Vol. 64 ■ No. 8 ■ August 2023

JNM

The Journal of Nuclear Medicine

**FEATURED ARTICLE**

Molecular Imaging of Myocardial Fibroblast Activation in Patients with Advanced Aortic Stenosis Before Transcatheter Aortic Valve Replacement: A Pilot Study. Johanna Diekmann et al. See page 1279.

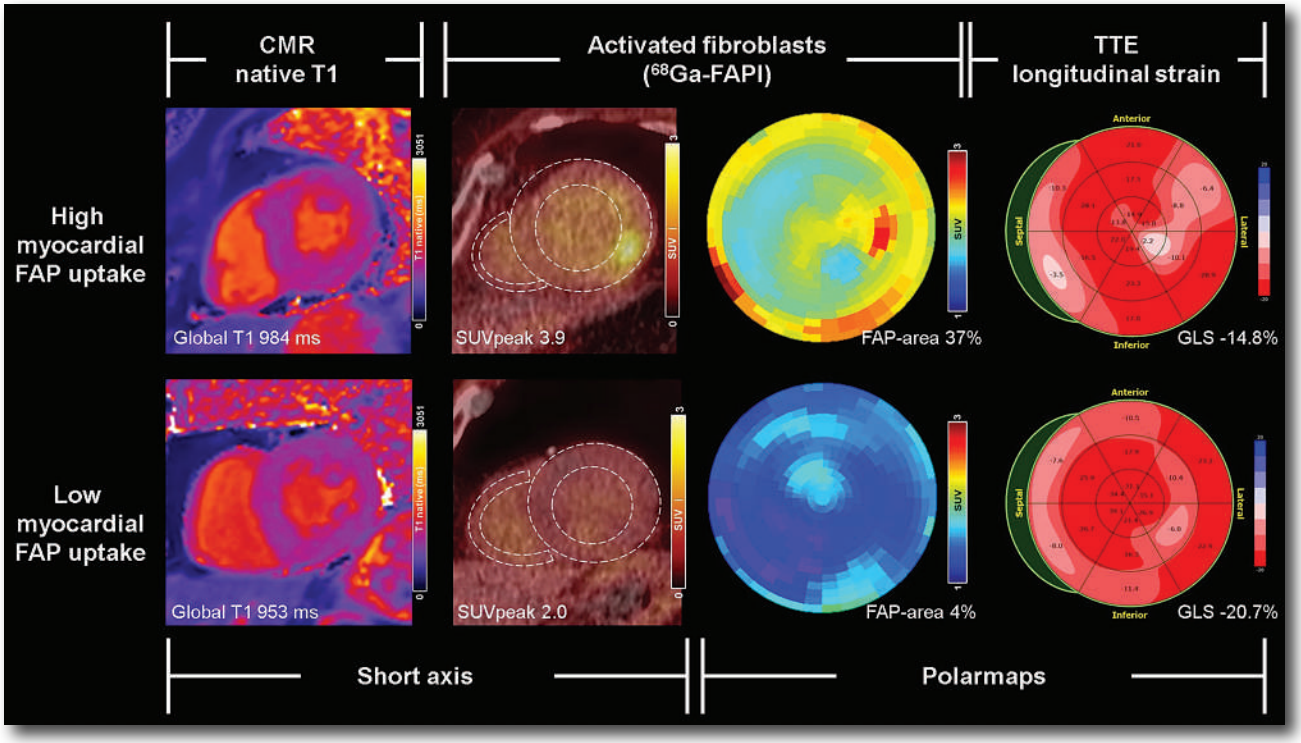


**Metformin and HER PET:** Preclinical implications for antibody targeting in novel cancer treatment and molecular imaging. Sandeep Panikar et al. See page 1195.

SNMMI SOCIETY OF NUCLEAR MEDICINE & MOLECULAR IMAGING


# Explore IAC Accreditation

IAC offers a **unique approach to accreditation** and is leading the field with **innovative, customized solutions** for your facility.

IAC is a nonprofit, nationally recognized accrediting organization, founded by medical professionals to advance appropriate utilization, standardization and quality of diagnostic imaging, interventional and therapeutic procedures.

- **Customer Service:** Facilities are busy caring for their patients and accreditation should not interfere with that. IAC clinical staff are available to guide applicant facilities through the accreditation process via phone, live chat or e-mail quickly and efficiently.
- **Quality & Safety Focused:** Offering a meaningful clinical peer review of case studies (with pathology) to evaluate diagnostic quality, report accuracy and report completeness, IAC is a partner in quality. IAC provides quality improvement-focused solutions such as the IAC QI Self-Assessment Tool, to help facilities optimize processes and improve patient safety and outcomes.
- **Continuous Improvement:** Accreditation must be thorough to truly affect the quality of care provided; however, IAC continues to explore ways to enhance the application process to make it simpler, more efficient and cost-effective to applicants including a base application fee reduction for facilities applying in 2023 and discounts on multiple site applications.

**Join the more than 14,000 IAC-accredited facilities who consistently express the highest levels of satisfaction with IAC's customer service and resources. IAC offers accreditation for:**

**Vascular Testing**
**Echocardiography**
**Nuclear/PET**
**MRI · CT / Dental CT**
**Carotid Stenting**
**Cardiac Electrophysiology**
**Cardiovascular Catheterization**
**Vascular Interventional**

IAC

*Improving health care through accreditation®*

**intersocietal.org** | 800.838.2110

**IAC Offering 20% Reduction on Base Application Fees for 2023**

To learn more or access our Online Fee Estimator, scan the QR code to the left or visit our website at ***intersocietal.org/iac/2023fees***.

JNM
Volume 64 • Number 8 • August 2023

JNM The Journal of NUCLEAR MEDICINE

The Official Publication of **SNMMI**



**MISSION STATEMENT:** *The Journal of Nuclear Medicine* advances the knowledge and practice of molecular imaging and therapy and nuclear medicine to improve patient care through publication of original basic science and clinical research.

*JNM* (ISSN 0161-5505 [print]; ISSN 2159-662X [online]) is published monthly by SNMMI, 1850 Samuel Morse Drive, Reston, VA 20190-5316. Periodicals postage is paid at Herndon, VA, and additional mailing offices. Postmaster, send address changes to *The Journal of Nuclear Medicine,* 1850 Samuel Morse Drive, Reston, VA 20190-5316. The costs of publication of all nonsolicited articles in *JNM* were defrayed in part by the payment of page charges. Therefore, and solely to indicate this fact, these articles are hereby designated "advertisements" in accordance with 18 USC section 1734.

**DISCLOSURE OF COMMERCIAL INTEREST:** Johannes Czernin, MD, editor-in-chief of *The Journal of Nuclear Medicine,* has indicated that he is a founder of Sofie Biosciences and holds equity in the company and in intellectual property invented by him, patented by the University of California, and licensed to Sofie Biosciences. He is also a founder and board member of Trethera Therapeutics and holds equity in the company and in intellectual property invented by him, patented by the University of California, and licensed to Triangle. He also serves on the medical advisory board of Actinium Pharmaceuticals and on the scientific advisory boards of POINT Biopharma, RayzeBio, and Jubilant Pharma and is a consultant for Amgen. No other potential conflicts of interest were reported. Manuscripts submitted to *JNM* with potential conflicts are handled by a guest editor.

**EDITORIAL COMMUNICATIONS** should be sent to: Editor-in-Chief, Johannes Czernin, MD, *JNM* Office, SNMMI, 1850 Samuel Morse Drive, Reston, VA 20190-5316. Phone: (703) 326-1185; Fax: (703) 708-9018. To submit a manuscript, go to https://submit-jnm.snmjournals.org.

**BUSINESS COMMUNICATIONS** concerning permission requests should be sent to the publisher, SNMMI, 1850 Samuel Morse Drive, Reston, VA 20190-5316; (703) 708-9000; home page address: jnm.snmjournals.org. Subscription requests and address changes should be sent to Membership Department, SNMMI at the address above. Notify the Society of change of address and telephone number at least 30 days before date of issue by sending both the old and new addresses. Claims for copies lost in the mail are allowed within 90 days of the date of issue. Claims are not allowed for issues lost as a result of insufficient notice of change of address. For information on advertising, contact Team SNMMI (Kevin Dunn, Rich Devanna, and Charlie Meitner; (201) 767-4170; fax: (201) 767-8065; TeamSNMMI@cunnasso.com). Advertisements are subject to editorial approval and are restricted to products or services pertinent to nuclear medicine. Closing date is the first of the month preceding the date of issue.

**INDIVIDUAL SUBSCRIPTION RATES** for the 2023 calendar year are $633 within the United States and Canada; $680 elsewhere. Make checks payable to the SNMMI. CPC IPM Sales Agreement No. 1415158. Sales of individual back copies from 1999 through the current issue are available for $60 at http://www.snmmi.org/subscribe (subscriptions@snmmi.org; fax: (703) 667-5134). Individual articles are available for sale online at http://jnm.snmjournals.org.

**Discussions with leaders:** Jadvar talks with Carolyn C. Meltzer, MD, Dean of the University of Southern California Keck School of Medicine, about her career in academic radiology and institutional leadership. . . . . ***Page 1167***

**PET Braak staging in AD:** Macedo and colleagues summarize current efforts to implement Braak staging of Alzheimer disease using PET and assess correspondence between Braak histopathologic descriptions and PET AD biomarkers. . . . . ***Page 1171***

**Tracking environmental pollutants:** Delaney and colleagues focus on the potential roles of molecular imaging and radiochemistry in characterizing the pharmacokinetic profiles of pollutants at environmentally relevant doses. . . . ***Page 1179***

**SSTR PET in meningioma**: Milosevic and colleagues report on institutional experience with somatostatin receptor–targeted [$^{68}$Ga]-DOTATOC PET/MRI in suspected or diagnosed meningiomas and compare results with those from conventional MRI. . . . . ***Page 1185***

**$SUV_{max}$ and CUP:** Zaun and colleagues identify an $SUV_{max}$ threshold on $^{18}$F-FDG PET/CT imaging as a favorable prognostic factor at initial diagnostic workup in patients with cancer of unknown primary. . . . . ***Page 1191***

**Metformin and membrane HER:** Panikar and colleagues use human epidermal growth factor receptor–targeted PET to study antibody–tumor binding in mice treated with metformin, with implications for both cancer imaging and therapy. . . . . ***Page 1195***

**Host–guest chemistry and pretargeted PET:** Jallinoja and colleagues describe a cucurbituril host and adamantane guest molecule pairing for antibody-based pretargeted PET in both in vitro and preclinical studies. . . . . ***Page 1203***

**$^{68}$Ga-FAPI-RGD PET:** Zhao and colleagues evaluate the clinical cancer imaging characteristics of a $^{68}$Ga-labeled heterodimer recognizing both fibroblast-activation protein and integrin $\alpha_v\beta_3$. . . . . ***Page 1210***

**Oncologic FAPI PET/CT:** Wass and colleagues provide a systematic review and metaanalysis to assess the diagnostic performance of fibroblast-activation protein inhibitor PET/CT in comparison with [$^{18}$F]FDG PET/CT. . . . . ***Page 1218***

**[$^{18}$F]FAPI-74 oncologic PET:** Watabe and colleagues detail the diagnostic performance of [$^{18}$F]-labeled fibroblast-activation protein inhibitor-74 PET in patients with various histopathologically confirmed cancers or suspected malignancies. . . . . ***Page 1225***

**[$^{68}$Ga]FAPI-46 PET in pancreatic tumors:** Rasinski and colleagues assess the diagnostic accuracy of [$^{68}$Ga]-fibroblast activation protein inhibitor-46 PET/CT in pancreatic cancer and look at data needed to verify that this technique improves characterization of equivocal lesions. . . . . ***Page 1232***

**PSMA PET/CT in unfavorable PCa:** Hagens and colleagues determine the diagnostic value of PSMA PET/CT in staging men with newly diagnosed and unfavorable intermediate-risk prostate cancer. . . . . ***Page 1238***

**[$^{177}$Lu]-PSMA RLT in elderly patients:** Tauber and colleagues analyze the efficacy and safety of PSMA radioligand therapy in octogenarian patients with metastatic castration-resistant prostate cancer, including data on response and toxicity rates and on predictors of survival. . . . ***Page 1244***

**TheraP PSMA PET eligibility criteria:** Karimzadeh and colleagues evaluate outcomes for patients with metastatic castration-resistant prostate cancer treated with PSMA radioligand therapy, focusing on comparisons with TheraP and TheraP-based PET inclusion criteria. . . . . ***Page 1252***

**Reader agreement VISION substudy:** Kuo and colleagues research interreader variability and intrareader reproducibility of visual assessments of $^{68}$Ga-PSMA-11 PET/CT scans using the VISION trial read criteria, looking at agreement with VISION study results. . . . . ***Page 1259***

**$^{177}$Lu-PSMA RLT in treatment-naïve mCRPC:** Satapathy and colleagues explore the impact of prior taxane chemotherapy on response and survival outcomes after [$^{177}$Lu]Lu-PSMA radioligand therapy in patients with metastatic castration-resistant prostate cancer. . . . . ***Page 1266***

**BMI and overall survival in PSMA RLT:** Hartrampf and colleagues investigate fat-related and body composition parameters in patients undergoing PSMA-directed radioligand therapy to assess associated predictive values for overall survival. . . . . ***Page 1272***

**Fibroblast activation in TAVR candidates:** Diekmann and colleagues use multimodal imaging, including $^{68}$Ga-fibroblast activation protein inhibitor-46 PET, to determine the extent and functional correlates of myocardial fibroblast activation in patients with aortic stenosis scheduled for transcatheter aortic valve replacement. . . . . ***Page 1279***

**PET/CT in hyperglycemia and infection:** Pijl and colleagues describe the effects of blood glucose levels on the performance of $^{18}$F-FDG PET/CT for detecting infection foci in patients with bacteremia. . . . . ***Page 1287***

**Comparative evaluation of MIRDcalc:** Carter and colleagues report on validation of this internal dosimetry software and provide a compendium of radiopharmaceutical dose coefficients obtained with MIRDcalc. . . . . ***Page 1295***

**Facial anonymization and total-body PET:** Selfridge and colleagues detail development of a workflow that obscures a subject's face in 3-dimensional volumetric data, with validation in total-body PET/CT imaging. . . . . ***Page 1304***

**PET and opioid release after orgasm:** Jern and colleagues use [$^{11}$C]carfentanil PET and PET/MRI to test the hypothesis that sexual arousal peaking in orgasm leads to endogenous opioid release in men. . . . . ***Page 1310***

**[$^{18}$F]FASu and [$^{18}$F]FSPG:** Colovic and colleagues report on a comparison of these amino acid radiopharmaceuticals targeting system $x_C^-$, a PET biomarker for oxidative stress, including uptake specificity and ability to image glioma and lung cancer xenografts in vivo. . . . . ***Page 1314***

**$^{161}$Tb-PSMA SPECT/CT:** Al-Ibraheem and colleagues present whole-body scintigraphic and SPECT/CT images acquired with this promising agent in a case of metastatic prostate cancer refractory to hormonal therapy and chemotherapy referred for PSMA radioligand treatment. . . . . ***Page 1322***

# A Life Study in Academic Leadership

## A Conversation Between Carolyn C. Meltzer and Hossein Jadvar

Carolyn C. Meltzer and Hossein Jadvar

*Department of Radiology, Keck School of Medicine, University of Southern California, Los Angeles, California*

Hossein Jadvar, MD, PhD, MPH, MBA, a tenured professor in the Department of Radiology at the Keck School of Medicine of the University of Southern California (USC) in Los Angeles, talked with Carolyn C. Meltzer, MD, about her career in science and academic leadership. Dr. Meltzer became the Dean of the USC Keck School of Medicine and the John and May Hooval Dean's Chair in Medicine on March 1, 2022. In this position, she oversees the operation and academic affairs of 26 basic and clinical academic departments and 16 major research institutes that sponsor training of more than 1,200 medical students, resident physicians, and graduate students in more than 70 specialty or subspecialty programs each year. She was recruited from Emory University School of Medicine (Atlanta, GA), where she served as the William P. Timmie Professor and Chair of Radiology and Imaging Sciences for 15 years. At Emory she also served as the Executive Associate Dean of Faculty Academic Advancement, Leadership, and Inclusion and as the Chief Diversity and Inclusion Officer. Dr. Meltzer has conducted research in multimodality imaging evaluation of neuropsychiatric disorders, Alzheimer disease, brain structure and function in normal aging, and cancer.

***Dr. Jadvar:*** *Could tell me about your career journey? What made you interested in a life of medicine and science, and what propelled you toward leadership in academic radiology?*

**Dr. Meltzer:** I was always interested in science and math and was also a very visual person. Even early on, I played competitive chess, seeing the moves on the chessboard and always thinking about how to solve problems. As a teenager, I would often read about the brain. I was fascinated by behavior, mood, and the workings of the brain—and how little we knew. At college, I decided that I was interested in medical school. I couldn't decide whether I wanted to be a neuroscientist or a physician. I spent a summer doing student research in Chicago, helping in a translational lab at Michael Reese Hospital (which closed in 2009). There, a distant relative invited me to her home for dinner. She and her husband were lovely people. It turned out that he was Robert N. Beck, who developed one of the first PET scanners at the University of Chicago. I had been reading about PET imaging and spent much of the evening asking about his work. He showed me scans that helped in understanding the inner workings of the brain. This was in the early days of functional imaging, and this moment was very influential in my life. When I went on to study at the Johns Hopkins Medical School, I volunteered as a control subject for a PET imaging study to make some money. This was one of the earliest such studies using a neuroreceptor tracer. I ended up working for these scientists and then spending another year on a PET research fellowship. These experiences fueled my excitement about brain imaging, particularly nuclear medicine and neuroradiology, which led me eventually to board certifications in both fields.

Carolyn C. Meltzer, MD

***Dr. Jadvar:*** *Did you know Henry N. Wagner, Jr., MD, and the group in nuclear medicine at Hopkins?*

**Dr. Meltzer:** Absolutely. Henry Wagner was leading nuclear medicine when I was a medical student and resident physician, and I worked with him. Just an extraordinary person.

***Dr. Jadvar:*** *Please tell me what propelled you to leadership in academic radiology, becoming a department chair and now our dean at USC?*

**Dr. Meltzer:** Serendipity, as for many of us. In my first post-training attending role at the University of Pittsburgh, I was thrust into an interim leadership role after a senior faculty member suddenly departed the institution. I was only 2 years into being an assistant professor and really was just flying by the seat of my pants. I didn't know much about leadership and management as a field or as a science, something that could be studied. I don't think many people did at that time, outside of the business world. In medicine, if you were good at your research or clinical care, then often it happened that you were asked to run something. I was working in the PET center and ended up being its medical director. I really enjoyed bringing people together, trying to have an impact, listening to lots of viewpoints, and having some say in how things are done to achieve the best possible outcomes for patients, staff, and students. I later had the opportunity to become a fellow of the Executive Leadership in Academic Medicine program (Drexel University School of Medicine; Philadelphia, PA), where I really learned leadership skills that reinforced what I had figured out the hard way and taught me to evaluate what worked and didn't. I became a lifelong student of leadership. I take it as an incredible opportunity and responsibility and have found that my approach is most aligned with the servant leadership model. I've been fortunate that people have wanted me to work with them. I am truly honored to be here at USC as the dean.

***Dr. Jadvar:*** *Let's talk about mentors. As you know, good mentors have a major impact on one's career. I can personally attest to that because I had many good mentors who influenced me. Who were your mentors that you want to acknowledge in your personal and professional life?*

**Dr. Meltzer:** There are so many. J. James Frost, MD, PhD, MBA, was one of my mentors in PET. My first mentor in the PET world was Dean Wong, MD, PhD. Dean took me on as a student and was

Published online Jul. 13, 2023.

DOI: 10.2967/jnumed.123.266097

really my first influential mentor in science and medicine. R. Nick Bryan, MD, PhD, who was at the time the chief of neuroradiology at Johns Hopkins, has been like a second father to me through my whole career. I consider him one of the most influential people in supporting my career and my personal life. I adore him and his wife, Jean, and we keep in touch. I can call him anytime and know that he'll always give me his honest opinion. Charles F. (Chip) Reynolds, MD, is another mentor who was in psychiatry at Pittsburgh when I did neuropsychiatry research. Also, Steven T. DeKosky, MD, who was chair of neurology and led the Alzheimer Disease Research Center at the University of Pittsburgh.

***Dr. Jadvar:*** *Tell me about your parents. Was anybody in medicine or in math? How did you become interested in math?*

**Dr. Meltzer:** My mom was a secretary and had a high school education. My dad was an immigrant from Greece. He wanted to be a physician but moved to the United States with no resources and ended up going to optometry school and becoming an optometrist. I was the kid who, like him, loved math, science, and taking things apart and putting them back together. He always wanted me to go into medicine and encouraged a belief that I could do whatever I wanted. He passed away about 5 years ago—an incredibly generous and supportive father.

***Dr. Jadvar:*** *Any siblings?*

**Dr. Meltzer:** I have an older sister, who also became an optometrist.

***Dr. Jadvar:*** *I want to focus a bit on your life as a clinician/scientist. You have received several prestigious awards for your research, including the Gold Medal and Distinguished Investigator Award from the Academy for Radiology & Biomedical Imaging Research and the Outstanding Researcher Award from the Radiological Society of North America. Can you tell me a little bit more about your research in brain imaging? What were your findings?*

**Dr. Meltzer:** I've had a couple of paths in my scholarly work, and one was in technology development. When I was engaged with PET imaging at Johns Hopkins and had done a year of research fellowship and worked throughout my residency in radiology and fellowship in neuroradiology and nuclear medicine, I kept up with research in Jim Frost's lab. One of the technologic barriers to making quantitative assessments in PET imaging was the challenge of partial-volume averaging of the signal. I was interested in normal aging and Alzheimer disease. Comparing quantitation of receptors or any other measurements in a brain that had significant atrophy with those from a more age-appropriate brain was very difficult, because of partial-volume averaging of cerebrospinal fluid and brain tissue due to the low spatial resolution of early PET images. I became very interested in how to do those corrections and published my work developing a new method (*J Comput Assist Tomogr*. 1990;14:561–570). This initially received little attention, although eventually it became something of a landmark paper in the field. I also worked on coregistration of MRI and CT with PET. My early work focused on technology development, including evaluation of the first human combined PET/CT scanner at the University of Pittsburgh. I also worked to acquire an early prototype human PET/MRI scanner at Emory for validation. The scientific questions for me were always around brain aging, sex differences in aging, and susceptibility to neuropsychiatric diseases and disorders such as late-life depression and eating disorders. A key project was evaluating serotonin receptor density in depression and implications for therapeutic effectiveness.

***Dr. Jadvar:*** *I gather that at Pittsburgh you came into contact with David Townsend, PhD, in PET/CT and the work of Chester Mathis, PhD, and William Klunk, MD, PhD, in developing $^{11}$C-Pittsburgh compound B amyloid scanning.*

**Dr. Meltzer:** Absolutely. David Townsend was the codeveloper of the first PET/CT scanner. He asked me to lead that first clinical evaluation of the first PET/CT scanner, opening a huge door for me. Same with Chet Mathis, who had codeveloped the $^{11}$C-Pittsburgh compound B tracer.

***Dr. Jadvar:*** *You are a neuroradiologist and a nuclear medicine physician. As you know, there have been incredible strides in molecular imaging and radiopharmaceutical therapy, especially with the recent approvals of new theranostic agents for precision imaging and treatment of patients with cancer. The Lancet Oncology Commission report on the Cancer Moonshot initiative (by former President Barack Obama and led by then–Vice President Joe Biden) identified and discussed nuclear medicine imaging and theranostics as priorities in fighting cancer. What are your thoughts on the future of translational theranostics, and how can we support this important priority that was also identified by the Cancer Moonshot Blue Ribbon panel?*

**Dr. Meltzer:** Theranostics is an incredible tool for being able to target specific molecular markers, not only for diagnosis but also for treatment. Under the bigger umbrella of synthetic biology, precision health, and cell-based therapies for cancer, such as CAR T cells and beyond, we're entering an age of precision in being able to diagnose and treat disease, particularly cancer. We know that individual molecular markers and rapid mutations can really affect how a cancer behaves. Being able to look at the molecular profile of individual tumors, the patient's genetic biologic makeup, and many other relevant parameters, coupled with increasing computing power, creates the opportunity to turn big data into actionable knowledge about how we can be more precise in treating patients.

> "… our most creative ideas come from … having people with different perspectives, different educational backgrounds, different life experiences, and from different fields working together. All the easy things that an individual contributor could do alone have been done."

***Dr. Jadvar:*** *Exactly. I want to switch gears now toward your distinguished service record in academic radiology. You have received notable awards, including those from the American Medical Association, Association of University Radiologists, American Society of Neuroradiology, and American Association of Women in Radiology, from the last of which you received the Marie Curie Award. I want to focus especially on this award, which is given to an individual with outstanding contributions to the advancement of women in radiology and radiation oncology. What are your thoughts on receiving this award? Where do you think we are now in academic medicine with regard to sex equity, and what are the remaining barriers in empowering women, especially in leadership positions? How many women are deans of medical schools in the United States?*

**Dr. Meltzer:** About 20% of department chairs are women, a percentage that varies a little by discipline but remains low, even in fields where most of the physician workforce may be women,

such as pediatrics and obstetrics/gynecology. The percentage of medical school deans who are women is slowly moving up and is now at about 25%. But this is not where we need it to be. It was initially thought that these percentages would catch up to parity as a result of a more robust pipeline of women coming into the field. But with medical schools at 40%–50% women now for 20 years or more, we're still not seeing the proportional dramatic increases that we should see with more sex parity in tenured and leadership positions. This is something I've been passionate about my whole career. When I went to medical school I was very much in the minority, and I've been the first woman in many of the leadership positions to which I've been fortunate to be appointed. That shouldn't keep happening. I was very much honored by the American Association of Women in Radiology when I received the Marie Curie Award. There are so many other deserving individuals who are trying to make sure people from groups historically underrepresented in medicine and science benefit from having our voices at the table. That has been a thread through my whole career: a strong focus on equity and on creating inclusive environments where we can come together and have better ideas. The American Medical Association award was specifically for the work I did on unconscious bias training and mitigation for physicians in the health-care environment. This is important work that still very much needs to be done. We've come a long way but not as far as we should have. The current challenges to women's reproductive health further indicate that there's still a lot of sex bias in every walk of life.

***Dr. Jadvar:*** *Am I correct that one of the things you did at Emory was look at compensation for women faculty, where you made changes?*

**Dr. Meltzer:** When I first became a department chair, I asked to see the compensation plan, because I couldn't really figure out why some faculty were paid X and others Y—salaries seemed highly variable. When I analyzed the data on assistant professors (the largest group and, one would think, the most uniform), there was a nearly statistically significant difference between men and women assistant professor salaries. I had to be transparent about it. I let the department faculty know we had a problem and that we were going to go to a compensation plan that was equitable and metrics-driven. In the absence of intentionality around equity, these patterns form as a result of our inherent and systemic biases.

***Dr. Jadvar:*** *Speaking about equity, you've been the chair of the Radiological Society of North America Committee on Diversity and Inclusion and also Chief Diversity and Inclusion Officer at Emory. Can you tell us about some of your activities in diversity, equity, and inclusion and why attention to this is important?*

**Dr. Meltzer:** It is now well known that our most creative ideas come from (the literature is quite clear in this) having people with different perspectives, different educational backgrounds, different life experiences, and from different fields working together. All the easy things that an individual contributor could do alone have been done. We now strive to tackle the most complex problems in human disease, which require a diverse and inclusive team approach. An environment that makes us all feel like we belong and can freely express ourselves is particularly critical. In my own leadership roles, I've always worked to flatten organizational hierarchy to make sure that we bring voices—all voices—to the table and that we check ourselves and hold each other accountable. We must also embrace grace and cultural humility, because although bias is a part of our human experience, we can learn from each other. That's been integral to my leadership throughout my career. It also requires intentionally striving to be reflective of the communities we serve, at both junior and senior levels. I'm in a new community now for the last year that looks different from the community I was in in Georgia. I am thankful that many leaders here feel strongly that we need to keep working to make sure that those we train and those we put in leadership positions reflect the rich diversity of the communities we serve and in whom we want to build trust.

***Dr. Jadvar:*** *You've been the dean of a major medical school within a large private research university for slightly more than 1 year. Can you describe the similarities, differences, and challenges you have encountered as a dean compared with your long experience as a chair of a major academic radiology department?*

**Dr. Meltzer:** If I had come directly from being a chair, I would have encountered more things that were new. In the 15 years that I was at Emory, I always had at least one other leadership role. These were mostly in the dean's office, including as Associate Dean for Research for 12 years. During the last 3 years I was there, in addition to being the chair of radiology, I served as Executive Associate Dean for Faculty and Chief Diversity and Inclusion Officer. I believe that these experiences of working not only in a scholarly domain but also in the clinical practice arena (and, of course, in radiology we interact with everybody) made it easier for me to work in the dean's office, bringing people together around research, faculty matters, professional advancement, leadership development, diversity, equity, and inclusion. That combination of experiences has prepared me well to step into the role of dean. There are new challenges every day, but at this point in my career I don't get easily flustered. I've seen a lot of challenges and try to take an inclusive approach in dealing with them, involving my executive team and stakeholders from all aspects of the institution and beyond, depending on the issue.

***Dr. Jadvar:*** *What advice do you have for young doctors considering a fulfilling career in academic medicine in general and in nuclear medicine in particular, especially our young women doctors?*

**Dr. Meltzer:** It's funny that you ask that today, because it's Match Day. I just had the opportunity this morning to offer advice to our senior medical students about their journey ahead. I talked about the importance of lifelong learning. We've prepared them well for the next step, but information and knowledge in medicine and science are now increasing exponentially. I suggested that they embrace an ever-curious mindset. When doors open, they should step through with courage and creativity. One is never sure where something's going to lead, so we need to explore and innovate. No career path is straight. I hope today's students will challenge the way we've done things and bring their own passions to the table. In radiology and nuclear medicine, where technology is constantly evolving, we have to continue innovating. That's certainly one of the aspects of imaging science that attracted me. I think it's very exciting for those who are particularly curious, creative, and want to just keep learning and growing.

***Dr. Jadvar:*** *I want to ask about your love of photography. I didn't know previously about your remarkable talent. As a serious amateur photographer myself, I can say that your work is truly exceptional. I believe that if you had not achieved an illustrious career in medicine and science, you would have had an eminent professional career in photography. How did you become interested in photography, and do you still have time to pursue this interest? Please tell me and our* JNM *readers about your story of creative imaging through photography.*

**Dr. Meltzer:** Very kind of you. It goes back to my dad. He and I would always build things, take things apart, and look at the

world together. I took after him in terms of being very visually oriented and excited about technology and science. He loved cameras, taking them apart, putting them back together, and trying different ones. He wasn't a very good photographer, but he would say, "Well, I don't think that I like this camera anymore. You take it." So, I would go off and try it. Although I loved the technology, I especially loved looking through the lens. When I ended up in imaging, I already had this creative side where I loved looking at the world from different perspectives. Early on, I kept those 2 worlds very separate; nobody I worked with knew that I had this love of photography. Later in life I felt comfortable openly sharing this other side of me, and artistic photography remains very much part of my life. It doesn't detract from my focus as a physician, scientist, and leader. In fact, I think the more I photograph the more I'm able to feel centered and bring my best self to my work. So, yes, I do continue to photograph. I do it in spurts when I travel. Or when there's a crazy storm in the sky I'll run out. But I do love it. It really is a natural proclivity for imaging scientists such as yourself who understand the magic of imaging in every aspect.

***Dr. Jadvar:*** *And you have a website?*

**Dr. Meltzer:** It's at carolynmeltzer.com.

***Dr. Jadvar:*** *I want to thank you again so much for taking time to speak with me and our* JNM *readers. Fight on and heal on!*

# The Use of Tau PET to Stage Alzheimer Disease According to the Braak Staging Framework

Arthur C. Macedo[1], Cécile Tissot[1], Joseph Therriault[1], Stijn Servaes[1], Yi-Ting Wang[1], Jaime Fernandez-Arias[1], Nesrine Rahmouni[1], Firoza Z. Lussier[2], Marie Vermeiren[1], Gleb Bezgin[1], Paolo Vitali[1], Kok Pin Ng[3], Eduardo R. Zimmer[4], Marie-Christine Guiot[5], Tharick A. Pascoal[2], Serge Gauthier[1], and Pedro Rosa-Neto[1]

*[1]Department of Neurology and Neurosurgery, McGill University, Montréal, Québec, Canada; [2]Department of Psychiatry and Neurology, University of Pittsburgh, Pittsburgh, Pennsylvania; [3]Department of Neurology, National Neuroscience Institute, Singapore, Singapore; [4]Department of Pharmacology, Universidade Federal do Rio Grande do Sul, Porto Alegre, Brazil; and [5]Department of Pathology, McGill Hospital Center, Montréal, Québec, Canada*

Amyloid-β plaques and neurofibrillary tangles (NFTs) are the 2 histopathologic hallmarks of Alzheimer disease (AD). On the basis of the pattern of NFT distribution in the brain, Braak and Braak proposed a histopathologic staging system for AD. Braak staging provides a compelling framework for staging and monitoring of NFT progression in vivo using PET imaging. Because AD staging remains based on clinical features, there is an unmet need to translate neuropathologic staging to a biologic clinical staging system. Such a biomarker staging system might play a role in staging preclinical AD or in improving recruitment strategies for clinical trials. Here, we review the literature regarding AD staging with the Braak framework using tau PET imaging, here called PET-based Braak staging. Our aim is to summarize the efforts of implementing Braak staging using PET and assess correspondence with the Braak histopathologic descriptions and with AD biomarkers. **Methods:** We conducted a systematic literature search in May 2022 on PubMed and Scopus combining the terms "Alzheimer" AND "Braak" AND ("positron emission tomography" OR "PET"). **Results:** The database search returned 262 results, and after assessment for eligibility, 21 studies were selected. Overall, most studies indicate that PET-based Braak staging may be an efficient method to stage AD since it presents an adequate ability to discriminate between phases of the AD continuum and correlates with clinical, fluid, and imaging biomarkers of AD. However, the translation of the original Braak descriptions to tau PET was done taking into account the limitations of this imaging technique. This led to important interstudy variability in the anatomic definitions of Braak stage regions of interest. **Conclusion:** Refinements in this staging system are necessary to incorporate atypical variants and Braak-nonconformant cases. Further studies are needed to understand the possible applications of PET-based Braak staging to clinical practice and research. Furthermore, there is a need for standardization in the topographic definitions of Braak stage regions of interest to guarantee reproducibility and methodologic homogeneity across studies.

**Key Words:** Alzheimer disease; Braak staging; PET; neurofibrillary tangles; cognitive impairment

**J Nucl Med 2023; 64:1171–1178**
DOI: 10.2967/jnumed.122.265200

Alzheimer disease (AD) is a progressive neurodegenerative disease whose neuropathologic hallmarks are amyloid-β (Aβ) plaques and neurofibrillary changes (*1*). Three types of neurofibrillary changes underlie AD pathogenesis: neuritic plaques, neurofibrillary tangles (NFTs), and neuropil threads. NFT and neuropil thread accumulation in the cerebral cortex present a well-defined distribution and progression pattern, allowing the differentiation of AD into stages (*2–5*). On this basis, Braak and Braak proposed a neuropathologic staging system comprising 6 successive stages (*6*). In 2006, this framework was revised, incorporating modern immunohistochemical techniques to improve its applicability and accuracy (*7*).

Braak stages are hierarchic, meaning that a given stage encompasses the abnormalities observed in the earlier ones (*6,7*). Stages I and II are marked by the involvement of the transentorhinal and entorhinal cortices, respectively (*7*). At stage III, modest damage is seen in the hippocampus, amygdala, and adjacent neocortical areas (*7*). Stage IV defines the initial extension of the pathologic process to neocortical association areas, encompassing the insular cortex and basal frontal areas (*7*). Stage V shows an impairment of neocortical association areas, especially in temporal, parietal, and associative occipital regions (*7*). In stage VI, degeneration spreads to primary motor and sensory fields. For practical purposes, these stages may be simplified into 3 categories: transentorhinal (I–II), limbic (III–IV), and isocortical (V–VI) (*8*). In 2012, this staging system was integrated into the AD neuropathologic diagnostic criteria (*9,10*). Figure 1 displays the topography of Braak stages according to the original histopathologic descriptions.

Because AD staging remains based on clinical features, there is an unmet need to translate neuropathologic staging to a biologic clinical staging system. Such a biomarker staging system might play a role in diagnosing preclinical AD and in improving recruitment strategies for clinical trials. The development of tau PET ligands created a way to map tau accumulation in the brain of living humans over time and stratify individuals on the AD continuum on the basis of in vivo Braak staging (*11*). By contrast, pathology remains limited in detecting longitudinal changes in tau accumulation, in establishing correlations to other biomarkers, and in its applicability in clinical practice and research. Compared with

Received Nov. 18, 2022; revision accepted Apr. 25, 2023.
For correspondence or reprints, contact Pedro Rosa-Neto (pedro.rosa@mcgill.ca).
Published online Jun. 15, 2023.

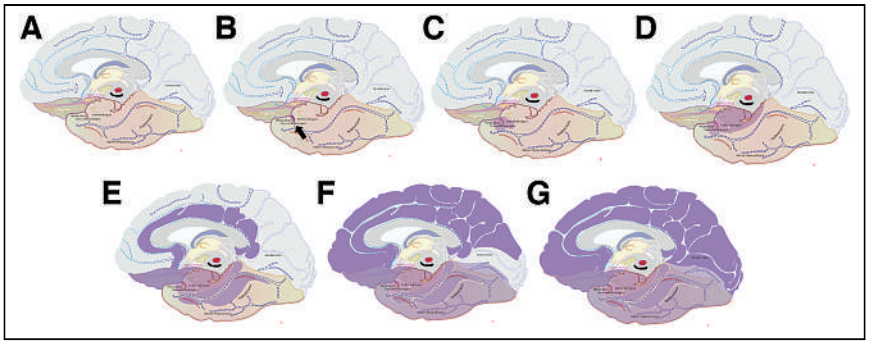


**FIGURE 1.** Topographic representation of Braak stages 0 (absence of tau accumulation) (A), I (B), II (C), III (D), IV (E), V (F), and VI (G) according to original histopathologic descriptions, displaying sagittal section of brain in midline. Affected brain regions are colored in different shades of purple.

histopathologic Braak assessment, which is conducted in a limited number of regions, PET provides an overview of tau pathology across the entire brain. PET limitations, in turn, include poorer resolution and sensitivity than neuropathology, as well as contamination of the early stages of NFT accumulation with off-target binding, especially in first-generation tau PET agents (*12*). Together, these limitations impose significant variability to parallel the in vivo classification system with the Braak histopathological scheme.

The recently developed second-generation tau PET ligands ($^{18}$F-MK6240, $^{18}$F-PI2620, and $^{18}$F-RO948) presenting higher sensitivity to tau and less off-target binding mitigated some of the limitations of first-generation agents ($^{18}$F-AV1451 and $^{18}$F-THK5351) and raised expectations about the implementation of Braaklike systems using in vivo techniques (*13–17*). Here, we review the literature regarding AD staging with the Braak histopathologic framework using tau PET imaging, hereafter called PET-based Braak staging. Our aim is to summarize the efforts to implement Braak staging using PET and assess their correspondence with the Braak histopathologic descriptions and with AD biomarkers.

## MATERIALS AND METHODS

A literature search was conducted on May 9, 2022, on PubMed and Scopus, using the following terms: "Alzheimer" AND "Braak" AND ("positron emission tomography" OR "PET"). No restrictions regarding language, year of publication, or type of report were applied. Two authors independently screened titles, abstracts, and full texts on the basis of the following inclusion criteria: cross-sectional, cohort, or case-control studies testing the applicability of PET-based Braak staging in the AD continuum. The exclusion criteria were unpublished manuscripts, animal or in vitro studies, reviews, clinical trials, case reports or series, conference papers, editorials, letters, responses, comments, book chapters, and guidelines.

The following data were extracted by 2 independent assessors: authors, year of publication, study design, population size and diagnoses, type of tau PET ligand used, statistical or practical approach to assessing PET-based Braak stages, main results, topographic definition of Braak stage regions of interest (ROIs), and meta-ROIs. Disagreements were resolved by consensus or by consulting a third investigator.

**NOTEWORTHY**

- Because AD staging remains based on clinical features, there is an unmet need to translate neuropathologic staging to a biologic clinical staging system.
- The development of tau PET ligands created a way to map tau accumulation in the brain of living humans over time and stratify individuals on the AD continuum based on in vivo Braak staging.
- Most studies indicate that tau PET performs well in staging AD when using Braak ROIs, even when compared with other biomarkers and clinical predictors.
- Refinements in the PET-based Braak staging system are necessary to incorporate atypical and Braak-nonconformant cases.
- The harmonization of Braak ROIs might represent a further step for ascertaining reproducibility.

## RESULTS

### Study Selection

The database search returned 132 and 130 results from PubMed and Scopus, respectively. After extraction of 117 duplicates, 145 records had their titles and abstracts screened for inclusion, leading to 31 reports selected for full-text evaluation. Ten reports were excluded for not assessing the use of PET-based Braak staging in the AD continuum, leaving 21 studies to be included in our review. Figure 2 displays the flowchart of study selection, and Table 1 shows the characteristics and main results of the studies included.

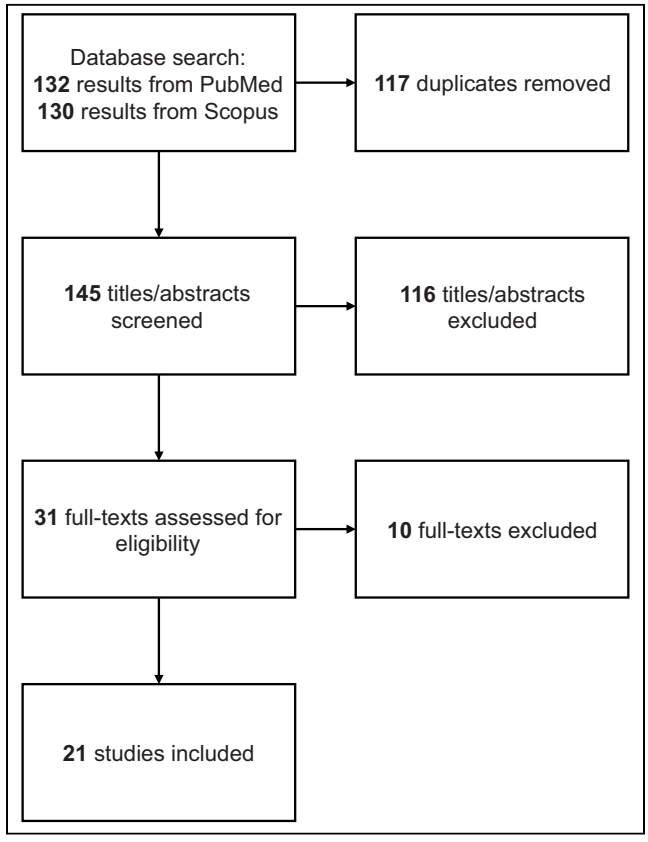


**FIGURE 2.** Flowchart of study selection.

**TABLE 1**
Characteristics and Main Results of Included studies

| Study | Design | Sample and clinical diagnoses | Tau PET ligand | Main results |
|---|---|---|---|---|
| Schöll (*11*) | Cohort | 15 AD (1 fvAD, 1 amnestic EOAD, 3 amnestic LOAD, 4 lvPPA, 6 PCA), 38 CU | $^{18}$F-AV1451 | Tracer retention corresponded well with Braak staging and was related to cognitive measures |
| Schwarz (*24*) | Cross-sectional | 44 AD*, 87 MCI, 56 CU | $^{18}$F-AV1451 | Binding strongly followed Braak scheme, but atypical patterns were also seen; Braak stages correlated with cognitive decline, diagnosis, and Aβ load |
| Lowe (*36*) | Cross-sectional | 5 AD, 3 MCI, 7 CU, 21 non-AD | $^{18}$F-AV1451 | Binding did not completely reflect early-stage tau progression suggested by Braak in atypical AD |
| Maass (*18*) | Cross-sectional | Sample 1: 48 AD†, 12 MCI, 86 CU/sample 2: 9 amnestic LOAD, 19 MCI, 42 CU | $^{18}$F-AV1451 | Braak-based staging, whole-brain, and regional tau measures had similar accuracies to distinguish MCI and AD from CU individuals |
| Marquié (*35*) | Cross-sectional | 22 NR | $^{18}$F-AV1451 | Autoradiographic $^{18}$F-AV1451 binding correlated with NFT accumulation and matched Braak stage progression |
| Lowe (*34*) | Cross-sectional | 51 AD†, 35 MCI, 601 CU | $^{18}$F-AV1451 | Distribution of tau PET signal in CU individuals was similar but not identical to Braak descriptions |
| Cho (*33*) | Cohort | 25 amnestic AD, 31 MCI, 52 CU | $^{18}$F-AV1451 | Tau accumulation supported Braak model and was associated with cognitive dysfunction |
| Timmers (*31*) | Cross-sectional | 52 AD†, 6 MCI, 42 CU | $^{18}$F-AV1451 | $^{18}$F-AV1451 in Braak I–II, III–IV, and V–VI was related to cortical atrophy in MCI/AD patients |
| Baek (*32*) | Cohort | 29 AD*, 39 MCI, 164 CU | $^{18}$F-AV1451 | Observed sequence of tau accumulation supported spreading model proposed by Braak and Braak |
| Betthauser (*19*) | Cohort | 167 CU | $^{18}$F-MK6240 | Binding mostly followed Braak stages and seemed to be disease-dependent |
| Franzmeier (*20*) | Cross-sectional | 11 amnestic AD, 85 MCI, 348 CU | $^{18}$F-AV1451 | Tau deposition in AD did not always follow Braak scheme, as may be explained by variability in tau epicenters |
| Leuzy (*29*) | Cross-sectional | 100 AD*, 154 MCI, 257 CU, 102 non-AD | $^{18}$F-RO948 | Braak ROI SUV ratio could discriminate AD from other neurodegenerative diseases, MCI, and controls |
| Pascoal (*17*) | Cross-sectional | 54 AD (30 EOAD, 21 LOAD, 3 NR), 67 MCI, 168 CU, 12 FTD | $^{18}$F-MK6240 | Ligand uptake recapitulated Braak stages, which were related to Aβ status, neurodegeneration, and cognitive impairment |
| Shokouhi (*21*) | Cross-sectional | 160 MCI, 301 CU | $^{18}$F-AV1451 | Tau-based network architecture mirrored Braak stage progression |
| Kim (*30*) | Cross-sectional | 26 AD*, 55 MCI, 32 CU | $^{18}$F-THK5351 | MRI brain volumetry and Braak ROI SUV ratio showed robust performance in discriminating AD spectrum |
| Kreisl (*22*) | Cross-sectional | 40 AD*, 22 MCI, 39 CU | $^{18}$F-MK6240 | Binding followed Braaklike progression and correlated with amyloid positivity, CSF biomarkers, cognition, and clinical diagnosis |
| Pascoal (*25*) | Cohort | 17 AD*, 21 MCI, 87 CU | $^{18}$F-MK6240 | Tau progression followed Braak stages and might be detected in vivo in individuals with and without symptoms of AD |
| Seemiller (*28*) | Cross-sectional | 39 AD*, 39 CU | $^{18}$F-AV1451 | Tau distribution was consistent with Braak staging model and supported network degeneration hypothesis |
| Nihashi (*23*) | Cross-sectional | 17 AD*, 9 MCI, 43 CU | $^{18}$F-THK5351 | Binding in Braak ROIs was higher in MCI and AD than in CU but did not differ significantly between MCI and AD |
| Rullmann (*27*) | Cross-sectional | 37 AD*, 26 CU | $^{18}$F-PI2620 | $^{18}$F-PI-2620 binding widely recapitulated Braak descriptions, and tau signal correlated with poorer cognition in all stages but VI |
| Therriault (*26*) | Cohort | 65 AD†, 80 MCI, 179 CU | $^{18}$F-MK6240 | PET-based Braak staging presented stage-specific correlations with Aβ PET abnormality, CSF and plasma phosphorylated tau biomarkers, and dementia severity |

*Study did not specify whether different AD variants were included.
†Study included different AD variants but did not provide number of participants with each variant.
fvAD = frontal variant AD; EOAD = early-onset AD; LOAD = late-onset AD; FTD = frontotemporal dementia; lvPPA = logopenic variant primary progressive aphasia; PCA = posterior cortical atrophy; NR = not reported.

### Variability in Definitions of PET-Based Braak Stages Across Studies

The ROIs used to define PET-based Braak stages showed some variability across studies (Supplemental Table 1; supplemental materials are available at http://jnm.snmjournals.org). Stage I was characterized as the entorhinal cortex in 7 studies (*11,18–23*) and as the transentorhinal cortex in 6 studies (*17,24–27*). All definitions for stage II included the hippocampus, with 3 also comprising the entorhinal cortex (*17,25,26*).

Ten of 16 studies identified stage III as a composite of amygdala, parahippocampal gyrus, fusiform gyrus, and lingual gyrus (*11,17,18,20–23,25,26,28*). The ROIs characterizing stage IV differed widely among studies, but the most cited ones were the inferior and middle temporal cortices, the insula, and the posterior cingulate. One study using $^{18}$F-AV1451 (*21*) included, in stage IV, the caudal and rostral anterior cingulate, a structure indicated to be in stage V by 4 studies using $^{18}$F-MK6240 (*17,22,25,26*).

The neocortical areas selected to define stage V varied considerably. Still, the definitions captured the notion that tau accumulation is extensive across the neocortex, with the exception of the primary motor and sensory areas. For stage VI, the topographic definition was relatively similar among studies, with the presence of the paracentral, postcentral, and precentral gyri highlighted in most descriptions (*11,17,18,20,22,28*). Divergence was found in the allocation of the cuneus: studies using second-generation ligands associated this structure with stage V (*17,22,25,26*), and those using first-generation ligands associated it with stage VI (*11,18,20,21,23,28*).

Some variability was also observed in the definitions of meta-ROIs based on the Braak simplified scheme (Supplemental Table 2). Two studies (*28,29*) defined Braak I/II as the entorhinal cortex, whereas 2 others (*30,31*) included the hippocampus along with the entorhinal cortex. The choice of regions for Braak III/IV and V/VI meta-ROIs is aligned with the fact that they represent, respectively, the limbic and neocortical stages of NFT accumulation. However, the insula, the posterior cingulate, and the lingual gyrus were linked to stage V/VI in one study (*29*) and to stage III/IV in others (*30–32*). A discrepancy was again observed regarding the anterior cingulate, which belonged to stage III/IV in one study (*30*) and to V/VI in another (*29*).

Figure 3 provides examples of imaging representation of PET-based Braak stages used in studies included in this review.

### Variability in Methodologic Approaches to PET-Based Braak Staging

Different methods to evaluate PET-based Braak stages were observed (Supplemental Table 3). Most studies used more than one statistical or practical approach, the most common being to treat the measures of ligand uptake as continuous variables (*11,17–19, 21–33*). Thresholds to define abnormal tau accumulation in Braak ROIs were also largely used (*11,17,18,22,24–27,29,32,34*). Seven studies assigned an individual-level PET-based Braak stage to participants, which usually followed a hierarchic pattern (i.e., individuals with abnormality in later stages also presented abnormalities in earlier stages) (*11,17,18,24,25,26,27*). However, this condition was not reported in 2 studies (*11,18*) and was not achieved in a small percentage of participants in other studies, whose Braak nonconformant status was disclaimed (*17,24,26,27*). Other approaches included identifying peaks of tau signal (*28*) or applying gaussian mixture modeling to assess the tau positivity probability (*20*) in Braak ROIs.

### Correspondence of Postmortem Tau Autoradiography Binding to Braak Histopathologic Staging

In an autoradiographic study including 22 brains, $^{18}$F-AV1451 binding correlated with the NFT accumulation pattern, demonstrating a promising ability for in vivo estimation of Braak staging (*35*). Another study found that $^{18}$F-AV1451 binding in subjects with atypical AD did not entirely follow the early-stage progression as in the Braak scheme, showing moderate correspondence to tau accumulation in cases at stages 0–VI (*36*).

### Recapitulation of Histopathologic Staging by PET-Based Braak Staging

Most studies indicated that the PET-based Braak staging framework corresponds well with the Braak histopathologic descriptions. Both cross-sectional and longitudinal studies showed that the binding patterns strongly resemble the Braak histopathologic staging (*11,17–22,24–28,32–35*), even though atypical patterns of NFT accumulation were also observed (*17,19,20,24,26–28,34,36*). Notably, similarities in NFT accumulation patterns were found in postmortem neuropathology and antemortem $^{18}$F-MK6240 PET data from 2 AD patients who died 12 and 22 mo after the imaging acquisition (*25*).

Nonetheless, Franzmeier et al. suggested that tau accumulation and epicenters can vary spatially and that tau deposition begins locally and disseminates subsequently throughout functionally connected brain regions (*20*). Therefore, tau spreading may not always follow the Braak scheme and may be tracked at an individual level according to the normative connectivity patterns of tau epicenters (*20*). Seemiller et al. used $^{18}$F-AV1451 PET and resting-state functional MRI to research the relationship between Braak staging and the network degeneration hypothesis, according to which AD degenerative changes affect large brain networks and display functional connectivity patterns (*28,37–39*). Their results indicate that the connectivity of individual regions displaying tau pathology could predict its progression into higher Braak stages and an increase of tau deposition in earlier Braak stages (*28*). Thus, these findings agree with the Braak histopathologic staging proposal and corroborate the network degeneration hypothesis (*28*).

In a cross-sectional study, tau deposition in cognitively unimpaired (CU) individuals observed on $^{18}$F-AV1451 PET resembled but was not identical to Braak and Braak's descriptions of early NFT distribution (*34*). Both elevated tau PET signal in Braak III–VI ROIs and widespread early tau pathology were observed in CU individuals (*34*). Differences in NFT accumulation were also seen between younger-onset and older-onset AD, with the former presenting higher tau signal in frontal regions (*34*). This provides evidence of possible variability in NFT deposition, which may be associated with disease phenotypes (*34*).

### Association of PET-Based Braak Staging with Clinical Measures and Diagnoses

Schöll et al. reported cross-sectional and longitudinal associations between $^{18}$F-AV1451 uptake and cognitive decline in Braak ROIs (*11*). These findings were subsequently replicated in other cross-sectional studies, with PET-based Braak stages correlating not only with cognitive impairment but also with global disease severity and clinical diagnosis (*17,18,22,23,24,27*). Therriault et al., in turn, used individual-level PET-based Braak staging and observed that cognitive decline started at stages II–IV and progressed with the advance of Braak stages (*26*). Specifically, whereas early Braak stages featured isolated memory deficits, late stages had poorer clinical dementia ratings (*26*).

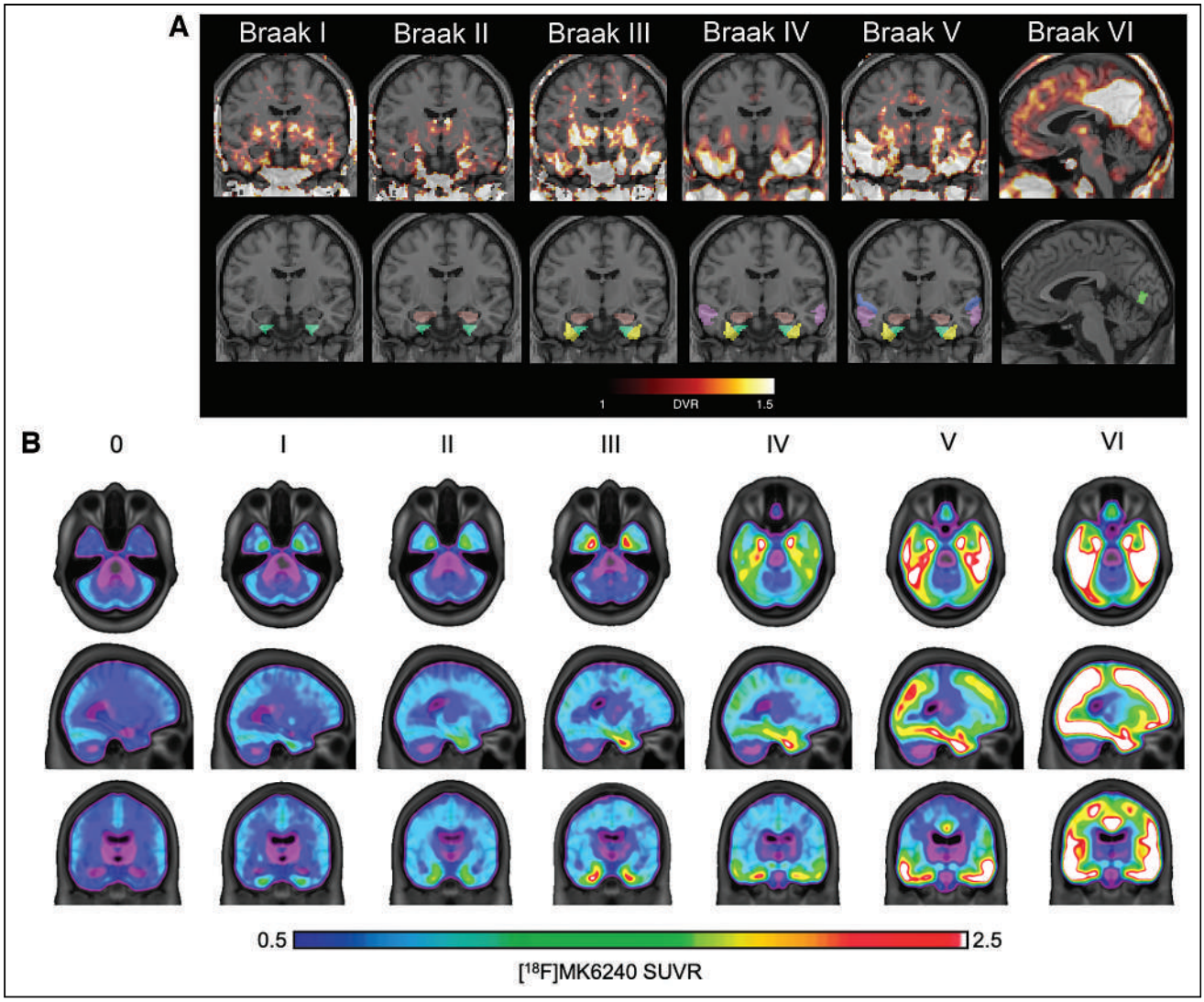


**FIGURE 3.** Examples of application of Braak staging in PET imaging studies. (A) Cases representative of each PET-based Braak stage included in Rullman et al. (*27*). Left column includes parametric $^{18}$F-PI2620 PET images merged with standard MRI, whereas right column shows MRI images with atlas regions corresponding to each Braak stage (*27*). (B) Average $^{18}$F-MK6240 SUV ratios across brains of participants in each PET-based Braak stage group included in Therriault et al. (*26*). (Adapted with permission of (*26,27*).)

Moreover, Cho et al. demonstrated that a higher tau accumulation rate in stages I–II was observed in mild cognitive impairment (MCI) patients, followed, respectively, by AD dementia and CU individuals (*33*). Tau accumulation reached higher rates in Braak III–IV ROIs in the AD dementia group. Moreover, the progression in tau accumulation in areas of higher Braak stage was associated with cognitive decline in AD (*33*). In another study, individuals classified as Aβ-negative CU, Aβ-positive CU, Aβ-positive MCI, and Aβ-positive AD showed a trend toward longitudinal tau accumulation predominantly in Braak I–II, I–III, IV–V, and V–VI ROIs, respectively (*25*). In Nihashi et al., $^{18}$F-THK5351 binding in Braak ROIs did not differ between Aβ-positive and Aβ-negative CU individuals (*23*). MCI and AD individuals had higher binding than CU participants in Braak I–IV ROIs and in all Braak ROIs, respectively (*23*). No significant difference was found between the MCI and AD groups. Finally, a cross-sectional study found that $^{18}$F-RO948 uptake was greater in individuals with AD dementia in all Braak ROIs than in Aβ-positive MCI and Aβ-negative CU patients (*29*). The Aβ-positive MCI group also presented a higher retention rate in I–II, III–IV, and I–IV ROIs than did Aβ-negative CU participants (*29*).

### Correspondence of In Vivo PET-Based Braak Staging with Cerebrospinal Fluid (CSF), Plasma, and Neuroimaging Biomarkers of AD

The association of Aβ positivity or load with PET-based Braak staging was pointed out in several studies (*11,17–19,22–24,26*). Correlations were also shown with several CSF biomarkers (*22,26*), plasma phosphorylated tau (*26*), and decreased hippocampal volume (*11,17,18,23*).

Among MCI or AD patients, $^{18}$F-AV1451 uptake in the entorhinal cortex was linked to local cortical atrophy and, in Braak III–IV and V–VI ROIs, to atrophy in local and distant locations (*31*). In CU individuals, tau had no effect on gray matter density (*31*). These findings suggest that tau spatial deposition is closely associated

with neurodegeneration in symptomatic individuals in the AD continuum (*31*).

### Comparisons of PET-Based Braak Staging and Other Strategies to Stage Individuals in the AD Continuum

Braak ROI-based staging demonstrated performance similar to that of whole-brain and regional tau measures in differentiating individuals with MCI and AD from Aβ-negative CU individuals. Nonetheless, PET-based Braak staging showed an enhanced potential to determine the initial stages of tau deposition (*18*). Furthermore, Braak ROI SUV ratio outperformed MRI and CSF measures when distinguishing AD and MCI from CU and non-AD groups (*29*).

In Kim et al., $^{18}$F-THK5351 PET was compared with MRI brain volumetry of selected regions (cingulate isthmus, inferior parietal lobule, and hippocampus) and with the combination of these tools regarding their ability to discriminate AD from CU and MCI (*30*). The combined model presented better performance than the SUV ratio of Braak ROIs alone in distinguishing AD from CU but not AD from MCI. Comparable performance was found for the combined model and MRI brain volumetry. In sum, all methods demonstrated good performance in distinguishing the phases of the AD continuum, with an additional value of brain volumetry in the distinction between AD and CU (*30*).

## DISCUSSION

With this review, we aimed to examine the literature about the use of tau PET to stage AD using ROIs and meta-ROIs that resemble the Braak histopathologic classification. The Braak histopathologic framework shows a good correspondence with clinical status across the AD spectrum (*40–42*), and tau PET is a promising tool to make possible in vivo AD staging using this classification. Despite the limited literature on the topic, most of the available studies indicate that tau PET performs well in staging AD when using Braak ROIs or meta-ROIs, even when compared with other biomarkers and clinical predictors.

The adaptation of the original histopathologic descriptions of Braak stages to their use in tau PET imaging studies has been done taking into account the limitations of PET imaging. This is evidenced by the variability in the anatomic definitions of Braak ROIs and meta-ROIs across studies, which may result from factors such as variability in imaging acquisition technique, tracers used, and the aims of the study. Also, it should be noted that the Braak histopathologic scheme was revised after the improvement of histopathology techniques. Some minor discrepancies in the topographic definitions of the stages are observed between different reports by Braak et al. (*6,7,43–45*). Insula involvement, for instance, was associated with stage V in the original description (*6*) but with stage IV in more recent studies (*7,44,45*). Changes in the description of the progression of neocortical damage are also seen between the initial and subsequent studies (*6,7,43–45*).

We observed multiple definitions of Braak I as the entorhinal cortex, which was described by Braak and Braak to be uninvolved or minimally involved at this stage (*6,7*). Partial anatomic descriptions were observed for stage II, whose hallmarks are the entorhinal cortex and hippocampal sector CA1 involvement (*6,7*). The limited spatial resolution of PET may partially account for these discrepancies since it hampers tau pathology identification in small areas of the medial temporal lobe and signal discrimination in the transentorhinal and entorhinal cortices. Braak I–II ROI definitions in $^{18}$F-AV1451 PET studies may be also affected by off-target binding to the choroid plexus, which limits the evaluation of early Braak ROIs (*12*). Even though some incompleteness was seen in stage III descriptions, the choice of ROIs had a high interstudy agreement and adequate correspondence with postmortem observations (*6,7*). The ROIs representing stages IV and V varied considerably but were in line with the fact that NFT pathology progresses more broadly into the associative neocortex in stage IV and extends to nearly all remaining neocortical areas (sparing primary fields) in stage V (*6,7*). For stage VI, definitions were fairly similar among studies and agreed with the histopathology framework (*6,7*). The definition of meta-ROIs also showed discrepancies, with incompleteness for Braak I/II and inclusion of regions linked mainly to stages III/IV (the insula, the posterior cingulate, and the lingual gyrus) in the V/VI meta-ROI (*6,7*). The relevance of these inconsistencies constitutes a knowledge gap and might be affected by the size of those regions relative to the Braak ROIs and by the resolution of tau PET imaging. Since the Braak framework serves as a benchmark for AD progression, the standardization of Braak ROIs might be important to test its accuracy as a staging and prognostic tool and to allow reproducibility.

Regardless of those discrepancies, most studies demonstrated that the tau accumulation seen in PET seems to follow the Braak histopathologic framework (*11,17–22,24–28,32–35*). Different clinical, fluid, and imaging biomarkers of AD severity were found to be associated with progressive tau deposition in subsequent Braak stages or a stronger signal in Braak ROIs: cognitive decline (*11,17,22–24, 26,27,33*), dementia severity (*17,26*), amyloid positivity or load (*11,17–19,22–24,26*), CSF measures (*22,26*), plasma phosphorylated tau (*26*), diminished hippocampal volume (*11,17,18,23*), and cortical atrophy (*31*). Furthermore, PET-based Braak staging appears to present a comparable or superior performance in relation to other AD staging methods (*18,29,30*). These findings reinforce the potential use of the proposed staging scheme in living individuals. Nonetheless, further studies comparing PET-based Braak staging to other methods assessing AD severity (e.g., fluid biomarkers or tau PET signal quantification in specific ROIs) are needed, especially concerning cost-effectiveness.

PET-based Braak staging also performed well in identifying the preclinical phases of AD. This ability is relevant in the context of population enrichment strategies for disease-modifying clinical trials. Indeed, this clinically silent period has become an attractive stage for preventive therapeutic interventions (*46*). Apart from that, this staging strategy could be useful for earlier AD diagnosis, before symptom onset, and for the proposition of personalized care strategies (*47*).

The existence of patterns of tau deposition other than the one proposed by Braak and Braak has been highlighted in several studies (*17,19,20,24,26–28,34,36*). One of these studies (*20*) proposes links between Braak-nonconformant patterns and tau spreading based on brain connectivity patterns. Furthermore, Vogel et al. proposed, via network diffusion models, the occurrence of different spatiotemporal patterns of tau accumulation in AD: limbic-predominant, medial temporal lobe–sparing, and posterior and lateral resembling atypical AD phenotypes (*48*). These data-driven techniques refine the concept of hierarchic patterns of tau propagation by emphasizing the role of brain connectivity in shaping their sequence. Moreover, studies on atypical AD have led to the emerging perspective that some individuals, because of their atypical NFT distribution, do not fit the Braak staging framework. Here, it is important to consider what a lack of fit to the Braak staging framework means. For example, do individuals with a significantly greater frontal tau load than

typically observed go against the Braak staging system? What if the medial temporal lobe is concurrently affected, albeit to a lesser degree? Although tau PET studies have indicated that the regional distribution of tau pathology at the individual level is indeed highly variable, it is presently unclear to what extent different clinical variants of AD have tau patterns that go against the Braak staging framework.

Some limitations were identified in the available literature on PET-based Braak staging. First, Braak histopathologic staging relies on the use of staining techniques to detect specific tau phosphorylation sites (*49*), but the extent of their contribution to the tau PET signal is yet to be clarified. Moreover, the fact that there is no established framework for defining Braak-based ROIs or meta-ROIs may lead to the misrepresentation of Braak histopathologic stages in imaging studies. Similarly, there is no standardization regarding the methods to establish thresholds for Braak ROI positivity. This includes the choice of the reference control group, which varied especially with respect to age across studies. Furthermore, the most used ligand in the available studies is $^{18}$F-AV1451, whose off-target binding may compromise the assessment of early Braak ROIs (*12*). Other ligands are still underrepresented in the literature, and there is a need for more studies testing and comparing their staging properties. Further studies comparing PET-based Braak staging with other biomarkers of disease severity are also necessary to understand the real potential of this staging method. Here, we suggest, for example, evaluating both its individual and combined efficiencies with other CSF, plasma, and imaging biomarkers. Also, most studies are not clear regarding which clinical variants of AD are evaluated. Studies addressing different patterns of tau deposition in early- and late-onset AD and comparing the typical and atypical phenotypes of AD are warranted to increase our understanding of the limitations of PET-based Braak staging.

It is also critical to consider the limitations of neuropathologic Braak staging itself, which was developed more than 30 y ago using techniques insensitive to the detection of NFT heterogeneity across various brain regions (*6*). Recent neuropathologic studies refined the initial contributions of Braak and Braak by identifying subtypes of AD with alternative distributions of NFTs at autopsy (*50*). Since it is based on autopsy assessments, another caveat of Braak and Braak's description is due to the cross-sectional nature of pathologic observations, which prevents longitudinal analyses. Furthermore, the relatively small number of cortical areas typically needed for neuropathology staging limits the observation of interindividual differences in tau distribution. Braak neuropathologic staging is also based on semiquantitative measures, making it difficult to classify cases in a transitional state.

## CONCLUSION

Overall, most studies suggest that PET-based Braak staging may be a logical starting point for staging AD, as it showed a valuable ability to discriminate between the phases of the AD continuum and correlated with clinical, laboratory, and imaging biomarkers of disease severity. Refinements in this staging system are necessary to incorporate atypical and Braak-nonconformant cases. Further studies are needed to validate tau staging systems in research and clinical practice. They should address, for instance, the correspondence with other clinical (e.g., performance in activities of daily living) and biologic markers of AD, include comparisons between in vivo PET and postmortem neuropathologic observations, and check the progression of PET-based Braak stages at an individual level, preferably for longer follow-up periods. Also, the harmonization of Braak ROIs and methods to define thresholds for tau abnormality might represent a further step for ascertaining reproducibility across studies.

## DISCLOSURE

Serge Gauthier has served as a scientific advisor to Cerveau Therapeutics. Eduardo Zimmer serves on the scientific advisory board of Next Innovative Therapeutics. No other potential conflict of interest relevant to this article was reported.

## ACKNOWLEDGMENTS

We thank Rullman et al. (*27*) and Therriault et al. (*26*), as well as the respective journals, for authorizing the reproduction of Figure 3.

## REFERENCES

1. McKhann G, Drachman D, Folstein M, Katzman R, Price D, Stadlan EM. Clinical diagnosis of Alzheimer's disease: report of the NINCDS-ADRDA Work Group under the auspices of Department of Health and Human Services Task Force on Alzheimer's Disease. *Neurology.* 1984;34:939–944.
2. Dayan AD. Quantitative histological studies on the aged human brain. I. Senile plaques and neurofibrillary tangles in normal patients. *Acta Neuropathol (Berl).* 1970; 16:85–94.
3. Hubbard BM, Fenton GW, Anderson JM. A quantitative histological study of early clinical and preclinical Alzheimer's disease. *Neuropathol Appl Neurobiol.* 1990; 16:111–121.
4. Kemper TL. Senile dementia: a focal disease in the temporal lobe. In; Nandy E, ed. *Senile Dementia: A Biomedical Approach.* Elsevier; 1978:105–113.
5. Wilcock GK, Esiri MM. Plaques, tangles and dementia: a quantitative study. *J Neurol Sci.* 1982;56:343–356.
6. Braak H, Braak E. Neuropathological stageing of Alzheimer-related changes. *Acta Neuropathol (Berl).* 1991;82:239–259.
7. Braak H, Alafuzoff I, Arzberger T, Kretzschmar H, Del Tredici K. Staging of Alzheimer disease-associated neurofibrillary pathology using paraffin sections and immunocytochemistry. *Acta Neuropathol (Berl).* 2006;112:389–404.
8. Nagy Z, Yilmazer-Hanke DM, Braak H, Braak E, Schultz C, Hanke J. Assessment of the pathological stages of Alzheimer's disease in thin paraffin sections: a comparative study. *Dement Geriatr Cogn Disord.* 1998;9:140–144.
9. Hyman BT, Phelps CH, Beach TG, et al. National Institute on Aging-Alzheimer's Association guidelines for the neuropathologic assessment of Alzheimer's disease. *Alzheimers Dement.* 2012;8:1–13.
10. Montine TJ, Phelps CH, Beach TG, et al. National Institute on Aging-Alzheimer's Association guidelines for the neuropathologic assessment of Alzheimer's disease: a practical approach. *Acta Neuropathol (Berl).* 2012;123:1–11.
11. Schöll M, Lockhart SN, Schonhaut DR, et al. PET imaging of tau deposition in the aging human brain. *Neuron.* 2016;89:971–982.
12. Marquié M, Normandin MD, Vanderburg CR, et al. Validating novel tau positron emission tomography tracer [F-18]-AV-1451 (T807) on postmortem brain tissue. *Ann Neurol.* 2015;78:787–800.
13. Wong DF, Comley RA, Kuwabara H, et al. Characterization of 3 novel tau radiopharmaceuticals, $^{11}$C-RO-963, $^{11}$C-RO-643, and $^{18}$F-RO-948, in healthy controls and in Alzheimer subjects. *J Nucl Med.* 2018;59:1869–1876.
14. Kuwabara H, Comley RA, Borroni E, et al. Evaluation of $^{18}$F-RO-948 PET for quantitative assessment of tau accumulation in the human brain. *J Nucl Med.* 2018; 59:1877–1884.
15. Hostetler ED, Walji AM, Zeng Z, et al. Preclinical characterization of $^{18}$F-MK-6240, a promising PET tracer for in vivo quantification of human neurofibrillary tangles. *J Nucl Med.* 2016;57:1599–1606.
16. Pascoal TA, Shin M, Kang MS, et al. In vivo quantification of neurofibrillary tangles with [$^{18}$F]MK-6240. *Alzheimers Res Ther.* 2018;10:74.
17. Pascoal TA, Therriault J, Benedet AL, et al. $^{18}$F-MK-6240 PET for early and late detection of neurofibrillary tangles. *Brain.* 2020;143:2818–2830.
18. Maass A, Landau S, Baker SL, et al. Comparison of multiple tau-PET measures as biomarkers in aging and Alzheimer's disease. *Neuroimage.* 2017;157:448–463.
19. Betthauser TJ, Koscik RL, Jonaitis EM, et al. Amyloid and tau imaging biomarkers explain cognitive decline from late middle-age. *Brain.* 2020;143:320–335.

20. Franzmeier N, Dewenter A, Frontzkowski L, et al. Patient-centered connectivity-based prediction of tau pathology spread in Alzheimer's disease. *Sci Adv.* 2020;6: eabd1327.
21. Shokouhi S, Taylor WD, Albert K, et al. In vivo network models identify sex differences in the spread of tau pathology across the brain. *Alzheimers Dement (Amst).* 2020;12:e12016.
22. Kreisl WC, Lao PJ, Johnson A, et al. Patterns of tau pathology identified with $^{18}$F-MK-6240 PET imaging. *Alzheimers Dement.* 2022;18:272–282.
23. Nihashi T, Sakurai K, Kato T, et al. Patterns of distribution of $^{18}$F-THK5351 positron emission tomography in Alzheimer's disease Continuum. *J Alzheimers Dis.* 2022;85:223–234.
24. Schwarz AJ, Yu P, Miller BB, et al. Regional profiles of the candidate tau PET ligand $^{18}$F-AV-1451 recapitulate key features of Braak histopathological stages. *Brain.* 2016;139:1539–1550.
25. Pascoal TA, Benedet AL, Tudorascu DL, et al. Longitudinal $^{18}$F-MK-6240 tau tangles accumulation follows Braak stages. *Brain.* 2021;144:3517–3528.
26. Therriault J, Pascoal TA, Lussier FZ, et al. Biomarker modeling of Alzheimer's disease using PET-based Braak staging. *Nat Aging.* 2022;2:526–535.
27. Rullmann M, Brendel M, Schroeter ML, et al. Multicenter $^{18}$F-PI-2620 PET for in vivo Braak staging of tau pathology in Alzheimer's disease. *Biomolecules.* 2022;12:458.
28. Seemiller J, Bischof GN, Hoenig MC, Tahmasian M, van Eimeren T, Drzezga A. Indication of retrograde tau spreading along Braak stages and functional connectivity pathways. *Eur J Nucl Med Mol Imaging.* 2021;48:2272–2282.
29. Leuzy A, Smith R, Ossenkoppele R, et al. Diagnostic performance of RO948 F 18 tau positron emission tomography in the differentiation of Alzheimer disease from other neurodegenerative disorders. *JAMA Neurol.* 2020;77:955–965.
30. Kim M, Kim SJ, Park JE, et al. Combination of automated brain volumetry on MRI and quantitative tau deposition on THK-5351 PET to support diagnosis of Alzheimer's disease. *Sci Rep.* 2021;11:10343.
31. Timmers T, Ossenkoppele R, Wolters EE, et al. Associations between quantitative [$^{18}$F] flortaucipir tau PET and atrophy across the Alzheimer's disease spectrum. *Alzheimers Res Ther.* 2019;11:60.
32. Baek MS, Cho H, Lee H, et al. Temporal trajectories of in vivo tau and amyloid-β accumulation in Alzheimer's disease. *Eur J Nucl Med Mol Imaging.* 2020;47: 2879–2886.
33. Cho H, Choi JY, Lee HS, et al. Progressive tau accumulation in Alzheimer disease: 2-year follow-up study. *J Nucl Med.* 2019;60:1611–1621.
34. Lowe VJ, Wiste HJ, Senjem ML, et al. Widespread brain tau and its association with ageing, Braak stage and Alzheimer's dementia. *Brain.* 2018;141:271–287.
35. Marquié M, Siao Tick Chong M, Antón-Fernández A, et al. [F-18]-AV-1451 binding correlates with postmortem neurofibrillary tangle Braak staging. *Acta Neuropathol (Berl).* 2017;134:619–628.
36. Lowe VJ, Curran G, Fang P, et al. An autoradiographic evaluation of AV-1451 tau PET in dementia. *Acta Neuropathol Commun.* 2016;4:58.
37. Buckner RL. Molecular, structural, and functional characterization of Alzheimer's disease: evidence for a relationship between default activity, amyloid, and memory. *J Neurosci.* 2005;25:7709–7717.
38. Tahmasian M, Shao J, Meng C, et al. Based on the network degeneration hypothesis: separating individual patients with different neurodegenerative syndromes in a preliminary hybrid PET/MR study. *J Nucl Med.* 2016;57:410–415.
39. Therriault J, Pascoal TA, Savard M, et al. Intrinsic connectivity of the human brain provides scaffold for tau aggregation in clinical variants of Alzheimer's disease. *Sci Transl Med.* 2022;14:eabc8693.
40. Nelson PT, Alafuzoff I, Bigio EH, et al. Correlation of Alzheimer disease neuropathologic changes with cognitive status: a review of the literature. *J Neuropathol Exp Neurol.* 2012;71:362–381.
41. Riley KP, Snowdon DA, Markesbery WR. Alzheimer's neurofibrillary pathology and the spectrum of cognitive function: findings from the Nun Study. *Ann Neurol.* 2002;51:567–577.
42. Serrano-Pozo A, Frosch MP, Masliah E, Hyman BT. Neuropathological alterations in Alzheimer disease. *Cold Spring Harb Perspect Med.* 2011;1:a006189.
43. Braak H, Braak E, Bohl J. Staging of Alzheimer-related cortical destruction. *Eur Neurol.* 1993;33:403–408.
44. Braak H, Braak E, Yilmazer D, Jansen EN, Bohl J. Pattern of brain destruction in Parkinson's and Alzheimer's diseases. *J Neural Transm.* 1996;103:455–490.
45. Braak H, Braak E. Staging of Alzheimer-related cortical destruction. *Int Psychogeriatr.* 1997;9:257–261.
46. Sperling RA, Rentz DM, Johnson KA, et al. The A4 study: stopping AD before symptoms begin? *Sci Transl Med.* 2014;6:228fs13.
47. Lima-Silva TB, Mioshi E, Bahia VS, et al. Disease progression in frontotemporal dementia and Alzheimer disease: the contribution of staging scales. *J Geriatr Psychiatry Neurol.* 2021;34:397–404.
48. Vogel JW, Young AL, Oxtoby NP, et al. Four distinct trajectories of tau deposition identified in Alzheimer's disease. *Nat Med.* 2021;27:871–881.
49. Wesseling H, Mair W, Kumar M. Tau PTM profiles identify patient heterogeneity and stages of Alzheimer's disease. *Cell.* 2020;183:1699–1713.e13.
50. Murray ME, Graff-Radford NR, Ross OA, Petersen RC, Duara R, Dickson DW. Neuropathologically defined subtypes of Alzheimer's disease with distinct clinical characteristics: a retrospective study. *Lancet Neurol.* 2011;10:785–796.

# Molecular Imaging, Radiochemistry, and Environmental Pollutants

Samantha Delaney[1–3], Joni Sebastiano[1–3], Brian M. Zeglis[1–5], and Outi M. Keinänen[1,2,6]

*[1]Department of Chemistry, Hunter College, City University of New York, New York, New York; [2]Department of Radiology, Memorial Sloan Kettering Cancer Center, New York, New York; [3]Ph.D. Program in Biochemistry, Graduate Center of City University of New York, New York, New York; [4]Ph.D. Program in Chemistry, Graduate Center of City University of New York, New York, New York; [5]Department of Radiology, Weill Cornell Medical College, New York, New York; and [6]Department of Chemistry, University of Helsinki, Helsinki, Finland*

The worldwide proliferation of persistent environmental pollutants is accelerating at an alarming rate. Not surprisingly, many of these pollutants pose a risk to human health. In this review, we examine recent literature in which molecular imaging and radiochemistry have been harnessed to study environmental pollutants. Specifically, these techniques offer unique ways to interrogate the pharmacokinetic profiles and bioaccumulation patterns of pollutants at environmentally relevant concentrations, thereby helping to determine their potential health risks.

**Key Words:** environmental pollutants; molecular imaging; PET imaging; SPECT imaging; fluorescence imaging

**J Nucl Med 2023; 64:1179–1184**
DOI: 10.2967/jnumed.122.265209

Over the last half century, human activity has caused a devastating rise in environmental pollution. The scientific community has sounded the alarm about the potential effects of certain pollutants—including micro- and nanosized plastics, metal oxides, and per- and poly-fluoroalkyl substances (PFAS)—on human health, especially in light of recent studies showing these compounds to have become ubiquitous in human biological systems (*1–5*). For example, micro- and nanosized plastics have recently been isolated from human blood, fecal matter, and placental tissue. As science seeks to unravel the toxicologic and biological effects of pollutants, understanding their pharmacokinetic profiles and bioaccumulation patterns is critical. To this end, scientists have begun to turn to molecular imaging, as it offers an accurate and noninvasive way to monitor the in vivo behavior of pollutants in living systems and, in so doing, identify potential sites of interaction and toxicity.

In this review, we discuss recent efforts to use molecular imaging and radiochemistry to study environmental pollutants. We are not the first to cover this topic; several excellent reviews have been published on work at the intersection of molecular imaging, radiochemistry, and environmental science (*6–9*). Although the field remains young, it has grown in recent years and—in our estimation—is poised to break out into the mainstream soon. We will cover how various molecular imaging and radiochemical methods have been used to study the pharmacokinetic profiles of five types of environmental pollutants: micro- and nanoplastics, PFAS, metal oxides, particulate matter (PM), and graphene. Ultimately, we hope that this review will shed light on how these techniques offer unique tools for probing the pharmacological behavior and biological impact of environmental pollutants and thus may help determine how to mitigate their risks to human health.

## Micro- and Nanoplastics

Contamination of the environment with microplastics (<5 mm in diameter) and nanoplastics (<100 nm in diameter) has grown substantially over the past few decades, and numerous studies have linked plastic pollution with adverse health effects in humans. Indeed, high levels of micro- and nanoplastic exposure have been associated with inflammatory effects as well as respiratory and cardiovascular diseases (*1,2*). However, the in vivo fate of micro- and nanoplastics in mammalian systems is relatively poorly understood, opening the door for molecular imaging to be used in this arena. In 2017, Deng et al. administered fluorophore-bearing polystyrene microplastics (5 and 20 μm) to mice via oral gavage (*10*). Although these particles could not be tracked in vivo because of the low tissue penetration of the fluorescent signal, ex vivo methods revealed accumulation of the particles in the liver, kidneys, and gut. In addition, the cohort that received the highest dose of microplastic particles exhibited inflamed livers, decreased body weights, decreased adenosine triphosphate levels, and increased lactate dehydrogenase activity. In another study, the translocation and fetal deposition of 20 nm rhodamine-labeled polystyrene nanoparticles were interrogated in pregnant rats (*11*). Again, the poor tissue penetration of visible light fluorescence prevented in vivo imaging, but ex vivo detection methods identified plastics in the maternal lung, heart, and spleen as well as several fetal tissues, suggesting translocation of the plastics through the placenta. Fluorophore-labeled polystyrene particles have, however, been harnessed for in vivo tracking in another, more transparent animal model: zebrafish. Pitt et al. reported that fluorescent polystyrene nanoparticles (50 nm) accumulated in the chorion of developing zebrafish embryos, resulting in toxicity due to the particles' penetration of the nutrient-rich yolk sac (*12*). These results align with those of van Pomeren et al., who studied the distribution of fluorophore-bearing polystyrene nanoparticles of several sizes

Received Apr. 24, 2023; revision accepted Jun. 21, 2023.
For correspondence or reprints, contact Outi Keinänen (ok510@hunter.cuny.edu).
Published online Jul. 13, 2023.

(25, 50, 250, and 700 nm) in zebrafish embryos at various stages of development (Fig. 1A) (*13*).

Several methods for the radiolabeling of micro- and nanoplastics have been developed to facilitate their study via autoradiography and nuclear imaging. For example, Al-Sid-Cheikh et al. used whole-body autoradiography to determine that $^{14}$C-labeled plastics accumulated in the muscles, gonads, mantle, gills, intestines, and kidneys of scallops, with the highest concentration detected in the hepatopancreas (*14,15*). Recently, our group reported the first (to our knowledge) study in which PET was used to track radiolabeled micro- and nanoplastic particles (*16*). In this work, $^{89}$Zr was used to radiolabel micro- and nanosized polystyrene particles (20 nm, 220 nm, 1 μm, and 6 μm) modified with the chelator desferrioxamine. PET imaging experiments revealed that after administration via oral gavage, these $^{89}$Zr-labeled radioplastics traveled through the gastrointestinal tract without reaching the systemic circulation (Fig. 1B). More recently, Im et al. labeled 200 nm polystyrene microplastic particles with the positron-emitting radiometal $^{64}$Cu and used PET to follow their in vivo behavior in mice (Fig. 1C) (*17*). In this case, the data revealed high activity concentrations in the stomach, intestines, and liver. However, this phenomenon could be due to translocation of the radioplastics or inadvertent release and redistribution of [$^{64}$Cu]$Cu^{2+}$, because the chelator used in this system—DOTA—has been shown to be an inadequate platform for the stable in vivo sequestration of $Cu^{2+}$ (*18*). Finally, radioiodination methods have recently been developed for polyvinylchloride particles (*19*). Although this technology has not yet been used to facilitate nuclear imaging, it is nonetheless exciting, as it could pave the way for PET imaging studies with the positron-emitting isotope of iodine, $^{124}$I.

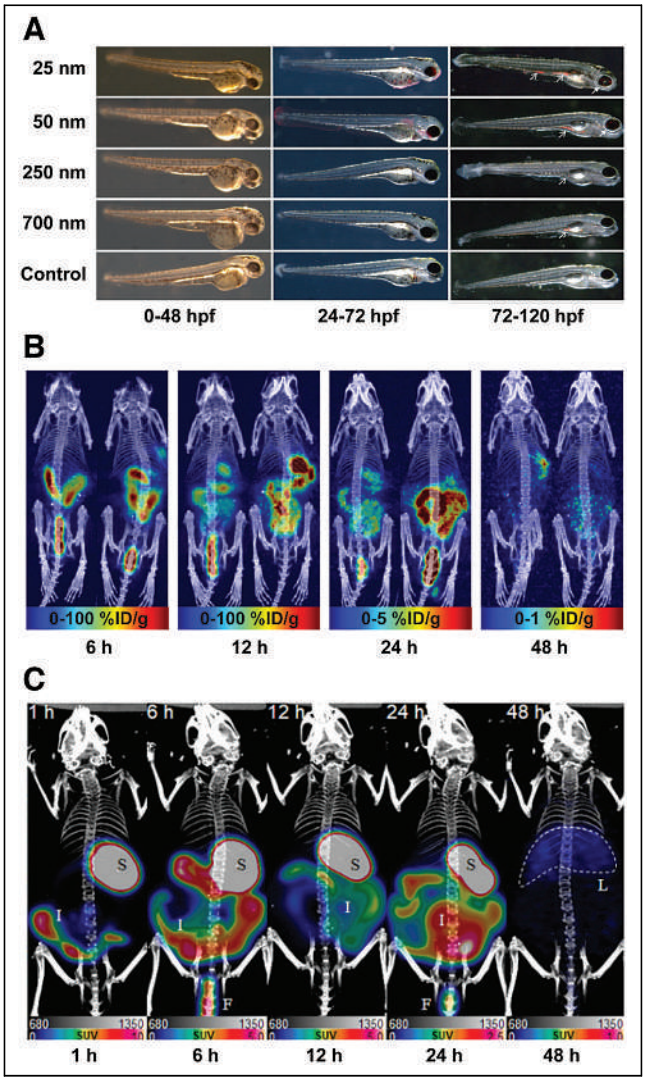


**FIGURE 1.** (A) Fluorescence microscopy images of different-sized polystyrene particles (25, 50, 250, and 700 nm) in zebrafish embryos (*13*). (B) Maximum-intensity-projection PET/CT images of mice at 6, 12, 24, and 48 h after administration of [$^{89}$Zr]Zr-desferrioxamine-polystyrene (20 nm; 1.85 MBq; 0.1 mg) via oral gavage (*16*). (C) Maximum-intensity-projection PET/CT images of mice at 1, 6, 12, 24, and 48 h after oral administration of [$^{64}$Cu]Cu-DOTA-polystyrene (200 nm; 4.81 MBq; 57.8 μg) (*17*). %ID = percent injected dose; hpf = hours postfertilization.

## PFAS

PFAS are classes of organofluorine compounds widely used in both industrial and consumer applications. From a chemical standpoint, PFAS offer numerous advantages—such as high inertness due to the strength of their carbon-fluorine bonds—but they come with a significant drawback: unfavorably long half-lives within environmental and biological systems (*4*). Recent monitoring studies have confirmed the pervasive presence of PFAS in water and land environments, as well as in aquatic species at all levels of the food web. Human exposure to PFAS has been linked to several negative health effects, such as impaired immunological function, chronic autoimmune diseases, hepatotoxicity, cancer, decreased fertility, and toxic developmental effects (*20,21*). Because of their small size, PFAS cannot reliably be labeled with fluorophores without disturbing their in vivo behavior. Instead, the field has turned to radiochemistry. Bogdanska et al., for example, administered $^{35}$S-labeled perfluorooctane sulfonate orally to adult mice and used whole-body autoradiography and scintillation counting to study the compound's biodistribution, ultimately finding the highest concentrations in the liver, bone, blood, skin, and muscle (*22*). More recently, Bartels et al. labeled perfluorooctanoic acid (PFOA), perfluorohexanoic acid, and perfluorobutanoic acid with the positron-emitting radiohalogen $^{18}$F (*23*). Ex vivo biodistribution data collected 4 h after the intravenous administration of these radiopollutants revealed that the highest concentrations of [$^{18}$F]F-PFOA and [$^{18}$F]F-perfluorohexanoic acid were in the liver, whereas that of [$^{18}$F]F-perfluorobutanoic acid was in the stomach. As an aside, it is worth noting that all of the mouse tissues examined in the aforementioned studies contained background levels of unlabeled PFAS, a result that aligns with postmortem analyses of human tissues.

Since high levels of exposure to PFAS can lead to birth defects, researchers have been particularly interested in investigating the fate of PFAS in gravid mice and in their fetuses and pups. In a study by Borg et al., gravid mice were administered $^{35}$S-labeled perfluorooctane sulfonate either intravenously or orally, and the bioaccumulation of the radiopollutant was subsequently measured in the dams, fetuses (on gestational days 18 and 20), and pups (on postnatal day 1) via whole-body autoradiography and scintillation counting (*24*). Surprisingly, the activity concentrations of [$^{35}$S]S-perfluorooctane sulfonate in the blood of the fetuses and pups were 1.1–2.3 times higher than that in the dam's blood. The activity concentrations in the livers of the fetuses were significantly lower than that in the maternal liver but were still about 2.5-fold higher than that in the maternal blood. Autoradiography also revealed heterogeneous uptake of [$^{35}$S]S-perfluorooctane sulfonate in the brains of fetuses and pups. In another

study, Bartels et al. used dynamic PET and biodistribution studies to explore the biologic fate of two $^{18}$F-labeled PFAS—[$^{18}$F]F-PFOA and [$^{18}$F]F-perfluorohexanoic acid—in pregnant mice after intravenous and oral administration (*25*). PET images revealed uptake of both compounds in the placentae, though the rate of accumulation was slower after oral administration (Figs. 2A and 2B). The radiolabeled PFAS were found in all tissues examined, with the highest concentrations in the blood (after intravenous injection) and in the gastrointestinal tract and lungs (after oral administration). Taken together, the studies described in this section effectively illustrate the intrinsic advantages and disadvantages of certain radionuclides for pollutant studies. Although the 87.4-d half-life of $^{35}$S allows for longitudinal monitoring, its emissions do not permit in vivo imaging; $^{18}$F (half-life, 109.8 min), on the other hand, can be imaged via PET, but its short half-life limits follow-up times.

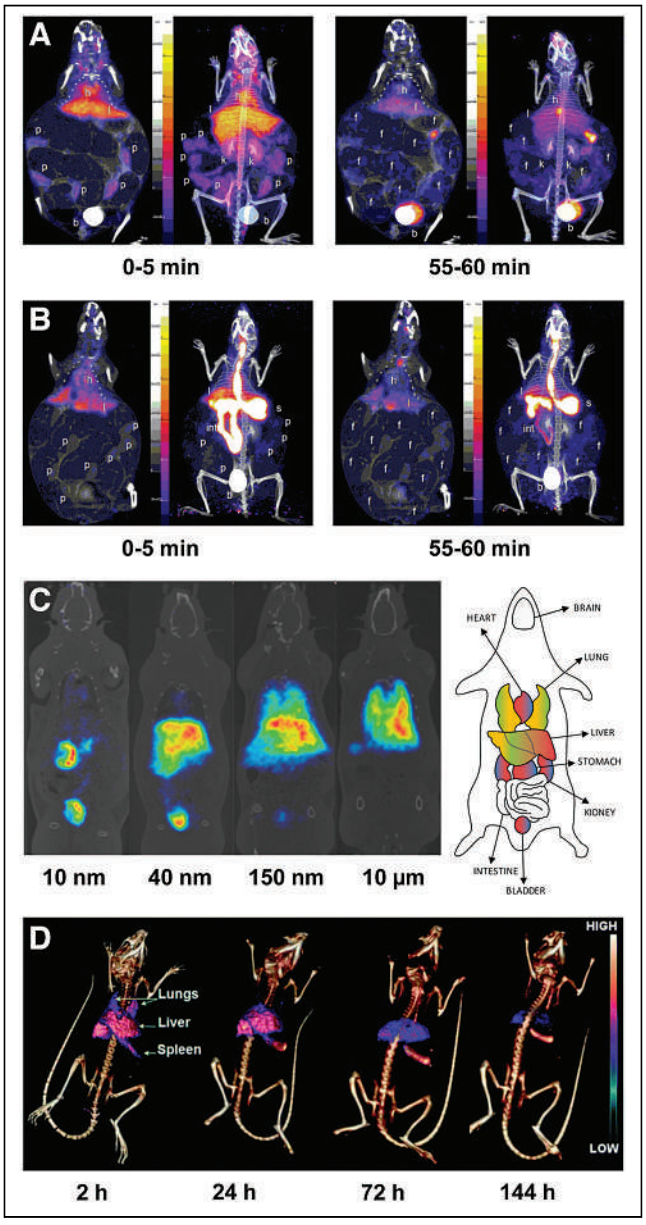


**FIGURE 2.** (A and B) Representative PET images illustrating uptake of [$^{18}$F]PFOA in mice at 2 time points after administration via tail vein injection (4.44 MBq) (A) and oral gavage (3.7 MBq) (B). b = bladder; f = fetus; h = heart; int = intestine; k = kidney; l = liver; p = placenta; s = stomach. (Reprinted with permission of (*25*).) (C) PET images of mice at 60 min after intravenous administration of 10 nm, 40 nm, 150 nm, or 10 μm of $^{13}$N-labeled $Al_2O_3$ nanoparticles (10–15 MBq, 5–8 mg). (Reprinted with permission of (*27*).) (D) SPECT/CT images of mice at 2, 24, 72, and 144 h after intravenous administration of $^{141}$Ce-labeled cerium oxide nanoparticles (6.7 MBq, 3.6 nmol). (Reprinted with permission of (*29*).)

### Metal Oxides

Nanoparticulate metal oxides have been used in a vast array of applications, including food additives, cosmetics, semiconductors, electronics, and medicine. This widespread use has inadvertently led to their proliferation as environmental pollutants, which, in turn, has fueled the study of their potential long-term biological effects. Radionuclides are the most common reporter for the in vivo study of metal oxides. Along these lines, Pérez-Campaña et al. have developed a robust proton beam methodology for the production of metal oxides radiolabeled with short-lived positron emitters (*26–28*). For example, they used the direct irradiation of $^{18}$O-enriched $Al_2O_3$ to generate $^{18}$F-labeled particles that were then administered intravenously to rats (*26*). PET imaging revealed that most of the aluminum oxide nanoparticles accumulated in the liver, though considerable uptake was also observed in the lungs, heart, kidneys, urine, and stomach. In a similar study, the same group produced $^{18}$F-labeled $TiO_2$ nanoparticles and administered them to rats both orally and intravenously (*28*). Subsequent PET imaging revealed the accumulation of these nanoparticles in the upper gastrointestinal tract and liver on oral and intravenous administration, respectively. Finally, Pérez-Campaña et al. have also investigated the effect of particle size on the biodistribution of metal oxides. After the production of $^{13}$N-labeled $Al_2O_3$ nanoparticles of different sizes via proton beam activation, in vivo biodistribution results showed that larger nanoparticles (i.e., 40 nm, 150 nm, and 10 μm) accumulated in the liver and lungs whereas smaller nanoparticles (i.e., 10 nm) accreted in excretory organs such as the bladder and kidneys (Fig. 2C) (*27*).

Shifting gears, a study performed by Yang et al. leveraged longer-lived radionuclides and SPECT to investigate the in vivo behavior of cerium oxide nanoparticles in mice up to 1 wk after intravenous injection (*29*). To this end, cerium oxide nanoparticles were radiolabeled with $^{141}$Ce, $^{111}$In, or $^{65}$Zn. SPECT imaging revealed high levels of accumulation in the lungs, liver, and spleen at early time points after intravenous administration (Fig. 2D). The particles gradually cleared from the lungs over time but remained in the liver and spleen until the end of the observation period.

### PM

*Particulate matter* is a general term for airborne particulate pollutants that are small enough to cause serious health issues on inhalation. PM, a mixture of solids and liquids that can contain hundreds of different chemicals, is categorized into 2 groups based on the size of the particles: those with a diameter of less than 10 μm ($PM_{10}$) and those with a diameter of less than 2.5 μm ($PM_{2.5}$). Recent years have played witness to a surge of reports linking PM to chronic respiratory issues, cardiovascular disease, cancer development, and even—in severe cases—death. In an effort to study this, Park et al. used $^{89}$Zr to radiolabel an analog of pyrene that was then used to prepare a suspension of diesel PM, a subset of PM that is emitted by diesel engines (*3*). This radioactive diesel PM (average size, ~200 nm) was then administered to mice orally, intratracheally, or intravenously. PET imaging revealed that the mice that received the $^{89}$Zr-labeled diesel PM orally

excreted the particles within a day (Fig. 3A). In contrast, the particles administered via the other 2 routes were retained in several organs. More specifically, intratracheally administered particles accumulated principally in the lungs (Fig. 3B), whereas those administered intravenously accreted in the heart, liver, and spleen (Fig. 3C). A few years earlier, Lee et al. leveraged SPECT imaging to track diesel exhaust particulates in vivo (*30*). In this investigation, an $^{125}$I-labeled variant of pyrene was incorporated in diesel PM (average size, ~200 nm) and administered intratracheally to mice. SPECT imaging and biodistribution experiments revealed that most of the radiolabeled particulates persisted in the lungs (Fig. 3D), reinforcing the dangers of pulmonary exposure in humans. Recently, Li et al. developed a fluorescence imaging method to determine the rate and pattern of $PM_{2.5}$ deposition in murine lung tissue (*31*). Two sizes of fluorescent latex microspheres—0.2 and 2 μm—were used to simulate the small and large components of $PM_{2.5}$ in the air. The deposition patterns were nonuniform, revealing higher rates of deposition in the acinar area than those predicted using the current state-of-the-art deposition model. Pan et al. embarked on the study of another particulate material when they modified $SiO_2$ with ethyl cellulose (*32*). This modification provided a facile route to radioiodination, and $^{131}$I-labeled ethyl cellulose/$SiO_2$ (1.2 μm) was synthesized and administered to rats via inhalation. SPECT images at 6 and 24 h after inhalation showed high initial uptake in the lungs that decreased significantly with time.

### Graphene

Graphene and its derivatives are relative newcomers in biological research. However, their attractive physicochemical properties and high biocompatibility have fueled a rise in their use across several industries. Graphene nanomaterials are 2-dimensional lattices of carbon atoms that, once released into the environment, are prone to aggregation and settlement into sediment layers (*33,34*). It is estimated that the world's production of graphene will reach 3,800 tons by 2027, so gaining an improved understanding of the pollutant's in vivo behavior is of paramount importance. In one study, Jasim et al. functionalized graphene oxide (GO) sheets with DOTA, radiolabeled them with $^{111}$In, and found that the highest levels of accumulation after intravenous injection were in the urine and spleen (*35*). In a follow-up study, the same team investigated the effect of the thickness of graphene on its biodistribution by labeling both thick and thin DOTA-bearing GO sheets with $^{64}$Cu (~0.8 μm in the largest dimension; thin flakes = 4–8 nm thick; thick flakes = 20–50 nm thick) (*34*). The intravenous injection of both variants produced rapid urinary excretion as well as high levels of persistent uptake in the liver and spleen, though the thick sheets accumulated in these tissues more quickly (Fig. 4A). Jasim et al. also investigated the biodistribution profiles of $^{111}$In-labeled GO sheets with 3 different sizes in lateral dimension: 1–35 μm, 30–1,900 nm, and 10–550 nm (*36*). All 3 varieties accumulated in the liver and spleen and were excreted through the urine. Interestingly, however, the largest sheets exhibited lung uptake that was not seen with the smaller variants.

Shifting to other laboratories, Li et al. radiolabeled nanoscale GO (10–800 nm) with $^{125}$I and administered it intratracheally to mice (*37*). SPECT imaging and biodistribution experiments revealed high concentrations of [$^{125}$I]I-nanoscale GO in the lungs at early time points, followed by a gradual decrease over several hours (Fig. 4B). Later, Mao et al. administered $^{14}$C-labeled few-layer graphene (60–590 nm in the largest dimension; 1–4 nm thick) to mice intratracheally and used ex vivo measurements to track its biodistribution over 28 d (*38*). Although the $^{14}$C-labeled few-layer graphene was increasingly excreted via the feces, almost 50% of the dose remained in the lungs after 4 wk. Lu et al. also synthesized $^{14}$C-labeled few-layer graphene but added their construct to water and sediment and subsequently quantified its bioaccumulation and biodistribution in loaches (*M. anguillicaudatus*), a type of freshwater, bottom-dwelling fish that ingests large amounts of sediment and

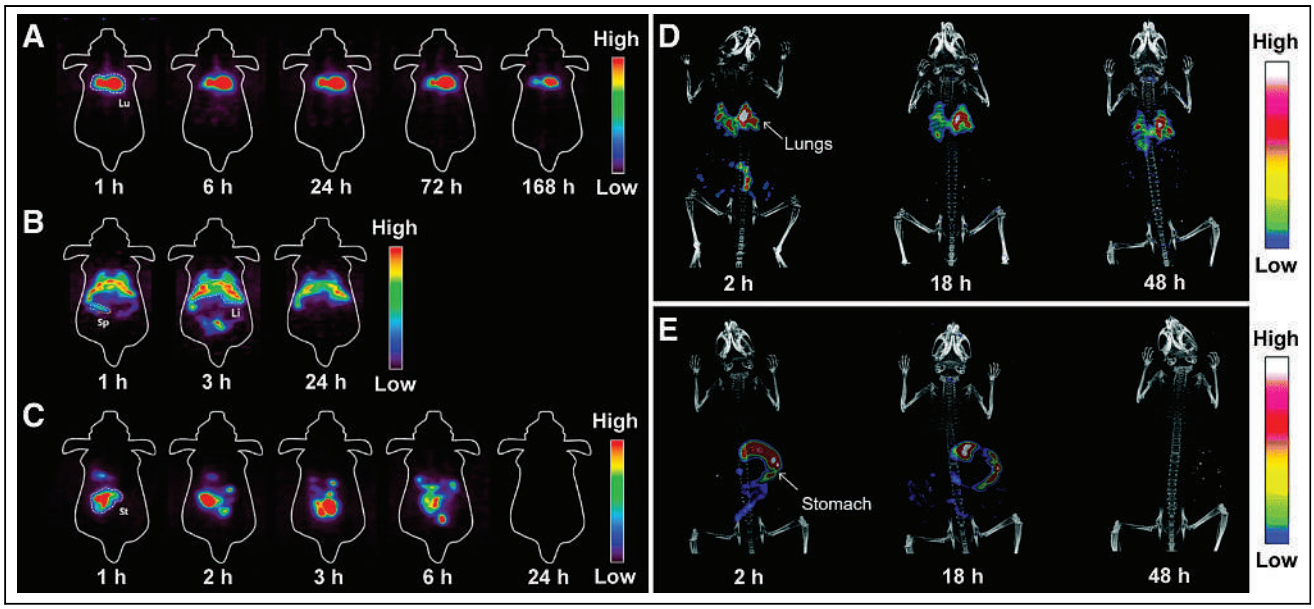


**FIGURE 3.** (A–C) Representative PET images of mice at 168 h after intratracheal administration (A), 24 h after oral administration (B), and 24 h after intravenous injection (C) of [$^{89}$Zr]Zr-desferrioxamine-pyr-diesel PM (1.85 MBq). Li = liver; Lu = lungs; Sp = spleen; St = stomach. (Reprinted with permission of (*3*).) (D–E) Whole-body SPECT/CT images of mice at 2, 18, and 48 h after intratracheal (D) and oral (E) administration of $^{125}$I-labeled diesel exhaust particulates (3.7 MBq) (*30*).

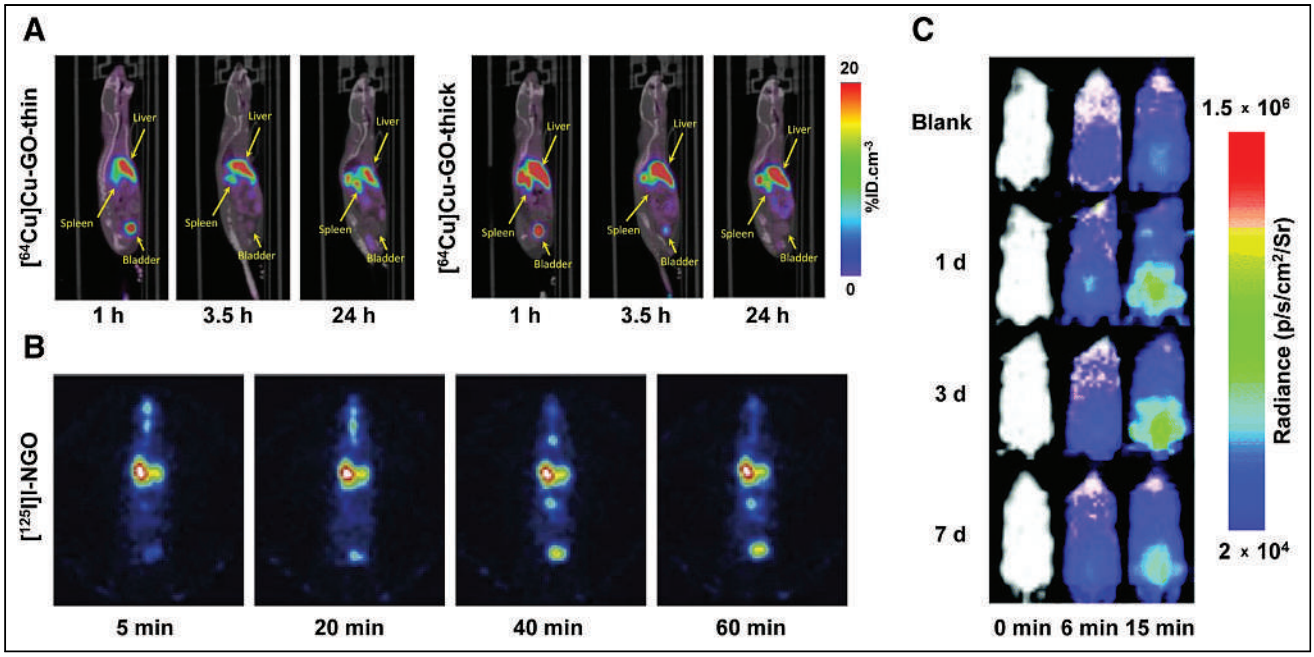


**FIGURE 4.** (A) Whole-body PET/CT images of mice at 1, 3.5, and 24 h after intravenous administration of 2.51–4.55 MBq (50 μg) of [$^{64}$Cu]Cu-GO-thin (left) or [$^{64}$Cu]Cu-GO-thick (right). (Reprinted with permission of (*34*).) (B) SPECT images of mice at 5, 20, 40, and 60 min after intratracheal administration of [$^{125}$I]I-nanoscale GO (1.85 MBq) (*37*). (C) Bioluminescence images of mice at 1, 3, and 7 d after intravenous administration of $Hg^{2+}$ (0.02 μmol) and facilitated using intraperitoneally injected $Hg^{2+}$-sensitive probe. (Reprinted with permission of (*38*).) %ID = percent injected dose.

are consumed by humans and other water-dwelling animals (*33*). After only 72 h in a container with sediment mixed with $^{14}$C-labeled few-layer graphene, radioactivity was found in the gut and liver of the loaches. In a very recent proof-of-principle study, autoradiography and mass spectrometry imaging were used to visualize $^{14}$C-labeled GO particles (50–400 nm, 1 nm thick) in mouse tissue sections 15 min after intravenous injection (*39*). The study validated mass spectrometry imaging as an efficient tool for the determination of the microscopic distribution of GOs. The four organs collected—lungs, liver, spleen, and kidneys—contained more than 96% of the total injected dose, with the highest uptake in the liver (>50% injected dose).

### Other Pollutants

Although much of the research at the intersection of molecular imaging, radiochemistry, and environmental pollutants has focused on the five types of contaminants discussed above, the literature contains a handful of reports in which these techniques have been used to study other pollutants. Al-Sid-Cheikh et al., for example, created $^{110m}$Ag-labeled silver nanoparticles and studied their bioaccumulation in Arctic char via quantitative whole-body autoradiography (*40*). $^{110m}$Ag-labeled silver nanoparticles are widely used in the production of nanomaterials as well as consumer products (*41*). In this study, uptake was observed in several organs on exposure of the fish via three administration methods—waterborne exposure, intravenous injection, and force-feeding—with the highest overall accumulation seen after intravenous exposure. Waterborne exposure, the most environmentally relevant method, yielded accretion levels lower than those produced by the other methods.

Using a dramatically different approach, Ke et al. created a bioluminescence imaging probe for tracking the accumulation of mercury in mice (*42*). Mercury is a naturally occurring environmental pollutant that can cause DNA damage and a wide variety of systemic diseases in humans and animals. The team synthesized a probe that reacts with $Hg^{2+}$ to release luciferin, a substrate for luciferase, resulting in bioluminescence. This $Hg^{2+}$-activated probe was administered intraperitoneally to transgenic FVB-*luc*+ mice—which ubiquitously express firefly luciferase—1, 3, and 7 d after the intravenous injection of $Hg^{2+}$. The noninvasive visualization of the bioluminescence signal provided insight into the accumulation and clearance of $Hg^{2+}$: by 7 d after administration, the $Hg^{2+}$-driven luminescent signal significantly decreased (Fig. 4C).

## CONCLUSION

Despite the efforts of many, environmental pollution is a persistent, stubborn, and—in many cases—worsening problem. Many pollutants pose threats to human health, and thus it is critical to characterize the potential toxicity of these environmental contaminants. An important step in this process is determining where these pollutants go in the body after exposure via different routes. Molecular imaging and radiochemistry can be indispensable in this regard, as they can help determine the pharmacokinetic profiles of pollutants at environmentally relevant doses. As methods for the labeling and tracking of environmental pollutants are disseminated, we expect to see a surge in studies that use molecular imaging to examine these potentially hazardous compounds. Among the methods discussed in this work, we believe that nuclear imaging has the greatest potential. Indeed, the advantages of nuclear imaging include high sensitivity that allows for the interrogation of pollutants at environmentally relevant concentrations, nearly unlimited tissue penetration, the opportunity for long-term longitudinal studies, and a wide array of robust labeling methods using commercially available radionuclides. It is our hope that the pioneering work that we have described here helps usher in a new era in which molecular imaging and radiochemistry become standard tools for the in vivo study of environmental pollutants.

## DISCLOSURE

Financial support was received from the NIH (F31CA275334 to Samantha Delaney; K99ES034053 to Outi Keinänen; and R01CA240963, R01CA204167, and R01CA244327 to Brian Zeglis), the Academy of Finland (331659 to Outi Keinänen), and the Tow Foundation (Joni Sebastiano). No other potential conflict of interest relevant to this article was reported.

## REFERENCES

1. Stapleton PA. Microplastic and nanoplastic transfer, accumulation, and toxicity in humans. *Curr Opin Toxicol.* 2021;28:62–69.
2. López de las Hazas MC, Boughanem H, Dávalos A. Untoward effects of micro- and nanoplastics: an expert review of their biological impact and epigenetic effects. *Adv Nutr.* 2021;13:1310–1323.
3. Park JE, Lee JY, Chae J, et al. In vivo tracking of toxic diesel particulate matter in mice using radiolabeling and nuclear imaging. *Chemosphere.* 2023;313:137395.
4. Manojkumar Y, Pilli S, Rao PV, Tyagi RD. Sources, occurrence and toxic effects of emerging per- and polyfluoroalkyl substances (PFAS). *Neurotoxicol Teratol.* 2023;97:107174.
5. Pietroiusti A, Stockmann-Juvala H, Lucaroni F, Savolainen K. Nanomaterial exposure, toxicity, and impact on human health. *Wiley Interdiscip Rev Nanomed Nanobiotechnol.* 2018;10:e1513.
6. Cresswell T, Metian M, Golding LA, Wood MD. Aquatic live animal radiotracing studies for ecotoxicological applications: addressing fundamental methodological deficiencies. *J Environ Radioact.* 2017;178–179:453–460.
7. Lanctôt CM, Al-Sid-Cheikh M, Catarino AI, et al. Application of nuclear techniques to environmental plastics research. *J Environ Radioact.* 2018;192:368–375.
8. Lee JY, Mushtaq S, Park JE, Shin HS, Lee SY, Jeon J. Radioanalytical techniques to quantitatively assess the biological uptake and in vivo behavior of hazardous substances. *Molecules.* 2020;25:3985.
9. Fan Y, Pan D, Yang M, Wang X. Radiolabelling and in vivo radionuclide imaging tracking of emerging pollutants in environmental toxicology: a review. *Sci Total Environ.* 2023;866:161412.
10. Deng Y, Zhang Y, Lemos B, Ren H. Tissue accumulation of microplastics in mice and biomarker responses suggest widespread health risks of exposure. *Sci Rep.* 2017;7:46687.
11. Fournier SB, D'Errico JN, Adler DS, et al. Nanopolystyrene translocation and fetal deposition after acute lung exposure during late-stage pregnancy. *Part Fibre Toxicol.* 2020;17:55.
12. Pitt JA, Kozal JS, Jayasundara N, et al. Uptake, tissue distribution, and toxicity of polystyrene nanoparticles in developing zebrafish (*Danio rerio*). *Aquat Toxicol.* 2018;194:185–194.
13. van Pomeren M, Brun NR, Peijnenburg WJGM, Vijver MG. Exploring uptake and biodistribution of polystyrene (nano)particles in zebrafish embryos at different developmental stages. *Aquat Toxicol.* 2017;190:40–45.
14. Al-Sid-Cheikh M, Rowland SJ, Kaegi R, Henry TB, Cormier M-A, Thompson RC. Synthesis of $^{14}$C-labelled polystyrene nanoplastics for environmental studies. *Commun Mater.* 2020;1:97.
15. Al-Sid-Cheikh M, Rowland SJ, Stevenson K, Rouleau C, Henry TB, Thompson RC. Uptake, whole-body distribution, and depuration of nanoplastics by the scallop *Pecten maximus* at environmentally realistic concentrations. *Environ Sci Technol.* 2018;52:14480–14486.
16. Keinänen O, Dayts EJ, Rodriguez C, et al. Harnessing PET to track micro- and nanoplastics in vivo. *Sci Rep.* 2021;11:11463.
17. Im C, Kim H, Zaheer J, et al. PET tracing of biodistribution for orally administered $^{64}$Cu-labeled polystyrene in mice. *J Nucl Med.* 2022;63:461–467.
18. Boswell CA, Sun X, Niu W, et al. Comparative in vivo stability of copper-64-labeled cross-bridged and conventional tetraazamacrocyclic complexes. *J Med Chem.* 2004; 47:1465–1474.
19. Munir M, Sholikhah UN, Lestari E, et al. Iodine-131 radiolabeled polyvinylchloride: a potential radiotracer for micro and nanoplastics bioaccumulation and biodistribution study in organisms. *Mar Pollut Bull.* 2023;188:114627.
20. Ehsan MN, Riza M, Pervez MN, Khyum MMO, Liang Y, Naddeo V. Environmental and health impacts of PFAS: sources, distribution and sustainable management in North Carolina (USA). *Sci Total Environ.* 2023;878:163123.
21. Uhl M, Schoeters G, Govarts E, et al. PFASs: what can we learn from the European Human Biomonitoring Initiative HBM4EU. *Int J Hyg Environ Health.* 2023; 250:114168.
22. Bogdanska J, Borg D, Sundström M, et al. Tissue distribution of $^{35}$S-labelled perfluorooctane sulfonate in adult mice after oral exposure to a low environmentally relevant dose or a high experimental dose. *Toxicology.* 2011;284:54–62.
23. Bartels JL, Aweda TA, Rosenberg AJ, Lunderberg DM, Peaslee GF, Lapi SE. Radiosynthesis and biological distribution of $^{18}$F-labeled perfluorinated alkyl substances. *Environ Sci Technol Lett.* 2017;4:211–215.
24. Borg D, Bogdanska J, Sundström M, et al. Tissue distribution of $^{35}$S-labelled perfluorooctane sulfonate (PFOS) in C57Bl/6 mice following late gestational exposure. *Reprod Toxicol.* 2010;30:558–565.
25. Bartels JL, Fernandez SR, Aweda TA, et al. Comparative uptake and biological distribution of [$^{18}$F]-labeled C6 and C8 perfluorinated alkyl substances in pregnant mice via different routes of administration. *Environ Sci Technol Lett.* 2020;7:665–671.
26. Pérez-Campaña C, Gómez-Vallejo V, Martin A, et al. Tracing nanoparticles in vivo: a new general synthesis of positron emitting metal oxide nanoparticles by proton beam activation. *Analyst.* 2012;137:4902–4906.
27. Pérez-Campaña C, Gómez-Vallejo V, Puigivila M, et al. Biodistribution of different sized nanoparticles assessed by positron emission tomography: a general strategy for direct activation of metal oxide particles. *ACS Nano.* 2013;7:3498–3505.
28. Pérez-Campaña C, Sansaloni F, Gómez-Vallejo V, et al. Production of $^{18}$F-labeled titanium dioxide nanoparticles by proton irradiation for biodistribution and biological fate studies in rats. *Part Part Syst Charact.* 2014;31:134–142.
29. Yang L, Sundaresan G, Sun M, et al. Intrinsically radiolabeled multifunctional cerium oxide nanoparticles for in vivo studies. *J Mater Chem B.* 2013;1:1421–1431.
30. Lee CH, Shim HE, Song L, et al. Efficient and stable radiolabeling of polycyclic aromatic hydrocarbon assemblies: in vivo imaging of diesel exhaust particulates in mice. *Chem Commun (Camb).* 2019;55:447–450.
31. Li D, Li Y, Li G, Zhang Y, Li J, Chen H. Fluorescent reconstitution on deposition of $PM_{2.5}$ in lung and extrapulmonary organs. *Proc Natl Acad Sci USA.* 2019;116: 2488–2493.
32. Pan D-H, Sheng J, Wang X-Y, et al. In vivo SPECT imaging of an $^{131}$I-labeled $PM_{2.5}$ mimic substitute. *Nucl Sci Tech.* 2020;31:111.
33. Lu K, Zha Y, Dong S, et al. Uptake route altered the bioavailability of graphene in *Misgurnus anguillicaudatus*: comparing waterborne and sediment exposures. *Environ Sci Technol.* 2022;56:9435–9445.
34. Jasim DA, Boutin H, Fairclough M, et al. Thickness of functionalized graphene oxide sheets plays critical role in tissue accumulation and urinary excretion: a pilot PET/CT study. *Appl Mater Today.* 2016;4:24–30.
35. Jasim DA, Ménard-Moyon C, Bégin D, Bianco A, Kostarelos K. Tissue distribution and urinary excretion of intravenously administered chemically functionalized graphene oxide sheets. *Chem Sci.* 2015;6:3952–3964.
36. Jasim DA, Newman L, Rodrigues AF, et al. The impact of graphene oxide sheet lateral dimensions on their pharmacokinetic and tissue distribution profiles in mice. *J Control Release.* 2021;338:330–340.
37. Li B, Yang J, Huang Q, et al. Biodistribution and pulmonary toxicity of intratracheally instilled graphene oxide in mice. *NPG Asia Mater.* 2013;5:e44.
38. Mao L, Hu M, Pan B, Xie Y, Petersen EJ. Biodistribution and toxicity of radiolabeled few layer graphene in mice after intratracheal instillation. *Part Fibre Toxicol.* 2016;13:7.
39. Cazier H, Malgorn C, Georgin D, et al. Correlative radioimaging and mass spectrometry imaging: a powerful combination to study $^{14}$C-graphene oxide in vivo biodistribution. *Nanoscale.* 2023;15:5510–5518.
40. Al-Sid-Cheikh M, Rouleau C, Bussolaro D, Oliveira Ribeiro CA, Pelletier E. Tissue distribution of radiolabeled $^{110m}$Ag nanoparticles in fish: Arctic charr (*Salvelinus alpinus*). *Environ Sci Technol.* 2019;53:12043–12053.
41. Istiqola A, Syafiuddin A. A review of silver nanoparticles in food packaging technologies: regulation, methods, properties, migration, and future challenges. *J Chin Chem Soc (Taipei).* 2020;67:1942–1956.
42. Ke B, Chen H, Ma L, et al. Visualization of mercury(II) accumulation in vivo using bioluminescence imaging with a highly selective probe. *Org Biomol Chem.* 2018; 16:2388–2392.

# Evaluation of [$^{68}$Ga]-DOTATOC PET/MRI in Patients with Meningioma of the Subcranial and Intraorbital Space

Aleksandar Milosevic[1], Hanna Styczen[1], Johannes Grueneisen[1], Yan Li[1], Manuel Weber[2], Wolfgang P. Fendler[2], Julian Kirchner[3], Philipp Damman[4], Karsten Wrede[4], Lazaros Lazaridis[5], Martin Glas[5], Maja Guberina[6], Anja Eckstein[7], Tobias Blau[8], Ken Herrmann[2], Lale Umutlu[1], Michael Forsting[1], Cornelius Deuschl*[1], and Benedikt Schaarschmidt*[1]

[1]*Institute of Diagnostic and Interventional Radiology and Neuroradiology, University Hospital Essen, Düsseldorf, Germany;* [2]*Department of Nuclear Medicine, University Hospital Essen, Düsseldorf, Germany;* [3]*Institute of Radiology, University Hospital Düsseldorf, Düsseldorf, Germany;* [4]*Department of Neurosurgery and Spine Surgery, University Hospital Essen, Düsseldorf, Germany;* [5]*Department of Neurology and Neurooncology, University Hospital Essen, Düsseldorf, Germany;* [6]*Department of Radiotherapy, University Hospital Essen, Düsseldorf, Germany;* [7]*Department of Ophthalmology, University Hospital Essen, Düsseldorf, Germany; and* [8]*Department of Neuropathology, University Hospital Essen, Düsseldorf, Germany*

Meningiomas are known to express somatostatin receptor (SSTR) type 2 to a high degree. Therefore, radiolabeled somatostatin analogs, such as DOTATOC, have been introduced for PET imaging of meningiomas. However, the benefit of hybrid SSTR PET/MRI is still debated. Here, we report our experience with [$^{68}$Ga]-DOTATOC PET/MRI. **Methods:** PET/MRI was performed in 60 patients with suspected or diagnosed meningiomas of the skull plane and eye socket. Acquired datasets were reported by 2 independent readers regarding local tumor extent and signal characteristics. Histopathologic results and follow-up imaging served as the reference standard. SUVs of target lesions were analyzed according to the corresponding maximal tracer uptake. The diagnostic accuracy of PET/MRI and conventional MRI was determined independently and compared with the reference standard. **Results:** In total, 60 target lesions were identified, with 54 considered to be meningiomas according to the reference standard. Sensitivity and specificity of PET/MRI versus MRI alone were 95% versus 96% and 75% versus 66%, respectively. The McNemar test was not able to distinguish any differences between PET/MRI and the reference standard or MRI and the reference standard. No differences were found between the 2 modalities with respect to local infiltration. **Conclusion:** SSTR PET/MRI and MRI yielded similar accuracy for the detection of meningiomas of the skull base and intraorbital space. Here, sequential low-dose SSTR PET/CT might be helpful for the planning of radioligand therapy or radiotherapy.

**Key Words:** meningioma; oncologic imaging; DOTATOC; somatostatin receptor ligands; PET

**J Nucl Med 2023; 64:1185–1190**
DOI: 10.2967/jnumed.123.265424

Meningiomas are the most common tumors of the meninges and account for 25%–34% of all primary neurocranial tumors, with an estimated annual incidence ranging from 7.62 cases out of 100,000 people to 97.5 cases out of 100,000 people in the United States (*1,2*). Although mostly regarded as benign tumors, atypical or anaplastic meningiomas usually bear a higher rate of mutation and can display more aggressive characteristics (*3*). Clinical symptoms depend on the primary location and the consecutive compression or, rather rarely, infiltration of adjacent structures (*4*). Therefore, the accurate depiction of the tumor and its surroundings is key to a successful treatment, especially in anatomically complex regions such as the skull base. Due to excellent soft-tissue contrast and, in many cases, characteristic radiographic features, MRI is the current gold standard in meningioma diagnostics (*5*). However, the value of MRI is limited in select cases, especially if infiltration of the skull base or the cavernous sinus is suspected (*6*). Therefore, molecular imaging, most notably PET using tracer ligands bound to the somatostatin receptor subtype 2 ($SSTR_2$), is progressively considered to be an important adjunct in the diagnosis and therapeutic planning of meningiomas (*7,8*). $SSTR_2$ is a surface antigen that is expressed to a particularly high degree in meningiomas (*9*). Our institution has used the $^{68}$Ga-labeled somatostatin analog DOTATOC successfully because it features more favorable imaging characteristics than its predecessors (*10*). In terms of diagnostic accuracy, [$^{68}$Ga]-DOTATOC possesses properties similar to those of its [$^{68}$Ga]-DOTATATE counterpart (*11*). The introduction of modern PET/MRI systems into clinical practice has led to considerable advantages in neuroradiologic imaging (*12–14*). PET/MRI combines the high-resolution properties of MRI with molecular information derived from the PET dataset. Current studies emphasize the superiority of PET/MRI when compared with conventional MRI or PET/CT. According to the published literature, PET/MRI enhances delineation of tumor margins and has become a potential adjunct in pretreatment planning (*7,8,15*). In the present study, we evaluate the diagnostic accuracy of integrated [$^{68}$Ga]-DOTATOC PET/MRI for meningiomas of the skull base and the orbital space compared with the accuracy with MRI, which is the current gold standard.

## MATERIALS AND METHODS

### Patients and Reference Standard

This study was approved by the local ethics committee in accordance with the declaration of Helsinki (application number 22-10703-BO, approval date May 23, 2022). The requirement to obtain informed consent was waived because of its retrospective design.

Received Jan. 9, 2023; revision accepted Apr. 20, 2023.
For correspondence or reprints, contact Aleksandar Milosevic (aleksandar.milosevic@uk-essen.de).
*Contributed equally to this work.
Published online Jun. 29, 2023.

Patients who underwent [$^{68}$Ga]-DOTATOC PET/MRI for initial tumor or recurrence diagnostics of meningioma from August 2012 to April 2022 were included in this analysis. Because histologic sampling is not always available during meningioma treatment, a combined reference standard including histopathologic workup as well as imaging follow-up as proposed in the literature was used in the present study (*16*). Clinical information and data regarding treatment and the course of disease were obtained from digital patient files.

### PET/MRI

The examination was performed 45 ± 25 min after intravenous injection with a mean activity of 79 ± 21 MBq [$^{68}$Ga]-DOTATOC. All PET/MRI scans were performed on a 3-T Biograph mMR (Siemens Healthineers). The scan ranged from the skull cap to the neck. Using a dedicated 20-channel radiofrequency coil for the head area, we performed diagnostic MRI in parallel with a PET scan in list mode without respiratory gating (1 bed position, 20 min per bed position). Parallel imaging (generalized autocalibrating partially parallel acquisitions, acceleration factor 2) was used. PET images were reconstructed using the 3-dimensional ordered-subsets expectation-maximization method (3 iterations, 21 subsets, gaussian filter of 4 mm in full width at half maximum, 344 × 344 matrix size). Attenuation correction of PET data was performed by implementing a 4-compartment-model map, calculated from obtained Dixon sequences. MRI protocols are displayed in Supplemental Table 1 (supplemental materials are available at http://jnm.snmjournals.org).

### Image Analysis

Examinations were reviewed in random order by 2 radiologists with more than 2 y of experience in hybrid imaging using a dedicated viewing software for hybrid imaging (Syngo.Via; Siemens Healthineers). Both readers were unaware of the tumor location, histopathologic results, and consecutive therapy. In the first session, readers were instructed to identify meningioma on the basis of clinically established features as proposed by the meningioma task force of the European Association of Neuro-Oncology. These criteria include an isointense signal on T1-weighted sequences, a hyperintense signal on T2-weighted sequences, a strong contrast enhancement, and the presence of a dural tail at the perimeter of the target lesions (*5*). To evaluate the tumor size, transversal and coronal contrast-enhanced T1-weighted images were used. PET/MR images were analyzed in a second assessment 4 wk later to avoid recognition bias. SUVs ($SUV_{max}$, $SUV_{peak}$, and $SUV_{mean}$) were measured by implementation of an isocontour volume of interest, with a threshold level at 40% of the maximal uptake (Fig. 1). Both readers assessed PET datasets qualitatively. As proposed elsewhere (*17*), an $SUV_{max}$ of 2.3 or greater was considered indicative of meningioma. Furthermore, sites of tumor infiltration were evaluated during both assessments. Tumoral infiltration was assumed if one of the following criteria was met: there was morphologically visible infiltration of a surrounding structure, cuffing of a surrounding structure, visible compression of a surrounding structure, an atypically increased tracer uptake of the surrounding structures (valid only for PET/MRI; threshold, $SUV_{max}$, 2.3). The following structures were identified as relevant sites of infiltration: optic chiasm, contra- and ipsilateral optical nerve, contra- and ipsilateral internal carotid artery (ICA), pituitary fossa, and cavernous sinus. A Likert scale was used by the readers to assess the readers' certainty (ranging from 1 being absolutely certain to 6 being absolutely uncertain). Consensus reading of both readers in combination with provided clinical reports and follow-up imaging served as the reference standard for infiltration.

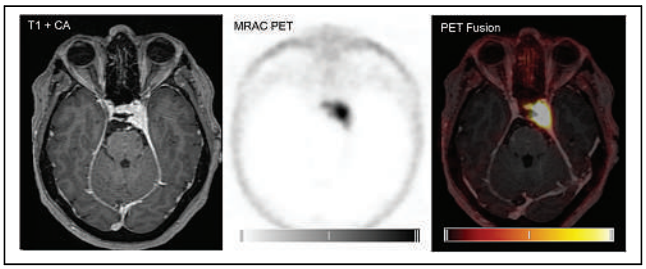


**FIGURE 1.** [$^{68}$Ga]-DOTATOC uptake in sphenoid wing meningioma. CA = contrast agent; MRAC = MR-based attenuation correction.

### Statistical Analysis

Diagnostic accuracy was calculated for MRI (first assessment) and PET/MRI (second assessment) in relation to the reference standard and compared using the McNemar test. Additionally, sensitivity, specificity, positive predictive value, and negative predictive value were calculated for each modality. Item scores were calculated using the provided Likert scales to depict certainty in the estimation of tumor infiltration. Likert scales were then compared by a Mann–Whitney *U* test. Cohen κ coefficient was calculated for both diagnosis and infiltration conspicuity to estimate the interreader variability. *P* values of 0.05 or less were considered to be statistically significant.

Excel 2013 (Microsoft Corp.) and SPSS Statistics 28 (IBM Technology Corp.) were used for statistical analysis.

## RESULTS

### Patients

Sixty patients (78% female [46/60]; 22% male [14/60], mean age, 57.1 ± 15.0 y) were subsequently included in our retrospective analysis. All patients suspected of recurrence of meningioma ($n$ = 14) had been treated at the primary diagnosis. Histopathologic assessment was available in 33.3% (20/60) of the cases after biopsy or resection. Follow-up MRI was performed at a median time point of 10.7 mo after the initial PET/MRI. Histopathologic analysis confirmed meningioma in 23.3% (14/60) of the cases. Histologic subtypes are displayed in Table 1. Seven percent (4/60) of patients displayed B-cell–type lymphoma, 5% (3/60) displayed marginal cell lymphoma, and 2% (1/60) displayed diffuse large B-cell lymphoma. Furthermore, sampling found cavernous venous malformation in 1 patient and lymphoid hyperplasia in another patient. Measured SUVs of lesions are displayed in Table 2. At the time point of data analysis, therapy for meningioma was concluded in 43 patients. In 16 cases, primary or partial surgical resection was performed. Four patients with involvement of the optic nerve received optic decompression. Thirty-nine patients received primary or adjuvant radiation therapy. Radionuclide therapy with $^{177}$Lu- or $^{90}$Y-DOTATOC was conducted in 5 patients.

**TABLE 1**
Distribution of Patients According to Histopathologic Sampling

| Histology | Number of patients with primary lesion | Number of patients with recurrent lesion |
|---|---|---|
| Meningothelial (WHO I) | 8.3% (5/60) | 10.0% (6/60) |
| Choroidal differentiation (WHO II) | 1.6% (1/60) | 0.0% (0/60) |
| Atypical (WHO II) | 0.0% (0/60) | 3.3% (2/60) |
| Other | 10.0% (6/60) | 0.0% (0/60) |

WHO = World Health Organization.

**TABLE 2**
SUV Analysis

| Group | Subtype | *n* | $SUV_{max}$ | $SUV_{peak}$ | $SUV_{mean}$ |
|---|---|---|---|---|---|
| All patients | Total | 60 | 12.9 | 9.4 | 5.9 |
| Meningioma | Total | 54 | 14.0 | 10.2 | 6.4 |
| | OSM | 20 | 6.2 | 4.2 | 3.8 |
| | SWM | 18 | 25.0 | 18.6 | 8.9 |
| | Other* | 16 | 11.4 | 8.3 | 6.9 |
| Nonmeningioma | Total | 6 | 2.5 | 1.9 | 1.5 |
| | MCL | 3 | 1.7 | 1.4 | 1.0 |
| | DLBCL | 1 | 3.6 | 2.9 | 2.2 |
| | CVM | 1 | 4.3 | 3.0 | 2.6 |
| | LH | 1 | 1.8 | 1.2 | 1.0 |

*Cavernous sinus, petroclival junction, planum sphenoidale.
OSM = optic sheath meningioma; SWM = sphenoid wing meningioma; MCL = marginal cell lymphoma; DLBCL = diffuse large B-cell lymphoma; CVM = cavernous venous malformation; LH = lymphoid hyperplasia.

### Lesion Detection

Sixty target lesions were identified, with 54 considered to be meningiomas according to the reference standard. Mean values for the maximal diameter of observed lesions was 2.7 ± 1.4 cm. Both PET/MRI and MRI detected all of the above-mentioned lesions. According to both reading sessions, MRI and PET/MRI misidentified meningioma as nonmeningioma in 3.7% (2/54) of patients. In contrast, MRI falsely diagnosed meningioma in 2 patients, and PET/MRI falsely diagnosed meningioma in 3 patients (Table 3). On the basis of this observation, we confirmed a sensitivity of 95%, a specificity of 75%, a positive predictive value of 98%, and a negative predictive value of 50% with PET/MRI and a sensitivity of 96%, a specificity of 66%, a positive predictive value of 96%, and a negative predictive value of 66% with MRI (Table 4). Diagnostic accuracy was 93% for both MRI and PET/MRI. The McNemar test was not able to discriminate any significant differences between PET/MRI and the reference standard ($P = 0.625$) or MRI and the reference standard ($P = 1.0$).

### Tumor Infiltration

Only 1 lesion (2%) displayed no signs of local invasion related to the above-mentioned criteria. According to MRI, invasion of the optic chiasm was found in 28% (16/60) of patients. The ipsilateral and contralateral optic nerves were affected in 85% (51/60) and 15% (9/60) of patients, respectively. PET/MRI confirmed infiltration of the optic chiasm in 30% (18/60) of patients and infiltration of the ipsilateral and contralateral optic nerves in 87% (52/60) and 15% (9/60) of patients, respectively. No differences were found between the 2 modalities concerning the infiltration of the pituitary fossa (60% [24/60]) and ipsilateral ICA (57% [34/60]). MRI found infiltration of contralateral ICA in 15% (9/60) of patients. In PET/MRI, infiltration of contralateral ICA was visible in 12% (7/60) of patients. Infiltration of the cavernous sinus was diagnosed in 57% (34/60) of patients by both MRI and PET/MRI. Rates of infiltration are displayed in Figure 2. Both readers were able to provide safe assumptions for infiltration in both assessments, according to the calculated item scores. Readouts for both MRI and PET/MRI achieved high confidence with respect to infiltration of surrounding structures. Mean item scores assumed a value between 1.0 (absolutely certain) and 2.0 (certain). Comparison of Likert scales via a Mann–Whitney *U* test revealed no significant differences in the assessment of infiltration between PET/MRI and MRI ($P > 0.05$). Interreader agreement is displayed in Supplemental Table 2.

## DISCUSSION

This retrospective study investigated our institutional experience with [$^{68}$Ga]-DOTATOC PET/MRI of meningiomas of the skull base. During our analysis, we were able to make one key observation. The inclusion of [$^{68}$Ga]-DOTATOC PET in a dedicated MRI protocol did not significantly improve the detection and differentiation of meningioma and nonmeningioma lesions. In fact, true-negative ratings were slightly lower than those of conventional MRI.

The implementation of somatostatin receptor (SSTR)–avid diagnostic radioligands such as [$^{68}$Ga]-DOTATOC into imaging workflows has been proven to facilitate the diagnosis of meningioma by providing additional information on SSTR density (*18,19*). Thus, hybrid imaging has rightfully established its position in high-quality diagnostics of meningioma and subsequent therapy planning (*19,20*). For instance, published data demonstrated a significantly improved detection of osseous infiltration in SSTR PET/CT when compared with detection with conventional contrast-enhanced MRI (*21*).

**TABLE 3**
Detection of Suspected Meningioma in MRI and PET/MRI

| | MRI | | | | PET/MRI | | | |
|---|---|---|---|---|---|---|---|---|
| Parameter | Total | OSM | SWM | Other* | Total | OSM | SWM | Other* |
| True positive | 52 | 18 | 18 | 16 | 53 | 19 | 18 | 16 |
| False positive | 2 | 2 | 0 | 0 | 3 | 3 | 0 | 0 |
| True negative | 4 | 4 | 0 | 0 | 3 | 3 | 0 | 0 |
| False negative | 2 | 2 | 0 | 0 | 1 | 1 | 0 | 0 |
| Total | 60 | 26 | 18 | 16 | 60 | 26 | 18 | 16 |

*Cavernous sinus, petroclival junction, planum sphenoidale.
OSM = optic sheath meningioma; SWM = sphenoid wing meningioma.

**TABLE 4**
Determined Values for Sensitivity, Specificity, Positive Predictive Value, and Negative Predictive Value

| | MRI (%) | | | | PET/MRI (%) | | | |
|---|---|---|---|---|---|---|---|---|
| Parameter | Total | OSM | SWM | Other* | Total | OSM | SWM | Other* |
| Sensitivity | 96 | 90 | 100 | 100 | 95 | 86 | 100 | 100 |
| Specificity | 66 | 67 | 100 | 100 | 75 | 75 | 100 | 100 |
| PPV | 96 | 90 | 100 | 100 | 98 | 95 | 100 | 100 |
| NPV | 66 | 67 | 100 | 100 | 50 | 50 | 100 | 100 |

*Cavernous sinus, petroclival junction, planum sphenoidale.
OSM = optic sheath meningioma; SWM = sphenoid wing meningioma.

Furthermore, hybrid imaging inherently influences treatment planning by enhancing delineation of meningioma volume before radiation therapy (*22*). Despite the overall outstanding diagnostic performance of PET/CT, its clinical application is limited because of potential adverse effects from ionizing radiation (*23*). Further limitations result from the confined range of β-radiation inside the tissue, which may produce inherent blurs in the imaging of intracranial structures. This is especially true for the skull base, a region of high anatomic complexity (*24*). Hence, the introduction of dedicated and simultaneously acquired PET/MRI datasets has positively influenced diagnostic security and enabled accurate depiction of morphologic relations. This is confirmed in established literature by a direct comparison of the diagnostic performance of PET/CT and PET/MRI, highlighting the superior sensitivity and specificity of PET/MRI (*18,25*). Further studies investigated additional benefits of PET/MRI in the diagnosis of meningiomas. A recently published study was able to accentuate the relevance of PET/MRI regarding therapeutic planning and differentiation of scar tissue versus a residual tumor (*26*). However, the current guideline on diagnosis and management of meningioma of the European Association of Neuro-Oncology lists MRI as the gold standard in initial and follow-up imaging of meningioma. According to the European Association of Neuro-Oncology guideline, PET imaging is recommended if the extension of meningioma or the diagnosis itself is uncertain (recommendation level C) (*5*). Although published data favor PET/MRI over PET/CT or conventional MRI, the limited availability of PET/MRI fuels debate about its actual clinical significance. However, further factors play a prominent role in this debate as well. Physiologic $SUV_{max}$ in [$^{68}$Ga]-DOTATOC imaging shows large intra- and interindividual differences as well as very heterogeneous distribution patterns (*27*). Kim et al. demonstrated that appropriate cutoff values for PET-assisted diagnosis of meningiomas still remain controversial and uncertain. They proposed an $SUV_{ratio}$ relative to the superior sagittal sinus with a threshold at 3.2, which may provide an optimal level of sensitivity (*26*). Rachinger et al. proposed a cutoff value at 2.3 for $SUV_{max}$ to discriminate between meningioma and nonmeningioma tissues (*17*).

In imaging of meningioma of the skull base, evidence regarding the clinical value of [$^{68}$Ga]-DOTATOC PET/MRI is still lacking. However, our results do not show a significant benefit for PET/MRI in this diagnostic scenario because sensitivity, specificity, positive predictive value, negative predictive value, and diagnostic accuracy displayed similar results. However, the specificity of PET/MRI was slightly superior (75%) to that of MRI (66%). These findings agree with previous studies on PET imaging of meningioma. Rachinger et al. provided comparable values for sensitivity (90%) and specificity (73%) in their DOTATATE PET assessment at a threshold of 2.3 for $SUV_{max}$ (*17*). At the same time, Kim et al. observed lower values for sensitivity (78%) while maintaining high values for specificity (98%) in their assessment (threshold, $SUV_{max}$, 4.7) (*26*). However, due to the different properties of DOTATOC and DOTATATE, a direct comparison with the above-mentioned studies is limited, although substantial differences in terms of diagnostic quality have not been demonstrated yet (*28,29*). As observed in our cohort, mischaracterization of lymphoma still poses a challenge in SSTR PET–assisted imaging. Individual studies have already demonstrated immunopositivity of lymphoma cells for $SSTR_2$, especially for diffuse large B-cell lymphoma subtypes (*30,31*). As observed in our cohort,

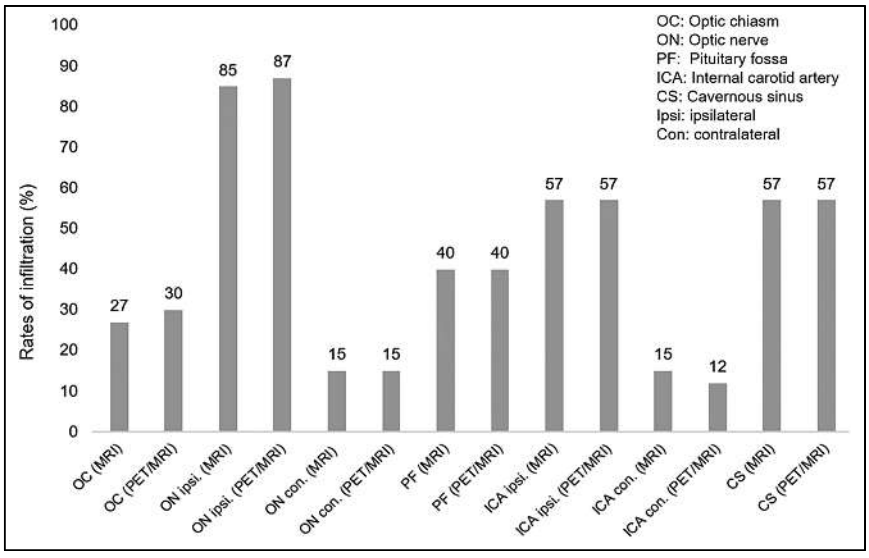


**FIGURE 2.** Rates of infiltration as detected by MRI and PET/MRI.

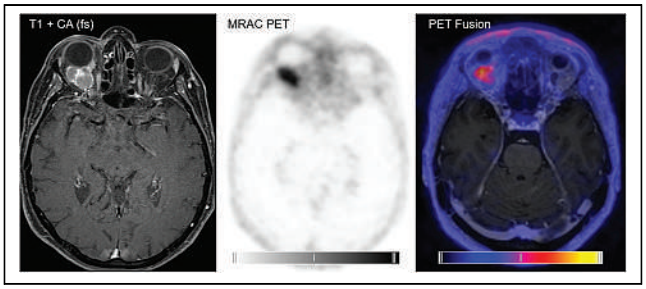


**FIGURE 3.** [$^{68}$Ga]-DOTATOC uptake in diffuse large B-cell lymphoma of right orbital space. CA = contrast agent; fs = fat saturation; MRAC = MR-based attenuation correction.

$SSTR_2$-positive lymphoma may mimic meningioma and lead to a false diagnosis (Fig. 3). Significantly increased tracer uptake was also found in a patient with a cavernous venous malformation of the intraconal space ($SUV_{max}$, 4.3). Cavernous venous malformations are among the most common benign intraorbital lesions in adults (*32*). The literature shows examples of hemangiomas and vascular formations in other locations that have shown increased tracer uptake in [$^{68}$Ga]-DOTATOC PET, most likely due to blood pooling (*33,34*).

Comparably, false positives and false negatives also predominantly involved suspected optic sheath meningioma in the MRI assessment. Atypical MRI signaling of 2 lesions in the course of the optic nerve evaluation led to misidentification of histologically proven optic sheath meningioma. Furthermore, MRI failed to expose the intraorbital cavernous venous malformation because it displayed characteristics of atypical meningioma. Another lesion could not be assigned definitively to a specific entity on MRI and was therefore wrongfully interpreted as atypical meningioma. This patient was later diagnosed with lymphoproliferative hyperplasia. This tumor can display morphologic similarity to optic sheath meningioma, especially considering its homogeneous contrast enhancement. Just as in the PET/MRI assessment, misdiagnoses in the MRI assessment were exclusively related to intraorbital tumors. Although malignant and benign lesions of the orbital space can be well differentiated on the basis of morphologic characteristics on cross-sectional imaging (*35*), pretherapeutic baseline imaging cannot replace surgical assessment for diagnostic differentiation (*36*). As the example of Tolosa–Hunt syndrome shows, space-occupying lesions in this area are difficult to differentiate morphologically and therefore often require further diagnostic measures (*37*). Hence, imaging of intraorbital lesions should be considered primarily for treatment planning and secondarily for confirmation of diagnosis.

Infiltration and compression of surrounding structures such as the cavernous sinus or ICA have a major impact on therapeutic planning and the eligibility for a surgical approach (*6,38*). Therefore, imaging must provide reliable information on contacts and infiltration of the neighboring structures. In particular, infiltration of the cavernous sinus is difficult to assess with MRI. Although PET/MRI provided us with complementary information on tumor characteristics, it did not provide a significant advantage for tumor infiltration when compared with the results from MRI in our study. Specifically, SSTR positivity of the pituitary gland posed a source of error in the evaluation of this region. Nevertheless, SSTR PET can be beneficial in therapeutic planning because of supplementary information gained by PET and improved delineation of tumor margins (*20,22,39*). The visualization of the $SSTR_2$ status is the basic requirement for radioligand therapy (*40*). Despite there being no current consensus on the detailed dosage and administration modality of peptide-receptor radioligand therapy in meningioma patients, SSTR PET has to be considered an important asset in the process of treatment planning of meningiomas and should therefore be widely available (*41*). This is particularly relevant for patients with inoperable meningiomas at the skull base. Due to the limited availability of PET/MRI, a 2-step approach consisting of a diagnostic MRI and a sequential low-dose PET/CT could provide a practical and cost-sensitive approach in such cases or in equivocal findings in morphologic imaging alone. Integrated [$^{68}$Ga]-DOTATOC PET/MRI should be reserved for tertiary care centers or clinical studies.

One of the limiting factors of our study was its retrospective characteristic. MRI protocols changed over the time span of the investigation, thus leading to slight alterations in imaging results. In particular, limited access to histopathologic data proved to be challenging for our evaluation. Additionally, there were no histopathologic data available to us with which to correlate the image features of infiltration and the actual infiltration. Surgical specimens of all suspected lesions would have been desirable as a reliable reference standard. However, current guidelines do not require histologic confirmation of meningioma before the initiation of therapy (*5*). Additionally, because our focus was on the skull base, most analyzed lesions were difficult to access. The risk of complications outweighed the benefit of histologic confirmation. In accordance with previous studies, the reference standard was composed of the available histopathologic data and cross-sectional imaging, including follow-up examinations.

## CONCLUSION

Our results demonstrate the comparable diagnostic performance of conventional MRI and [$^{68}$Ga]-DOTATOC PET/MRI for the detection and evaluation of meningioma of the skull plane and orbital space. However, PET assessment can give supplementary information on therapy-relevant factors. Furthermore, it provides the basis for radionuclide therapy by quantifying SSTR expression of meningioma. To optimize the acquisition of diagnostic information, we propose the inclusion of a 2-step approach consisting of high-quality MRI and sequential low-dose SSTR PET/CT in equivocal cases or before peptide-receptor radioligand therapy or radiotherapy.

## DISCLOSURE

Aleksandar Milosevic has received travel grants from Bayer AG. Wolfgang Fendler reports fees from SOFIE Biosciences (research funding), Janssen (consultant, speaker), Calyx (consultant), Bayer (consultant, speaker, research funding), Parexel (image review), Novartis (speaker), and Telix (speaker) outside of the submitted work. Manuel Weber reports fees from Boston Scientific, Terumo, Advanced Accelerator Applications, and Eli Lilly outside of the submitted work. Lazaros Lazaridis received honoraria and travel support from Novocure. Benedikt Schaarschmidt received report fees from AstraZeneca (speaker), PharmaCept (research grant), and the Else-Kröner-Fresenius foundation (research grant). No other potential conflict of interest relevant to this article was reported.

**KEY POINTS**

**QUESTION:** Are there any significant benefits of implementing SSTR PET/MRI into diagnostic workflows of meningioma patients when compared with MRI only?

**PERTINENT FINDINGS:** We observed no significant differences between the 2 modalities. There was no significant improvement in detection and evaluation of meningiomas on PET/MRI.

**IMPLICATIONS FOR PATIENT CARE:** Conventional MRI is sufficient to assess local tumor extent. Additional molecular characteristics, such as screening for peptide-receptor radioligand therapy, can be obtained by sequential PET/CT without loss of information.

## REFERENCES


1. Wiemels J, Wrensch M, Claus EB. Epidemiology and etiology of meningioma. *J Neurooncol.* 2010;99:307–314.
2. Dolecek TA, Dressler EVM, Thakkar JP, Liu M, Al-Qaisi A, Villano JL. Epidemiology of meningiomas post-public law 107-206: the benign brain tumor cancer registries amendment act. *Cancer.* 2015;121:2400–2410.
3. Bi WL, Prabhu VC, Dunn IF. High-grade meningiomas: biology and implications. *Neurosurg Focus.* 2018;44:E2.
4. Neuschmelting V, Goldbrunner R. Meningeome. In: Schmoll H-J, Höffken K, Possinger K, eds. *Kompendium Internistische Onkologie. Springer Reference Medizin.* Springer; 2021.
5. Goldbrunner R, Stavrinou P, Jenkinson MD, et al. EANO guideline on the diagnosis and management of meningiomas. *Neuro Oncol.* 2021;23:1821–1834.
6. Kotapka MJ, Kalia KK, Martinez AJ, Sekhar LN. Infiltration of the carotid artery by cavernous sinus meningioma. *J Neurosurg.* 1994;81:252–255.
7. Afshar-Oromieh A, Giesel FL, Linhart HG, et al. Detection of cranial meningiomas: comparison of $^{68}$Ga-DOTATOC PET/CT and contrast-enhanced MRI. *Eur J Nucl Med Mol Imaging.* 2012;39:1409–1415.
8. Mahase SS, Roth O'Brien DA, No D, et al. [$^{68}$Ga]-DOTATATE PET/MRI as an adjunct imaging modality for radiation treatment planning of meningiomas. *Neurooncol Adv.* 2021;3:vdab012.
9. Arena S, Barbieri F, Thellung S, et al. Expression of somatostatin receptor mRNA in human meningiomas and their implication in in vitro antiproliferative activity. *J Neurooncol.* 2004;66:155–166.
10. Frilling A, Sotiropoulos GC, Radtke A, et al. The impact of $^{68}$Ga-DOTATOC positron emission tomography/computed tomography on the multimodal management of patients with neuroendocrine tumors. *Ann Surg.* 2010;252:850–856.
11. Poeppel TD, Binse I, Petersenn S, et al. $^{68}$Ga-DOTATOC versus $^{68}$Ga-DOTATATE PET/CT in functional imaging of neuroendocrine tumors. *J Nucl Med.* 2011;52:1864–1870.
12. Deuschl C, Kirchner J, Poeppel T, et al. $^{11}$C-MET PET/MRI for detection of recurrent glioma. *Eur J Nucl Med Mol Imaging.* 2018;45:593–601.
13. Kirchner J, Schaarschmidt BM, Sauerwein W, et al. $^{18}$F-FDG PET/MRI vs MRI in patients with recurrent adenoid cystic carcinoma. *Head Neck.* 2019;41:170–176.
14. Schaarschmidt BM, Heusch P, Buchbender C, et al. Locoregional tumour evaluation of squamous cell carcinoma in the head and neck area: a comparison between MRI, PET/CT and integrated PET/MRI. *Eur J Nucl Med Mol Imaging.* 2016;43:92–102.
15. Graef J, Furth C, Kluge AK, et al. $^{68}$Ga-DOTATOC-PET/MRI: a secure one-stop shop imaging tool for robotic radiosurgery treatment planning in patients with optic nerve sheath meningioma. *Cancers (Basel).* 2021;13:3305.
16. Grueneisen J, Schaarschmidt BM, Heubner M, et al. Integrated PET/MRI for whole-body staging of patients with primary cervical cancer: preliminary results. *Eur J Nucl Med Mol Imaging.* 2015;42:1814–1824.
17. Rachinger W, Stoecklein VM, Terpolilli NA, et al. Increased $^{68}$Ga-DOTATATE uptake in PET imaging discriminates meningioma and tumor-free tissue. *J Nucl Med.* 2015;56:347–353.
18. Afshar-Oromieh A, Wolf MB, Kratochwil C, et al. Comparison of $^{68}$Ga-DOTATOC-PET/CT and PET/MRI hybrid systems in patients with cranial meningioma: initial results. *Neuro Oncol.* 2015;17:312–319.
19. Galldiks N, Albert NL, Sommerauer M, et al. PET imaging in patients with meningioma: report of the RANO/PET group. *Neuro Oncol.* 2017;19:1576–1587.
20. Gehler B, Paulsen F, Öksüz MÖ, et al. [$^{68}$Ga]-DOTATOC-PET/CT for meningioma IMRT treatment planning. *Radiat Oncol.* 2009;4:56.
21. Kunz WG, Jungblut LM, Kazmierczak PM, et al. Improved detection of transosseous meningiomas using $^{68}$Ga-DOTATATE PET/CT compared with contrast-enhanced MRI. *J Nucl Med.* 2017;58:1580–1587.
22. Graf R, Nyuyki F, Steffen IG, et al. Contribution of $^{68}$Ga-DOTATOC PET/CT to target volume delineation of skull base meningiomas treated with stereotactic radiation therapy. *Int J Radiat Oncol Biol Phys.* 2013;85:68–73.
23. Salmon E, Bernard Ir C, Hustinx R. Pitfalls and limitations of PET/CT in brain imaging. *Semin Nucl Med.* 2015;45:541–551.
24. Welsh JS. Beta radiation. *Oncologist.* 2006;11:181–183.
25. Einhellig HC, Siebert E, Bauknecht H-C, et al. Comparison of diagnostic value of $^{68}$Ga-DOTATOC PET/MRI and standalone MRI for the detection of intracranial meningiomas. *Sci Rep.* 2021;11:9064.
26. Kim SH, Roytman M, Madera G, et al. Evaluating diagnostic accuracy and determining optimal diagnostic thresholds of different approaches to [$^{68}$Ga]-DOTATATE PET/MRI analysis in patients with meningioma. *Sci Rep.* 2022;12:9256.
27. Mikat C, Boy C, Heusner T, et al. $^{68}$Ga-DOTATOC-PET/CT imaging and somatostatin receptor "fingerprints" in physiological human tissues: "SUVmax meets mRNA expression" [in German]. *Rofo.* 2010:182:VO101_4.
28. Johnbeck CB, Knigge U, Loft A, et al. Head-to-head comparison of $^{64}$Cu-DOTATATE and $^{68}$Ga-DOTATOC PET/CT: a prospective study of 59 patients with neuroendocrine tumors. *J Nucl Med.* 2017;58:451–457.
29. Velikyan I, Sundin A, Sörensen J, et al. Quantitative and qualitative intrapatient comparison of $^{68}$Ga-DOTATOC and $^{68}$Ga-DOTATATE: net uptake rate for accurate quantification. *J Nucl Med.* 2014;55:204–210.
30. Juntikka T, Vaittinen S, Vahlberg T, Jyrkkiö S, Minn H. Somatostatin receptors and chemokine receptor CXCR4 in lymphomas: a histopathological review of six lymphoma subtypes. *Front Oncol.* 2021;11:710900.
31. Ruuska T, Ramírez Escalante Y, Vaittinen S, et al. Somatostatin receptor expression in lymphomas: a source of false diagnosis of neuroendocrine tumor at $^{68}$Ga-DOTANOC PET/CT imaging. *Acta Oncol.* 2018;57:283–289.
32. Calandriello L, Grimaldi G, Petrone G, et al. Cavernous venous malformation (cavernous hemangioma) of the orbit: current concepts and a review of the literature. *Surv Ophthalmol.* 2017;62:393–403.
33. Gilardi L, Vadrucci M, Grana CM. Multiple vertebral hemangiomas: a potential pitfall in $^{68}$Ga-DOTATOC PET/CT interpretation. *Endocrine.* 2017;55:992–993.
34. Schreiter NF, Nogami M, Steffen I, et al. Evaluation of the potential of PET-MRI fusion for detection of liver metastases in patients with neuroendocrine tumours. *Eur Radiol.* 2012;22:458–467.
35. Ben Simon GJ, Annunziata CC, Fink J, Villablanca P, McCann JD, Goldberg RA. Rethinking orbital imaging: establishing guidelines for interpreting orbital imaging studies and evaluating their predictive value in patients with orbital tumors. *Ophthalmology.* 2005;112:2196–2207.
36. Eisen MD, Yousem DM, Loevner LA, Thaler ER, Bilker WB, Goldberg AN. Preoperative imaging to predict orbital invasion by tumor. *Head Neck.* 2000;22:456–462.
37. Kline LB, Hoyt WF. The Tolosa–Hunt syndrome. *J Neurol Neurosurg Psychiatry.* 2001;71:577–582.
38. Larson JJ, van Loveren HR, Balko MG, Tew JM. Evidence of meningioma infiltration into cranial nerves: clinical implications for cavernous sinus meningiomas. *J Neurosurg.* 1995;83:596–599.
39. Barone F, Inserra F, Scalia G, et al. $^{68}$Ga-DOTATOC PET/CT follow up after single or hypofractionated gamma knife ICON radiosurgery for meningioma patients. *Brain Sci.* 2021;11:375.
40. Unterrainer M, Niyazi M, Tonn J, Ilhan H, Bartenstein P, Albert NL. Current status of SSR-directed imaging and therapy in meningioma. *Clin Transl Imaging.* 2019;7:171–180.
41. Filippi L, Palumbo I, Bagni O, Schillaci O, Aristei C, Palumbo B. Somatostatin receptor targeted PET-imaging for diagnosis, radiotherapy planning and theranostics of meningiomas: a systematic review of the literature. *Diagnostics (Basel).* 2022;12:1666.

# $SUV_{max}$ Above 20 in $^{18}$F-FDG PET/CT at Initial Diagnostic Workup Associates with Favorable Survival in Patients with Cancer of Unknown Primary

Gregor Zaun[1], Manuel Weber[2], Martin Metzenmacher[1], Marcel Wiesweg[1], Thomas Hilser[1], Yasmin Zaun[1], Sven Liffers[3,4], Michael Pogorzelski[1], Isabel Virchow[1], Wilfried Eberhardt[1], Sarah Theurer[5], Tanja Abu Sabbah[1], Timm M. Reissig[1,4], Martin Stuschke[6], Cornelius Kürten[7], Timon Hussain[7], Stephan Lang[7], Stefan Kasper[1,3], Wolfgang P. Fendler[2], Ken Herrmann[2], and Martin Schuler[1,3]

*[1]Department of Medical Oncology, West German Cancer Center, University Hospital Essen, Essen, Germany; [2]Department of Nuclear Medicine, University Hospital Essen, Essen, Germany; [3]German Cancer Consortium, Partner Site University Hospital Essen, Essen, Germany; [4]Bridge Institute of Experimental Tumor Therapy, West German Cancer Center, University Hospital Essen, Essen, Germany; [5]Institute of Pathology, West German Cancer Center, University Hospital Essen, Essen, Germany; [6]Department of Radiation Oncology, West German Cancer Center, University Hospital Essen, Essen, Germany; and [7]Department of Otorhinolaryngology, West German Cancer Center, University Hospital Essen, Essen, Germany*

Cancer of unknown primary (CUP) is a heterogeneous entity with a limited prognosis. Novel prognostic markers are needed for patient stratification in prospective clinical trials exploring innovative therapies. **Methods:** In CUP patients treated at the West German Cancer Center Essen, the prognostic value of $^{18}$F-FDG PET/CT at the initial diagnostic workup was analyzed by comparing overall survival (OS) in patients who underwent $^{18}$F-FDG PET/CT with those who did not. **Results:** Of 154 patients with a CUP diagnosis, 76 underwent $^{18}$F-FDG PET/CT at the initial diagnostic workup. The median overall survival (OS) of the full analysis set was 20.0 mo. Within the PET/CT subgroup, an $SUV_{max}$ above 20 was associated with significantly superior OS (median OS, not reached vs. 32.0 mo; hazard ratio, 0.261; 95% CI, 0.095–0.713; $P = 0.009$). **Conclusion:** Our retrospective work shows that an $SUV_{max}$ above 20 on $^{18}$F-FDG PET/CT at the initial diagnostic workup is a favorable prognostic factor in patients with CUP. This finding deserves further prospective studies for validation.

**Key Words:** CUP; $^{18}$F-FDG PET/CT; $SUV_{max}$

**J Nucl Med 2023; 64:1191–1194**
DOI: 10.2967/jnumed.122.265161

Cancer of unknown primary (CUP) is a heterogeneous cancer entity in which the primary tumor remains unknown after a comprehensive diagnostic workup (*1*). CUP affects 2%–4% of all newly diagnosed malignancies. In the literature, 75%–85% of cases are described as diffusely metastatic at initial diagnosis. The median overall survival (OS) of patients with diffusely metastasized CUP remains poor, at only 8–11 mo (*2*). Unlike the multimodal concepts in solitary metastatic CUP syndrome with a curative approach, patients with diffuse metastasis usually receive only systemic palliative chemotherapy, with generally poor responses (*1–3*). To provide a basis toward future treatment approaches stratified by clinical and biologic markers, we analyzed a large cohort of CUP patients receiving treatment at a major German comprehensive cancer center.

In this study, particular attention was paid to the potential prognostic value of $^{18}$F-FDG PET/CT imaging in CUP patients.

## MATERIALS AND METHODS

### Patient Selection

The clinical cancer registry of the West German Cancer Center Essen was searched for patients who received an initial diagnosis of CUP between January 2015 and May 2021, with the data being cut off on December 23, 2021. We stringently applied the predefined CUP criteria of the current European Society for Medical Oncology guidelines to confirm the diagnosis (Fig. 1) (*1*).

### Image Acquisition and Analysis

Images were acquired in accordance with the European Association of Nuclear Medicine guidelines for tumor imaging using $^{18}$F-FDG PET (*4*), as follows: after the intravenous administration of a median of 289 MBq (interquartile range, 97 MBq) of $^{18}$F-FDG and a median uptake interval of 73 min (interquartile range, 16 min), image acquisition began. The $^{18}$F-FDG activity was based on body weight. Images

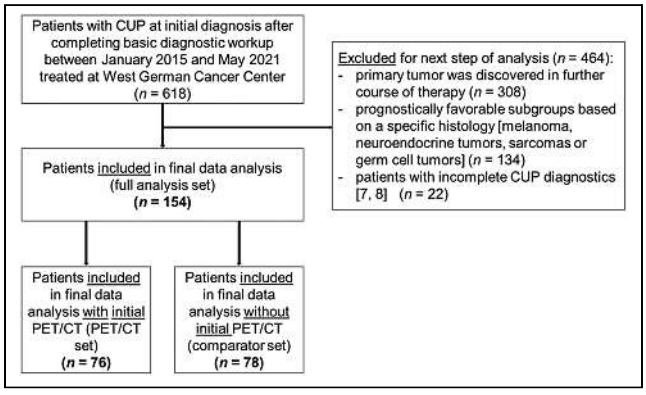


**FIGURE 1.** CONSORT (Consolidated Standards of Reporting Trials) flow diagram for patient inclusion in data analysis.

Received Nov. 8, 2022; revision accepted Apr. 4, 2023.
For correspondence or reprints, contact Gregor Zaun (gregor.zaun@uk-essen.de).
Published online Jun. 15, 2023.

**TABLE 1**
Baseline Characteristics

| Parameter | Characteristic | Full analysis set ($n$ = 154) | | PET/CT set ($n$ = 76) | | Comparator set ($n$ = 78) | |
|---|---|---|---|---|---|---|---|
| | | $n$ | % | $n$ | % | $n$ | % |
| Sex | Male | 82 | 53.25 | 41 | 53.95 | 41 | 52.56 |
| | Female | 72 | 46.75 | 35 | 46.05 | 37 | 47.44 |
| Age | >60 y | 84 | 54.55 | 39 | 51.32 | 45 | 57.69 |
| | ≤60 y | 70 | 45.45 | 37 | 48.68 | 33 | 42.31 |
| Metastasis | Solitary | 61 | 39.61 | 40 | 52.63 | 21 | 26.92 |
| | Diffuse | 93 | 60.39 | 36 | 47.37 | 57 | 73.08 |
| Histology | Adenocarcinoma | 66 | 42.86 | 25 | 32.89 | 41 | 52.56 |
| | Undifferentiated carcinoma | 10 | 6.49 | 6 | 7.89 | 4 | 5.13 |
| | Squamous cell carcinoma | 53 | 34.42 | 40 | 52.63 | 13 | 16.67 |
| | Neuroendocrine carcinoma | 25 | 16.23 | 5 | 6.58 | 20 | 25.64 |
| Secondary malignancy | Yes | 32 | 20.78 | 14 | 18.42 | 18 | 23.08 |
| | No | 122 | 79.22 | 62 | 81.58 | 60 | 76.92 |
| Pulmonary artery embolism or thrombosis | Yes | 28 | 18.18 | 13 | 17.11 | 15 | 19.23 |
| | No | 126 | 81.82 | 63 | 82.89 | 63 | 80.77 |
| Affected organ systems | 1 | 83 | 53.90 | 47 | 61.84 | 36 | 46.15 |
| | 2 | 41 | 26.62 | 20 | 26.32 | 21 | 26.92 |
| | ≥3 | 30 | 19.48 | 9 | 11.84 | 21 | 26.92 |
| $SUV_{max}$ | >20 | | | 22 | 28.95 | | |
| | ≤20 | | | 54 | 71.05 | | |

Median age was 62 y (range, 20–85 y). Median $SUV_{max}$ was 13.9 (range, 3.5–30.8).

were analyzed by 3 unmasked readers, among whom were at least 1 board-certified radiologist and 1 nuclear medicine physician, as per the clinical standard. If multiple lesions were present, the most representative malignant lesion was chosen as the target lesion for further analyses.

All analyses were performed on pseudonymized datasets. The institutional review board approved this retrospective study, and the requirement to obtain informed consent was waived; nevertheless, all subjects gave written informed consent to providing their data for scientific purposes.

### Statistical Analysis

In the initial, pretherapeutic, $^{18}$F-FDG PET/CT scan, we determined the $SUV_{max}$ of the detected tumor manifestations. The 75th percentile of $SUV_{max}$ was set as the discriminator between high and low $SUV_{max}$. OS was defined as the time from initial diagnosis to death from any cause. If the time point of death was not detectable, patients were censored at the time of last follow-up. Survival was analyzed using the Kaplan–Meier method and log-rank testing, and putative prognostic factors were correlated by multivariate analysis with Cox regression.

Statistical analyses were performed using Excel 2016 (version 2304; Microsoft) and SPSS Statistics (version 26; IBM). A $P$ value of 0.05 or less was defined as statistically significant.

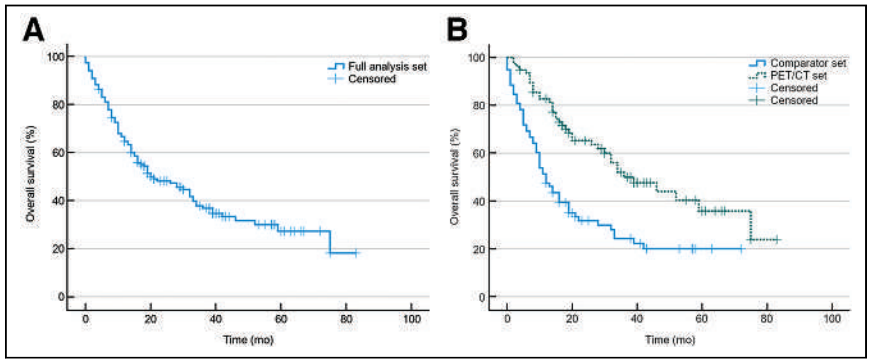


**FIGURE 2.** Median OS of full analysis set and patient subsets. (A) OS of full analysis set ($n$ = 154) was 20.0 mo (95% CI, 10.0–30.0). (B) At 36.0 mo (95% CI, 21.3–50.7), OS of PET/CT set ($^{18}$F-FDG PET/CT at initial diagnostic workup, $n$ = 76) was significantly higher than OS of comparator set (without $^{18}$F-FDG PET/CT at initial diagnostic workup, $n$ = 78), at 12.0 mo (95% CI, 8.7–15.3; $P$ < 0.001).

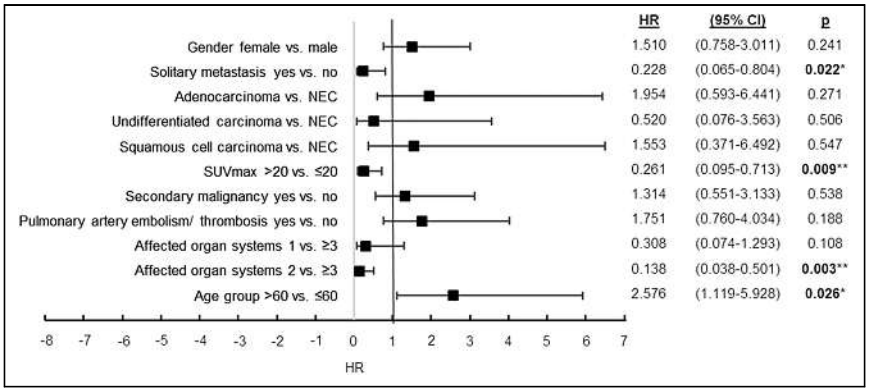


**FIGURE 3.** Multivariate analysis for prognostic parameters for PET/CT set ($n = 76$): hazard ratio with 95% CI and $P$ value. *$P < 0.05$. **$P < 0.01$. HR = hazard ratio; NEC = neuroendocrine carcinoma).

## RESULTS

### Patients

In total, 618 patients with a clinical diagnosis of CUP were identified, of whom 154 fulfilled all the prespecified inclusion criteria of the study (full analysis set). Of those, 76 (49%) had undergone $^{18}$F-FDG PET/CT at the initial diagnostic workup (PET/CT set), whereas 78 (51%) had no initial $^{18}$F-FDG PET/CT (comparator set, Fig. 1). The characteristics of the different subgroups are summarized in Table 1. The median $SUV_{max}$ of the PET/CT set was 13.9 (range, 3.5–30.8). The 75th percentile was approximately 20. At the time of data cutoff, 96 (62.3%) patients were deceased, 56 (36.4%) were alive, and 2 (1.3%) were lost to follow-up.

### Survival and Prognostic Factors

The OS was 20.0 mo (95% CI, 10.0–30.0 mo) for the full analysis set (Fig. 2A), 36.0 mo (95% CI, 21.3–50.7) for the PET/CT set (Fig. 2B), and 12.0 mo (95% CI, 8.7–15.3) for the comparator set (Fig. 2B).

Using multivariate Cox regression, we correlated OS with established prognostic clinical parameters. We identified a solitary metastasis as a significant favorable prognostic factor (Fig. 3; Supplemental Figs. 1 and 2; supplemental materials are available at http://jnm.snmjournals.org). Significant unfavorable prognostic factors were involvement of 3 or more organ systems (Fig. 3; Supplemental Figs. 1 and 3) and an age over 60 y (Fig. 3; Supplemental Fig. 1). These prognostic parameters were comparably relevant in the full analysis set, the PET/CT set, and the comparator set (Fig. 3; Supplemental Fig. 1), demonstrating overall a similar distribution of CUP biologies among these populations.

We next explored the prognostic impact of tumor metabolic activity as determined by $SUV_{max}$ at pretherapeutic $^{18}$F-FDG PET/CT. An $SUV_{max}$ of 20 clearly discriminated a favorable subgroup from an unfavorable subgroup in the PET/CT set (median OS, not reached vs. 32.0 mo [95% CI, 23.2–40.8]; hazard ratio, 0.261 [95% CI, 0.095–0.713]; $P = 0.009$) (Figs. 3 and 4).

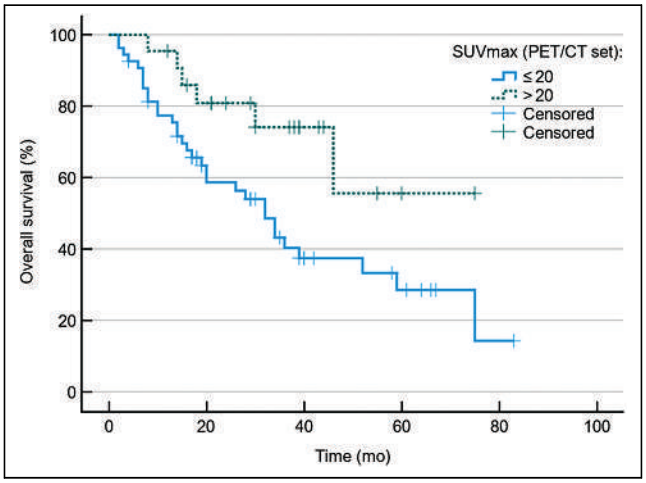


**FIGURE 4.** Median OS in relation to $SUV_{max}$ in PET/CT set. In subset with initial $^{18}$F-FDG PET/CT, patients with $SUV_{max}$ above 20 ($n = 22$) had significantly higher OS (not reached) than patients with $SUV_{max}$ of 20 or less ($n = 54$) (32.0 mo; 95% CI, 23.2–40.8; $P = 0.022$).

## DISCUSSION

With a poor OS of 11.0 mo, our data for patients with CUP and diffuse metastasis are consistent with data from other studies (*2*). Further progress in treatment is hampered by the heterogeneity of the CUP population, which may confound the results of studies exploring novel treatments. Current stratification factors such as age, a low number of metastatic sites, or solitary metastasis, which have already been described in the literature (*1,3*) and could also be confirmed in this work as prognostic factors, are of limited use. They do not reflect the biologic heterogeneity within the respective subgroups.

Using functional imaging, we here describe an independent association of tumor metabolic activity with survival of patients with a stringently defined CUP diagnosis. An $SUV_{max}$ above 20, as detected at the pretherapeutic workup by $^{18}$F-FDG PET/CT, is a strong predictor of a favorable outcome.

In contrast, Yılmaz et al. (*5*) among patients with stage III non–small cell lung cancer, and Werner et al. (*6*) among patients with laryngeal carcinoma, found no influence of $SUV_{max}$ on OS.

Other studies described a high $SUV_{max}$ as a negative prognostic factor in tumor entities such as hypopharyngeal or pancreatic cancer (*6,7*). These studies focused on nonmetastatic disease stages with a curative approach, corresponding to Union for International Cancer Control (UICC) stages I–III. An association of high $SUV_{max}$ with rapid disease recurrence has often been described and usually has not had a direct influence on OS.

By definition, CUP syndrome is already a metastatic, UICC stage IV disease at initial diagnosis.

For other aggressive tumor entities at stage IV and with palliative therapeutic intention, observations comparable to our results are available in the literature. A higher OS was described for patients with small cell lung cancer at UICC stage IV under systemic palliative therapy with a higher $SUV_{max}$, whereas at stages I–III a lower $SUV_{max}$ showed a better outcome (*8*). A possible interpretation of better OS with high $SUV_{max}$ at stage IV of tumor disease, and thus also in CUP syndrome, was provided by Liu et al. in a study of ovarian cancer (*9*). They were able to show a higher chemosensitivity at a high $SUV_{max}$. In future studies, the marker $SUV_{max}$ should be tested prospectively in patients with CUP syndrome.

## CONCLUSION

Our retrospective study found that an $SUV_{max}$ over 20 on $^{18}$F-FDG PET/CT is associated with favorable survival in patients with CUP at the initial diagnostic workup. This finding deserves further investigation in prospective studies. If they validate this finding, they could provide information that goes beyond staging to support the treatment of CUP. These results could optimize patient stratification in future studies of systemic therapies in CUP to increase the likelihood that a true therapeutic effect on survival will be detected.

## DISCLOSURE

Wolfgang Fendler reports fees from SOFIE Biosciences, Janssen, Calyx, Bayer, Novartis, and Telix. Ken Herrmann reports fees from Bayer, SOFIE Biosciences, SIRTEX, Adacap, Curium, Endocyte, BTG, IPSEN, Siemens Healthineers, GE Healthcare, Amgen, Novartis, ymabs, Aktis Oncology, Theragnostics, Pharma15, Debiopharm, AstraZeneca, and Janssen and nonfinancial support from ABX. Manuel Weber reports fees from Boston Scientific, Terumo, Advanced Accelerator Applications, and Eli Lilly. Martin Metzenmacher reports honoraria from AMGEN, AstraZeneca, Boehringer-Ingelheim, BMS, MSD, Novartis, Roche, and Takeda. Marcel Wiesweg received honoraria from Amgen, Boehringer-Ingelheim, Daiichi Sankyo, GlaxoSmithKline, Novartis, Pfizer, Roche, and Takeda and research funding from BMS and Takeda. Michael Pogorzelski received honoraria from Boehringer-Ingelheim, BMS, Lilly, Merck Healthcare KGaA, Merck Sharp & Dohme, Roche, Sanofi-Aventis, and Servier. Stefan Kasper received honoraria from Merck Serono, MSD, Novartis, BMS, Amgen, Roche, Sanofi-Aventis, Servier, Incyte, and Lilly and research funding from Merck Serono, Lilly, BMS and Roche. Martin Schuler received research funding from AstraZeneca and BMS; received honoraria from Amgen, Boehringer-Ingelheim, BMS, Janssen, and Novartis; and had a compensated consultant role for Amgen, AstraZeneca, BIOCAD, Boehringer-Ingelheim, BMS, GlaxoSmithKline, Janssen, Merck Serono, Novartis, Roche, Sanofi, and Takeda. No other potential conflict of interest relevant to this article was reported.

**KEY POINTS**

**QUESTION:** Is a high $SUV_{max}$ over 20 on pretherapeutic $^{18}$F-FDG PET/CT a prognostic factor in patients with CUP?

**PERTINENT FINDINGS:** We performed a retrospective analysis of 154 patients with CUP, 76 of whom received initial $^{18}$F-FDG PET/CT. Although other prognostic parameters were equivalent in the PET/CT and comparator sets, an $SUV_{max}$ over 20 was associated with significantly superior OS in the PET/CT set.

**IMPLICATIONS FOR PATIENT CARE:** $SUV_{max}$ should be used for patient stratification in future studies of CUP patients and can support shared decision-making regarding the initiation and type of therapy in current clinical practice.

## REFERENCES


1. Krämer A, Bochtler T, Pauli C, et al.; ESMO Guidelines Committee. Cancer of unknown primary: ESMO clinical practice guideline for diagnosis, treatment and follow-up. *Ann Oncol.* 2023;34:228–246.
2. Zaun G, Schuler M, Herrmann K, Tannapfel A. CUP syndrome: metastatic malignancy with unknown primary tumor. *Dtsch Arztebl Int.* 2018;115:157–162.
3. Pavlidis N, Pentheroudakis G. Cancer of unknown primary site: 20 questions to be answered. *Ann Oncol.* 2010;21(suppl 7):vii303–vii307.
4. Boellaard R, Delgado-Bolton R, Oyen WJG, et al. FDG PET/CT: EANM procedure guidelines for tumour imaging—version 2.0. *Eur J Nucl Med Mol Imaging.* 2015;42:328–354.
5. Yılmaz U, Batum Ö, Koparal H, Özbilek E, Kıraklı E. Prognostic value of primary tumor SUVmax on pre-treatment 18F-FDG PET/CT imaging in patients with stage III non-small cell lung cancer. *Rev Esp Med Nucl Imagen Mol (Engl Ed).* 2018;37:218–222.
6. Werner J, Hüllner MW, Rupp NJ, et al. Predictive value of pretherapeutic maximum standardized uptake value (SUVmax) in laryngeal and hypopharyngeal cancer. *Sci Rep.* 2019;9:8972.
7. McGahan W, Chikatamarla V, Thomas P, Cavallucci D, O'Rourke N, Burge M. High SUVmax on routine pre-operative FDG-PET predicts early recurrence in pancreatic and peri-ampullary cancer. *HPB (Oxford).* 2022;24:1387–1393.
8. van der Leest C, Smit EF, Baas J, et al. $SUV_{max}$ during $^{18}$FDG-PET scanning in small cell lung cancer: similar information as in non-small cell lung cancer? *Lung Cancer.* 2012;76:67–71.
9. Liu S, Feng Z, Wen H, et al. $^{18}$F-FDG PET/CT can predict chemosensitivity and proliferation of epithelial ovarian cancer via SUVmax value. *Jpn J Radiol.* 2018;36:544–550.

# Metformin-Induced Receptor Turnover Alters Antibody Accumulation in HER-Expressing Tumors

Sandeep Surendra Panikar[1], Nai Keltee[1], Na-Keysha Berry[1], Shayla Shmuel[1], Zachary T. Fisher[1], Emma Brown[1], Abbey Zidel[1,2], Alex Mabry[1,3], and Patrícia M.R. Pereira[1]

[1]*Department of Radiology, Mallinckrodt Institute of Radiology, Washington University School of Medicine, St. Louis, Missouri;* [2]*Department of Biology, Washington University School of Medicine, St. Louis, Missouri; and* [3]*Department of Biological and Biomedical Sciences, Washington University School of Medicine, St. Louis, Missouri*

Metformin has effects beyond its antihyperglycemic properties, including altering the localization of membrane receptors in cancer cells. Metformin decreases human epidermal growth factor receptor (HER) membrane density. Depletion of cell-surface HER decreases antibody–tumor binding for imaging and therapeutic approaches. Here, we used HER-targeted PET to annotate antibody–tumor binding in mice treated with metformin. **Methods:** Small-animal PET annotated antibody binding in HER-expressing xenografts on administration of an acute versus a daily dose schedule of metformin. Analyses at the protein level in the total, membrane, and internalized cell extracts were performed to determine receptor endocytosis, HER surface and internalized protein levels, and HER phosphorylation. **Results:** At 24 h after injection of radiolabeled anti-HER antibodies, control tumors had higher antibody accumulation than tumors treated with an acute dose of metformin. These differences were temporal, and by 72 h, tumor uptake in acute cohorts was similar to uptake in control. Additional PET imaging revealed a sustained decrease in tumor uptake on daily metformin treatment compared with control and acute metformin cohorts. The effects of metformin on membrane HER were reversible, and after its removal, antibody–tumor binding was restored. The time- and dose-dependent effects of metformin-induced HER depletion observed preclinically were validated with immunofluorescence, fractionation, and protein analysis cell assays. **Conclusion:** The findings that metformin decreases cell-surface HER receptors and reduces antibody–tumor binding may have significant implications for the use of antibodies targeting these receptors in cancer treatment and molecular imaging.

**Key Words:** metformin; PET imaging; HER family

**J Nucl Med 2023; 64:1195–1202**
DOI: 10.2967/jnumed.122.265248

Metformin is the most prescribed first-line drug to reduce blood glucose levels in patients with type 2 diabetes mellitus (*1,2*). Metformin is safe, well tolerated, and prescribed to more than 120 million people for the management of type 2 diabetes mellitus. Metformin has benefits beyond its antihyperglycemic properties that include reduction of body weight and fat content, antiaging effects, and anticancer effects in patients with diabetes who are prescribed metformin (*2–8*). Patients with metabolic dysregulation (metabolic syndrome, diabetes, or obesity) who take metformin have shown lower cancer risk and cancer-related mortalities (*7,9,10*). As clinical trials repurpose metformin in oncology (*11*), it is important to understand how alterations induced by this drug on cancer cells and the tumor microenvironment affect tumor response to therapies (*12,13*).

Epidermal growth factor receptor (EGFR) and human epidermal growth factor receptor 2 (HER2) are receptor tyrosine kinases overexpressed and dysregulated in cancer cells (*14*). This has led to the development of small-molecule drugs and monoclonal therapeutic antibodies targeting human epidermal growth factor receptor (HER). Examples of anti-HER therapeutic monoclonal antibodies are trastuzumab and panitumumab, which target the extracellular domains of HER2 and EGFR in cancer cells (*15,16*). Trastuzumab is used as first-line therapy, in combination with chemotherapy, for gastric cancer and is the standard-of-care treatment for women with metastatic and early-stage breast cancer (*15,17*). Panitumumab is approved to treat wild-type Kirsten rat sarcoma viral metastatic colorectal cancer (*18*). The efficacy of HER-targeted antibody drugs depends on the density and availability of HER at the membrane of cancer cells (*19,20*). Previous studies suggest that drugs interfering with the stability and membrane localization of HER receptors will affect tumor response to antibody therapies.

Previous preclinical studies in gastric, breast, and bladder cancer models have shown that cholesterol-depleting drugs increase HER cell-surface density, as visualized by HER-directed immuno-PET uptake (*19–21*). These previous studies have also shown improved therapeutic efficacy of antibody drugs combined with cholesterol-depleting drugs (*19–21*). Accumulating preclinical and clinical data indicate that metformin interferes with the cholesterol biosynthetic pathway and raft production, but the molecular mechanisms of how these processes occur remain unclear (*8,22–26*). Metformin alters the cholesterol content located at the cell membrane and intracellularly, and it affects the synthesis and stability of receptors that rely on GM1 ganglioside, lipid raft markers (such as HER) (*8,22–26*). How the timing, duration, and dose of metformin treatment affect HER membrane receptor turnover in cancer cells is still unclear.

Immuno-PET is a useful tool for monitoring the uptake and binding of antibodies to tumors in real time. In this study, it was used to visualize and quantify the uptake of anti-HER antibodies in mice treated with metformin.

## MATERIALS AND METHODS

### Radiolabeling

$^{89}$Zr-labeled trastuzumab and panitumumab were prepared with a specific activity of 22 MBq/nmol and immunoreactivity above 95%.

Received Nov. 23, 2022; revision accepted Mar. 30, 2023.
For correspondence or reprints, contact Patrícia M.R. Pereira (ribeiropereirap@wustl.edu).
Published online Jun. 2, 2023.

$^{64}$Cu-labeled trastuzumab was prepared with a specific activity of 32–34.04 MBq/nmol. Detailed protocols are described in the Supplemental Methods (supplemental materials are available at http://jnm.snmjournals.org).

### Metformin Treatment

In vitro treatments, Western blot, and immunofluorescence analyses are described in the Supplemental Methods. An acute dose of metformin (250 mg/kg) was orally administered 12 h before and at the same time as the tail vein injection of $^{89}$Zr-labeled antibody. Metformin (200 mg/kg dose) was then intraperitoneally administered for 7–11 consecutive days before the tail vein injection of $^{89}$Zr-DFO-trastuzumab or $^{89}$Zr-DFO-panitumumab. Detailed protocols are described in the Supplemental Methods.

### Small-Animal PET and Biodistribution Studies

PET imaging experiments were conducted on a nanoScan PET/CT scanner (Mediso). Images were reviewed using 3D Slicer software (version 5.0.3; https://www.slicer.org/). The mice were sacrificed, and organs were harvested, weighed, and assayed in the γ-counter for biodistribution studies. Radioactivity associated with each organ was expressed as percentage injected dose (%ID) per gram of the organ.

### Statistical Analyses

Data were analyzed using RStudio (Posit Software; http://www.rstudio.com/). Data are expressed as mean ± SD. Groups were compared using the Student *t* test. In biodistribution and imaging studies, each cohort included 3–4 mice per time point.

## RESULTS

### Metformin Induces Temporal Depletion of Cell-Surface HER2 or EGFR

Trastuzumab or panitumumab binding to tumors depends on HER2 or EGFR availability at the membrane of cancer cells (*19–21,27*). Previous in vitro studies have shown alterations in membrane receptors in cancer cells treated with metformin in the millimolar range (*28,29*). We initially determined membrane levels of HER2 or EGFR in HER2-positive NCIN87 or EGFR-positive A431 cancer cells treated with 5 mM metformin (Fig. 1). We found that metformin promotes loss of cell-surface HER between 0 and 4 h of incubation time compared with no metformin (Figs. 1A and 1B; Supplemental Fig. 1). Metformin did not affect HER2 or EGFR in total protein lysates. The effect of metformin-induced membrane HER depletion was transient, and protein levels similar to those of control were detected after 12–24 h of incubation time.

Caveolin-1 (CAV1), a crucial structural protein of cholesterol-rich caveolae, negatively correlates with membrane HER at the protein level and affects anti-HER antibody binding to cancer cells (*19,20,28,30–34*). Previous studies have shown an upregulation in CAV1 tumoral levels on treatment with metformin. Because NCIN87 and A431 cancer cells are rich in caveolae (*35*), we next hypothesized that metformin-induced depletion in membrane HER is accompanied by an increase in total CAV1 protein levels. HER2-positive NCIN87 and EGFR-positive A431 cancer cells showed a 1.8-fold and 1.6-fold increase in CAV1 total protein levels at 2 h after metformin treatment (Figs. 1A and 1B). CAV1 total protein levels at 24 h after incubation with metformin were similar to those of no-metformin control.

We next evaluated whether metformin-induced depletion in membrane HER would hamper antibody binding to cancer cells (Fig. 1C). Cellular fractionation of NCIN87 or A431 cells incubated with $^{89}$Zr-labeled trastuzumab or panitumumab showed a significant decrease in membrane-bound radioactivity at 2 h after incubation with metformin (Fig. 1D). At 24 h after cell incubation with metformin, membrane-bound antibody resembled those found at no-metformin control cells, confirming the transience and temporality of the metformin cell treatments.

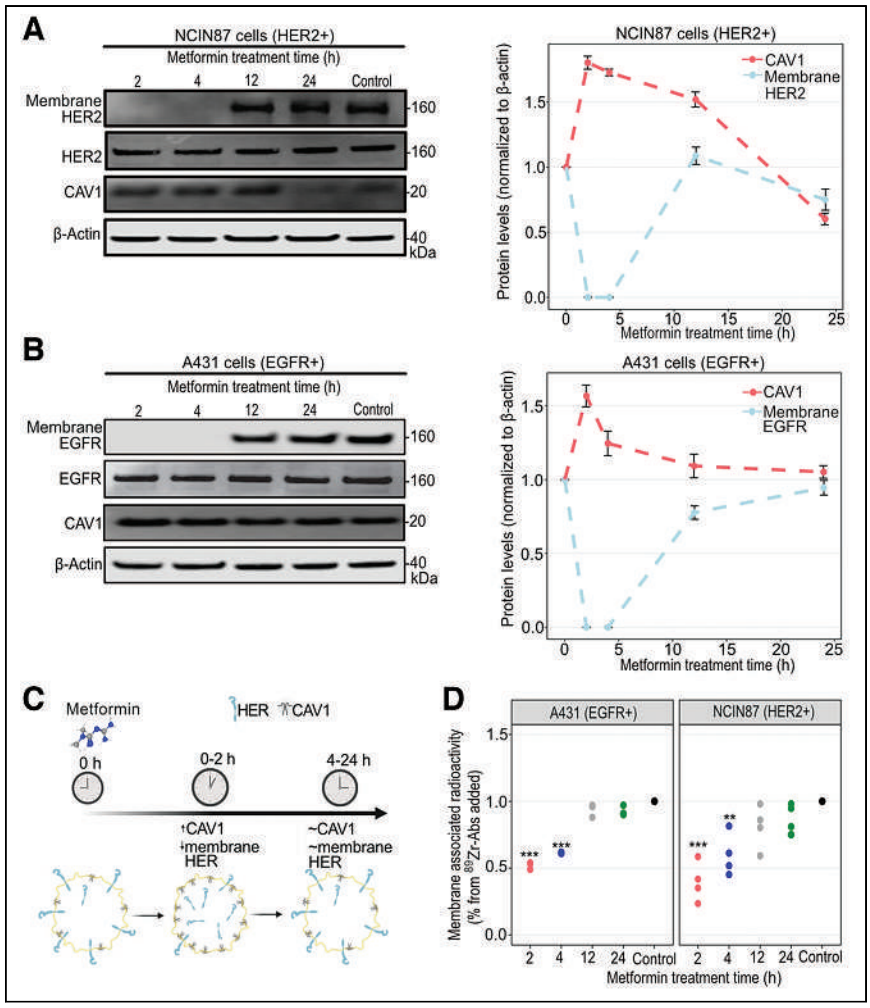


**FIGURE 1.** (A and B) Western blot of total CAV1, membrane and total HER2, and membrane and total EGFR after cancer cell treatment with metformin. NCIN87 or A431 cancer cells were incubated with 5 mM metformin for 2, 4, 12, and 24 h. Graphs show quantification of Western blots with protein levels normalized to no-metformin control (bars, $n = 3$, mean ± SD). (C) Schematic representation showing metformin-induced temporal changes in CAV1 and membrane HER. Schematic was made using BioRender. (D) Fractionation assay for membrane-bound and internalized $^{89}$Zr-labeled trastuzumab or $^{89}$Zr-labeled panitumumab after incubation of cancer cells with 5 mM metformin for 2, 4, 12, and 24 h. $^{**}P < 0.01$, based on Student *t* test and compared with untreated cells ($n = 3$–4, mean ± SD). $^{***}P < 0.001$, based on Student *t* test and compared with untreated cells ($n = 3$–4, mean ± SD).

Altogether, these results suggest that metformin temporarily enhances CAV1 total protein levels and decreases membrane HER and anti-HER membrane-bound antibody to cancer cells.

### Short-Term Cell Incubation with Metformin Enhances HER2 and EGFR Internalization

Premised on our initial in vitro findings, we anticipated that metformin-induced changes in membrane HER and total CAV1 protein levels would result in changes in HER internalization. This, in turn, would affect HER-mediated oncogenic signaling and the ability of trastuzumab or panitumumab to target and bind HER2- or EGFR-expressing cancer cells, respectively. Because we observed that short-term incubation with metformin decreased cell-surface HER and enhanced total CAV1 levels, we sought to investigate HER internalization and shedding in cancer cells treated with metformin for 2 h. Treatment with metformin did not induce significant changes in HER2 shedding in NCIN87 cancer cells (Supplemental Fig. 2). To determine HER intracellular localization, trastuzumab or panitumumab was allowed to bind on cancer cells treated with metformin for 2 h. Antibody-mediated internalization was then boosted in cancer cells for 90 min (Fig. 2A). Compared with untreated cells, an increase in HER internalization was observed in metformin-treated cancer cells (Figs. 2B and 2C; Supplemental Figs. 3 and 4). Metformin-induced depletion of membrane HER was accompanied by a decrease in phosphorylated HER2 or phosphorylated EGFR protein levels (Figs. 2B and 2C; Supplemental Figs. 3 and 4). Thus, our findings suggest that short-term incubation with metformin decreases membrane HER and phosphorylated HER oncogenic signaling pathways.

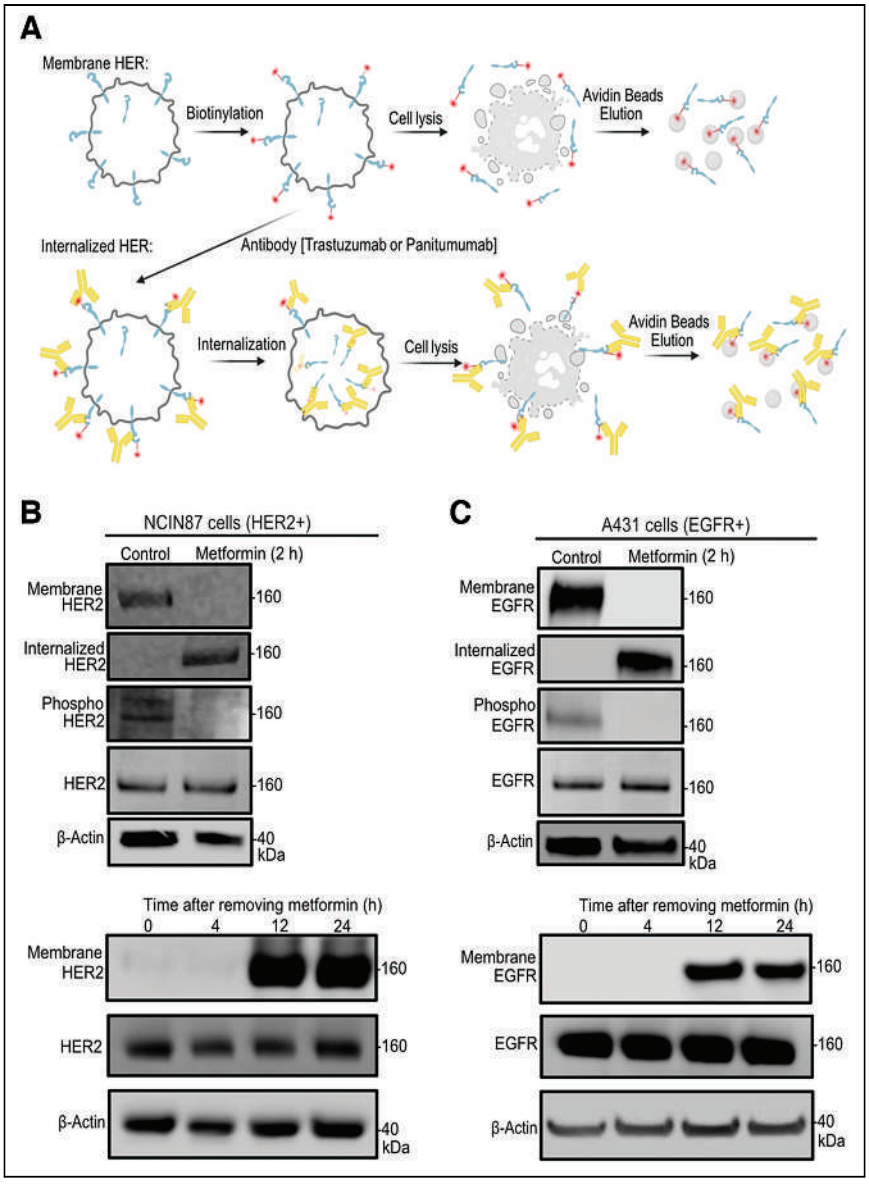


**FIGURE 2.** (A) Schematic representation of cell-surface biotinylation approach used to collect membrane-bound and internalized proteins. Schematic was made using BioRender. (B and C) Western blot analysis of biotinylated membrane; internalized, phosphorylated HER2; phosphorylated EGFR; total HER2; and total EGFR on NCIN87 or A431 cancer cells incubated with 5 mM metformin for 2 h. Western blot at bottom shows membrane HER2, membrane EGFR, total HER2, and total EGFR at 0, 4, 12, and 24 h after removing metformin from cancer cells. Cancer cells were incubated with 5 mM metformin for 2 h and washed with fresh culture medium before protein lysates were collected.

### Removal of Metformin Causes Rebound Effects on Cell-Surface HER Density

Our in vitro findings demonstrated that membrane HER decreases rapidly within 2 h after cell incubation with metformin (Fig. 1), becoming markedly lower than that of untreated cells. This abrupt decrease in membrane HER was accompanied by a decrease in membrane-bound antibodies (Fig. 1) and an increase in internalized HER (Fig. 2). We next analyzed membrane HER after metformin withdrawal in time-course immunoblotting experiments on cancer cells treated with metformin for 2 h and then released from treatment through a rapid washout procedure. We observed that the amount of membrane HER increased rapidly after metformin washout as it went back to control levels between 12 and 24 h after drug withdrawal (Figs. 2B and 2C). In conclusion, the removal of metformin restores membrane HER after drug washout.

### Preincubation with Metformin Reduces Anti-HER Antibody–Tumor Binding

We showed that metformin decreases membrane HER and membrane-bound anti-HER antibody and enhances total CAV1 (Fig. 1). We next performed immunofluorescence assays to determine the effect of metformin on trastuzumab or panitumumab binding to HER2-positive NCIN87 or EGFR-positive A431 cancer cells, respectively (Supplemental Fig. 5). We examined antibody binding to cancer cells preincubated versus coincubated with metformin.

The preincubation approach was applied to determine whether metformin-induced CAV1 expression could decrease antibody binding to cancer cells. When cancer cells were preincubated with metformin for 2 h, we observed an 8.3-fold or 2.6-fold decrease

in antibody binding to NCIN87 or A431 cancer cells, respectively (Fig. 3), compared with control.

Because metformin is usually prescribed as a daily dose, we evaluated antibody binding to cancer cells in the continuous presence of metformin (coincubation). Although trastuzumab or panitumumab binding decreased in cancer cells coincubated with metformin, the decrease was substantially lower than before metformin treatment (Fig. 3). In our studies, the antibody bound to NCIN87 or A431 cancer cells was 1.2-fold or 1.5-fold lower, respectively, in a coincubation treatment regimen.

These results demonstrate that a preincubation schedule of cancer cells with metformin highly reduces membrane HER, which in turn decreases anti-HER accumulation in cancer cells.

### Acute Metformin Treatment Induces Reversible Depletion in Anti-HER Antibody–Tumor Binding

The preceding in vitro data provided the rationale for preclinical imaging studies to annotate trastuzumab and panitumumab tumor binding in mice treated with metformin. In our studies, trastuzumab or panitumumab was conjugated with the Deferoxamine (DFO) chelator and labeled with $^{89}$Zr (Supplemental Figs. 6 and 7). Acute oral administration of metformin was performed 1 d before and at the same time as the radiolabeled antibody. This acute metformin treatment schedule was performed to validate our in vitro findings that the effects of metformin-induced depletion of trastuzumab or panitumumab tumor binding are reversible. The dose of metformin used in our imaging studies, 250 mg/kg for mice, corresponds to a human-equivalent dose of 1,219 mg, which is lower than the maximum recommended daily dose in humans of 2,550 mg/d. Control mice were administered saline instead of metformin in the same volume (Fig. 4A).

HER-targeted PET imaging at 24 h demonstrated a lower accumulation of antibody in tumors from metformin-treated mice than from saline cohorts (Fig. 4B; Supplemental Figs. 8–10). Additional PET imaging of these mice revealed similar antibody–tumor accumulation in mice treated with an acute dose of metformin and in control cohorts at 72 h after injection of the radioimmunoconjugate. Ex vivo biodistribution studies validated our findings from PET imaging at 72 h: 55.08 ± 3.84 %ID/g of tumor for $^{89}$Zr-trastuzumab in the saline cohort and 56.43 ± 0.54 %ID/g of tumor for $^{89}$Zr-trastuzumab in the metformin cohort (Fig. 4C; Supplemental Fig. 9).

These results indicate that the differences in antibody–tumor uptake in mice treated with an acute dose of metformin are temporal, with decreased uptake in metformin-treated tumors at 24 h and similar uptake values at 72 h after antibody injection versus control.

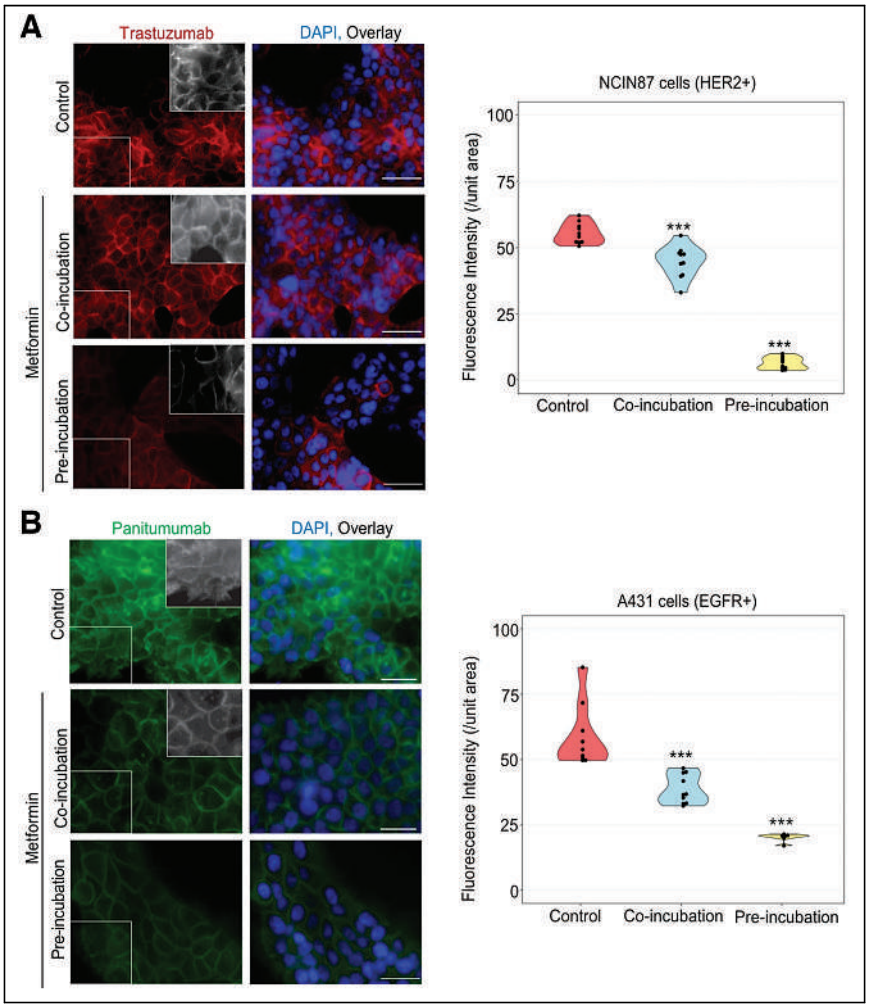


**FIGURE 3.** Representative fluorescence microscopy images and quantification of immunofluorescence staining of HER2 and EGFR receptors in NCIN87 (A) or A431 (B) cancer cells coincubated or preincubated with metformin. ***$P < 0.001$, based on Student $t$ test and compared with untreated cells ($n$ = 7–10, mean ± SD). DAPI = 4′,6-diamidino-2-phenylindole.

### Daily Administration of Metformin Reduces Anti-HER Accumulation in HER2- and EGFR-Expressing Tumor Xenografts

Because metformin is clinically prescribed once daily, we performed additional immuno-PET studies administering metformin daily before $^{89}$Zr-labeled antibody injection. The daily dose used in our preclinical studies (200 mg/kg for mice) was lower than the maximum recommended daily dose in humans. Previous studies using this daily dose of metformin demonstrated a high reduction in membrane receptor density (other than HER) without signs of preclinical toxicity (*29*). Control cohorts were administered saline instead of metformin (Fig. 4A).

Immuno-PET at 72 h after injection of $^{89}$Zr-labeled antibody demonstrated a reduction in antibody–tumor binding compared with the control or acute cohorts (Fig. 4B; Supplemental Figs. 8–10). Ex vivo biodistribution studies at 72 h after radiolabeled trastuzumab injection validated our findings from HER2-targeted PET imaging (Fig. 4C; Supplemental Fig. 9). HER2-positive NCIN87 xenografts of mice treated daily with metformin yielded tumor uptake of 15.01 ± 3.84 %ID/g, lower than that in saline cohorts (55.08 ± 7.54 %ID/g) or NCIN87 tumors from mice treated with an acute dose of metformin (56.43 ± 0.54 %ID/g). Similar results were obtained in tumors of mice treated daily with metformin and imaged with radiolabeled anti-EGFR panitumumab

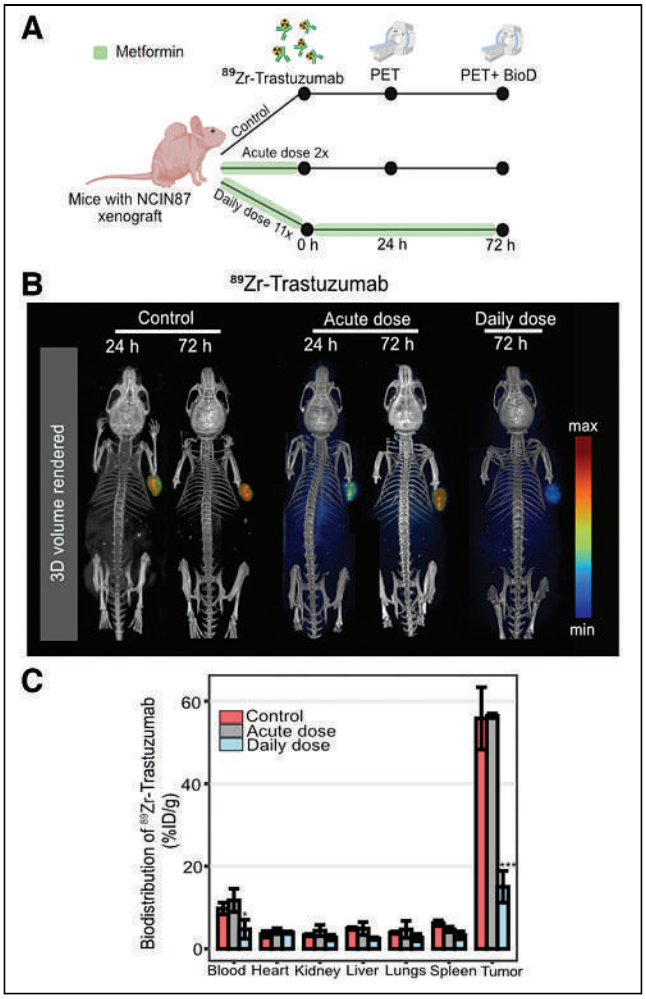


**FIGURE 4.** (A) Schematic representation of PET imaging in mice bearing tumor xenografts treated with acute or daily dose of metformin. (B) Representative 3-dimensional volume-rendered images of PET at 24 and 72 h after tail vein injection of $^{89}$Zr-labeled trastuzumab in mice bearing HER2-positive NCIN87 xenografts. Metformin (250 mg/kg) was orally administered 1 d before and at same time as $^{89}$Zr-DFO-trastuzumab (6.66–7.40 MBq, 45–80 μg of protein) in acute-dose cohort. In daily-dose cohort, metformin (200 mg/kg) was injected daily by intraperitoneal administration. Scale bar, percentage injected dose (%ID) per gram of the organ. (C) Biodistribution profile of control, acute-dose, and daily-dose cohorts at 72 h after injection of $^{89}$Zr-DFO-trastuzumab. MIP = maximum-intensity projection. Supplemental materials provide full list of organ biodistribution. $^{***}P < 0.001$, based on Student *t* test and compared with control (bars, $n = 3$, mean ± SD). $^{*}P < 0.05$, based on Student *t* test and compared with control (bars, $n = 3$, mean ± SD). BioD = biodistribution.

(Supplemental Fig. 10). However, the tumor uptake of a radiolabeled IgG control was low and comparable in mice treated with saline and those with daily administration of metformin (Supplemental Fig. 11).

These results suggest that the reduction in membrane HER by daily treatments with metformin is physiologically significant and clinically relevant.

### PET Imaging Allows Monitoring of Cell-Surface HER Rebound After Withdrawal of Metformin

To validate the temporality and reversibility effect of metformin on antibody–tumor binding, we performed PET imaging before, during, and after metformin treatment using trastuzumab labeled with the short-lived isotope $^{64}$Cu (Fig. 5A). Mice with HER2-positive NCIN87 xenografts imaged before initiating the metformin treatment demonstrated tumor uptake of 51.54 ± 10.41 %ID/g (Fig. 5B; Supplemental Figs. 12 and 13). PET images of mice treated with a daily dose of metformin showed a 1.8-fold reduction in tumor uptake (27.42 ± 7.5 %ID/g). Finally, PET images of mice at 7 d after stopping the metformin treatment demonstrated tumor uptake similar to that observed before metformin therapy (57.82 ± 15.39 %ID/g). These studies suggest that immuno-PET can effectively track the temporal and reversible changes in antibody–tumor binding as a result of metformin treatment.

## DISCUSSION

In addition to its antidiabetic properties, metformin induces antitumor effects by directly inhibiting the phosphatidylinositol-3-kinase mammalian-target-of-rapamycin and Ras-mitogen-activated protein kinase (MAPK) pathways (*2,4,5,8*). The indirect antitumor effects of metformin comprise reduction of glucose, insulin metabolism, and immune responses by regulation of T-cell differentiation and activity (*12,29*). In addition, metformin reduces cholesterol biosynthesis through its indirect activation of the adenosine monophosphate-activated protein kinase pathway (*8,25,26,36,37*). Drugs that deplete cholesterol content at cell membranes temporally enhance receptor availability on the surface of cancer cells and tumor xenografts (*19–21,28*). Here, we show that metformin reduces the surface

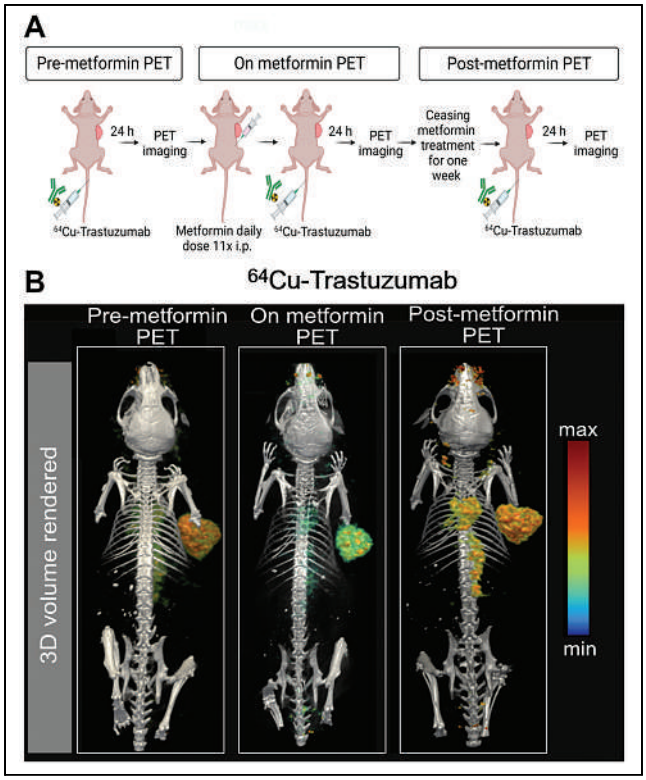


**FIGURE 5.** (A) Schematic representation of PET imaging before, during, and after treatment with daily dose of metformin. (B) Three-dimensional volume-rendered images of PET acquired at 24 h after injection of $^{64}$Cu-trastuzumab. Mice were imaged at 24 h after injection of $^{64}$Cu-trastuzumab (6.66–8.3 MBq or 45–56 μg of protein). PET images were acquired at baseline (pre-metformin PET), after daily administration of metformin (on metformin PET), and at 7 d after withdrawal of metformin (post-metformin PET). Scale bar, percentage injected dose (%ID) per gram of the organ.

availability of HER in a time-dependent manner. Metformin reduces membrane HER to decrease antibody binding to tumor xenografts. Our findings highlight the significance of monitoring the effects of over-the-counter medicines in oncology settings.

Treatment with metformin induces HER internalization (Fig. 2), decreasing the number of HER receptors available at the cell membrane for antibody–tumor binding (Fig. 4). A reduction in receptor density at the cell surface has been shown to decrease transphosphorylation, likely by reducing receptor dimerization. Loss of membrane HER in tumors not only decreases HER phosphorylation (Fig. 2) but also reduces antibody–tumor binding in mice treated with a prolonged dose of metformin (Fig. 4).

We found a decrease in the accumulation of trastuzumab or panitumumab binding to tumors as an acute response to oral administration of metformin. The effects induced by acute administration of metformin are reversible: progressive recovery in membrane HER (Figs. 2B and 2C) was detected after removing the metformin from cancer cells, and antibody–tumor accumulation recovered at 72 h in mice treated with only 2 doses of metformin (Fig. 4). However, mice treated daily with metformin showed a greater and more sustained reduction in antibody accumulation in tumors than did control mice or mice treated with an acute dose of metformin. Additional PET imaging studies performed before, during, and after metformin daily treatment demonstrated a rebound of cell-surface HER after withdrawal of the drug (Fig. 5). Because our imaging studies used a full-length antibody, it is possible that blocking of HER2 receptors could occur during the weekly imaging schedule. Therefore, future imaging studies will use a radiolabeled small molecule to monitor the dynamic changes induced by metformin in tumoral HER2. Future studies would be required to determine whether the depletion observed in antibody–tumor binding affects tumor response after treatment with an acute versus a prolonged dose of metformin in the presence or absence of anti-HER therapies.

The therapeutic efficacy of trastuzumab, trastuzumab–drug conjugates (trastuzumab emtansine or trastuzumab deruxtecan), cetuximab, and panitumumab depends on receptor density and HER-antibody trafficking (*19–21,38,39*). Our previous studies have shown that drugs altering rates of HER endocytosis and recycling result in changes in the surface pool of HER. We have previously reported that cholesterol-depleting drugs (*19–21*) enhance antibody–tumor binding and efficacy. Others have shown that metformin inhibits transcriptional and translational expression of key components of the cholesterol biosynthetic pathway (*8,22–26*). These previous reports could indicate that metformin may enhance antibody accumulation in tumors. However, our data suggest that daily administration of metformin reduces trastuzumab or panitumumab accumulation in tumors. Further studies are needed to understand the mechanisms, other than alterations in the cholesterol biosynthetic pathway, that occur in cancer cells treated with metformin.

The CAV1 protein, a major structural protein of cholesterol-rich, caveolae-mediated endocytosis, is involved in HER cell membrane dynamics, and the bioavailability of membrane HER is enhanced via temporal regulation of CAV1 (*19–21,27*). Others have shown that metformin-induced upregulation of AMP-activated protein kinase increases CAV1 expression in cancer cells, and pretreatment of cancer cells with metformin enhances trastuzumab emtansine efficacy (*28,40,41*). Here, we provide evidence that an acute dose of metformin upregulates CAV1 at early incubation times and leads to a rebound of membrane HER after the removal of metformin. However, a daily dose of metformin results in sustained depletion of membrane HER and reduces antibody accumulation in tumors. The discovery that metformin-induced depletion in cell-surface HER depends on time and dose may have direct implications for the use of anti-HER antibodies for imaging and therapy. Because many patients with cancer are prescribed metformin, our data provide a rationale to evaluate doses and regimens of metformin treatment that might affect the therapeutic or imaging outcomes in patients with HER2- or EGFR-expressing tumors.

In a recent phase 3 clinical trial (CCTG.MA.32), the addition of metformin to standard adjuvant chemotherapy did not improve progressive-free survival or overall survival for patients with hormone receptor–positive or hormone receptor–negative breast cancer (*42*). Metformin sensitizes HER-targeted therapies in vitro and in preclinical mouse models of cancer (*43,44*). The benefits of combining metformin with anti-HER therapies have also been tested in the clinical setting. Although the METTEN prospective clinical study demonstrated that nondiabetic breast cancer metformin users receiving trastuzumab and chemotherapy have a higher pathologic complete response than that of nonusers, the study was underpowered to show synergism (*44*).

Metformin is administered to humans with type 2 diabetes mellitus orally at therapeutic doses of 500–3,000 mg/d (*45*). After a single dose, the plasma concentrations peak in 3 h, resulting in concentrations ranging from 10 to 25 μM (*46,47*). In mice, administering metformin at a 250 mg/kg dose yields plasma concentrations of 125–150 μM after 1–2 h that rapidly decrease thereafter (*48*). However, metformin treatment of cancer cells requires high doses (in the millimolar range) to exert an anticancer effect or to deplete the cellular abundance of tumor targets. For example, previous studies reported that millimolar concentrations of metformin led to significant depletion of membrane programmed death-ligand 1 or HER (*29,49,50*). Similar to other studies reporting alterations in membrane receptor density on treatment with metformin (*28,29*), the in vitro concentrations reported here are higher than the micromolar-range concentrations detected in patients. Despite these differences in metformin dosage in clinical and preclinical settings, recent studies have shown that metformin can significantly reduce the expression of EGFR in clinical samples of oral squamous cell carcinoma (*51*). Therefore, it is necessary to explore how clinically relevant doses of metformin affect membrane HER and, subsequently, tumor uptake of anti-HER antibodies.

Our study has several limitations. Because the susceptibility of cancer cells to metformin depends on time, dose, and cell line, it is not clear whether the results described here will translate to other tumor types and membrane receptors. Given the ability of metformin to broadly affect cancer cells through multiple pathways, changes in CAV1 and membrane HER may partially explain the ability of metformin to decrease antibody binding in tumors. Although the dosage of metformin used in our in vitro studies is similar to that used in other studies reporting metformin-induced alterations in receptor density, a concentration in the millimolar range is higher than the concentration of metformin detected in serum samples of patients. In addition, the mechanisms by which metformin accumulates in cancer cells and how it confers beneficial effects in patients with cancer are incompletely understood. In our studies, an acute dose of metformin was administered orally to mimic clinical administration, whereas daily administration was performed through intraperitoneal injection with a nontoxic dosage schedule (*29*). Although intraperitoneal administration of a substance has similar pharmacokinetics to oral administration (*52*), further clinical studies are necessary to explore whether the route of administration of metformin can affect the uptake or biologic activity of anti-HER antibodies. Furthermore, it is not clear whether the alterations in HER observed in our studies using xenografts will translate into clinical changes due to differences in metformin pharmacokinetics in mice versus humans.

## CONCLUSION

Several clinical trials are under way to evaluate metformin for drug repurposing in patients with cancer. Our data suggest that short-term administration (2 d) of metformin treatment results in reversible depletion in membrane HER and, consequently, in temporal depletion of antibody–tumor accumulation. However, daily administration of metformin to mice with HER2-positive or EGFR-positive tumors reduces trastuzumab or panitumumab accumulation, respectively, as a result of reducing target density at the cell membrane. These results suggest that the daily use of metformin may influence the effectiveness of these cancer treatments and imaging outcomes and therefore should be carefully considered in the clinical setting.

## DISCLOSURE

This research was supported by internal funds provided by the Mallinckrodt Institute of Radiology (MIR) and in part by the American Cancer Society (IRG-21-133-64-03) and by the National Institutes of Health (NIH) (R37CA276498). Patrícia Pereira is supported by the NIH (R01 CA244233-01A1 and R37CA276498), American Cancer Society (IRG-21-133-64-03), Cancer Research Foundation (P22-03203), Elsa Pardee Foundation, Alvin J. Siteman Cancer Center (SSC) through the Foundation for Barnes-Jewish Hospital, and National Cancer Institute (NCI; P30 CA091842). Abbey Zidel's and Zachary Fisher's contributions to the research were supported through Washington University's biology undergraduate research program (Bio 200/500), MIR Summer Research Program, and the Summer Undergraduate Research Award. The Preclinical Imaging Facility was supported by NIH/NCI SCC support grant P30 CA091842, NIH instrumentation grants S10OD018515 and S10OD030403, and internal funds provided by MIR. The content is solely the responsibility of the authors and does not necessarily represent the official views of the NIH. No other potential conflict of interest relevant to this article was reported.

## ACKNOWLEDGMENTS

We thank the Washington University School of Medicine isotope production team for the production of $^{89}$Zr and $^{64}$Cu, and the small-animal imaging facility for help with the small-animal PET/CT image collection. We thank Dr. Luis Batista for letting us use the Odyssey Infrared Imaging System. We thank Dr. Luke Carter for his help with the 3D Slicer software. We acknowledge the SSC pharmacy for providing us with trastuzumab (Herceptin, Roche) and panitumumab (Vectibix, Amgen) antibodies.

### KEY POINTS

**QUESTION:** Can HER-targeted antibody PET imaging inform on metformin-induced alterations to the cell-surface density of tumor biomarkers?

**PERTINENT FINDINGS:** Metformin has both time- and dose-dependent effects on membrane HER density as visualized by immuno-PET.

**IMPLICATIONS FOR PATIENT CARE:** Metformin-induced downregulation of cell-surface HER reduces the accumulation of therapeutic anti-HER antibodies in tumors that could affect tumor response to therapy.

## REFERENCES

1. American Diabetes Association. Pharmacologic approaches to glycemic treatment: standards of medical care in diabetes—2021. *Diabetes Care.* 2021;44(suppl): S111–S124.
2. Foretz M, Guigas B, Bertrand L, Pollak M, Viollet B. Metformin: from mechanisms of action to therapies. *Cell Metab.* 2014;20:953–966.
3. Thomas I, Gregg B. Metformin; a review of its history and future: from lilac to longevity. *Pediatr Diabetes.* 2017;18:10–16.
4. Saraei P, Asadi I, Kakar MA, Moradi-Kor N. The beneficial effects of metformin on cancer prevention and therapy: a comprehensive review of recent advances. *Cancer Manag Res.* 2019;11:3295–3313.
5. Dowling RJ, Zakikhani M, Fantus IG, Pollak M, Sonenberg N. Metformin inhibits mammalian target of rapamycin-dependent translation initiation in breast cancer cells. *Cancer Res.* 2007;67:10804–10812.
6. Barzilai N, Crandall JP, Kritchevsky SB, Espeland MA. Metformin as a tool to target aging. *Cell Metab.* 2016;23:1060–1065.
7. Evans JM, Donnelly LA, Emslie-Smith AM, Alessi DR, Morris AD. Metformin and reduced risk of cancer in diabetic patients. *BMJ.* 2005;330:1304–1305.
8. Viollet B, Guigas B, Sanz Garcia N, Leclerc J, Foretz M, Andreelli F. Cellular and molecular mechanisms of metformin: an overview. *Clin Sci (Lond).* 2012;122: 253–270.
9. Decensi A, Puntoni M, Goodwin P, et al. Metformin and cancer risk in diabetic patients: a systematic review and meta-analysis. *Cancer Prev Res (Phila).* 2010;3: 1451–1461.
10. Kim J, Lee J, Jang SY, Kim C, Choi Y, Kim A. Anticancer effect of metformin on estrogen receptor-positive and tamoxifen-resistant breast cancer cell lines. *Oncol Rep.* 2016;35:2553–2560.
11. Schipper LJ, Zeverijn LJ, Garnett MJ, Voest EE. Can drug repurposing accelerate precision oncology? *Cancer Discov.* 2022;12:1634–1641.
12. Jin M-Z, Jin W-L. The updated landscape of tumor microenvironment and drug repurposing. *Signal Transduct Target Ther.* 2020;5:166.
13. Goldenberg JM, Cárdenas-Rodríguez J, Pagel MD. Preliminary results that assess metformin treatment in a preclinical model of pancreatic cancer using simultaneous [$^{18}$F]FDG PET and acidoCEST MRI. *Mol Imaging Biol.* 2018;20:575–583.
14. Lemmon MA, Schlessinger J, Ferguson KM. The EGFR family: not so prototypical receptor tyrosine kinases. *Cold Spring Harb Perspect Biol.* 2014;6:a020768.
15. Hudis CA. Trastuzumab: mechanism of action and use in clinical practice. *N Engl J Med.* 2007;357:39–51.
16. Alorabi M, Shonka NA, Ganti AK. EGFR monoclonal antibodies in locally advanced head and neck squamous cell carcinoma: what is their current role? *Crit Rev Oncol Hematol.* 2016;99:170–179.
17. Oh DY, Bang YJ. HER2-targeted therapies: a role beyond breast cancer. *Nat Rev Clin Oncol.* 2020;17:33–48.
18. Douillard JY, Oliner KS, Siena S, et al. Panitumumab-FOLFOX4 treatment and RAS mutations in colorectal cancer. *N Engl J Med.* 2013;369:1023–1034.
19. Pereira PMR, Mandleywala K, Monette S, et al. Caveolin-1 temporal modulation enhances antibody drug efficacy in heterogeneous gastric cancer. *Nat Commun.* 2022;13:2526.
20. Pereira PMR, Sharma SK, Carter LM, et al. Caveolin-1 mediates cellular distribution of HER2 and affects trastuzumab binding and therapeutic efficacy. *Nat Commun.* 2018;9:5137.
21. Pereira PMR, Mandleywala K, Ragupathi A, Lewis JS. Acute statin treatment improves antibody accumulation in EGFR- and PSMA-expressing tumors. *Clin Cancer Res.* 2020;26:6215–6229.
22. Wahdan-Alaswad RS, Cochrane DR, Spoelstra NS, et al. Metformin-induced killing of triple-negative breast cancer cells is mediated by reduction in fatty acid synthase via miRNA-193b. *Horm Cancer.* 2014;5:374–389.
23. Wahdan-Alaswad RS, Edgerton SM, Salem HS, Thor AD. Metformin targets cholesterol biosynthesis pathway, GM1 lipid raft stabilization, EGFR signaling and proliferation in triple negative breast cancers. *Cancer Ther Oncol Int J.* 2018;9: 555765.
24. Madsen A, Bozickovic O, Bjune J-I, Mellgren G, Sagen JV. Metformin inhibits hepatocellular glucose, lipid and cholesterol biosynthetic pathways by transcriptionally suppressing steroid receptor coactivator 2 (SRC-2). *Sci Rep.* 2015;5:16430.
25. Shaw RJ, Lamia KA, Vasquez D, et al. The kinase LKB1 mediates glucose homeostasis in liver and therapeutic effects of metformin. *Science.* 2005;310:1642–1646.
26. Mazière JC, Mazière C, Mora L, et al. The antidiabetic drug metformin decreases cholesterol metabolism in cultured human fibroblasts. *Atherosclerosis.* 1988;71: 27–33.
27. Pereira PMR, Mandleywala K, Ragupathi A, et al. Temporal modulation of HER2 membrane availability increases pertuzumab uptake and pretargeted molecular imaging of gastric tumors. *J Nucl Med.* 2019;60:1569–1578.

28. Chung Y-C, Chang C-M, Wei W-C, Chang T-W, Chang K-J, Chao W-T. Metformin-induced caveolin-1 expression promotes T-DM1 drug efficacy in breast cancer cells. *Sci Rep.* 2018;8:3930.
29. Cha JH, Yang WH, Xia W, et al. Metformin promotes antitumor immunity via endoplasmic-reticulum-associated degradation of PD-L1. *Mol Cell.* 2018;71:606–620.
30. Sekhar SC, Kasai T, Satoh A, et al. Identification of caveolin-1 as a potential causative factor in the generation of trastuzumab resistance in breast cancer cells. *J Cancer.* 2013;4:391–401.
31. Sung M, Tan X, Lu B, et al. Caveolae-mediated endocytosis as a novel mechanism of resistance to trastuzumab emtansine (T-DM1). *Mol Cancer Ther.* 2018;17:243–253.
32. Park SS, Kim JE, Kim YA, Kim YC, Kim SW. Caveolin-1 is down-regulated and inversely correlated with HER2 and EGFR expression status in invasive ductal carcinoma of the breast. *Histopathology.* 2005;47:625–630.
33. Indira Chandran V, Månsson AS, Barbachowska M, et al. Hypoxia attenuates trastuzumab uptake and trastuzumab-emtansine (T-DM1) cytotoxicity through redistribution of phosphorylated caveolin-1. *Mol Cancer Res.* 2020;18:644–656.
34. Chung Y-C, Kuo J-F, Wei W-C, Chang K-J, Chao W-T. Caveolin-1 dependent endocytosis enhances the chemosensitivity of HER-2 positive breast cancer cells to trastuzumab emtansine (T-DM1). *PLoS One.* 2015;10:e0133072.
35. Sigismund S, Woelk T, Puri C, et al. Clathrin-independent endocytosis of ubiquitinated cargos. *Proc Natl Acad Sci USA.* 2005;102:2760–2765.
36. Zhou G, Myers R, Li Y, et al. Role of AMP-activated protein kinase in mechanism of metformin action. *J Clin Invest.* 2001;108:1167–1174.
37. Teranishi T, Ohara T, Maeda K, et al. Effects of pioglitazone and metformin on intracellular lipid content in liver and skeletal muscle of individuals with type 2 diabetes mellitus. *Metabolism.* 2007;56:1418–1424.
38. Li BT, Michelini F, Misale S, et al. HER2-mediated internalization of cytotoxic agents in *ERBB2* amplified or mutant lung cancers. *Cancer Discov.* 2020;10:674–687.
39. Chew HY, De Lima PO, Gonzalez Cruz JL, et al. Endocytosis inhibition in humans to improve responses to ADCC-mediating antibodies. *Cell.* 2020;180:895–914.
40. Salis O, Bedir A, Ozdemir T, Okuyucu A, Alacam H. The relationship between anticancer effect of metformin and the transcriptional regulation of certain genes (CHOP, CAV-1, HO-1, SGK-1 and Par-4) on MCF-7 cell line. *Eur Rev Med Pharmacol Sci.* 2014;18:1602–1609.
41. Salani B, Maffioli S, Hamoudane M, et al. Caveolin-1 is essential for metformin inhibitory effect on IGF1 action in non-small-cell lung cancer cells. *FASEB J.* 2012;26:788–798.
42. Goodwin PJ, Dowling RJO, Ennis M, et al. Effect of metformin versus placebo on metabolic factors in the MA.32 randomized breast cancer trial. *NPJ Breast Cancer.* 2021;7:74.
43. Li L, Han R, Xiao H, et al. Metformin sensitizes EGFR-TKI-resistant human lung cancer cells in vitro and in vivo through inhibition of IL-6 signaling and EMT reversal. *Clin Cancer Res.* 2014;20:2714–2726.
44. Morgillo F, Sasso FC, Della Corte CM, et al. Synergistic effects of metformin treatment in combination with gefitinib, a selective EGFR tyrosine kinase inhibitor, in LKB1 wild-type NSCLC cell lines. *Clin Cancer Res.* 2013;19:3508–3519.
45. Bailey CJ, Turner RC. Metformin. *N Engl J Med.* 1996;334:574–579.
46. Lalau JD, Lemaire-Hurtel AS, Lacroix C. Establishment of a database of metformin plasma concentrations and erythrocyte levels in normal and emergency situations. *Clin Drug Investig.* 2011;31:435–438.
47. Owen MR, Doran E, Halestrap AP. Evidence that metformin exerts its antidiabetic effects through inhibition of complex 1 of the mitochondrial respiratory chain. *Biochem J.* 2000;348:607–614.
48. Hunter RW, Hughey CC, Lantier L, et al. Metformin reduces liver glucose production by inhibition of fructose-1-6-bisphosphatase. *Nat Med.* 2018;24:1395–1406.
49. Chen G, Huang AC, Zhang W, et al. Exosomal PD-L1 contributes to immunosuppression and is associated with anti-PD-1 response. *Nature.* 2018;560:382–386.
50. Vazquez-Martin A, Oliveras-Ferraros C, Menendez JA. The antidiabetic drug metformin suppresses HER2 (erbB-2) oncoprotein overexpression via inhibition of the mTOR effector p70S6K1 in human breast carcinoma cells. *Cell Cycle.* 2009;8:88–96.
51. Wang W-M, Yang S-S, Shao S-H, Nie H-Q, Zhang J, Su T. Metformin downregulates the expression of epidermal growth factor receptor independent of lowering blood glucose in oral squamous cell carcinoma. *Front Endocrinol (Lausanne).* 2022;13:828608.
52. Lukas G, Brindle SD, Greengard P. The route of absorption of intraperitoneally administered compounds. *J Pharmacol Exp Ther.* 1971;178:562–564.

# Pretargeting with Cucurbituril–Adamantane Host–Guest Pair in Xenograft Models

Vilma I.J. Jallinoja[1,2], Courtney H. Abbriano[1], Kavita Bhatt[1], Amritjyot Kaur[1], David J. Schlyer[1,3], Paul J. Yazaki[4], Brandon D. Carney[1], and Jacob L. Houghton[1]

*[1]Department of Radiology, Stony Brook University, Stony Brook, New York; [2]Chemical and Physical Biology Graduate Program, Vanderbilt University, Nashville, Tennessee; [3]Collider-Accelerator Department, Brookhaven National Laboratory, Upton, New York; and [4]Department of Immunology and Theranostics, Beckman Research Institute, City of Hope, Duarte, California*

The goal of reducing the total-body radiation dose of macromolecule-based nuclear medicine with a 2-step pretargeting strategy has been achieved with several pretargeting methodologies in preclinical and clinical settings. However, the lack of modularity, biocompatibility, and in vivo stability in existing pretargeting agents obstructs their respective platforms' wide clinical use. We hypothesized that host–guest chemistry would provide an optimal pretargeting methodology. A cucurbit[7]uril host and an adamantane guest molecule form a high-affinity host–guest complex (association constant, $\sim 10^{14}$ $M^{-1}$), and in this work, we explored the use of this noncovalent interaction as the basis for antibody-based pretargeted PET. Along with the straightforward modularity of these agents, cucurbit[7]uril and adamantane are recognized to have high in vivo stability and suitability for human use, which is why we proposed this methodology as the ideal approach for pretargeted nuclear medicine. **Methods:** Three $^{64}$Cu-labeled adamantane guest radioligands were developed, and their in vitro stability, lipophilicity, and in vivo blood half-lives were compared. The adamantane radioligands were analyzed for pretargeting using a cucurbit[7]uril-modified carcinoembryonic antigen–targeting full-length antibody, hT84.66-M5A, as the macromolecule pretargeting agent with 2 different dosing schedules. These molecules were evaluated for pretargeting in human pancreatic cancer BxPC3 and MIAPaCa-2 mouse xenografts using PET and in vivo biodistribution studies. The dosimetry of the cucurbit[7]uril–adamantane (CB7-Adma) pretargeting approach in men was calculated and compared with that of the directly $^{89}$Zr-labeled hT84.66-M5A. **Results:** The adamantane radioligands possessed high in vitro stability up to 24 h (>90%). Pretargeted PET with CB7-Adma methodology resulted in specific tumor uptake ($P < 0.05$) with low background signal. The in vivo formed CB7-Adma complex was demonstrated to be stable, with high tumor uptake up to 24 h after radioligand injection (12.0 ± 0.9 percentage injected dose/g). The total-body radiation dose of the pretargeting strategy was only 3.3% that of the directly $^{89}$Zr-labeled hT84.66-M5A. **Conclusion:** The CB7-Adma strategy is highly suitable for pretargeted PET. The exceptional stability of the pretargeting agents and the specific and high tumor uptake of the pretargeted adamantane radioligands provide great potential for the platform.

**Key Words:** pretargeting; host–guest chemistry; carcinoembryonic antigen; PET; adamantane

**J Nucl Med 2023; 64:1203–1209**
DOI: 10.2967/jnumed.122.265008

Pretargeted PET provides a quantitative, noninvasive whole-body in vivo profile of macromolecules with an overall lower total-body radiation dose than directly radiolabeled macromolecules (*1,2*). Pretargeting is a 2-step strategy involving administration of a target-binding macromolecule that accumulates at the target site over several days while the unbound macromolecule excretes from nontarget tissue. In a second step, a bioorthogonal small-molecule radioligand is administered (Fig. 1). The low molecular weight of the radioligand allows its target accumulation and excretion to occur more quickly than for the initial macromolecule. The work reported here harnesses host–guest complex formation as the specific pretargeting interaction between the macromolecule and the radioligand. We hypothesized that because of the high in vivo stability, modularity and low immunogenicity, the chosen host–guest pair, cucurbit[7]uril–adamantane (CB7-Adma; association constant, $\sim 10^{14}$ $M^{-1}$), makes an ideal interaction pair for pretargeted PET (*3–5*). The strong complex between the 2 molecules forms when the Adma guest with an adjacent positively charged moiety binds to the carbonyl framed cavity of the macrocyclic CB7 host molecule via multiple van der Waals and ion-dipole interactions. So far, the medical imaging applications using host–guest chemistry have been limited to preformed host–guest complexes to increase the stability or sensitivity of imaging agents (*6–8*). In nuclear medicine, the high-affinity noncovalent binding between CB7 and Adma molecules has remained minimally explored (*9*).

The reported work lays the foundation for the host–guest chemistry of the CB7-Adma–driven pretargeting platform. Three $^{64}$Cu-labeled Adma guest molecules were synthesized and characterized: [$^{64}$Cu]Cu-NOTA-Adma (**1**), [$^{64}$Cu]Cu-NOTA-polyethylene glycol $(PEG)_3$-Adma (**2**), and [$^{64}$Cu]Cu-NOTA-$PEG_7$-Adma (**3**) (Fig. 2A). The in vivo profile of the ligands for pretargeting was evaluated using a CB7-modified carcinoembryonic antigen (CEA) targeting humanized full-length antibody (CB7-M5A) as the secondary pretargeting agent. To study the potential of the platform, we investigated 2 pretargeting lag time schedules, 72 and 144 h. The pretargeting studies were performed on BxPC3 (CEA-positive) and MIAPaCa-2 (CEA-negative) human pancreatic cancer mouse xenografts (*10–12*).

The biodistribution and dosimetry of the pretargeted Adma radioligand were compared with those of a directly $^{89}$Zr-labeled M5A. We hypothesized that the high stability, mutual high affinity, and human compatibility of the proposed CB7-Adma pretargeting agents would provide a great basis for a widely applicable pretargeting platform.

Received Oct. 7, 2022; revision accepted Mar. 14, 2023.
For correspondence or reprints, contact Jacob Houghton (jacob.houghton@stonybrookmedicine.edu).
Published online Apr. 6, 2023.

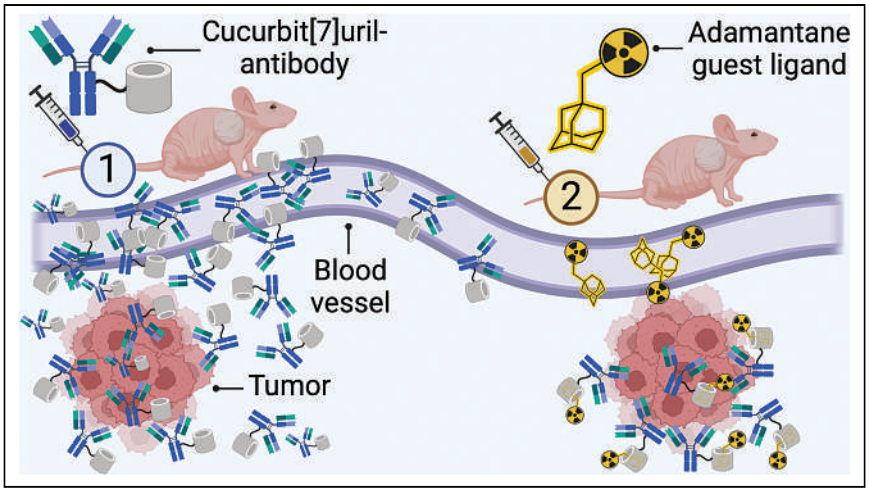


**FIGURE 1.** Illustration of 2-step CB7-Adma pretargeting approach.

## MATERIALS AND METHODS

### Development of Adma Radioligands

Detailed information on synthesis and characterization of the precursors for Adma radioligands **1**–**3** is provided in Supplemental Figures 1–3 (supplemental materials are available at http://jnm.snmjournals.org) To synthesize **1**–**3,** [$^{64}$Cu]$CuCl_2$ in 0.05 M HCl (1.5–7.4 μL; 47–260 MBq) was mixed with 0.2 M $NH_4OAc$ (pH 5.5; 50–150 μL) in an Eppendorf tube. The respective precursors for **1, 2,** and **3** (1–5 μL in DMSO) were added to the solution, followed by incubation of the reaction at room temperature for 10 min. The reaction was monitored with radio–high-performance liquid chromatography using a method described in the supplemental materials. Because of the high radiolabeling yield, no purification was required.

### Synthesis and Characterization of Modified M5A Molecules

CB7-M5A and deferoxamine-conjugated M5A (DFO-M5A) were prepared as previously described (*13,14*). The quality control of both modified antibodies was performed with size-exclusion chromatography, and the immunoreactivity was determined via cellular binding using the Lindmo assay (*15*) as previously reported (*14*). The number of CB7 moieties per monoclonal antibody (mAb) was determined as previously reported (*13*).

### $^{89}$Zr Labeling of DFO-M5A

[$^{89}$Zr]$Zr(C_2O_4)_2$ in 0.1 M oxalic acid (86.2 MBq; 46 μL) was neutralized to pH 7.4 using 1 M $NaHCO_3$. DFO-M5A (900 μg; 6 nmol in 450 μL in phosphate-buffered saline [PBS], pH 7.4) was added to the solution of $^{89}$Zr, and the labeling reaction was incubated at room temperature for 1 h. The labeling reaction yield was checked with radio–thin-layer chromatography using instant thin-layer chromatography silica gel glass microfiber chromatography paper and 50 mM ethylenediaminetetraacetic acid as the mobile phase. The synthesized [$^{89}$Zr]Zr-DFO-M5A was purified with a PD10 desalting column using PBS as the elution buffer. The radiochemical purity of the purified product was determined using the previously described radio–thin-layer chromatography method.

### In Vitro Stability and Plasma Protein Binding of 1–3

The in vitro stability of **1**–**3** was studied in PBS and in bovine plasma at 37°C. First, freshly synthesized radioligand (**1**–**3**; 1.5 nmol; 3.0–3.9 MBq in 100 μL of 0.2 M $NH_4OAc$, pH 5.5) was added to an Eppendorf tube with PBS (1 mL). The samples were incubated at 37°C for 1, 6, or 24 h, after which they were analyzed with radio–high-performance liquid chromatography. To study the ligands' stability in plasma, freshly synthesized radioligands **1**–**3** (1.4 MBq in 5 μL of 0.2 M $NH_4OAc$, pH 5.5) were mixed with bovine plasma (100 μL). The samples were incubated at 37°C for 1, 6, or 24 h followed by an addition of cold acetonitrile (100 μL). The sample was centrifuged for 5 min (10,000 rpm). Supernatant was collected and centrifuged for a second time, after which it was diluted with $H_2O$ (300 μL) and run on radio–high-performance liquid chromatography. The formed pellet was measured for radioactivity and compared with the initial total activity to determine the protein-bound fraction. Both stability assays were done in triplicate.

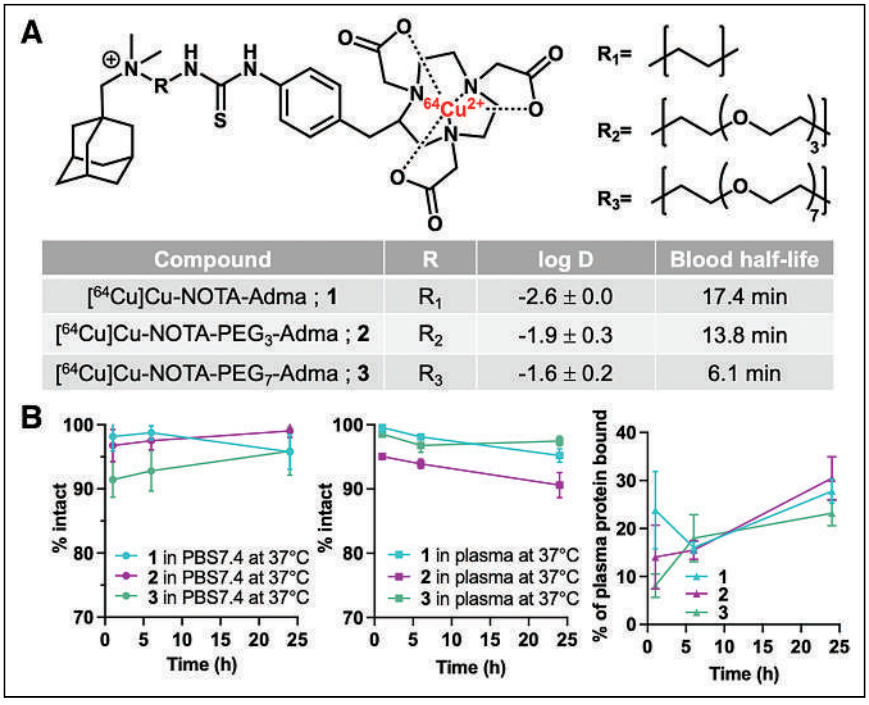


| Compound | R | log D | Blood half-life |
|---|---|---|---|
| [$^{64}$Cu]Cu-NOTA-Adma ; **1** | $R_1$ | -2.6 ± 0.0 | 17.4 min |
| [$^{64}$Cu]Cu-NOTA-$PEG_3$-Adma ; **2** | $R_2$ | -1.9 ± 0.3 | 13.8 min |
| [$^{64}$Cu]Cu-NOTA-$PEG_7$-Adma ; **3** | $R_3$ | -1.6 ± 0.2 | 6.1 min |

**FIGURE 2.** (A) Chemical structure of [$^{64}$Cu]Cu-NOTA-Adma (**1**), [$^{64}$Cu]Cu-NOTA-$PEG_3$-Adma (**2**), and [$^{64}$Cu]Cu-NOTA-$PEG_7$-Adma (**3**) and their respective log D and blood half-lives. (B) In vitro stability of **1–3** in PBS (pH 7.4) and in bovine plasma at 37°C and their plasma protein binding.

### Distribution Coefficient (Log D) Measurement of Guest Radioligands

Freshly synthesized radioligands **1**–**3** (586–610 kBq; 13 μL in 0.2 M $NH_4OAc$, pH 5.5) were added to an Eppendorf tube containing PBS (600 μL) and 1-octanol (600 μL). The mixture was stirred on a ThermoMixer (Eppendorf) for 10 min (900 rpm) at room temperature and was then centrifuged for 5 min (1,000 relative central force); 200 μL of each phase were transferred, and the samples were weighed and counted on a γ-counter to determine the relative amount of radioactivity in each phase. The log D value was calculated as $\log_{10}$ (% radioligand

in 1-octanol/% radioligand in PBS). The experiment was done in triplicate.

### BxPC3 Cell Interaction with 2

Freshly synthesized **2** (354 kBq; 10 μL) or [$^{64}$Cu]$CuCl_2$ in 0.2 M $NH_4OAc$, pH 5.5 (407 kBq; 10 μL), was mixed with RPMI-1640 medium containing a 0.3 g/L concentration of glutamine, 25 mM 4-(2-hydroxyethyl)-1-piperazineethanesulfonic acid, 1% (v/v) penicillin–streptomycin, and 10% (v/v) fetal bovine serum (12 mL). Medium (1 mL) was measured into the wells of a 6-well plate that had been plated with $0.75 \times 10^6$ BxPC3 cells the day before. The cells were incubated with the medium for 2, 4, or 6 h at 37°C followed by treatment with 0.05 M glycine, pH 2.8. Finally, the cells were lysed by being incubated with 1.0 M NaOH. The medium, glycine, and NaOH solutions were collected and measured with a γ-counter to determine the unbound, membrane-bound, and internalized fraction of each radioactive agent.

### 1–3 in Healthy Mice

To determine the blood half-life of each Adma radioligand, freshly synthesized radioligands **1**–**3** (13.6–14.8 MBq; 1.5 nmol in 100 μL of PBS) were injected intravenously into healthy female nude mice ($n = 3$). Blood was drawn from the saphenous vein at 6 different time points after injection (2, 5, 15, 30, 60, and 120 min). The collected blood samples were weighed and measured with a γ-counter to determine the percentage injected dose per gram (%ID/g) for each sample. In addition to studying the blood half-life of each radioligand, we studied the renal excretion of **2** at early time points in healthy female nude mice by collecting urine at 20 and 60 min after radioligand injection. Further descriptions of both experiments are detailed in the supplemental materials.

### Pretargeting with 1–3

Experimental cohorts of BxPC3 tumor–bearing female nude mice ($n = 4$–5/cohort) were injected intravenously with CB7-M5A (0.7 nmol; 100 μg in 150 μL in PBS) followed 72 h later with an intravenous injection of **1**–**3** (1.5 nmol; 10.2–13.9 MBq in 150 μL in PBS). For pretargeting with **2,** a 144-h lag time between the antibody and radioligand was also investigated. The cohorts were euthanized for in vivo biodistribution 4, 8, or 24 h after radioligand injection, and the 24-h cohort was also imaged with a small-animal PET/CT scanner (Siemens Inveon) at 4, 8, and 24 h after radioligand injection before euthanasia. An additional cohort per time point for pretargeted **2** was assigned, which was euthanized 2 h after radioligand injection for dosimetry calculations. The corresponding control cohort ($n = 4$/cohort) for each ligand was injected intravenously only with **1**–**3** and euthanized for in vivo biodistribution studies 24 h after injection.

### [$^{89}$Zr]Zr-DFO-M5A In Vivo Profile in Tumor Models

A cohort of BxPC3 and MIAPaCa-2 tumor–bearing female nude mice ($n = 4$/cohort) was injected intravenously with [$^{89}$Zr]Zr-DFO-M5A (0.7 nmol; 100 μg; 2.3–3.4 MBq in 200 μL in PBS). The mice were imaged with a small-animal PET/CT scanner 72 h after injection, followed by in vivo biodistribution studies.

### Pretargeting with 2 in MIAPaCa-2 Xenografts

A cohort of MIAPaCa-2 tumor–bearing female nude mice ($n = 4$) was injected with CB7-M5A (0.7 nmol; 100 μg in 150 μL in PBS) intravenously 72 h before an injection of **2** (1.5 nmol; 8.8–10.1 MBq in 150 μL in PBS). The mice were imaged with a small-animal PET/CT scanner 24 h after radioligand injection, followed by in vivo biodistribution studies.

### The Dosimetry of Pretargeted 2

The estimated dosimetry of the pretargeted **2** in a man (70 kg) was calculated on the basis of the in vivo biodistribution of the pretargeted **2** in BxPC3 tumor–bearing mice. The biodistribution data were fitted using a linear interpolation between time points. The linear function of each organ was used to interpolate the concentration at intervals of 1 h to better estimate the kinetics. The integration time was extended 48 h with the assumption that the %ID per organ was constant after the first 24 h and that the only change in concentration between 24 and 48 h was due to radioactive decay. A trapezoidal approximation was then used to obtain the integral over the time intervals. These residence times were used to estimate the absorbed dose to a human subject using the OLINDA program (*16*) with the adult human male model and no bladder clearance. The %ID to the large intestine was divided equally between the right and left colon for input into the OLINDA model for a man. The dose to the rest of the body was not used in this calculation.

### Statistical Analysis

Statistical analysis for all data from the biodistribution and in vitro assays was performed with 2-tailed unpaired *t* tests using Prism (GraphPad Software, Inc.). A *P* value between 2 groups of less than 0.05 was considered significant. At least 4 mice were used for each pretargeting cohort. All in vitro experiments were performed in triplicate unless otherwise noted.

## RESULTS

### Development of Pretargeting Agents

Each of the 3 radioligands was synthesized and radiolabeled efficiently and in good yields. Precursors for **1, 2,** and **3** were synthesized with overall yields of 14.5%, 36.2%, and 14.1%, respectively, and with respective chemical purities of 97.6%, 97.2%, and 95.8% (Supplemental Figs. 4–6). Radioligands **1**–**3** were produced by radiolabeling their corresponding precursors with high radiochemical yields of 97.6% ± 1.5%, 98.5% ± 0.7%, and 96.7% ± 0.0%, respectively, and with purity of 97.5% ± 1.0%, 98.3% ± 1.8%, and 98.9% ± 0.7%, respectively ($n = 3$) (Supplemental Figs. 7–9).

CB7 conjugated antibody was synthesized with an overall recovery yield of 83%. Each M5A was determined to have 0.8 ± 0.0 CB7 ($n = 3$) moieties on average. Quality control testing of the CB7-M5A indicated that no aggregation or fragments were present (Supplemental Fig. 10). The immunoreactivity of the CB7-conjugated antibody was 95.7% ± 0.7% ($n = 3$).

### In Vitro Characterization of 1–3

To compare the 3 radioligands, we performed in vitro analysis on each to determine their relative pharmacologic characteristics and suitability for in vivo pretargeting experiments. **1**–**3** demonstrated great in vitro stability in PBS and in bovine plasma (Fig. 1B; Supplemental Tables 1 and 2). At 24 h, 95.8% ± 2.2%, 99.0% ± 0.8%, and 95.9% ± 3.1% of **1, 2,** and **3,** respectively, was still intact in PBS and 95.2% ± 0.9%, 90.6% ± 1.6%, and 97.5% ± 0.6%, respectively, remained intact in bovine plasma samples. No free $^{64}$Cu was observed in any of the stability samples, suggesting that the radioligands were sufficiently stable for the application. At the 1-h time point, the Adma radioligands exhibited decreased plasma binding as the length of polyethylene glycol (PEG) linker increased (23.8 ± 6.6 [**1**], 14.0 ± 5.4 [**2**], and 8.1 ± 2.0 [**3**]). Additionally, the fraction of protein-bound radioligand grew over time to the last time point of 24 h (27.8 ± 2.1 [**1**], 30.5 ± 3.7 [**2**], and 23.2 ± 2.1 [**3**]). These differences among the molecules were not significant ($P > 0.05$).

On the basis of the cell internalization assay in BxPC3 cells, **2** did not bind to the cell membrane (0.1% ± 0.1%) or get internalized (0.0% ± 0.0%) even after a 6-h incubation period (Supplemental Fig. 11). [$^{64}$Cu]$CuCl_2$ demonstrated significantly higher internalization (5.2% ± 0.3%; $P = 0.002$) than **2,** confirming that

the $^{64}$Cu-NOTA complex of **2** remained intact for the duration of the experiment.

### Development of DFO-Modified Antibody

Quality control testing indicated that the DFO-conjugated M5A antibody was intact, and no fragments or aggregates were detected (Supplemental Fig. 10). The overall recovery yield was 85%. The immunoreactive fraction of DFO-M5A was 89.6% ± 2.1%, which was suitable for in vivo analysis.

### 1–3 in Healthy Mice

To determine the route and relative rate of clearance of the radioligands, we investigated their blood half-life. Additionally, because we expected a combination of both renal and hepatobiliary clearance, we collected urine at time points earlier than the first biodistribution time point. The in vivo blood half-life experiments revealed that the blood half-life correlated negatively with the number of PEG units incorporated in the radioligand (Fig. 2A; Supplemental Fig. 12). The ligands' blood half-lives decreased as the PEG-linker length increased (**1,** 17.4 min; **2,** 13.8 min; **3,** 6.1 min). Urine samples at 20 and 60 min after injection of **2** into healthy mice indicated that the radioligand demonstrated high renal clearance at these early time points (680 ± 210 and 1,050 ± 450 %ID/g, respectively) (Supplemental Table 3).

### In Vivo Biodistribution of Pretargeted 1–3

In vivo biodistribution studies were performed to assess the relative effectiveness of the 3 radioligands for pretargeting of tumors in a mouse model. Of the 3 Adma radioligands that were studied with a 72-h lag time schedule, only pretargeted **1** and **2** demonstrated significantly higher tumor uptake than their respective control cohorts (**1,** $P = 0.005$; **2,** $P = 0.003$; Supplemental Tables 4 and 5). Pretargeted **3** resulted in almost 4 times higher average tumor uptake than control (3.9 ± 2.1 %ID/g and 0.0 ± 0.0 %ID/g, respectively; Supplemental Table 6). However, differences in tumor uptake between the cohorts were not significant ($P = 0.053$). Tumor uptake increased over time in all cohorts, yet the highest average tumor uptake was with pretargeted **2** (**1,** 8.9 ± 2.0 %ID/g; **2,** 12.0 ± 0.9 %ID/g; **3,** 3.9 ± 2.1 %ID/g) (Fig. 3). To demonstrate that our pretargeting platform may be suitable for clinical applications without the use of clearing agents, we also explored the best-performing radioligand (**2**) with a 144-h lag time, which is more aligned with the biologic half-life of mAbs in humans. For the pretargeted **2,** tumor uptake was lower when administration was at 144 h than at 72 h after CB7-M5A injection (144 h: 5.3 ± 1.4 %ID/g; $P = 0.01$), but the tumor-to-blood uptake ratio was substantially higher for the 144-h cohorts (Supplemental Tables 7 and 8).

The presence of all Adma radioligands in the blood pool was significantly higher in the pretargeting cohorts than in their corresponding control cohorts ($P = 0.001$, $P = 0.0006$, and $P = 0.01$ for **1, 2,** and **3,** respectively, with a 72-h lag time), revealing that the Adma radioligands bound to the remaining CB7-M5A circulating in the blood. However, when the lag time was extended from 72 to 144 h, the presence of the pretargeted **2** in the blood was not significantly higher than in control studies when only **2** was administered ($P = 0.13$), suggesting that less of **2** was binding to the CB7-M5A in the blood with the longer lag time (Supplemental Table 7). The lower presence of **2**-bound CB7-M5A circulating in the blood pool likely contributed to the fact that tumor uptake of pretargeted **2** was lower at later time points with the extended lag time. Initially at the 4-h time point, tumor uptake of pretargeted **2** was similar with 72- and 144-h lag times (3.5 ± 1.1 %ID/g and 3.2 ± 1.4 %ID/g, respectively).

All 3 pretargeted radioligands were excreted through the kidneys/bladder and gastrointestinal tract. With a 72-h lag time, excretion was the slowest for pretargeted **3.** For pretargeted **2,** excretion through the intestine was suggested to be slower with a longer lag time of 144 h. However, the SDs of the %ID/g values were large for the organ since feces were not removed from the large-intestine samples, a fact that could partly explain the difference between the lag time cohorts. By 24 h after injection, the excretion was complete for **1**–**3.** Despite the low kidney retention at 4 h with pretargeted **1**–**3** (<1.0 %ID/g; Supplemental Tables 4 and 7), **2** demonstrated early renal clearance in healthy mice (Supplemental Table 3).

As expected, tumor-to-blood ratios increased over time with the pretargeted ligands (Supplemental Table 8). The difference between the first and last time points was significant only with pretargeted **2** with a 72-h lag time (4 h, 2.3 ± 1.5; 24 h, 5.8 ± 0.4 [$P = 0.008$]). The low presence of **2** in the blood pool with the 144-h lag time resulted in a higher tumor-to-blood ratio at 24 h (16.7 ± 4.6) than under any other studied conditions.

As was expected from the CEA expression differences in BxPC3 and MIAPaCa-2 cells (Supplemental Fig. 13), tumor uptake of the pretargeted **2** was significantly lower in MIAPaCa-2 tumor models than in BxPC3 (0.5 ± 0.1 vs. 12.0 ± 0.9 %ID/g, respectively; $P = 0.003$), demonstrating the specificity of interaction of the radioligands with the tumors (Fig. 4D).

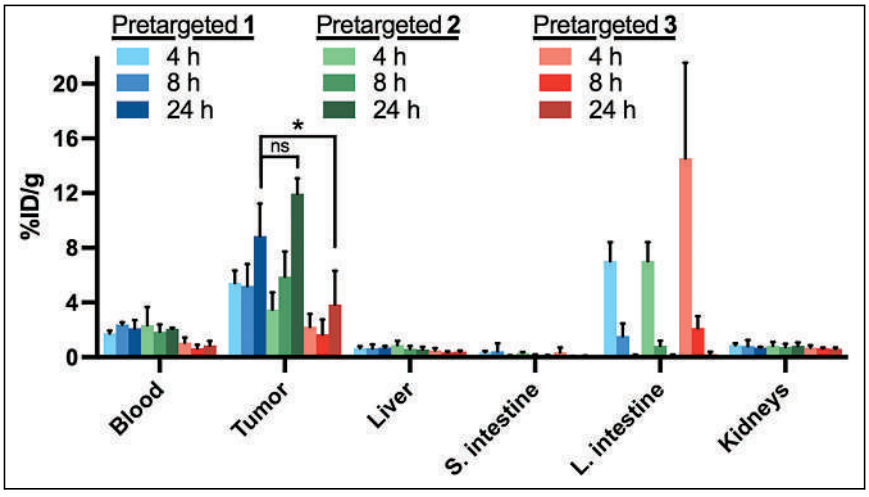


**FIGURE 3.** In vivo biodistribution of pretargeted [$^{64}$Cu]Cu-NOTA-Adma (**1**), [$^{64}$Cu]Cu-NOTA-PEG$_3$-Adma (**2**), and [$^{64}$Cu]Cu-NOTA-PEG$_7$-Adma (**3**) in BxPC3 tumor–bearing nude mice. *$P < 0.05$. ns = not significant.

### Pretargeted PET 1–3

PET imaging of the pretargeted radioligands **1**–**3** in BxPC3 tumor–bearing nude mice successfully delineated the tumor mass at all time points (Fig. 5; Supplemental Fig. 14). The images confirmed the in vivo biodistribution data, showing that the tumor uptake and tumor-to-background signal increased over time up to the last time point. Tumor uptake of the pretargeted radioligands **1**–**3** varied, at 3.8–17.1, 14.5–24.0, and

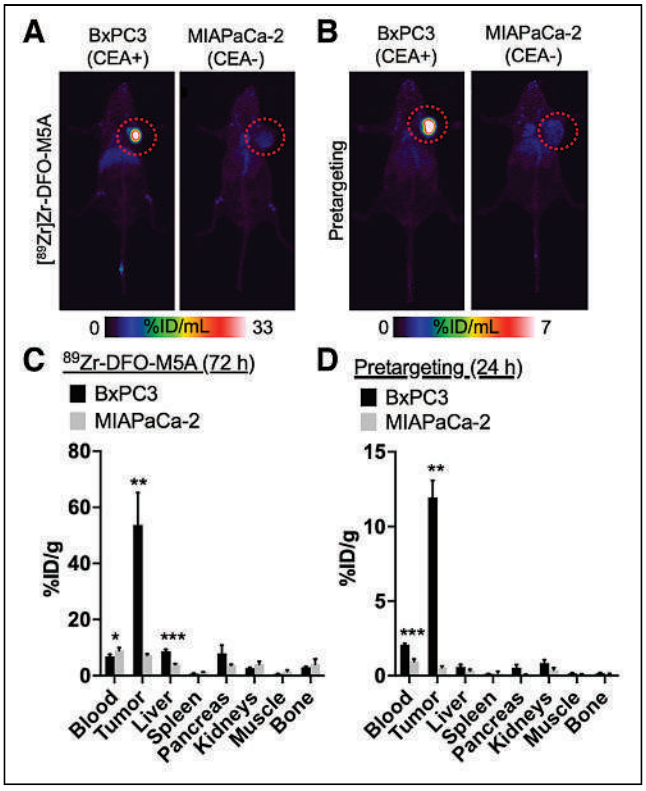


**FIGURE 4.** In vivo profile of [$^{89}$Zr]Zr-DFO-M5A at 72 h after injection and pretargeted **2** at 24 h after injection in BxPC3 and MIAPaCa-2 tumor–bearing female nude mice. Maximum-intensity-projection PET images of [$^{89}$Zr]Zr-DFO-M5A (A) and pretargeted **2** (B), and in vivo biodistribution of [$^{89}$Zr]Zr-DFO-M5A (C) and pretargeted **2** (D). Mice administered **2** were injected with CB7-M5A 72 h beforehand. Location of tumor on right shoulder is encircled.

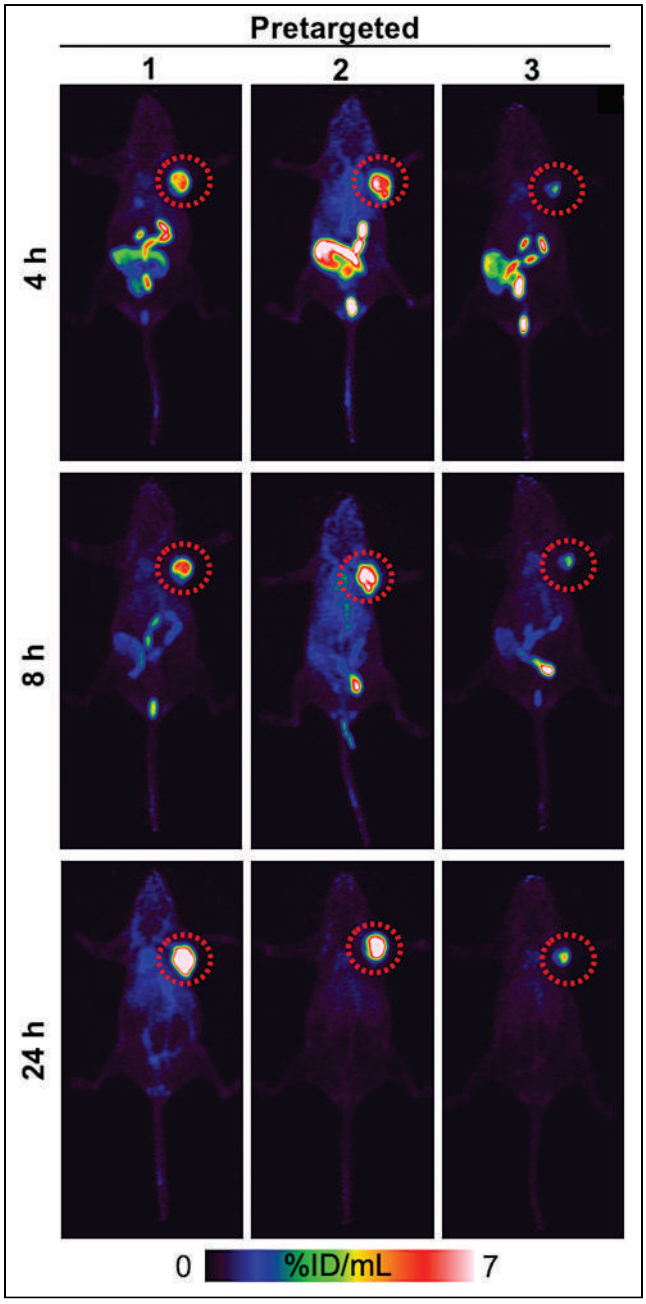


**FIGURE 5.** Maximum-intensity-projection PET images of pretargeted [$^{64}$Cu]Cu-NOTA-Adma (**1**), [$^{64}$Cu]Cu-NOTA-PEG$_3$-Adma (**2**), and [$^{64}$Cu]Cu-NOTA-PEG$_7$-Adma (**3**) in BxPC3 tumor–bearing nude mice at 4, 8, and 24 h after radioligand injection with 72-h lag time in pretargeting schedule. Location of tumor on right shoulder is encircled.

2.8–13.1 %ID/mL, respectively, with the 72-h lag time and 3.8–7.9 %ID/mL with the 144-h lag time at 24 h after radioligand injection. For the pretargeted **2** in MIAPaCa-2 tumor–bearing mice, the tumor uptake values were between 0.8 and 1.4 %ID/mL, indicating that there was no specific uptake in the tumors due to the lack of CEA expression (Fig. 4B).

### In Vivo Profile of [$^{89}$Zr]Zr-DFO-M5A in Xenograft Models

To compare uptake in antigen-expressing and antigen-negative cell lines with M5A, we used directly labeled [$^{89}$Zr]Zr-DFO-M5A. The in vivo profile of [$^{89}$Zr]Zr-DFO-M5A in the subcutaneous tumor mouse models of BxPC3 and MIAPaCa-2 revealed varying tumor uptake between the models. The findings aligned with the Western blotting results on the CEA expression of the cell lines, as well as with previously published results from the same cell lines (Supplemental Fig. 13) (*10–12*). The CEA-positive BxPC3 xenografts demonstrated higher tumor uptake than the CEA-negative xenografts of MIAPaCa-2 (53.7 ± 10.0 vs. 7.3 ± 0.3 %ID/g, respectively; $P$ = 0.004) (Fig. 4C). On the basis of these imaging experiments, the tumor-to-background signal was higher in the BxPC3 cohort than in MIAPaCa-2, and the tumor uptake values in both tumor models supported the findings of the in vivo biodistribution studies (BxPC3, 50.4 ± 8.9 %ID/mL; MIAPaCa-2, 4.8 ± 0.2 %ID/g) (Fig. 4A).

### Dosimetry of Pretargeted 2

To determine the dosimetric advantages of our pretargeting method, we calculated the dosimetry for our approach and compared it with that of the directly labeled [$^{89}$Zr]Zr-DFO-M5A. The estimated dose of a man for pretargeted **2** demonstrated that the CB7-Adma pretargeting approach resulted in much lower organ doses than did use of [$^{89}$Zr]Zr-DFO-M5A, whose dosimetry analysis was reported earlier by our laboratory (Supplemental Table 9) (*14*). In all investigated organs, the dose of pretargeted **2** was reduced severalfold compared with the directly radiolabeled M5A. The dose-limiting organ for use of directly radiolabeled antibodies is often red marrow, and here its dose with [$^{89}$Zr]Zr-DFO-M5A was found to be almost 70-fold higher than that of the pretargeted **2.** The reported injected clinical doses of $^{89}$Zr-labeled mAbs vary between 37 and

185 MBq (*17,18*). In this regard, with an estimated 110-MBq clinical dose of [$^{89}$Zr]Zr-DFO-M5A, the effective dose would be 95.5 mSv. A clinical dose of 150 MBq of pretargeted **2,** however, would give rise to a lower effective dose of 6.0 mSv while still providing the necessary tumor–to–nontarget tissue uptake ratios to clearly delineate CEA-expressing tumors.

## DISCUSSION

We have demonstrated in this work that host–guest CB7-Adma pretargeted PET shows specific and exceptionally high tumor uptake and tumor-to-background signal (Fig. 3; Supplemental Tables 4–8). The efficacy of the pretargeting methodology was evaluated with 3 $^{64}$Cu-labeled Adma radioligands. The pretargeted radioligand with the best in vivo profile, **2,** was also studied with an additional lag time. Since the motivation for the studies was development of a pretargeting platform, the dosimetry of a directly radiolabeled [$^{89}$Zr]Zr-DFO-M5A and CB7-M5A pretargeted **2** was compared (Supplemental Table 9). Although the isotopes were not matched for these experiments, [$^{89}$Zr]Zr-DFO-M5A was chosen because $^{89}$Zr is the most clinically relevant isotope for PET imaging with mAbs and provides information on the biologic fate of the mAbs at 5–7 d after injection, whereas $^{64}$Cu-based PET with mAbs is useful for only about 2 d after injection, when there is still very low tumor–to–nontarget tissue uptake, especially in the blood.

The difference among **1, 2,** and **3** was observed in their respective blood half-lives and log D values, which resulted in the ligands' having variance in their tumor uptake and clearance profile. The number of PEG units incorporated in the Adma radioligand correlated negatively with the compound's log D value and blood half-life. The same correlation between the number of PEG units and the log D value was observed earlier by our laboratory with ferrocene radioligands designed for pretargeting (*14*). As has been reported earlier, with a higher number of hydrophilic PEG units the expectation is to have lower respective log D values (*19*). In addition to exploring the use of other linkers, our laboratory is investigating why the opposite trend was observed with **1**–**3**.

In turn, the log D values of **1**–**3** negatively correlated with the blood half-lives. This trend toward diffusion of more hydrophilic compounds from the bloodstream through the cell membrane at a lower rate, resulting in a longer blood half-life, has been established before (*20,21*). The difference in tumor uptake of pretargeted **1** and **2** was not significant, despite their relative difference in blood half-life. However, the Adma radioligand with the shortest blood half-life, **3,** resulted in the lowest tumor uptake, which was determined to be significant compared with pretargeted **1** and **2.** This positive correlation between blood half-life and tumor uptake was reported earlier by us and other laboratories (*14,19*). As the radioligand remains in the blood pool longer, the molecule has more time to accumulate at the target site.

M5A demonstrated high specificity toward the CEA, which was validated with in vivo experiments with directly labeled M5A ([$^{89}$Zr]Zr-DFO-M5A) and pretargeted **2** in CEA-positive (BxPC3) and CEA-negative (MIAPaCa-2) tumor–bearing mice (Fig. 4). Both imaging experiments in the 2 tumor models showed that the high specificity and excellent tumor-to-background signal that antibody-based imaging provides is not lost when the antibody imaging is done with the CB7-Adma pretargeting strategy. The obtained tumor-to-blood ratio of pretargeted **2** at 24 h after injection with the longer lag time schedule of 144 h was higher than that of [$^{89}$Zr]Zr-DFO-M5A at 72 h after injection (16.7 ± 4.6 and 7.5 ± 1.1, respectively) (Supplemental Tables 8 and 9). Interestingly, the fact that we were able to obtain excellent tumor targeting with a 144-h lag time suggests that even longer lag times may still be possible, which would further improve the dosimetry by reducing exposure in nontarget tissues, including blood and marrow. This would potentially improve image contrast using our pretargeted approach, as well as the therapeutic index when turning this strategy to targeted radionuclide therapy.

Previously, our laboratory reported the use of ferrocene radioligand–driven host–guest chemistry methodology for pretargeted PET (*13,14*). Comparing the CB7-ferrocene pair with the CB7-Adma pair as the pretargeting agents, we can note several advantages in the latter approach. All the investigated Adma radioligands maintained high in vitro stability in plasma up to 24 h, unlike the reported ferrocene radioligands (70%–80% intact at 4 h). Additionally, the formed Adma-CB7 host–guest complex exhibited higher in vivo stability than the previously reported CB7-ferrocene complex. We observed increasing tumor uptake in pretargeting experiments with **1**–**3** from the first studied time point (4 h) to the last (24 h), whereas the opposite trend was observed in the CB7-ferrocene pretargeting approach, and dissociation of the ferrocene radioligand from the CB7 over time is observed. All in all, when the same antibody, pretargeting schedule, dosing, and mouse tumor model were used, the highest tumor uptake values experienced with our lead Adma radioligand candidate (**2**) were several times higher (8 h, 5.9 ± 1.6 %ID/g; 24 h, 12.0 ± 0.9 ID/g) than for the previously reported ferrocene radioligand (8 h, 3.1 ± 0.6 %ID/g; 24 h, 1.5 ± 0.5 %ID/g) (*14*). The in vivo stability of a preformed CB7-Adma complex has been explored earlier with $^{11}$C- and $^{18}$F-labeled Adma guests in rodents (*9*). The complexes exhibited high stability in vivo; however, the stability was studied up to only 1 h. Our work expands knowledge on the in vivo formed host–guest complexes and their stability.

We hypothesize that a major advantage of host–guest pretargeting lies in the high stability of the CB7-Adma components, allowing pretargeting with flexible pretargeting dosing schedules and preferably longer lag times (>3 d). The reported pretargeting strategy excels with varying lag times, making the strategy clinically approachable. Importantly, the feasibility of longer lag times potentially allows the methodology to further decrease the whole-body radiation dose and increase the tumor-to-background signal—a motivation for shifting to pretargeting technologies from the use of directly radiolabeled antibodies.

## CONCLUSION

We have reported the development and characterization of 3 Adma radioligands for CB7-Adma host–guest pretargeted PET. The use of a $^{64}$Cu-labeled Adma radioligand along with a CB7-modified anti-CEA full-length antibody as the pretargeting agent pair for pretargeted PET in BxPC3 tumor–bearing nude mice resulted in high, enduring target uptake of the radioligand. To our knowledge, this is the first reported pretargeting study using CB7-Adma complex formation as the pretargeting interaction for antibody-based PET.

## DISCLOSURE

This research was funded by the National Institutes of Health via the National Institute of Biomedical Imaging and Bioengineering under awards 1R21EB027982 and 1S10RR023680-1. No other potential conflict of interest relevant to this article was reported.

## ACKNOWLEDGMENTS

We thank the Stony Brook University Small-Animal PET/SPECT/CT In Vivo Imaging Core, supported by the Departments of Radiology and Chemistry, for its assistance. We acknowledge the Stony Brook Cancer Center (Biological Mass Spectrometry Shared Resources) for characterization of the small molecules.

## KEY POINTS

**QUESTION:** Can host–guest complexation between a cucurbit[7]uril and an adamantane be used for pretargeting?

**PERTINENT FINDINGS:** A cucurbit[7]uril-modified antibody and a $^{64}$Cu-labeled adamantane were administered separately intravenously to a mouse, and the biodistribution findings revealed that $^{64}$Cu-labeled Adma specifically bound to the CB7-modified antibody.

**IMPLICATIONS FOR PATIENT CARE:** Clinical studies of pretargeting technologies have been hindered by the immunogenicity and lack of modularity of the pretargeting agents. The reported work reveals a promising new strategy for pretargeted nuclear medicine.

## REFERENCES

1. Altai M, Membreno R, Cook B, Tolmachev V, Zeglis BM. Pretargeted imaging and therapy. *J Nucl Med.* 2017;58:1553–1559.
2. Jallinoja VI, Houghton JL. Current landscape in clinical pretargeted radioimmunoimaging and therapy. *J Nucl Med.* 2021;62:1200–1206.
3. Assaf KI, Nau WM. Cucurbiturils: from synthesis to high-affinity binding and catalysis. *Chem Soc Rev.* 2015;44:394–418.
4. Wanka L, Iqbal K, Schreiner PR. The lipophilic bullet hits the targets: medicinal chemistry of adamantane derivatives. *Chem Rev.* 2013;113:3516–3604.
5. Shetty D, Khedkar JK, Park KM, Kim K. Can we beat the biotin-avidin pair?: cucurbit[7]uril-based ultrahigh affinity host-guest complexes and their applications. *Chem Soc Rev.* 2015;44:8747–8761.
6. Zhao XB, Kang JY, Shi YP. Noncovalent dual-locked near-infrared fluorescent probe for precise imaging of tumor via hypoxia/glutathione activation. *Anal Chem.* 2022;94:6574–6581.
7. Sembo-Backonly BS, Estour F, Gouhier G. Cyclodextrins: promising scaffolds for MRI contrast agents. *RSC Advances.* 2021;11:29762–29785.
8. Wu H, Chen Z, Qi S, et al. Evaluation of the stability of cucurbit[8]uril-based ternary host-guest complexation in physiological environment and the fabrication of a supramolecular theranostic nanomedicine. *J Nanobiotechnology.* 2021;19:330.
9. Strebl MG, Yang J, Isaacs L, Hooker JM. Adamantane/cucurbituril: a potential pretargeted imaging strategy in immuno-PET. *Mol Imaging.* 2018;17:1536012118799838.
10. Girgis MD, Olafse T, Kenanova V, McCabe KE, Wu AM, Tomlinson JS. Targeting CEA in pancreas cancer xenografts with a mutated scFv-Fc antibody fragment. *EJNMMI Res.* 2011;1:24.
11. Yunis AA, Arimura GK, Russin DJ. Human pancreatic carcinoma (MIA PaCa-2) in continuous culture: sensitivity to asparaginase. *Int J Cancer.* 1977;19:128–135.
12. Tan MH, Nowak NJ, Loor R, et al. Characterization of a new primary human pancreatic tumor line. *Cancer Invest.* 1986;4:15–23.
13. Jallinoja VIJ, Carney BD, Zhu M, Bhatt K, Yazaki PJ, Houghton JL. Cucurbituril-ferrocene: host-guest based pretargeted positron emission tomography in a xenograft model. *Bioconjug Chem.* 2021;32:1554–1558.
14. Jallinoja VIJ, Carney BD, Bhatt K, et al. Investigation of copper-64-based host-guest chemistry pretargeted positron emission tomography. *Mol Pharm.* 2022;19:2268–2278.
15. Lindmo T, Bunn PA Jr. Determination of the true immunoreactive fraction of monoclonal antibodies after radiolabeling. *Methods Enzymol.* 1986;121:678–691.
16. Stabin MG, Sparks RB, Crowe E. OLINDA/EXM: the second-generation personal computer software for internal dose assessment in nuclear medicine. *J Nucl Med.* 2005;46:1023–1027.
17. Ulaner GA, Hyman DM, Lyashchenko SK, Lewis JS, Carrasquillo JA. $^{89}$Zr-trastuzumab PET/CT for detection of human epidermal growth factor receptor 2–positive metastases in patients with human epidermal growth factor receptor 2–negative primary breast cancer. *Clin Nucl Med.* 2017;42:912–917.
18. Menke-van der Houven van Oordt CW, Gootjes EC, Huisman MC, et al. $^{89}$Zr-cetuximab PET imaging in patients with advanced colorectal cancer. *Oncotarget.* 2015;6:30384–30393.
19. Meyer JP, Kozlowski P, Jackson J, et al. Exploring structural parameters for pretargeting radioligand optimization. *J Med Chem.* 2017;60:8201–8217.
20. Obach RS, Lombardo F, Waters NJ. Trend analysis of a database of intravenous pharmacokinetic parameters in humans for 670 drug compounds. *Drug Metab Dispos.* 2008;36:1385–1405.
21. Lewis JS, Windhorst AD, Zeglis BM. *Radiopharmaceutical Chemistry.* Springer Cham; 2019:125–127.

# Clinical Evaluation of $^{68}$Ga-FAPI-RGD for Imaging of Fibroblast Activation Protein and Integrin $\alpha_v\beta_3$ in Various Cancer Types

Liang Zhao*[1–4], Xuejun Wen*[5], Weizhi Xu*[1], Yizhen Pang[1,2], Long Sun[1], Xiaoming Wu[6], Pengfei Xu[3,4,7], Jingjing Zhang[3,4,7], Zhide Guo[5], Qin Lin[2], Xiaoyuan Chen[3,4,7], and Haojun Chen[1]

[1]*Department of Nuclear Medicine and Minnan PET Center, Xiamen Cancer Center, First Affiliated Hospital of Xiamen University, School of Medicine, Xiamen University, Xiamen, China;* [2]*Department of Radiation Oncology, Xiamen Key Laboratory of Radiation Oncology, Xiamen Cancer Center, First Affiliated Hospital of Xiamen University, School of Medicine, Xiamen University, Xiamen, China;* [3]*Departments of Diagnostic Radiology, Surgery, Chemical and Biomolecular Engineering, and Biomedical Engineering, Yong Loo Lin School of Medicine and Faculty of Engineering, National University of Singapore, Singapore;* [4]*Clinical Imaging Research Centre, Centre for Translational Medicine, Yong Loo Lin School of Medicine, National University of Singapore, Singapore;* [5]*State Key Laboratory of Molecular Vaccinology and Molecular Diagnostics and Center for Molecular Imaging and Translational Medicine, School of Public Health, Xiamen University, Xiamen, China;* [6]*College of Nuclear Science and Technology, Harbin Engineering University, Harbin, China; and* [7]*Nanomedicine Translational Research Program, NUS Center for Nanomedicine, Yong Loo Lin School of Medicine, National University of Singapore, Singapore*

Radiolabeled fibroblast activation protein (FAP) inhibitors (FAPIs) and Arg-Gly-Asp (RGD) peptides have been extensively investigated for imaging of FAP- and integrin $\alpha_v\beta_3$–positive tumors. In this study, a FAPI-RGD heterodimer was radiolabeled with $^{68}$Ga and evaluated in patients with cancer. We hypothesized that the heterodimer, recognizing both FAP and integrin $\alpha_v\beta_3$, would be advantageous because of its dual-receptor–targeting property. **Methods:** The effective dose of $^{68}$Ga-FAPI-RGD was evaluated in 3 healthy volunteers. The clinical feasibility of $^{68}$Ga-FAPI-RGD PET/CT was evaluated in 22 patients with various types of cancer, and the results were compared with those of $^{18}$F-FDG and $^{68}$Ga-FAPI-46. **Results:** $^{68}$Ga-FAPI-RGD was tolerated well, with no adverse events in any of the healthy volunteers or patients. The effective dose from $^{68}$Ga-FAPI-RGD PET/CT was $1.01 \times 10^{-2}$ mSv/MBq. In clinical investigations with different types of cancer, the radiotracer uptake and tumor-to-background ratio (TBR) of primary and metastatic lesions in $^{68}$Ga-FAPI-RGD PET/CT were significantly higher than those in $^{18}$F-FDG PET/CT (primary tumors: $SUV_{max}$, 18.0 vs. 9.1 [$P < 0.001$], and TBR, 15.2 vs. 5.5 [$P < 0.001$]; lymph node metastases: $SUV_{max}$, 12.1 vs. 6.1 [$P < 0.001$], and TBR, 13.3 vs. 4.1 [$P < 0.001$]), resulting in an improved lesion detection rate and tumor delineation, particularly for the diagnosis of lymph node (99% vs. 91%) and bone (100% vs. 80%) metastases. $^{68}$Ga-FAPI-RGD PET/CT also yielded a higher radiotracer uptake and TBR than $^{68}$Ga-FAPI-46 PET/CT did. **Conclusion:** $^{68}$Ga-FAPI-RGD exhibited improved tumor uptake and TBR compared with $^{18}$F-FDG and $^{68}$Ga-FAPI PET/CT. This study demonstrated the safety and clinical feasibility of $^{68}$Ga-FAPI-RGD PET/CT for imaging of various types of cancer.

**Key Words:** fibroblast activation protein; integrin $\alpha_v\beta_3$; heterodimer; cancer-associated-fibroblasts; PET

**J Nucl Med 2023; 64:1210–1217**
DOI: 10.2967/jnumed.122.265383

Tumor receptor imaging is an important component of oncologic molecular imaging and plays a key role in cancer diagnosis and management. It is made possible by the intense expression of specific biomarkers in the cellular membrane. Integrin $\alpha_v\beta_3$ is a heterodimeric transmembrane glycoprotein that is highly expressed in activated endothelial cells, newly formed blood vessels, and several types of tumor cells. In contrast, it exhibits low or no expression in normal cells (*1*). Therefore, integrin $\alpha_v\beta_3$ is a promising target for tumor imaging and therapy (*2*). The tripeptide Arg-Gly-Asp (RGD) moiety exhibits a high binding affinity and specificity for integrin $\alpha_v\beta_3$. Various RGD-based cyclic peptides have been labeled with radionuclides and extensively evaluated for PET or SPECT imaging of cancers (*2*). However, the rapid blood clearance of RGD peptides is one of the reasons that their application is limited in radionuclide therapy (*3*). The need to improve the pharmacokinetics of RGD peptides has led to multimeric strategies or conjugation with albumin-binding moieties (*3,4*). These approaches allow the transformation of a drug into a theranostic agent for use as both an imaging agent and a therapeutic agent.

The importance of the tumor microenvironment in cancer development and clinical prognosis is now widely appreciated (*5*). Besides tumor cells and tumor angiogenesis, cancer-associated fibroblasts of the tumor microenvironment are the major components of solid tumors (*6*). Fibroblast activation protein (FAP)–α is highly expressed in cancer-associated fibroblasts in most epithelial cancers but is weakly expressed in normal tissues, making it an attractive target for cancer imaging and therapy (*7*). In the past few years, quinoline-based FAP inhibitor (FAPI) PET/CT has become an active field in nuclear oncology (*7,8*). Various studies have demonstrated that

Received Dec. 30, 2022; revision accepted Mar. 17, 2023.
For correspondence or reprints, contact Haojun Chen (leochen0821@foxmail.com) or Xiaoyuan Chen (chen.shawn@nus.edu.sg).
*Contributed equally to this work.
Published online May 4, 2023.

FAPI-based radiopharmaceuticals are promising radiotracers for cancer diagnosis, staging, and restaging. They may be better alternatives for cancer types that exhibit low to moderate uptake of $^{18}$F-FDG, including gastric, pancreatic, and liver cancers (*9*).

Recently, a heterodimeric peptide, denoted as FAPI-RGD, was synthesized from FAPI-02 and cyclo-RGD-D-Phe-Lys (c[RGDfK]) for targeting both FAP and integrin $\alpha_v\beta_3$ receptors (*10*). It was radiolabeled with $^{68}$Ga for preclinical evaluation and was further assessed in a pilot clinical study. The tumor uptake and retention of $^{68}$Ga-FAPI-RGD were significantly greater than those of $^{68}$Ga-FAPI-46 and $^{68}$Ga-c(RGDfK) in mouse xenografts (*10*). Furthermore, this pilot clinical study on 6 patients demonstrated that $^{68}$Ga-FAPI-RGD PET/CT enabled visualization of tumor lesions with favorable imaging contrast. These results encouraged us to further explore the role of $^{68}$Ga-FAPI-RGD PET/CT for cancer imaging.

The aim of this study was to evaluate, in patients with various types of cancer, the radiotracer uptake and clinical feasibility of $^{68}$Ga-FAPI-RGD PET/CT compared with those of $^{18}$F-FDG and $^{68}$Ga-FAPI-46 PET/CT.

## MATERIALS AND METHODS

### Chemistry and Radiochemistry

The detailed synthesis procedure for FAPI-RGD was reported recently (*10*). Information on the chemicals and reagents is briefly presented in the supplemental materials (available at http://jnm.snmjournals.org). $^{68}$Ga-radiolabeling of FAPI-02, FAPI-46, c(RGDfK), and FAPI-RGD variants was performed as previously described (*11–13*). In brief, 25 nmol of FAPI-RGD in 1 mL of sodium acetate buffer (0.25 M) were reacted with 4 mL of $^{68}$Ga-solution (1.1 GBq in 0.6 M HCl) at 100°C for 15 min. For clinical imaging, the final product was passed through a 0.22-μm Millipore filter for sterilization of each preparation of $^{68}$Ga-FAPI-RGD. Quality control was performed using ultraviolet and radio-high-performance liquid chromatography (supplemental materials). The stability of the radiolabeled compound was determined by incubating the product in phosphate-buffered saline at 37°C and analyzing it via radio-high-performance liquid chromatography after 1, 2, and 4 h of incubation.

### Clinical PET/CT Imaging in Healthy Volunteers and Patients with Cancer

The prospective clinical study protocol was approved by the institutional review board of the First Affiliated Hospital of Xiamen University and was registered at ClinicalTrials.gov (NCT05543317). Written informed consent was obtained from all healthy volunteers and patients. The dose of intravenously injected $^{68}$Ga-FAPI-RGD was calculated according to the participants' body weight (3.0–3.7 MBq/kg), which corresponds to approximately 7–8 nmol per subject. Safety data (blood pressure, heart rate, and temperature) and adverse events were recorded before and 4 h after injection of $^{68}$Ga-FAPI-RGD. The PET/CT scanning and reconstruction protocols are presented in the supplemental materials. For dosimetry evaluation, $^{68}$Ga-FAPI-RGD PET imaging was performed at 30, 60, and 180 min after tracer injection. Time–activity curve fitting and subsequent dose calculations were performed using OLINDA/EXM software, version 1.1 (*14*).

All patients underwent paired $^{68}$Ga-FAPI-RGD and $^{18}$F-FDG PET/CT scans. An additional $^{68}$Ga-FAPI-46 PET/CT scan was performed for comparative purposes depending on the patient's willingness. We evaluated the in vivo distribution pattern of $^{68}$Ga-FAPI-RGD at later time points, by performing 3-h-delayed $^{68}$Ga-FAPI-RGD PET/CT scans for all patients (because of the relatively short half-life [68 min] of $^{68}$Ga). All PET images were evaluated by 2 board-certified and experienced nuclear medicine physicians. Disagreements were resolved via consensus.

For quantitative analysis, the $SUV_{max}$ was used to quantify radiopharmaceutical uptake by normal organs and tumor tissues. Tracer uptake in normal organs (background) was quantified by $SUV_{mean}$, which was delineated with a sphere that had a diameter of 1 cm (for small organs, including thyroid, salivary gland, and pancreas) to 2 cm (for other organs, including brain, heart, liver, kidney, spleen, muscle, and bone marrow) placed inside the organ parenchyma. The tumor-to-background ratio (TBR) was calculated as tumor $SUV_{max}$/background $SUV_{mean}$.

To evaluate the diagnostic performance of $^{68}$Ga-FAPI-RGD and $^{18}$F-FDG PET imaging, the results of the visually interpreted PET images were compared with the histopathologic results (via surgery or biopsy), which were used as the gold standard for the final diagnosis. For patients for whom tissue diagnosis was not applicable, clinical and radiographic follow-up data were used as the reference standard to validate the PET/CT findings. Lesions were considered malignant on the basis of any of the following follow-up criteria: typical malignant features confirmed by multimodal medical imaging, significant progression on follow-up imaging, or a significant decrease in posttreatment tumor size. The minimum follow-up period was 3 mo. Histopathologic staining of surgical and biopsy samples was performed as previously described (*15*).

### Statistical Analysis

All statistical analyses were conducted using Prism (version 8.0; GraphPad Software Inc.) and SPSS Statistics (version 22.0; IBM Corp.). All quantitative data are expressed as the mean. The Wilcoxon matched-pairs signed-rank test was used to compare SUVs derived from $^{18}$F-FDG, $^{68}$Ga-FAPI-RGD, and $^{68}$Ga-FAPI-46 PET/CT. The McNemar test was used to compare the lesion detectability of the different PET/CT scans. Statistical significance was defined as a $P$ value of less than 0.05.

## RESULTS

### Synthesis and Radiolabeling

$^{68}$Ga-FAPI-RGD was radiolabeled at a specific activity of approximately 33 GBq/μmol, with over 99% radiochemical purity after purification (Supplemental Fig. 1A). High-performance liquid chromatography analysis revealed that $^{68}$Ga-FAPI-RGD had a high stability for up to 4 h, with no significant demetallation observed in phosphate-buffered saline (>99%) (Supplemental Figs. 1B–1D).

### Safety and Radiation Dosimetry in Healthy Volunteers

All observed vital signs (including temperature, heart rate, and blood pressure) remained normal during the injection and 4-h post-injection follow-up. $^{68}$Ga-FAPI-RGD was tolerated well, with no adverse events in any of the healthy volunteers or patients. Representative PET images and biodistribution data of healthy volunteers ($n = 3$) are provided in Figure 1. Tracer uptake rapidly decreased in most normal organs from 30 to 180 min, particularly in the thyroid, pancreas, and salivary glands. The $^{68}$Ga-FAPI-RGD effective dose was $1.01 \times 10^{-2}$ mSv/MBq (Supplemental Table 1), which was comparable to that of $^{68}$Ga-FAPI-02 ($1.80 \times 10^{-2}$ mSv/MBq) (*16*). The organ with the highest effective dose was the thyroid ($3.01 \times 10^{-3}$ mSv/MBq), followed by the urinary bladder wall ($1.37 \times 10^{-3}$ mSv/MBq), liver ($1.10 \times 10^{-3}$ mSv/MBq), and lungs ($1.09 \times 10^{-3}$ mSv/MBq).

### Patients' Characteristics

From July 1 to September 15, 2022, 22 patients with cancer (15 men; median age, 57 y; range, 34–79 y; 17 for staging and 5 for restaging) who underwent paired $^{68}$Ga-FAPI-RGD and $^{18}$F-FDG PET/CT were enrolled in this study. The median interval between

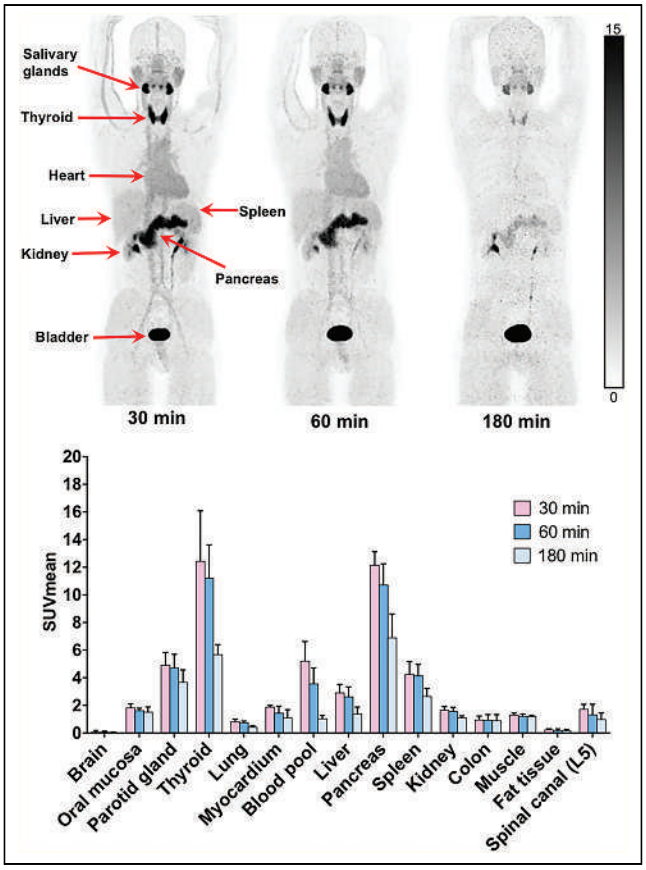


**FIGURE 1.** $^{68}$Ga-FAPI-RGD at 30, 60, and 180 min after injection in healthy volunteers, and $SUV_{mean}$ of normal organs at corresponding time points ($n = 3$).

the 2 scans was 4 d (range, 1–7 d). Furthermore, 7 of the 22 patients underwent additional $^{68}$Ga-FAPI-46 PET/CT for comparison. Among the 22 patients, the final diagnosis was based on the histopathologic results for 20 and diagnostic radiology results for 2. Detailed information on the enrolled patients is provided in Supplemental Table 2.

### Dual-Time-Point $^{68}$Ga-FAPI-RGD PET/CT Imaging in Patients with Cancer

To evaluate the in vivo distribution pattern of the radiotracer and tumor uptake over time, dual-time-point $^{68}$Ga-FAPI-RGD PET/CT (1 vs. 3 h) was performed for all patients. As demonstrated in Figure 2, most tumor lesions demonstrated increased uptake over time. Specifically, $SUV_{max}$ derived from the delayed scan (3 h) was significantly higher than $SUV_{max}$ derived from routine scans (1 h) in the primary tumors (18.0 vs. 12.6; $P < 0.001$), lymph node metastases (12.1 vs. 9.3; $P < 0.001$), lung metastases (median, 8.0 vs. 4.6; $P < 0.001$), and bone metastases (16.2 vs. 13.2; $P < 0.001$). Interestingly, background activity decreased greatly over time. Consequently, TBR improved significantly in primary tumors with involved lymph nodes and with lung, liver, peritoneal, and bone metastases. Detailed data are presented in Supplemental Table 3.

### Comparison of $^{68}$Ga-FAPI-RGD and $^{18}$F-FDG Uptake in Patients with Cancer

Among the 17 patients who underwent paired $^{68}$Ga-FAPI-RGD and $^{18}$F-FDG PET/CT for initial staging, $^{68}$Ga-FAPI-RGD PET/CT allowed detection of all primary tumors (19/19) with intense radiotracer uptake, whereas $^{18}$F-FDG PET/CT resulted in 3 missed tumor lesions in 1 patient with multifocal breast cancer. In all primary tumors, $SUV_{max}$ was significantly higher when derived from $^{68}$Ga-FAPI-RGD PET/CT than from $^{18}$F-FDG (18.0 vs. 9.1, $P < 0.001$). Furthermore, the TBRs of the primary tumors from $^{68}$Ga-FAPI-RGD PET/CT were approximately 3 times greater than those from $^{18}$F-FDG PET/CT (15.2 vs. 5.5, $P < 0.001$). Detailed data and representative images are presented in Table 1 and Figure 3, respectively.

Among the 22 patients who underwent paired $^{68}$Ga-FAPI-RGD and $^{18}$F-FDG PET/CT, 129 lymph node metastases and 149 bone and visceral metastases were evaluated (including bone [$n = 80$], lung [$n = 25$], liver [$n = 14$], peritoneal [$n = 17$], and other [$n = 13$] metastases). $^{68}$Ga-FAPI-RGD PET/CT revealed a significantly higher $SUV_{max}$ and TBR than did $^{18}$F-FDG PET/CT in most metastatic lesions. Interestingly, the $SUV_{max}$ and TBR of lymph node metastases derived from $^{68}$Ga-FAPI-RGD PET/CT were 2 to 3 times greater than those derived from $^{18}$F-FDG PET/CT ($SUV_{max}$, 12.1 vs. 6.1 [$P < 0.001$]; TBR, 13.3 vs. 4.1 [$P < 0.001$]), resulting in a greater number of metastatic lesions detected by $^{68}$Ga-FAPI-RGD than by $^{18}$F-FDG PET/CT (99% [128/129] vs. 91% [117/129], $P = 0.003$). Regarding imaging of bone and visceral metastases, $^{68}$Ga-FAPI-RGD PET/CT demonstrated significantly higher radiotracer uptake and a 2- to 3-fold higher TBR than did $^{18}$F-FDG PET/CT in most tumor lesions, including the lung, liver, bone, and peritoneal metastases. Consequently, $^{68}$Ga-FAPI-RGD PET/CT yielded significantly higher lesion detection rates than $^{18}$F-FDG for the diagnosis of bone and visceral metastases (96% [143/149] vs. 79% [118/149], $P < 0.001$). Representative PET/CT images with FAP and integrin $\alpha_v\beta_3$ staining are presented in Figure 4.

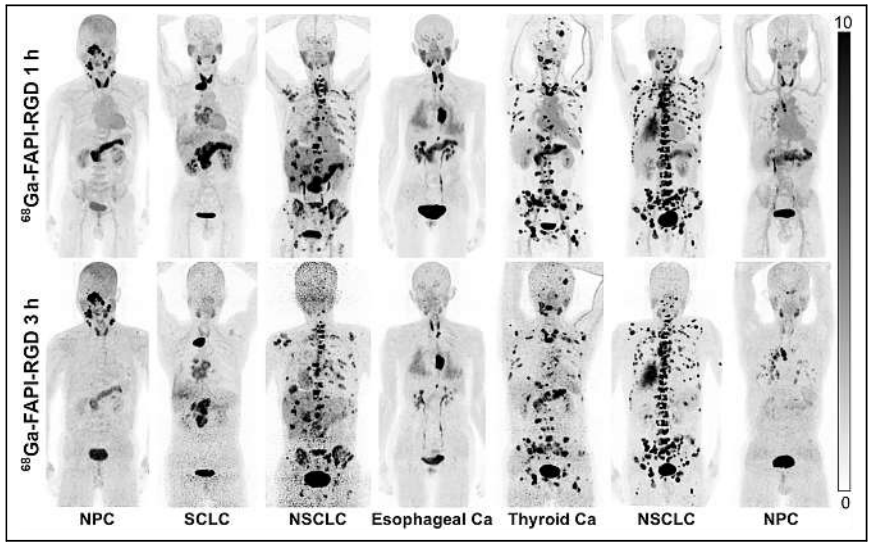


**FIGURE 2.** Maximum-intensity-projection images of $^{68}$Ga-FAPI-RGD PET/CT at 1 and 3 h after injection in different types of cancer. Ca = cancer; NPC = nasopharyngeal carcinoma; SCLC = small cell lung cancer.

**TABLE 1**
Comparison of $SUV_{max}$ from $^{68}$Ga-FAPI-RGD and $^{18}$F-FDG PET/CT in Primary and Metastatic Tumors

| | | | $^{68}$Ga-FAPI-RGD PET/CT | | | $^{18}$F-FDG PET/CT | | | *P* (FAPI-RGD vs. FDG) | |
|---|---|---|---|---|---|---|---|---|---|---|
| Tumor type | *n* | Size (cm) | Positive tumors (*n*) | $SUV_{max}$ | TBR | Positive tumors (*n*) | $SUV_{max}$ | TBR | Median $SUV_{max}$ | TBR |
| Primary | | | | | | | | | | |
| Total | 19 | 2.5 (0.6–6.5) | 19 | 18.0 (7.0–40.3) | 15.2 (7.0–57.6) | 16 | 9.1 (1.7–15.5) | 5.5 (1.7–14.3) | <0.001 | <0.001 |
| NPC | 3 | 1.9 (1.3–2.4) | 3 | 19.3 (16.5–25.8) | 13.8 (10.3–15.2) | 3 | 10.9 (7.8–11.8) | 5.5 (4.9–7.9) | 0.109 | 0.109 |
| Breast cancer* | 3 | 0.8 (0.6–0.8) | 3 | 16.2 (7.1–18.9) | 27.0 (11.8–31.5) | 0 | 2.1 (1.7–2.4) | 2.1 (1.7–2.4) | 0.109 | 0.109 |
| Esophageal cancer | 4 | 2.4 (1.8–2.7) | 4 | 30.1 (21.3–40.3) | 33.4 (23.7–57.6) | 4 | 12.1 (9.1–15.5) | 7.2 (5.4–10.2) | 0.068 | 0.068 |
| NSCLC | 3 | 2.6 (2.5–6.5) | 3 | 14.8 (12.9–18.0) | 16.1 (14.5–24.7) | 3 | 7.8 (6.8–12.9) | 10.4 (3.2–14.3) | 0.18 | 0.109 |
| SCLC | 2 | 4.2 (3.6–4.8) | 2 | 9.1 (8.9–9.2) | 7.5 (6.1–8.9) | 2 | 6.7 (5.5–7.8) | 3.4 (3.2–3.5) | NA | NA |
| Pancreatic cancer | 1 | 4.3 (NA) | 1 | 36.3 (NA) | 51.9 (NA) | 1 | 13.8 (NA) | 6.6 (NA) | NA | NA |
| Ovarian cancer | 3 | 3.8 (3.2–4.5) | 3 | 12.4 (7.0–25.6) | 12.4 (7.0–14.2) | 3 | 9.9 (8.1–12.6) | 5.7 (5.0–6.8) | 0.285 | 0.109 |
| Metastases | | | | | | | | | | |
| Lymph node mets (total) | 129 | 1.1 (0.4–3.6) | 128 | 12.1 (2.0–27.1) | 13.3 (1.8–38.7) | 117 | 6.1 (1.0–13.7) | 4.1 (1.0–14.2) | <0.001 | <0.001 |
| Lung mets | 25 | 0.9 (0.3–3.5) | 19 | 8.0 (0.9–15.7) | 15.6 (1.1–39.3) | 17 | 4.9 (0.7–7.1) | 10.0 (0.9–22.3) | <0.001 | <0.001 |
| Liver mets | 14 | 1.4 (0.6–3.9) | 14 | 11.2 (3.9–19.4) | 7.3 (3.6–16.8) | 11 | 5.3 (2.3–12.0) | 1.9 (1.0–5.0) | 0.005 | 0.001 |
| Bone mets | 80 | 1.3 (0.5–8.2) | 80 | 16.2 (5.6–49.6) | 15.6 (6.3–70.9) | 64 | 5.2 (0.9–11.8) | 4.7 (0.9–13.8) | <0.001 | <0.001 |
| Peritoneal mets | 17 | NA† | 17 | 16.0 (6.4–18.8) | 16.8 (3.6–22.9) | 17 | 10.3 (4.7–14.1) | 7.1 (2.6–10.1) | <0.001 | <0.001 |
| Other mets‡ | 13 | 0.8 (0.4–2.3) | 13 | 8.6 (4.0–10.0) | 10.0 (6.3–207.5) | 9 | 6.6 (3.4–11.9) | 3.4 (1.0–6.0) | 0.196 | 0.001 |

*One patient was diagnosed with multifocal breast cancer (4 primary tumors).
†Lesion size cannot be calculated because of diffuse type of peritoneal metastasis (irregular shape).
‡Other mets included splenic ($n = 2$), pleural ($n = 1$), adrenal ($n = 1$), brain ($n = 4$), and subcutaneous ($n = 5$) mets.
NPC = nasopharyngeal carcinoma; SCLC = small lung cancer; mets = metastases; NA = not applicable.
Continuous data are median and range. Quantitative data from $^{68}$Ga-FAPI-RGD and $^{18}$F-FDG PET/CT were acquired at 3 h and 1 h after injection, respectively.

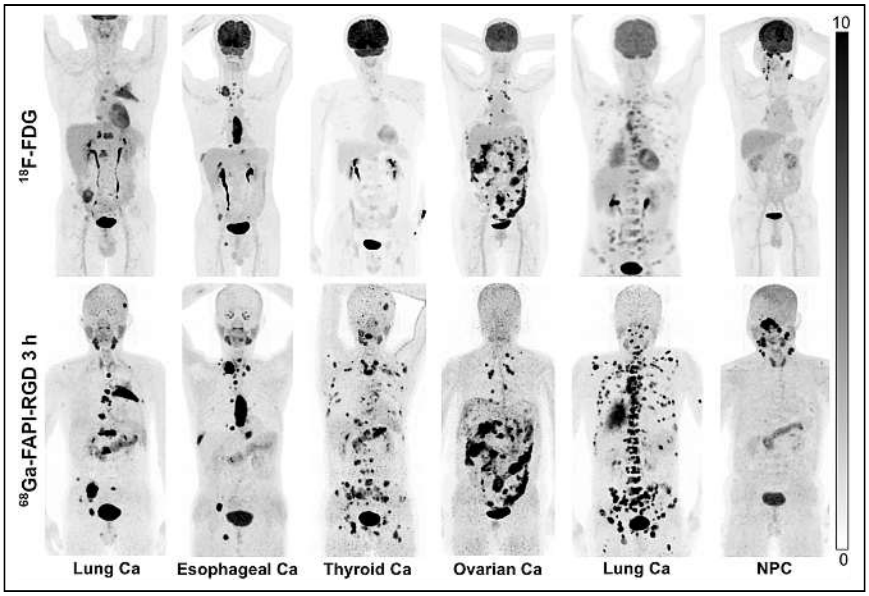


**FIGURE 3.** Maximum-intensity-projection images of $^{18}$F-FDG and $^{68}$Ga-FAPI-RGD PET/CT in patients with different types of cancer. Ca = cancer; NPC = nasopharyngeal carcinoma.

### Comparison of $^{68}$Ga-FAP-RGD and $^{68}$Ga-FAPI-46 Uptake in Patients with Cancer

$^{68}$Ga-FAPI-RGD and $^{68}$Ga-FAPI-46 PET/CT were compared among 7 patients with 5 types of cancer. Three patients were treatment-naïve, and 4 had recurrent or progressive disease. Although the $SUV_{max}$ and TBR of primary tumors from $^{68}$Ga-FAPI-RGD PET/CT seemed higher than those from $^{68}$Ga-FAPI-46 ($SUV_{max}$, 25.8 vs. 14.5 [$P = 0.109$]; TBR, 15.2 vs. 7.6 [$P = 0.109$]), no statistical difference was observed (Table 2). Regarding the 102 metastatic lesions evaluated, $^{68}$Ga-FAPI-RGD PET/CT yielded a significantly higher $SUV_{max}$ and TBR than did $^{68}$Ga-FAPI-46 in lymph node metastases ($SUV_{max}$, 15.5 vs. 8.7 [$P < 0.001$]; TBR, 13.2 vs. 8.1 [$P < 0.001$]), lung metastases ($SUV_{max}$, 9.5 vs. 6.4 [$P = 0.004$]; TBR, 18.8 vs. 12.5 [$P = 0.003$]), and bone metastases ($SUV_{max}$, 13.7 vs. 6.8 [$P < 0.001$]; TBR, 14.5 vs. 6.3 [$P < 0.001$]) (Fig. 5). Representative PET images are presented in Figure 6. Interestingly, in 1 patient with small cell lung cancer, 4 bone metastases and 3 liver metastases exhibited no abnormal uptake of $^{68}$Ga-FAPI-46, but uptake of $^{68}$Ga-FAPI-RGD was increased. Immunohistochemical staining of a liver metastasis demonstrated negative FAP expression but positive integrin $\alpha_v\beta_3$ expression (Fig. 7A). Notably, in another patient with nasopharyngeal carcinoma, both tracers exhibited similar uptake in several metastatic lung lesions, which demonstrated positive FAP expression and negative integrin $\alpha_v\beta_3$ expression (Fig. 7B).

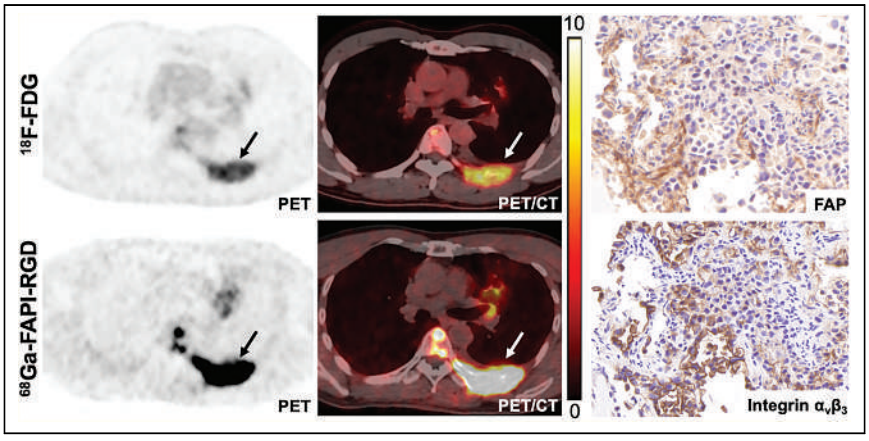


**FIGURE 4.** $^{68}$Ga-FAPI-RGD and $^{18}$F-FDG PET/CT images in patient with metastatic lung adenocarcinoma. Immunohistochemical staining from left rib metastasis (arrow) revealed positive FAP and integrin $\alpha_v\beta_3$ expression.

## DISCUSSION

As pan-cancer biomarkers, FAP with radiolabeled FAPI-based molecules (including FAPI-04/46) have yielded encouraging results for PET imaging of cancer (*7,9*). However, the relatively short tumor retention time may hamper the use of FAP molecules for radioligand therapy applications. We and others have applied the polyvalence effect to develop homomultimers to enhance tumor uptake and retention, and dimeric FAPI-based tracers have been synthesized and evaluated (*17,18*). A dual-receptor–targeting approach with a heterodimer is another strategy to improve the tumor-targeting efficacy, especially for imaging probes that recognize only 1 receptor (*19*). Considering that our previous data showed tumor uptake and retention of $^{68}$Ga-FAPI-RGD to be significantly greater than those of $^{68}$Ga-FAPI-46 and $^{68}$Ga-c(RGDfK) in mouse xenografts (*10*), we speculated that $^{68}$Ga-FAPI-RGD would be a promising radiotracer for imaging tumors expressing either FAP or integrin $\alpha_v\beta_3$. In the present study, $^{68}$Ga-FAPI-RGD, a heterodimeric PET tracer that targets both FAP and integrin $\alpha_v\beta_3$, was evaluated in 3 healthy volunteers and 22 patients with cancer. Our clinical studies demonstrated $^{68}$Ga-FAPI-RGD to be a promising PET agent that allows imaging of various types of cancer. Its dual-receptor–targeting property results in improved tumor uptake and retention, allowing imaging of tumors with either or both receptor expression patterns.

$^{68}$Ga-FAPI-RGD was safe and well tolerated in all healthy volunteers and patients with cancer. The average effective whole-body dose of $^{68}$Ga-FAPI-RGD was $1.01 \times 10^{-2}$ mSv/MBq, which is comparable to the effective doses of $^{68}$Ga-FAPI-02 and $^{68}$Ga-FAPI-04 ($1.64 \times 10^{-2}$ mSv/MBq and $1.80 \times 10^{-2}$ mSv/MBq) (*16*). However, intense physiologic $^{68}$Ga-FAPI-RGD uptake was observed in the thyroid and pancreas, with a distribution pattern similar to that of $^{68}$Ga-FAPI dimers previously reported by us and others (*17,18*). Interestingly, significantly decreased $^{68}$Ga-FAPI-RGD activity was observed in normal organs (particularly in the thyroid, pancreas, and salivary glands), whereas increased uptake was observed in tumor lesions from 0.5 to 3 h after injection, resulting in optimized lesion contrast in delayed scans. Therefore, we speculate that additional delayed $^{68}$Ga-FAPI-RGD PET/CT scans may help improve the lesion

**TABLE 2**
Comparison of $SUV_{max}$ on $^{68}$Ga-FAPI-RGD and $^{68}$Ga-FAPI-46 PET/CT Images in Primary and Metastatic Lesions

| Tumor type | *n* | Tumor size (cm) | Tracer | Positive lesions (*n*) | $SUV_{max}$ Median | $SUV_{max}$ *P* | TBR Median | TBR *P* |
|---|---|---|---|---|---|---|---|---|
| Primary tumors | | | | | | | | |
| NPC | 1 | 2.4 (NA) | $^{68}$Ga-FAPI-RGD | | 25.8 | NA | 15.2 | NA |
| | | | $^{68}$Ga-FAPI-46 | | 14.5 | | 7.6 | |
| SCLC | 1 | 4.8 (NA) | $^{68}$Ga-FAPI-RGD | | 9.2 | NA | 6.1 | NA |
| | | | $^{68}$Ga-FAPI-46 | | 5.8 | | 3.4 | |
| Pancreatic cancer | 1 | 4.3 (NA) | $^{68}$Ga-FAPI-RGD | | 36.3 | NA | 51.9 | NA |
| | | | $^{68}$Ga-FAPI-46 | | 31.1 | | 38.9 | |
| Total | 3 | 4.3 (2.4–4.8) | $^{68}$Ga-FAPI-RGD | | 25.8 (9.2–36.3) | 0.109 | 15.2 (6.1–51.9) | 0.109 |
| | | | $^{68}$Ga-FAPI-46 | | 14.5 (5.8–31.1) | | 7.6 (3.4–38.9) | |
| Metastases | | | | | | | | |
| Lymph node mets (total) | 46 | 1.1 (0.6–2.8) | $^{68}$Ga-FAPI-RGD | 46 | 15.5 (4.3–27.1) | <0.001 | 13.2 (3.3–38.7) | <0.001 |
| | | | $^{68}$Ga-FAPI-46 | 46 | 8.7 (3.3–23.3) | | 8.1 (2.7–18.2) | |
| Brain mets | 4 | 0.7 (0.4–0.7) | $^{68}$Ga-FAPI-RGD | 4 | 5.8 (4.0–8.3) | 0.068 | 143.8 (80.0–207.5) | 0.068 |
| | | | $^{68}$Ga-FAPI-46 | 4 | 3.0 (2.5–4.2) | | 83.7 (65.0–85.0) | |
| Lung mets | 15 | 1.1 (0.5–1.4) | $^{68}$Ga-FAPI-RGD | 13 | 9.5 (2.0–15.7) | 0.004 | 18.8 (2.0–39.3) | 0.003 |
| | | | $^{68}$Ga-FAPI-46 | 13 | 6.4 (1.6–13.3) | | 12.5 (1.6–33.3) | |
| Liver mets | 7 | 1.1 (0.6–1.4) | $^{68}$Ga-FAPI-RGD | 7 | 6.9 (3.9–16.8) | 0.028 | 6.3 (3.6–16.8) | 0.028 |
| | | | $^{68}$Ga-FAPI-46 | 4 | 3.4 (1.8–16.2) | | 3.4 (1.8–16.2) | |
| Subcutaneous mets | 5 | 0.8 (0.7–0.9) | $^{68}$Ga-FAPI-RGD | 5 | 8.6 (6.6–10.0) | 0.138 | 7.2 (5.5–10.0) | 0.08 |
| | | | $^{68}$Ga-FAPI-46 | 5 | 7.2 (6.1–9.0) | | 5.1 (3.6–8.2) | |
| Bone mets | 29 | 1.2 (0.5–8.2) | $^{68}$Ga-FAPI-RGD | 29 | 13.7 (6.1–27.6) | <0.001 | 14.5 (6.3–27.6) | <0.001 |
| | | | $^{68}$Ga-FAPI-46 | 25 | 6.8 (1.2–19.6) | | 6.3 (1.8–21.8) | |

NPC = nasopharyngeal carcinoma; NA = not applicable; SCLC = small lung cancer; mets = metastases.
Data in parentheses are ranges.

detection rate and offer advantages for discrimination of tumor and nontumor lesions. However, the clinical benefits of delayed scans require further investigation in a larger patient population.

The $SUV_{max}$ and TBR of primary tumors from $^{68}$Ga-FAPI-RGD PET/CT were significantly higher than those from $^{18}$F-FDG PET/CT, particularly in non–small cell lung cancer (NSCLC) and in esophageal, breast, and pancreatic cancers. The reason for this finding is that all primary tumors (19/19) were satisfactorily visualized via $^{68}$Ga-FAPI-RGD, whereas 3 breast cancer lesions were missed via $^{18}$F-FDG. $^{68}$Ga-FAPI-RGD PET/CT also demonstrated significantly greater radiotracer uptake in lymph node, bone, and visceral metastases and a significantly higher TBR than $^{18}$F-FDG PET/CT, resulting in an improved lesion detection rate, particularly for the diagnosis of lymph node (99% vs. 91%) and bone (100% vs. 80%) metastases. However, in our previous $^{68}$Ga-FAPI-RGD PET/CT study on 6 patients, the tumor uptake of $^{68}$Ga-FAPI-RGD did not differ from that of $^{18}$F-FDG (*10*). Possible explanations may be the limited number of patients, different cancer types investigated, and different acquisition time after injection (30–120 min vs. 60–180 min). According to the results of the present study, $^{68}$Ga-FAPI-RGD may be more suitable for imaging tumors with both FAP and integrin $\alpha_v\beta_3$ expression, particularly for NSCLC and esophageal cancer (*20,21*). First, the radiotracer uptake and TBR derived from $^{68}$Ga-FAPI-RGD PET/CT were higher than those from $^{18}$F-FDG in these cancer types, resulting in improved lesion detectability, particularly of liver, bone, and brain metastases. These results suggest that $^{68}$Ga-FAPI-RGD PET/CT may contribute to the diagnosis of NSCLC and esophageal cancer, especially in detecting

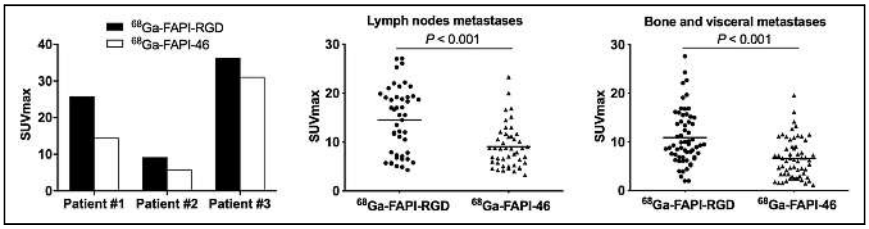


**FIGURE 5.** Quantitative comparison between $^{68}$Ga-FAPI-RGD and $^{68}$Ga-FAPI-46 in primary tumor (left), lymph node (middle), and bone and visceral metastases (right).

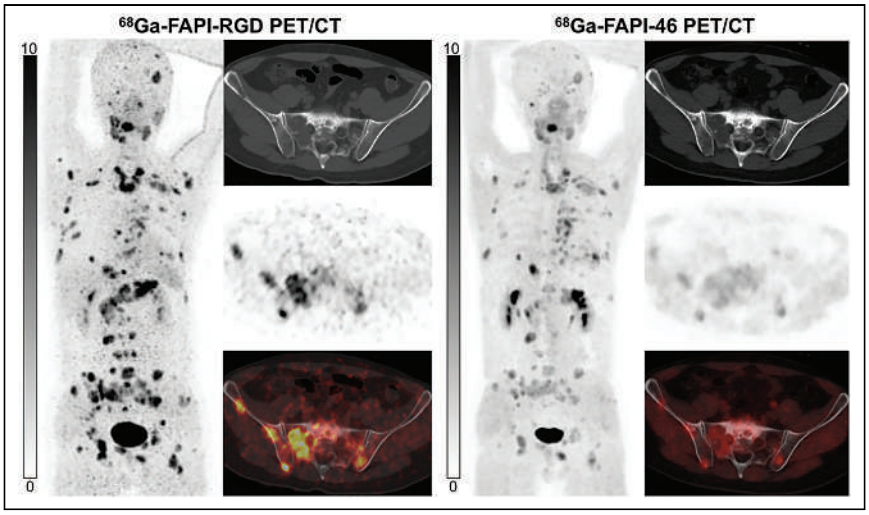


**FIGURE 6.** $^{68}$Ga-FAPI-RGD PET/CT shows significantly higher radiotracer uptake than $^{68}$Ga-FAPI-46 in patient with metastatic thyroid cancer.

small metastases with low-to-moderate uptake on $^{18}$F-FDG PET/CT. Second, false-positive findings in the mediastinal lymph nodes often confound interpretation of preoperative $^{18}$F-FDG PET/CT images in NSCLC and esophageal cancer. On the basis of previous publications, nonmetastatic reactive lymph nodes presenting increased $^{18}$F-FDG uptake might be correctly diagnosed either by FAP or by integrin $\alpha_v\beta_3$–targeting radiotracers (*21–24*). Therefore, $^{68}$Ga-FAPI-RGD PET/CT may be more suitable than $^{18}$F-FDG PET/CT for determining the preoperative lymph node status in these cancer types. Taken together, the results indicate that NSCLC and esophageal cancer may be potential indications for future clinical use of $^{68}$Ga-FAPI-RGD, and further prospective studies are warranted to confirm this possibility.

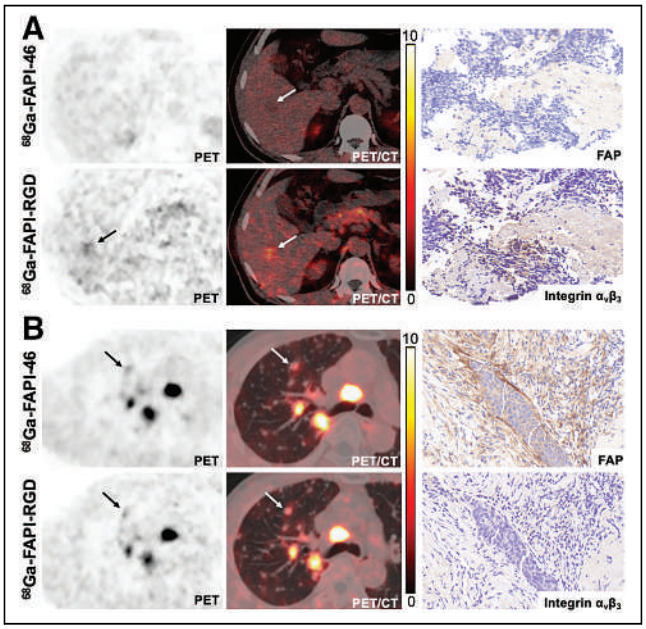


**FIGURE 7.** $^{68}$Ga-FAPI-RGD and $^{68}$Ga-FAPI-46 PET/CT images and immunohistochemical staining in patients with metastatic small cell lung cancer (A) and nasopharyngeal carcinoma (B). Biopsy site is indicated by arrow.

PET imaging demonstrated that the radiotracer uptake and TBR of $^{68}$Ga-FAPI-RGD were significantly higher than those of $^{68}$Ga-FAPI-46, especially in the involved lymph node, bone, and visceral metastases. Interestingly, we noted that several lesions from metastatic small cell lung cancer and thyroid cancer exhibited low uptake of $^{68}$Ga-FAPI-46 but higher uptake of $^{68}$Ga-FAPI-RGD. Histopathologic results revealed low expression of FAP but higher expression of integrin $\alpha_v\beta_3$. Therefore, $^{68}$Ga-FAPI-RGD PET/CT may be used to image tumors that are either FAP-positive or integrin $\alpha_v\beta_3$–positive, whereas $^{68}$Ga-FAPI-46 failed to visualize lesions that were FAP-negative and integrin $\alpha_v\beta_3$–positive. Moreover, both tracers showed similar uptake in lesions with FAP-positive and integrin $\alpha_v\beta_3$–negative expression, suggesting comparable FAP-targeting ability between $^{68}$Ga-FAPI-RGD and $^{68}$Ga-FAPI-46. On the basis of these findings, we speculate that $^{68}$Ga-FAPI-RGD PET/CT would be superior to $^{68}$Ga-FAPI-46 PET/CT for the diagnosis of cancer, especially when $^{68}$Ga-FAPI-46 PET/CT findings are inconclusive.

With the rather rapid washout from tumors and unsatisfactory therapeutic efficacy, $^{177}$Lu-FAPI-04/46 may not be an optimal targeting vector for radioligand therapy (*25,26*). Besides the improved tumor uptake of $^{68}$Ga-FAPI-RGD, the prolonged tumor retention was an unexpected finding in this study, as may be explained by the synergistic interaction between the 2 binding motifs in the heterodimer. It is possible that the binding of the first motif, even if only temporary, may first direct $^{68}$Ga-FAPI-RGD to the target surface or reduce the off-rate of $^{68}$Ga-FAPI-RGD, allowing the second binding motif to also attach to the tumor and therefore increasing the overall binding and the probability of adhering to the tumor (*27*). Improved tumor accumulation and prolonged tumor retention are the potential advantages of FAPI-RGD over the current FAPI variants, making it a suitable targeting vector after labeling with $^{177}$Lu/$^{90}$Y/$^{225}$Ac for therapeutic applications. In addition, the rapid clearance of $^{68}$Ga-FAPI-RGD in normal organs, particularly in the thyroid, salivary glands, and blood pool, may decrease the absorbed dose delivered to normal human tissues. This possibility should be extensively studied in nuclear oncology research in the future.

Our study had several limitations. First, because of the relatively short half-life of $^{68}$Ga, the in vivo distribution pattern and tumor retention of FAPI-RGD could not be fully investigated. Second, because few patients underwent paired $^{68}$Ga-FAPI-RGD/$^{18}$F-FDG ($n = 22$) or $^{68}$Ga-FAPI-RGD/$^{68}$Ga-FAPI-46 PET/CT imaging ($n = 7$), only a descriptive comparison was possible. Third, this study focused primarily on lesion detection rates, and the specificity of $^{68}$Ga-FAPI-RGD PET/CT requires further investigations with histopathologic confirmation. Furthermore, we were unable to compare $^{68}$Ga-FAPI-RGD PET/CT with $^{68}$Ga-RGD PET/CT in the same group of patients because of ethical considerations. $^{68}$Ga-FAPI-RGD and $^{68}$Ga-RGD PET/CT should be compared in future clinical research.

## CONCLUSION

The study demonstrated the safety and clinical feasibility of $^{68}$Ga-FAPI-RGD PET/CT for imaging of various types of cancer.

Further investigation of the diagnostic accuracy of $^{68}$Ga-FAPI-RGD as a PET tracer, as well as its antitumor efficacy after labeling with therapeutic radionuclides, is necessary.

## DISCLOSURE

This work was funded by the National Natural Science Foundation of China (82071961), Key Scientific Research Program for Young Scholars in Fujian (2021ZQNZD 016), Fujian Natural Science Foundation for Distinguished Young Scholars (2022J01310623), Fujian Research and Training Grants for Young and Middle-aged Leaders in Healthcare, Key Medical and Health Projects in Xiamen (3502Z20209002), The National University of Singapore Start-up Grant (NUHSRO/2020/133/Startup/08), NUS School of Medicine Nanomedicine Translational Research Programme (NUHSRO/2021/034/TRP/09/Nanomedicine), and National Medical Research Council (NMRC) Centre Grant Programme (CG21APR1005). Liang Zhao was partially funded by the China Scholarship Council (CSC). No other potential conflict of interest relevant to this article was reported.

## KEY POINTS

**QUESTION:** Will a heterodimer that recognizes both FAP and integrin $\alpha_v\beta_3$ yield improved tumor uptake compared with $^{18}$F-FDG or $^{68}$Ga-FAPI-46?

**PERTINENT FINDINGS:** This clinical study revealed that the tumor uptake and TBR of $^{68}$Ga-FAPI-RGD were significantly higher than those of either $^{18}$F-FDG or $^{68}$Ga-FAPI-46 in various types of cancer.

**IMPLICATIONS FOR PATIENT CARE:** The dual-receptor–targeting property of $^{68}$Ga-FAPI-RGD results in improved tumor uptake compared with $^{18}$F-FDG or $^{68}$Ga-FAPI-46, enabling imaging of tumors with either or both receptor expression patterns.

## REFERENCES

1. Pang X, He X, Qiu Z, et al. Targeting integrin pathways: mechanisms and advances in therapy. *Signal Transduct Target Ther.* 2023;8:1–42.
2. Chen H, Niu G, Wu H, Chen X. Clinical application of radiolabeled RGD peptides for PET imaging of integrin $\alpha_v\beta_3$. *Theranostics.* 2016;6:78–92.
3. Zhao L, Chen H, Guo Z, et al. Targeted radionuclide therapy in patient-derived xenografts using $^{177}$Lu-EB-RGD. *Mol Cancer Ther.* 2020;19:2034–2043.
4. Carlsen EA, Loft M, Loft A, et al. Prospective phase II trial of [$^{68}$Ga]Ga-NODAGA-E[c(RGDyK)]$_2$ PET/CT imaging of integrin $\alpha_v\beta_3$ for prognostication in patients with neuroendocrine neoplasms. *J Nucl Med.* 2023;64:252–259.
5. Bejarano L, Jordao MJC, Joyce JA. Therapeutic targeting of the tumor microenvironment. *Cancer Discov.* 2021;11:933–959.
6. Kalluri R. The biology and function of fibroblasts in cancer. *Nat Rev Cancer.* 2016;16:582–598.
7. Kratochwil C, Flechsig P, Lindner T, et al. $^{68}$Ga-FAPI PET/CT: tracer uptake in 28 different kinds of cancer. *J Nucl Med.* 2019;60:801–805.
8. Loktev A, Lindner T, Mier W, et al. A tumor-imaging method targeting cancer-associated fibroblasts. *J Nucl Med.* 2018;59:1423–1429.
9. Sollini M, Kirienko M, Gelardi F, Fiz F, Gozzi N, Chiti A. State-of-the-art of FAPI-PET imaging: a systematic review and meta-analysis. *Eur J Nucl Med Mol Imaging.* 2021;48:4396–4414.
10. Zang J, Wen X, Lin R, et al. Synthesis, preclinical evaluation and radiation dosimetry of a dual targeting PET tracer [$^{68}$Ga]Ga-FAPI-RGD. *Theranostics.* 2022;12:7180–7190.
11. Wen X, Xu P, Shi M, et al. Evans blue-modified radiolabeled fibroblast activation protein inhibitor as long-acting cancer therapeutics. *Theranostics.* 2022;12:422–433.
12. Pang Y, Zhao L, Meng T, et al. PET imaging of fibroblast activation protein in various types of cancer using $^{68}$Ga-FAP-2286: comparison with $^{18}$F-FDG and $^{68}$Ga-FAPI-46 in a single-center, prospective study. *J Nucl Med.* 2023;64:386–394.
13. Mitsuyuki K, Watabe T, Naka S, et al. Evaluation of integrin $\alpha_v\beta_3$ expression in murine xenograft models: [$^{68}$Ga]Ga-DOTA-C(RGDfK) PET study with immunohistochemical confirmation. *Diagnostics (Basel).* 2021;11:1295–1303.
14. Stabin MG, Sparks RB, Crowe E. OLINDA/EXM: the second-generation personal computer software for internal dose assessment in nuclear medicine. *J Nucl Med.* 2005;46:1023–1027.
15. Chen H, Zhao L, Fu K, et al. Integrin $\alpha_v\beta_3$-targeted radionuclide therapy combined with immune checkpoint blockade immunotherapy synergistically enhances antitumor efficacy. *Theranostics.* 2019;9:7948–7960.
16. Giesel FL, Kratochwil C, Lindner T, et al. $^{68}$Ga-FAPI PET/CT: biodistribution and preliminary dosimetry estimate of 2 DOTA-containing FAP-targeting agents in patients with various cancers. *J Nucl Med.* 2019;60:386–392.
17. Moon ES, Ballal S, Yadav MP, et al. Fibroblast activation protein (FAP) targeting homodimeric FAP inhibitor radiotheranostics: a step to improve tumor uptake and retention time. *Am J Nucl Med Mol Imaging.* 2021;11:476–491.
18. Zhao L, Niu B, Fang J, et al. Synthesis, preclinical evaluation, and a pilot clinical PET imaging study of $^{68}$Ga-labeled FAPI dimer. *J Nucl Med.* 2022;63:862–868.
19. Boinapally S, Lisok A, Lofland G, et al. Hetero-bivalent agents targeting FAP and PSMA. *Eur J Nucl Med Mol Imaging.* 2022;49:4369–4381.
20. Gao S, Wu H, Li W, et al. A pilot study imaging integrin αvβ3 with RGD PET/CT in suspected lung cancer patients. *Eur J Nucl Med Mol Imaging.* 2015;42:2029–2037.
21. Dong Y, Wei Y, Chen G, et al. Relationship between clinicopathological characteristics and PET/CT uptake in esophageal squamous cell carcinoma: [$^{18}$F]alfatide versus [$^{18}$F]FDG. *Mol Imaging Biol.* 2019;21:175–182.
22. Jin X, Liang N, Wang M, et al. Integrin imaging with $^{99m}$Tc-3PRGD2 SPECT/CT shows high specificity in the diagnosis of lymph node metastasis from non-small cell lung cancer. *Radiology.* 2016;281:958–966.
23. Shang Q, Zhao L, Pang Y, Meng T, Chen H. Differentiation of reactive lymph nodes and tumor metastatic lymph nodes with $^{68}$Ga-FAPI PET/CT in a patient with squamous cell lung cancer. *Clin Nucl Med.* 2022;47:458–461.
24. Zhou X, Wang S, Xu X, et al. Higher accuracy of [$^{68}$Ga]Ga-DOTA-FAPI-04 PET/CT comparing with 2-[$^{18}$F]FDG PET/CT in clinical staging of NSCLC. *Eur J Nucl Med Mol Imaging.* 2022;49:2983–2993.
25. Assadi M, Rekabpour SJ, Jafari E, et al. Feasibility and therapeutic potential of $^{177}$Lu-fibroblast activation protein inhibitor-46 for patients with relapsed or refractory cancers: a preliminary study. *Clin Nucl Med.* 2021;46:e523–e530.
26. Zhao L, Chen J, Pang Y, et al. Fibroblast activation protein-based theranostics in cancer research: a state-of-the-art review. *Theranostics.* 2022;12:1557–1569.
27. Chittasupho C. Multivalent ligand: design principle for targeted therapeutic delivery approach. *Ther Deliv.* 2012;3:1171–1187.

# Evaluation of the Diagnostic Accuracy of FAPI PET/CT in Oncologic Studies: Systematic Review and Metaanalysis

Grayson Wass[1], Kari Clifford[2], and Rathan M. Subramaniam[1,3,4]

[1]*Department of Medicine, Dunedin School of Medicine, University of Otago Medical School, Dunedin, New Zealand;*
[2]*Surgical Outcomes Research Centre, Department of Surgical Sciences, University of Otago Medical School, Dunedin, New Zealand;*
[3]*Department of Radiology, Duke University, Durham, North Carolina; and* [4]*Faculty of Medicine, Nursing, Midwifery, and Health Sciences, University of Notre Dame Australia, Sydney, Australia*

Fibroblast-activation protein is a promising target for oncologic molecular imaging. Studies show that fibroblast activation protein inhibitor (FAPI) radiotracers are accurate diagnostics with favorable tumor-to-background ratios across various cancers. Therefore, we performed a systematic review and metaanalysis to assess the diagnostic performance of FAPI PET/CT in comparison with [$^{18}$F]FDG PET/CT, the most widely used radiotracer in oncology. **Methods:** We conducted a systematic search in MEDLINE, Embase, Scopus, PubMed, Cochrane Central Register of Controlled Trials, relevant trial registries, and bibliographies. The search consisted of combinations of terms for 3 topics: neoplasia, PET/CT, and FAPI. Two authors independently screened retrieved articles using predefined inclusion and exclusion criteria and extracted the data. Study quality was assessed using the criteria of QUADAS-2 (Quality Assessment of Diagnostic Accuracy Studies 2). For each study, the sensitivity, specificity, and 95% CIs were calculated to determine diagnostic accuracy for primary, nodal, and metastatic lesions. A random-effects metaanalysis was used for pooling the data, and heterogeneity was assessed ($I^2$ index). **Results:** Thirty-nine studies (1,259 patients) investigating the use of FAPI PET/CT were included. On a patient-based analysis, pooled sensitivity was 0.99 (95% CI, 0.97–1.0) for the detection of primary lesions. Pooled sensitivity for nodal and distant metastases was 0.91 (95% CI, 0.81–0.96) and 0.99 (95% CI, 0.96–1.0), respectively. On a paired analysis between FAPI and [$^{18}$F]FDG PET/CT, FAPI had a higher sensitivity in the detection of primary, nodal, and metastatic lesions (all $P <$ 0.001). The differences in sensitivities between FAPI and [$^{18}$F]FDG were statistically significant. In terms of heterogeneity, analyses on primary lesions were moderately affected, distant metastatic lesions were highly affected, and the nodal metastatic analyses had negligible heterogeneity. **Conclusion:** The diagnostic performance of FAPI PET/CT is superior to that of [$^{18}$F]FDG in the detection of primary, nodal, and distant metastases. However, further studies are needed to better evaluate its utility and indication in specific cancer types and clinical settings.

**Key Words:** FAPI; metaanalysis; neoplasia; PET/CT; radiology

**J Nucl Med 2023; 64:1218–1224**
DOI: 10.2967/jnumed.123.265471

PET scans are used in the diagnosis and staging of various cancers, with [$^{18}$F]FDG the most widely used radiotracer (*1*). The glucose analog FDG utilizes the increased glucose demand of many tumors (Warburg effect); however, this can result in nonspecific uptake in glucose-avid organs or areas of inflammation (*1*). More recent research into the tumor microenvironment resulted in the development of fibroblast activation protein inhibitor (FAPI) radiotracers, such as [$^{68}$Ga]FAPI-04 (*2*). This protein is a type II transmembrane serine protease that is overexpressed on cancer-associated fibroblasts, a heterogeneous population of fibroblastlike cells and a predominant component of the tumor microenvironment (*2,3*). These fibroblasts are implicated in several aspects of tumorigenesis, such as immunosuppression and extracellular matrix remodeling (*3,4*). This protein is also expressed in wound healing, in inflammatory conditions such as arthritis, in fibrosis, and in areas of extracellular matrix remodeling such as myocardial infarction and liver cirrhosis (*3,5,6*). Fibroblast activation protein is detected during embryogenesis and tissue remodeling but is otherwise expressed at low levels in healthy tissue (*3,5*). Studies show fibroblast activation protein expression on tumor cells, with increased expression correlating with poorer prognosis (*7*). These features make fibroblast activation protein an attractive target for oncologic imaging.

Since FAPI radiotracers were first described in 2018 (*8*), multiple studies have investigated their diagnostic accuracy in the detection of various cancers, reporting high accuracy and favorable tumor-to-background ratios (*9,10*). Comparisons are made between FAPI PET/CT, [$^{18}$F]FDG PET/CT, and other imaging modalities (CT and MRI) (*11,12*). There are currently 4 metaanalyses investigating the diagnostic accuracy of FAPI PET (*13–16*). Compared with prior analyses, this current metaanalysis includes a larger number of studies, covering multiple cancer types, and directly comparing FAPI and [$^{18}$F]FDG PET/CT.

This systematic review and metaanalysis synthesize the current literature on various FAPI radiotracers and the diagnostic accuracy of FAPI PET/CT in comparison with [$^{18}$F]FDG PET/CT for the detection of cancers and associated metastatic lesions.

## MATERIALS AND METHODS

### Literature Search

We conducted this systematic review and metaanalysis in line with the Preferred Reporting Items for Systematic Reviews and Meta-Analyses guidelines. The study protocol is registered in PROSPERO (International Prospective Register of Systematic Reviews) (CRD42 021270480).

Received Feb. 2, 2023; revision accepted Apr. 14, 2023.
For correspondence or reprints, contact Rathan M. Subramaniam (rathan.subramaniam@otago.ac.nz).
Published online Jun. 8, 2023.

A systematic search of the literature on FAPI PET/CT was performed in November 2021 and updated in April 2022. Relevant studies were identified from the following electronic databases: MEDLINE, Embase, Scopus, PubMed, and the Cochrane Central Register of Controlled Trials. To identify trials, we searched the U.S. National Institutes of Health Ongoing Trials Register, World Health Organization International Clinical Trials Registry Platform, and the Australian New Zealand Clinical Trials Registry. The search strategy utilized medical subject headings and free-text terms centered around neoplasia, PET/CT, and FAPI. No language or publication period limitations were used in the search. Additional studies were manually retrieved through citation searches and the reference lists of included articles.

### Eligibility Criteria

We applied the following criteria for study inclusion: use of FAPI PET/CT imaging for suspected or proven tumors (initial detection, staging, or recurrence detection), adult participants (≥18 y), tumor presence confirmed by reference standard (histopathologic or imaging), data available for primary outcome, and studies with ethical approval. The following were excluded: nonhuman studies, studies in fields other than oncology, case reports, review articles, editorials, letters, commentaries, and conference proceedings.

### Data Extraction

All identified studies were screened using the predefined eligibility criteria by 2 investigators. Studies were screened first for inclusion or exclusion using titles and abstracts and then using full texts. A third investigator resolved any discrepancies in study inclusion and exclusion. If studies had insufficient data to construct 2 × 2 contingency tables, the corresponding authors were contacted for data before the study was excluded. If 2 or more studies by the same group had overlapping study periods and populations, the study with the largest cohort was included. In these cases, the corresponding authors were also contacted to check for any potential study overlap.

We extracted the following data: publication details, study design, study methodology, patient demographics, imaging modalities used, number of accurately diagnosed primary and metastatic lesions, number of accurately diagnosed lesions, number of inaccurately diagnosed primary and metastatic lesions, number of inaccurately diagnosed lesions, and PET radiopharmaceuticals used. If the studies did not report the raw diagnostic data, we reconstructed 2 × 2 tables from the diagnostic estimates given in the text.

### Study Quality Assessment

All included studies were screened and assessed for quality using the QUADAS-2 (Quality Assessment of Diagnostic Accuracy Studies 2) criteria by 2 of the investigators independently. The risk of bias and applicability were evaluated for patient selection, index test, and reference standard, with the flow and timing domain being used only to assess bias.

### Data Synthesis and Statistical Analysis

We assessed the diagnostic performance of FAPI PET/CT and [$^{18}$F]FDG PET/CT for primary tumors (patient-based and lesion-based), lymph nodes, and metastases. We calculated sensitivity, specificity, and 95% CIs for each study and determined the pooled relative diagnostic accuracy of FAPI PET/CT and [$^{18}$F]FDG PET/CT with a random-effects metaanalysis. Analyses were performed using a frequentist framework in R (version 4.1.2) with *lme4, meta,* and *lmtest* packages. Data were summarized and presented in paired forest plots and summary receiver-operating characteristic curves for each analysis using Revman (version 5.4, ReviewManager). Heterogeneity was evaluated using general linear models to evaluate between-study variance. Publication and any other potential biases were assessed visually using funnel plots. A *P* value of 0.05 or less was considered statistically significant.

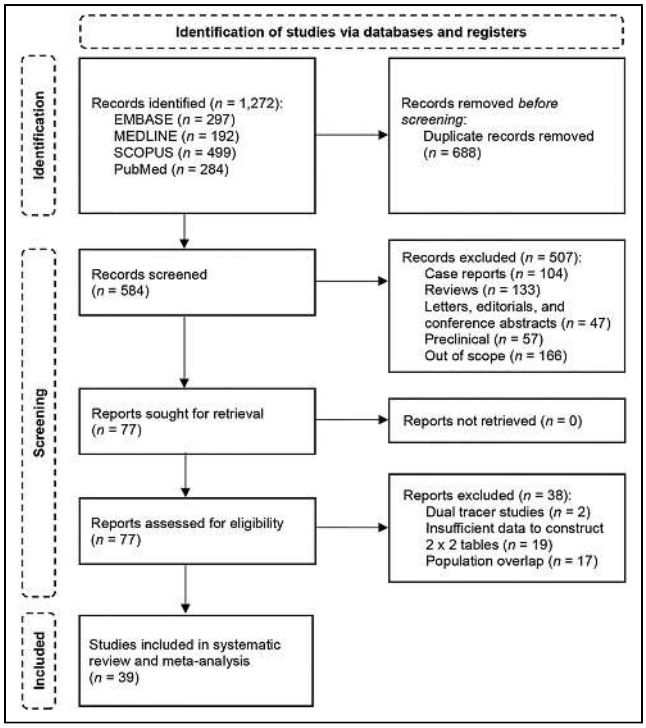


**FIGURE 1.** Flowchart of study inclusions.

## RESULTS

### Study Selection and Characteristics

Electronic database searches identified 1,272 articles. Duplicate screening removed 688 articles, and a further 507 articles were removed after title and abstract screening, resulting in full-text retrieval of 77 relevant articles. After full-text review, 39 studies met the inclusion criteria, constituting 1,259 patients. Nineteen studies were excluded because of insufficient data, 17 studies had overlapping populations, and 2 studies investigated only dual-tracer scans (Fig. 1).

Study quality was assessed using the QUADAS-2 criteria (Fig. 2). The main issues in study quality were uncertainty about consecutive enrollment, lack or uncertainty of masking, lack of inclusion of all patients in the final analysis, and the use of different reference standards.

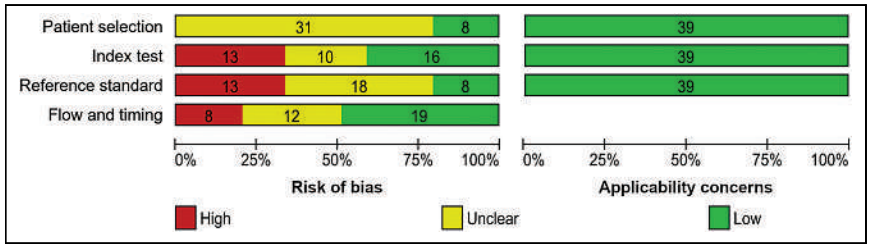


**FIGURE 2.** QUADAS-2 criteria assessment results for included studies. Judgments about each domain are presented as percentages, and number of studies is presented within bars.

**TABLE 1**
Study Demographics

| Study | Patients (*n*) | Study design | Age (y) | Cancer type |
|---|---|---|---|---|
| Ballal (2021, India) | 54 (20 M, 34 F) | Prospective | 48.4 | Various |
| Çermik (2022, Turkey) | 42 (26 M, 16 F) | Prospective | 58.5 | Various |
| Chen (2021, China) | 68 (40 M, 28 F) | Prospective | 57* | Various |
| Chen (2022, China) | 36 (29 M, 7 F) | Prospective | 61.6 | Oral squamous cell carcinoma |
| Elboğa (2022, Turkey) (*17*) | 37 (23 M, 14 F) | Retrospective | 62.8 | Colorectal, gastric, pancreaticobiliary |
| Elboğa (2022, Turkey) (*48*) | 14 (7 M, 7 F) | Retrospective | 59 | Multiple myeloma |
| Gu (2022, China) | 45 (24 M, 21 F) | Prospective | 46* | Soft-tissue sarcoma |
| Gündoğan (2022, Turkey) | 21 (12 M, 9 F) | Prospective | 61* | Gastric adenocarcinoma |
| Guo (2021, China) | 34 (25 M, 9 F) | Retrospective | 60.6 | Hepatic |
| Hu (2022, China) | 22 (12 M, 10 F) | Prospective | 55.5* | Various |
| Jiang (2022, China) | 38 (29 M, 9 F) | Retrospective | 63.7 | Gastric |
| Jin (2022, China) | 73 (37 M, 36 F) | Prospective | 51.6 | Lymphoma |
| Kessler (2022, Germany) | 47 (24 M, 23 F) | Prospective | 48.1 | Sarcoma |
| Kömek (2021, Turkey) | 20 (0 M, 20 F) | Prospective | 44* | Breast |
| Kreppel (2021, Germany) | 13 (8 M, 5 F) | Retrospective | 66.8 | Liver metastases in neuroendocrine tumors |
| Kuten (2022, Israel) | 13 (6 M, 7 F) | Prospective | 70* | Gastric adenocarcinoma |
| Lan (2022, China) | 123 (69 M, 54 F) | Prospective | 56.11 | Various |
| Li (2022, China) | 34 (25 M, 9 F) | Prospective | 62* | Lung adenocarcinoma |
| Lin (2022, China) | 56 (40 M, 16 F) | Prospective | 63.8* | Gastric |
| Linz (2021, Germany) | 10 (8 M, 2 F) | Prospective | 62 | Oral squamous cell carcinoma |
| Mona (2022, United States) | 15 (8 M, 7 F) | Prospective | 60.7 | Various |
| Pang (2021, China) | 35 (18 M, 17 F) | Retrospective | 64* | Gastric, colorectal, duodenal |
| Pang (2022, China) | 36 (25 M, 11 F) | Retrospective | 60* | Pancreatic |
| Promteangtrong (2022, Thailand) | 40 (27 M, 13 F) | Prospective | 57 | Head and neck squamous cell carcinoma |
| Qin (2021, China) | 15 (8 M, 7 F) | Prospective | 51.2 | Nasopharyngeal carcinoma |
| Qin (2022, China) | 20 (9 M, 11 F) | Prospective | 56* | Gastric |
| Ristau (2020, Germany) | 7 (5 M, 2 F) | Retrospective | 63.5* | Esophageal |
| Röhrich (2021, Germany) | 19 (10 M, 9 F) | Retrospective | 64* | Pancreatic adenocarcinoma |
| Şahin (2021, Turkey) | 31 (19 M, 12 F) | Retrospective | 61.9 | Liver metastases in gastrointestinal cancer |
| Serfling (2021, Germany) | 8 (6 M, 2 F) | Retrospective | 62 | Tonsil carcinoma |
| Shi (2021, China) | 20 (18 M, 2 F) | Prospective | 58 | Hepatic |
| Siripongsatian (2022, Thailand) | 27 (21 M, 6 F) | Retrospective | 68* | Hepatic |
| Wang (2021, China) | 25 (24 M, 1 F) | Retrospective | 59.4 | Hepatic |
| Wang (2022, China) | 34 (20 M, 14 F) | Prospective | 64* | Lung |
| Wei (2022, China) | 28 (16 M, 12 F) | Prospective | 59.8 | Various |
| Windisch (2020, Germany) | 13 (5 M, 8 F) | Prospective | 60.9 | Glioblastoma |
| Zhang (2022, China) | 33 (19 M, 14 F) | Prospective | 68.8 | Pancreatic |
| Zhao (2021, China) (*31*) | 21 (18 M, 3 F) | Retrospective | 60* | Esophageal |
| Zhao (2021, China) (*35*) | 45 (35 M, 10 F) | Retrospective | 50* | Nasopharyngeal carcinoma |

*Median.

**Systematic Review**

Study demographic and index test characteristics are summarized in Table 1 and Supplemental Table 1, respectively (supplemental materials are available at http://jnm.snmjournals.org). The included studies were published between 2020 and 2022. Twenty-four studies were prospective, and 15 were retrospective. More than half the studies were conducted in China. The included studies focused on gastrointestinal cancers (*12,17–31*), head and neck cancer (*11,32–36*), various cancers (*9,10,37–41*), lung cancer (*42,43*), sarcoma (*44,45*), breast cancer (*46*), lymphoma (*47*), multiple myeloma (*48*), glioblastoma (*49*), and liver metastases (*50,51*).

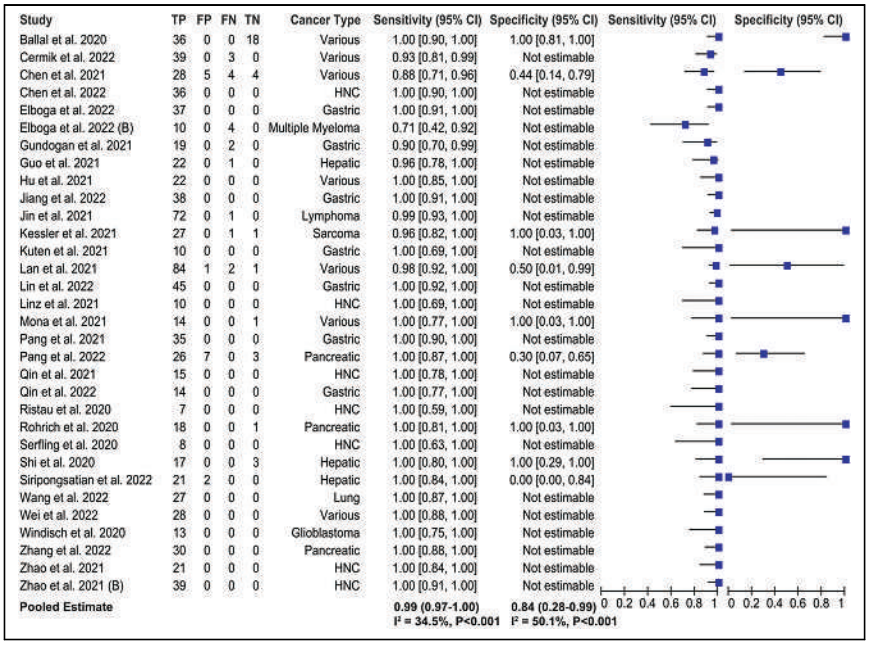


**FIGURE 3.** Forest plot showing random-effects estimates and individual study sensitivity and specificity for detection of primary lesions by FAPI PET/CT. FN = false-negative; FP = false-positive; HNC = head and neck cancer; TN = true-negative; TP = true-positive.

PET/CT was used as the index test imaging modality in 34 studies, PET/MRI was used in 3 studies, and both PET/CT and PET/MRI were used in 2 studies. The studies used various FAPI ligands (FAPI-02, FAPI-04, FAPI-42, FAPI-46, DOTA.SA.FAPI, and DATA$^{5m}$.SA.FAPI) and isotopes ($^{18}$F and $^{68}$Ga). The injected activity of the radiotracer varied among studies (Supplemental Table 1). The most common acquisition time was 60 min (24 studies), 5 studies used acquisition times shorter than 60 min, and 10 studies used a range of acquisition times (30–113 min) (Supplemental Table 1). The FAPI scans were compared with [$^{18}$F]FDG in 34 studies, MRI in 3 studies, contrast-enhanced CT in 2 studies, and a second FAPI ligand in 1 study; 2 studies had no comparator.

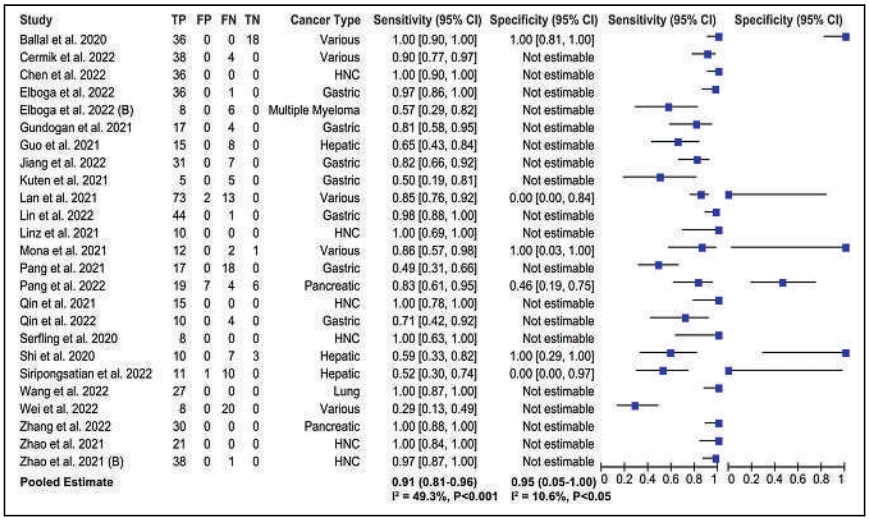


**FIGURE 4.** Forest plot showing random-effects estimate and individual study sensitivity and specificity for detection of primary lesions by [$^{18}$F]FDG PET/CT. FN = false-negative; FP = false-positive; HNC = head and neck cancer; TN = true-negative; TP = true-positive.

### Metaanalysis

We used per-patient data for primary lesions and per-lesion data for the nodal and distant metastatic lesions. The overall pooled sensitivity of FAPI was 0.99 (95% CI, 0.97–1.00; heterogeneity index [$I^2$] = 34.5%), 0.91 (95% CI, 0.81–0.96; $I^2$ = 0.0%), and 0.99 (95% CI, 0.96–1.00; $I^2$ = 96.8%) for the detection of primary, nodal, and distant metastatic lesions, respectively (Fig. 3; Supplemental Fig. 1). The overall pooled specificity of FAPI was 0.84 (95% CI, 0.28–0.99; $I^2$ = 50.1%) for the detection of primary lesions. The forest plot in Figure 3 shows the pooled estimates of sensitivity and specificity for the detection of primary lesions. The estimated metastatic pooled per-lesion sensitivity was not reliable because of high heterogeneity ($I^2$ = 96.8%). Forest plots for the detection of nodal and distant metastases and summary receiver-operating characteristic curves are shown in Supplemental Figures 1 and 2, respectively. The limited number of studies reporting true-negative data reduced the certainty of the pooled specificity results.

A paired analysis including studies comparing both radiotracers showed that sensitivity was higher for FAPI than for [$^{18}$F]FDG in the detection of primary lesions (1.00 [95% CI, 0.95–1.00] vs. 0.91 [95% CI, 0.81–0.96]), nodal metastases (0.91 [95% CI, 0.81–0.96] vs. 0.78 [95% CI, 0.66–0.87]), and distant metastatic lesions (0.99 [95% CI, 0.96–1.00] vs. 0.73 [95% CI, 0.53–0.87]). There was a significant difference in sensitivity between FAPI and [$^{18}$F]FDG in the detection of primary lesions ($P < 0.001$), nodal metastases ($P < 0.001$), and distant metastatic lesions ($P < 0.001$). The study estimates of sensitivity and specificity for the detection of primary lesions by [$^{18}$F]FDG PET/CT are shown in Figure 4, and paired summary receiver-operating characteristic curves are shown in Figure 5. The paired analysis for primary lesions had moderate heterogeneity ($I^2$ = 29.0% for FAPI; $I^2$ = 49.3% for [$^{18}$F]FDG), nodal metastases had negligible heterogeneity ($I^2$ = 0.0% for both), and metastatic lesions had high heterogeneity ($I^2$ = 96.8% for FAPI; $I^2$ = 96.6% for [$^{18}$F]FDG). The overall pooled specificity for the detection of primary lesions was higher for [$^{18}$F]FDG than for FAPI (0.95 [95% CI, 0.05–1.00] vs. 0.87 [95% CI, 0.05–1.00]); however, the limited number of studies reporting true-negative data reduced the certainty of the specificity analyses. Forest plots for the detection of nodal and distant metastases are shown in Supplemental Figure 3. Funnel plot asymmetry (Supplemental Figs. 4–6) suggests slight study bias, particularly for lymph node and metastatic analyses.

A subgroup analysis comparing FAPI and [$^{18}$F]FDG PET/CT in gastrointestinal cancers demonstrated that FAPI PET/CT had a higher sensitivity (1.00 [95% CI, 0.84–0.99] vs. 0.81 [95% CI, 0.66–0.90])

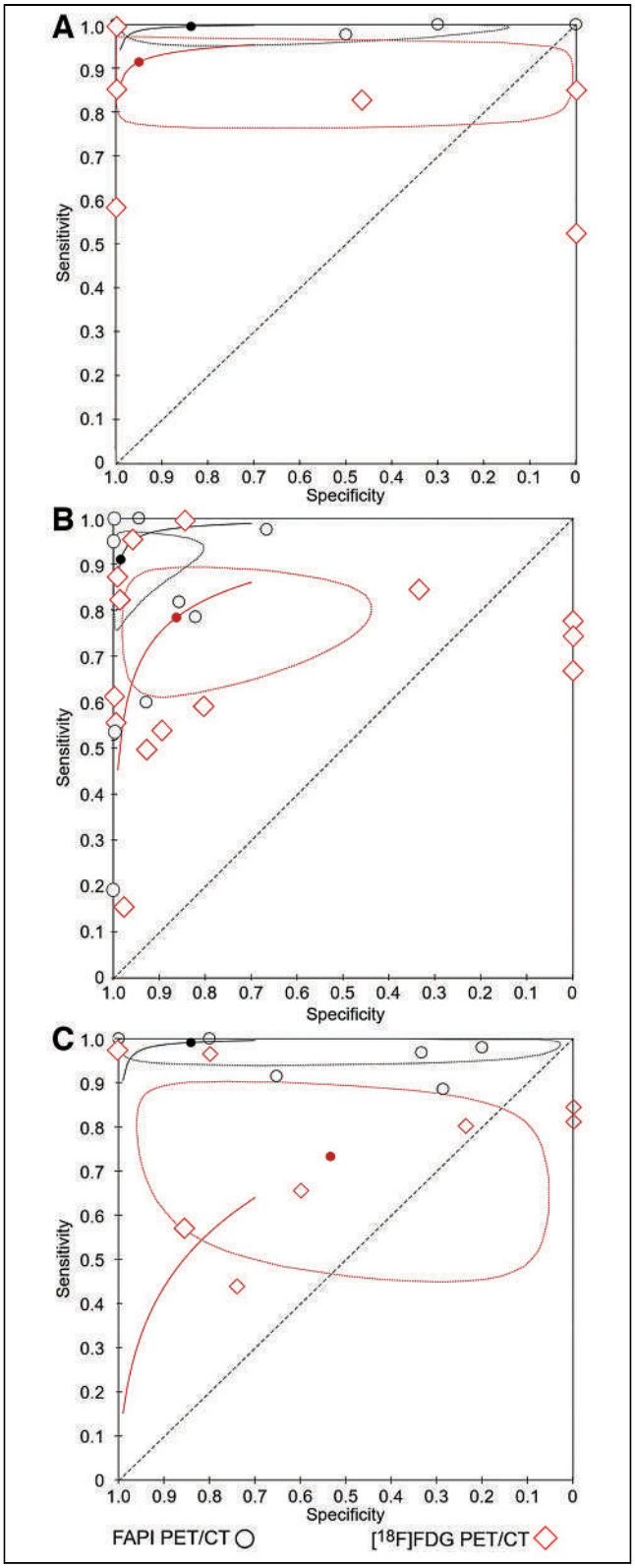


**FIGURE 5.** Summary receiver-operating characteristic curve analysis comparing diagnostic performance of FAPI PET/CT and [$^{18}$F]FDG PET/CT for studies that reported on both tracers: primary lesions (A), nodal metastases (B), and metastatic lesions (C). Each circle represents FAPI PET/CT data, and each diamond represents [$^{18}$F]FDG PET/CT data for individual study. Shaded circles represent summary points, and dotted circles show 95% CIs.

and specificity (0.54 [95% CI, 0.05–0.96] vs. 0.52 [95% CI, 0.26–0.77]) than [$^{18}$F]FDG PET/CT in the detection of primary gastrointestinal lesions (Supplemental Fig. 7). There was a significant difference in sensitivity between [$^{18}$F]FDG and FAPI ($P < 0.001$), but not specificity ($P = 0.42$), and both analyses had high heterogeneity ($I^2 = 87.9\%$ and $I^2 = 87.8\%$, respectively). FAPI PET/CT had a higher sensitivity than [$^{18}$F]FDG PET/CT in the detection of nodal [0.90 (95% CI, 0.65–0.98) vs 0.64 (95% CI, 0.43–0.81)] and distant (0.99 [95% CI, 0.88–0.99] vs. 0.61 [95% CI, 0.43–0.78]) metastatic lesions in gastrointestinal cancers (Supplemental Figs. 8 and 9). Both analyses were significant ($P < 0.001$), and they had moderate ($I^2 = 57.9\%$) and high ($I^2 = 98.2\%$) heterogeneity, respectively.

## DISCUSSION

This systematic review and metaanalysis showed that FAPI is highly sensitive in the detection of primary, nodal, and metastatic lesions. We demonstrated that FAPI is significantly more sensitive than [$^{18}$F]FDG for primary, nodal, and metastatic lesions, across studies examining both radiotracers. Our analyses showed that [$^{18}$F]FDG had a higher specificity than FAPI for the detection of primary lesions; however, the lack of studies reporting true-negative data reduces our confidence in pooled specificities.

Several metaanalyses investigated the diagnostic accuracy of FAPI PET/CT in the detection of oncologic lesions (*13–16*). Compared with previous metaanalyses, our comprehensive analysis provides an up-to-date evaluation of the diagnostic applicability of FAPI PET/CT radiotracers and a direct comparison to [$^{18}$F]FDG PET/CT for primary lesions, nodal metastases, and distant metastases.

An early metaanalysis of 14 studies on [$^{68}$Ga]FAPI by Sollini et al. (*13*) reported a patient-based pooled sensitivity and specificity of 0.99 and 0.87, respectively. On a lesion-based analysis, they reported sensitivities of 1.00 and 0.93 for the detection of primary and distant metastases, respectively. However, the results were highly heterogeneous, and the study design of the included papers prevented the calculation of pooled specificity for both primary tumors and metastases. Our lesion-based analysis for the detection of distant metastases was also heterogeneous ($I^2 = 96.6\%$). Sollini et al., however, did not report or compare [$^{68}$Ga]FAPI PET/CT with [$^{18}$F]FDG PET/CT or other imaging modalities (*13*). A metaanalysis by Roustaei et al. directly compared the detection rates of [$^{68}$Ga]FAPI and [$^{18}$F]FDG PET using odds ratios (OR) and risk differences for various cancers across 9 studies (*14*). They found that gastrointestinal tumors had the highest estimated OR (32.079; 95% CI, 4.001–257.212; $P = 0.001$) for the detection of primary tumors (*14*). For nodal and distant metastases, they found that hepatobiliary tumors (OR, 11.609) and nasopharyngeal carcinomas (OR, 77.451) had the highest ORs, respectively (*14*). Their analysis of different cancer types had high heterogeneity, similar to our analysis of distant metastases across various cancer types (*14*). Gege et al. compared [$^{68}$Ga]FAPI and [$^{18}$F]FDG PET/CT for the detection of peritoneal metastases, showing [$^{68}$Ga]FAPI to have superior sensitivity in both patient-based analysis (98.2% vs. 55.9%, 9 studies) and lesion-based analyses (99.9% vs. 27.35, 4 studies) (*15*). Finally, Huang et al. analyzed the detection rates of [$^{68}$Ga]FAPI in digestive system tumors in 18 studies (*16*), reporting a patient-based sensitivity of 0.98 and a lesion-based sensitivity of 0.97 (*16*), as well as a pooled sensitivity of 0.94 for the detection of nonprimary (lymph node and distant metastases) lesions (*16*). Specificity was statistically pooled by neither Gege et al. nor Huang et al. because of a

lack of true-negative data, a common limitation in these diagnostic studies (*15,16*).

FAPI PET/CT appears to be a promising diagnostic radiotracer for tumors and lesions that are inconclusive on [$^{18}$F]FDG imaging, such as tumors in the gut and liver with variable [$^{18}$F]FDG uptake due to metabolic alterations (*24*). A study by Chen et al. (*9*) showed that [$^{68}$Ga]DOTA-FAPI PET/CT had higher tumor uptake and a more favorable tumor-to-background ratio in tumors with inconclusive [$^{18}$F]FDG findings.

Our metaanalysis has some limitations. First, because of the limited number of studies available on FAPI PET/CT, we included all studies that used FAPI PET/CT in an oncologic setting. These studies were heterogeneous, with various cancers and patients. As study of FAPI PET/CT continues, further analyses can be conducted on specific cancer types to better determine its diagnostic utility. Second, a small number of studies reporting true-negative data resulted in wide pooled CIs for specificity and limited conclusions on overall diagnostic accuracy. The fact that some studies also excluded patients with benign disease or included only patients who already had a confirmed malignancy highlights the need for adequate studies on patients who do not have histologic confirmation of cancer. Third, in terms of the detection of nodal and metastatic lesions, patients in some studies had already undergone treatment whereas others were treatment-naïve, which may underestimate FAPI's ability to detect these treated lesions. Finally, many of the included studies were retrospective or focused on tumors with suboptimal [$^{18}$F]FDG sensitivity, resulting in a risk of pretest selection bias.

## CONCLUSION

This systematic review demonstrates that FAPI has high sensitivity in the detection of primary and nodal lesions. Additionally, the sensitivity of FAPI in the detection of primary, nodal, and metastatic lesions was significantly higher than that of [$^{18}$F]FDG across various cancers. However, our findings on distant metastases were biased by high heterogeneity. Although FAPI is a promising radiotracer, the high risk of bias and study heterogeneity suggest that further trials are required to evaluate the role of FAPI in an oncologic setting and its utility alongside or over [$^{18}$F]FDG PET/CT.

## DISCLOSURE

This study was supported by the Department of Medicine, Dunedin School of Medicine, University of Otago Medical School, Dunedin, New Zealand. No other potential conflict of interest relevant to this article was reported.

**KEY POINTS**

**QUESTION:** What is the diagnostic accuracy of FAPI PET/CT alone and compared with [$^{18}$F]FDG PET/CT for the detection of primary and metastatic lesions?

**PERTINENT FINDINGS:** This systematic review and metaanalysis found that FAPI has high sensitivity in the detection of primary lesions (0.99; 95% CI, 0.97–1.00), nodal metastases (0.91; 95% CI, 0.81–0.96), and distant metastases (0.99; 95% CI, 0.96–1.00). In a paired analysis, the sensitivity of FAPI was superior to that of [$^{18}$F]FDG PET/CT, with statistical significance.

**IMPLICATIONS FOR PATIENT CARE:** These findings show that FAPI is a promising radiotracer in oncology, but further studies are required to better evaluate its indications and role.

## REFERENCES

1. Lopci E, Fanti S. Non-FDG PET/CT. *Recent Results Cancer Res.* 2020;216: 669–718.
2. Siveke JT. Fibroblast-activating protein: targeting the roots of the tumor microenvironment. *J Nucl Med.* 2018;59:1412–1414.
3. Hicks RJ, Roselt PJ, Kallur KG, Tothill RW, Mileshkin L. FAPI PET/CT: will it end the hegemony of $^{18}$F-FDG in oncology? *J Nucl Med.* 2021;62:296–302.
4. Liu T, Han C, Wang S, et al. Cancer-associated fibroblasts: an emerging target of anti-cancer immunotherapy. *J Hematol Oncol.* 2019;12:86.
5. Lindner T, Loktev A, Giesel F, Kratochwil C, Altmann A, Haberkorn U. Targeting of activated fibroblasts for imaging and therapy. *EJNMMI Radiopharm Chem.* 2019;4:16.
6. Uitte de Willige S, Malfliet JJ, Janssen HL, Leebeek FW, Rijken DC. Increased N-terminal cleavage of alpha-2-antiplasmin in patients with liver cirrhosis. *J Thromb Haemost.* 2013;11:2029–2036.
7. Liu F, Qi L, Liu B, et al. Fibroblast activation protein overexpression and clinical implications in solid tumors: a meta-analysis. *PLoS One.* 2015;10:e0116683.
8. Loktev A, Lindner T, Mier W, et al. A tumor-imaging method targeting cancer-associated fibroblasts. *J Nucl Med.* 2018;59:1423–1429.
9. Chen H, Zhao L, Ruan D, et al. Usefulness of [$^{68}$Ga]Ga-DOTA-FAPI-04 PET/CT in patients presenting with inconclusive [$^{18}$F]FDG PET/CT findings. *Eur J Nucl Med Mol Imaging.* 2021;48:73–86.
10. Lan L, Liu H, Wang Y, et al. The potential utility of [$^{68}$Ga]Ga-DOTA-FAPI-04 as a novel broad-spectrum oncological and non-oncological imaging agent-comparison with [$^{18}$F]FDG. *Eur J Nucl Med Mol Imaging.* 2022;49:963–979.
11. Linz C, Brands RC, Kertels O, et al. Targeting fibroblast activation protein in newly diagnosed squamous cell carcinoma of the oral cavity: initial experience and comparison to [$^{18}$F]FDG PET/CT and MRI. *Eur J Nucl Med Mol Imaging.* 2021; 48:3951–3960.
12. Guo W, Pang Y, Yao L, et al. Imaging fibroblast activation protein in liver cancer: a single-center post hoc retrospective analysis to compare [$^{68}$Ga]Ga-FAPI-04 PET/CT versus MRI and [$^{18}$F]-FDG PET/CT. *Eur J Nucl Med Mol Imaging.* 2021; 48:1604–1617.
13. Sollini M, Kirienko M, Gelardi F, Fiz F, Gozzi N, Chiti A. State-of-the-art of FAPI-PET imaging: a systematic review and meta-analysis. *Eur J Nucl Med Mol Imaging.* 2021;48:4396–4414.
14. Roustaei H, Kiamanesh Z, Askari E, Sadeghi R, Aryana K, Treglia G. Could fibroblast activation protein (FAP)-specific radioligands be considered as pan-tumor agents? *Contrast Media Mol Imaging.* 2022;2022:3948873.
15. Gege Z, Xueju W, Bin J. Head-to-head comparison of $^{68}$Ga-FAPI PET/CT and FDG PET/CT for the detection of peritoneal metastases: systematic review and meta-analysis. *AJR.* February 15, 2023 [Epub ahead of print].
16. Huang D, Wu J, Zhong H, et al. [$^{68}$Ga]Ga-FAPI PET for the evaluation of digestive system tumors: systematic review and meta-analysis. *Eur J Nucl Med Mol Imaging.* 2023;50:908–920.
17. Elboğa U, Sahin E, Kus T, et al. Comparison of $^{68}$Ga-FAPI PET/CT and $^{18}$FDG PET/CT modalities in gastrointestinal system malignancies with peritoneal involvement. *Mol Imaging Biol.* 2022;24:789–797.
18. Gündoğan C, Komek H, Can C, et al. Comparison of $^{18}$F-FDG PET/CT and $^{68}$Ga-FAPI-04 PET/CT in the staging and restaging of gastric adenocarcinoma. *Nucl Med Commun.* 2022;43:64–72.
19. Jiang D, Chen X, You Z, et al. Comparison of [$^{68}$Ga]Ga-FAPI-04 and [$^{18}$F]-FDG for the detection of primary and metastatic lesions in patients with gastric cancer: a bicentric retrospective study. *Eur J Nucl Med Mol Imaging.* 2022;49:732–742.
20. Kuten J, Levine C, Shamni O, et al. Head-to-head comparison of [$^{68}$Ga]Ga-FAPI-04 and [$^{18}$F]-FDG PET/CT in evaluating the extent of disease in gastric adenocarcinoma. *Eur J Nucl Med Mol Imaging.* 2022;49:743–750.
21. Lin R, Lin Z, Chen Z, et al. [$^{68}$Ga]Ga-DOTA-FAPI-04 PET/CT in the evaluation of gastric cancer: comparison with [$^{18}$F]FDG PET/CT. *Eur J Nucl Med Mol Imaging.* 2022;49:2960–2971.
22. Pang Y, Zhao L, Luo Z, et al. Comparison of $^{68}$Ga-FAPI and $^{18}$F-FDG uptake in gastric, duodenal, and colorectal cancers. *Radiology.* 2021;298:393–402.
23. Pang Y, Zhao L, Shang Q, et al. Positron emission tomography and computed tomography with [$^{68}$Ga]Ga-fibroblast activation protein inhibitors improves tumor detection and staging in patients with pancreatic cancer. *Eur J Nucl Med Mol Imaging.* 2022;49:1322–1337.
24. Qin C, Shao F, Gai Y, et al. $^{68}$Ga-DOTA-FAPI-04 PET/MR in the evaluation of gastric carcinomas: comparison with $^{18}$F-FDG PET/CT. *J Nucl Med.* 2022;63:81–88.
25. Röhrich M, Naumann P, Giesel FL, et al. Impact of $^{68}$Ga-FAPI PET/CT imaging on the therapeutic management of primary and recurrent pancreatic ductal adenocarcinomas. *J Nucl Med.* 2021;62:779–786.
26. Shi X, Xing H, Yang X, et al. Comparison of PET imaging of activated fibroblasts and $^{18}$F-FDG for diagnosis of primary hepatic tumours: a prospective pilot study. *Eur J Nucl Med Mol Imaging.* 2021;48:1593–1603.

27. Siripongsatian D, Promteangtrong C, Kunawudhi A, et al. Comparisons of quantitative parameters of Ga-68-labelled fibroblast activating protein inhibitor (FAPI) PET/CT and [$^{18}$F]F-FDG PET/CT in patients with liver malignancies. *Mol Imaging Biol.* 2022;24:818–829.
28. Wang H, Zhu W, Ren S, et al. $^{68}$Ga-FAPI-04 versus $^{18}$F-FDG PET/CT in the detection of hepatocellular carcinoma. *Front Oncol.* 2021;11:693640.
29. Zhang Z, Jia G, Pan G, et al. Comparison of the diagnostic efficacy of $^{68}$Ga-FAPI-04 PET/MR and $^{18}$F-FDG PET/CT in patients with pancreatic cancer. *Eur J Nucl Med Mol Imaging.* 2022;49:2877–2888.
30. Ristau J, Giesel FL, Haefner MF, et al. Impact of primary staging with fibroblast activation protein specific enzyme inhibitor (FAPI)-PET/CT on radio-oncologic treatment planning of patients with esophageal cancer. *Mol Imaging Biol.* 2020;22: 1495–1500.
31. Zhao L, Chen S, Chen S, et al. $^{68}$Ga-fibroblast activation protein inhibitor PET/CT on gross tumour volume delineation for radiotherapy planning of oesophageal cancer. *Radiother Oncol.* 2021;158:55–61.
32. Promteangtrong C, Siripongsatian D, Jantarato A, et al. Head-to-head comparison of $^{68}$Ga-FAPI-46 and $^{18}$F-FDG PET/CT for evaluation of head and neck squamous cell carcinoma: a single-center exploratory study. *J Nucl Med.* 2022;63:1155–1161.
33. Qin C, Liu F, Huang J, et al. A head-to-head comparison of $^{68}$Ga-DOTA-FAPI-04 and $^{18}$F-FDG PET/MR in patients with nasopharyngeal carcinoma: a prospective study. *Eur J Nucl Med Mol Imaging.* 2021;48:3228–3237.
34. Serfling S, Zhi Y, Schirbel A, et al. Improved cancer detection in Waldeyer's tonsillar ring by $^{68}$Ga-FAPI PET/CT imaging. *Eur J Nucl Med Mol Imaging.* 2021;48: 1178–1187.
35. Zhao L, Pang Y, Zheng H, et al. Clinical utility of [$^{68}$Ga]Ga-labeled fibroblast activation protein inhibitor (FAPI) positron emission tomography/computed tomography for primary staging and recurrence detection in nasopharyngeal carcinoma. *Eur J Nucl Med Mol Imaging.* 2021;48:3606–3617.
36. Chen S, Chen Z, Zou G, et al. Accurate preoperative staging with [$^{68}$Ga]Ga-FAPI PET/CT for patients with oral squamous cell carcinoma: a comparison to 2-[$^{18}$F]FDG PET/CT. *Eur Radiol.* 2022;32:6070–6079.
37. Ballal S, Yadav MP, Moon ES, et al. Biodistribution, pharmacokinetics, dosimetry of [$^{68}$Ga]Ga-DOTA.SA.FAPi, and the head-to-head comparison with [$^{18}$F]F-FDG PET/CT in patients with various cancers. *Eur J Nucl Med Mol Imaging.* 2021;48: 1915–1931.
38. Çermik TF, Ergul N, Yilmaz B, Mercanoglu G. Tumor imaging with $^{68}$Ga-DOTA-FAPI-04 PET/CT: comparison with $^{18}$F-FDG PET/CT in 22 different cancer types. *Clin Nucl Med.* 2022;47:e333–e339.
39. Hu K, Wang L, Wu H, et al. [$^{18}$F]FAPI-42 PET imaging in cancer patients: optimal acquisition time, biodistribution, and comparison with [$^{68}$Ga]Ga-FAPI-04. *Eur J Nucl Med Mol Imaging.* 2022;49:2833–2843.
40. Wei Y, Zheng J, Ma L, et al. [$^{18}$F]AlF-NOTA-FAPI-04: FAP-targeting specificity, biodistribution, and PET/CT imaging of various cancers. *Eur J Nucl Med Mol Imaging.* 2022;49:2761–2773.
41. Mona CE, Benz MR, Hikmat F, et al. Correlation of $^{68}$Ga-FAPi-46 PET biodistribution with FAP expression by immunohistochemistry in patients with solid cancers: a prospective translational exploratory study. *J Nucl Med.* 2022;63:1021–1026.
42. Wang L, Tang G, Hu K, et al. Comparison of $^{68}$Ga-FAPI and $^{18}$F-FDG PET/CT in the evaluation of advanced lung cancer. *Radiology.* 2022;303:191–199.
43. Li Y, Lin X, Li Y, et al. Clinical utility of F-18 labeled fibroblast activation protein inhibitor (FAPI) for primary staging in lung adenocarcinoma: a prospective study. *Mol Imaging Biol.* 2022;24:309–320.
44. Gu B, Liu X, Wang S, et al. Head-to-head evaluation of [$^{18}$F]FDG and [$^{68}$Ga]Ga-DOTA-FAPI-04 PET/CT in recurrent soft tissue sarcoma. *Eur J Nucl Med Mol Imaging.* 2022;49:2889–2901.
45. Kessler L, Ferdinandus J, Hirmas N, et al. $^{68}$Ga-FAPI as a diagnostic tool in sarcoma: data from the $^{68}$Ga-FAPI PET prospective observational trial. *J Nucl Med.* 2022;63:89–95.
46. Kömek H, Can C, Güzel Y, et al. $^{68}$Ga-FAPI-04 PET/CT, a new step in breast cancer imaging: a comparative pilot study with the $^{18}$F-FDG PET/CT. *Ann Nucl Med.* 2021;35:744–752.
47. Jin X, Wei M, Wang S, et al. Detecting fibroblast activation proteins in lymphoma using $^{68}$Ga-FAPI PET/CT. *J Nucl Med.* 2022;63:212–217.
48. Elboğa U, Sahin E, Cayirli YB, et al. Comparison of [$^{68}$Ga]-FAPI PET/CT and [$^{18}$F]-FDG PET/CT in multiple myeloma: clinical experience. *Tomography.* 2022; 8:293–302.
49. Windisch P, Rohrich M, Regnery S, et al. Fibroblast activating protein specific PET for advanced target volume delineation in glioblastoma. *Radiother Oncol.* 2020;150:159–163.
50. Şahin E, Elboğa U, Çelen YZ, Sever ÖN, Çayırlı YB, Çimen U. Comparison of $^{68}$Ga-DOTA-FAPI and $^{18}$FDG PET/CT imaging modalities in the detection of liver metastases in patients with gastrointestinal system cancer. *Eur J Radiol.* 2021;142: 109867.
51. Kreppel B, Gonzalez-Carmona MA, Feldmann G, et al. Fibroblast activation protein inhibitor (FAPi) positive tumour fraction on PET/CT correlates with Ki-67 in liver metastases of neuroendocrine tumours. *Nuklearmedizin.* 2021;60:344–354.

# Initial Evaluation of [$^{18}$F]FAPI-74 PET for Various Histopathologically Confirmed Cancers and Benign Lesions

Tadashi Watabe[1,2], Sadahiro Naka[3], Mitsuaki Tatsumi[4], Takashi Kamiya[4], Toru Kimura[5], Yasushi Shintani[5], Kaori Abe[6], Tomohiro Miyake[6], Kenzo Shimazu[6], Shogo Kobayashi[7], Yukinori Kurokawa[7], Hidetoshi Eguchi[7], Yuichiro Doki[7], Hidenori Inohara[8], Hiroki Kato[1,2], Yuriko Mori[9], Jens Cardinale[9], and Frederik L. Giesel[2,9]

*[1]Department of Nuclear Medicine and Tracer Kinetics, Graduate School of Medicine, Osaka University, Osaka, Japan; [2]Institute for Radiation Sciences, Osaka University, Osaka, Japan; [3]Department of Pharmacy, Osaka University Hospital, Osaka, Japan; [4]Department of Radiology, Osaka University Hospital, Osaka, Japan; [5]Department of Thoracic Surgery, Graduate School of Medicine, Osaka University, Osaka, Japan; [6]Department of Breast and Endocrine Surgery, Graduate School of Medicine, Osaka University, Osaka, Japan; [7]Department of Gastroenterological Surgery, Graduate School of Medicine, Osaka University, Osaka, Japan; [8]Department of Otorhinolaryngology–Head and Neck Surgery, Graduate School of Medicine, Osaka University, Osaka, Japan; and [9]Department of Nuclear Medicine, University Hospital Duesseldorf, Heinrich Heine University, Duesseldorf, Germany*

The $^{18}$F-labeled fibroblast activation protein inhibitor (FAPI) [$^{18}$F]FAPI-74 has the benefit of a higher synthetic yield and better image resolution than $^{68}$Ga-labeled FAPI. We preliminarily evaluated the diagnostic performance of [$^{18}$F]FAPI-74 PET in patients with various histopathologically confirmed cancers or suspected malignancies. **Methods:** We enrolled 31 patients (17 men and 14 women) with lung cancer ($n$ = 7), breast cancer ($n$ = 5), gastric cancer ($n$ = 5), pancreatic cancer ($n$ = 3), other cancers ($n$ = 5), and benign tumors ($n$ = 6). Twenty-seven of the 31 patients were treatment-naïve or preoperative, whereas recurrence was suspected in the remaining 4 patients. Histopathologic confirmation was obtained for the primary lesions of 29 of the 31 patients. In the remaining 2 patients, the final diagnosis was based on the clinical course. [$^{18}$F]FAPI-74 PET scanning was performed 60 min after the intravenous injection of [$^{18}$F]FAPI-74 (240 ± 31 MBq). The [$^{18}$F]FAPI-74 PET images were compared between the primary or local recurrent lesions of malignant tumors ($n$ = 21) and nonmalignant lesions ($n$ = 8: type-B1 thymomas, granuloma, solitary fibrous tumor, and postoperative or posttherapeutic changes). The uptake and number of detected lesions on [$^{18}$F]FAPI-74 PET were also compared with those on [$^{18}$F]FDG PET for available patients ($n$ = 19). **Results:** [$^{18}$F]FAPI-74 PET showed higher uptake in primary lesions of various cancers than in nonmalignant lesions (median $SUV_{max}$, 9.39 [range, 1.83–25.28] vs. 3.49 [range, 2.21–15.58]; $P$ = 0.053), but some of the nonmalignant lesions showed high uptake. [$^{18}$F]FAPI-74 PET also showed significantly higher uptake than [$^{18}$F]FDG PET (median $SUV_{max}$, 9.44 [range, 2.50–25.28] vs. 5.45 [range, 1.22–15.06] in primary lesions [$P$ = 0.010], 8.86 [range, 3.51–23.33] vs. 3.84 [range, 1.01–9.75] in lymph node metastases [$P$ = 0.002], and 6.39 [range, 0.55–12.78] vs. 1.88 [range, 0.73–8.35] in other metastases [$P$ = 0.046], respectively). In 6 patients, [$^{18}$F]FAPI-74 PET detected more metastatic lesions than [$^{18}$F]FDG PET. **Conclusion:** [$^{18}$F]FAPI-74 PET showed higher uptake and detection rates in primary and metastatic lesions than did [$^{18}$F]FDG PET. [$^{18}$F]FAPI-74 PET is a promising novel diagnostic modality for various tumors, especially for precise staging before treatment, including characterization of tumor lesions before surgery. Moreover, $^{18}$F-labeled FAPI ligand might serve a higher demand in clinical care in the future.

**Key Words:** fibroblast activation protein; [$^{18}$F]FAPI-74; cancer-associated fibroblast; PET; oncology

**J Nucl Med 2023; 64:1225–1231**
DOI: 10.2967/jnumed.123.265486

Cancer-associated fibroblasts are major components of the cancer stroma and play an important role in cancer invasion and metastasis in the tumor microenvironment (*1*). Cancer-associated fibroblasts interact with cancer cells by secreting numerous chemokines and cytokines, such as transforming growth factor β, inducing immunosuppression in the tumor microenvironment (*1*). Cancer-associated fibroblasts express fibroblast activation protein (FAP), and the expression levels of FAP have been reported to correlate with the prognosis in patients with cancer (*1*). In addition, FAP expression has been confirmed in various cancer types, with minimal expression observed in normal organs (*2,3*). The FAP inhibitor (FAPI) has gained attention as an excellent PET probe that can accurately detect many types of cancer compared with the conventional glucose analog [$^{18}$F]FDG. $^{68}$Ga-labeled FAPI ([$^{68}$Ga]FAPI-04 or [$^{68}$Ga]FAPI-46) and $^{18}$F-labeled FAPI ([$^{18}$F]FAPI-74) are most commonly available for clinical use (*4–6*). Recently, the number of published papers reporting the excellent performance of FAPI PET has increased, and clinical trials are being conducted (NCT05262855 and NCT05641896). FAPI PET is expected to be used increasingly in cancer diagnosis and treatment planning for optimized patient management.

However, the short half-life of $^{68}$Ga (68 min) can cause problems in production and delivery. It requires onsite production by a $^{68}$Ga generator or cyclotron production using a solid target of $^{68}$Zn. It also has a limitation in that one production cycle of $^{68}$Ga allows the acquisition of only 2–3 patient scans because of the relatively low yield and short half-life. Labeling with $^{18}$F (half-life, 110 min), such as [$^{18}$F]FDG, will enable more practical large-scale production. For prostate-specific membrane antigen PET, [$^{68}$Ga]PSMA-11 is being replaced by $^{18}$F-labeled prostate-specific membrane antigen

Received Jan. 22, 2023; revision accepted Mar. 14, 2023.
For correspondence or reprints, contact Tadashi Watabe (watabe.tadashi.med@osaka-u.ac.jp).
Published online Jun. 2, 2023.

probes, such as [$^{18}$F]DCFPyL, because of the increasing cost of $^{68}$Ga generators. Thus, $^{18}$F-labeled FAPI ligands, such as [$^{18}$F]FAPI-74, may be the best option for widespread use in the global market with the added benefit of a higher synthetic yield and delivery from centralized large-scale production (*5*).

In this study, we preliminarily evaluated the diagnostic performance of [$^{18}$F]FAPI-74 PET in patients with various histopathologically confirmed cancers or suspected malignancies.

## MATERIALS AND METHODS

### Patients

We enrolled 31 patients (age range, 38–83 y; 17 men and 14 women) in this prospective study. The inclusion criteria were as follows: patients who had been diagnosed with a malignant tumor or suspected malignancy before treatment and had undergone CT or [$^{18}$F]FDG PET, patients who had been diagnosed with a malignant tumor and had undergone or were to undergo chemotherapy or radiotherapy, and patients with suspected recurrence based on the clinical findings or other diagnostic imaging, such as CT or [$^{18}$F]FDG PET, after treatment. The patient characteristics are summarized in Table 1. The study included patients with lung cancer ($n = 7$), breast cancer ($n = 5$), gastric cancer ($n = 5$), pancreatic cancer ($n = 3$), other cancers ($n = 5$), and benign tumors ($n = 6$). Twenty-seven of the 31 patients were treatment-naïve or preoperative, whereas recurrence was suspected in the remaining 4 patients. Patients who were pregnant or suspected to be pregnant, pediatric patients who required sedation, and patients considered unsuitable for participation in the study were excluded. Histopathologic confirmation was obtained for the primary lesions of 29 of the 31 patients (94%) and for the metastatic lesions of 10 patients who underwent surgical resection. In 2 patients (2/31), the final diagnosis was based on the clinical course, including the results of follow-up imaging. Postoperative fibrosis was suspected in 1 patient because no remarkable changes were observed on the follow-up MRI. In another case, the patient had been followed up for more than 10 y after surgery for breast cancer. Multiple metastases in the lymph nodes (LNs), liver, and bone were detected on CT and [$^{18}$F]FDG PET in this patient. Among the patients with LN metastasis ($n = 12$), the histopathology of the LN was confirmed via surgical resection or biopsy in 6 patients and was based on comprehensive interpretation by a nuclear medicine specialist who reported a high possibility of metastasis in the other 6 patients.

The study protocol was approved by the Institutional Review Board of the Osaka University Hospital (approval 21472-4), and the study was performed in accordance with the ethical standards laid down in the 1964 Declaration of Helsinki. Written informed consent was obtained from all patients before their inclusion in the study.

### Synthesis of [$^{18}$F]FAPI-74 and [$^{18}$F]FDG

[$^{18}$F]FAPI-74 solution was synthesized using CFN-MPS200 (Sumitomo Heavy Industries), according to a previous study (*6*). [$^{18}$F]fluoride eluted with 0.5 M sodium acetate buffer and precursor solution (a mixture of dimethyl sulfoxide, 10 mM aluminum chloride, 20% w/v ascorbic acid, and 4 mM FAPI-74 precursor) was mixed and fluorinated for 5 min at room temperature, followed by 15 min at 95°C. [$^{18}$F]FAPI-74 was purified from the reaction solution using an hydrophilic–lipophilic balance cartridge and ethanol. Finally, the [$^{18}$F]FAPI-74 solution was obtained by diluting with 10 mM phosphate-buffered saline (pH 6.7) containing 100 mg of sodium ascorbate and filtering through a sterile 0.22-μm Millex GV filter. The radioactivity of the [$^{18}$F]FAPI-74 solution was 10,201 ± 593 MBq at the end of synthesis by the irradiation condition at 25 μA for 30–35 min. The radiochemical purity was 97.3% ± 0.3%.

The [$^{18}$F]FDG solution was synthesized using the F200 synthesizer (Sumitomo Heavy Industries). After eluting [$^{18}$F]fluoride with Kryptofix 222 (Merck KGaA) and potassium carbonate solution and drying completely, we fluorinated [$^{18}$F]FDG with mannose triflate and then deprotected with 0.3 M NaOH. [$^{18}$F]FDG was subsequently purified using solid-phase extraction cartridges (IC-H, PS-2, and Alumina N) and passed through a sterile 0.22-μm vented Millex GS filter. The radiochemical purity of [$^{18}$F]FDG was more than 95%.

### PET/CT Scanning

PET/CT scanning was performed 60 min after the intravenous injection of [$^{18}$F]FAPI-74 (240 ± 31 MBq). The patients were monitored for adverse events from the time of administration to the end of the PET scan. PET/CT images were acquired using a Biograph Vision 600 (Siemens Healthineers) in continuous bed motion (matrix, 440 × 440; pixel size, 1.65 mm) at 3.5 mm/s for 4 frames. The PET images were reconstructed to a slice thickness of 3 mm with an increment of 3 mm using ordered-subset expectation maximization with 3 iterations per 5 subsets and was gauss-filtered to a transaxial resolution of 3 mm in full width at half maximum. Attenuation was corrected using unenhanced low-dose CT data (effective dose, 50 mAs). The CT scans were reconstructed to a slice thickness of 3 mm in increments of 3 mm. [$^{18}$F]FDG PET scanning was performed 60 min after the intravenous injection of [$^{18}$F]FDG (3.7 MBq/kg) according to the institutional protocol.

**TABLE 1**
Patient Characteristics

| Characteristic | Data |
|---|---|
| Number of patients | 31 |
| Sex | |
| Male | 17 |
| Female | 14 |
| Age range (y) | 38–83 (median, 68) |
| Diagnosis | Lung cancer (adenocarcinoma [$n = 6$] and squamous cell carcinoma [$n = 1$]), breast cancer (invasive ductal carcinoma [$n = 5$]), gastric cancer ($n = 5$), pancreatic cancer (adenocarcinoma [$n = 3$]), oropharyngeal cancer ($n = 1$), thyroid cancer (papillary carcinoma [$n = 1$]), thymic cancer and thymoma (type B3) ($n = 3$), and benign tumors ($n = 6$) |
| Patient status | Before treatment or surgery ($n = 27$, including after chemotherapy [$n = 5$] or after chemoradiation therapy [$n = 1$]); suspected recurrence ($n = 4$) |
| Histologic findings of benign tumors | Thymoma (type B1 [$n = 2$]), granuloma ($n = 1$), solitary fibrous tumor ($n = 1$), and postoperative changes ($n = 2$) |

### Image Analysis

SUV measurements were performed via volume-of-interest analysis of the [$^{18}$F]FAPI-74 PET images using Syngovia software (Siemens Healthineers). $SUV_{max}$ and the tumor–to–normal background (T/N) ratio were compared between the primary or local recurrent lesions of malignant tumors ($n$ = 21) and nonmalignant lesions ($n$ = 8). Volumes of interest of normal background were placed on the normal areas surrounding each tumor lesion where physiologic accumulation did not overlap. We defined nonmalignant lesions as postoperative/therapeutic changes and benign/low-malignancy tumors, such as thymoma (type B1), granuloma, and solitary fibrous tumor (intermediate lesion with low malignancy potential). The $SUV_{max}$ of the primary lesions, LN metastases, and other metastases, as well as the number of detected metastatic lesions on [$^{18}$F]FAPI-74 PET, were compared with those of [$^{18}$F]FDG PET (within 8 wk) for available cases of malignant tumors ($n$ = 19). The median interval between [$^{18}$F]FAPI-74 PET and [$^{18}$F]FDG PET was 18 d (range, 6 − 56 d). [$^{18}$F]FDG PET images obtained using different PET scanners ($n$ = 12) were also included.

### Statistical Analyses

Comparisons between the 2 groups were performed using the Wilcoxon signed-rank test for paired data or Mann–Whitney $U$ test for unpaired data by SPSS (version 25.0; IBM Corp.). The differences were considered statistically significant at a $P$ value of less than 0.05.

## RESULTS

All patients were monitored for adverse or serious adverse events due to the [$^{18}$F]FAPI-74 injection. The symptoms were monitored after injection until the end of the PET scan, and no adverse events occurred due to its administration. No clinically significant changes were observed in heart rate, oxygen saturation, or body temperature before or after administration of the [$^{18}$F]FAPI-74 solution (Supplemental Table 1; supplemental materials are available at http://jnm.snmjournals.org).

In the comparison between malignant tumors and nonmalignant lesions, [$^{18}$F]FAPI-74 PET showed higher uptake in primary lesions of various cancers (median $SUV_{max}$, 9.39 [range, 1.83–25.28]; median T/N ratio, 9.36 [range, 1.87–35.61]) than that in nonmalignant lesions (median $SUV_{max}$, 3.49 [range, 2.21–15.58]; T/N ratio, 4.27 [range, 1.67–10.74]) ($P$ = 0.053 and $P$ = 0.008, respectively) (Figs. 1A and B). However, some of the benign tumors and treatment-related changes showed high uptake on [$^{18}$F]FAPI-74 PET, such as granuloma, postoperative changes, and radiation pneumonitis (Supplemental Table 2). Compared with [$^{18}$F]FDG PET, [$^{18}$F]FAPI-74 PET also showed significantly higher uptake in the primary lesions (median $SUV_{max}$, 9.44 [range, 2.50–25.28]

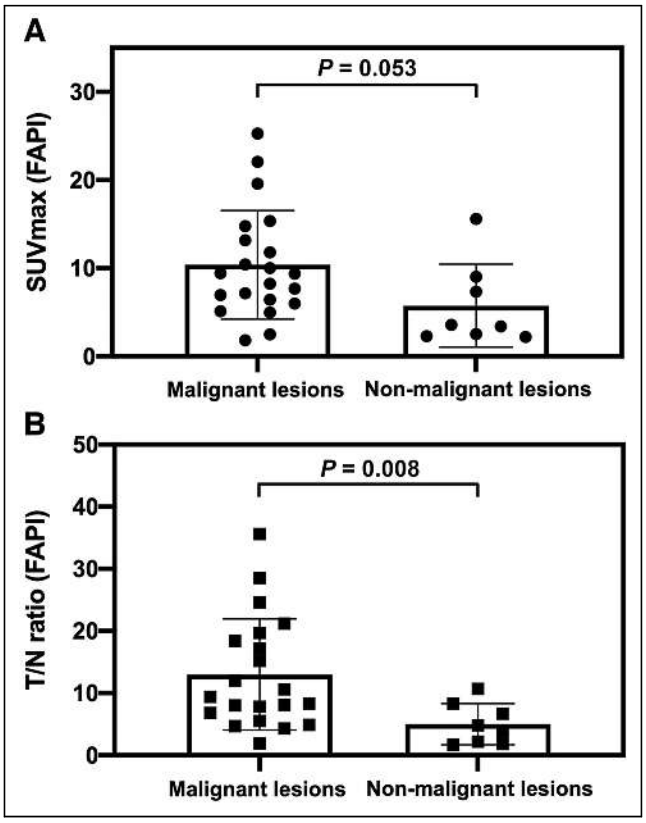


**FIGURE 1.** Comparison of uptake on [$^{18}$F]FAPI-74 PET between malignant tumors and nonmalignant lesions: $SUV_{max}$ (A) and T/N ratio (B) (with $P$ value by Mann–Whitney $U$ test).

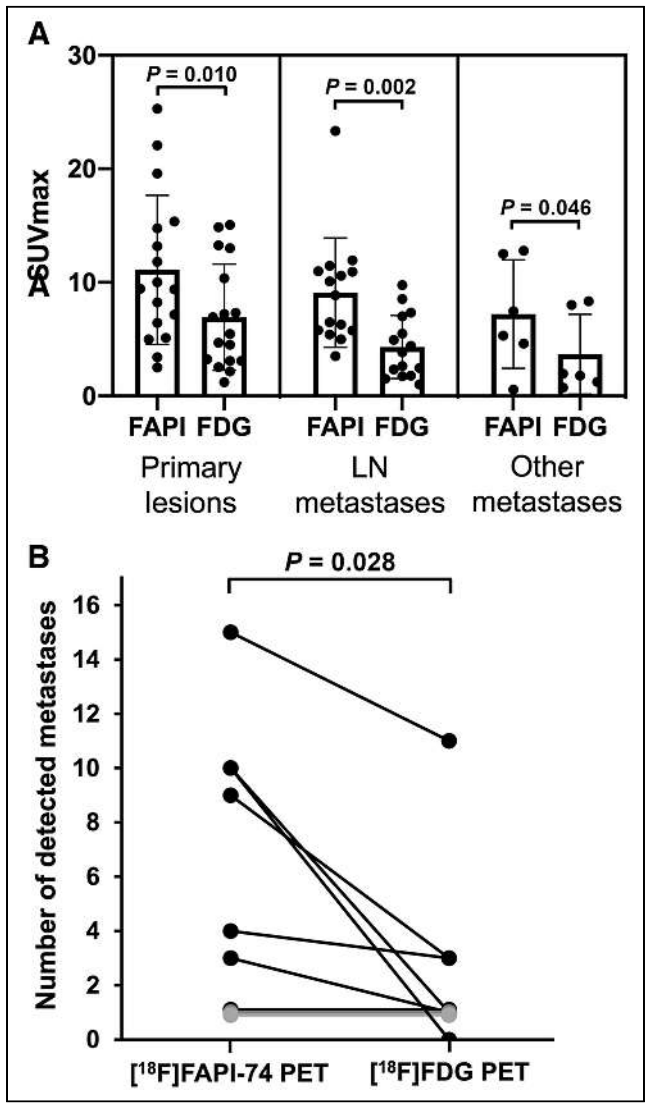


**FIGURE 2.** Comparison of uptake between [$^{18}$F]FAPI-74 PET and [$^{18}$F]FDG PET: $SUV_{max}$ in primary lesions, LN metastases, and other metastases (A) and number of detected metastatic lesions on [$^{18}$F]FAPI-74 PET compared with [$^{18}$F]FDG PET (B) (with $P$ value by Wilcoxon signed-rank test).

**TABLE 2**
Head-to-Head Comparison of $SUV_{max}$ Between [$^{18}$F]FAPI-74 PET and [$^{18}$F]FDG PET

| | | [$^{18}$F]FAPI-74 PET | | | | | [$^{18}$F]FDG PET | | | | |
|---|---|---|---|---|---|---|---|---|---|---|---|
| Cancer type | State | Primary lesion | LN metastasis (1) | LN metastasis (2) | Other metastases | Location | Primary lesion | LN metastasis (1) | LN metastasis (2) | Other metastases | Location |
| Breast cancer | Before surgery | 25.3 | 10.1 | | | | 6.9 | 2.6 | | | |
| Breast cancer | Before treatment | 22.1 | 6.3 | 5.8* | | | 7.3 | 1.7 | ND (1.0) | | |
| Breast cancer (case shown in Fig. 4) | Before treatment | 19.6 | 23.3 | 11.9* | | | 13.0 | 8.5 | 7.4 | | |
| Breast cancer | Recurrence | | 11.0 | 10.9* | 12.8, 12.5 | Liver | | 3.8 | 2.5 | 8.0, 8.4 | Liver |
| Esophageal cancer | Before treatment | 10.0 | | | | | 7.2 | | | | |
| Gastric cancer | Before treatment | 5.0 | | | | | 2.2 | | | | |
| Gastric cancer | After NAC | 8.2 | | | | | 5.5 | | | | |
| Gastric cancer | After NAC | ND | 5.8 | | | | ND | 9.8 | | | |
| Gastric cancer | After NAC | 3.4 | | | | | 3.1 | | | | |
| Gastric cancer | After NAC | 7.2 | | | | | 10.4 | | | | |
| Lung cancer | Before surgery | 15.4 | | | | | 13.3 | | | | |
| Lung cancer | Before surgery | 6.4 | | | | | 4.7 | | | | |
| Lung cancer | Before surgery | 5.1 | | | | | 2.5 | | | | |
| Lung cancer (case shown in Fig. 5) | Before surgery | 2.5 | | | | | 1.2 | | | | |
| Lung cancer | Before surgery | 11.8 | 3.5 | | | | 14.9 | 4.9 | | | |
| Head and neck | Before treatment | 14.8 | 11.5 | 8.9* | | | 15.1 | 7 | 4.4 | | |
| Pancreatic cancer | Before treatment | 13.2 | | | | | 3.1 | | | | |
| Pancreatic cancer (case shown in Fig. 3) | Before treatment | 9.4 | 5.4 | 6.5* | 7.5, 5.3 | Peritoneum | 3.2 | ND (2.3) | ND (1.5) | ND (2.0, 1.8) | Peritoneum |
| Pancreatic cancer | Recurrence | 9.4 | 10.6 | 5.0* | 4.6 | Peritoneum | 4.5 | 5.5 | 1.8 | ND (1.2) | Peritoneum |
| Thymoma (type B3) | Recurrence | | | | ND (0.6) | Pleura | | | | ND (0.7) | Pleura |

*Number of detected LN metastases is more than 3, and 2 major sites are shown here.
ND = not detected; NAC = neoadjuvant chemotherapy.

vs. 5.45 [range, 1.22–15.06]; $P = 0.010$), LN metastases (median $SUV_{max}$, 8.86 [range, 3.51–23.33] vs. 3.84 [range, 1.01–9.75]; $P = 0.002$), and other metastases (median $SUV_{max}$, 6.39 [range, 0.55–12.78] vs. 1.88 [range, 0.73–8.35]; $P = 0.046$) (Fig. 2A; Table 2). The number of metastatic lesions detected on [$^{18}$F]FAPI-74 PET was significantly higher than that on [$^{18}$F]FDG PET (Fig. 2B). In 6 patients, [$^{18}$F]FAPI-74 PET detected more metastatic lesions than [$^{18}$F]FDG PET, especially LN and peritoneal metastases in pancreatic cancer and LN metastases in breast cancer (Figs. 3 and 4). [$^{18}$F]FAPI-74 PET showed clearer uptake in patients with lung adenocarcinoma ($n = 2$), even when [$^{18}$F]FDG PET showed only faint uptake (Fig. 5).

## DISCUSSION

In this study, we evaluated patients with various histopathologically confirmed cancers and benign lesions using [$^{18}$F]FAPI-74 PET as an initial evaluation for a prospective clinical trial. [$^{18}$F]FAPI-74 PET showed higher uptake in cancerous lesions than in nonmalignant lesions. [$^{18}$F]FAPI-74 PET also showed significantly higher uptake in primary and metastatic lesions than did [$^{18}$F]FDG PET. Reporting the superiority of [$^{18}$F]FAPI-74 PET as an initial evaluation would aid the research community since the number of reports on [$^{18}$F]FAPI-74 remains very limited.

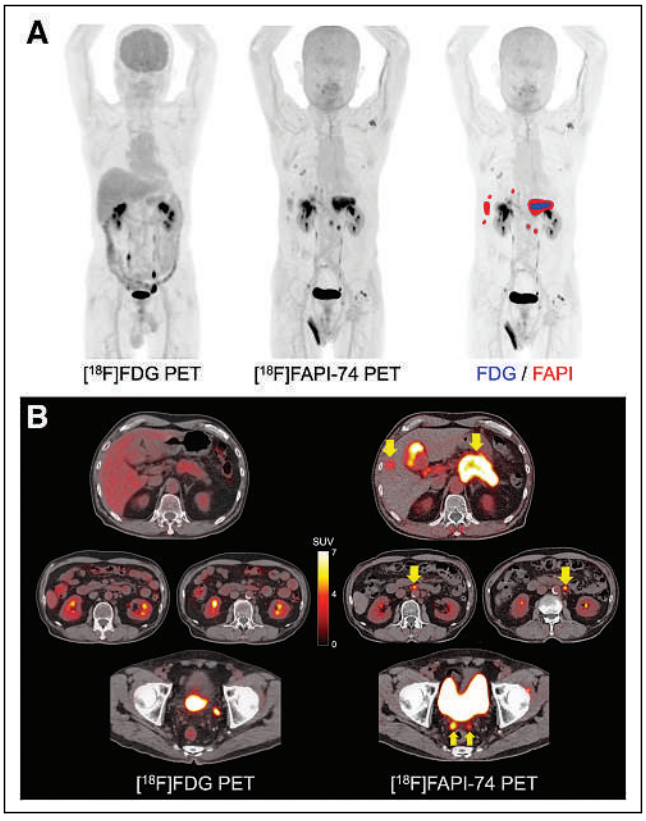


**FIGURE 3.** A 68-y-old man with multiple LN and peritoneal metastases of pancreatic cancer. (A) Comparison of maximum-intensity projection images: image on right shows fusion with positive lesions on [$^{18}$F]FAPI-74 PET (red area) and [$^{18}$F]FDG PET (blue area). (B) PET/CT images on [$^{18}$F]FAPI-74 PET and [$^{18}$F]FDG PET (arrows indicate metastatic lesions). [$^{18}$F]FAPI-74 PET detected more metastatic lesions than [$^{18}$F]FDG PET ($SUV_{max}$ of primary lesion is 9.4 and 3.2, respectively). Brain uptake is decreased on [$^{18}$F]FDG PET because of high blood glucose level (277 mg/dL).

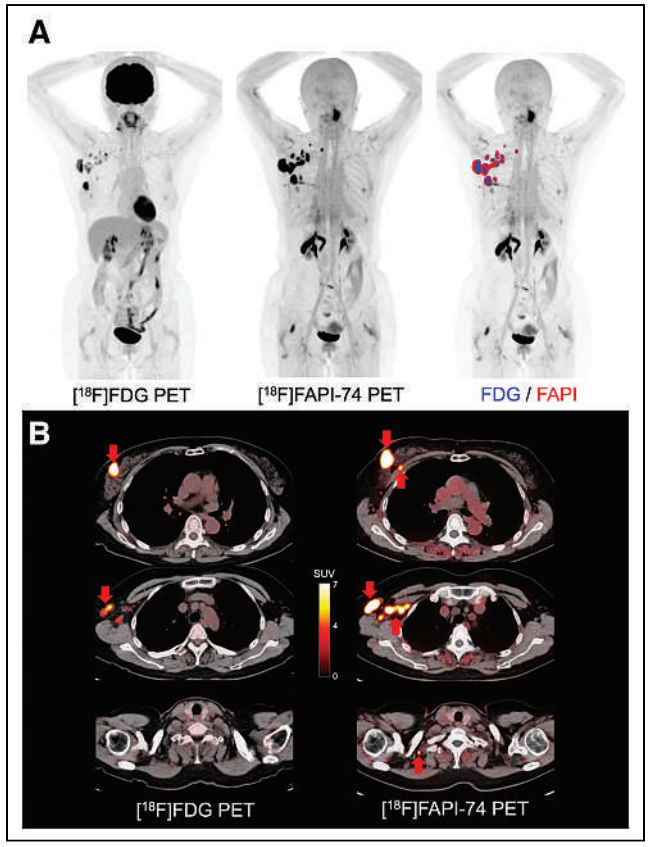


**FIGURE 4.** A 59-y-old woman with multiple LN metastases of breast cancer. (A) Comparison of maximum-intensity projection images: image on right shows fusion with positive lesions on [$^{18}$F]FAPI-74 PET (red area) and [$^{18}$F]FDG PET (blue area), (B) PET/CT images on [$^{18}$F]FAPI-74 PET and [$^{18}$F]FDG PET (arrows indicate metastatic lesions). [$^{18}$F]FAPI-74 PET detected more metastatic lesions than [$^{18}$F]FDG PET ($SUV_{max}$ of primary lesion is 19.6 and 13.0, respectively).

Previous studies reported higher uptake of FAPI PET than of [$^{18}$F]FDG in many types of cancers, including gastric, pancreatic, ovarian, and head and neck (*7–10*). It has been reported that

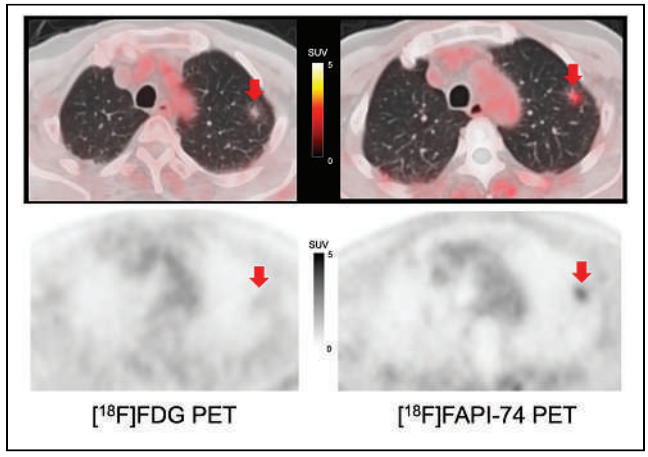


**FIGURE 5.** Comparison of PET/CT images on [$^{18}$F]FAPI-74 PET and [$^{18}$F]FDG PET of 80-y-old man with lung adenocarcinoma with ground-glass opacity (arrows indicate primary lesions). [$^{18}$F]FAPI-74 PET showed clearer uptake than [$^{18}$F]FDG PET ($SUV_{max}$ of primary lesion is 2.5 and 1.2, respectively).

FAPI PET detected a higher number of metastatic lesions than [$^{18}$F]FDG PET did in patients with various types of cancers presenting with inconclusive [$^{18}$F]FDG PET findings (*7*). The number of positive lesions was significantly higher in patients with gastric, lung, liver, and nasopharyngeal cancers. FAPI PET showed excellent sensitivity for peritoneal carcinomatosis of gastric, pancreatic, and ovarian cancers (*8–10*). We also observed peritoneal carcinomatosis in patients with pancreatic cancer, which could not be detected on [$^{18}$F]FDG PET (Fig. 3). FAPI PET, including [$^{18}$F]FAPI-74 PET, will contribute to accurate clinical staging and lead to proper patient management.

Two studies compared the uptake between FAPI PET and [$^{18}$F]FDG PET in patients with histopathologically confirmed non–small cell lung cancer (*11,12*). Both studies reported that there was no statistically significant difference in the primary lesions in terms of $SUV_{max}$, T/N ratio, or lesion detection. However, FAPI PET was significantly superior to [$^{18}$F]FDG PET in the detection of LN, pleural, and bone metastases. In our cohort, we enrolled mainly preoperative patients without metastatic lesions. Although primary lesion detectability was similar in larger tumors, consistent with previous reports, [$^{18}$F]FAPI-74 PET showed higher uptake in the ground-glass opacity lesions than did [$^{18}$F]FDG PET, as shown in Figure 5.

FAPI PET is reported to be superior to [$^{18}$F]FDG PET in detecting primary tumors, with high sensitivity in patients with breast cancer, as well as in detecting LN, hepatic, bone, and cerebral metastases because of its lower background activity (*13–16*). In our cohort, [$^{18}$F]FAPI-74 PET showed a higher uptake than [$^{18}$F]FDG, as shown in Figure 4. Additional LN metastasis was detected on [$^{18}$F]FAPI-74 PET with histologic confirmation, which was not detected on [$^{18}$F]FDG PET.

FAPI PET images must be interpreted carefully in terms of specificity. There are several pitfalls of noncancer uptake in benign lesions. A previous study reported that benign uptake occurs in bone degeneration, wound healing, the endometrium, and inflammation, including pancreatitis and pneumonia (*17,18*). Benign tumors sometimes show high FAPI uptake in renal angiomyolipomas, thyroid adenomas, necrotizing granulomas, and splenic hemangioma (*18*). Therefore, it is necessary to carefully interpret the possibility of benign or inflammatory uptake on [$^{18}$F]FAPI-74 PET.

In this study, we observed a high uptake in postoperative changes or scars, granulomas, and radiation pneumonitis. One case study reported that FAPI PET showed high uptake in tuberculous granuloma (*19*). Although there have been no systematic reports of FAP expression in granulomas, granulomatous lesions may show high FAP expression. Regarding radiation pneumonitis, Qin et al. reported increased FAP expression and FAPI uptake in a rat model of radiation-induced lung damage (*20*). Further, Röhrich et al. reported increased uptake in fibrotic lung disease (*21*). In our study, there were no residual tumors among the high-uptake lesions on FAPI PET in a patient with lung cancer after chemoradiation therapy. It has been suggested that FAP expression is associated with radiation-induced fibrotic changes. Therefore, caution is required when using [$^{18}$F]FAPI-74 PET to assess the therapeutic efficacy in lung cancer after radiation therapy.

Compared with [$^{68}$Ga]-labeled FAPI PET probes, [$^{18}$F]FAPI-74 might have the advantage of the shorter positron range of $^{18}$F (mean range in water, 0.6 mm) than of $^{68}$Ga (3.5 mm), thereby yielding a better image resolution, especially in small lesions (*22*). However, hepatobiliary excretion might affect the detectability of biliary tract cancer on [$^{18}$F]FAPI-74 PET.

This study had some limitations. First, the number of patients was small, which should be finalized in the final report with a certain number of patients for each cancer type. Second, we performed [$^{18}$F]FAPI-74 PET after [$^{18}$F]FDG PET with a median interval of 18 d, and some [$^{18}$F]FDG PET images were acquired using different PET scanners; thus, there may have been some resulting bias in the comparison. Third, we did not perform a comparison between immunohistochemical staining and FAP. Such a comparison should be included in future studies to confirm the specific uptake of [$^{18}$F]FAPI-74 on PET and elucidate the FAP pathology in cancer-associated fibroblasts in greater detail.

## CONCLUSION

[$^{18}$F]FAPI-74 PET showed higher uptake and detection rates in primary and metastatic lesions than did [$^{18}$F]FDG PET. [$^{18}$F]FAPI-74 PET is a promising novel diagnostic modality for various tumors, especially for precise staging before treatment, including characterization of tumor lesions before surgery. Moreover, $^{18}$F-labeled FAPI ligand might serve a higher demand in clinical care in the future.

## DISCLOSURE

This study was funded by the QiSS program of OPERA (grant JPMJOP1721) from the Japan Science and Technology Agency. Frederik Giesel is an advisor at ABX, Telix, SOFIE Biosciences, and α-Fusion and has shares in a consultancy group for iTheranostics. No other potential conflict of interest relevant to this article was reported.

## ACKNOWLEDGMENTS

We thank the doctors of the Departments of Thoracic Surgery, Breast and Endocrine Surgery, Gastroenterological Surgery, and Otorhinolaryngology–Head and Neck Surgery for introducing patients, and we thank the technologists Hidetaka Sasaki and Kosei Ichinose for their excellent technical assistance. The precursor of FAPI was provided by SOFIE Biosciences, which holds a license to the FAPI family of compounds for diagnostic use.

**KEY POINTS**

**QUESTION:** Does [$^{18}$F]FAPI-74 PET have higher uptake and detection rates in primary and metastatic lesions than [$^{18}$F]FDG PET?

**PERTINENT FINDINGS:** [$^{18}$F]FAPI-74 PET showed significantly higher uptake in primary and metastatic lesions of various histopathologically confirmed cancers than did [$^{18}$F]FDG PET.

**IMPLICATIONS FOR PATIENT CARE:** The $^{18}$F-labeled FAPI ligand [$^{18}$F]FAPI-74 PET is a promising novel diagnostic probe for various tumors that can serve a future higher demand with large-scale production.

## REFERENCES

1. Kobayashi H, Enomoto A, Woods SL, Burt AD, Takahashi M, Worthley DL. Cancer-associated fibroblasts in gastrointestinal cancer. *Nat Rev Gastroenterol Hepatol.* 2019;16:282–295.
2. Giesel FL, Kratochwil C, Lindner T, et al. $^{68}$Ga-FAPI PET/CT: biodistribution and preliminary dosimetry estimate of 2 DOTA-containing FAP-targeting agents in patients with various cancers. *J Nucl Med.* 2019;60:386–392.
3. Kratochwil C, Flechsig P, Lindner T, et al. $^{68}$Ga-FAPI PET/CT: tracer uptake in 28 different kinds of cancer. *J Nucl Med.* 2019;60:801–805.

4. Loktev A, Lindner T, Burger EM, et al. Development of fibroblast activation protein-targeted radiotracers with improved tumor retention. *J Nucl Med.* 2019;60:1421–1429.
5. Giesel FL, Adeberg S, Syed M, et al. FAPI-74 PET/CT using either $^{18}$F-AlF or cold-kit $^{68}$Ga labeling: biodistribution, radiation dosimetry, and tumor delineation in lung cancer patients. *J Nucl Med.* 2021;62:201–207.
6. Naka S, Watabe T, Lindner T, et al. One-pot and one-step automated radiosynthesis of [$^{18}$F]AlF-FAPI-74 using a multi purpose synthesizer: a proof-of-concept experiment. *EJNMMI Radiopharm Chem.* 2021;6:28.
7. Chen H, Zhao L, Ruan D, et al. Usefulness of [$^{68}$Ga]Ga-DOTA-FAPI-04 PET/CT in patients presenting with inconclusive [$^{18}$F]FDG PET/CT findings. *Eur J Nucl Med Mol Imaging.* 2021;48:73–86.
8. Zhao L, Pang Y, Luo Z, et al. Role of [$^{68}$Ga]Ga-DOTA-FAPI-04 PET/CT in the evaluation of peritoneal carcinomatosis and comparison with [$^{18}$F]-FDG PET/CT. *Eur J Nucl Med Mol Imaging.* 2021;48:1944–1955.
9. Pang Y, Zhao L, Luo Z, et al. Comparison of $^{68}$Ga-FAPI and $^{18}$F-FDG uptake in gastric, duodenal, and colorectal cancers. *Radiology.* 2021;298:393–402.
10. Chen H, Pang Y, Li J, et al. Comparison of [$^{68}$Ga]Ga-FAPI and [$^{18}$F]FDG uptake in patients with gastric signet-ring-cell carcinoma: a multicenter retrospective study. *Eur Radiol.* 2023;33:1329–1341.
11. Wu J, Deng H, Zhong H, et al. Comparison of $^{68}$Ga-FAPI and $^{18}$F-FDG PET/CT in the evaluation of patients with newly diagnosed non-small cell lung cancer. *Front Oncol.* 2022;12:924223.
12. Can C, Kepenek F, Kömek H, et al. Comparison of $^{18}$F-FDG PET/CT and $^{68}$Ga-FAPI-04 PET/CT in patients with non-small cell lung cancer. *Nucl Med Commun.* 2022;43:1084–1091.
13. Kömek H, Can C, Güzel Y, et al. $^{68}$Ga-FAPI-04 PET/CT, a new step in breast cancer imaging: a comparative pilot study with the $^{18}$F-FDG PET/CT. *Ann Nucl Med.* 2021;35:744–752.
14. Eshet Y, Tau N, Apter S, et al. The role of $^{68}$Ga-FAPI PET/CT in detection of metastatic lobular breast cancer. *Clin Nucl Med.* 2023;48:228–232.
15. Dendl K, Koerber SA, Finck R, et al. $^{68}$Ga-FAPI-PET/CT in patients with various gynecological malignancies. *Eur J Nucl Med Mol Imaging.* 2021;48:4089–4100.
16. Backhaus P, Burg MC, Roll W, et al. Simultaneous FAPI PET/MRI targeting the fibroblast-activation protein for breast cancer. *Radiology.* 2022;302:39–47.
17. Kessler L, Ferdinandus J, Hirmas N, et al. Pitfalls and common findings in $^{68}$Ga-FAPI PET: a pictorial analysis. *J Nucl Med.* 2022;63:890–896.
18. Hotta M, Rieger AC, Jafarvand MG, et al. Non-oncologic incidental uptake on FAPI PET/CT imaging. *Br J Radiol.* 2023;96:20220463.
19. Liu W, Gong W, Yang X, Xu T, Chen Y. Increased FAPI activity in pulmonary tuberculosis. *Clin Nucl Med.* 2023;48:188–189.
20. Qin X, Wang S, Liu X, et al. Diagnostic value of $^{18}$F-NOTA-FAPI PET/CT in a rat model of radiation-induced lung damage. *Front Oncol.* 2022;12:879281.
21. Röhrich M, Leitz D, Glatting FM, et al. Fibroblast activation protein-specific PET/CT imaging in fibrotic interstitial lung diseases and lung cancer: a translational exploratory study. *J Nucl Med.* 2022;63:127–133.
22. Braune A, Oehme L, Freudenberg R, et al. Comparison of image quality and spatial resolution between $^{18}$F, $^{68}$Ga, and $^{64}$Cu phantom measurements using a digital Biograph Vision PET/CT. *EJNMMI Phys.* 2022;9:58.

# Tumor Characterization by [$^{68}$Ga]FAPI-46 PET/CT Can Improve Treatment Selection for Pancreatic Cancer Patients: An Interim Analysis of a Prospective Clinical Trial

Pawel Rasinski[1,2], Siri af Burén[1,2], Maria Holstensson[1,2], Ted Nilsson[2], Louiza Loizou[1,3], Thuy A. Tran[4,5], Ernesto Sparrelid[1,6], J. Matthias Löhr[1,6], and Rimma Axelsson[2,7]

[1]*Department of Clinical Science, Intervention, and Technology, Karolinska Institutet, Stockholm, Sweden;* [2]*Department of Medical Radiation Physics and Nuclear Medicine, Karolinska University Hospital, Huddinge, Sweden;* [3]*Department of Radiology, Karolinska University Hospital, Huddinge, Sweden;* [4]*Department of Oncology–Pathology, Karolinska Institutet, Stockholm, Sweden;* [5]*Department of Radiopharmacy, Karolinska University Hospital, Stockholm, Sweden;* [6]*Department of Upper Gastrointestinal Diseases, Karolinska University Hospital, Huddinge, Sweden; and* [7]*Department of Molecular Medicine and Surgery, Karolinska Institutet, Stockholm, Sweden*

Correct and timely diagnosis of pancreatic cancer (PC) is essential for treatment selection but is still clinically challenging. Standard-of-care imaging methods can sometimes not differentiate malignancies from inflammatory lesions or detect malignant transformation in premalignant lesions. This interim analysis of a prospective clinical trial aimed to evaluate the diagnostic accuracy of [$^{68}$Ga]fibroblast activation protein inhibitor (FAPI)-46 PET/CT for PC and determine the sample size needed to demonstrate whether this imaging technique improves the characterization of equivocal lesions detected by standard-of-care imaging methods. **Methods:** [$^{68}$Ga]FAPI-46 PET/CT imaging was performed on 30 patients scheduled for surgical resection of suspected PC. Target lesions were delineated, $SUV_{max}$ and $SUV_{mean}$ were determined, and the results were compared with those of standard-of-care imaging. Receiver operating characteristics were calculated for the whole cohort and a subcohort of 11 patients with an equivocal clinical imaging work-up preoperatively. Postoperative histopathologic findings served as a reference standard, and the statistical power was determined. **Results:** Histopathologic examination revealed malignancy in 20 patients and benign lesions in 10 patients. Significantly elevated [$^{68}$Ga]FAPI-46 uptake was observed in malignant tumors compared with benign lesions ($P < 0.001$). Receiver-operating-characteristic analyses established optimal cutoffs for both SUVs for differentiation of malignant from nonmalignant pancreatic tumors. The optimal $SUV_{max}$ cutoff was 10.2 and showed 95% sensitivity and 80% specificity for the whole cohort, as well as 100% diagnostic accuracy when considering the subcohort with equivocal imaging work-up only. For sufficient statistical power, 38 equivocal observations are needed. **Conclusion:** We conclude that [$^{68}$Ga]FAPI-46 PET/CT can accurately differentiate malignant from benign pancreatic lesions deemed equivocal by standard-of-care imaging. This trial will therefore continue to recruit a total of 120 patients to reach those 38 equivocal observations needed for sufficient statistical power. On the basis of our findings, we propose that [$^{68}$Ga]FAPI-46 PET/CT not only can be clinically applied as a complement but also could become a necessary tool when standard-of-care imaging is inconclusive.

**Key Words:** fibroblast activation protein; PET/CT; pancreatic cancer; $^{68}$Ga-FAPI-46

Received Jan. 18, 2023; revision accepted Apr. 14, 2023.
For correspondence or reprints, contact Rimma Axelsson (rimma.axelsson@ki.se).
Published online Jun. 22, 2023.


**J Nucl Med 2023; 64:1232–1237**
DOI: 10.2967/jnumed.123.265481

Pancreatic cancer (PC) is a leading cause of cancer-related deaths worldwide, with a 5-y relative survival rate of 11% for all stages combined (*1*). Among the reasons for this dismal outcome is the challenge of establishing a correct and timely diagnosis (*2*). Most patients are diagnosed in advanced stages of disease (*3*), and surgical resection combined with chemotherapy is the only potentially curative therapy.

Imaging plays an essential role in several aspects of PC management, including diagnosis and evaluation of resectability. Multiphase contrast-enhanced CT (CECT) is the current preferred standard-of-care imaging modality for diagnosis of PC and is recommended as the primary imaging modality by the guidelines of both the National Comprehensive Cancer Network and the European Society for Medical Oncology (*4,5*). The differential diagnosis of a pancreatic mass, however, does encompass a range of clinical entities, including benign lesions, such as mass-forming chronic, autoimmune, or paraduodenal pancreatitis (*6*), all of which may mimic PC on CECT, making correct characterization challenging (*7*). Additionally, small isoattenuating adenocarcinomas can be overlooked on CECT (*8*). Correct preoperative diagnosis is crucial, as misinterpretation may lead to a major pancreatic resection for benign disease, failure to operate on a potentially curable lesion, or even surgery in patients with disseminated disease, in whom systemic treatment would have been more appropriate. Previous studies show that inflammation accounts for 5%–10% of surgical resection for clinically suspected cancer (*9*).

For detection of malignant transformation within pancreatic intraductal papillary mucinous neoplasia (IPMN), 3 current international guidelines recommend both CECT and MRI in the diagnostic work-up, with MRI being the preferred method (*10–12*). The accuracy of either method, or even both combined, for a specific diagnosis is, however, relatively low (61%) (*13*). Approximately 10% of all pancreatectomies performed in the United States are for IPMN (*14*). As a significant number of these operated IPMNs do not show invasive or high-grade histology, and since the morbidity

associated with resection is similar regardless of pathology, improved diagnostic accuracy is needed to aid in surgical selection. $^{68}$Ga-labeled fibroblast activation protein inhibitor (FAPI), a new tracer for PET, targets fibroblast activation protein expressed on the surface of cancer-associated fibroblasts (*15,16*). As cancer-associated fibroblasts represent the most abundant cell type in the tumor stroma (*17*), application of FAPI-based tracers in PET imaging of various types of cancers with a high stromal content, including PC, has been proven successful (*18,19*). The purpose of this interim analysis, part of a prospective clinical trial, was to evaluate the diagnostic accuracy of [$^{68}$Ga]FAPI-46 PET/CT for PC and to determine the sample size needed to demonstrate the superiority of this imaging technique in characterizing equivocal lesions detected by standard-of-care imaging methods. We tested this hypothesis by performing [$^{68}$Ga]FAPI-46 PET/CT imaging on patients with suspected PC who were scheduled for surgery, comparing the results with those of standard-of-care imaging, using postoperative histopathology as a reference standard.

## MATERIALS AND METHODS

### Clinical Study Design and Patient Cohort

The presented study was part of an ongoing phase II exploratory trial approved by the Swedish Ethical Review Authority (diarienummer 2020-03400) and Medical Products Agency (EudraCT 2020-002568-30) and registered on ClinicalTrials.gov (NCT05172310). All patients provided written informed consent. As the origin of the cancer is sometimes difficult to determine before surgery (*20*), we enrolled subjects with suspected periampullary tumors other than PC as part of the consecutive patient group. These include duodenal and ampullary cancers as well as distal cholangiocarcinoma. Patients scheduled for surgical resection of the primary tumor were screened for eligibility during multidisciplinary conferences according to the inclusion and exclusion criteria listed in Supplemental Table 1 (supplemental materials are available at http://jnm.snmjournals.org). Subjects with nonmalignant tumors on postoperative histopathology served as a comparator group. [$^{68}$Ga]FAPI-46 PET/CT imaging was performed within 2 wk before surgery. The surgery was performed at Karolinska University Hospital, with an individual treatment strategy decided for every patient at multidisciplinary conferences according to clinical routine and the Swedish National Cancer Control Program. The diagnosis for the primary tumor and resected regional lymph nodes was confirmed after surgery as per the clinical routine. Operating surgeons did not know the [$^{68}$Ga]FAPI-46 PET/CT imaging results until after surgery, preventing any impact on choice of therapy. A CECT or MRI including MR cholangiopancreatography was performed on all patients as per the clinical routine and before inclusion in this study.

### Radiopharmaceuticals and Image Acquisition

[$^{68}$Ga]FAPI-46 was radiosynthesized at the Karolinska Radiopharmacy facilities on an Eckert & Ziegler Modular-Lab PharmTracer synthesis module, using $^{68}GaCl_3$ eluate from a $^{68}$Ge/$^{68}$Ga generator, as earlier described (*21*). FAPI-46 precursor was acquired from Sofie Biosciences. The amount of radioactivity injected depended on labeling yield and patient weight (4.0 MBq/kg if possible; minimum, 50 MBq; maximum, 370 MBq). Whole-body scanning was performed 1 h after injection, previously shown to be a suitable time point for tumor imaging with [$^{68}$Ga]FAPI-46 (*18,22–24*). A Biograph mCT PET/CT scanner (Siemens) and a Discovery MI scanner (GE Healthcare) were used.

Preceded by a low-dose non-CECT scan for attenuation correction, PET images were acquired from vertex to mid thigh (4 min/bed position). The obtained emission data were corrected for scatter, randoms, and decay and were reconstructed with an ordered-subset expectation maximization algorithm. The reconstruction parameters were carefully designed to ensure equivalent (within ±10% variation) SUV and contrast in a PET body phantom with spheres. Finally, diagnostic CECT was performed for anatomic correlation of PET findings and diagnostic-quality image fusion.

### Image Analysis and Interpretation

[$^{68}$Ga]FAPI-46 PET/CT images were analyzed using Syngo.via (Siemens) individually by 2 readers, both board-certified radiologists, one of whom was a board-certified nuclear medicine specialist and the other a specialist in training. Both readers had access to patients' clinical imaging workup to facilitate localization of the target lesion. However, neither knew the histopathologic results. Differences in opinion were resolved by consensus, and previously described pitfalls in [$^{68}$Ga]FAPI PET/CT imaging were taken into consideration (*25*).

Lesions suspected of representing malignancy, with focal tracer uptake exceeding that of the surrounding background, were regarded as positive. SUV parameters were extracted from volumes of interest, defined using 40% threshold isocontouring. These were used for receiver-operating-characteristic (ROC) analyses. Positive [$^{68}$Ga]FAPI-46 PET/CT findings were defined as either an $SUV_{max}$ or an $SUV_{mean}$ at or above the respective optimal cutoff. Anatomic information from CT images was used to avoid inclusion of activity from adjacent nontumoral tissues and to exclude other potential causes of tracer uptake.

The clinical imaging work-up was interpreted by board-certified radiologists specialized in abdominal radiology and presented at multidisciplinary conferences as per the clinical routine. For this study, an additional reading was performed retrospectively by a board-certified radiologist who was specialized in abdominal radiology and did not know either the [$^{68}$Ga]FAPI-46 PET/CT or the histopathology results, and the results were classified as either positive, negative, or equivocal. To compare the performance of [$^{68}$Ga]FAPI-46 PET/CT with that of standard-of-care imaging in characterizing pancreatic tumors, $SUV_{max}$ and $SUV_{mean}$ were analyzed individually.

### Statistical Analysis

For all statistical analyses, R software, version 4.2.1., was used, including the "pROC" and "cutpointr" packages for ROC analyses and cutoff determination for both PET parameters. Values below the cutoff were coded as [$^{68}$Ga]FAPI-46 PET–negative, whereas values equal to or above were coded as [$^{68}$Ga]FAPI-46 PET–positive. True-positive patients were defined as [$^{68}$Ga]FAPI-46 PET–positive with malignant histopathology; false-positive, as [$^{68}$Ga]FAPI-46 PET–positive with benign histopathology; false-negative, as [$^{68}$Ga]FAPI-46 PET–negative with malignant histopathology; and true negative, as [$^{68}$Ga]FAPI-46 PET–negative with benign histopathology. Accuracy, sensitivity, specificity, and positive and negative predictive values, including corresponding 95% CIs, were calculated using the "epiR" package. Power calculation was performed using the package "pwr," with CECT specificity set to 0.9 (*26*), the statistical significance level set to 0.05, and power set to 0.8. In all statistical tests, *P* values of less than 0.05 were considered statistically significant.

## RESULTS

### Patient Cohort and Imaging Acquisition

Thirty patients were recruited between September 2021 and May 2022 (17 men and 13 women; mean age, 66.9 ± 12.4 y; range, 27–85 y) with suspected pancreatic or periampullary cancer. All underwent [$^{68}$Ga]FAPI-46 PET/CT and subsequent surgery after a median of 5.5 d (interquartile range, 2.3–12.8 d). The mean injected activity was 272.5 ± 74.8 MBq, and the mean uptake time was 60.5 ± 2.5 min (range, 56–67 min). Six patients were reported

**TABLE 1**
Patient Demographics and Clinical Characteristics

| Patient no. | Sex | Age (y) | Clinical imaging work-up | Clinical work-up findings | [$^{68}$Ga]FAPI-46 PET/CT findings | $SUV_{max}$ | $SUV_{mean}$ | Histologic diagnosis |
|---|---|---|---|---|---|---|---|---|
| 1 | M | 62 | CECT | Positive | Positive | 18.4 | 10.9 | Cholangiocarcinoma |
| 2 | F | 69 | CECT | Positive | Positive | 15.1 | 9.9 | PC |
| 3 | F | 85 | CECT | Positive | Positive | 23.9 | 14.4 | PC |
| 4 | F | 74 | CECT + MRI | Positive | Positive | 19.0 | 10.7 | PC |
| 5 | M | 60 | CECT | Equivocal | Negative | 7.1 | 4.0 | Distal choledocholithiasis |
| 6 | F | 72 | CECT | Positive | Positive | 24.9 | 15.0 | PC |
| 7 | F | 80 | CECT | Positive | Positive | 18.5 | 11.1 | Ampullary carcinoma |
| 8 | M | 66 | CECT | Positive | Positive | 22.0 | 12.4 | PC |
| 9 | M | 64 | CECT + MRI | Positive | Positive | 15.0 | 8.4 | PC |
| 10 | F | 49 | MRI | Positive | Positive | 18.5 | 11.4 | PC |
| 11 | M | 75 | CECT | Positive | Positive | 10.5 | 6.2 | Autoimmune pancreatitis |
| 12 | F | 27 | CECT | Equivocal | Negative | 1.0 | 0.7 | Duodenal adenoma |
| 13 | F | 80 | CECT + MRI | Positive | Positive | 17.4 | 10.9 | PC |
| 14 | M | 83 | CECT | Equivocal | Positive | 15.4 | 8.5 | Ampullary carcinoma |
| 15 | M | 63 | CECT + MRI | Negative | Positive | 15.4 | 8.2 | Chronic pancreatitis |
| 16 | F | 58 | CECT | Positive | Positive | 16.6 | 9.8 | PC |
| 17 | M | 73 | CECT | Equivocal | Negative | 2.2 | 1.3 | IPMN |
| 18 | M | 53 | CECT | Positive | Positive | 10.4 | 6.0 | Cholangiocarcinoma |
| 19 | M | 78 | CECT | Equivocal | Positive | 10.2 | 5.9 | Duodenal carcinoma |
| 20 | M | 57 | CECT + MRI | Equivocal | Negative | 3.7 | 2.2 | PanIN |
| 21 | M | 73 | CECT + MRI | Positive | Positive | 12.1 | 7.3 | PC |
| 22 | F | 69 | MRI | Equivocal | Negative | 2.2 | 1.5 | IPMN |
| 23 | M | 74 | CECT | Positive | Positive | 18.8 | 11.5 | PC |
| 24 | M | 65 | CECT | Positive | Positive | 15.6 | 9.0 | PC |
| 25 | M | 69 | CECT + MRI | Equivocal | Negative | 1.1 | 0.5 | PanIN |
| 26 | F | 59 | CECT + MRI | Equivocal | Positive | 11.4 | 7.9 | Ampullary carcinoma |
| 27 | F | 47 | MRI | Equivocal | Negative | 1.4 | 1.0 | IPMN |
| 28 | M | 66 | CECT + MRI | Equivocal | Negative | 5.3 | 2.9 | IPMN |
| 29 | F | 79 | CECT | Positive | Positive | 9.9 | 6.3 | PC |
| 30 | M | 78 | CECT | Positive | Positive | 22.5 | 13.6 | PC |

PanIN = pancreatic intraepithelial neoplasia.

as unresectable because of macroscopic peritoneal carcinomatosis ($n = 3$), extensive venous involvement ($n = 1$), excessive inflammation and fibrosis ($n = 1$), or significant celiac trunk stenosis ($n = 1$). The diagnosis in these patients was confirmed either by perioperative cryosection in the case of peritoneal carcinomatosis or by perioperative core-needle biopsy or endoscopic ultrasound-guided fine-needle biopsy in the remaining cases deemed irresectable.

Histopathologic analysis revealed carcinoma in 20 patients and benign lesions in 10 patients. The demographics and clinical characteristics of the participants are presented in Table 1.

**TABLE 2**
$SUV_{max}$ and $SUV_{mean}$ in Pancreatic Lesions with Malignant Vs. Benign Histopathology

| | Malignant | | Benign | | |
|---|---|---|---|---|---|
| Parameter | Mean ± SD | Range | Mean ± SD | Range | *P* |
| $SUV_{max}$ | 17.0 ± 5.0 | 9.9–24.9 | 5.0 ± 5.0 | 1.0–15.4 | <0.001 |
| $SUV_{mean}$ | 10.0 ± 2.7 | 5.9–15.0 | 2.8 ± 2.6 | 0.5–8.2 | <0.001 |

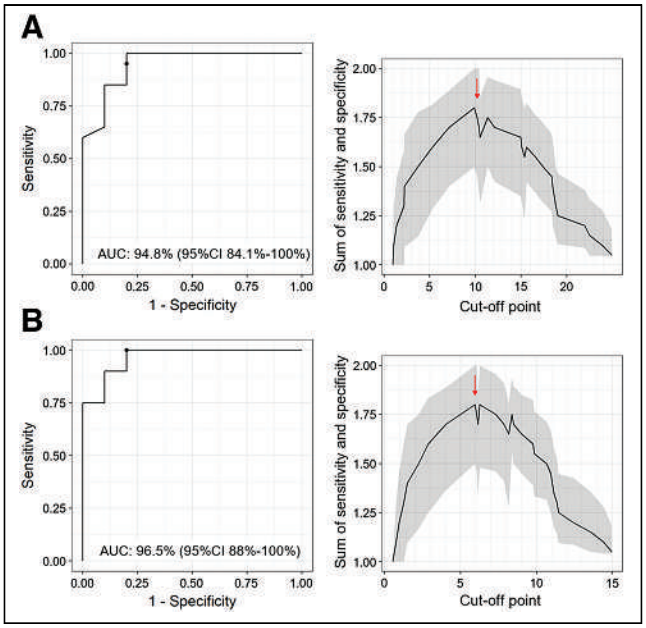


**FIGURE 1.** ROC curves depicting sensitivity and specificity of $SUV_{max}$ (A) and $SUV_{mean}$ (B) for diagnosis of PC. Graphs to right show optimum for different potential cutoffs; arrow indicates optimal cutoff for each parameter. AUC = area under curve.

### Patient Safety

All subjects were monitored during examination, with blood pressure, heart rate, and body temperature registered before [$^{68}$Ga]FAPI-46 injection and after examination (~1.5-h interval). No related pharmacologic or physiologic effects were recorded, and none of the participants reported any new symptoms.

### Image Interpretation and Diagnostic Performance

Visual assessment showed high tracer activity in primary tumors and low background tracer activity, especially in the brain, but also in the uninvolved parts of the pancreatic parenchyma and in the liver, heart, and gastrointestinal tract, yielding a purposive image contrast. All 20 malignant lesions showed intense [$^{68}$Ga]FAPI-46 uptake (Table 2). At the same time, 2 of the benign lesions also showed tracer uptake above the cutoffs (Supplemental Fig. 1). ROC analyses rendered optimal cutoffs of 10.2 for $SUV_{max}$ and 5.9 for $SUV_{mean}$ as presented in Figure 1. Table 3 provides the diagnostic performance data with corresponding 95% CIs for both parameters, regarding differentiation of malignancies from benign lesions, in the whole cohort and in the subcohort with equivocal clinical imaging work-up.

### Comparison with Standard-of-Care Imaging

All patients classified as equivocal on standard-of-care imaging ($n = 11$) were correctly classified as either positive or negative for PC by [$^{68}$Ga]FAPI-46 PET/CT, for both $SUV_{max}$ and $SUV_{mean}$ ($P < 0.001$) (Table 1; Fig. 2).

### Power Analysis

At trial initiation, power analysis was not possible because of a lack of published data. An interim analysis was therefore included in this study to serve as a basis for calculating the sample size needed to detect a significant difference in specificity between CECT and [$^{68}$Ga]FAPI-46 PET/CT. On the basis of a recently reported CECT specificity of 90% (*26*) and that of [$^{68}$Ga]FAPI-46 PET/CT for the whole cohort (80%), 195 observations are needed. When considering the equivocal cohort only, with [$^{68}$Ga]FAPI-46 PET/CT specificity of 100%, 38 observations are needed.

## DISCUSSION

The differential diagnosis of pancreatic masses remains a challenge for diagnostic imaging despite modern cross-sectional techniques with CECT and MRI. To improve the diagnostic yield, we applied a new tracer with high affinity for epithelial cancers, FAPI. In this interim analysis, we evaluated the accuracy of [$^{68}$Ga]FAPI-46 PET/CT for the diagnosis of pancreatic tumors and determined the sample size needed for sufficient power. We observed a significantly higher [$^{68}$Ga]FAPI-46 uptake in malignant tumors than in benign lesions (Table 2), demonstrating high accuracy for diagnosis of PC, for both $SUV_{max}$ and $SUV_{mean}$ (Table 3). In patients with equivocal standard-of-care imaging results, sample size calculations show that 38 observations are needed for sufficient statistical power. This trial will therefore continue to recruit a total of 120 patients to reach 38 equivocal observations by standard-of-care imaging.

CECT has a reported sensitivity of 89%–91% and a specificity of 85%–90% for the diagnosis of PC in recent metaanalyses (*26,27*). Our data indicate that [$^{68}$Ga]FAPI-46 PET/CT has at least an equally high diagnostic accuracy as CECT for the diagnosis of primary PC, within a 95% CI. In fact, in all 11 cases in which the clinical imaging workup findings were equivocal, [$^{68}$Ga]FAPI-46 PET/CT correctly differentiated malignant from benign lesions, yielding a diagnostic accuracy of 100%. $SUV_{mean}$ had a slightly larger area under the ROC curve than $SUV_{max}$ (96.5% vs. 94.8%),

**TABLE 3**
Diagnostic Performance of $SUV_{max}$ with Cutoff of 10.2 and $SUV_{mean}$ with Cutoff of 5.9 in Diagnosis of PC

| | Whole cohort ($n = 30$) | | Subcohort with equivocal clinical imaging ($n = 11$) | |
|---|---|---|---|---|
| Parameter | $SUV_{max}$ | $SUV_{mean}$ | $SUV_{max}$ | $SUV_{mean}$ |
| Sensitivity | 95 (75–100) | 100 (83–100) | 100 (29–100) | 100 (29–100) |
| Specificity | 80 (44–97) | 80 (44–97) | 100 (63–100) | 100 (63–100) |
| Positive predictive value | 90 (70–99) | 91 (71–99) | 100 (29–100) | 100 (29–100) |
| Negative predictive value | 89 (52–100) | 100 (63–100) | 100 (63–100) | 100 (63–100) |
| Overall accuracy | 90 (73–98) | 93 (78–99) | 100 (72–100) | 100 (72–100) |

Data are percentages, with 95% CIs in parentheses.

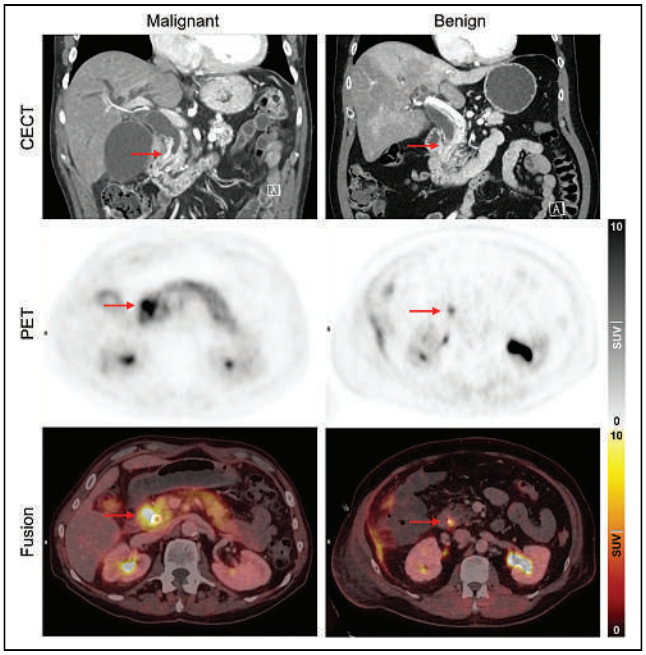


**FIGURE 2.** CECT, axial PET, and fused images of malignant (left) and benign (right) periampullary lesion obstructing bile duct (arrow).

suggesting that the parameter might be somewhat more accurate (Fig. 1). However, both parameters are convincing because of their high diagnostic accuracy, and as more data are collected, new ROC analyses will be performed. In the subanalysis of patients with an equivocal imaging work-up, both parameters showed 100% accuracy. To our knowledge, we are the first to report such high accuracy for the method in the diagnosis of PC, and on the basis of these results, we expect [$^{68}$Ga]FAPI-46 PET/CT imaging to have a significant impact on the diagnostic work-up of PC patients. The wide span of the 95% CI for [$^{68}$Ga]FAPI-46 PET/CT is probably due to the relatively few cases in our study and should narrow as more subjects are included.

The high [$^{68}$Ga]FAPI-46 uptake in malignant lesions and the significantly lower uptake in benign lesions, together with negligible background activity, gave satisfactory image contrast and is consistent with the results of previous [$^{68}$Ga]Ga-FAPI PET/CT studies on pancreatic and other cancers (*28,29*). Röhrich et al. evaluated the clinical impact of PET/CT using [$^{68}$Ga]FAPI-4 and [$^{68}$Ga]FAPI-46 in the staging of primary and recurrent pancreatic ductal adenocarcinoma, reporting clinically meaningful changes in the staging of both groups (*30*). Similarly, Pang et al. observed that [$^{68}$Ga]FAPI-4 PET/CT improves tumor detection and staging in PC (*31*). Lang et al. also concluded that [$^{68}$Ga]FAPI-74 PET/CT could predict malignant transformation within IPMN with high accuracy (*32*). Our study sets itself apart from these studies because our findings were histologically validated and inclusion of nonmalignant conditions allowed the accuracy of [$^{68}$Ga]FAPI-46 PET/CT for the diagnosis of PC to be determined, an essential step for application to clinical practice. The high sensitivity suggests that no malignancy would be missed and that the specificity we assessed is acceptable and comparable to that of the current best standard. The 2 false-positive cases represented inflammation (Supplemental Fig. 1). However, this issue has been addressed in previous publications, showing that the addition of multiple-time-point and dynamic imaging techniques facilitates differentiation of malignancy from pancreatitis (*30,31,33*).

A major limitation of this study is the small sample size, especially with regard to patients with equivocal results on standard-of-care imaging, and conclusions from these data should therefore be drawn with caution. Larger exploratory studies are needed as our power calculations suggest. Furthermore, even though small (±10%), the variations in image quality and SUV measurements resulting from the use of different cameras could have affected the results, especially in patients with an SUV in the vicinity of the cutoffs.

## CONCLUSION

Characterization of pancreatic mass lesions remains clinically challenging because various inflammatory tumors may mimic PC on imaging, leading to major pancreatic surgery for benign disease in a substantial number of patients (*6–9,34*). Such surgery is associated with high costs, high morbidity rates, and a significant decline in quality of life (*35–39*) and should therefore be avoided if possible. Our results show that [$^{68}$Ga]FAPI-46 PET/CT can accurately differentiate malignant from benign pancreatic lesions deemed equivocal by standard-of-care imaging. For this differentiation, we propose semiquantitative cutoffs for both $SUV_{max}$ and $SUV_{mean}$. In this trial, we will therefore continue to recruit a total of 120 patients to reach those 38 equivocal observations needed for sufficient statistical power. On the basis of our findings, we conclude that [$^{68}$Ga]FAPI-46 PET/CT not only might represent a new complementary imaging technique in primary diagnosis of PC but also could become a necessary tool when standard-of-care imaging results are inconclusive. A prospective clinical trial is currently ongoing in our department, but even larger, multicenter trials will be needed for clinical translation of [$^{68}$Ga]FAPI-46 PET/CT in PC.

## DISCLOSURE

The study was financed by grants from the Swedish government under the ALF agreement (SLL20200025) and from the Swedish Cancer Society (200695). No other potential conflict of interest relevant to this article was reported.

## ACKNOWLEDGMENTS

We thank Laura Vossen Engblom (Department of Medicine, Huddinge, Karolinska Institutet) for the statistical data analyses, and we thank the Swedish Association for the Advancement of Pancreatology for its support.

## KEY POINTS

**QUESTION:** Can [$^{68}$Ga]FAPI-46 PET/CT improve characterization of equivocal pancreatic lesions detected by standard-of-care imaging, and how many observations are needed for sufficient statistical power?

**PERTINENT FINDINGS:** In this interim analysis of a prospective clinical trial, analysis of 30 surgical patients showed that [$^{68}$Ga]FAPI-46 PET/CT can accurately differentiate malignant from benign pancreatic lesions deemed equivocal by standard-of-care imaging. For sufficient statistical power, this trial will continue to recruit a total of 120 patients to reach 38 equivocal observations by standard-of-care imaging.

**IMPLICATIONS FOR PATIENT CARE:** Our findings suggest that [$^{68}$Ga]FAPI-46 PET/CT not only can be clinically applied as a complement but also could become a necessary tool when standard-of-care imaging on PC is inconclusive.

## REFERENCES


1. Siegel RL, Miller KD, Fuchs HE, Jemal A. Cancer statistics, 2022. *CA Cancer J Clin.* 2022;72:7–33.
2. Michl P, Lohr M, Neoptolemos JP, et al. UEG position paper on pancreatic cancer. Bringing pancreatic cancer to the 21st century: prevent, detect, and treat the disease earlier and better. *United European Gastroenterol J.* 2021;9:860–871.
3. Li D, Xie K, Wolff R, Abbruzzese JL. Pancreatic cancer. *Lancet.* 2004;363: 1049–1057.
4. Ducreux M, Cuhna AS, Caramella C, et al. Cancer of the pancreas: ESMO clinical practice guidelines for diagnosis, treatment and follow-up. *Ann Oncol.* 2015; 26(suppl 5):v56–v68.
5. Tempero MA, Malafa MP, Al-Hawary M, et al. Pancreatic adenocarcinoma, version 2.2017, NCCN clinical practice guidelines in oncology. *J Natl Compr Canc Netw.* 2017;15:1028–1061.
6. Conrad C, Fernandez-Del Castillo C. Preoperative evaluation and management of the pancreatic head mass. *J Surg Oncol.* 2013;107:23–32.
7. Schima W, Bohm G, Rosch CS, Klaus A, Fugger R, Kopf H. Mass-forming pancreatitis versus pancreatic ductal adenocarcinoma: CT and MR imaging for differentiation. *Cancer Imaging.* 2020;20:52.
8. Elbanna KY, Jang HJ, Kim TK. Imaging diagnosis and staging of pancreatic ductal adenocarcinoma: a comprehensive review. *Insights Imaging.* 2020;11:58.
9. Dutta AK, Chacko A. Head mass in chronic pancreatitis: inflammatory or malignant. *World J Gastrointest Endosc.* 2015;7:258–264.
10. European Study Group on Cystic Tumours of the Pancreas. European evidence-based guidelines on pancreatic cystic neoplasms. *Gut.* 2018;67:789–804.
11. Tanaka M, Fernandez-Del Castillo C, Kamisawa T, et al. Revisions of international consensus Fukuoka guidelines for the management of IPMN of the pancreas. *Pancreatology.* 2017;17:738–753.
12. Vege SS, Ziring B, Jain R, Moayyedi P; Clinical Guidelines Committee, American Gastroenterology Association. American Gastroenterological Association Institute guideline on the diagnosis and management of asymptomatic neoplastic pancreatic cysts. *Gastroenterology.* 2015;148:819–822.
13. Del Chiaro M, Segersvard R, Pozzi Mucelli R, et al. Comparison of preoperative conference-based diagnosis with histology of cystic tumors of the pancreas. *Ann Surg Oncol.* 2014;21:1539–1544.
14. Khoury RE, Kabir C, Maker VK, Banulescu M, Wasserman M, Maker AV. What is the incidence of malignancy in resected intraductal papillary mucinous neoplasms? An analysis of over 100 US institutions in a single year. *Ann Surg Oncol.* 2018;25:1746–1751.
15. Öhlund D, Handly-Santana A, Biffi G, et al. Distinct populations of inflammatory fibroblasts and myofibroblasts in pancreatic cancer. *J Exp Med.* 2017;214: 579–596.
16. Shi M, Yu DH, Chen Y, et al. Expression of fibroblast activation protein in human pancreatic adenocarcinoma and its clinicopathological significance. *World J Gastroenterol.* 2012;18:840–846.
17. Micke P, Ostman A. Exploring the tumour environment: cancer-associated fibroblasts as targets in cancer therapy. *Expert Opin Ther Targets.* 2005;9:1217–1233.
18. Kratochwil C, Flechsig P, Lindner T, et al. $^{68}$Ga-FAPI PET/CT: tracer uptake in 28 different kinds of cancer. *J Nucl Med.* 2019;60:801–805.
19. Hirmas N, Hamacher R, Sraieb M, et al. Fibroblast-activation protein PET and histopathology in a single-center database of 324 patients and 21 tumor entities. *J Nucl Med.* 2023;64:711–716.
20. Sarmiento JM, Nagomey DM, Sarr MG, Farnell MB. Periampullary cancers: are there differences? *Surg Clin North Am.* 2001;81:543–555.
21. Jussing E, Milton S, Samen E, et al. Clinically applicable cyclotron-produced gallium-68 gives high-yield radiolabeling of DOTA-based tracers. *Biomolecules.* 2021;11:1118.
22. Lindner T, Loktev A, Altmann A, et al. Development of quinoline-based theranostic ligands for the targeting of fibroblast activation protein. *J Nucl Med.* 2018;59: 1415–1422.
23. Giesel FL, Kratochwil C, Lindner T, et al. $^{68}$Ga-FAPI PET/CT: biodistribution and preliminary dosimetry estimate of 2 DOTA-containing FAP-targeting agents in patients with various cancers. *J Nucl Med.* 2019;60:386–392.
24. Loktev A, Lindner T, Burger EM, et al. Development of fibroblast activation protein-targeted radiotracers with improved tumor retention. *J Nucl Med.* 2019;60: 1421–1429.
25. Kessler L, Ferdinandus J, Hirmas N, et al. Pitfalls and Common Findings in $^{68}$Ga-FAPI PET: a pictorial analysis. *J Nucl Med.* 2022;63:890–896.
26. Treadwell JR, Zafar HM, Mitchell MD, Tipton K, Teitelbaum U, Jue J. Imaging tests for the diagnosis and staging of pancreatic adenocarcinoma: a meta-analysis. *Pancreas.* 2016;45:789–795.
27. Toft J, Hadden WJ, Laurence JM, et al. Imaging modalities in the diagnosis of pancreatic adenocarcinoma: a systematic review and meta-analysis of sensitivity, specificity and diagnostic accuracy. *Eur J Radiol.* 2017;92:17–23.
28. Gilardi L, Airo Farulla LS, Demirci E, Clerici I, Omodeo Sale E, Ceci F. Imaging cancer-associated fibroblasts (CAFs) with FAPi PET. *Biomedicines.* 2022;10:523.
29. Sollini M, Kirienko M, Gelardi F, Fiz F, Gozzi N, Chiti A. State-of-the-art of FAPI-PET imaging: a systematic review and meta-analysis. *Eur J Nucl Med Mol Imaging.* 2021;48:4396–4414.
30. Röhrich M, Naumann P, Giesel FL, et al. Impact of $^{68}$Ga-FAPI PET/CT imaging on the therapeutic management of primary and recurrent pancreatic ductal adenocarcinomas. *J Nucl Med.* 2021;62:779–786.
31. Pang Y, Zhao L, Shang Q, et al. Positron emission tomography and computed tomography with [$^{68}$Ga]Ga-fibroblast activation protein inhibitors improves tumor detection and staging in patients with pancreatic cancer. *Eur J Nucl Med Mol Imaging.* 2022;49:1322–1337.
32. Lang M, Spektor AM, Hielscher T, et al. Static and dynamic $^{68}$Ga-FAPI PET/CT for the detection of malignant transformation of intraductal papillary mucinous neoplasia of the pancreas. *J Nucl Med.* 2023;64:244–251.
33. Glatting FM, Hoppner J, Liew DP, et al. Repetitive early $^{68}$Ga-FAPI PET acquisition comparing $^{68}$Ga-FAPI-02, $^{68}$Ga-FAPI-46, and $^{68}$Ga-FAPI-74: methodologic and diagnostic implications for malignant, inflammatory/reactive, and degenerative lesions. *J Nucl Med.* 2022;63:1844–1851.
34. Holländer S, Birk D. Pancreatic cancer within the uncinate process. In: Beger HG, Warshaw AL, Hruban RH, et al., eds. *The Pancreas: An Integrated Textbook of Basic Science, Medicine, and Surgery.* Wiley; 2018:724–727.
35. Billings BJ, Christein JD, Harmsen WS, et al. Quality-of-life after total pancreatectomy: is it really that bad on long-term follow-up? *J Gastrointest Surg.* 2005;9:1059–1066.
36. Eaton AA, Gonen M, Karanicolas P, et al. Health-related quality of life after pancreatectomy: results from a randomized controlled trial. *Ann Surg Oncol.* 2016;23: 2137–2145.
37. Balzano G, Capretti G, Callea G, Cantu E, Carle F, Pezzilli R. Overuse of surgery in patients with pancreatic cancer: a nationwide analysis in Italy. *HPB (Oxford).* 2016;18:470–478.
38. Vollmer CM Jr. The economics of pancreas surgery. *Surg Clin North Am.* 2013;93: 711–728.
39. Dominguez-Comesana E, Gonzalez-Rodriguez FJ, Ulla-Rocha JL, Lede-Fernandez A, Portela-Serra JL, Pinon-Cimadevila MA. Morbidity and mortality in pancreatic resection [in Spanish]. *Cir Esp.* 2013;91:651–658.

# The Diagnostic Value of PSMA PET/CT in Men with Newly Diagnosed Unfavorable Intermediate-Risk Prostate Cancer

Marinus J. Hagens[1–3], Wietske I. Luining[2,3], Auke Jager[2,3], Maarten L. Donswijk[4], Zing Cheung[4], Maurits Wondergem[4], Daniela E. Oprea-Lager[5], André N. Vis[2,3], Pim J. van Leeuwen[1,3], and Henk G. van der Poel[1–3]

*[1]Department of Urology, Netherlands Cancer Institute–Antoni van Leeuwenhoek Hospital, Amsterdam, The Netherlands; [2]Department of Urology, Amsterdam University Medical Center, Location VUmc, Amsterdam, The Netherlands; [3]Prostate Cancer Network Netherlands, Amsterdam, The Netherlands; [4]Department of Nuclear Medicine, Netherlands Cancer Institute–Antoni van Leeuwenhoek Hospital, Amsterdam, The Netherlands; and [5]Department of Radiology and Nuclear Medicine, Amsterdam University Medical Center, Location VUmc, Amsterdam, The Netherlands*

Our objective was to determine the diagnostic value of prostate-specific membrane antigen (PSMA) PET/CT in staging men with newly diagnosed unfavorable intermediate-risk prostate cancer (PCa). **Methods:** Patients with newly diagnosed unfavorable intermediate-risk PCa, in whom PSMA PET/CT was performed as a primary staging modality, were retrospectively studied. PSMA PET/CT was performed at several diagnostic centers and reported by expert nuclear medicine physicians within 2 high-volume PCa centers. A multivariate logistic regression analysis, taking into account clinical, biochemical, pathologic, and radiologic variables, was performed to identify potential independent predictors for metastatic disease on PSMA PET/CT. **Results:** In total, 396 men with newly diagnosed unfavorable intermediate-risk PCa were studied. Metastatic disease was observed in 37 (9.3%) men, of whom 29 (7.3%) had molecular imaging locoregional lymph node metastases (miN1) and 16 (4.0%) had distant metastases (miM1). A radiologic tumor stage of at least T3 on MRI (odds ratio, 2.72 [95% CI, 1.27–5.83]; $P = 0.01$) and more than 50% positive prostate biopsies (odds ratio, 3.87 [95% CI, 1.74–8.62]; $P = 0.001$) were found to be independently associated with metastatic disease on PSMA PET/CT. **Conclusion:** Given that metastatic disease was observed in nearly 1 in 10 men with newly diagnosed unfavorable intermediate-risk PCa, PSMA PET/CT is considered to be of diagnostic value within this population. Further stratification using the radiologic tumor stage and the percentage of positive prostate biopsies could aid in identifying those patients at risk of having metastatic disease on PSMA PET/CT.

**Key Words:** prostate cancer; unfavorable intermediate-risk; diagnostic value; PSMA PET/CT

**J Nucl Med 2023; 64:1238–1243**
DOI: 10.2967/jnumed.122.265205

Metastatic screening using prostate-specific membrane antigen (PSMA) PET/CT in men with prostate cancer (PCa) is increasingly being adopted in urologic practice. Compared with conventional imaging techniques (such as CT and bone scintigraphy), PSMA PET/CT appears to have greater accuracy in detecting metastases, is more likely to lead to management changes, produces fewer equivocal findings, and has lower radiation exposure (*1–3*).

To avoid overdiagnosis, adequate selection of patients at risk of having metastatic disease is of paramount importance. The presence of metastases on PSMA PET/CT has been shown to be directly associated with prostate-specific antigen (PSA) levels, clinical tumor stages, and biopsy International Society of Urological Pathology (ISUP) grade groups (GGs) (*3–6*). Therefore, the decision on whether to perform PSMA PET/CT is based on the stratification of patients according to the American Urological Association risk groups (i.e., low, favorable intermediate, unfavorable intermediate, and high risk; Table 1) (*7,8*). Consequently, the Society of Nuclear Medicine and Molecular Imaging recommends performing metastatic screening using PSMA PET/CT in patients with unfavorable intermediate-risk and high-risk PCa (*9*).

Even though the diagnostic value of PSMA PET/CT in men with high-risk PCa has already been demonstrated, the clinical benefit of PSMA PET/CT in men with newly diagnosed unfavorable intermediate-risk PCa remains questionable and literature on this topic is scarce (*3,4,10*). Therefore, this study aimed to determine the diagnostic value of PSMA PET/CT for metastatic screening within the largest known dataset of newly diagnosed unfavorable intermediate-risk PCa patients.

## MATERIALS AND METHODS

### Study Design and Patient Population

A retrospective cohort study was performed at The Netherlands Cancer Institute and the Amsterdam University Medical Center. The institutional review board approved this retrospective study and waived the requirement to obtain informed consent.

Patients found to have unfavorable PCa on diagnostic prostate biopsies and on whom PSMA PET/CT was performed between January 2018 and December 2021 as a primary staging modality were retrospectively studied. Excluded from the analysis were patients with any high-risk factors, such as a PSA level of at least 20 ng/mL or a clinical tumor stage of at least T3a on digital rectal examination. Patients who had received prior PCa treatments were excluded as well.

Patient characteristics were collected from patient charts, and PSMA PET/CT results were collected from nuclear medicine reports.

### MRI Acquisition and Analysis

Before undergoing prostate biopsies, the men underwent MRI. Prostate MRI was performed using a 3.0-T scanner according to the European Society of Urological Radiology MRI protocol in high-volume

Received Nov. 16, 2022; revision accepted Feb. 21, 2023.
For correspondence or reprints, contact Marinus J. Hagens (m.hagens@nki.nl).
Published online Jun. 29, 2023.

**TABLE 1**
American Urological Association Risk Groups for Localized PCa

| Risk group | Description |
|---|---|
| Low risk | PSA < 10 ng/mL and Gleason score < 7 (ISUP GG1) and cT1–2a |
| Intermediate risk | |
| Favorable | PSA 10–20 ng/mL or Gleason score 7 (ISUP GG2) or cT2b–c |
| Unfavorable | PSA 10–20 ng/mL or Gleason score 7 (ISUP GG3) or cT2b–c |
| High risk | PSA > 20 ng/mL or Gleason score > 7 (ISUP GG4–5) or cT3–4 |

cT stage = clinical tumor stage.

diagnostic PCa centers (*11*). All MRI scans were reviewed by experienced radiologists according to the standardized Prostate Imaging Reporting and Data System (PI-RADS) classification system, version 2.1 (*12*). Following Dutch guidelines, all radiologists were experienced enough to independently read prostate MR images (*13*).

### Prostate Biopsies and Histopathologic Assessment

All prostate biopsies took place in high-volume diagnostic PCa centers within the Prostate Cancer Network Netherlands by experienced urologists with at least 5 y of experience performing prostate biopsies. The biopsies were performed transrectally or transperineally, using either MRI/transrectal ultrasound fusion software or cognitive fusion. If an MRI-positive lesion (defined as PI-RADS classification 3–5) was visible, systematic prostate biopsies were preceded by targeted prostate biopsies. If MRI had negative findings (defined as PI-RADS classification 1–2) or was not performed, only systematic prostate biopsies were obtained. Given the fact that not all hospitals were yet performing targeted prostate biopsies, some MRI-positive patients underwent only systematic prostate biopsies. Prostate biopsies were processed and reported according to the ISUP protocol by specialized uropathologists with at least 5 y of experience in assessing prostate biopsies (*14*). MRI-directed targeted prostate biopsies were pooled and reported as 1 biopsy core in a systematic biopsy set. Before PSMA PET/CT was performed, prostate biopsies were not reassessed. If the presence of a cribriform growth pattern was reported, then it was considered.

### PSMA PET/CT Imaging and Analysis

Although PSMA PET/CT was performed at several diagnostic centers, all scans were revised and reported by expert nuclear medicine physicians within 2 high-volume PCa centers (Netherlands Cancer Institute and Amsterdam University Medical Center). PSMA PET/CT images were analyzed and classified according to the European Association of Nuclear Medicine PSMA guidelines (*15*). A PSMA PET/CT scan was reported as positive when the lesion was compatible with or suggestive of PCa. According to the molecular imaging classification (mi), locoregional lymph node metastases (miN1) were defined as lymph node metastases in the pelvic region, whereas distant metastases (miM1) were defined as either extrapelvic lymph node (miM1a), bone (miM1b), or visceral metastases (miM1c).

For logistic reasons, several PSMA radiotracers were used for metastatic screening during the study time frame: [$^{18}$F]DCFPyL, [$^{18}$F]PSMA-1007, [$^{18}$F]PSMA-JK7, and [$^{68}$Ga]PSMA-11. PET images were acquired from mid thigh to skull base or vertex. Incubation times and doses differed among tracers and sites, according to local protocols: a median of 99 min (interquartile range [IQR], 60–120 min) after a median dose of 280 MBq (IQR, 198–313 MBq) for [$^{18}$F]DCFPyL, a median of 90 min (IQR, 90–120 min) after a median dose of 258 MBq (IQR, 208–293 MBq) for [$^{18}$F]PSMA-1007, a median of 77 min (IQR, 60–90 min) after a median dose of 201 MBq (IQR, 194–265 MBq) for [$^{18}$F]PSMA-JK7, and a median of 49 min (IQR, 45–60 min) after a median dose of 133 MBq (IQR, 103–154 MBq) for [$^{68}$Ga]PSMA-11. PET images were combined with either a low-dose CT scan (120–140 kV, 40–80 mAs) or a diagnostic CT scan (130 kV, 110 mAs) for anatomic correlation and attenuation correction.

### Statistical Analysis

Categoric variables were reported as frequency distributions and percentages, and continuous variables were expressed as medians with IQR.

To study the diagnostic value of PSMA PET/CT, the number needed to image (NNI) was assessed. The NNI was defined as the number of PSMA PET/CT imaging examinations performed for every PSMA PET/CT scan with metastatic disease (i.e., miN1 and higher) (*16*). Univariate and multivariate logistic regression analyses were performed to identify possible predictive variables for metastatic disease on PSMA PET/CT imaging. First, univariate analyses were performed to assess the association between clinical, biochemical, pathologic, and radiologic variables and metastatic disease on PSMA PET/CT imaging. Variables included in the model were age, PSA level, prostate volume, PSA density, radiologic tumor stage on MRI, PI-RADS assessment category, percentage of positive prostate biopsies, percentage of ISUP GG3 PCa in prostate biopsies, and cribriform growth. Univariate statistically significant variables were applied in the multivariate conditional logistic regression analysis using a backward stepwise variable selection method. For clinical applicability, the percentage of positive prostate biopsies and the percentage of ISUP GG3 in prostate biopsies were used as binary (≤50% and >50%) and categoric (≤25%, 25%–50%, 50%–75%, and >75%) variables. Subsequently, through further stratification in subgroups, precisely those patients at risk for metastatic disease on PSMA PET/CT were identified.

A $P$ value of less than 0.05 was considered to indicate statistical significance. All statistical analyses were performed with the statistical package SPSS, version 27 (IBM), for MacOS (Apple).

## RESULTS

In total, 396 men with newly diagnosed unfavorable intermediate-risk PCa were studied. Patient characteristics and PSMA PET/CT results are presented in Tables 2 and 3, respectively. PSMA-expressing metastases were observed in 37 (9.3%) men, resulting in an NNI of approximately 10. No patients were found to have miM1c. Metastatic disease was observed significantly more often in men undergoing PSMA PET/CT scans using [$^{18}$F]PSMA-1007 than using the other PSMA tracers ($P$ = 0.01; Table 3). No statistically significant differences regarding clinical variables were observed among the applied PSMA radiotracers.

**TABLE 2**
Patient Characteristics of Both Entire Study Population and Subgroups With and Without PSMA-Expressing Metastases

| Characteristic | Overall ($n$ = 396) | Patients without metastases ($n$ = 359) | Patients with metastases ($n$ = 37) | $P$ |
|---|---|---|---|---|
| Age (y) | 69 (63–73) | 68 (63–73) | 70 (66–75) | 0.16 |
| Clinical tumor stage | | | | 0.30 |
| cT1c | 162 (40.9%) | 150 (41.8%) | 12 (32.4%) | |
| cT2 | 234 (59.1%) | 209 (58.2%) | 25 (67.6%) | |
| PSA (ng/mL) | 8.5 (6.2–11.3) | 8.3 (5.9–11.0) | 10.0 (7.3–14.8) | 0.001 |
| Prostate volume (mL) | 41 (31–53) | 40 (31–52) | 47 (31–63) | 0.13 |
| PSA density (ng/mL/cm$^3$) | 0.20 (0.13–0.30) | 0.19 (0.13–0.29) | 0.22 (0.13–0.35) | 0.16 |
| Prebiopsy MRI | 381 (96.2%) | 349 (97.2%) | 32 (86.5%) | 0.01 |
| PI-RADS category | | | | 0.54 |
| ≤2 | 12 (3.1%) | 12 (3.4%) | — | |
| 3 | 22 (5.6%) | 21 (5.8%) | 1 (2.7%) | |
| 4 | 154 (38.9%) | 143 (39.8%) | 11 (29.7%) | |
| 5 | 186 (47.0%) | 166 (46.2%) | 20 (54.1%) | |
| Missing | 22 (5.6%) | 17 (4.7%) | 5 (13.5%) | |
| Radiologic tumor stage | | | | 0.001 |
| rT1c | 12 (3.0%) | 12 (3.3%) | — | |
| rT2 | 267 (67.4%) | 252 (70.2%) | 16 (42.1%) | |
| rT3a | 73 (18.4%) | 61 (17.0%) | 12 (32.4%) | |
| rT3b | 27 (6.8%) | 22 (6.1%) | 5 (13.5%) | |
| Missing | 17 (4.3%) | 12 (3.3%) | 5 (13.5%) | |
| Biopsy approach | | | | 0.93 |
| SBx | 168 (42.4%) | 151 (42.1%) | 17 (45.9%) | |
| TBx | 27 (6.8%) | 25 (7.0%) | 2 (5.4%) | |
| SBx+TBx | 199 (50.3%) | 181 (50.4%) | 18 (48.6%) | |
| Missing | 2 (0.5%) | 2 (0.6%) | — | |
| Type of core ISUP GG3 was found in … | | | | 0.47 |
| TBx | 123 (31.1%) | 114 (31.9%) | 9 (24.3%) | |
| SBx | 200 (50.5%) | 181 (50.7%) | 19 (51.4%) | |
| TBx and SBx | 71 (17.9%) | 62 (17.4%) | 9 (24.3%) | |
| Missing | 2 (0.5%) | 2 (0.6%) | — | |
| Percentage of positive biopsies | 41.7 (23.1–62.5) | 40.0 (22.2–59.2) | 70.0 (40.7–88.1) | <0.001 |
| Percentage of ISUP GG3 in biopsies | 26.7 (14.3–44.4) | 25.0 (13.8–43.7) | 40.8 (28.0–74.1) | 0.001 |
| Cribriform growth | 220 (55.6%) | 194 (54.3%) | 25 (65.8%) | 0.16 |

Radiologic tumor stage refers to tumor stage indicated on MRI. Prostate volume was manually assessed on MRI following suggested measurements for ellipsoid formula in PI-RADS, version 2.1. Continuous variables are shown as median with IQR, and categoric variables are shown as numbers and percentages.

#### Univariate and Multivariate Logistic Regression Analysis

Univariate logistic regression analyses showed that initial PSA level ($P$ = 0.001), radiologic tumor stage on MRI ($P$ = 0.001), percentage of positive prostate biopsies ($P$ < 0.001), and percentage of ISUP GG3 PCa in prostate biopsies ($P$ = 0.001) were associated with the presence of metastatic disease on PSMA PET/CT (Table 2). After backward selection, 2 variables remained independently statistically significantly associated with the presence of PSMA-expressing metastases (Table 4). More precisely, a radiologic tumor stage of at least T3 (odds ratio, 2.72 [95% CI, 1.27–5.83]; $P$ = 0.01) and more than 50% positive prostate biopsies (odds ratio, 3.87 [95% CI, 1.74–8.62]; $P$ = 0.001) were found to be associated with metastatic disease on PSMA PET/CT.

**TABLE 3**
PSMA PET/CT Results for All Unfavorable Intermediate-Risk PCa Patients by Applied PSMA Radiotracer

| Result | Overall ($n$ = 396) | [$^{18}$F]DCFPyL ($n$ = 182) | [$^{18}$F]PSMA-JK7 ($n$ = 45) | [$^{18}$F]PSMA-1007 ($n$ = 24) | [$^{68}$Ga]PSMA-11 ($n$ = 145) | $P$ |
|---|---|---|---|---|---|---|
| Positive scan | 378 (95.5%) | 174 (95.6%) | 42 (93.3%) | 24 (100.0%) | 138 (95.2) | 0.65 |
| Metastatic disease | 37 (9.3%) | 10 (5.5%) | 4 (8.9%) | 6 (25.0%) | 17 (11.7) | 0.01 |
| miN1 | 29 (7.3%) | 9 (4.9%) | 4 (8.9%) | 3 (12.5%) | 13 (9.0%) | 0.36 |
| miM1a | 3 (0.8%) | 2 (1.1%) | — | — | 1 (0.7%) | 0.41 |
| miM1b | 14 (3.5%) | 5 (2.7%) | — | 5 (20.8%) | 4 (2.8%) | 0.02 |

### The Prostate Cancer Network Netherlands Subclassification

PSMA-expressing metastases were particularly common in men with a radiologic tumor stage of at least T3a and higher proportions of positive prostate biopsies. Especially men with more than 75% positive prostate biopsies were at increased risk of having metastatic disease on PSMA PET/CT (odds ratio, 3.88 [95% CI, 1.23–12.21]; $P = 0.02$; Supplemental Table 1; supplemental materials are available at http://jnm.snmjournals.org). Therefore, further risk stratification was investigated.

By further stratification, according to radiologic tumor stage and percentage of positive prostate biopsies, patients at higher risk of metastatic disease on PSMA PET/CT could be identified. Three subgroups were created: low, moderate, and high metastatic potential (Table 5). The NNIs were 32, 10, and 5 for patients with low, moderate, and high metastatic potential, respectively. Patients with high metastatic potential might benefit most from metastatic screening with PSMA PET/CT. The incidence of PSMA-expressing metastases was significantly higher in patients with high metastatic potential than in those with low metastatic potential (18.5% vs. 3.0%; $P < 0.001$). No significant difference was observed between patients with moderate and high metastatic potential (9.4% vs. 18.5%; $P = 0.18$).

**TABLE 4**
Detection of PSMA-Expressing Locoregional Lymph Node or Distant Metastases on PET/CT Multivariate Logistic Regression Analysis

| Result | Odds ratio | $P$ |
|---|---|---|
| Positive needle biopsy cores (%) | | — |
| ≤50 | Reference | |
| >50 | 3.87 (95% CI, 1.74–8.62) | 0.001 |
| Radiologic tumor stage | | — |
| rT1–2 | Reference | |
| rT3 | 2.72 (95% CI, 1.27–5.83) | 0.01 |

Univariate significant variables added to analysis: PSA level ($P = 0.001$), radiologic tumor stage on MRI ($P = 0.001$), percentage of positive prostate biopsies ($P < 0.001$), and percentage of ISUP GG3 in prostate biopsies ($P = 0.001$). Percentage of positive prostate biopsies (≤50% and >50%) and percentage of ISUP GG3 in prostate biopsies (≤50% and >50%) were included as ordinal variables for clinical relevance.

## DISCUSSION

We evaluated the diagnostic value of PSMA PET/CT within the largest known dataset of newly diagnosed unfavorable intermediate-risk PCa patients. Given that 9.3% of patients had PSMA-expressing metastases, resulting in an NNI of approximately 10, this study supports the diagnostic value of PSMA PET/CT within this specific yet important patient population. However, as a relatively expensive diagnostic tool with only limited availability, careful consideration should be given to who will benefit most from PSMA PET/CT (*17*). In this study, we showed that a radiologically more advanced stage of disease on MRI and a higher proportion of positive prostate biopsies were independently associated with metastatic disease on PSMA PET/CT.

Even though the proPSMA study has demonstrated the diagnostic value of PSMA PET/CT in men with newly diagnosed ISUP GG3 PCa, data on its diagnostic value within the intermediate-risk group, and in particular the unfavorable intermediate-risk group, are lacking (*1*). There are only a few reports on the incidence of PSMA-expressing metastases within the intermediate-risk PCa population, which do not elaborate on the incidence of metastases within the different prognostic subgroups (*3,6,18–21*). In the retrospective cohort study by Yaxley et al., the incidence of PSMA-expressing metastases was studied in 638 intermediate-risk PCa patients. Metastatic disease was identified in 5.2% of the patients (*3*). On the other hand, Chikatamarla et al. found higher incidence rates for metastatic disease (*6*). Within their intermediate-risk PCa population, 8.5% (6/71) of men had bone metastases on PSMA PET/CT. Their higher metastatic rates may be attributed to the PSMA radiotracer used, namely [$^{18}$F]PSMA-1007, which is known to have higher rates of nonspecific bone lesions (*22–24*). This was likewise observed in our cohort, as 20.8% of men with unfavorable intermediate-risk PCa had bone metastases. Their lower observed incidence of metastatic disease, compared with our study, may be explained by the fact that Yaxley et al. and Chikatamarla et al. included both favorable and unfavorable intermediate-risk PCa patients. Therefore, the incidence of metastatic disease in their unfavorable intermediate-risk populations might be higher and hence similar to ours.

In our study, a radiologic stage of at least T3 was found to be a statistically independent prognostic factor for PSMA-expressing metastases. Similar outcomes were shown by Yaxley et al. as they reported metastatic disease in 35.2% of men with radiologic stages of at least T3a (*2*). However, this increased incidence was observed in a population with low-, intermediate- and high-risk patients, and specific data regarding the unfavorable intermediate-risk PCa population were lacking. The clinical benefit of the radiologic tumor stage for stratification of patients before metastatic screening may be partially explained by the improved ability of local staging

**TABLE 5**
Incidence of Metastatic Disease and NNI According to Prostate Cancer Network Netherlands Subclassification

| Result | Low metastatic potential: rT1–2 and ≤50% positive prostate biopsies | Moderate metastatic potential: rT1–2 and >50% and ≤75% positive prostate biopsies | High metastatic potential: rT3–4 or >75% positive prostate biopsies |
|---|---|---|---|
| Metastatic disease | 6/197 (3.0%) | 5/53 (9.4%) | 24/130 (18.5%) |
| miN1 | 4/6 (66.7%) | 4/5* (80.0%) | 20/24* (83.3%) |
| miM1a | — | — | 3/24* (12.5%) |
| miM1b | 2/6 (33.3%) | 2/5* (20.0%) | 8/24* (33.3%) |
| NNI | 32 | 10 | 5 |

*Patients could have multiple metastatic lesions simultaneously.
rT = radiologic tumor stage.

by MRI compared with digital rectal examination and the predictive value of the tumor stage on the presence of nodal metastases (*25,26*).

Along with the radiologic tumor stage, the proportion of positive prostate biopsies was associated with the presence of metastatic disease on PSMA PET/CT in our study. This is equally the case for the proportion of ISUP GG3 in prostate biopsies and in line with preexisting literature (*27*). The presence of these associations may be explained by potential improper grading at the time of biopsy. The proportion of highest ISUP GG in biopsies has been shown to be a significant predictor of both up- and downgrading in radical prostatectomy—the lower the proportion, the greater the likelihood of downgrading and, consequently, an inaccurate indication (*28*). The fact that both targeted and systematic biopsies were taken in most men may also have influenced our unfavorable intermediate-risk group, as the original American Urological Association risk groups were based on ISUP GG from systematic sextant biopsies. Systematic biopsies are more frequently upgraded at radical prostatectomy than targeted biopsies (*29*).

Our study is not devoid of limitations. First, given the retrospective nature of this study, the presence of selection bias cannot be ruled out, meaning results should be interpreted with caution. Second, the lack of histopathologic reevaluation when prostate biopsies were not performed within the Netherlands Cancer Institute and Amsterdam University Medical Center may have influenced the ISUP GG and potentially our results. Furthermore, given that PSMA PET/CT scans were performed in several hospitals, scan protocols may have differed, which might have influenced our findings. In addition, multiple PSMA radiotracers were used within this cohort. Since experience with particular PSMA radiotracers is essential for interpreting scans, the variety of tracers used may have influenced the assessments (*24*). Finally, because of the lack of histopathologic confirmation, it remains unclear whether these PSMA-avid metastases were indeed PCa metastases. Considering the limitations discussed, future prospective studies are needed to further investigate the diagnostic value of PSMA PET/CT within this specific yet important patient population.

## CONCLUSION

PSMA PET/CT is of diagnostic value in men with newly diagnosed unfavorable intermediate-risk PCa. Our data show that nearly 1 in 10 men who underwent metastatic screening with PSMA PET/CT showed metastatic disease. Especially men with more advanced radiologic tumor stages and higher percentages of positive prostate biopsies might benefit most from PSMA-based metastatic screening. On the basis of our analyses, further stratification of unfavorable intermediate-risk PCa patients using the proposed Prostate Cancer Network Netherlands subclassification could aid in identifying those patients at risk of having metastatic disease on PSMA PET/CT. However, given the paucity of data on the diagnostic value of PSMA PET/CT within this distinct patient population, further research is needed to support and externally validate our findings.

## DISCLOSURE

No potential conflict of interest relevant to this article was reported.

## KEY POINTS

**QUESTION:** Should PSMA PET/CT be recommended in men with newly diagnosed unfavorable intermediate-risk PCa?

**PERTINENT FINDINGS:** In a retrospective analysis with 396 newly diagnosed unfavorable intermediate-risk PCa patients, PSMA-expressing metastases were observed in 37 (9.3%) men. A radiologically more advanced stage of disease on MRI and a higher percentage of positive prostate biopsies were found to be independently associated with the presence of PSMA-expressing metastases.

**IMPLICATIONS FOR PATIENT CARE:** Further stratification of unfavorable intermediate-risk PCa patients using the proposed Prostate Cancer Network Netherlands subclassification could aid in identifying those patients at risk of having metastatic disease on PSMA PET/CT.

## REFERENCES


1. Hofman MS, Lawrentschuk N, Francis RJ, et al. Prostate-specific membrane antigen PET-CT in patients with high-risk prostate cancer before curative-intent surgery or radiotherapy (proPSMA): a prospective, randomised, multicentre study. *Lancet.* 2020;395:1208–1216.
2. Donswijk ML, van Leeuwen PJ, Vegt E, et al. Clinical impact of PSMA PET/CT in primary prostate cancer compared to conventional nodal and distant staging: a retrospective single center study. *BMC Cancer.* 2020;20:723.
3. Yaxley JW, Raveenthiran S, Nouhaud FX, et al. Risk of metastatic disease on $^{68}$gallium-prostate-specific membrane antigen positron emission tomography/computed

tomography scan for primary staging of 1253 men at the diagnosis of prostate cancer. *BJU Int.* 2019;124:401–407.
4. Rogasch JM, Cash H, Zschaeck S, et al. Ga-68-PSMA PET/CT in treatment-naïve patients with prostate cancer: which clinical parameters and risk stratification systems best predict PSMA-positive metastases? *Prostate.* 2018;78:1103–1110.
5. Dekalo S, Kuten J, Campbell J, et al. $^{68}$Ga-prostate-specific membrane antigen positron emission tomography/computed tomography for patients with favorable intermediate-risk prostate cancer. *Can Urol Assoc J.* 2022;16:E381–E385.
6. Chikatamarla VA, Okano S, Jenvey P, et al. Risk of metastatic disease using [$^{18}$F]PSMA-1007 PET/CT for primary prostate cancer staging. *EJNMMI Res.* 2021;11:128.
7. Mohler JL, Antonarakis ES, Armstrong AJ, et al. Prostate cancer, version 2.2019, NCCN clinical practice guidelines in oncology. *J Natl Compr Canc Netw.* 2019; 17:479–505.
8. Sanda MG, Cadeddu JA, Kirkby E, et al. Clinically localized prostate cancer: AUA/ASTRO/SUO guideline. Part I: risk stratification, shared decision making, and care options. *J Urol.* 2018;199:683–690.
9. Jadvar H, Calais J, Fanti S, et al. Appropriate use criteria for prostate-specific membrane antigen PET imaging. *J Nucl Med.* 2022;63:59–68.
10. Meijer D, de Barros HA, van Leeuwen PJ, et al. The predictive value of preoperative negative prostate specific membrane antigen positron emission tomography imaging for lymph node metastatic prostate cancer. *J Urol.* 2021;205:1655–1662.
11. Barentsz JO, Richenberg J, Clements R, et al. ESUR prostate MR guidelines 2012. *Eur Radiol.* 2012;22:746–757.
12. Turkbey B, Rosenkrantz AB, Haider MA, et al. Prostate imaging reporting and data system version 2.1: 2019 update of prostate imaging reporting and data system version 2. *Eur Urol.* 2019;76:340–351.
13. de Rooij M, Israël B, Tummers M, et al. ESUR/ESUI consensus statements on multi-parametric MRI for the detection of clinically significant prostate cancer: quality requirements for image acquisition, interpretation and radiologists' training. *Eur Radiol.* 2020;30:5404–5416.
14. van Leenders GJLH, van der Kwast TH, Grignon DJ, et al. The 2019 International Society of Urological Pathology (ISUP) consensus conference on grading of prostatic carcinoma. *Am J Surg Pathol.* 2020;44:e87–e99.
15. Ceci F, Oprea-Lager DE, Emmett L, et al. E-PSMA: the EANM standardized reporting guidelines v1.0 for PSMA-PET. *Eur J Nucl Med Mol Imaging.* 2021;48:1626–1638.
16. Haller S. The concept of "number needed to image." *AJNR.* 2017;38:E79–E80.
17. de Feria Cardet RE, Hofman MS, Segard T, et al. Is prostate-specific membrane antigen positron emission tomography/computed tomography imaging cost-effective in prostate cancer: an analysis informed by the proPSMA trial. *Eur Urol.* 2021;79:413–418.
18. Cytawa W, Seitz AK, Kircher S, et al. $^{68}$Ga-PSMA I&T PET/CT for primary staging of prostate cancer. *Eur J Nucl Med Mol Imaging.* 2020;47:168–177.
19. Kulkarni SC, Sundaram PS, Padma S. In primary lymph nodal staging of patients with high-risk and intermediate-risk prostate cancer, how critical is the role of gallium-68 prostate-specific membrane antigen positron emission tomography-computed tomography? *Nucl Med Commun.* 2020;41:139–146.
20. Simsek DH, Sanli Y, Engin MN, Erdem S, Sanli O. Detection of metastases in newly diagnosed prostate cancer by using $^{68}$Ga-PSMA PET/CT and its relationship with modified D'Amico risk classification. *Eur J Nucl Med Mol Imaging.* 2021;48: 1639–1649.
21. Kopp D, Kopp J, Bernhardt E, et al. $^{68}$Ga-prostate-specific membrane antigen positron emission tomography-computed tomography-based primary staging and histological correlation after extended pelvic lymph node dissection in intermediate-risk prostate cancer. *Urol Int.* 2022;106:56–62.
22. Arnfield EG, Thomas PA, Roberts MJ, et al. Clinical insignificance of [$^{18}$F]PSMA-1007 avid non-specific bone lesions: a retrospective evaluation. *Eur J Nucl Med Mol Imaging.* 2021;48:4495–4507.
23. Grünig H, Maurer A, Thali Y, et al. Focal unspecific bone uptake on [$^{18}$F]-PSMA-1007 PET: a multicenter retrospective evaluation of the distribution, frequency, and quantitative parameters of a potential pitfall in prostate cancer imaging. *Eur J Nucl Med Mol Imaging.* 2021;48:4483–4494.
24. Hagens MJ, Oprea-Lager DE, Vis AN, et al. Reproducibility of PSMA PET/CT imaging for primary staging of treatment-naïve prostate cancer patients depends on the applied radiotracer: a retrospective study. *J Nucl Med.* 2022;63:1531–1536.
25. de Rooij M, Hamoen EH, Witjes JA, Barentsz JO, Rovers MM. Accuracy of magnetic resonance imaging for local staging of prostate cancer: a diagnostic meta-analysis. *Eur Urol.* 2016;70:233–245.
26. Meijer D, van Leeuwen PJ, Donswijk ML, et al. Predicting early outcomes in patients with intermediate- and high-risk prostate cancer using prostate-specific membrane antigen positron emission tomography and magnetic resonance imaging. *BJU Int.* 2022;129:54–62.
27. Aydos U, Çetin S, Akdemir ÜÖ, et al. The role of histopathological and biochemical parameters for predicting metastatic disease on $^{68}$Ga-PSMA-11 PET in prostate cancer. *Prostate.* 2021;81:1337–1348.
28. Yoo S, Suh J, Park J, et al. Proportion of cores with the highest Gleason grade group among positive cores on prostate biopsy: does this affect the probability of upgrading or downgrading? *Scand J Urol.* 2019;53:372–377.
29. Goel S, Shoag JE, Gross MD, et al. Concordance between biopsy and radical prostatectomy pathology in the era of targeted biopsy: a systematic review and meta-analysis. *Eur Urol Oncol.* 2020;3:10–20.

# Safety and Efficacy of [$^{177}$Lu]-PSMA-I&T Radioligand Therapy in Octogenarians with Metastatic Castration-Resistant Prostate Cancer: Report on 80 Patients over the Age of 80 Years

Robert Tauber[1], Karina Knorr[2], Margitta Retz[1], Isabel Rauscher[2], Sonia Grigorascu[2], Kimberley Hansen[2], Calogero D'Alessandria[2], Hans-Jürgen Wester[3], Jürgen Gschwend[1], Wolfgang Weber[2], Matthias Eiber[2], and Thomas Langbein[2]

[1]*Department of Urology, Klinikum Rechts der Isar, School of Medicine, Technical University of Munich, Munich, Germany;* [2]*Department of Nuclear Medicine, Klinikum Rechts der Isar, School of Medicine, Technical University of Munich, Munich, Germany; and* [3]*Chair of Radiopharmacy, Technical University of Munich, Munich, Germany*

$^{177}$Lu-labeled prostate-specific membrane antigen (PSMA) radioligand therapy (RLT) is a new treatment option for metastatic castration-resistant prostate cancer (mCRPC). Its low toxicity profile favors use in elderly patients or in patients with critical comorbidities. The purpose of this analysis was to evaluate the efficacy and safety of [$^{177}$Lu]-PSMA RLT in mCRPC patients at least 80 y old. **Methods:** Eighty mCRPC patients at least 80 y old underwent [$^{177}$Lu]-PSMA-I&T RLT and were retrospectively selected. The patients were previously treated by androgen receptor–directed therapy, received taxane-based chemotherapy, or were chemotherapy-ineligible. The best prostate-specific antigen (PSA) response was calculated, as well as clinical progression-free survival (cPFS) and overall survival (OS). Toxicity data were acquired until 6 mo after the last treatment cycle. **Results:** Of 80 patients, 49 (61.3%) were chemotherapy-naïve and 16 (20%) had visceral metastases. The median number of previous mCRPC treatment regimens was 2. In total, 324 cycles (median, 4 cycles; range, 1–12) with a median cumulative activity of 23.8 GBq (interquartile range, 14.8–42.2) were applied. A PSA decline of 50% was achieved in 37 (46.3%) patients. Chemotherapy-naïve patients showed higher 50% PSA response rates than chemotherapy-pretreated patients (51.0% vs. 38.7%, respectively). Overall, median cPFS and OS were 8.7 and 16.1 mo, respectively. The median cPFS and OS of chemotherapy-naïve patients were significantly longer than those of chemotherapy-pretreated patients (10.5 vs. 6.5 mo and 20.7 vs. 11.8 mo, respectively, $P < 0.05$). A lower hemoglobin level and higher lactate dehydrogenase level at baseline were independent predictors of shorter cPFS and OS. Treatment-emergent grade 3 toxicities were anemia in 4 patients (5%), thrombocytopenia in 3 patients (3.8%), and renal impairment in 4 patients (5%). No nonhematologic grade 3 and no grade 4 toxicities were observed. The most frequent clinical side effects were grade 1–2 xerostomia, fatigue, and inappetence. **Conclusion:** [$^{177}$Lu]-PSMA-I&T RLT in mCRPC patients at least 80 y old is safe and effective, comparable to previously published data on non–age-selected cohorts with a low rate of high-grade toxicities. Chemotherapy-naïve patients showed a better and longer response to therapy than taxane-pretreated patients. [$^{177}$Lu]-PSMA RLT seems to be a meaningful treatment option for older patients.

**Key Words:** metastatic castration-resistant prostate cancer; radioligand therapy; prostate-specific membrane antigen; [$^{177}$Lu]-PSMA; elderly patients

Received Dec. 6, 2022; revision accepted Mar. 14, 2023.
For correspondence or reprints, contact Robert Tauber (robert.tauber@tum.de).
Published online Jun. 15, 2023.


**J Nucl Med 2023; 64:1244–1251**
DOI: 10.2967/jnumed.122.265259

Octogenarians represent a considerable proportion of patients with prostate cancer (*1*). Future projections indicate a growth due to the global increase in life expectancy and more life-prolonging treatments (*2*). Management of late-stage disease in elderly men is challenging given the reduced normal organ function or higher frequency of drug interactions related to treatment of comorbidities (*3*). Elderly patients have higher incidences of cardiovascular diseases, impaired renal function, and a lower bone marrow function. Therapy-related side effects are often less tolerated by senescent patients (*4*). In some age-stratified analyses of cytotoxic and androgen receptor–targeted agents in older patients with metastatic castration-resistant prostate cancer (mCRPC), increased toxicity rates were observed, necessitating dose reductions (*5*). Enzalutamide can be associated with cognitive impairment (*6*), and cabazitaxel has shown higher rates of adverse events in men older than 75 y (*7*).

In clinical studies, often only the fittest of elderly patients are included (*8*). Consequently, despite the fact that approximately 42% of cancer patients are at least 70 y old, they comprise less than 10% of the patients in clinical trials (*9*). [$^{177}$Lu]-labeled prostate-specific membrane antigen (PSMA) radioligand therapy (RLT) has demonstrated a substantial antitumor effect and low rates of toxicities in mCRPC. However, in the pivotal VISION trial, only 1.7% ($n = 14/831$) of patients were 85 y or older (*10*).

The primary aim of this retrospective analysis was to assess the efficacy and safety of PSMA RLT in octogenarian mCRPC patients. Response and toxicity rates in chemotherapy-pretreated and chemotherapy-naïve patients were compared, and predictors for clinical progression-free survival (cPFS) and overall survival (OS) were investigated.

## MATERIALS AND METHODS

### Patients and Data Collection

mCRPC patients aged 80 y or older and treated with [$^{177}$Lu]-PSMA-I&T RLT between October 2014 and February 2022 were identified from our institutional database. [$^{177}$Lu]-PSMA-I&T was prepared according to good manufacturing practices and the German Medicinal Products Act (Arzneimittelgesetz §13 2b). All patients gave written informed

consent and were treated under the conditions of Declaration of Helsinki article 37, "Unproven Interventions in Clinical Practice." The responsible institutional review board approved the retrospective analysis (reference 115/18S).

Institutional eligibility criteria were previously published and were in accordance with the interdisciplinary German guideline for the treatment of prostate cancer after interdisciplinary tumor board decisions (*11–13*). Briefly, the study included mCRPC patients with pretreatment consisting of at least 1 line of androgen receptor–targeted agents and at least 1 line of taxane-based chemotherapy using a docetaxel or cabazitaxel regimen. Furthermore, patients who were ineligible for taxane-based chemotherapy because of poor Eastern Oncology Cooperative Group (ECOG) performance status (PS), higher-grade comorbidities, or refusal of chemotherapy were included in this retrospective data collection. Pretherapeutic PSMA PET was performed, and uptake was required to be higher in the tumor lesions than in the liver.

### [$^{177}$Lu]-PSMA RLT Procedure

Radiolabeling of [$^{177}$Lu]-PSMA-I&T and administration of RLT were performed as previously reported (*11,12,14*). Patients usually underwent RLT at 6-wk intervals at a standard dose of 7.4 GBq. Treatment could be intensified with doses of up to 9 GBq or a 4-wk interval, or dosing could be reduced to 6 GBq depending on clinical factors such as organ function (e.g., impaired kidney or bone marrow function) and high or low tumor load, similar to other reports (*15,16*). The patients underwent PSMA PET/CT every 12 wk during treatment.

Intravenous treatment with [$^{177}$Lu]-PSMA-I&T was continued up to a maximum of 12 cycles in patients with absence of radiographic or clinical progression and lack of severe toxicity. Androgen-deprivation therapy was continued during [$^{177}$Lu]-PSMA-I&T RLT (Fig. 1). No other systemic treatments were allowed.

### Efficacy and Safety Assessment

Assessment of treatment efficacy was based on best prostate-specific antigen (PSA) response (PSA decline of ≥ 0%, ≥50%, or ≥90% during treatment). PSA progression-free survival (PFS) according to the recommendations of the Prostate Cancer Trials Clinical Working Group 3 (*17*) and OS were calculated. cPFS was defined as the time from treatment initiation to clinical or imaging progression or death, as previously published (*12*). Clinical progression included disease-related symptoms, reduced ECOG PS, and new cancer-related complications. Treatment-related toxicity was documented until 6 mo after the last RLT cycle and graded according to the Common Terminology Criteria for Adverse Events (version 5.0). Changes in ECOG PS after RLT were recorded. Assessment of renal function was based on the estimated glomerular filtration rate using the Chronic Kidney Disease Epidemiology Collaboration 2012 equation.

### Statistical Analyses

Descriptive analyses were used to assess PSA response. The Kaplan–Meier curve method with corresponding 95% CI was used to analyze PSA PFS, cPFS, and OS. In a subgroup analysis, chemotherapy-naïve and chemotherapy-pretreated patients were compared for treatment outcome parameters.

Previously reported baseline parameters were used to evaluate potential predictions of cPFS and OS using the Cox proportional-hazards

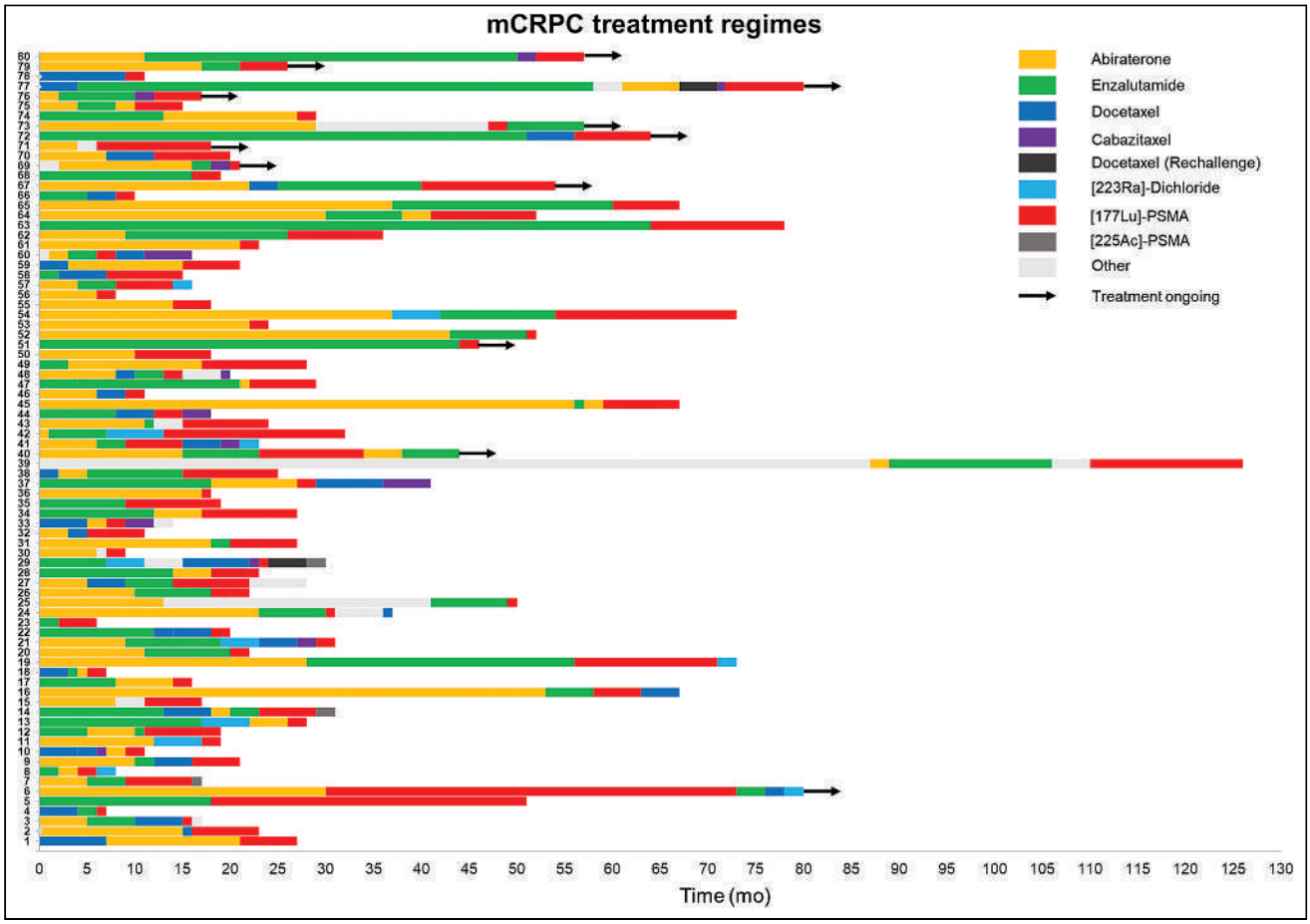


**FIGURE 1.** Swimmer plot of mCRPC treatments. Length of each bar symbolizes duration for which patient was on specific treatment.

regression model. The following baseline variables were investigated: PS, PSA level, hemoglobin level, alkaline phosphatase level, lactate dehydrogenase (LDH) level, time between initial diagnosis and RLT initiation, presence of bone metastases, presence of visceral metastases, prior taxane-based chemotherapy, and primary metastatic disease. Only variables with significant differences from the univariate model ($P < 0.05$) were included in the multivariable analysis. Results are reported as hazard ratios (HRs) with 95% CIs.

A matched-pair subanalysis of 30 chemotherapy-naïve versus 30 chemotherapy-pretreated patients was conducted to adjust for possible bias at baseline. One patient of the chemotherapy-pretreated cohort could not be matched. Matching parameters were clinical and imaging-based parameters, consisting of time between first diagnosis and initiation of [$^{177}$Lu]-PSMA-I&T RLT, initial Gleason score/International Society of Urological Pathology grade, primary metastatic disease, pretreatments for mCRPC, PSA at diagnosis and at RLT initiation, baseline AP and baseline LDH levels, and tumor distribution on baseline PSMA PET/CT. The patient characteristics of chemotherapy-naïve and chemotherapy-pretreated subgroups were compared using the Fisher exact test and the Mann–Whitney *U* test. Results were reported as frequency (percentage), median with 25th–75th percentiles, or median with range. A 2-sided *P* value of less than 0.05 was considered statistically significant. Statistical analysis was performed using SPSS software (version 24; IBM).

## RESULTS

### Patient Population and Treatment with [$^{177}$Lu]-PSMA-I&T

Overall, 80 patients with mCRPC were analyzed. Their median age was 82 y (range, 80–91 y) at the initiation of [$^{177}$Lu]-PSMA-I&T RLT. The median time between initial diagnosis and the start of RLT was 9 y (range, 1–25 y). Of 80 patients, 49 (61.3%) were chemotherapy-naïve. A median of 2 (range, 1–6) previous mCRPC treatment regimens had been applied, and 24 (30%) patients had received 3 or more mCRPC treatments before RLT. A swimmer plot was constructed to visualize mCRPC therapy lines (Fig. 1). Baseline characteristics, including site of metastases, baseline PSA levels, and details for the chemotherapy-naïve and chemotherapy-pretreated subgroups are presented in Table 1.

In total, 324 cycles of [$^{177}$Lu]-PSMA-I&T had been administered, with a median of 4 (interquartile range [IQR], 2–6) cycles per

**TABLE 1**
Baseline Patient Characteristics

| Characteristic | Entire cohort | Chemotherapy-naïve patients | Chemotherapy-pretreated patients |
|---|---|---|---|
| Patients | 80 | 49 | 31 |
| Age (y) | 82 (range, 80–91) | 83 (range, 80–91) | 81 (range 80–90) |
| iPSA (ng/mL) | 18.6 (IQR, 7.9–61.8) | 14.0 (IQR, 6.2–30.0) | 23.0 (IQR, 12.5–71.5) |
| Time between initial diagnosis and start of [$^{177}$Lu]-PSMA (y) | 9 (range, 1–25) | 9 (range, 1–25) | 8 (range, 1–20) |
| Gleason score | 8 (range, 5–10) | 8 (range, 6–10) | 8 (range, 5–10) |
| Primary metastasized | 24 (30%) | 15 (30.6%) | 9 (29.0%) |
| mCRPC pretreatments | 2 (range, 1–6) | 2 (range, 1–6) | 3 (1–5) |
| 3 or more prior mCRPC lines | 24 (30%) | 7 (14.3%) | 17 (54.8%) |
| Baseline ECOG | | | |
| 0 | 21 (26.6%) | 12 (24.5%) | 9 (29.0%) |
| 1 | 51 (63.8%) | 32 (65.3%) | 19 (61.3%) |
| 2 | 8 (10.0%) | 5 (10.2%) | 3 (9.7%) |
| Baseline miTNM | | | |
| N1 | 42 (52.5%) | 23 (46.9%) | 19 (61.3%) |
| M1a | 46 (57.5%) | 25 (51.0%) | 21 (67.7%) |
| M1b | 73 (91.3%) | 44 (89.8%) | 29 (93.5%) |
| M1c | 16 (20.0%) | 4 (8.2%) | 12 (38.7) |
| Baseline LDH (U/L) | 253 (IQR, 216.0–309.0) | 253 (IQR, 219.8–300.3) | 255 (IQR, 213.5–331.5) |
| Baseline AP (U/L) | 102.5 (IQR, 72.5–146) | 116 (IQR, 85–215) | 85 (IQR, 59–135) |
| Baseline PSA (ng/mL) | 71.8 (IQR, 18.3–189.4) | 108.0 (77.0–146.0) | 149 (IQR, 21.1–348.5) |
| Cycles | 4 (range, 1–12) | 4 (range, 1–12) | 3 (range, 1–8) |
| Dose per cycle (GBq) | 7.3 (IQR, 7.1–7.5) | 7.4 (IQR, 7.0–7.5) | 7.3 (IQR, 7.1–7.4) |
| Cumulative activity (GBq) | 23.8 (IQR, 14.8–42.2) | 26.8 (IQR, 15.0–44.7) | 21.8 (IQR, 14.7–36.0) |
| Therapy duration (mo) | 4 (IQR, 1–7) | 4 (IQR, 1–10) | 1 (1–6) |
| Follow-up time (mo) | 11.4 (IQR, 5.8–16.7) | 13.4 (IQR, 8.9–19.7) | 7.7 (3.4–11.7) |

iPSA = initial PSA; miTNM = molecular imaging TNM; AP = alkaline phosphatase.
Qualitative data are number and percentage; continuous data are median and range or IQR.

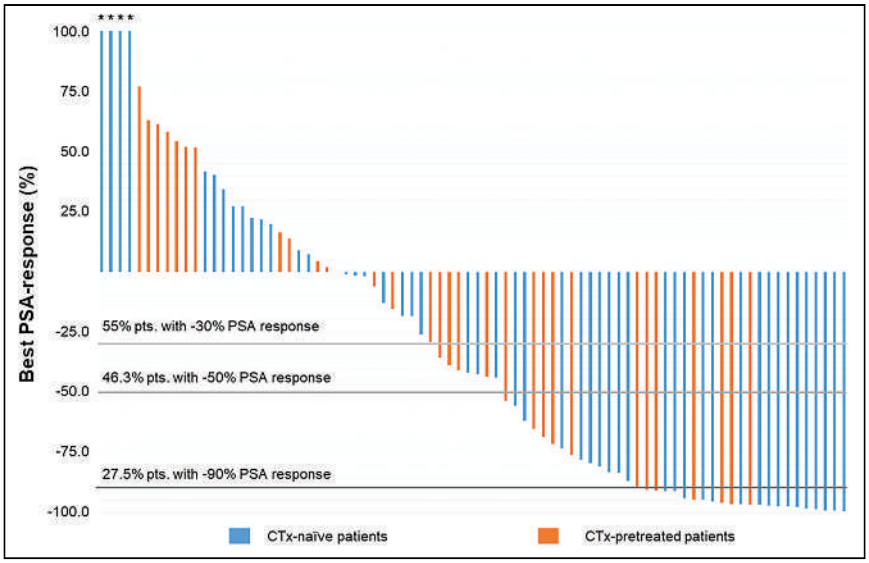


**FIGURE 2.** Waterfall plot of best PSA response during [$^{177}$Lu]-PSMA-I&T RLT. Blue and orange bars indicate chemotherapy-naïve and chemotherapy-pretreated patients, respectively. *PSA increase of >100%. CTx = chemotherapy; pts. = patients.

patient, a median dose of 7.3 GBq per cycle (IQR, 7.1–7.5 GBq), and a median cumulative activity of 23.8 GBq (IQR, 14.8–42.2 GBq). The median duration of RLT was 4 mo (IQR, 1–7 mo), and the median follow-up time was 11.4 mo (IQR, 5.8–16.7 mo). Supplemental Figure 1 shows details of the RLT cycles of the cohort (supplemental materials are available at http://jnm.snmjournals.org).

On the basis of the predefined criteria, 30 chemotherapy-pretreated patients could be matched to 30 chemotherapy-naïve patients from the total cohort of 80 patients. The baseline and treatment characteristics of the matched-pair subcohorts are shown in Supplemental Table 1.

### Treatment Efficacy and Clinical Outcomes

A maximum PSA response of at least 30%, at least 50%, and at least 90% was achieved in 44 (55%), 37 (46.3%), and 22 (27.5%) of the patients, respectively (Fig. 2). A trend toward a higher PSA response in chemotherapy-naïve than in chemotherapy-pretreated patients was observed but was not statistically significant (e.g., ≥50% PSA decline in 51.0% vs. 38.7%, respectively; Supplemental Fig. 2). This tendency was confirmed in the matched-pair subanalysis (Supplemental Table 2).

Median PSA PFS, cPFS, and OS were 6.1 mo (95% CI, 3.7–9.2 mo), 8.7 mo (95% CI, 5.9–10.5 mo), and 16.1 mo (95% CI, 13.3–20.9 mo), respectively. Median cPFS and median OS were significantly longer in chemotherapy-naïve patients than in chemotherapy-pretreated patients (10.5 vs. 6.5 mo and 20.7 vs. 11.8 mo; $P = 0.01$ and $<0.01$, respectively). A strong trend toward a longer PSA PFS in chemotherapy-naïve patients than in chemotherapy-pretreated patients was also observed but was not statistically significant (6.2 vs. 3.8 mo, respectively; $P = 0.09$) (Fig. 3). The results for PSA PFS, cPFS, and OS were comparable in the matched-pair subanalysis (Supplemental Fig. 2).

Overall, 5 (6.3%) patients improved from ECOG PS 1 to 0. PS was stable in 56 (70.0%) patients (in 11 [13.8%] patients with ECOG 0, 37 [46.3%] patients with ECOG 1, and 8 [10.0%] patients with ECOG 2) after RLT. PS worsened by 1 and 2 grades in 14 (17.5%) and 4 (5%) patients after RLT, respectively. In 2 patients, RLT was stopped at the patient's request, and in 7 patients RLT was stopped because of a worsening of the patient's general condition or other reasons.

### Predicting Factors in OS and cPFS

The results of the univariate and multivariable analyses are shown in Table 2. For OS, a shorter time from initial diagnosis (HR, 2.1 [95% CI, 1.0–4.2]; $P = 0.04$), a hemoglobin level below the median of 11.9 g/dL (HR, 2.8 [95% CI, 1.4–5.6]; $P < 0.01$), a LDH level above the median of 253 U/L (HR, 3.3 [95% CI, 1.6–6.9]; $P < 0.01$), and pretreatment with taxane-based chemotherapy (HR, 3.0 [95% CI, 1.6–5.7]; $P < 0.01$) were associated with a worse outcome on univariate analysis. However, in a multivariable Cox regression model, only a lower hemoglobin level (HR, 2.2 [95% CI, 1.1–4.4]; $P = 0.02$), a higher LDH level (HR, 2.3 [95% CI,

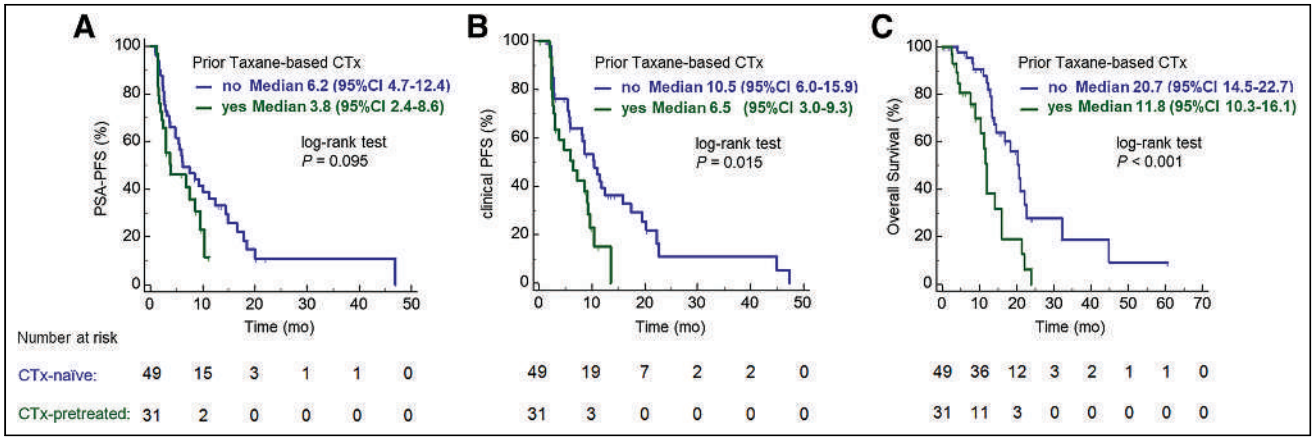


**FIGURE 3.** PSA PFS (A), cPFS (B), and OS (C) in chemotherapy-naïve patients ($n = 49$) vs. chemotherapy-pretreated patients ($n = 31$). CTx = chemotherapy.

**TABLE 2**
Univariate and Multivariable Analysis of OS and cPFS in Entire Cohort (80 Patients)

| Subgroup | Univariate analysis | | | | | | Multivariable analysis | | | | | |
|---|---|---|---|---|---|---|---|---|---|---|---|---|
| | OS | | | cPFS | | | OS | | | cPFS | | |
| | HR | 95% CI | *P* | HR | 95% CI | *P* | HR | 95% CI | *P* | HR | 95% CI | *P* |
| Baseline ECOG > 0 | 1.4 | 0.6–3.1 | 0.46 | 0.8 | 0.4–1.4 | 0.38 | NA | NA | | NA | NA | |
| Baseline PSA > 71.8 ng/mL | 1.6 | 0.8–3.1 | 0.12 | 1.3 | 0.7–2.2 | 0.38 | NA | NA | | NA | NA | |
| Baseline hemoglobin < 11.9 g/dL | 2.8 | 1.4–5.6 | <0.01 | 2.5 | 1.4–4.3 | <0.01 | 2.2 | 1.1–4.4 | 0.02 | 2.2 | 1.2–3.9 | <0.01 |
| Time from diagnosis to first [$^{177}$Lu]-PSMA-I&T therapy < 9 y | 2.1 | 1.0–4.2 | 0.04 | 2.0 | 1.1–3.4 | 0.02 | 1.7 | 0.9–3.5 | 0.13 | 1.7 | 1.0–3.0 | 0.07 |
| Baseline bone metastases present | 1.6 | 0.6–4.6 | 0.36 | 1.5 | 0.6–3.6 | 0.34 | NA | NA | | NA | NA | |
| Baseline visceral metastases present | 1.9 | 0.9–3.9 | 0.11 | 1.9 | 0.9–4.0 | 0.07 | NA | NA | | NA | NA | |
| Baseline alkaline phosphatase > 102.5 U/L | 1.3 | 0.7–2.4 | 0.43 | 1.2 | 0.7–2.0 | 0.55 | NA | NA | | NA | NA | |
| Primary metastatic disease | 0.9 | 0.5–1.8 | 0.85 | 1.0 | 0.6–1.8 | 1.0 | NA | NA | | NA | NA | |
| LDH > 253 U/L | 3.3 | 1.6–6.9 | <0.01 | 2.2 | 1.3–3.9 | <0.01 | 2.3 | 1.1–5.0 | 0.03 | 1.8 | 1.0–3.2 | 0.04 |
| Prior taxane-based chemotherapy received | 3.0 | 1.6–5.7 | <0.01 | 2.0 | 1.1–3.7 | 0.02 | 2.0 | 1.0–4.0 | 0.04 | 1.7 | 0.9–3.1 | 0.09 |

1.1–5.0]; $P = 0.03$), and prior taxane-based chemotherapy (HR, 2.0 [95% CI, 1.0–4.0]; $P = 0.04$) remained independent predictors of a shorter OS.

For shorter cPFS, significant independent predictors were a lower baseline hemoglobin level (HR, 2.2 [95% CI, 1.3–3.9]; $P < 0.01$) and a higher baseline LDH level (HR, 1.8 [95% CI, 1.0–3.2]; $P = 0.04$). A shorter time from initial diagnosis and pretreatment with taxane-based chemotherapy could not be confirmed as a significant predictor of a shorter cPFS on multivariable analysis. Univariate and multivariable analyses of OS and cPFS in the chemotherapy-naïve and chemotherapy-pretreated patients are presented in Supplemental Tables 3 and 4.

### Toxicity

Treatment with [$^{177}$Lu]-PSMA-I&T was well tolerated, with a low number of treatment-emergent grade 3 adverse events, such as grade 3 anemia in 4 (5%) patients (Table 3). No grade 4 adverse events occurred. The most frequent treatment-emergent low-grade adverse events were hematotoxicity, in particular anemia in 46% of the patients and thrombocytopenia in 16%. Renal toxicity of grade 3 or less, based on the estimated glomerular filtration rate changes, occurred in 20 (25%) of 80 patients, and grade 3 renal toxicity occurred in 4 (5%) patients. In 3 (3.8%) of 80 patients, a treatment-emergent decline in renal function led to termination of [$^{177}$Lu]-PSMA-I&T RLT. The most frequent nonhematologic side effects were xerostomia of grade 2 or less and fatigue in 32% of the patients. The frequency of adverse events was similar between chemotherapy-naïve and chemotherapy-pretreated patients.

## DISCUSSION

We retrospectively report on the treatment outcome and safety of [$^{177}$Lu]-PSMA-I&T RLT in 80 mCRPC octogenarians. The patients underwent a median of 4 cycles with a favorable safety profile and a low frequency (<10%) of higher-grade toxicities. Rates of 50% PSA decline (46.3%), median PSA PFS (6.1 mo), and OS (16.1 mo) were comparable to those in a non–age-selected population. A more favorable outcome was observed in chemotherapy-naïve patients.

So far, studies on PSMA-targeted RLT report data on patients with a median age ranging between 70 and 72 y (*10,12,16*). Specifically, in the VISION trial only 1.7% ($n = 14/831$) of patients were at the age of 85 y or older (*10*). Because of reduced organ function and capability to tolerate side effects, oncologic treatments in senescent patients are challenging. For our retrospective analysis, we specifically selected octogenarians with a median age of 82 y at treatment initiation. In this selected group, treatment with [$^{177}$Lu]-PSMA-I&T was overall safe and well tolerated, comparable to previously published data on RLT with [$^{177}$Lu]-PSMA (*10,12,16*).

We acknowledge a high variation in reported toxicity rates in the literature for PSMA RLT in non–age-selected cohorts. Rates of anemia, for example, have varied: 19% of the patients in the TheraP-trial, 32% of the patients in the VISION trial, and 36% of the patients in a retrospective single-center study (*10,12,18*). The occurrence of posttherapeutic fatigue ranges between 20% and 70%, similar to xerostomia, which was observed in 24%–87% (*10,12,16*). These distinct variations most likely underline differences between retrospective and prospective studies and the limited comparability and standardization of subjective, patient-reported symptoms.

Given their reduced organ function, comorbidities, and impaired general condition, octogenarians are frequently designated as unfit for chemotherapy. We specifically investigated and compared side effects in chemotherapy-naïve and chemotherapy-pretreated patients

**TABLE 3**
[$^{177}$Lu]-PSMA-I&T RLT Emergent Toxicities

| Toxicity | Entire cohort | Chemotherapy-naïve patients | Chemotherapy-pretreated patients | *P** |
|---|---|---|---|---|
| Hematologic toxicities | | | | |
| Anemia | | | | |
| All grades | 37 (46.3%) | 23 (46.9%) | 14 (45.2%) | 0.64 |
| Grade 3 or 4 | 4 (5.0%) | 1 (2.0) | 3 (9.7%) | |
| Leukocytopenia | | | | |
| All grades | 12 (15.0%) | 5 (10.2%) | 7 (22.6%) | 0.18 |
| Grade 3 or 4 | 0 (0%) | 0 (0%) | 0 (0%) | |
| Thrombocytopenia | | | | |
| All grades | 13 (16.3%) | 7 (14.3%) | 6 (19.4%) | 0.20 |
| Grade 3 or 4 | 3(3.8%) | 1 (2.0%) | 2 (6.5%) | |
| Renal toxicity | | | | |
| Estimated glomerular filtration rate | | | | |
| All grades | 20 (25%) | 15 (30.6%) | 5 (16.1%) | 0.29 |
| Grade 3 or 4 | 4 (5.0%) | 2 (4.1%) | 2 (6.5%) | |
| Nonhematologic toxicities | | | | |
| Xerostomia | | | | |
| All grades | 26 (32.5%) | 19 (38.8%) | 7 (22.6%) | 0.39 |
| Grade 3 | 0 (0%) | 0 (0%) | 0 (0%) | |
| Fatigue | | | | |
| All grades | 26 (32.5%) | 14 (28.6%) | 12 (38.7%) | 0.53 |
| Grade 3 or 4 | 0 (0%) | 0 (0%) | 0 (0%) | |
| Loss of appetite | | | | |
| All grades | 16 (20.0%) | 11 (22.4%) | 5 (16.1%) | 0.79 |
| Grade 3 or 4 | 0 (0%) | 0 (0%) | 0 (0%) | |
| Diarrhea | | | | |
| All grades | 4 (5.0%) | 4 (8.2%) | 0 (0%) | 0.70 |
| Grade 3 or 4 | 0 (0%) | 0 (0%) | 0 (0%) | |
| Constipation | | | | |
| All grades | 7 (8.8%) | 6 (12.2%) | 1 (3.2%) | 0.91 |
| Grade 3 or 4 | 0 (0%) | 0 (0%) | 0 (0%) | |
| Nausea | | | | |
| All grades | 2 (2.5%) | 2 (4.1%) | 1 (3.2%) | 0.89 |
| Grade 3 or 4 | 0 (0%) | 0 (0%) | 0 (0%) | |

*$\chi^2$ test.

and observed no substantial differences. A recent retrospective analysis of 83 chemotherapy-pretreated versus 84 chemotherapy-naïve non–age-selected mCRPC patients reported equal rates of side effects in both groups (*19*).

In comparison to taxane-based chemotherapy, the rates of side effects of [$^{177}$Lu]-PSMA-I&T RLT are similar, with a trend toward a lower number of high-grade toxicities and lower rates of treatment discontinuation. A multicenter study of docetaxel as the first mCRPC treatment line in a comparable patient cohort of 123 octogenarians (median age, 82 y) reported toxicity with grade 3–4 neutropenia in 10.6%, fatigue in 9.7%, and diarrhea in 4.1%, but toxicity-related treatment discontinuation occurred in 15.4% (*20*). In a smaller cohort, Wong et al. reported distinctly higher rates of grade 3–4 hematologic toxicity in 9 of 20 (45%) patients and hospitalization of 5 patients because of chemotherapy-related complications (*21*). In the TROPIC trial, mCRPC patients older than 75 y and pretreated with docetaxel ($n = 70$) showed higher rates of diarrhea and neutropenia after cabazitaxel than did younger patients ($n = 301$) (55.7% and 24.2% vs. 44.5% and 17.6%, respectively) (*7*). Consistent with that, multivariable analysis of data from the European early-access program for cabazitaxel showed higher age to be a predictor of neutropenia of grade 3 or higher (*22*).

Similar observations with higher rates of toxicities in elderly patients have been reported for other mCRPC treatments. For the androgen receptor–targeting agent abiraterone, slightly higher rates of cardiac disorders such as atrial fibrillation and tachycardia were observed in mCRPC patients older than 75 y (*5*), and more frequent toxicity-caused treatment discontinuation was observed in octogenarians (*23*). For enzalutamide, similar tendencies were reported in elderly patients (*24*).

Impaired renal function is a known comorbidity in elderly patients (*25*). Currently, the impact of [$^{177}$Lu]-PSMA RLT on renal function is not entirely clear. In early retrospective studies, no grade 3–4 renal toxicity was described (*11*). Assuming a similar delayed onset of kidney toxicity for [$^{177}$Lu]-PSMA RLT, as known from, for example, peptide receptor radionuclide therapy, the current study protocols and the limited life span of mCRPC patients might not adequately capture its potential long-term effects. For instance, adverse events in patients in the pivotal phase III (VISION) trial were detected only up to 30 d after the last administration (*10*). However, our group recently reported 3 mCRPC patients showing histopathologically confirmed radiation nephropathy after high cumulative doses of [$^{177}$Lu]-PSMA-I&T RLT (*26*). In the current study, 3 of 80 elderly patients eventually had to stop [$^{177}$Lu]-PSMA-I&T RLT because of progressive renal impairment.

A PSA decline of at least 50% in 37 (46.3%) patients, a median PSA PFS of 6.1 mo, and a median OS of 16.1 mo are in the range of reports for a general mCRPC population and document the high antitumor effect of [$^{177}$Lu]-PSMA RLT in elderly patients. Not unexpectedly, chemotherapy-naïve patients showed a significantly longer median cPFS and median OS of 10.5 and 20.7 mo, respectively. This finding was confirmed in a matched-pair subgroup analysis of 30 chemotherapy-naïve patients versus 30 chemotherapy-pretreated patients (median OS, 20.7 vs. 11.8 mo, respectively). Previously, Barber et al. reported similar differences for both groups (27.1 vs. 10.7 mo, respectively) in a general mCRPC cohort (*19*). These data compare well with docetaxel in a first-line mCRPC setting. In a similar patient cohort of 123 octogenarians (median age, 82 y), a PFS of 7 mo and a median OS of 20 mo were reported (*20*).

In our study, a lower hemoglobin level and a higher LDH level at treatment initiation were independent baseline predictors of both inferior cPFS and inferior OS, a finding that is in line with data on non–age-selected investigations (*12,27*). Likewise, prior taxane-based chemotherapy was associated with a poorer OS in a multivariable Cox regression model (*19*). The presence of visceral metastases, a significant predictor of OS in previous studies, was not related to OS in this analysis, possibly because of the limited number of patients.

The presented data have several limitations. The main limitation is the retrospective nature of the study, potentially missing side effects occurring outside the usual treatment and follow-up visits. Second, comparing rates of adverse events with data from the literature is prone to potential bias from different patient characteristics. Third, we could not perform further analysis with respect to the predictive nature of pretherapeutic PSMA PET, as patients in this cohort underwent PET with different PSMA ligands.

## CONCLUSION

[$^{177}$Lu]-PSMA-I&T RLT in mCRPC patients at least 80 y old is safe and effective, comparable to previously published data on non–age-selected cohorts with only a low rate of high-grade toxicities. Therefore, this treatment can be considered an alternative option in patients who are not eligible for taxane-based chemotherapy because of comorbidities or other relevant medical conditions. Similar to other agents, [$^{177}$Lu]-PSMA-I&T RLT showed higher rates of biochemical response and a longer duration of response in chemotherapy-naïve patients. A prospective evaluation in earlier stages of mCRPC is already being explored in different studies (e.g., PSMAfore and SPLASH) to better define the role of [$^{177}$Lu]-PSMA RLT in the therapy sequence of prostate cancer. The results might provide further insight into potential long-term toxicities (e.g., renal impairment), which are currently not fully known because of the limited life expectancy of mCRPC patients.

## DISCLOSURE

Robert Tauber reports prior consulting activities for AstraZeneca, Bayer, BMS, Eisei, EUSA, Ipsen, Janssen, MSD, Philogen, Roche, and Sanofi; travel support from Bayer, BMS, Ipsen, Janssen, and Roche; and owning shares of Bayer. Hans-Jürgen Wester and Matthias Eiber are named in a patent application for rhPSMA and received funding from Blue Earth Diagnostics Ltd. (BED), Oxford, U.K. (licensee for rhPSMA), as part of an academic collaboration. Hans-Jürgen Wester is a founder, shareholder, and advisory board member of Scintomics GmbH, Fuerstenfeldbruck, Germany. Matthias Eiber reports prior consulting activities for BED, Novartis, Telix, Progenics, Bayer, Point Biopharma, and Janssen. Thomas Langbein reports consulting activities for BED. No other potential conflict of interest relevant to this article was reported.

**KEY POINTS**

**QUESTION:** The purpose of this retrospective analysis was to evaluate the efficacy and safety of [$^{177}$Lu]-PSMA RLT in metastatic castration-resistant prostate cancer (mCRPC) patients at least 80 y old.

**PERTINENT FINDINGS:** In a retrospective analysis of patients at least 80 y old with mCRPC, [$^{177}$Lu]-PSMA RLT showed comparable efficacy and safety to the published data. In the total cohort, 46.3% of the patients had a PSA response of at least 50%. In the subgroup analysis, there was a certain but nonsignificant advantage for patients without prior chemotherapy (PSA response, 51.0% vs. 38.7%). The therapy was well tolerated by the elderly patients. Critical grade 3 side effects occurred only rarely (e.g., anemia, 5%). No grade 4 toxicity was observed.

**IMPLICATIONS FOR PATIENT CARE:** [$^{177}$Lu]-PSMA RLT seems to be a meaningful treatment option for older patients.

## REFERENCES


1. Scosyrev E, Messing EM, Mohile S, Golijanin D, Wu G. Prostate cancer in the elderly: frequency of advanced disease at presentation and disease-specific mortality. *Cancer.* 2012;118:3062–3070.
2. Ferlay J, Soerjomataram I, Dikshit R, et al. Cancer incidence and mortality worldwide: sources, methods and major patterns in GLOBOCAN 2012. *Int J Cancer.* 2015;136:E359–E386.
3. Droz JP, Aapro M, Balducci L, et al. Management of prostate cancer in older patients: updated recommendations of a working group of the International Society of Geriatric Oncology. *Lancet Oncol.* 2014;15:e404–e414.
4. Handforth C, Clegg A, Young C, et al. The prevalence and outcomes of frailty in older cancer patients: a systematic review. *Ann Oncol.* 2015;26:1091–1101.
5. Mulders PF, Molina A, Marberger M, et al. Efficacy and safety of abiraterone acetate in an elderly patient subgroup (aged 75 and older) with metastatic

castration-resistant prostate cancer after docetaxel-based chemotherapy. *Eur Urol.* 2014;65:875–883.
6. Ryan C, Wefel JS, Morgans AK. A review of prostate cancer treatment impact on the CNS and cognitive function. *Prostate Cancer Prostatic Dis.* 2020;23:207–219.
7. de Bono JS, Oudard S, Ozguroglu M, et al. Prednisone plus cabazitaxel or mitoxantrone for metastatic castration-resistant prostate cancer progressing after docetaxel treatment: a randomised open-label trial. *Lancet.* 2010;376:1147–1154.
8. Shenoy P, Harugeri A. Elderly patients' participation in clinical trials. *Perspect Clin Res.* 2015;6:184–189.
9. Sedrak MS, Freedman RA, Cohen HJ, et al. Older adult participation in cancer clinical trials: a systematic review of barriers and interventions. *CA Cancer J Clin.* 2021;71:78–92.
10. Sartor O, de Bono J, Chi KN, et al. Lutetium-177-PSMA-617 for metastatic castration-resistant prostate cancer. *N Engl J Med.* 2021;385:1091–1103.
11. Heck MM, Retz M, D'Alessandria C, et al. Systemic radioligand therapy with $^{177}$Lu labeled prostate specific membrane antigen ligand for imaging and therapy in patients with metastatic castration resistant prostate cancer. *J Urol.* 2016;196:382–391.
12. Heck MM, Tauber R, Schwaiger S, et al. Treatment outcome, toxicity, and predictive factors for radioligand therapy with $^{177}$Lu-PSMA-I&T in metastatic castration-resistant prostate cancer. *Eur Urol.* 2019;75:920–926.
13. Prostatakarzinom. Leitlinienprogramm Onkologie website. http://www.leitlinienprogramm-onkologie.de/leitlinien/prostatakarzinom/. Accessed May 16, 2023.
14. Weineisen M, Simecek J, Schottelius M, Schwaiger M, Wester HJ. Synthesis and preclinical evaluation of DOTAGA-conjugated PSMA ligands for functional imaging and endoradiotherapy of prostate cancer. *EJNMMI Res.* 2014;4:63.
15. Rasul S, Hartenbach M, Wollenweber T, et al. Prediction of response and survival after standardized treatment with 7400 MBq $^{177}$Lu-PSMA-617 every 4 weeks in patients with metastatic castration-resistant prostate cancer. *Eur J Nucl Med Mol Imaging.* 2021;48:1650–1657.
16. Hofman MS, Violet J, Hicks RJ, et al. [$^{177}$Lu]-PSMA-617 radionuclide treatment in patients with metastatic castration-resistant prostate cancer (LuPSMA trial): a single-centre, single-arm, phase 2 study. *Lancet Oncol.* 2018;19:825–833.
17. Scher HI, Morris MJ, Stadler WM, et al. Trial design and objectives for castration-resistant prostate cancer: updated recommendations from the Prostate Cancer Clinical Trials Working Group 3. *J Clin Oncol.* 2016;34:1402–1418.
18. Hofman MS, Emmett L, Sandhu S, et al. [$^{177}$Lu]Lu-PSMA-617 versus cabazitaxel in patients with metastatic castration-resistant prostate cancer (TheraP): a randomised, open-label, phase 2 trial. *Lancet.* 2021;397:797–804.
19. Barber TW, Singh A, Kulkarni HR, Niepsch K, Billah B, Baum RP. Clinical outcomes of $^{177}$Lu-PSMA radioligand therapy in earlier and later phases of metastatic castration-resistant prostate cancer grouped by previous taxane chemotherapy. *J Nucl Med.* 2019;60:955–962.
20. Veccia A, Caffo O, De Giorgi U, et al. Clinical outcomes in octogenarians treated with docetaxel as first-line chemotherapy for castration-resistant prostate cancer. *Future Oncol.* 2016;12:493–502.
21. Wong HL, Lok SW, Wong S, Parente P, Rosenthal M. Docetaxel in very elderly men with metastatic castration-resistant prostate cancer. *Prostate Int.* 2015;3:42–46.
22. Heidenreich A, Bracarda S, Mason M, et al. Safety of cabazitaxel in senior adults with metastatic castration-resistant prostate cancer: results of the European compassionate-use programme. *Eur J Cancer.* 2014;50:1090–1099.
23. Leibowitz-Amit R, Templeton AJ, Alibhai SM, et al. Efficacy and toxicity of abiraterone and docetaxel in octogenarians with metastatic castration-resistant prostate cancer. *J Geriatr Oncol.* 2015;6:23–28.
24. Graff JN, Baciarello G, Armstrong AJ, et al. Efficacy and safety of enzalutamide in patients 75 years or older with chemotherapy-naive metastatic castration-resistant prostate cancer: results from PREVAIL. *Ann Oncol.* 2016;27:286–294.
25. Mallappallil M, Friedman EA, Delano BG, McFarlane SI, Salifu MO. Chronic kidney disease in the elderly: evaluation and management. *Clin Pract (Lond).* 2014;11:525–535.
26. Schäfer H, Mayr S, Büttner-Herold M, et al. Extensive $^{177}$Lu-PSMA radioligand therapy can lead to radiation nephropathy with a renal thrombotic microangiopathy-like picture. *Eur Urol.* 2023;83:385–390.
27. Ahmadzadehfar H, Schlolaut S, Fimmers R, et al. Predictors of overall survival in metastatic castration-resistant prostate cancer patients receiving [$^{177}$Lu]Lu-PSMA-617 radioligand therapy. *Oncotarget.* 2017;8:103108–103116.

# The Impact of PSMA PET–Based Eligibility Criteria Used in the Prospective Phase II TheraP Trial in Metastatic Castration-Resistant Prostate Cancer Patients Undergoing Prostate-Specific Membrane Antigen–Targeted Radioligand Therapy

Amir Karimzadeh[1,2], Matthias Heck[3], Robert Tauber[3], Esteban Solaris[1], Stephan Nekolla[1], Karina Knorr[1], Bernhard Haller[4], Calogero D'Alessandria[1], Wolfgang A. Weber[1], Matthias Eiber*[1], and Isabel Rauscher*[1]

[1]*Department of Nuclear Medicine, School of Medicine, Technical University of Munich, Munich, Germany;* [2]*Department of Diagnostic and Interventional Radiology and Nuclear Medicine, University Medical Center Hamburg–Eppendorf, Hamburg, Germany;* [3]*Department of Urology, School of Medicine, Technical University of Munich, Munich, Germany; and* [4]*Institute of AI and Informatics in Medicine, School of Medicine, Technical University of Munich, Munich, Germany*

Prostate-specific membrane antigen (PSMA) radioligand therapy (RLT) has shown encouraging results for treatment of metastatic castration-resistant prostate cancer (mCRPC) in the prospective, multicenter, randomized phase II TheraP study. The inclusion criteria for that study comprised a pretherapeutic $^{68}$Ga-PSMA-11 PET scan showing sufficient tumor uptake using a predefined threshold and the absence of $^{18}$F-FDG–positive, PSMA ligand–negative tumor lesions. However, the prognostic value of these PET-based inclusion criteria remains unclear. Therefore, we evaluated the outcome of mCRPC patients treated with PSMA RLT using TheraP as well as other TheraP-based PET inclusion criteria. **Methods:** First, patients were dichotomized into 2 groups whose PSMA PET scans did (TheraP contrast-enhanced PSMA [cePSMA] PET–positive) or did not (TheraP cePSMA PET–negative) fulfill the inclusion criteria of TheraP. Notably, unlike in TheraP, $^{18}$F-FDG PET was not performed on our patients. Prostate-specific antigen (PSA) response (PSA decline ≥ 50% from baseline), PSA progression-free survival, and overall survival (OS) were compared. Additionally, patients were further dichotomized according to predefined $SUV_{max}$ thresholds different from those used in TheraP to analyze their potential impact on outcome as well. **Results:** In total, 107 mCRPC patients were included in this analysis (TheraP cePSMA PET–positive, $n = 77$; TheraP cePSMA PET–negative, $n = 30$). PSA response rates were higher in TheraP cePSMA PET–positive patients than in TheraP cePSMA PET–negative patients (54.5% vs. 20%, respectively; $P = 0.0012$). The median PSA progression-free survival ($P = 0.007$) and OS ($P = 0.0007$) of patients were significantly longer in the TheraP cePSMA PET–positive group than in the TheraP cePSMA PET–negative group. Moreover, being in the TheraP cePSMA PET–positive group was identified as a significant prognosticator of longer OS ($P = 0.003$). The application of different $SUV_{max}$ thresholds for a single hottest lesion demonstrated no influence on outcome in patients eligible for PSMA RLT. **Conclusion:** Patient selection for PSMA RLT according to the inclusion criteria of TheraP led to a better treatment response and outcome in our preselected patient cohort. However, a relevant number of patients not fulfilling these criteria also showed substantial rates of response.

**Key Words:** metastatic castration-resistant prostate cancer; mCRPC; TheraP; $^{68}$Ga-PSMA-11 PET; prostate-specific membrane antigen targeted radioligand therapy; PSMA RLT

**J Nucl Med 2023; 64:1252–1258**
DOI: 10.2967/jnumed.122.265346

In patients with metastatic castration-resistant prostate cancer (mCRPC), prostate-specific membrane antigen (PSMA) radioligand therapy (RLT) has emerged as a promising option with favorable efficacy and low toxicity and was recently approved by the Food and Drug Administration and the European Medicines Agency (*1–4*). Patients who received prior treatment usually undergo PET imaging (e.g., using $^{68}$Ga-PSMA-11) to assess for sufficient PSMA ligand uptake (*5*). To date, the criteria used to select patients are inconsistent in clinical use and even differ between prospective clinical trials (*6*).

Recently, the prospective, multicenter, randomized phase II TheraP study was published comparing $^{177}$Lu-PSMA-617 with cabazitaxel in 200 mCRPC patients (*7*). It reported a significantly higher treatment response and less toxicity in patients receiving $^{177}$Lu-PSMA-617. This trial used strict PSMA ligand PET–based selection criteria requiring high $^{68}$Ga-PSMA-11 tumor uptake with an $SUV_{max}$ of at least 20 for at least 1 metastatic site, an $SUV_{max}$ of greater than 10 for all other measurable (diameter, ≥10 mm) lesions, and absence of $^{18}$F-FDG–positive, PSMA ligand–negative tumor lesions (*7*). $^{177}$Lu-PSMA-I&T is another PSMA ligand showing promising results for therapy of mCRCP and is currently being explored in a prospective, multicenter, randomized phase III trial on mCRPC prior chemotherapy (SPLASH, NCT04647526) after second-line hormonal treatment (*3,8*). However, with the first results being expected in 2023, the PSMA PET avidity criteria required in this trial are so far unknown and cannot be addressed. High tumor uptake of $^{68}$Ga-PSMA-11 correlates with higher tumor radiation doses (*9*) and—despite not being proven for PSMA RLT—yields

Received Dec. 19, 2022; revision accepted Mar. 24, 2023.
For correspondence or reprints, contact Amir Karimzadeh (amir.karimzadeh@uke.de).
*Contributed equally to this work.
Published online Jun. 8, 2023.

**TABLE 1**
Baseline Patient Characteristics

| Characteristic | Data |
|---|---|
| No. of patients | 107 |
| Age (y) | 73 (66–76) |
| PSA (ng/mL) | 115 (19–324) |
| Lactate dehydrogenase (U/L) | 266 (217–350) |
| Alkaline phosphatase (U/L) | 101 (72–229) |
| Hemoglobin (g/dL) | 11.5 (10.1–12.4) |
| Prior systemic therapies for mCRPC | |
| Docetaxel | 82 |
| Cabazitaxel | 20 |
| Abiraterone | 87 |
| Enzalutamide | 63 |
| $^{223}$Ra | 19 |
| Previous chemotherapy | 82 |
| Site of metastasis | |
| Lymph node, overall | 87 |
| Lymph node only (N1+/M1a) | 7 |
| Bone overall | 97 |
| Bone (M1b, without visceral metastases) | 71 |
| Visceral, overall (M1c) | 31 |
| Liver | 10 |
| Lung | 14 |
| Adrenal | 10 |

Qualitative data are number and percentage; continuous data are median and interquartile range ($n$ = 107).

promise of better treatment effects. Therefore, following the theranostic paradigm, it seems reasonable to limit RLT to patients with high $^{68}$Ga-PSMA-11 tumor uptake and avoid including patients with a lower chance of response but still at risk for side effects. However, it remains unclear how well the selected $SUV_{max}$ thresholds separate patients who do benefit from RLT from those do not, as biologic differences in the tumor might also play a substantial role.

Thus, the aim of this retrospective analysis was to evaluate the prognostic value of predefined $SUV_{max}$-based thresholds, including those applied in TheraP for the outcome of PSMA RLT. Outcome was measured by a prostate-specific antigen (PSA) decline of at least 50% from baseline, PSA progression-free survival (PFS), and overall survival (OS). Of note, the investigation included our large cohort of mCRPC patients previously treated with RLT using less restrictive criteria than in TheraP and therefore also encompasses patients who would not have been selected for RLT in this trial.

## MATERIALS AND METHODS

### Patients and $^{177}$Lu-PSMA-I&T RLT

From our institutional database of patients who underwent PSMA RLT using $^{177}$Lu-PSMA-I&T from December 2014 to July 2020 at the Department of Nuclear Medicine, School of Medicine, Technical University of Munich, 120 patients with $^{68}$Ga-PSMA-11 PET/CT imaging before treatment were screened, and 107 consecutive patients with PSMA PET imaging performed at our institution were selected. This patient population includes 73 patients for whom the safety and antitumor effect of PSMA RLT, but not the prognostic value of pretherapeutic $^{68}$Ga-PSMA-11 PET, have already been reported by Heck et al. (*3*). All patients had previously received second-line hormonal therapy with abiraterone or enzalutamide as well as chemotherapy or were unfit for chemotherapy. The patient characteristics are shown in Table 1. Before treatment, uptake in tumor lesions was confirmed by $^{68}$Ga-PSMA-11 PET imaging, and patients needed to present with lesions showing PSMA ligand uptake at least as high as liver background uptake. $^{177}$Lu-PSMA-I&T was synthesized and radiolabeled as reported by Weineisen et al. (*10*). $^{177}$Lu-PSMA-I&T was prepared according to good manufacturing practices and the German Medicinal Products Act (Arzneimittelgesetz §13 2b). In total, 444 cycles of PSMA RLT with a median of 4 cycles per patient (range, 2–20 cycles) were applied. Treatment was discontinued in patients with radiographic or clinical signs of progression or the appearance of severe toxicity according to the investigator. Patients received an intravenous treatment using a standard activity of 7.4 GBq of $^{177}$Lu-PSMA-I&T every 4–10 wk (median, 6 wk), which could be slightly adapted on the basis of, for example, lab test results and tumor burden. All patients gave written informed consent and were treated under the conditions of Declaration of Helsinki article 37, "Unproven Interventions in Clinical Practice." The retrospective analysis was approved by the local ethics committee under reference number 115/18 S.

### Image Analysis and Definition of PET Eligibility

$^{68}$Ga-PSMA-11 was synthesized according to Eder et al. (*11*). $^{68}$Ga-PSMA-11 was given to patients via an intravenous bolus followed by an intravenous injection of diuretic (furosemide). The PET acquisition began about 60 min after injection. All patients were examined on a Biograph mCT scanner (Siemens Medical Solutions). A diagnostic CT scan was initially performed in the portal venous phase 80 s after

**TABLE 2**
PET-Based Eligibility Criteria

| Criterion | PET-based eligibility in TheraP using $^{68}$Ga-PSMA-11 and $^{18}$F-FDG PET (*7*) | Institutional PET-based eligibility criteria using $^{68}$Ga-PSMA-11 and contrast-enhanced CT |
|---|---|---|
| Inclusion | PSMA-positive disease with at least $SUV_{max}$ of 20 at site of disease; $SUV_{max}$ greater than 10 at all other sites of measurable (diameter, ≥10 mm) metastatic disease | PSMA ligand uptake at least as high as liver background uptake in most metastatic lesions |
| Exclusion | Metastatic site of disease with discordant $^{18}$F-FDG–positive and $^{68}$Ga-PSMA-11–negative findings | Any negative visceral metastases (>1 cm) or relevant fraction (~>25%) of soft-tissue lesions in contrast-enhanced CT with PSMA ligand uptake lower than liver uptake |

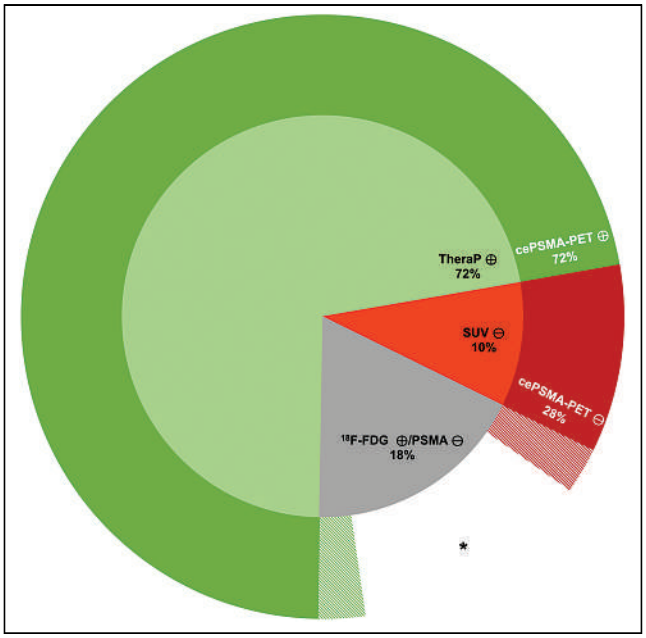


**FIGURE 1.** Comparison of PET eligibility criteria used in TheraP (inner pie chart) and our retrospective stratification of patients (outer pie chart). In inner pie chart, green fill is patients who fulfilled PET eligibility criteria according to TheraP (TheraP–positive, 72%), gray fill is patients who were excluded because of discordant $^{18}$F-FDG–positive, PSMA-negative metastatic disease (18%), and red fill is patients who were not included because of low uptake on $^{68}$Ga-PSMA-11 PET/CT ($SUV_{max}$-negative, 10%). In outer pie chart (not drawn to scale), green is patients who retrospectively fulfilled inclusion criteria from TheraP (TheraP cePSMA PET–positive, 72%), and red is patients who retrospectively did not fulfill PSMA ligand PET-based $SUV_{max}$ inclusion criteria (TheraP cePSMA PET–negative, 28%). Asterisk in gap represents patient cohort that was excluded from TheraP on basis of $^{18}$F-FDG–positive, PSMA-negative disease and was also not treated with PSMA RLT at our institution because of PSMA-negative visceral or soft-tissue lesions. Hatched areas represent patients in our cohort who were treated with PSMA RLT but might have been excluded from TheraP because of $^{18}$F-FDG–positive, PSMA-negative bone disease. ⊕ = positive; ⊖ = negative.

intravenous injection of an iodinated contrast agent (Imeron 300; Bracco Imaging) and was followed by the PET scan. All patients received a diluted oral contrast agent (300 mg of Telebrix; Guerbet). The PET scans were acquired in 3-dimensional mode with an acquisition time of 3–4 min per bed position or 1.1–1.5 mm/s using flow technique. Emission data were corrected for randoms, dead time, scatter, and attenuation and were reconstructed iteratively using ordered-subsets expectation maximization (4 iterations, 8 subsets) followed by a postreconstruction smoothing gaussian filter (5 mm in full width at half maximum). All patients were assessed as to whether they fulfilled the $SUV_{max}$-based criteria for $^{68}$Ga-PSMA-11 uptake of TheraP (TheraP contrast-enhanced PSMA [cePSMA] PET–positive vs. TheraP cePSMA PET–negative). The criteria from TheraP used for this analysis are shown in Table 2. In an additional analysis, we further explored the impact of the $SUV_{max}$ threshold of 20 required to be fulfilled by at least 1 lesion in TheraP. For this analysis, exploratory thresholds between an $SUV_{max}$ of 10 and an $SUV_{max}$ of 50 were used, and the patients were restratified. The requirement of the $SUV_{max}$-based TheraP criteria of an $SUV_{max}$ of at least 10 at all other sites of measurable (diameter, ≥10 mm) metastatic disease remained unchanged for this analysis. To determine the $SUV_{max}$ of the tumor lesions, all were semiautomatically segmented using a predefined threshold and annotated regarding their malignancy (benign vs. malignant) and anatomic location (tissue type, organ) using the prototype software as described by Capobianco et al. (*12*). Our approach consisted of the following steps: first, all PSMA-avid foci with an $SUV_{max}$ of at least 10 were automatically preselected, and foci with a PET volume smaller than 0.5 mL were discarded. Second, missed foci or foci falsely marked as physiologic were manually adjusted, if needed. Third, after the semiautomatic preselection of appropriate PSMA-avid foci, all $^{68}$Ga-PSMA-11 PET/CT scans were reread to assess whether they fulfilled the requirement of measurable metastatic disease.

Notably, in comparison to TheraP, our patients do not undergo $^{18}$F-FDG PET before $^{177}$Lu-PSMA RLT. However, our institutional PET eligibility criteria (Table 2) require the use of contrast-enhanced CT, which, in comparison to $^{68}$Ga-PSMA-11 PET, can identify PSMA ligand–negative visceral and soft-tissue lesions. With this approach, only potential nonsclerotic PSMA-negative and $^{18}$F-FDG–positive disease might be missed.

### Clinical Parameters, PSA Response, and PSA Progression

The following pretherapeutic parameters were collected and correlated with patient outcome: age, alkaline phosphatase, lactate dehydrogenase, hemoglobin, PSA, prior systemic therapies (including abiraterone, enzalutamide, first- and second-line chemotherapy, and $^{223}$Ra), lymph node–only metastases (N+/M1a), and visceral metastases (M1c). According to Prostate Cancer Clinical Trials Working Group 3, a PSA decline of at least 50% from baseline was defined as a PSA response (*12*). PSA progression was defined as either a PSA increase of at least 25% and at least 2 ng/mL above the nadir after an initial PSA decline or a PSA increase of at least 25% and at least 2 ng/mL from baseline in cases with no PSA decline (*13*).

### Statistical Analysis

The primary outcome measures were PSA response, PSA PFS, and OS. The Kaplan–Meier method was used to estimate event time

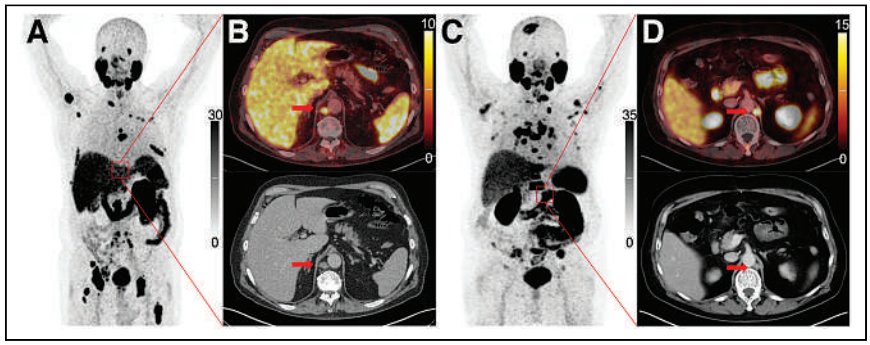


**FIGURE 2.** Examples of $^{68}$Ga-PSMA-11 PET/CT in mCRPC patients. (A and B) Maximum-intensity projection (A) and PSMA ligand PET/CT (B, top) and corresponding CT dataset (B, bottom) in 67-y-old patient from TheraP cePSMA PET–negative group with bone and lymph node metastases presenting with retrocrural lymph node metastasis with short-axis diameter of 14 mm and $SUV_{max}$ of 8.1 (arrows). (C and D) Maximum-intensity projection (C) and PSMA ligand PET/CT (D, top) with corresponding CT dataset (D, bottom) in 74-y-old patient from TheraP cePSMA PET–positive group with bone and lymph node metastases presenting with retrocrural lymph node metastasis with short-axis diameter of 11 mm and $SUV_{max}$ of 10.8 (arrows). PSA PFS and OS were 11 wk and 8 mo, respectively, in patient shown in A and B and 45 wk and 45 mo, respectively, in patient shown in C and D.

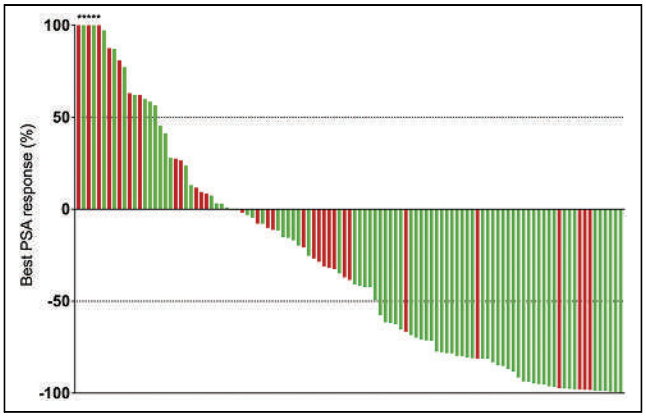


**FIGURE 3.** Waterfall plot showing response to treatment as measured by serum PSA. Color-coded best PSA response is defined as smallest increase or greatest decrease in PSA from baseline. Green indicates patients who fulfilled PET eligibility criteria (TheraP cePSMA PET–positive, $n = 77$). Red indicates patients who did not fulfill TheraP PET-based inclusion criteria (TheraP cePSMA PET–negative, $n = 30$). Asterisks indicate patients with increase of more than 100% in best PSA response.

distributions, and log-rank tests were used for group comparisons. The frequencies of PSA response between the cePSMA PET–positive and cePSMA PET–negative groups within each $SUV_{max}$ threshold group were compared using $\chi^2$ tests. Univariate and multivariate Cox regression analyses were performed to determine the association of pretherapeutic parameters with PSA PFS and OS. The corresponding hazard ratios (HRs) and 95% CIs are presented. A $P$ value of less than 0.05 was considered statistically significant.

$\chi^2$ tests, Kaplan–Meier estimation, and log-rank tests were performed using Prism, version 8.4.3 (GraphPad Software), for Mac (Apple). Uni- and multivariate Cox regression analyses were performed using SPSS Statistics, version 25.0. (IBM Corp.), for Windows (Microsoft).

## RESULTS

In total, 107 patients were analyzed. The median time on treatment was 4 mo (range, 1–57 mo). At baseline, lymph node, bone, and visceral metastases were present in 87 (81.3%), 97 (90.7%), and 31 (29.0%) patients, respectively. The median follow-up time was 11 mo (range, 1–63 mo). Forty-eight (44.9%) patients achieved a PSA response after PSMA-targeted RLT. Median OS and PSA PFS were 14.0 mo (95% CI, 11.0–17.0 mo) and 17.6 wk (95% CI, 14.6–29.7 wk), respectively. At the time of analysis, 88 patients showed PSA progression and 97 had died.

### Clinical Outcome of TheraP cePSMA PET–Positive and TheraP cePSMA PET–Negative Patients

Seventy-seven (72%) patients were classified as TheraP cePSMA PET–positive, and 30 patients were classified as TheraP cePSMA PET–negative (28%; 9 patients with no metastatic lesion with an $SUV_{max} \geq 20$, and 21 patients with ≥1 measurable metastatic lesion with an $SUV_{max} < 10$), who would not have been treated in TheraP on the basis of PSMA PET $SUV_{max}$ criteria. Visceral metastases were present in 20 (26%) and 11 (37%) patients classified as TheraP cePSMA PET–positive and TheraP cePSMA PET–negative, respectively. Figure 1 compares the PET eligibility criteria used in TheraP with the retrospective stratification of patients treated in our compassionate-use program. Figures 2A–2D show an example of a TheraP cePSMA PET–positive patient and a TheraP cePSMA PET–negative patient.

PSA response was achieved by 54.5% ($n = 42$) and 20% ($n = 6$) of patients in the TheraP cePSMA PET–positive and TheraP cePSMA PET–negative groups, respectively ($P = 0.0012$). A PSA waterfall plot (Fig. 3) shows the correlation between TheraP $SUV_{max}$ criteria and the best PSA response. The median PSA PFS and OS were 6.0 versus 3.2 mo, respectively (HR, 0.5; 95% CI, 0.3–0.8; $P = 0.007$; Fig. 4A), for the TheraP cePSMA PET–positive group and 15.0 versus 10.0 mo, respectively (HR, 0.4; 95% CI, 0.2–0.7; $P = 0.0007$; Fig. 4B) for the TheraP cePSMA PET–negative group.

Both univariate and multivariate Cox regression analyses indicated that a TheraP cePSMA PET–positive status is a significant positive prognosticator for OS ($P = 0.001$ and $P = 0.003$ for uni- and multivariate analysis, respectively; Table 3). On univariate analysis, further parameters associated with worse OS were rising levels of lactate dehydrogenase and PSA, decreasing levels of hemoglobin, and the presence of visceral metastases at baseline PET (Table 3). In the multivariate Cox regression model, only rising lactate dehydrogenase, decreasing hemoglobin, and the presence of visceral metastases remained independent predictors of poor OS apart from the TheraP cePSMA PET–positive status (Table 3).

### Correlation Between Adapted SUV Thresholds for the Hottest Lesion on Clinical Outcome

When adjusting the $SUV_{max}$ threshold required for at least 1 lesion without other changes in the PSMA ligand PET–based stratification, we obtained the following numbers of patients in the respective cePSMA PET–positive groups: 78 for an $SUV_{max}$ of more than 10 or 15, 72 for an $SUV_{max}$ of more than 25, 63 for an $SUV_{max}$ of more than 30, 56 for an $SUV_{max}$ of more than 35, 51 for an $SUV_{max}$ of more than 40, and 47 for an $SUV_{max}$ of more than 45 or 50 (Supplemental Table 1; supplemental materials are available at http://jnm.snmjournals.org).

The results on the PSA response, PSA PFS, and OS of the exploratory cePSMA PET–positive and cePSMA PET–negative groups using $SUV_{max}$ thresholds of between 10 and 50 are presented in Supplemental Table 1. PSA responses significantly differed between the cePSMA PET–positive and cePSMA PET–negative groups when the threshold $SUV_{max}$ for the hottest lesions was between 10 and 35 (all $P < 0.05$).

Further, the relative risk of death for the exploratory cePSMA PET–positive group showed a decreasing trend from a high to low adjusted $SUV_{max}$. It was lowest for an $SUV_{max}$ of 20 (HR, 0.4; 95% CI, 0.3–0.9),

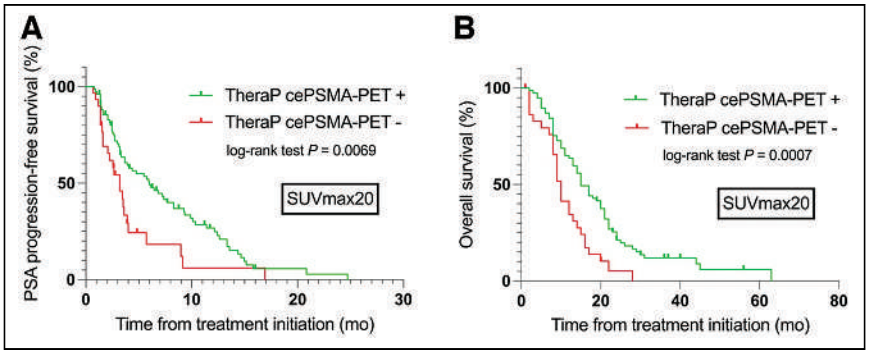


**FIGURE 4.** Kaplan–Meier survival curves for PSA PFS (A) and OS (B) in TheraP cePSMA PET–positive and TheraP cePSMA PET–negative patients.

**TABLE 3**
Uni- and Multivariate Cox Regression Analysis

| Parameter | Patients (*n*) | Univariate analysis | | | Multivariate analysis | | |
|---|---|---|---|---|---|---|---|
| | | HR | 95% CI | *P* | HR | 95% CI | *P* |
| TheraP criteria | 107 | | | | | | |
| TheraP cePSMA PET–negative | 30 | Reference | | | | | |
| TheraP cePSMA PET–positive | 77 | 0.5 | 0.3–0.8 | 0.001* | 0.5 | 0.3–0.8 | 0.003* |
| Visceral metastases | 107 | | | | | | |
| No | | Reference | | | | | |
| Yes | | 1.7 | 1.2–2.6 | 0.02* | 2.2 | 1.3–.2.7 | 0.005* |
| Lymph node only | 107 | | | | | | |
| No | | Reference | | | | | |
| Yes | | 0.4 | 0.2–1.1 | 0.07 | 0.6 | 0.2–1.6 | 0.3 |
| Previous abiraterone | 107 | | | | | | |
| No | | Reference | | | | | |
| Yes | | 1.1 | 0.7–1.9 | 0.7 | 1.5 | 0.9–2.7 | 0.2 |
| Previous enzalutamide | 107 | | | | | | |
| No | | Reference | | | | | |
| Yes | | 0.9 | 0.6–1.4 | 0.7 | 0.7 | 0.5–1.1 | 0.2 |
| Previous $^{223}$Ra | 107 | | | | | | |
| No | | Reference | | | | | |
| Yes | | 0.9 | 0.5–1.5 | 0.7 | 0.7 | 0.4–1.2 | 0.2 |
| Previous chemotherapy | 107 | | | | | | |
| Yes | | Reference | | | | | |
| No | | 0.7 | 0.5–1.2 | 0.2 | 1.3 | 0.7–2.5 | 0.3 |
| Age, risk change with 10 y increase | 107 | | | | | | |
| Continuous | | 1.0 | 0.8–1.4 | 0.9 | 1.1 | 0.8–1.5 | 0.7 |
| PSA, risk change with 50 ng/mL increase | 107 | | | | | | |
| Continuous | | 1.0 | 1.0–1.0 | 0.02* | 1.0 | 1.0–1.0 | 0.5 |
| Hemoglobin (g/dL) | 107 | | | | | | |
| Continuous | | 0.8 | 0.7–0.8 | <0.0001* | 0.7 | 0.6–0.9 | <0.001* |
| AP, risk change with 50 U/L increase | 107 | | | | | | |
| Continuous | | 1.0 | 1.0–1.0 | 0.05 | 1.0 | 1.0–1.1 | 0.9 |
| LDH, risk change with 50 U/L increase | 107 | | | | | | |
| Continuous | | 1.0 | 1.0–1.1 | <0.0001* | 1.1 | 1.0–1.1 | 0.03* |

*Statistically significant.
AP = alkaline phosphatase; LDH = lactate dehydrogenase.

followed by an $SUV_{max}$ of 10, 15, 25, and 30 (HR, 0.5; 95% CI, 0.3–0.8 each) (Supplemental Table 1). OS significantly differed between the cePSMA PET–positive and cePSMA PET–negative groups with an exploratory $SUV_{max}$ of between 10 and 35 (all $P < 0.05$; Figs. 5A–5D).

The different exploratory $SUV_{max}$ thresholds had no substantial effect on PSA response (range, 52.8%–55.6%) or median OS (range, 15.0–18.5 mo) in the group of cePSMA PET–positive patients. In the different exploratory cePSMA PET–negative groups, PSA response (range, 17.2%–38.3%) and median OS (range, 9.5–12.0 mo) declined in lower $SUV_{max}$ thresholds (Supplemental Table 1).

## DISCUSSION

Our retrospective analysis indicates that quantitative thresholds for PSMA ligand PET used in TheraP are predictive for response in patients treated with $^{177}$Lu-PSMA RLT selected on the basis of visual $^{68}$Ga-PSMA-11 uptake. Patients who fulfilled these criteria showed higher rates of maximum PSA response (54.5% vs. 20%, $P = 0.0012$), significantly longer PSA PFS (median, 6.0 vs. 3.2 mo, $P = 0.007$), and OS (median, 15.0 vs. 10.0 mo, $P = 0.0007$). Further, multivariate Cox regression analysis identified PSMA ligand PET–based criteria from TheraP (TheraP cePSMA PET–positive) as a new prognosticator for outcome in addition to known variables. In an additional exploratory analysis, adjustment of the

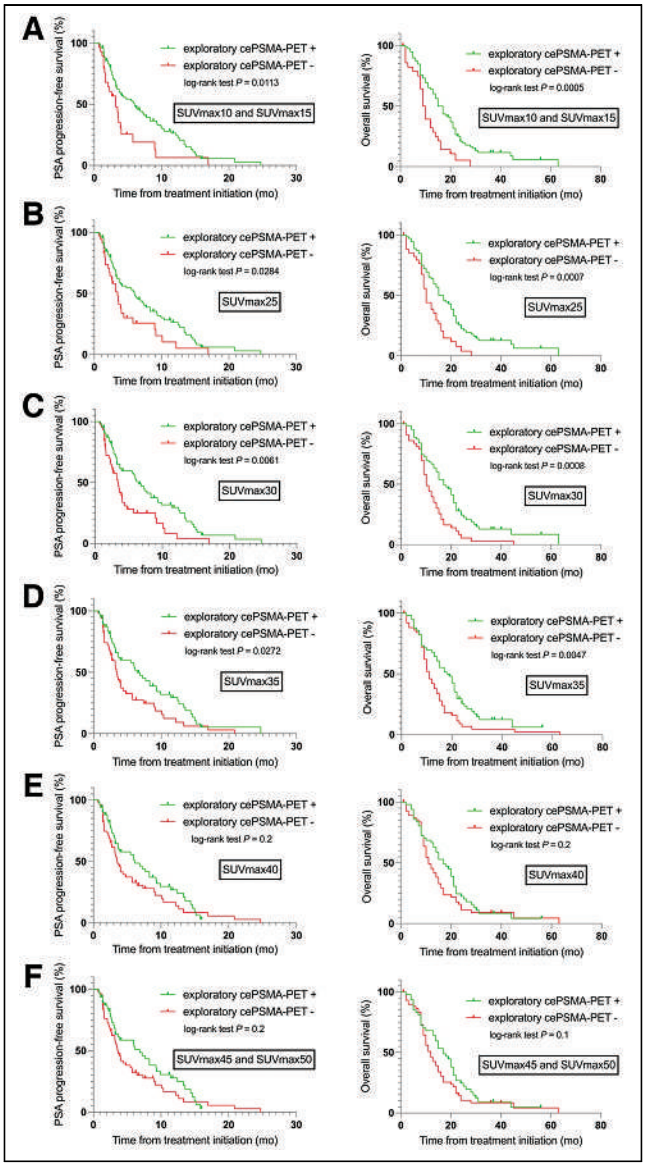


**FIGURE 5.** Kaplan–Meier survival curves for PSA PFS and OS in exploratory cePSMA PET–positive and exploratory cePSMA PET–negative patients stratified according to presence of PSMA-positive disease with $SUV_{max}$ of at least 10 and 15 (A), 25 (B), 30 (C), 35 (D), 40 (E), and 45 and 50 (E).

$SUV_{max}$ threshold required for the hottest lesion did not further select for higher response in the group fulfilling these criteria.

In TheraP, a maximum PSA decline of at least 50% was achieved in 66% of patients receiving $^{177}$Lu-PSMA RLT, compared with 54.5% in our TheraP cePSMA PET–positive cohort. The corresponding OS in TheraP patients was 19.1 mo, compared with 15.0 mo in our TheraP cePSMA PET–positive cohort (*14*). The slight shift toward a lower PSA response rate and shorter OS in our analysis might be explained by the more advanced disease stage in our TheraP cePSMA PET–positive cohort (visceral metastases in 26% of TheraP cePSMA PET–positive patients [$n = 20$] vs. 7% in TheraP patients [$n = 7$]), given the known negative association of visceral metastases with outcome (*15*). Another possible contributor might be the inclusion of patients with nonsclerotic PSMA-negative and $^{18}$F-FDG–positive bone disease in our TheraP cePSMA PET–positive cohort. We do not perform $^{18}$F-FDG PET at treatment selection for $^{177}$Lu-PSMA RLT, yet we strongly believe that our approach including contrast-enhanced CT within the PSMA ligand PET/CT reliably identifies PSMA-negative visceral lesions that are potentially $^{18}$F-FDG PET–positive. Consequently, this type of disease does not constitute a further confounder in our data compared with TheraP. Our institutional approach is also supported by recent results from Seifert et al., who reported a substantial level of agreement in findings between PSMA ligand PET/CT and combined $^{18}$F-FDG PET and PSMA ligand PET/CT for the assessment of therapy eligibility according to the VISION inclusion criteria (*16*). Although $^{18}$F-FDG PET and PSMA PET provide complementary information, in only 5% of patients was incremental information derived from dual-tracer PET/CT imaging (*16*). However, in a recently published analysis by Buteau et al., an increased $^{18}$F-FDG tumor volume (metabolic tumor volume $\geq$ 200 mL) in TheraP participants was significantly associated with lower rates of a maximum PSA decline of at least 50% (OR, 0.44; $P = 0.01$) and significantly correlated with a shorter PSA PFS (HR, 1.44; 95% CI, 1.28–2.52; $P = 0.03$) (*17*). Furthermore, in a retrospective analysis on patients who underwent $^{177}$Lu-PSMA, the median OS was significantly shorter (6.0 mo) in patients with discordant $^{18}$F-FDG–avid disease than in those without any $^{18}$F-FDG–positive, PSMA-negative lesions (16.0 mo) (*18*). This finding further underpins the potential prognostic value of combined $^{18}$F-FDG–negative, PSMA-negative PET imaging for treatment selection.

Sufficient PSMA ligand uptake of metastases in pretherapeutic PET is a prerequisite before PSMA RLT. However, no consensus on what should be considered sufficient exists (*19*). It is hypothesized that higher $^{68}$Ga-PSMA-11 uptake correlates with higher absorbed doses of $^{177}$Lu-PSMA, resulting in a favorable treatment response (*9*). Thus, it seems reasonable to restrict RLT to patients presenting with high $^{68}$Ga-PSMA-11 tumor uptake to increase treatment response and avoid unnecessary side effects in patients unlikely to respond. In our exploratory analysis using different $SUV_{max}$ thresholds between 10 and 50 for the hottest lesion, no clear trend on patient outcome as measured by PSA response (range, 52.8%–55.6%) or OS (range, 15.0–18.5 mo) in the cePSMA PET–positive group was observed (Supplemental Table 1). This observation is in line with results from Seifert et al., who demonstrated no significant correlation between the highest $SUV_{max}$ in a single lesion and OS (*20*). Similarly, Ferdinandus et al. found no significant correlation between uptake in pretherapeutic PET ($SUV_{max}$ of different types of metastases and different tumor-to-normal organ ratios) (*21*).

In the cePSMA PET–negative group, outcome measurements tend to be worse in the lower than higher $SUV_{max}$ threshold groups. PSA response ranged from 17.2% to 38.3% and median OS from 9.5 to 12.0 mo using $SUV_{max}$ thresholds from 10 to 50 (Supplemental Table 1). One possible explanation could be that at decreasing $SUV_{max}$ thresholds for the hottest lesion, the cePSMA PET–negative group contains a higher rate of patients with lesions below an $SUV_{max}$ of 10. For example, at $SUV_{max}$ thresholds of 50, 35, and 10 for the hottest lesion, 14 of 60, 21 of 30, and 29 of 29 patients, respectively, were classified as cePSMA PET–negative based on measurable lesions with an $SUV_{max}$ of below 10 (Supplemental Table 1). This demonstrates an increasing selection of patients with a generally lower lesion uptake in the cePSMA PET–negative group, potentially explaining the lower response. Thus, a hypothesis might be that insufficient PSMA ligand uptake in lesions in general might be more relevant for PSMA RLT outcome than a single

hottest lesion. This hypothesis is also supported by a substudy from Kuo et al. investigating the association between imaging parameters from baseline $^{68}$Ga-PSMA-11 PET/CT scans in the $^{177}$Lu-PSMA-617 arm of the VISION trial and clinical outcome (*22*). In this study, no significant correlation between $SUV_{max}$ and treatment response or OS was found. However, a rising whole-body $SUV_{mean}$ correlated with survival and treatment response, supporting our hypothesis that insufficient PSMA ligand uptake in lesions in general might play a crucial role for the outcome of PSMA RLT. This result is also in line with results from Gafita et al. demonstrating rising values of tumor $SUV_{mean}$ to be significantly correlated with better outcome (*23*).

There are several limitations to our analysis, including its retrospective nature. In addition, although we could assess the impact of the TheraP criteria used in $^{68}$Ga-PSMA-11 PET on treatment outcome, our cohort did not undergo additional $^{18}$F-FDG PET. Thus, exact comparison with the TheraP cohort is not possible. Nevertheless, we believe that our approach including contrast-enhanced CT in the pretherapeutic workup selects most $^{18}$F-FDG–positive, PSMA-negative disease, as discussed.

## CONCLUSION

The results of our analysis demonstrate a better treatment response and outcome in mCRPC patients who underwent $^{177}$Lu-PSMA RLT and retrospectively fulfilled the $^{68}$Ga-PSMA-11–based TheraP inclusion criteria. However, as a relevant number of patients not fulfilling these stricter criteria also showed substantial rates of response, it remains to be discussed whether PSMA RLT needs to be withheld from these patients. Finally, our exploratory analyses using different $SUV_{max}$ thresholds for the hottest lesion indicate that this criterion in TheraP is less prognostic than insufficient PSMA ligand uptake of lesions in general.

## DISCLOSURE

Matthias Eiber reports fees from Blue Earth Diagnostics Ltd. (consultant, research funding), Novartis/AAA (consultant), Telix (consultant), Bayer (consultant, research funding), RayzeBio (consultant), Point Biopharma (consultant), Janssen Pharmaceuticals (consultant, speakers' bureau), Parexel (image review), and Bioclinica (image review) outside the submitted work and a patent application for rhPSMA. No other potential conflict of interest relevant to this article was reported.

**KEY POINTS**

**QUESTION:** Is retrospective application of different TheraP PET-based inclusion criteria in mCRPC patients treated with RLT associated with higher rates of maximum PSA decline of at least 50%, and does it correlate with longer PSA PFS and OS?

**PERTINENT FINDINGS:** Retrospective application of the criteria was associated with higher rates of maximum PSA decline of at least 50% and significantly correlated with longer PSA PFS and OS.

**IMPLICATIONS FOR PATIENT CARE:** The $^{68}$Ga-PSMA-11–based PET selection criteria used in TheraP are highly prognostic of better treatment outcome. The $SUV_{max}$ threshold for the hottest lesions seems to be less relevant than insufficient PSMA ligand uptake in lesions in general.

## REFERENCES


1. Rahbar K, Ahmadzadehfar H, Kratochwil C, et al. German multicenter study investigating $^{177}$Lu-PSMA-617 radioligand therapy in advanced prostate cancer patients. *J Nucl Med.* 2017;58:85–90.
2. Hofman MS, Violet J, Hicks RJ, et al. [$^{177}$Lu]-PSMA-617 radionuclide treatment in patients with metastatic castration-resistant prostate cancer (LuPSMA trial): a single-centre, single-arm, phase 2 study. *Lancet Oncol.* 2018;19:825–833.
3. Heck MM, Tauber R, Schwaiger S, et al. Treatment outcome, toxicity, and predictive factors for radioligand therapy with $^{177}$Lu-PSMA-I&T in metastatic castration-resistant prostate cancer. *Eur Urol.* 2019;75:920–926.
4. Sartor O, de Bono J, Chi KN, et al. Lutetium-177-PSMA-617 for metastatic castration-resistant prostate cancer. *N Engl J Med.* 2021;385:1091–1103.
5. Kratochwil C, Fendler WP, Eiber M, et al. EANM procedure guidelines for radionuclide therapy with $^{177}$Lu-labelled PSMA-ligands ($^{177}$Lu-PSMA-RLT). *Eur J Nucl Med Mol Imaging.* 2019;46:2536–2544.
6. Iravani A, Violet J, Azad A, Hofman MS. Lutetium-177 prostate-specific membrane antigen (PSMA) theranostics: practical nuances and intricacies. *Prostate Cancer Prostatic Dis.* 2020;23:38–52.
7. Hofman MS, Emmett L, Sandhu S, et al. [$^{177}$Lu]Lu-PSMA-617 versus cabazitaxel in patients with metastatic castration-resistant prostate cancer (TheraP): a randomised, open-label, phase 2 trial. *Lancet.* 2021;397:797–804.
8. Karimzadeh A, Heck M, Tauber R, et al. $^{177}$Lu-PSMA-I&T for treatment of metastatic castration-resistant prostate cancer: prognostic value of scintigraphic and clinical biomarkers. *J Nucl Med.* 2023;64:402–409.
9. Violet J, Jackson P, Ferdinandus J, et al. Dosimetry of $^{177}$Lu-PSMA-617 in metastatic castration-resistant prostate cancer: correlations between pretherapeutic imaging and whole-body tumor dosimetry with treatment outcomes. *J Nucl Med.* 2019;60:517–523.
10. Weineisen M, Simecek J, Schottelius M, Schwaiger M, Wester HJ. Synthesis and preclinical evaluation of DOTAGA-conjugated PSMA ligands for functional imaging and endoradiotherapy of prostate cancer. *EJNMMI Res.* 2014;4:63.
11. Eder M, Neels O, Müller M, et al. Novel preclinical and radiopharmaceutical aspects of [$^{68}$Ga]Ga-PSMA-HBED-CC: a new PET tracer for imaging of prostate cancer. *Pharmaceuticals (Basel).* 2014;7:779–796.
12. Capobianco N, Sibille L, Chantadisai M, et al. Whole-body uptake classification and prostate cancer staging in $^{68}$Ga-PSMA-11 PET/CT using dual-tracer learning. *Eur J Nucl Med Mol Imaging.* 2022;49:517–526.
13. Scher HI, Morris MJ, Stadler WM, et al. Trial design and objectives for castration-resistant prostate cancer: updated recommendations from the Prostate Cancer Clinical Trials Working Group 3. *J Clin Oncol.* 2016;34:1402–1418.
14. Hofman MS, Emmet L, Sandhu S, et al. TheraP: [$^{177}$Lu]Lu-PSMA-617 versus cabazitaxel in patients with metastatic castration-resistant prostate cancer (mCRPC) progressing after docetaxel—overall survival after median follow-up of 3 years (ANZUP 1603). *J Clin Oncol* [abstract]. 2022;40(suppl 16):5000.
15. Manafi-Farid R, Harsini S, Saidi B, et al. Factors predicting biochemical response and survival benefits following radioligand therapy with [$^{177}$Lu]Lu-PSMA in metastatic castrate-resistant prostate cancer: a review. *Eur J Nucl Med Mol Imaging.* 2021;48:4028–4041.
16. Seifert R, Telli T, Hadaschik B, Fendler WP, Kuo PH, Herrmann K. Is $^{18}$F-FDG PET needed to assess $^{177}$Lu-PSMA therapy eligibility? A VISION-like, single-center analysis. *J Nucl Med.* 2023;64:731–737.
17. Buteau JP, Martin AJ, Emmett L, et al. PSMA PET and FDP PET as predictors of response and prognosis in a randomized phase 2 trial of $^{177}$Lu-PSMA-617 (LuPSMA) versus cabazitaxel in metastatic, castration-resistant prostate cancer (mCRPC) progressing after docetaxel (TheraP ANZUP 1603). *J Clin Oncol* [abstract]. 2022;40(suppl 6):10.
18. Michalski K, Ruf J, Goetz C, et al. Prognostic implication of dual tracer PET/CT: PSMA ligand and [$^{18}$F] FDG PET/CT in patients undergoing [$^{177}$Lu] PSMA radioligand therapy. *Eur J Nucl Med Mol Imaging.* 2021;48:2024–2030.
19. Kratochwil C, Fendler WP, Eiber M, et al. EANM procedure guidelines for radionuclide therapy with $^{177}$Lu-labelled PSMA-ligands ($^{177}$Lu-PSMA-RLT). *Eur J Nucl Med Mol Imaging.* 2019;46:2536–2544.
20. Seifert R, Seitzer K, Herrmann K, et al. Analysis of PSMA expression and outcome in patients with advanced prostate cancer receiving $^{177}$Lu-PSMA-617 radioligand therapy. *Theranostics.* 2020;10:7812–7820.
21. Ferdinandus J, Eppard E, Gaertner FC, et al. Predictors of response to radioligand therapy of metastatic castrate-resistant prostate cancer with $^{177}$Lu-PSMA-617. *J Nucl Med.* 2017;58:312–319.
22. Kuo PH, Hesterman J, Amstrong AJ, et al. [$^{68}$Ga]Ga-PSMA-11 PET baseline imaging as a prognostic tool for clinical outcomes to [$^{177}$Lu]Lu-PSMA-617 in patients with mCRPC. *J Clin Oncol* [abstract]. 2022;40(suppl 16):5002.
23. Gafita A, Calais J, Grogan TR, et al. Nomograms to predict outcomes after $^{177}$Lu-PSMA therapy in men with metastatic castration-resistant prostate cancer: an international, multicentre, retrospective study. *Lancet Oncol.* 2021;22:1115–1125.

# A VISION Substudy of Reader Agreement on $^{68}$Ga-PSMA-11 PET/CT Scan Interpretation to Determine Patient Eligibility for $^{177}$Lu-PSMA-617 Radioligand Therapy

Phillip H. Kuo[1], Don C. Yoo[2], Ryan Avery[3], Marc Seltzer[4], Jeremie Calais[5], James Nagarajah[6], Wolfgang A. Weber[7], Wolfgang P. Fendler[8], Michael S. Hofman[9,10], Bernd J. Krause[11], Marcia Brackman[12], Euloge Kpamegan[13], Samson Ghebremariam[13], Taylor Benson[14], Ana M. Catafau[15], and Ayse T. Kendi[16]

[1]*University of Arizona, Tucson, Arizona;* [2]*Warren Alpert Medical School of Brown University, Providence, Rhode Island;* [3]*Northwestern University, Evanston, Illinois;* [4]*Geisel School of Medicine at Dartmouth, Hanover, New Hampshire;* [5]*Ahmanson Translational Theranostics Division, Department of Molecular and Medical Pharmacology, UCLA, Los Angeles, California;* [6]*Department of Medical Imaging, Radboud University Medical Center, Nijmegen, The Netherlands;* [7]*TUM School of Medicine, Technical University of Munich, Munich, Germany;* [8]*Department of Nuclear Medicine, University of Duisburg–Essen and German Cancer Consortium–University Hospital Essen, Essen, Germany;* [9]*Cancer Imaging, Prostate Theranostics and Imaging Centre of Excellence, Peter MacCallum Cancer Centre, Melbourne, Victoria, Australia;* [10]*Sir Peter MacCallum Department of Oncology, University of Melbourne, Melbourne, Victoria, Australia;* [11]*Rostock University Medical Center, Rostock, Germany;* [12]*Novartis Pharmaceuticals Corporation, Indianapolis, Indiana;* [13]*Novartis Pharmaceuticals Corporation, East Hanover, New Jersey;* [14]*Novartis Pharmaceuticals Corporation, St. George, Utah;* [15]*Advanced Accelerator Applications, Geneva, Switzerland; and* [16]*Mayo Clinic, Rochester, Minnesota*

[$^{68}$Ga]Ga-PSMA-11 ($^{68}$Ga-PSMA-11) is used to identify prostate-specific membrane antigen (PSMA)–positive tumors on PET scans. In the VISION study, $^{68}$Ga-PSMA-11 was used to determine the eligibility of patients with metastatic castration-resistant prostate cancer for treatment with [$^{177}$Lu]Lu-PSMA-617 ($^{177}$Lu-PSMA-617), based on predefined read criteria. This substudy aimed to investigate the interreader variability and intrareader reproducibility of visual assessments of $^{68}$Ga-PSMA-11 PET/CT scans using the VISION read criteria and evaluate the agreement between read results for this and the VISION study. **Methods:** In VISION, $^{68}$Ga-PSMA-11 PET/CT scans were centrally read as inclusion cases if they had at least 1 PSMA-positive lesion and no PSMA-negative lesions that fulfilled the exclusion criteria. In this substudy, 125 PET/CT scans (75 inclusion and 50 exclusion cases) were randomly selected from VISION and retrospectively assessed by 3 independent central readers. A random subset of 20 cases (12 inclusion and 8 exclusion cases) was recoded for assessment of intrareader reproducibility. Classification of cases as inclusion or exclusion cases was based on the VISION read criteria. Overall interreader variability was assessed by Fleiss κ-statistics, and pairwise variability and intrareader reproducibility were assessed by Cohen κ-statistics. **Results:** For interreader variability, the readers agreed on 77% of cases (overall average agreement rate, 0.85; Fleiss κ, 0.60 [95% CI, 0.50–0.70]). The pairwise agreement rate was 0.82, 0.88, and 0.84, and the corresponding Cohen κ was 0.54 (95% CI, 0.38–0.71), 0.67 (95% CI, 0.52–0.83), and 0.59 (95% CI, 0.43–0.75), respectively. For intrareader reproducibility, the agreement rate was 0.90, 0.90, and 0.95, and the corresponding Cohen κ was 0.78 (95% CI, 0.49–0.99), 0.76 (95% CI, 0.46–0.99), and 0.89 (95% CI, 0.67–0.99), respectively. The number of actual VISION inclusion cases out of the total number of cases scored as inclusion in this substudy was 71 of 93 (agreement rate, 0.76; 95% CI, 0.66–0.85) for reader 1, 70 of 88 (0.80; 0.70–0.87) for reader 2, and 73 of 96 (0.76; 0.66–0.84) for reader 3. All readers agreed on 66 of 75 VISION inclusion cases. **Conclusion:** Moderate-to-substantial interreader agreement and substantial-to-almost perfect intrareader reproducibility for $^{68}$Ga-PSMA-11 PET/CT scan assessment using the VISION read criteria were observed. The read rules applied in VISION can be readily learned and demonstrate good reproducibility.

**Key Words:** PSMA; prostate cancer; PET/CT

**J Nucl Med 2023; 64:1259–1265**
DOI: 10.2967/jnumed.122.265077

Prostate-specific membrane antigen (PSMA) is a transmembrane glutamate carboxypeptidase that is highly expressed in prostate cancer cells, with limited expression in non-prostate-cancer cells (*1–3*). This makes PSMA an important actionable theranostic target for patients with prostate cancer.

[$^{68}$Ga]Ga-PSMA-11 (also known as $^{68}$Ga-PSMA-11) is an approved radioligand imaging agent used to identify PSMA-positive tumors on PET scans. In the pivotal phase 3 VISION study, $^{68}$Ga-PSMA-11 imaging was used to determine the eligibility of patients with metastatic castration-resistant prostate cancer (mCRPC) for radioligand therapy with [$^{177}$Lu]Lu-PSMA-617 (also known as $^{177}$Lu-PSMA-617), based on predefined read criteria (*4*). These $^{68}$Ga-PSMA-11 PET/CT read rules were intended to select patients who were most likely to benefit from $^{177}$Lu-PSMA-617 in the VISION trial, following a population enrichment approach (*5*). VISION read rules were also designed to reduce future issues with reimbursement in using both $^{18}$F-FDG and PSMA PET scans (*5*).

Received Nov. 7, 2022; revision accepted Mar. 24, 2023.
For correspondence or reprints, contact Phillip H. Kuo (pkuo@email.arizona.edu).
Guest Editor: Lisa Bodei, Memorial Sloan Kettering Cancer Center
Published online May 25, 2023.

There is reported evidence on the reliability of $^{68}$Ga-PSMA-11 PET scan reads in identifying PSMA-positive lesions across a range of diagnostic evaluation criteria and prostate cancer populations (*6–11*). Of note, the ProPSMA phase 3 study in the setting of staging demonstrated high reporter agreement between local and central review for $^{68}$Ga-PSMA-11 PET/CT, with κ-values of 0.87 for nodal and 0.88 for distant metastases (*12*). However, the reliability of read rules to establish the eligibility of patients with mCRPC for treatment with $^{177}$Lu-PSMA-617 in the VISION trial is yet to be determined.

In this independent VISION substudy, we aimed to assess the robustness of read rules used for scan interpretation in the VISION study. Specifically, we investigated the interreader variability and intrareader reproducibility of visual assessments of $^{68}$Ga-PSMA-11 PET/CT scans using the VISION read criteria for $^{177}$Lu-PSMA-617 therapy eligibility.

## MATERIALS AND METHODS

### Overview and Objectives

VISION was an open-label, international, randomized, phase 3 trial investigating the efficacy and safety of $^{177}$Lu-PSMA-617 in patients with progressive PSMA-positive mCRPC, previously treated with at least 1 androgen receptor pathway inhibitor and 1–2 taxane regimens. Details of the study design have been published elsewhere (*4*). This retrospective, independent, masked VISION substudy aimed to assess the variability across different readers (interreader variability) and the variability between different reads performed by the same reader (intrareader reproducibility) of $^{68}$Ga-PSMA-11 PET/CT scans, based on the VISION read rules used to determine patient eligibility for $^{177}$Lu-PSMA-617 therapy in the VISION study. The results from the eligibility determination in this reader agreement VISION substudy were also compared with the original eligibility results from the VISION study. Reader training, proficiency testing, and independent masked reads were conducted virtually on May 9–11, 2020.

### VISION $^{68}$Ga-PSMA-11 PET/CT Read Rules

In VISION, $^{68}$Ga-PSMA-11 scans were centrally read by 1 reader from a pool of 3 board-certified nuclear medicine physicians/radiologists. Readers were trained in person on the VISION read rules. VISION $^{68}$Ga-PSMA-11 PET/CT read rules have been reported and discussed in detail elsewhere (*4,5*). Briefly, patients with mCRPC with at least 1 PSMA-positive lesion identified by $^{68}$Ga-PSMA-11 PET/CT and no PSMA-negative lesion fulfilling the exclusion criteria were enrolled in the study, provided all other inclusion criteria were met (*4*). PSMA-positive lesions, of any size and present in any organ system, were identified first. These lesions were defined as those that had uptake greater than observed in the liver by visual assessment. PSMA-negative lesions were defined as those that had activity equal to or less than observed in the liver by visual assessment. Patients were excluded if one or more PSMA-negative lesions fulfilled the following size criteria measured on diagnostic imaging: lymph node at least 2.5 cm in short-axis diameter anywhere in the body, bone metastasis with soft-tissue component at least 1 cm in short-axis diameter, or solid-organ metastasis at least 1 cm in short-axis diameter (Supplemental Fig. 1; supplemental materials are available at http://jnm.snmjournals.org).

### Readers and Reader Training

Three independent central readers, each from a different institution, who were not previously involved in VISION $^{68}$Ga-PSMA-11 PET scan reads were asked to participate in this substudy. Readers were U.S. board-certified nuclear medicine physicians from different institutions; 2 readers were dual board-certified in radiology. Readers were experienced in reading PET/CT scans but not in reading $^{68}$Ga-PSMA-11 PET/CT scans or with the VISION read rules. A nuclear medicine radiologist involved in the development of the VISION read criteria and training of the central readers for the VISION study was assigned as the trainer. Because of the coronavirus disease 2019 pandemic, the readers were trained virtually, via the Zoom teleconference platform. The readers were guided through an approved independent-review training manual (developed by Invicro and Advanced Accelerator Applications), image software, the basics of PSMA PET/CT interpretation, and the VISION PET/CT scan read criteria. After completion of the training session, the readers were required to correctly assess at least 80% of 10 allocated training cases. The training cases were scored in a similar manner to the actual masked read to allow readers to familiarize themselves with the software and imaging evaluation. A reader with a score of below 80% would be provided with additional training and be reassessed for proficiency.

### Scan Selection and Coding

A random generator was used to select a total of 125 $^{68}$Ga-PSMA-11 PET scans and corresponding diagnostic CT/MRI scans from VISION to obtain a predetermined number of 75 inclusion cases (60%; patient enrolled) and 50 exclusion cases (40%; screen failure). These percentages intentionally deviated from the approximately 85% of inclusion cases in VISION to allow for a more robust exclusion case sample size for the evaluation of interreader variability. A randomly selected subset of 20 cases (12 inclusion cases and 8 exclusion cases) was also recoded for the evaluation of intrareader reproducibility. Scans for the 125 cases, plus 20 recoded repeats, and an additional 29 reader training cases were uploaded by the Invicro Image Management team to the Imaging Picture Archiving and Communication System, version 2.03. Digital Imaging and Communications in Medicine tags were modified with new patient identification randomization codes, and scans were uploaded to the mint Lesion software application (Mint Medical Inc.). All codes and files were reviewed and verified by Invicro, and scans were evaluated for anatomic coverage and quality.

### Independent Masked Read

*Conduct.* The readers could seek assistance on case loading and assessment recording from a proctor via Zoom; proctors were not able to comment on the assessments. The readers were provided with a list of PET/CT scans in a predefined read order that was unique to each reader. All cases, including the 20 recoded repeat cases, were read independently for 3 consecutive days, for approximately 8 h per day. The readers were allowed to take breaks whenever they wanted and were unaware of the patient data and each other's results.

*Assessment.* The readers recorded their visual assessment of each scan on an electronic case report form and assessed whether a case was considered an inclusion or exclusion case for VISION enrollment (Supplemental Fig. 2).

### Statistical Analyses

Interreader variability was assessed by Fleiss κ-statistics, and interpretation was based on the Landis and Koch scale, whereby values of less than 0.00 were defined as poor disagreement, 0.00–0.20 as slight agreement, 0.21–0.40 as fair agreement, 0.41–0.60 as moderate agreement, 0.61–0.80 as substantial agreement, and 0.81–1.00 as almost perfect agreement (*13,14*). An overall average agreement rate (Pbar) for the Fleiss κ-analysis was calculated as the average agreement rate across the 3 readers for each of the 125 cases. Pairwise variability and intrareader reproducibility were assessed by Cohen κ-statistics. The agreement rate between independent reads in the substudy and VISION eligibility reads was calculated as the percentage of inclusion cases in VISION

**TABLE 1**
Concordance Combinations Among 3 Readers (125 Cases)

| Reader outcomes | | | Results | |
|---|---|---|---|---|
| Reader 1 | Reader 2 | Reader 3 | Frequency (*n*) | Proportion (%) |
| Inclusion | Inclusion | Inclusion | 76 | 61 |
| Inclusion | Inclusion | Exclusion | 3 | 2 |
| Inclusion | Exclusion | Inclusion | 11 | 9 |
| Inclusion | Exclusion | Exclusion | 3 | 2 |
| Exclusion | Inclusion | Inclusion | 6 | 5 |
| Exclusion | Inclusion | Exclusion | 3 | 2 |
| Exclusion | Exclusion | Inclusion | 3 | 2 |
| Exclusion | Exclusion | Exclusion | 20 | 16 |

compared with cases assessed as inclusion by each independent reader. Statistical analyses were performed by an external consultant designated by Advanced Accelerator Applications.

### Study Oversight

VISION was registered on ClinicalTrials.gov (NCT03511664) and was conducted in accordance with the principles of the Declaration of Helsinki, the International Conference on Harmonization Good Clinical Practice, and any applicable local regulations. All patients in the pivotal study provided written informed consent before enrollment, and independent ethical review boards approved the VISION study protocol. This substudy was conducted by Invicro and funded by Advanced Accelerator Applications, a Novartis Company.

## RESULTS

### Conduct

Day 1 consisted of 4 h of reader training, followed by 2 h for the assessment of the 10 allocated training cases and 1.5 h for actual read time. Days 2 and 3 consisted of 7.5 h each for actual read time. The average number of cases read per hour was 8.8.

### Reader Proficiency Testing

After completion of the training session, all 3 readers scored 80% or higher in the correct assessment of the 10 training cases and required no further training.

### Interreader Variability

The readers agreed on the assessment of 96 of 125 cases (77%), of which 76 (79%) were scored as inclusion cases and 20 (21%) were scored as exclusion cases (Table 1). The agreement rates for inclusion and exclusion cases were 88% and 60%, respectively. The Pbar between readers was 0.85; the Fleiss κ was 0.60 (95% CI, 0.50, 0.70), representing moderate-to-substantial interreader agreement.

The pairwise agreement rate between readers 1 and 2, readers 1 and 3, and readers 2 and 3, was 0.82, 0.88, and 0.84, respectively; the corresponding Cohen κ was 0.54 (95% CI, 0.38, 0.71), 0.67 (95% CI, 0.52, 0.83), and 0.59 (95% CI, 0.43, 0.75), respectively, representing moderate-to-substantial agreement between all 3 pairs of readers (Fig. 1).

Of the 29 of 125 (23%) discordant cases, some of which belonged to multiple regions, the readers differed in their assessment of lymph node (6 cases) and of bone metastasis, liver, or cases with no positive lesion (5 each). There were 9 discordant cases that included lesions in the prostate/urinary bladder ($n = 4$), lung ($n = 2$), adrenal gland ($n = 2$), and kidney ($n = 1$). Illustrative examples of PET/CT scans for discordant exclusion cases are shown in Figure 2, whereby one reader did not see a bone lesion with a PET-negative soft-tissue component in a patient with multiple positive PET-positive lesions, and another did not see a PET-negative lung lesion among multiple PET-positive lesions.

### Intrareader Reproducibility

For the 20 recoded cases that were read twice by each reader, the agreement rate was 0.90, 0.90, and 0.95 for readers 1, 2, and 3, respectively. The corresponding Cohen κ was 0.78 (95% CI, 0.49,

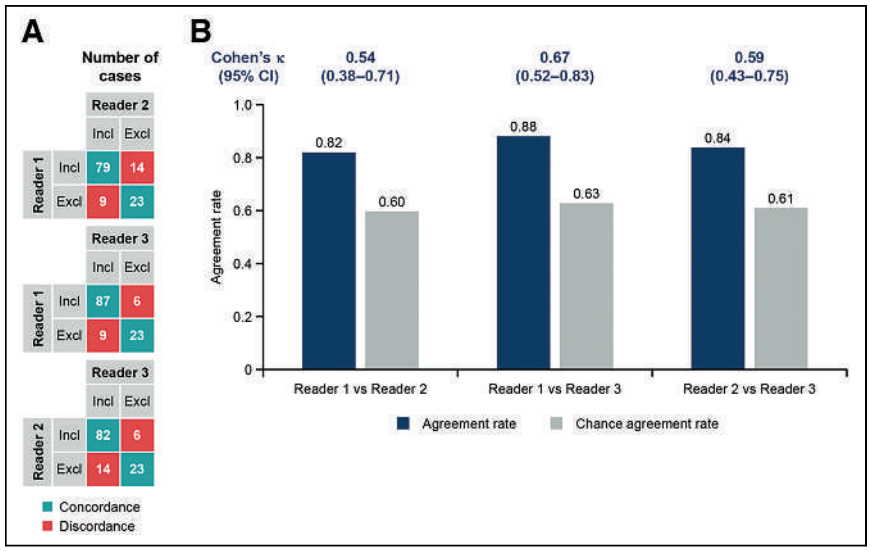


**FIGURE 1.** Pairwise interreader agreement (125 cases). (A) Pairwise concordance combinations. (B) Cohen κ-analysis. κ-statistic is calculated as (observed agreement − chance agreement)/(1 − chance agreement). Chance agreement is probability that readers randomly agree. Excl = cases assessed as exclusion; Incl = cases assessed as inclusion.

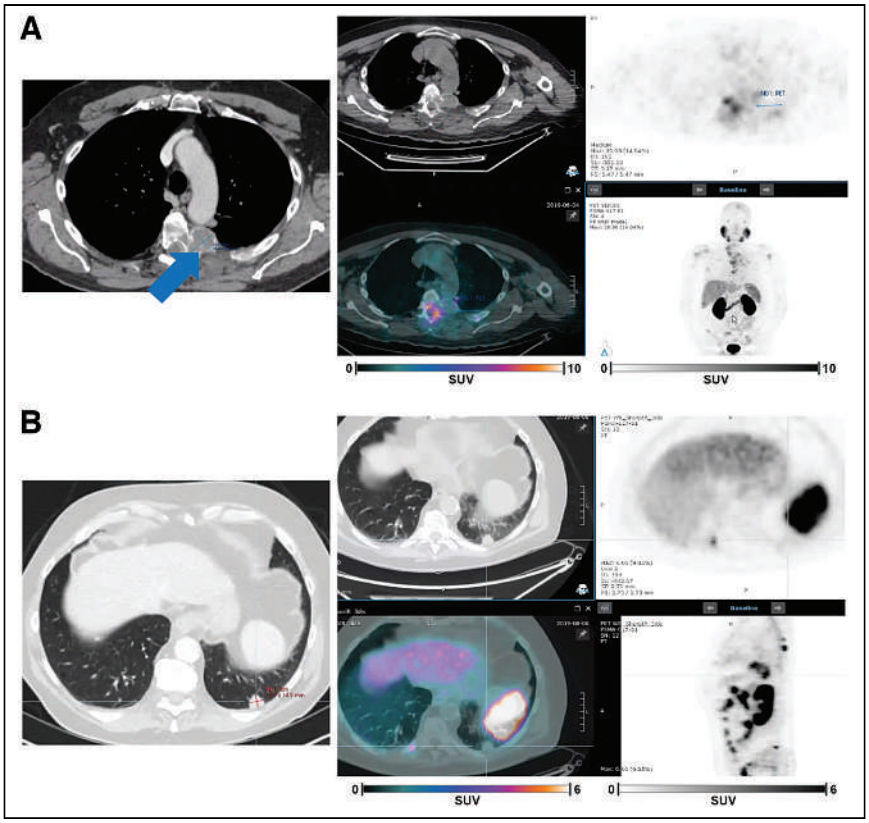


**FIGURE 2.** Illustrative PSMA PET/CT and diagnostic CT scans for discordant cases. (A) In the left panel, transaxial slice from diagnostic CT with intravenous contrast at level of aortic arch shows left thoracic vertebral metastasis (arrow) with soft-tissue component greater than 1 cm in short axis. In the right panel, PSMA PET/CT transaxial and maximum-intensity-projection images from mint Lesion were captured from annotations by 2 of 3 readers who correctly identified PSMA-negative vertebral lesion. (B) In the left panel, transaxial slice from diagnostic CT with intravenous contrast medium at level of lung bases demonstrates left lung nodule measuring 1.5 cm in short axis. In the right panel, PSMA PET/CT transaxial and sagittal PET images from mint Lesion were captured from annotations by 2 of 3 readers who classified lung nodule as PSMA-negative. One reader may not have identified this lesion as PSMA-negative since other nodules (not shown) were PSMA-positive.

0.99), 0.76 (95% CI, 0.46, 0.99), and 0.89 (95% CI, 0.67, 0.99), respectively, representing substantial-to-almost perfect agreement for all 3 readers (Fig. 3).

### Agreement Rates with VISION Eligibility Read Results

Read results from this study were compared with the VISION eligibility read results used to determine patient enrollment. The agreement rate, defined as the proportion of actual inclusion cases in VISION, out of the number of cases scored as inclusion by each reader in the reader agreement study, was 0.76 (95% CI, 0.66, 0.85), 0.80 (95% CI, 0.70, 0.87), and 0.76 (95% CI, 0.66, 0.84) (Fig. 4). Of the 75 inclusion cases from VISION, there was complete agreement among the 3 readers on the assessment of 66 (88%) cases as inclusion cases. The remaining 9 (12%) cases that the readers disagreed on were unique to each reader. Better concordance was observed for inclusion cases than for exclusion cases for all 3 readers.

## DISCUSSION

To date, the reported reader agreement on $^{68}$Ga-PSMA-11 PET scans has been based on diagnostic criteria (*6–11,15*). In this independent substudy of the phase 3 VISION study, we assessed the robustness of the VISION read criteria for enrollment of patients with mCRPC, previously treated with at least 1 androgen receptor pathway inhibitor and 1–2 taxane regimens, for treatment with $^{177}$Lu-PSMA-617 in VISION. According to the Landis and Koch scale, interpretation of $^{68}$Ga-PSMA-11 PET/CT scans using the VISION read criteria showed moderate-to-substantial interreader agreement and substantial-to-almost perfect intrareader reproducibility. Substantial agreement between read results in this substudy and the VISION study was also observed. Overall, agreement rates were consistently higher for inclusion cases than for exclusion cases.

In VISION, the CT scan was used to identify more aggressive lesions (i.e., anatomically measurable lesions according to the read rules for exclusion) and visual assessments were used instead of quantitative assessments for PSMA positivity criteria, using liver uptake as a reference organ (*4*). Using this approach, the need for an additional $^{18}$F-FDG PET/CT scan or PET quantification was avoided. Overall, the moderate-to-substantial level of interreader agreement (Pbar, 0.85; Fleiss κ, 0.60 [95% CI, 0.50, 0.70]) in $^{68}$Ga-PSMA-11 PET/CT scan interpretation in this VISION substudy was similar to what has been previously reported, although it should be noted that these studies use different study criteria and are in different disease settings (Supplemental Table 1). Intrareader reproducibility for repeated reads by the same reader was 90%–95%, with a corresponding Cohen κ of 0.76–0.89, showing excellent agreement for all 3 readers. These results indicate that the reproducibility of read rules for patient selection is high. To our knowledge, this substudy is the first to determine reader agreement in the visual interpretation of $^{68}$Ga-PSMA-11 PET/CT scans in patients with mCRPC for eligibility assessment of $^{177}$Lu-PSMA-617, in the context of applying a population enrichment approach within a clinical trial. In clinical practice, selection of patients for treatment with $^{177}$Lu-PSMA-617 may require multidisciplinary consultation for borderline or difficult-to-interpret scans by a single reader (*16*).

Comparison of read results in this study and VISION eligibility read results demonstrated an agreement rate of between 76% and 80%, with better concordance among inclusion cases. All readers agreed on the assessment of 66 of 75 VISION inclusion cases. The remaining cases, which the readers did not agree on, were unique, and although these were assessed as inclusion cases in VISION, there is a possibility that the central reader was incorrect in their assessment.

There were several study limitations that could have resulted in variability between readers and between VISION read results. First, in the VISION study, the readers were trained in person. The same was initially planned for this substudy; however, because of the coronavirus disease 2019 pandemic, training, proficiency testing, and the retrospective reading of PET/CT scans were conducted

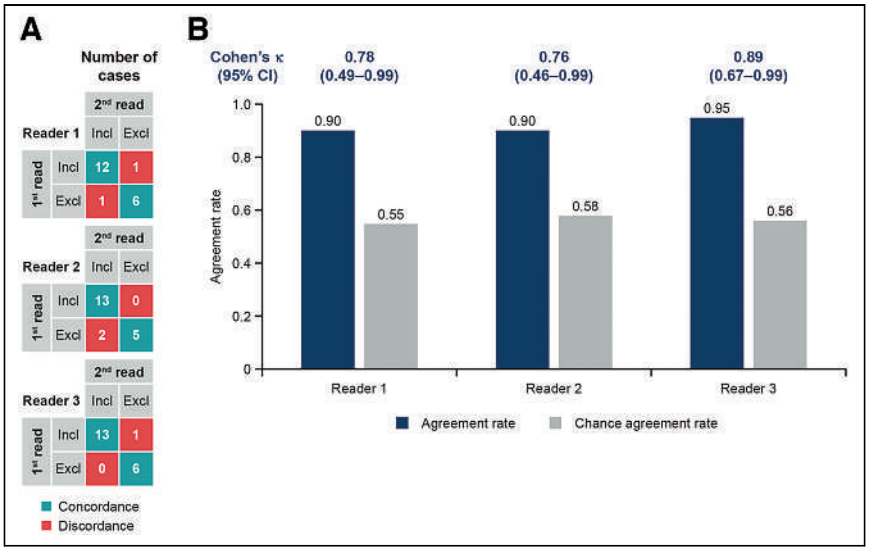


**FIGURE 3.** Intrareader agreement (20 cases). (A) Concordance combinations. (B) Cohen κ-analysis. κ-statistic is calculated as (observed agreement – chance agreement)/(1 – chance agreement). Chance agreement is probability that readers randomly agree. Excl = cases assessed as exclusion; Incl = cases assessed as inclusion.

virtually. Mitigation strategies were implemented to reduce potential study variability, including the provision of identical multimonitor workstations and pretesting of the transfer of data-heavy PET/CT images using residential Internet service. However, caveats to the virtual approach included potentially less comprehensive training and technical issues such as delays in high-resolution image display and scrolling, which may have led to reader fatigue. Second, and leading on from this, reads in VISION were performed for just a few cases per session during VISION enrollment, but in this study, the readers assessed an average of 8.8 cases per hour. Therefore, another cause of reader fatigue in this study may have resulted from the 8-h sessions over 3 consecutive days, which may have also affected visual search patterns (*17*). This aspect could particularly affect the search for CT-measurable but PSMA-negative lesions, which may account for the higher variability found in exclusion cases. Third, the readers had little or no experience with PSMA PET/CT scans, which is different from the current standard of care now that PSMA PET agents are U.S. Food and Drug Administration-approved and in wider use. Fourth, unlike what we expect for implementation in standard practice, no prior imaging or reports were available, which may have complicated the interpretation of the true metastatic nature of lesions and also identification of all relevant lesions on CT.

A higher agreement rate was observed between inclusion cases than between exclusion cases. Overall, 40% of cases were exclusion cases, compared with the 12.6% in VISION that did not meet the imaging criteria. A higher proportion of exclusion cases was included in this study to support statistical analyses; however, challenges associated with the interpretation of exclusion cases may have also contributed to increased interreader variability. For example, the identification of negative lesions requires readers to search for anatomic lesions on CT/MRI scans with no or low corresponding image tracer uptake on PET. It is generally easier to identify hot lesions than cold ones. Therefore, oversight of an anatomic lesion on CT/MRI may lead to misclassification of an exclusion case as an inclusion case. In addition, lack of access to prior diagnostic imaging or reports may have been a limiting factor in identifying lesions and characterizing whether lung and adrenal nodules, for example, were truly metastatic. Finally, reader variability associated with the identification of different lesion types such as PSMA-negative lymph nodes and bone metastases with soft-tissue components—because of more challenging tumors with necrotic components, for example—could have been another limiting factor. Indeed, 11 of 29 discordant cases in this substudy were attributed to the assessment of lymph node and bone metastases.

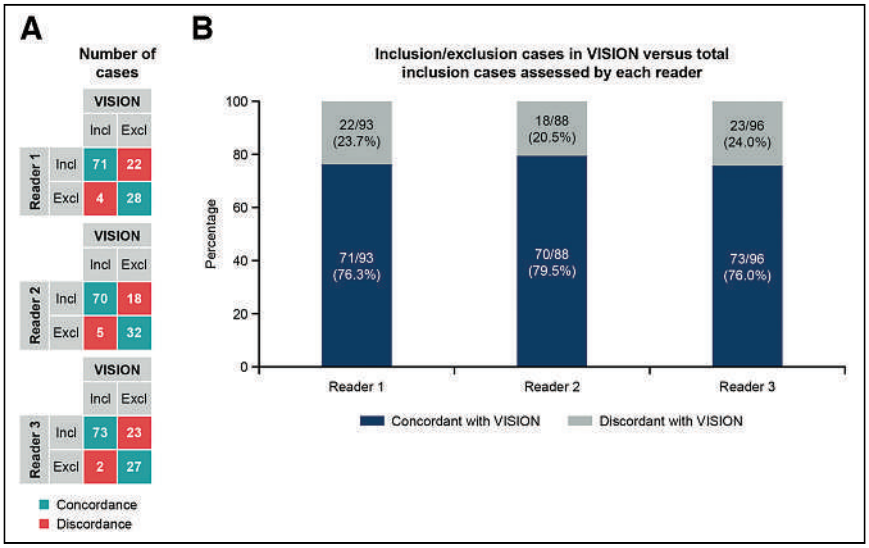


**FIGURE 4.** Agreement between substudy read results and VISION eligibility read results (125 cases). (A) Concordance combinations between individual readers in substudy and eligibility assessments in VISION. (B) Proportion of actual inclusion and exclusion cases in VISION among total number of inclusion cases assessed by reader in this substudy. Excl = cases assessed as exclusion; Incl = cases assessed as inclusion.

To minimize discordance in case assessment in clinical practice, careful reading of the diagnostic CT scan using region-anatomic and organ-specific windows is recommended. The often very high uptake of metastatic lesions in mCRPC can tempt readers to view the PET imaging at too wide a window. Since the threshold for PSMA positivity or negativity is the liver, active windowing of the PET imaging, with the liver initially placed in the middle of the window, is recommended. Specifically for extensive PSMA-positive adenopathy, focal areas of decreased uptake should be carefully assessed for negative nodes. For prostate bed or urinary bladder assessments,

viewing in coronal and sagittal planes and multiple window intensities is recommended. For aggressive disease invading the urinary bladder and surrounding structures, the CT scan is critical since uptake by the disease may be similar to the urinary activity. For bone metastases, CT scans should be read on both bone and soft-tissue windows, and PET and PET/CT images should be assessed for mild activity outside the margins of the cortical bone. For liver metastases, careful reading of the CT scan is essential to identify lesions since PSMA-negative metastases will often be invisible against the background of normal liver uptake. Viewing the region of the metastasis in multiple axes on the PET scan is suggested given the frequency of motion artifacts. Finally, one should recognize the critical difference between this read paradigm and the typical use of PSMA PET for staging or recurrence. For approximately 95% of cases, the goal is not to identify all sites of PSMA-positive disease but rather to ensure that any PSMA-negative lesion meeting the size criteria is identified. It is inherently easier to see PSMA-positive than PSMA-negative disease and thus fall into the trap of "satisfaction of search." Therefore, the reader needs to tune out the often numerous PSMA-positive lesions and tune in to finding lesions at or below the level of liver uptake—a task that may be feasible only by first identifying the metastasis on CT.

## CONCLUSION

This VISION substudy demonstrated moderate-to-substantial interreader agreement and substantial-to-almost perfect intrareader agreement on visual assessment of $^{68}$Ga-PSMA-11 PET/CT scans, according to predefined VISION rules. The read rules used in VISION to determine patient eligibility for treatment with $^{177}$Lu-PSMA-617 were readily learned and demonstrated good reproducibility among independent reviewers, despite the limitations of this substudy.

## DISCLOSURE

This work was funded by Advanced Accelerator Applications, a Novartis Company. Phillip H. Kuo was an employee of Invicro LLC and reports consulting or speaker fees from Amgen, Bayer AG, Chimerix, Eisai, Fusion Pharma, GE Healthcare, Invicro, Novartis, and UroToday and research funding from Blue Earth Diagnostics and GE Healthcare. Don C. Yoo and Ryan Avery report consulting fees for Invicro LLC. Jeremie Calais reports prior consulting activities for Advanced Accelerator Applications, Astellas, Blue Earth Diagnostics, Curium Pharma, DS Pharma, EXINI, GE Healthcare, IBA RadioPharma, Isoray, Janssen Pharmaceuticals, Lightpoint Medical, Lantheus, Monrol, Novartis, POINT Biopharma, Progenics, Radiomedix, Sanofi, and Telix Pharmaceuticals. James Nagarajah reports consulting fees from Curium Pharma and POINT Biopharma, speaker fees from Bayer AG, and research funding from Advanced Accelerator Applications. Wolfgang A. Weber reports consulting or speaker/advisory fees from Advanced Accelerator Applications, Bayer AG, Blue Earth Diagnostics, GSK, ITM, Pentixapharm, Rayzebio, Reflexion, and Vida Ventures and research funding from BMS, Imaginab, Ipsen, Nuclidium, Piramal, and TRIMT. Wolfgang P. Fendler reports consulting fees or speaker fees from Advanced Accelerator Applications, Bayer AG, Calyx, Janssen Pharmaceuticals, and Parexel and research funding from Bayer AG and Sofie Biosciences. Michael S. Hofman reports consulting fees from Astellas, AstraZeneca, Janssen Pharmaceuticals, Merck/MSD, Mundipharma, and POINT Biopharma and research funding from Advanced Accelerator Applications. Bernd J. Krause reports consulting fees from Advanced Accelerator Applications, Bayer AG, and ITM and research funding from Advanced Accelerator Applications. Marcia Brackman, Euloge Kpamegan, Samson Ghebremariam, and Taylor Benson are employees and stockholders of Novartis, and Ana M. Catafau is an employee and stockholder of Advanced Accelerator Applications. Ayse T. Kendi reports consulting fees and research funding from Novartis. Under the direction of the authors, Sarah Sabir from Oxford PharmaGenesis, Oxford, U.K., provided medical writing support, which was funded by Novartis, in accordance with Good Publication Practice 3 guidelines (https://www.ismpp.org/gpp3). No other potential conflict of interest relevant to this article was reported.

## ACKNOWLEDGMENTS

We thank the patients, their families, and all site investigators and personnel who participated in the study. We also thank Shannon Ricard, Marianne Gauthier, Nicholas Sandella, and Kyle LoPresto, members of the Invicro team, for their assistance in preparing and conducting the study.

### KEY POINTS

**QUESTION:** This study investigated the interreader variability and intrareader reproducibility of visual assessment of $^{68}$Ga-PSMA-11 PET/CT scans using the VISION read criteria and evaluated agreement between read results for this and the VISION study.

**PERTINENT FINDINGS:** This was a retrospective, masked VISION substudy in which 3 independent readers assessed 125 PET/CT scans from VISION, according to the VISION read criteria. The 3 readers agreed on the assessment of 77% of cases, showing moderate-to-substantial interreader agreement (Fleiss κ, 0.60 [95% CI, 0.50, 0.70]). The intrareader reproducibility of $^{68}$Ga-PSMA-11 PET/CT scan assessment was substantial to almost perfect (Cohen κ, 0.78 [95% CI, 0.49, 0.99], 0.76 [95% CI, 0.46, 0.99], and 0.89 [95% CI, 0.67, 0.99]). Comparison of the reader results in this study and the VISION eligibility read results demonstrated an agreement rate of between 76% and 80%.

**IMPLICATIONS FOR PATIENT CARE:** Visual assessment of $^{68}$Ga-PSMA-11 PET/CT scans using the VISION read criteria to enrich the patient population in VISION can be readily learned and demonstrates good reproducibility. In clinical practice, variations of this approach for patient selection may apply.

## REFERENCES

1. Liu H, Rajasekaran AK, Moy P, et al. Constitutive and antibody-induced internalization of prostate-specific membrane antigen. *Cancer Res.* 1998;58:4055–4060.
2. Minner S, Wittmer C, Graefen M, et al. High level PSMA expression is associated with early PSA recurrence in surgically treated prostate cancer. *Prostate.* 2011;71:281–288.
3. Schutz FA, Buzaid AC, Sartor O. Taxanes in the management of metastatic castration-resistant prostate cancer: efficacy and management of toxicity. *Crit Rev Oncol Hematol.* 2014;91:248–256.

4. Sartor O, de Bono J, Chi KN, et al. Lutetium-177-PSMA-617 for metastatic castration-resistant prostate cancer. *N Engl J Med.* 2021;385:1091–1103.
5. Kuo PH, Benson T, Messmann R, Groaning M. Why we did what we did: PSMA-PET/CT selection criteria for the VISION trial. *J Nucl Med.* 2022;63:816–818.
6. Basha MAA, Hamed MAG, Hussein O, et al. $^{68}$Ga-PSMA-11 PET/CT in newly diagnosed prostate cancer: diagnostic sensitivity and interobserver agreement. *Abdom Radiol (NY).* 2019;44:2545–2556.
7. Derwael C, Lavergne O, Lovinfosse P, et al. Interobserver agreement of [$^{68}$Ga]Ga-PSMA-11 PET/CT images interpretation in men with newly diagnosed prostate cancer. *EJNMMI Res.* 2020;10:15.
8. Fanti S, Minozzi S, Morigi JJ, et al. Development of standardized image interpretation for $^{68}$Ga-PSMA PET/CT to detect prostate cancer recurrent lesions. *Eur J Nucl Med Mol Imaging.* 2017;44:1622–1635.
9. Fendler WP, Calais J, Allen-Auerbach M, et al. $^{68}$Ga-PSMA-11 PET/CT interobserver agreement for prostate cancer assessments: an international multicenter prospective study. *J Nucl Med.* 2017;58:1617–1623.
10. Lawhn-Heath C, Flavell RR, Behr SC, et al. Single-center prospective evaluation of $^{68}$Ga-PSMA-11 PET in biochemical recurrence of prostate cancer. *AJR.* 2019; 213:266–274.
11. Miksch J, Bottke D, Krohn T, et al. Interobserver variability, detection rate, and lesion patterns of $^{68}$Ga-PSMA-11-PET/CT in early-stage biochemical recurrence of prostate cancer after radical prostatectomy. *Eur J Nucl Med Mol Imaging.* 2020;47:2339–2347.
12. Hofman MS, Lawrentschuk N, Francis RJ, et al. Prostate-specific membrane antigen PET-CT in patients with high-risk prostate cancer before curative-intent surgery or radiotherapy (proPSMA): a prospective, randomised, multicentre study. *Lancet.* 2020;395:1208–1216.
13. Landis JR, Koch GG. The measurement of observer agreement for categorical data. *Biometrics.* 1977;33:159–174.
14. Fleiss JL. Measuring nominal scale agreement among many raters. *Psychol Bull.* 1971;76:378–382.
15. van Kalmthout LWM, van Melick HHE, Lavalaye J, et al. Prospective validation of gallium-68 prostate specific membrane antigen-positron emission tomography/computerized tomography for primary staging of prostate cancer. *J Urol.* 2020; 203:537–545.
16. Locametz. Package insert. Advanced Accelerator Applications; 2022.
17. Ganesan A, Alakhras M, Brennan PC, Mello-Thoms C. A review of factors influencing radiologists' visual search behaviour. *J Med Imaging Radiat Oncol.* 2018;62:747–757.

# [$^{177}$Lu]Lu-PSMA-Radioligand Therapy Efficacy Outcomes in Taxane-Naïve Versus Taxane-Treated Patients with Metastatic Castration-Resistant Prostate Cancer: A Systematic Review and Metaanalysis

Swayamjeet Satapathy[1], Ranjit K. Sahoo[2], and Chandrasekhar Bal[1]

*[1]Department of Nuclear Medicine, All India Institute of Medical Sciences, New Delhi, India; and [2]Department of Medical Oncology, B.R. Ambedkar Institute Rotary Cancer Hospital, All India Institute of Medical Sciences, New Delhi, India*

Radioligand therapy (RLT) with $^{177}$Lu-prostate-specific membrane antigen (PSMA) inhibitors ([$^{177}$Lu]Lu-PSMA) is currently approved for patients with metastatic castration-resistant prostate cancer (mCRPC) after progression with at least 1 taxane and 1 androgen-receptor–pathway inhibitor. However, the impact of prior chemotherapy on [$^{177}$Lu]Lu-PSMA-RLT outcomes is debatable, with various studies showing inconsistent results. This study was conducted to precisely evaluate the impact of prior taxane chemotherapy on response and survival outcomes in mCRPC patients after [$^{177}$Lu]Lu-PSMA-RLT. **Methods:** This review followed the Preferred Reporting Items for Systematic Reviews and Meta-Analyses (PRISMA) guidelines. Searches in PubMed, Scopus, and Embase were made using relevant key words, and articles up to December 2022 were included. The endpoints included prostate-specific antigen (PSA) response rate (RR), progression-free survival, and overall survival (OS). Individual patient data were pooled when feasible. Univariate odds ratios (ORs) and hazard ratios (HRs) were extracted from the individual articles, and pooled estimates and 95% CIs were generated using metaanalysis. **Results:** Thirteen articles comprising 2,068 patients were included. In 6 articles (553 patients), taxane-naïve patients had significantly better odds of biochemical response after [$^{177}$Lu]Lu-PSMA-RLT (pooled OR, 1.82; 95% CI, 1.21–2.71). Individual patient data metaanalysis for PSA RRs in 3 articles revealed a significantly higher PSA RR in the taxane-naïve versus taxane-treated patients (57.1% vs. 39.5%; difference, 17.6%; 95% CI, 5.6%–28.9%). Further, taxane-naïve status was also a predictor of significantly better progression-free survival (5 articles; 1,027 patients; pooled HR, 0.60; 95% CI, 0.51–0.69) and OS (8 articles; 1,594 patients; pooled HR, 0.54; 95% CI, 0.43–0.68) after [$^{177}$Lu]Lu-PSMA-RLT. There was no evidence of publication bias. **Conclusion:** mCRPC patients with no prior taxanes had significantly better outcomes after [$^{177}$Lu]Lu-PSMA-RLT than did taxane-treated patients. Further trials evaluating [$^{177}$Lu]Lu-PSMA-RLT in the taxane-naïve setting are now required.

**Key Words:** mCRPC; [$^{177}$Lu]Lu-PSMA; radioligand therapy; chemotherapy; metaanalysis

**J Nucl Med 2023; 64:1266–1271**
DOI: 10.2967/jnumed.123.265414

Prostate cancer is currently ranked as the second most common cancer and the fifth leading cause of cancer-related death in men globally (*1*). Metastatic prostate cancer, particularly castration-resistant disease, presents a considerable therapeutic challenge (*2,3*). Over the past 2 decades, few drugs have shown efficacy and a proven survival benefit in metastatic castration-resistant prostate cancer (mCRPC) (*4*). However, more often than not, disease progression eventually ensues. In this context, radioligand therapy (RLT) with $^{177}$Lu-labeled prostate-specific membrane antigen ([$^{177}$Lu]Lu-PSMA) inhibitors has emerged as a viable treatment option.

PSMA is a type II transmembrane glycoprotein that is overexpressed in almost all prostate cancer cells, thereby making it an ideal target for therapy in mCRPC (*5*). In the landmark phase 3 VISION trial, [$^{177}$Lu]Lu-PSMA-617-RLT has been proven to improve overall survival (OS), when added to the standard of care, in patients with end-stage, PSMA-positive mCRPC previously treated with at least 1 androgen-receptor–pathway inhibitor (ARPI) and 1 taxane regimen (*6*). The phase 2 trial, TheraP, also demonstrated better biochemical and radiologic response outcomes, as well as longer progression-free survival (PFS), with [$^{177}$Lu]Lu-PSMA-617 than with cabazitaxel in mCRPC patients having previously progressed on docetaxel (*7*). Subsequently, [$^{177}$Lu]Lu-PSMA-617-RLT was granted Food and Drug Administration approval for progressive end-stage PSMA-positive mCRPC. The recent American Society of Clinical Oncology update also recommended its use as a treatment option in patients with PSMA-positive mCRPC who have progressed on 1 prior line of ARPI and at least 1 line of prior chemotherapy (*8*).

Despite these successes, there is a need to further optimize patient selection for PSMA-RLT to ensure better outcomes. The impact of prior taxane chemotherapy on [$^{177}$Lu]Lu-PSMA-RLT outcomes is debatable at present, with various studies showing inconsistent results (*9*). Given that the current treatment guidelines recommend [$^{177}$Lu]Lu-PSMA-RLT in only the postchemotherapy setting, it is essential to address this conundrum. This systematic review and metaanalysis was therefore conducted to precisely evaluate the effect of prior taxane chemotherapy on biochemical response and survival outcomes in patients with mCRPC treated with [$^{177}$Lu]Lu-PSMA-RLT.

## MATERIALS AND METHODS

This systematic review was conducted as per a prespecified protocol (supplemental materials; available at http://jnm.snmjournals.org) in

Received Jan. 5, 2023; revision accepted Mar. 10, 2023.
For correspondence or reprints, contact Chandrasekhar Bal (csbal@hotmail.com).
Published online May 11, 2023.

accordance with the Preferred Reporting Items for Systematic Reviews and Meta-Analyses (PRISMA) guidelines (*10*).

### Search Strategy and Study Selection

Two reviewers made independent systematic searches in PubMed, Scopus, and Embase for articles published until December 19, 2022. The search key words used were (lutetium OR Lu) AND (PSMA OR "prostate specific membrane antigen") AND (chemotherapy OR taxane) AND (response OR survival OR prognosis). The reviewers also undertook a manual search and searches through the references of various articles. We selected studies that assessed the impact of prior taxane chemotherapy on prostate-specific antigen (PSA) response in patients with mCRPC after treatment with [$^{177}$Lu]Lu-PSMA-RLT using univariate binary logistic regression analysis. Studies that provided the PSA response rates (RRs) in the taxane-naïve and taxane-treated patients separately were also included. PSA response was defined as per the Prostate Cancer Clinical Trials Working group 3 criteria—that is, at least a 50% decline in serum PSA levels from baseline (*11*). We also included studies with [$^{177}$Lu]Lu-PSMA-RLT that evaluated prior taxane chemotherapy status as predictors for PFS or OS using the univariate Cox proportional-hazards model. PFS was estimated from the date of the first [$^{177}$Lu]Lu-PSMA-RLT till documented PSA progression or radiologic progression or death. OS was estimated from the date of first treatment till death from any cause. No restriction was placed on country, language, or date of publication or on the type of ligand used for therapy; both [$^{177}$Lu]Lu-PSMA-617 and [$^{177}$Lu]Lu-PSMA-I&T were considered. Only full-length articles that included at least 30 patients were included in this review. Reviews, case reports, letters to the editor, conference abstracts, and articles reporting exclusively on dosimetry or toxicity were excluded. In the case of multiple studies from the same center, the study with the largest number of patients was included; however, if 2 studies from the same center assessed different outcomes, they were also included separately. Studies with RLT other than [$^{177}$Lu]Lu-PSMA, such as $^{90}$Y-PSMA, $^{225}$Ac-PSMA, or tandem [$^{225}$Ac]Ac-PSMA/[$^{177}$Lu]Lu-PSMA, were also excluded. Discrepancies, if any, were resolved in consultation with the third reviewer. Institutional review board approval was not required since only prior published studies were evaluated.

### Data Extraction

The following data were extracted from the included articles by 2 reviewers independently: name of first author; publication year; study design; sample size; baseline patient characteristics such as age and serum PSA; treatment characteristics such as agent administered, number of cycles, interval between each cycle, and activity administered per cycle; and available treatment outcomes (namely PSA RR or PFS or OS). For evaluating the impact of prior chemotherapy on treatment outcomes, we extracted the univariate odds ratios (ORs) for PSA response and the univariate hazard ratios (HRs) for PFS and OS in taxane-naïve versus taxane-treated patients, as available. Natural logarithmic transformations of the ratios (OR or HR) and their corresponding 95% CIs were done, and SEs for the ratios in the individual articles were calculated (*12*).

Quality assessment of the included studies was done as per the adapted Newcastle–Ottawa scale for single-arm cohort studies by 2 reviewers independently. The scale consists of 2 parameters—selection and outcome—with a total score of at least 4 for a study to be considered of good quality (*13*).

### Statistical Analysis

All statistical analyses were performed using RevMan (version 5.3; Nordic Cochrane Centre) and Stata (version 14.2; Stata Corp.). Statistical heterogeneity was assessed using $I^2$ statistics, with an $I^2$ value of 30%–50% representing moderate heterogeneity and more than 50% suggesting substantial heterogeneity. The pooled OR and HR estimates were calculated using the generic inverse-variance method with random-effects model. Forest plots were generated to summarize the results. Sensitivity analysis was done to explore heterogeneity, if any, by calculating the pooled estimates after consecutively excluding each study from the metaanalysis. Subgroup analyses were based on the type of the study, sample size, and RLT agent used. Funnel plots and Egger regression tests were also undertaken to assess for publication bias. A $P$ value of less than 0.05 was considered statistically significant.

## RESULTS

### Study Characteristics

In total, 591 articles were found through a systematic search of the databases: 148 from PubMed, 148 from Scopus, and 295 from Embase. After screening of titles and abstracts and removal of duplicate records, 47 full-text articles were assessed for eligibility. Thirteen articles were finally included, comprising 2,068 patients (Fig. 1; Supplemental Tables 1–2) (*14–26*). All studies were single-arm interventional studies and, barring 2 studies (*19,20*), were retrospective. All studies included mCRPC patients who had progressive disease despite prior treatments with antiandrogens with or without chemotherapy and who had been administered [$^{177}$Lu]Lu-PSMA-RLT as salvage or compassionate treatment. The prior taxane chemotherapy status was available for 2,067 patients, of whom 590 (28.5%) were taxane-naïve and 1,477 (71.5%) had received prior taxane. The median of the median and mean age of the patients in the evaluable articles was 71.6 y (range, 30–92 y). The median of the median and mean pretreatment PSA of the patients was 214 ng/mL (range, 0.07–11,830 ng/mL). Most studies used RLT with [$^{177}$Lu]Lu-PSMA-617 ($n$ = 8); however, 3 studies used [$^{177}$Lu]Lu-PSMA-I&T (*17,25,26*) and 2 other studies used both agents in their respective cohorts (*16,21*). [$^{177}$Lu]Lu-PSMA-RLT was administered intravenously at activities of up to 11.6 GBq/cycle (usually 6.0–7.4 GBq/cycle), 3–12 wk apart over 1–20 cycles. The patients were followed up for a median of 9.9 mo (range, 0.5–72 mo). The characteristics of the included articles are detailed in Supplemental Table 1. The impact of prior chemotherapy

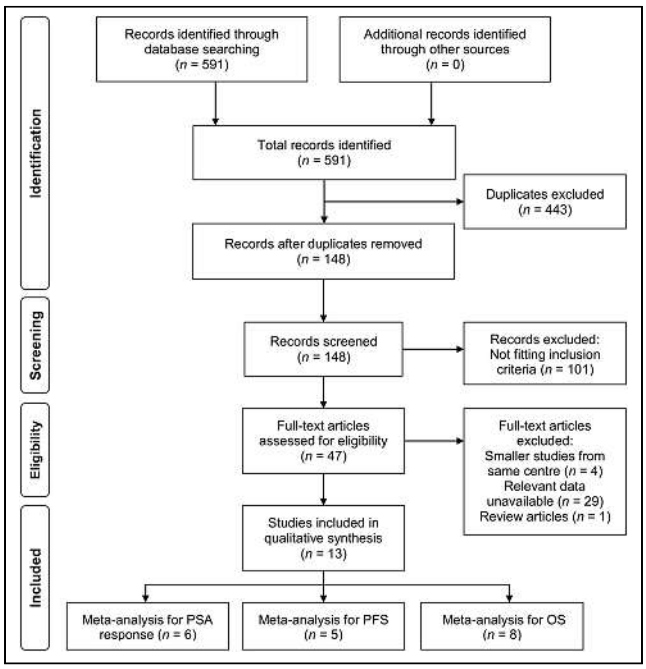


**FIGURE 1.** Flowchart describing study selection process.

**TABLE 1**
Prior Chemotherapy Status and Impact on Response and Survival Outcomes in Included Studies (Taxane-Naïve vs. Taxane-Treated Patients)

| Study | Sample size (*n*) | Prior status | | Univariate OR for PSA response | Univariate HR for PFS | Univariate HR for OS |
|---|---|---|---|---|---|---|
| | | Taxane-naïve (*n*) | Taxane-treated (*n*) | | | |
| Bräuer (*14*) | 59 | 12 (20.3%) | 47 (79.7%) | NS | NS | 0.62 (0.22–1.79) |
| Rahbar (*15*) | 145 | 66 (45.5%) | 79 (54.5%) | 1.94 (0.87–4.33)* | NS | NS |
| Barber (*16*) | 167 | 84 (50.3%) | 83 (49.7%) | 1.97 (0.99–3.95)† | 0.59 (0.41–0.83) | 0.39 (0.25–0.62) |
| Heck (*17*) | 100 | 16 (16.0%) | 84 (84.0%) | 1.33 (0.45–3.93) | Excluded‡ | Excluded‡ |
| Ahmadzadehfar (*18*) | 416 | 102 (24.5%) | 314 (75.5%) | NS | NS | 0.67 (0.51–0.87) |
| Yadav (*19*) | 90 | 6 (6.7%) | 84 (93.3%) | 1.29 (0.24–6.82) | NS | NS |
| Khreish (*20*) | 254 | 66 (26.0%) | 188 (74.0%) | NS | 0.71 (0.53–0.97) | 0.63 (0.39–1.01) |
| Meyrick§ (*21*) | 191 | 72 (37.7%) | 118 (61.8%) | NS | 0.58 (0.42–0.80) | 0.29 (0.18–0.47) |
| Rasul (*22*) | 61 | 19 (31.1%) | 42 (68.9%) | 1.27 (0.42–3.80) | NS | NS |
| Widjaja (*23*) | 71 | 12 (16.9%) | 59 (83.1%) | 4.08 (1.00–16.63) | NS | NS |
| Yadav (*24*) | 121 | 20 (16.5%) | 101 (83.5%) | NS | 0.63 (0.34–1.13) | 0.50 (0.27–0.91) |
| Hartrampf (*25*) | 92 | 28 (30.4%) | 64 (69.6%) | NS | NS | 0.67 (0.40–1.13) |
| Karimzadeh (*26*) | 301 | 87 (28.9%) | 214 (71.1%) | NS | 0.53 (0.40–0.69)‖ | 0.67 (0.45–0.98)‖ |

*OR for PSA RR evaluated in 99 patients: 44 taxane-naïve and 55 taxane-treated.
†OR for PSA RR evaluated in 132 patients: 70 taxane-naïve and 62 taxane-treated.
‡Results excluded because corresponding estimates were available in larger study from same center (*26*).
§Prior chemotherapy status available for 190 patients.
‖HR for PFS and OS evaluated in 295 patients: 84 taxane-naïve and 211 taxane-treated.
NS = not specified.
Data in parentheses are percentages or 95% CIs.

on treatment outcomes in the individual studies is summarized in Table 1. All included studies were of good quality as per the Newcastle–Ottawa scale, with 11 of the 13 articles having a total score of 6 each (Table 2).

**TABLE 2**
Quality Assessment of Included Studies Using Adapted Newcastle–Ottawa Scale

| Study | Selection | Outcome | Total score |
|---|---|---|---|
| Bräuer (*14*) | 3 | 2 | 5 |
| Rahbar (*15*) | 3 | 2 | 5 |
| Barber (*16*) | 3 | 3 | 6 |
| Heck (*17*) | 3 | 3 | 6 |
| Ahmadzadehfar (*18*) | 3 | 3 | 6 |
| Yadav (*19*) | 3 | 3 | 6 |
| Khreish (*20*) | 3 | 3 | 6 |
| Meyrick (*21*) | 3 | 3 | 6 |
| Rasul (*22*) | 3 | 3 | 6 |
| Widjaja (*23*) | 3 | 3 | 6 |
| Yadav (*24*) | 3 | 3 | 6 |
| Hartrampf (*25*) | 3 | 3 | 6 |
| Karimzadeh (*26*) | 3 | 3 | 6 |

### Pooled OR for PSA Response

The PSA RRs, that is, the proportions of patients achieving at least a 50% decline in serum PSA from baseline, ranged from 34% to 61% in the evaluable articles. Six articles consisting of 553 patients provided univariate ORs to assess the impact of prior taxane chemotherapy status on PSA response (*15–17,19,22,23*). These included 167 (30.2%) taxane-naïve patients and 386 (69.8%) taxane-treated patients. The estimated pooled OR for PSA response in taxane-naïve versus taxane-treated patients was 1.82 (95% CI, 1.21–2.71; $P = 0.004$). No statistical heterogeneity was observed ($I^2 = 0\%$, $P = 0.810$) (Fig. 2A).

Individual patient data for PSA RRs were available in 3 articles comprising 303 patients (*16,17,23*). The pooled PSA RR after [$^{177}$Lu]Lu-PSMA-RLT was significantly higher in the taxane-naïve patients than in patients who received chemotherapy (56/98 [57.1%] vs. 81/205 [39.5%]; difference, 17.6%; 95% CI, 5.6%–28.9%; $P = 0.004$).

### Pooled HR for PFS

In the evaluable articles, the median PFS ranged from 4.0 to 12.0 mo. The impact of prior chemotherapy status on PFS was evaluated in 5 articles (1,027 patients) comprising 326 (31.7%) taxane-naïve and 701 (68.3%) taxane-treated patients (*16,20,21,24,26*). Three of these articles evaluated PFS based on PSA progression (*20,24,26*), one assessed radiologic PFS (*16*), and another evaluated both PSA PFS and radiologic PFS (*21*). The pooled HR estimate for overall PFS in taxane-naïve versus taxane-treated patients was 0.60 (95% CI, 0.51–0.69; $P < 0.001$) (Fig. 2B). No significant statistical

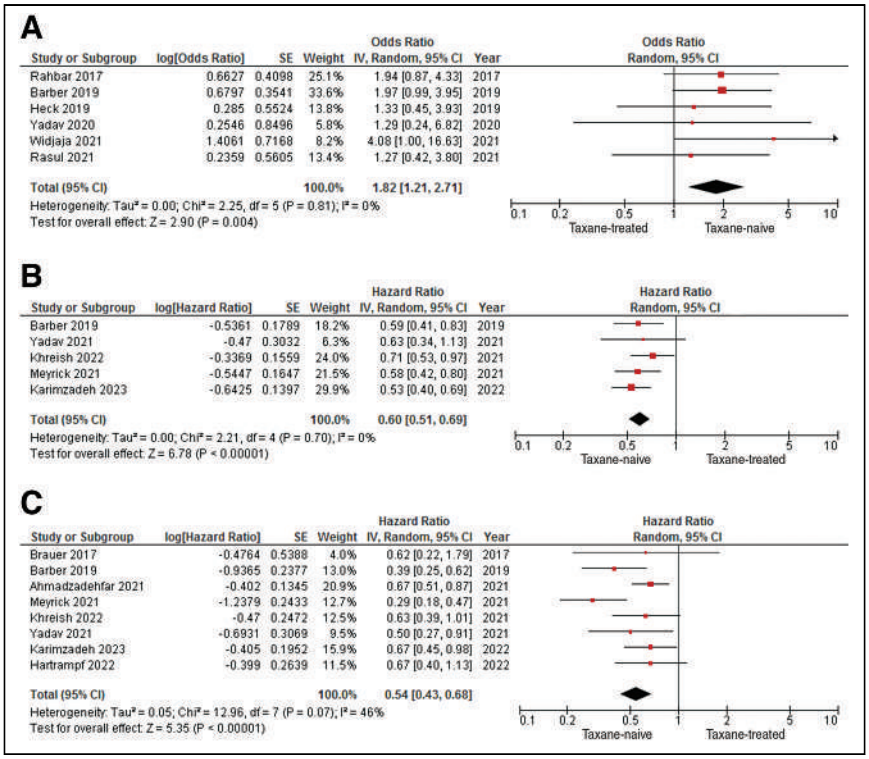


**FIGURE 2.** Forest plots showing pooled estimates of univariate OR for PSA response (A), univariate HR for PFS (B), and univariate HR for OS (C) in taxane-naïve vs. taxane-treated patients after $^{177}$Lu-PSMA-RLT.

heterogeneity was noted ($I^2$ = 0%, $P$ = 0.70). The corresponding pooled HR estimates for PSA PFS and radiologic PFS were 0.60 (95% CI, 0.51–0.71; $P < 0.001$; $I^2$ = 0%) and 0.55 (95% CI, 0.43–0.70; $P < 0.001$; $I^2$ = 0%), respectively.

### Pooled HR for OS

The median OS in the included articles ranged from 8.0 to 27.1 mo. Eight articles comprising 1,594 patients evaluated the impact of prior chemotherapy in predicting OS using univariate analysis (*14,16,18,20,21,24–26*). The estimated pooled univariate HR for taxane-naïve patients ($n$ = 468/1,594, 29.4%) versus taxane-treated patients ($n$ = 1,126/1,594, 70.6%) was 0.54 (95% CI, 0.43–0.68; $P < 0.001$) (Fig. 2C). Moderate statistical heterogeneity was observed ($I^2$ = 46%, $P$ = 0.07). Sensitivity analysis indicated that the source of heterogeneity was the study by Meyrick et al. (*21*). After exclusion of this particular result from the meta-analysis, the pooled HR for OS was 0.61 (95% CI, 0.52–0.71; $P < 0.001$) and did not exhibit any statistical heterogeneity ($I^2$ = 0%, $P$ = 0.58).

### Subgroup Analyses

Table 3 shows the results of subgroup analyses of the pooled estimates based on the study design, sample size, and RLT agent used. Significantly better PFS and OS outcomes were observed with both [$^{177}$Lu]Lu-PSMA-617 (HR for PFS, 0.69; HR for OS, 0.64) and [$^{177}$Lu]Lu-PSMA-I&T (HR for PFS, 0.53; HR for OS, 0.67) in the taxane-naïve than in the taxane-treated patients.

### Publication Bias

Visual assessment of funnel plots for the efficacy outcomes did not indicate any publication bias. Egger regression test results were not statistically significant (Fig. 3).

## DISCUSSION

With the results of the landmark VISION and TheraP trials, [$^{177}$Lu]Lu-PSMA-RLT has been proven to improve outcomes in mCRPC patients in the postchemotherapy setting (*6,7*). Given its encouraging efficacy and safety profiles in end-stage mCRPC, use in earlier treatment lines is expected to result in even better outcomes. However, the absence of definite evidence of improvement in outcomes has so far hindered the acceptability of [$^{177}$Lu]Lu-PSMA-RLT earlier in the disease course. Further, retrospective

**TABLE 3**
Subgroup Analyses of Pooled Estimates

| | Pooled OR for PSA response | | Pooled HR for PFS | | Pooled HR for OS | |
|---|---|---|---|---|---|---|
| Variable | 95% CI | $I^2$ | 95% CI | $I^2$ | 95% CI | $I^2$ |
| Study design | | | | | | |
| Retrospective | 1.85 (1.22–2.81) | 0% | 0.56 (0.47–0.67) | 0% | 0.53 (0.41–0.68) | 53% |
| Prospective | 1.29 (0.24–6.82) | NA | 0.71 (0.53–0.97) | NA | 0.63 (0.39–1.01) | NA |
| Sample size | | | | | | |
| <100 patients | 1.87 (1.07–3.25) | 0% | NA | NA | 0.66 (0.42–1.05) | 0% |
| ≥100 patients | 1.76 (0.98–3.16) | 0% | NA | NA | 0.52 (0.39–0.68) | 60% |
| RLT agent | | | | | | |
| $^{177}$Lu-PSMA-617 | 1.87 (1.07–3.25) | 0% | 0.69 (0.53–0.91) | 0% | 0.64 (0.51–0.78) | 0% |
| $^{177}$Lu-PSMA-I&T | 1.33 (0.45–3.93) | NA | 0.53 (0.40–0.69) | NA | 0.67 (0.49–0.91) | 0% |

NA = not applicable.

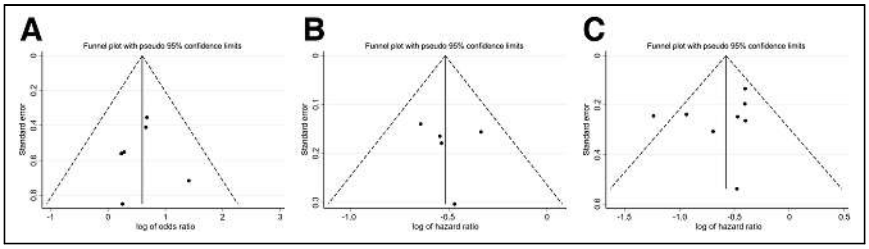


**FIGURE 3.** Funnel plots evaluating publication bias for PSA RR (A), PFS (B), and OS (C)

studies evaluating [$^{177}$Lu]Lu-PSMA-RLT outcomes in taxane-naïve versus taxane-treated patients have so far given conflicting results (*14–26*). To address this evidence gap, this systematic review and metaanalysis comprehensively pooled 13 studies to evaluate the impact of prior chemotherapy status on [$^{177}$Lu]Lu-PSMA-RLT outcomes. Our results clearly indicate that [$^{177}$Lu]Lu-PSMA-RLT resulted in significantly better PSA response, PFS, and OS when administered in the taxane-naïve setting than in the post-taxane setting. Specifically, in taxane-naïve patients receiving [$^{177}$Lu]Lu-PSMA-RLT, the odds of having a PSA response were 1.8 times better than in taxane-treated patients, with a reduction of 40% and 46% in the risk of progression and deaths, respectively.

Nevertheless, the results of this metaanalysis, although highly relevant, are no substitute for those of a randomized controlled trial. To date, only a single prospective phase 2 trial has evaluated [$^{177}$Lu]Lu-PSMA-RLT in taxane-naïve mCRPC. The trial compared [$^{177}$Lu]Lu-PSMA-617 with docetaxel in 40 taxane-naïve mCRPC patients and showed that [$^{177}$Lu]Lu-PSMA-617 had response outcomes similar and noninferior to docetaxel. Further, patients receiving [$^{177}$Lu]Lu-PSMA-617 experienced fewer grade 3–5 adverse events (30% vs. 50%, respectively), with a significantly better quality of life, than those receiving docetaxel (*27*). These results, when coupled with those of our metaanalysis, support the notion that [$^{177}$Lu]Lu-PSMA-RLT can safely be instituted in the prechemotherapy space, at least in the second-line setting (post-ARPI) in mCRPC, with better long-term outcomes. Upcoming phase 3 trials with [$^{177}$Lu]Lu-PSMA-RLT in the taxane-naïve setting—such as PSMAfore (NCT04689828) and SPLASH (NCT04647526)—will help elucidate its impact on survival outcomes.

The reasons underlying better outcomes with [$^{177}$Lu]Lu-PSMA-RLT in the taxane-naïve setting need exploration. In a series of 167 patients, Barber et al. observed that the patients receiving [$^{177}$Lu]Lu-PSMA-RLT and, previously, taxane-based chemotherapy had more aggressive baseline features than did their taxane-naïve counterparts, such as a higher tumor burden, lower hemoglobin levels, poorer performance status, and a greater number of prior treatments (*16*). A baseline poor performance status before [$^{177}$Lu]Lu-PSMA-RLT affects tolerance of the complete RLT course and negatively impacts survival outcomes. Further, chemotherapy-induced systemic toxicities often result in a relatively lower threshold for tolerating RLT-related adverse events, thereby further compromising patient tolerance of RLT. It is known that higher cumulative activities of [$^{177}$Lu]Lu-PSMA-RLT are necessary for an adequate tumor-absorbed dose and for causing a tumor response (*28,29*). Poor tolerance and the resultant inability to complete the RLT course in taxane-treated patients, especially in the face of highly aggressive, high-volume disease, is therefore likely to contribute to poor post-RLT outcomes, often coupled with added toxicity. In contrast, taxane-naïve patients are likely to have a better performance status, less aggressive disease, fewer toxicities, better tolerance to [$^{177}$Lu]Lu-PSMA-RLT, and, hence, better efficacy and safety outcomes.

Another parameter bearing significance is tumor heterogeneity, especially in the presence of visceral metastases. In the era of extensive use of novel ARPIs, the prevalence of visceral metastasis in mCRPC has increased manifold, with a possible contribution from the prolonged androgen suppression leading to neuroendocrine transdifferentiation (*30*). PSMA expression in these metastases is often low and accompanied by increased metabolic activity on 2-[$^{18}$F]FDG PET/CT (*31*). Patients with these low–PSMA-expressing or discordant metastases therefore respond poorly to [$^{177}$Lu]Lu-PSMA-RLT and are better suited for chemotherapy (*32,33*). On the basis of our observations, we believe that mCRPC patients after progression with ARPIs can safely and effectively be treated with [$^{177}$Lu]Lu-PSMA-RLT in cases of adequate PSMA expression and preferably in the absence of visceral metastases. If patients progress on [$^{177}$Lu]Lu-PSMA-RLT or already have discordant visceral metastases at initial presentation, chemotherapy might be an option. A crossover randomized controlled trial comparing the sequencing of [$^{177}$Lu]Lu-PSMA-RLT and taxane chemotherapy in the post-ARPI setting will be necessary to validate our hypothesis.

The current metaanalysis is not without limitations. The number of studies included for each outcome analyzed was quite limited to obtain definitive conclusions. Most studies were retrospective and single-armed and thus had an inherent high risk of bias. Further, the numbers of taxane-naïve and taxane-treated patients were not equally matched. Pooled estimates of univariate ORs and HRs might also have been affected by other clinical variables.

## CONCLUSION

The current metaanalysis comprehensively pooled the largest series—to our knowledge—of taxane-naïve mCRPC patients treated with [$^{177}$Lu]Lu-PSMA-RLT. Our results highlight the better response and long-term survival outcomes with [$^{177}$Lu]Lu-PSMA-RLT in such patients with no prior exposure to taxane chemotherapy. Although data from phase 3 trials are awaited, our results show a promising role for [$^{177}$Lu]Lu-PSMA-RLT in the taxane-naïve space. This will be especially beneficial for those patients who are ineligible for or unwilling to undergo chemotherapy because of its potential toxicities and adverse impact on quality of life. Further trials evaluating [$^{177}$Lu]Lu-PSMA-RLT in the taxane-naïve setting are now required.

## DISCLOSURE

No potential conflict of interest relevant to this article was reported.

**KEY POINTS**

**QUESTION:** Will [$^{177}$Lu]Lu-PSMA-RLT be more effective when administered before taxane chemotherapy than after?

**PERTINENT FINDINGS:** This systematic review and metaanalysis comprised 13 articles with 2,068 patients. In 6 articles comprising 553 patients, taxane-naïve patients had significantly better odds of a biochemical response after [$^{177}$Lu]Lu-PSMA-RLT (pooled OR, 1.82; 95% CI, 1.21–2.71). A taxane-naïve status was also a predictor of significantly better PFS (5 articles; 1,027 patients; pooled HR, 0.60; 95% CI, 0.51–0.69) and OS (8 articles; 1,594 patients; pooled HR, 0.54; 95% CI, 0.43–0.68) after [$^{177}$Lu]Lu-PSMA-RLT.

**IMPLICATIONS FOR PATIENT CARE:** Although [$^{177}$Lu]Lu-PSMA-RLT has been proven effective in end-stage disease, our results suggest even better outcomes in patients with no prior exposure to chemotherapy.

## REFERENCES


1. Bray F, Ferlay J, Soerjomataram I, Siegel RL, Torre LA, Jemal A. Global cancer statistics 2018: GLOBOCAN estimates of incidence and mortality worldwide for 36 cancers in 185 countries. *CA Cancer J Clin.* 2018;68:394–424.
2. Helgstrand JT, Røder MA, Klemann N, et al. Trends in incidence and 5-year mortality in men with newly diagnosed, metastatic prostate cancer: a population-based analysis of 2 national cohorts. *Cancer.* 2018;124:2931–2938.
3. Cornford P, Bellmunt J, Bolla M, et al. EAU-ESTRO-SIOG guidelines on prostate cancer. Part II: treatment of relapsing, metastatic, and castration-resistant prostate cancer. *Eur Urol.* 2017;71:630–642.
4. Ingrosso G, Detti B, Scartoni D, et al. Current therapeutic options in metastatic castration-resistant prostate cancer. *Semin Oncol.* 2018;45:303–315.
5. Wright GL Jr, Haley C, Beckett ML, Schellhammer PF. Expression of prostate-specific membrane antigen in normal, benign, and malignant prostate tissues. *Urol Oncol.* 1995;1:18–28.
6. Sartor O, de Bono J, Chi KN, et al. Lutetium-177-PSMA-617 for metastatic castration-resistant prostate cancer. *N Engl J Med.* 2021;385:1091–1103.
7. Hofman MS, Emmett L, Sandhu S, et al. [$^{177}$Lu]Lu-PSMA-617 versus cabazitaxel in patients with metastatic castration-resistant prostate cancer (TheraP): a randomised, open-label, phase 2 trial. *Lancet.* 2021;397:797–804.
8. Garje R, Rumble RB, Parikh RA. Systemic therapy update on $^{177}$lutetium-PSMA-617 for metastatic castration-resistant prostate cancer: ASCO rapid recommendation. *J Clin Oncol.* 2022;40:3664–3666.
9. Manafi-Farid R, Harsini S, Saidi B, et al. Factors predicting biochemical response and survival benefits following radioligand therapy with [$^{177}$Lu]Lu-PSMA in metastatic castrate-resistant prostate cancer: a review. *Eur J Nucl Med Mol Imaging.* 2021;48:4028–4041.
10. Page MJ, McKenzie JE, Bossuyt PM, et al. The PRISMA 2020 statement: an updated guideline for reporting systematic reviews. *BMJ.* 2021;372:n71.
11. Scher HI, Morris MJ, Stadler WM, et al. Trial design and objectives for castration-resistant prostate cancer: updated recommendations from the Prostate Cancer Clinical Trials Working Group 3. *J Clin Oncol.* 2016;34:1402–1418.
12. Tierney JF, Stewart LA, Ghersi D, Burdett S, Sydes MR. Practical methods for incorporating summary time-to-event data into meta-analysis. *Trials.* 2007;8:16.
13. Schmitz S, Maguire Á, Morris J, et al. The use of single armed observational data to closing the gap in otherwise disconnected evidence networks: a network meta-analysis in multiple myeloma. *BMC Med Res Methodol.* 2018;18:66.
14. Bräuer A, Grubert LS, Roll W, et al. $^{177}$Lu-PSMA-617 radioligand therapy and outcome in patients with metastasized castration-resistant prostate cancer. *Eur J Nucl Med Mol Imaging.* 2017;44:1663–1670.
15. Rahbar K, Ahmadzadehfar H, Kratochwil C, et al. German multicenter study investigating $^{177}$Lu-PSMA-617 radioligand therapy in advanced prostate cancer patients. *J Nucl Med.* 2017;58:85–90.
16. Barber TW, Singh A, Kulkarni HR, Niepsch K, Billah B, Baum RP. Clinical outcomes of $^{177}$Lu-PSMA radioligand therapy in earlier and later phases of metastatic castration-resistant prostate cancer grouped by previous taxane chemotherapy. *J Nucl Med.* 2019;60:955–962.
17. Heck MM, Tauber R, Schwaiger S, et al. Treatment outcome, toxicity, and predictive factors for radioligand therapy with $^{177}$Lu-PSMA-I&T in metastatic castration-resistant prostate cancer. *Eur Urol.* 2019;75:920–926.
18. Ahmadzadehfar H, Rahbar K, Baum RP, et al. Prior therapies as prognostic factors of overall survival in metastatic castration-resistant prostate cancer patients treated with [$^{177}$Lu]Lu-PSMA-617. A WARMTH multicenter study (the 617 trial). *Eur J Nucl Med Mol Imaging.* 2021;48:113–122.
19. Yadav MP, Ballal S, Bal C, et al. Efficacy and safety of $^{177}$Lu-PSMA-617 radioligand therapy in metastatic castration-resistant prostate cancer patients. *Clin Nucl Med.* 2020;45:19–31.
20. Khreish F, Ghazal Z, Marlowe RJ, et al. $^{177}$Lu-PSMA-617 radioligand therapy of metastatic castration-resistant prostate cancer: initial 254-patient results from a prospective registry (REALITY study). *Eur J Nucl Med Mol Imaging.* 2022;49:1075–1085.
21. Meyrick D, Gallyamov M, Sabarimurugan S, Falzone N, Lenzo N. Real-world data analysis of efficacy and survival after lutetium-177 labelled PSMA ligand therapy in metastatic castration-resistant prostate cancer. *Target Oncol.* 2021;16:369–380.
22. Rasul S, Hartenbach M, Wollenweber T, et al. Prediction of response and survival after standardized treatment with 7400 MBq $^{177}$Lu-PSMA-617 every 4 weeks in patients with metastatic castration-resistant prostate cancer. *Eur J Nucl Med Mol Imaging.* 2021;48:1650–1657.
23. Widjaja L, Werner RA, Ross TL, Bengel FM, Derlin T. PSMA expression predicts early biochemical response in patients with metastatic castration-resistant prostate cancer under $^{177}$Lu-PSMA-617 radioligand therapy. *Cancers (Basel).* 2021;13:2938.
24. Yadav MP, Ballal S, Sahoo RK, et al. Long-term outcome of $^{177}$Lu-PSMA-617 radioligand therapy in heavily pre-treated metastatic castration-resistant prostate cancer patients. *PLoS One.* 2021;16:e0251375.
25. Hartrampf PE, Seitz AK, Weinzierl FX, et al. Baseline clinical characteristics predict overall survival in patients undergoing radioligand therapy with [$^{177}$Lu]Lu-PSMA I&T during long-term follow-up. *Eur J Nucl Med Mol Imaging.* 2022;49:4262–4270.
26. Karimzadeh A, Heck M, Tauber R, et al. $^{177}$Lu-PSMA-I&T for treatment of metastatic castration resistant prostate cancer: prognostic value of scintigraphic and clinical biomarkers. *J Nucl Med.* 2023;64:402–409.
27. Satapathy S, Mittal BR, Sood A, et al. $^{177}$Lu-PSMA-617 versus docetaxel in taxane-naïve metastatic castration-resistant prostate cancer: a randomized, controlled, phase 2 non-inferiority trial. *Eur J Nucl Med Mol Imaging.* 2022;49:1754–1764.
28. Violet J, Jackson P, Ferdinandus J, et al. Dosimetry of $^{177}$Lu-PSMA-617 in metastatic castration-resistant prostate cancer: correlations between pretherapeutic imaging and whole-body tumor dosimetry with treatment outcomes. *J Nucl Med.* 2019;60:517–523.
29. Ling SW, de Blois E, Hooijman E, van der Veldt A, Brabander T. Advances in $^{177}$Lu-PSMA and $^{225}$Ac-PSMA radionuclide therapy for metastatic castration-resistant prostate cancer. *Pharmaceutics.* 2022;14:2166.
30. Makino T, Izumi K, Mizokami A. Undesirable status of prostate cancer cells after intensive inhibition of AR signaling: post-AR era of CRPC treatment. *Biomedicines.* 2021;9:414.
31. Shen K, Liu B, Zhou X, et al. The evolving role of $^{18}$F-FDG PET/CT in diagnosis and prognosis prediction in progressive prostate cancer. *Front Oncol.* 2021;11:683793.
32. Satapathy S, Mittal BR, Sood A. Visceral metastases as predictors of response and survival outcomes in patients of castration-resistant prostate cancer treated with $^{177}$Lu-labeled prostate-specific membrane antigen radioligand therapy: a systematic review and meta-analysis. *Clin Nucl Med.* 2020;45:935–942.
33. Michalski K, Ruf J, Goetz C, et al. Prognostic implications of dual tracer PET/CT: PSMA ligand and [$^{18}$F]FDG PET/CT in patients undergoing [$^{177}$Lu]PSMA radioligand therapy. *Eur J Nucl Med Mol Imaging.* 2021;48:2024–2030.

# Elevated Body Mass Index Is Associated with Improved Overall Survival in Castration-Resistant Prostate Cancer Patients Undergoing Prostate-Specific Membrane Antigen–Directed Radioligand Therapy

Philipp E. Hartrampf*[1], Patrick W. Mihatsch*[2], Anna Katharina Seitz[3], Lilja B. Solnes[4], Steven P. Rowe[4], Martin G. Pomper[4], Hubert Kübler[3], Thorsten A. Bley[2], Andreas K. Buck[1], and Rudolf A. Werner[1,4]

[1]*Department of Nuclear Medicine, University Hospital of Würzburg, Würzburg, Germany;* [2]*Department of Diagnostic and Interventional Radiology, University Hospital of Würzburg, Würzburg, Germany;* [3]*Department of Urology and Paediatric Urology, University Hospital of Würzburg, Würzburg, Germany; and* [4]*Russell H. Morgan Department of Radiology and Radiological Science, Johns Hopkins University School of Medicine, Baltimore, Maryland*

In patients with prostate cancer scheduled for systemic treatment, being overweight is linked to prolonged overall survival (OS), whereas sarcopenia is associated with shorter OS. We investigated fat-related and body composition parameters in patients undergoing prostate-specific membrane antigen (PSMA)–directed radioligand therapy (RLT) to assess their predictive value for OS. **Methods:** Body mass index (BMI, in kg/m$^2$) and CT-derived body composition parameters (total, subcutaneous, visceral fat area, and psoas muscle area at the L3–L4 level) were determined for 171 patients scheduled for PSMA-directed RLT. After normalization for stature, the psoas muscle index was used to define sarcopenia. Outcome analysis was performed using Kaplan–Meier curves and Cox regression including fat-related and other clinical parameters (Gleason score, C-reactive protein [CRP], lactate dehydrogenase [LDH], hemoglobin, and prostate-specific antigen levels). The Harrell C-index was used for goodness-of-fit analysis. **Results:** Sixty-five patients (38%) had sarcopenia, and 98 patients (57.3%) had increased BMI. Relative to the 8-mo OS in normal-weight men (BMI $< 25$), overweight men ($25 \geq$ BMI $> 30$) and obese men (BMI $\geq 30$) achieved a longer OS of 14 mo (hazard ratio [HR], 0.63; 95% CI, 0.40–0.99; $P = 0.03$) and 13 mo (HR, 0.47; 95% CI, 0.29–0.77; $P = 0.004$), respectively. Sarcopenia showed no impact on OS (11 vs. 12 mo; HR, 1.4; 95% CI, 0.91–2.1; $P = 0.09$). Most of the body composition parameters were tightly linked to OS on univariable analyses, with the highest C-index for BMI. In multivariable analysis, a higher BMI (HR, 0.91; 95% CI, 0.86–0.97; $P = 0.006$), lower CRP (HR, 1.09; 95% CI, 1.03–1.14; $P < 0.001$), lower LDH (HR, 1.08; 95% CI, 1.03–1.14; $P < 0.001$), and longer interval between initial diagnosis and RLT (HR, 0.95; 95% CI, 0.91–0.99; $P = 0.02$) were significant predictors of OS. **Conclusion:** Increased fat reserves assessed by BMI, CRP, LDH, and interval between initial diagnosis and RLT, but not CT-derived body composition parameters, were relevant predictors for OS. As BMI can be altered, future research should investigate whether a high-calorie diet before or during PSMA RLT may improve OS.

**Key Words:** PSMA; prostate cancer; radioligand therapy; overall survival; body composition

**J Nucl Med 2023; 64:1272–1278**
DOI: 10.2967/jnumed.122.265379

With more than 1.4 million new cases globally, prostate cancer (PC) is a major health burden (*1*), and androgen deprivation therapy alone or in combination with androgen receptor–targeted agents or chemotherapy is essential for treating patients with metastatic PC (*2*). Therapeutic options for evolving tumor biology leading to a castration-resistant tumor stage are still limited but include androgen receptor–targeted agents, for example, abiraterone and enzalutamide (*3,4*), or taxane-containing chemotherapies (*5,6*). In recent years, prostate-specific membrane antigen (PSMA)–directed radioligand therapy (RLT) has penetrated the clinical arena, demonstrating remarkable outcome benefits (*7–9*). For instance, the prospective VISION trial reported on a relevant improvement in overall survival (OS) when added to standard care (*10*), leading to recent U.S. Food and Drug Administration approval (*11*).

First-line therapeutic regimens used in hormone-sensitive stages, including androgen deprivation therapy, can influence body composition in PC (*12–15*). Body composition parameters were also tightly linked to outcome for men with castration-resistant PC (CRPC) (*16*). For instance, several studies have reported that overweight or obesity is favorable for prognosis in patients with CRPC, such as those receiving taxane-based chemotherapy (*17–19*), whereas high visceral fat is suspected of being a predictor of worse outcome (*19–21*). Moreover, defined as gradual skeletal muscle loss, sarcopenia still has a debatable impact on disease progression under second-line therapies such as docetaxel (*19,22,23*).

In the present study, the prevalence of sarcopenia and obesity in men with PSMA-targeted RLT using [$^{177}$Lu]Lu-PSMA I&T was assessed. We also aimed to determine the impact of fat-related and other CT-derived body composition parameters, as well as laboratory values and clinical characteristics, on outcome.

## MATERIALS AND METHODS

### Patient Cohort

One hundred seventy-one CRPC patients treated with [$^{177}$Lu]Lu-PSMA I&T were included in this investigation. The local ethics

Received Dec. 29, 2022; revision accepted Mar. 21, 2023.
For correspondence or reprints, contact Philipp E. Hartrampf (hartrampf_p@ukw.de).
*Contributed equally to this work.
Published online Jun. 8, 2023.

committee waived the need for further approval of this retrospective study (waiver 20210422 04). All patients gave written informed consent for the conducted procedures. Parts of this cohort have previously been reported (*24–28*), without focusing on fat-related and body composition parameters and their predictive performance for OS.

### Treatment with [$^{177}$Lu]Lu-PSMA I&T

The synthesis of [$^{177}$Lu]Lu-PSMA I&T was previously described (*28*). Details on the standardized pretherapy work-up in our department were also previously published (*24*). In brief, blood panels including prostate-specific antigen (PSA) level, C-reactive protein (CRP), lactate dehydrogenase (LDH), and hemoglobin were collected at cycle 1, day 1, and the patient's history was available in an electronic health database. Information on processing of blood samples and dedicated laboratory analyses was previously published (*28*). For treatment, we administered 6.0 GBq of [$^{177}$Lu]Lu-PSMA I&T every 8 wk (maximum, 9 cycles per patient).

### Assessment of Body Composition

As part of serial hybrid imaging, PSMA-directed PET along with respective CT was performed before initiation of PSMA-directed RLT, defined as baseline. CT images were assessed on a workstation equipped with syngo.via imaging software, version VB60A_HF01 (Siemens Healthineers AG). The scans were evaluated by an observer with 4 y of experience in reading PSMA-targeted PET/CT, who underwent a previous training session, and were reviewed by experienced readers, if needed. The hybrid imaging protocol was previously published (*29*).

CT-based assessment of body composition was performed as previously described (*23*). Cross-sectional areas of different tissue compartments, including total, subcutaneous, and visceral fat areas, as well as the psoas muscle area, were segmented on axial CT scans at the level of the third and fourth lumbar vertebrae (L3–L4) by manually drawing a region of interest for each compartment and applying the respective tissue-typical Hounsfield unit threshold: −190 to −30 for adipose tissue and −29 to +150 for muscle tissue (Fig. 1). Body mass index (BMI, in kg/m$^2$), visceral fat–to–subcutaneous fat ratio, and subcutaneous fat–to–muscle ratio were calculated. BMI was classified as normal (<25), preobese (25 ≤ BMI < 30), or obese (≥30) (*30*). Subcutaneous fat area, visceral fat area, and psoas muscle area were then normalized for slice thickness, and all of those parameters were also normalized for stature to derive respective indices (subcutaneous fat index, visceral fat index, and psoas muscle index [PMI], in cm$^2$/m$^2$). Sarcopenia was then defined as an L3 PMI of less than 5.7 cm$^2$/m$^2$ according to the literature (*22,23*).

### Statistical Analyses

We used GraphPad Prism, version 9.3.0 (GraphPad Software), for statistical analyses. Descriptive data are presented as median and range. We defined OS as the interval from the day of the first cycle until the day of death (presented as median). Univariable Cox regression was performed with all parameters for OS after exclusion of outliers ($n = 7$). For multivariable analysis, we then selected significant parameters from the univariable analysis. Parallel inclusion of multiple body composition parameters in 1 model was not possible because of multicollinearity (e.g., BMI + weight + total fat area or psoas muscle area + PMI). Thus, we decided for the relevant clinical parameter BMI (as a fat-related parameter) and PMI (as an established marker of sarcopenia) in the multivariable analyses (*22,23*). Different Cox regression models were compared with each other and with a null model (without any parameter) using the Akaike information criterion (*31*) and the Harrell C-statistic (*32*). In this regard, a lower Akaike information criterion and a higher Harrell C value indicate a better-fit model (*31,32*). The hazard ratio (HR) of death and 95% CI are presented. Kaplan–Meier curves and log-rank comparison were also calculated to illustrate different survivals between high- and low-risk patients. We present median survival in months, with the HR of death and 95% CI. A $P$ value of less than 0.05 was considered statistically significant.

## RESULTS

### Patient Characteristics

The median age of the 171 included patients was 71 y (range, 46–95 y), and the median Gleason score at original diagnosis was 9 (range, 5–10). The patients received a median of 2 systemic treatment lines before PSMA RLT, with 71%, 65%, 68%, and 8% of patients receiving taxane-based chemotherapy, enzalutamide, abiraterone, and $^{223}$Ra, respectively. The median baseline laboratory values were 158 ng/mL (range, 0.07–5,000 ng/mL), 0.56 mg/dL (range, 0.02–29.34 mg/dL), 268 U/L (range, 118–1,800 U/L), and 11.6 g/dL (range, 6.0–16.1 g/dL) for PSA, CRP, LDH, and hemoglobin, respectively. Men underwent a median of 2 cycles (range, 1–9) of RLT with [$^{177}$Lu]Lu-PSMA I&T. The median follow-up was 7 mo (range, 1–53 mo), and the median OS was 11 mo. Ninety-four patients died during follow-up. At baseline, 73 patients (42.7%) showed a normal BMI, 56 patients (32.7%) were preobese, and the remaining 42 patients (24.6%) were obese. Sarcopenia was recorded in 65 patients (38%; Table 1). Table 1 provides a comprehensive overview of the baseline patient characteristics.

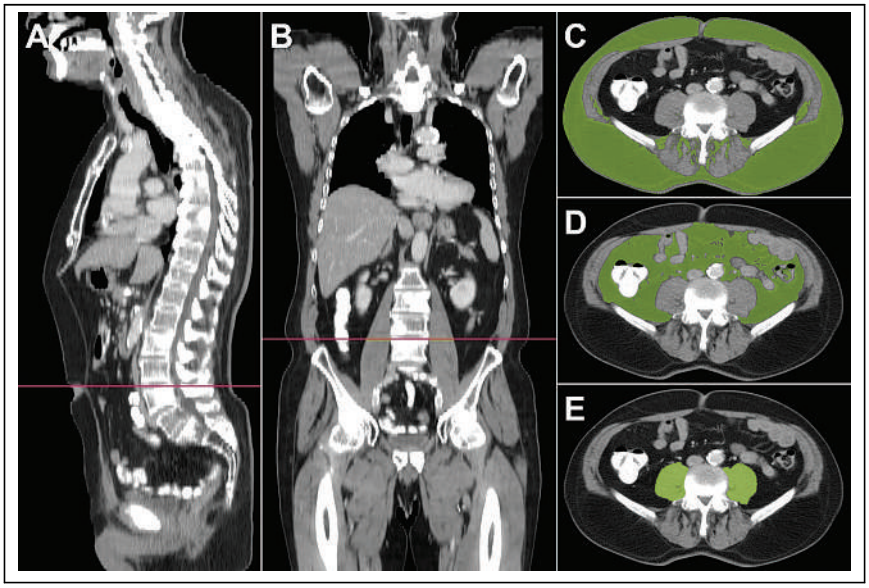


**FIGURE 1.** Example of 68-y-old patient with PC. As part of hybrid imaging (PSMA PET/CT), body composition of CT was investigated. Sagittal (A), coronal (B), and axial (C–E) CT images show segmentation of separate tissue compartments at level of third and fourth lumbar vertebrae (L3–L4) applying different Hounsfield units: subcutaneous fat cross-sectional area (−190 to −30) (C), visceral fat cross-sectional area (−190 to −30) (D), and psoas muscle area (−29 to +150) (E).

### Identification of Patients Prone to Shorter Survival Through BMI but Not CT-Derived Body Composition Parameters

Univariable Cox regression for different body composition parameters revealed total fat area (per 50 cm$^2$; HR, 0.93; 95% CI, 0.88–0.99; $P = 0.03$), psoas muscle area

**TABLE 1**
Patient Characteristics

| Characteristic at initiation of RLT | Data |
|---|---|
| Age (y) | 71 (46–95) |
| PSA (ng/mL) | 158 (0.07–5,000) |
| CRP (mg/dL) | 0.56 (0.02–29.34) |
| LDH (U/L) | 268 (118–1,800) |
| Hemoglobin (g/dL) | 11.6 (6.0–16.1) |
| Interval between initial diagnosis and RLT (mo) | 71 (9–364) |
| Gleason score | 9 (5–10) |
| BMI ($kg/m^2$) | 25.8 (18.4–49.7) |
| Normal (BMI $<$ 25) | 73 (42.7%) |
| Preobese (25 $\leq$ BMI $<$ 30) | 56 (32.7%) |
| Obese (BMI $\geq$ 30) | 42 (24.6%) |
| Body composition before initiation of RLT | |
| Psoas muscle area ($cm^2$) | 19.0 (7.9–37.2) |
| PMI ($cm^2/m^2$) | 6.1 (2.5–11.9) |
| Sarcopenia (PMI $<$ 5.7 $cm^2/m^2$) | 65 (38.0%) |
| Total fat area ($cm^2$) | 416.7 (104.8–1,372) |
| Visceral fat area ($cm^2$) | 166.9 (23.3–478.9) |
| Visceral fat index ($cm^2/m^2$) | 53.8 (6.5–160.4) |
| Subcutaneous fat area ($cm^2$) | 229.5 (70.2–1,053) |
| Subcutaneous fat index ($cm^2/m^2$) | 76.4 (22.8–307.6) |
| Visceral fat–to–subcutaneous fat ratio | 0.77 (0.25–1.96) |
| Subcutaneous fat–to–muscle ratio | 12.4 (3.7–42.5) |
| RLT cycles (*n*) | 2 (1–9) |
| RLT in castration-resistant stage as … | |
| First-line therapy | 6/171 (3.5%) |
| Second-line therapy | 25/171 (14.6%) |
| Third-line therapy | 71/171 (41.5%) |
| Fourth-line therapy | 60/171 (35.1%) |

Qualitative data are number and percentage; continuous data are median and range.

(HR, 0.95; 95% CI, 0.91–0.99; $P = 0.02$), PMI (HR, 0.85; 95% CI, 0.75–0.97; $P = 0.01$), visceral fat index (HR, 0.99; 95% CI, 0.99–1.00; $P = 0.05$), BMI (HR, 0.91; 95% CI, 0.86–0.96; $P = 0.001$), and weight (HR, 0.97; 95% CI, 0.96–0.99; $P = 0.005$) as significantly associated with OS. Sarcopenia, however, failed to reach significance ($P = 0.14$, Table 2). Investigating clinical parameters, CRP (HR, 1.16; 95% CI, 1.11–1.20; $P = 0.001$), LDH (per 50 U/L; HR, 1.16; 95% CI, 1.11–1.20; $P = 0.001$), hemoglobin (HR, 0.71; 95% CI, 0.61–0.81; $P < 0.001$), PSA (HR, 1.01; 95% CI, 1.00–1.03; $P = 0.04$), and interval between initial diagnosis and RLT (per year; HR, 0.94; 95% CI, 0.89–0.98; $P = 0.003$) were significant predictors of OS. Age and Gleason score, however, were not significant ($P \geq 0.31$). However, the largest improvements in the models compared with a model without parameters (null model) were seen for BMI among the body composition and fat parameters (Akaike information criterion, 728.5 vs. 738.2 in the null model; C-index, 0.64).

The multivariable analysis included BMI, CRP, LDH, interval between initial diagnosis and RLT, hemoglobin, baseline PSA value, and PMI (C-index, 0.80). CRP (HR, 1.09; 95% CI, 1.03–1.14; $P < 0.001$), LDH (per 50 U/L; HR, 1.08; 95% CI, 1.03–1.14; $P < 0.001$), interval between initial diagnosis and RLT (per year; HR, 0.95; 95% CI, 0.91–0.99; $P = 0.02$), and BMI (HR, 0.91; 95% CI, 0.86–0.97; $P = 0.006$) remained significant predictors of OS (Table 3).

Relative to 8 mo in patients with a normal BMI, preobese men achieved a longer OS of 14 mo in Kaplan–Meier analysis (HR, 0.63; 95% CI, 0.40–0.99; $P = 0.03$). Similar results were recorded for obese subjects (OS, 13 mo; HR, 0.47; 95% CI, 0.29–0.77; $P = 0.004$ vs. normal BMI; Fig. 2). There was no significant difference in OS between preobese and obese subjects ($P = 0.39$). Patients with sarcopenia at baseline did not have a shorter OS than patients without sarcopenia (11 vs. 12 mo; HR, 1.4; 95% CI, 0.91–2.1; $P = 0.09$; Fig. 3).

## DISCUSSION

Investigating fat-related and CT-derived body composition parameters along with other clinical parameters of 171 PC patients

**TABLE 2**
Univariable Cox Regression Model

| Parameter | HR | 95% CI | AIC | Harrell C | *P* |
|---|---|---|---|---|---|
| Null model | | | 738.2 | | |
| CRP (per mg/dL) | 1.16 | 1.11–1.20 | 700.0 | 0.76 | 0.001 |
| LDH (per 50 U/L) | 1.16 | 1.11–1.20 | 703.2 | 0.75 | 0.001 |
| Hemoglobin (per g/dL) | 0.71 | 0.61–0.81 | 716.5 | 0.69 | 0.001 |
| BMI (per $kg/m^2$) | 0.91 | 0.86–0.96 | 728.5 | 0.64 | 0.001 |
| Interval between initial diagnosis and RLT (per year) | 0.94 | 0.89–0.98 | 729.4 | 0.62 | 0.003 |
| Weight (per kg) | 0.97 | 0.96–0.99 | 731.5 | 0.63 | 0.005 |
| PMI ($cm^2/m^2$) | 0.85 | 0.75–0.97 | 733.8 | 0.59 | 0.01 |
| Psoas muscle area (per $cm^2$) | 0.95 | 0.91–0.99 | 734.2 | 0.59 | 0.02 |
| Total fat area (per 50 $cm^2$) | 0.93 | 0.88–0.99 | 735.3 | 0.57 | 0.03 |
| Visceral fat area (per 50 $cm^2$) | 0.89 | 0.79–1.00 | 736.0 | 0.55 | 0.05 |
| Visceral fat index (per $cm^2/m^2$) | 0.99 | 0.99–1.00 | 736.1 | 0.56 | 0.05 |
| PSA (per 50 ng/mL) | 1.01 | 1.00–1.03 | 736.6 | 0.59 | 0.04 |
| Subcutaneous fat index (per $cm^2/m^2$) | 1.00 | 0.99–1.00 | 736.6 | 0.58 | 0.07 |
| Subcutaneous fat area (per 50 $cm^2$) | 0.91 | 0.82–1.01 | 737.1 | 0.57 | 0.09 |
| Sarcopenia present | 1.39 | 0.90–2.12 | 738.0 | 0.55 | 0.14 |
| Visceral fat–to–subcutaneous fat ratio | 0.71 | 0.39–1.22 | 738.7 | 0.50 | 0.24 |
| Age (per year) | 0.99 | 0.96–1.01 | 739.2 | 0.54 | 0.31 |
| Gleason score* | 1.12 | 0.89–1.42 | | 0.53 | 0.35 |
| Subcutaneous fat–to–muscle ratio | 0.99 | 0.96–1.03 | 740.1 | 0.51 | 0.74 |

*Because of missing values, another null model was used and comparison was not possible.
AIC = Akaike information criterion.
Lower Akaike information criterion and higher Harrell C values indicate better-fit model (*31,32*).

scheduled for RLT, we found that a higher BMI of at least 25 $kg/m^2$, a lower CRP, a lower LDH, and a longer interval between initial diagnosis and RLT were significant predictors for prolonged OS. The prevalence of sarcopenia or any other CT-derived body composition parameter, however, had no relevant impact on OS in a multivariable analysis.

In the present cohort, the occurrence of sarcopenia (38%) was comparable to that in prior studies for patients scheduled for docetaxel chemotherapy (*19,22*). However, this prevalence is higher than reported for people aged 60–70 y in the United States and parts of Europe, with those values ranging from 5% to 13% (*33*). As a possible explanation, this difference may be caused by an advanced tumor biology as included in the present study, which can result in increased catabolism and malnutrition (*34*). In addition, RLT patients have usually undergone extensive pretreatment with androgen deprivation therapy, enzalutamide/abiraterone, and chemotherapy with

**TABLE 3**
Multivariable Cox Regression

| Parameter | HR | 95% CI | AIC | Harrell C | *P* |
|---|---|---|---|---|---|
| Null model | | | 738.2 | | |
| CRP (per mg/dL) | 1.09 | 1.03–1.14 | 675.8 | 0.80 | <0.0001 |
| LDH (per 50 U/L) | 1.08 | 1.03–1.14 | | | <0.001 |
| BMI (per $kg/m^2$) | 0.91 | 0.86–0.97 | | | 0.006 |
| Interval between initial diagnosis and RLT (per year) | 0.95 | 0.91–0.99 | | | 0.02 |
| Hemoglobin (per g/dL) | 0.86 | 0.74–1.00 | | | 0.06 |
| PMI (per $cm^2/m^2$) | 0.92 | 0.80–1.01 | | | 0.25 |
| PSA (per 50 ng/mL) | 1.00 | 0.98–1.01 | | | 0.97 |

AIC = Akaike information criterion.

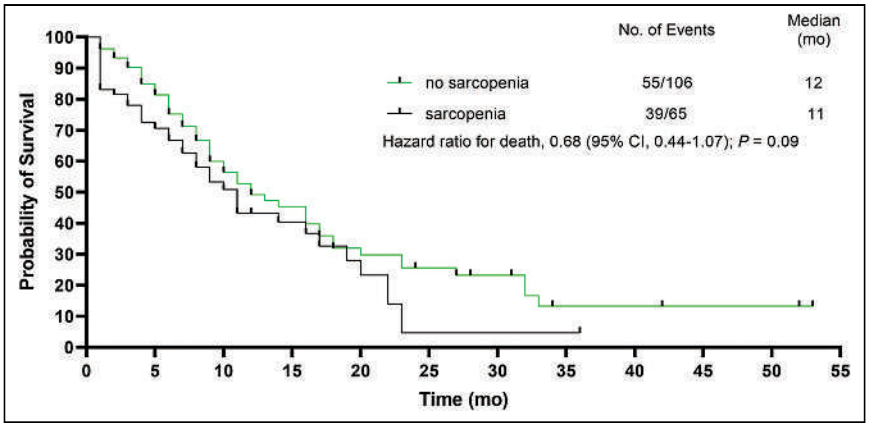


**FIGURE 2.** Kaplan–Meier curves and log rank comparisons for patients with and without sarcopenia and treated with RLT, revealing no relevant differences in OS for men allocated to either group.

docetaxel, which may also result in loss of skeletal muscle. In our investigated mCRPC patients treated with [$^{177}$Lu]Lu-PSMA I&T, sarcopenia was not associated with OS, as is in line with the findings on subjects scheduled for other last-line therapies such as docetaxel chemotherapy (*19*). Of note, Ohtaka et al. reported a shortened OS in sarcopenic patients undergoing taxane-based chemotherapy (*22*). Thus, given those varying results depending on the treatment regimen, further studies are needed to corroborate our findings of no relevant impact of muscle loss on outcome by investigating other PSMA-targeted therapeutic compounds, such as [$^{177}$Lu]Lu-PSMA-617 or rhPSMA-7.3 (*10,35*).

Investigating a large single-center experience with men treated with [$^{177}$Lu]Lu-PSMA-I&T to date, we found that most of the body composition parameters were tightly linked to OS on univariable analyses, thereby demonstrating their clinical relevance in patients treated with RLT. In this regard, a rather time-consuming assessment of CT-derived body composition parameters yielded comparable results to BMI. The latter parameter, however, is easily obtainable, for example, on a first-time visit when taking the patient's history before initiation of RLT.

In addition, BMI also achieved the highest C-index of all body composition parameters, further emphasizing the importance of this parameter in clinical routine to identify high-risk individuals experiencing treatment failure. On multivariable analysis including other relevant clinical parameters, BMI then again remained a significant predictor of OS along with CRP, LDH, and interval between initial diagnosis and RLT, whereas PMI as a CT body composition parameter failed to reach significance (Table 3). In this regard, PMI may still be prone to observer bias, but BMI as an easily obtainable clinical variable can be recorded in a standardized fashion on a first visit for RLT. Those considerations are further fueled by the fact that the recent Food and Drug Administration approval may increase the number of men anticipated for PSMA-directed RLT in the near future (*36*), thereby not allowing for laborious CT assessments in a busy theranostic practice. In this regard, we found that patients with a BMI of more than 25 kg/m$^2$ showed a significantly longer OS, which corroborates previous results for CRPC patients (*17,18*), in particular when treated with standard docetaxel chemotherapy (*19,21*).

As a possible explanation, patients with higher BMIs have greater fat reserves, thereby resisting tumor-associated cachexia for a substantially longer time after starting PSMA RLT. As such, this observation may have further clinical implications, as future studies may include high-calorie diet protocols before initiation of RLT or on repeated cycles, particularly when other therapies such as docetaxel have already been applied. In this regard, the observed impact of body habitus on OS is a variable that could be modified by the referring treating physician, whereas all other clinical variables that remained significant in multivariate analyses (including blood-based values or interval between initial diagnosis and RLT) cannot be modified. Nonetheless, the most appropriate dietary control would then have to be defined, as preclinical studies have reported stronger PC growth on high-fat than high-carbohydrate diets in murine studies (*37*). In this regard, our study may then also pave the way for future investigations, which should assess whether underweight patients scheduled for RLT may be at higher risk for treatment failure and whether those high-risk individuals may benefit from such modified dietary protocols.

Similar to previous studies, other clinical parameters have reached significance on univariable regression analysis, including CRP, LDH, and interval between initial diagnosis and RLT (*24,38,39*). The assumption that patients with a high visceral fat–to–subcutaneous fat ratio exhibit shorter OS than patients with a low visceral fat–to–subcutaneous fat ratio (*20,21*) could not be verified in our cohort of patients undergoing RLT. Interestingly, relative to CRP, LDH, or hemoglobin, BMI or CT-derived body composition parameters such as total fat area, visceral fat area, and psoas muscle area predict OS to a lesser extent. This may be partially explained by an observer bias for CT assessment, in particular as blood-based biomarkers are analyzed following highly standardized protocols. Baseline PSA values also failed to reach significance in multivariable

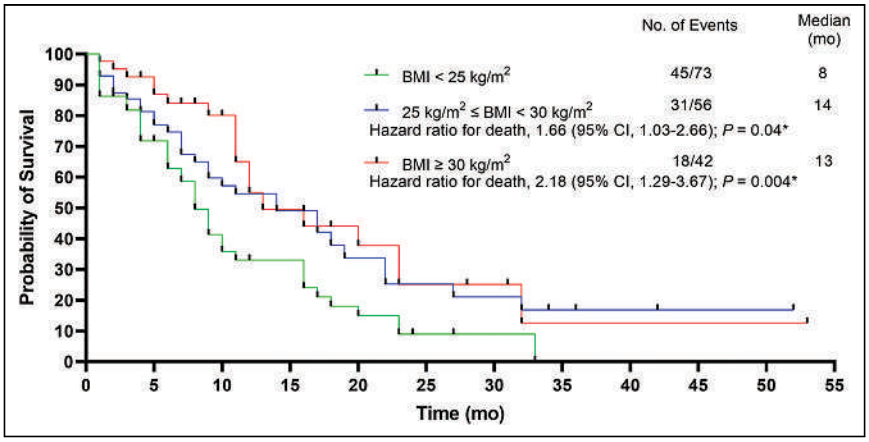


**FIGURE 3.** Kaplan–Meier curves and log rank comparisons for patients treated with RLT and stratified according to their BMI. Higher BMI was associated with longer median survival, in particular for obese subjects with BMI ≥ 30 kg/m$^2$. *Compared with patients with BMI < 25 kg/m$^2$.

Cox regression. This, however, is in line with previous findings for predicting survival using [$^{177}$Lu]Lu-PSMA-617 (*40–42*) and [$^{177}$Lu]Lu-PSMA I&T (*24,38*).

This study has limitations, including its retrospective design and its not individually determined, but fixed activity, regimens. PSMA RLT is usually given 4–6 times (*43*). As a real-world dataset obtained from routine care, not all patients were able to complete all 4–6 cycles, explaining the drop-out rate of approximately 20% after every cycle. Another partial explanation is that when the first patients were included in this analysis, respective restrictions on the number of cycles were nonexistent, for example, because of the missing results of the Vision Trial (*10*). Nonetheless, the number of cycles is of importance, as this is also recommended by the respective guidelines (*43*), and thus, future investigations may include only subjects with no more than 6 cycles. Although previous studies have shown no relevant outcome differences in a matched-pair analysis comparing the 2 most widely used therapeutic radiotracers, [$^{177}$Lu]Lu-PSMA I&T and [$^{177}$Lu]Lu-PSMA-617 (*25*), future studies should determine the predictive performance of baseline BMI and body composition in other PSMA-targeted agents recently introduced for therapy, including [$^{177}$Lu]Lu-rhPSMA-7.3 (*35*). Other studies may also incorporate sophisticated nomograms along with fat-related parameters to provide an even more refined selection of candidates who are likely to respond to treatment (*44*). Last, performance status, such as Eastern Cooperative Oncology Group status, should be investigated to determine the predictive value relative to BMI or CT-based body composition (*45*).

## CONCLUSION

In CRPC patients scheduled for RLT, patients with higher BMIs showed longer OS in multivariable analyses, whereas CT-derived body composition parameters reached significance only in univariate analyses. BMI as an easily obtainable parameter was also predictive of survival, along with blood-based parameters (CRP and LDH) and time between diagnosis and initiation of RLT. Although the latter clinical variables cannot be modified by the referring physician, future studies should determine whether a preceding high-calorie diet in individuals with lower fat reserves may also improve outcome.

## DISCLOSURE

This work was supported by the IZKF Wuerzburg (grant Z-02/85 to Philipp Hartrampf). Rudolf Werner and Andreas Buck received speaker honoraria from Novartis (Triple A). No other potential conflict of interest relevant to this article was reported.

**KEY POINTS**

**QUESTION:** How do body composition parameters (e.g., fat parameters, BMI, or sarcopenia) influence OS in CRPC patients undergoing PSMA RLT?

**PERTINENT FINDINGS:** In PC patients scheduled for RLT, sarcopenia is present in 38% of cases but is not associated with survival. However, increased fat reserves, as determined by BMI, are associated with a better outcome.

**IMPLICATIONS FOR PATIENT CARE:** Future studies should investigate whether alteration of BMI before treatment initiation may improve OS.

## ACKNOWLEDGMENT

We thank Dr. Dirk Mügge (Adelebsen) for his statistical advice.

## REFERENCES

1. Sung H, Ferlay J, Siegel RL, et al. Global cancer statistics 2020: GLOBOCAN estimates of incidence and mortality worldwide for 36 cancers in 185 countries. *CA Cancer J Clin.* 2021;71:209–249.
2. Parker C, Castro E, Fizazi K, et al. Prostate cancer: ESMO Clinical Practice Guidelines for diagnosis, treatment and follow-up. *Ann Oncol.* 2020;31:1119–1134.
3. Ryan CJ, Smith MR, de Bono JS, et al. Abiraterone in metastatic prostate cancer without previous chemotherapy. *N Engl J Med.* 2013;368:138–148.
4. Beer TM, Armstrong AJ, Rathkopf DE, et al. Enzalutamide in metastatic prostate cancer before chemotherapy. *N Engl J Med.* 2014;371:424–433.
5. Tannock IF, de Wit R, Berry WR, et al. Docetaxel plus prednisone or mitoxantrone plus prednisone for advanced prostate cancer. *N Engl J Med.* 2004;351:1502–1512.
6. de Bono JS, Oudard S, Ozguroglu M, et al. Prednisone plus cabazitaxel or mitoxantrone for metastatic castration-resistant prostate cancer progressing after docetaxel treatment: a randomised open-label trial. *Lancet.* 2010;376:1147–1154.
7. Calais J, Gafita A, Eiber M, et al. Prospective phase 2 trial of PSMA-targeted molecular RadiothErapy with $^{177}$Lu-PSMA-617 for metastatic castration-reSISTant Prostate Cancer (RESIST-PC): efficacy results of the UCLA cohort. *J Nucl Med.* 2021; 62:1440–1446.
8. Hofman MS, Violet J, Hicks RJ, et al. [$^{177}$Lu]-PSMA-617 radionuclide treatment in patients with metastatic castration-resistant prostate cancer (LuPSMA trial): a single-centre, single-arm, phase 2 study. *Lancet Oncol.* 2018;19:825–833.
9. Hofman MS, Emmett L, Sandhu S, et al. [$^{177}$Lu]Lu-PSMA-617 versus cabazitaxel in patients with metastatic castration-resistant prostate cancer (TheraP): a randomised, open-label, phase 2 trial. *Lancet.* 2021;397:797–804.
10. Sartor O, de Bono J, Chi KN, et al. Lutetium-177-PSMA-617 for metastatic castration-resistant prostate cancer. *N Engl J Med.* 2021;385:1091–1103.
11. FDA Approves Pluvicto/Locametz for metastatic castration-resistant prostate cancer. *J Nucl Med.* 2022;63(5):13N.
12. Smith MR, Saad F, Egerdie B, et al. Sarcopenia during androgen-deprivation therapy for prostate cancer. *J Clin Oncol.* 2012;30:3271–3276.
13. Smith MR. Changes in fat and lean body mass during androgen-deprivation therapy for prostate cancer. *Urology.* 2004;63:742–745.
14. Hamilton EJ, Gianatti E, Strauss BJ, et al. Increase in visceral and subcutaneous abdominal fat in men with prostate cancer treated with androgen deprivation therapy. *Clin Endocrinol (Oxf).* 2011;74:377–383.
15. Saylor PJ, Smith MR. Metabolic complications of androgen deprivation therapy for prostate cancer. *J Urol.* 2013;189(suppl):S34–S42.
16. Antoun S, Bayar A, Ileana E, et al. High subcutaneous adipose tissue predicts the prognosis in metastatic castration-resistant prostate cancer patients in post chemotherapy setting. *Eur J Cancer.* 2015;51:2570–2577.
17. Halabi S, Ou SS, Vogelzang NJ, Small EJ. Inverse correlation between body mass index and clinical outcomes in men with advanced castration-recurrent prostate cancer. *Cancer.* 2007;110:1478–1484.
18. Vidal AC, Howard LE, de Hoedt A, et al. Obese patients with castration-resistant prostate cancer may be at a lower risk of all-cause mortality: results from the shared equal access regional cancer hospital (SEARCH) database. *BJU Int.* 2018; 122:76–82.
19. Cushen SJ, Power DG, Murphy KP, et al. Impact of body composition parameters on clinical outcomes in patients with metastatic castrate-resistant prostate cancer treated with docetaxel. *Clin Nutr ESPEN.* 2016;13:e39–e45.
20. Stangl-Kremser J, Suarez-Ibarrola R, Andrea D, et al. Assessment of body composition in the advanced stage of castration-resistant prostate cancer: special focus on sarcopenia. *Prostate Cancer Prostatic Dis.* 2020;23:309–315.
21. Wu W, Liu X, Chaftari P, et al. Association of body composition with outcome of docetaxel chemotherapy in metastatic prostate cancer: a retrospective review. *PLoS One.* 2015;10:e0122047.
22. Ohtaka A, Aoki H, Nagata M, et al. Sarcopenia is a poor prognostic factor of castration-resistant prostate cancer treated with docetaxel therapy. *Prostate Int.* 2019;7:9–14.
23. Sheikhbahaei S, Reyes DK, Rowe SP, Pienta KJ. CT-based assessment of body composition following neoadjuvant chemohormonal therapy in patients with castration-naive oligometastatic prostate cancer. *Prostate.* 2021;81:127–134.
24. Hartrampf PE, Seitz AK, Weinzierl FX, et al. Baseline clinical characteristics predict overall survival in patients undergoing radioligand therapy with [$^{177}$Lu]Lu-PSMA I&T during long-term follow-up. *Eur J Nucl Med Mol Imaging.* 2022;49: 4262–4270.

25. Hartrampf PE, Weinzierl FX, Buck AK, et al. Matched-pair analysis of [$^{177}$Lu]Lu-PSMA I&T and [$^{177}$Lu]Lu-PSMA-617 in patients with metastatic castration-resistant prostate cancer. *Eur J Nucl Med Mol Imaging.* 2022;49:3269–3276.
26. Hartrampf PE, Bundschuh RA, Weinzierl FX, et al. mCRPC patients with PSA fluctuations under radioligand therapy have comparable survival benefits relative to patients with sustained PSA decrease. *Eur J Nucl Med Mol Imaging.* 2022;49:4727–4735.
27. Hartrampf PE, Weinzierl FX, Seitz AK, et al. Any decline in prostate-specific antigen levels identifies survivors scheduled for prostate-specific membrane antigen-directed radioligand therapy. *Prostate.* 2022;82:1406–1412.
28. Hartrampf PE, Weinzierl FX, Serfling SE, et al. Hematotoxicity and nephrotoxicity in prostate cancer patients undergoing radioligand therapy with [$^{177}$Lu]Lu-PSMA I&T. *Cancers (Basel).* 2022;14:647.
29. Hartrampf PE, Heinrich M, Seitz AK, et al. Metabolic tumour volume from PSMA PET/CT scans of prostate cancer patients during chemotherapy: do different software solutions deliver comparable results? *J Clin Med.* 2020;9:1390.
30. Yumuk V, Tsigos C, Fried M, et al. European guidelines for obesity management in adults. *Obes Facts.* 2015;8:402–424.
31. Cavanaugh JE, Neath AA. The Akaike information criterion: background, derivation, properties, application, interpretation, and refinements. *Wiley Interdiscip Rev Comput Stat.* 2019;11:e1460.
32. Longato E, Vettoretti M, Di Camillo B. A practical perspective on the concordance index for the evaluation and selection of prognostic time-to-event models. *J Biomed Inform.* 2020;108:103496.
33. Waters DL, Baumgartner RN, Garry PJ, Vellas B. Advantages of dietary, exercise-related, and therapeutic interventions to prevent and treat sarcopenia in adult patients: an update. *Clin Interv Aging.* 2010;5:259–270.
34. Cavka L, Pohar Perme M, Zakotnik B, Rotovnik Kozjek N, Seruga B. Nutritional status and health-related quality of life in men with advanced castrate-resistant prostate cancer. *Nutr Cancer.* 2022;74:472–481.
35. Feuerecker B, Chantadisai M, Allmann A, et al. Pretherapeutic comparative dosimetry of $^{177}$Lu-rhPSMA-7.3 and $^{177}$Lu-PSMA I&T in patients with metastatic castration-resistant prostate cancer. *J Nucl Med.* 2022;63:833–839.
36. Jadvar H. The VISION forward: recognition and implication of PSMA-/$^{18}$F-FDG+ mCRPC. *J Nucl Med.* 2022;63:812–815.
37. Huang M, Narita S, Numakura K, et al. A high-fat diet enhances proliferation of prostate cancer cells and activates MCP-1/CCR2 signaling. *Prostate.* 2012;72:1779–1788.
38. Heck MM, Tauber R, Schwaiger S, et al. Treatment outcome, toxicity, and predictive factors for radioligand therapy with $^{177}$Lu-PSMA-I&T in metastatic castration-resistant prostate cancer. *Eur Urol.* 2019;75:920–926.
39. Karimzadeh A, Heck M, Tauber R, et al. $^{177}$Lu-PSMA-I&T for treatment of metastatic castration-resistant prostate cancer: prognostic value of scintigraphic and clinical biomarkers. *J Nucl Med.* 2023;64:402–409.
40. Rathke H, Holland-Letz T, Mier W, et al. Response prediction of $^{177}$Lu-PSMA-617 radioligand therapy using prostate-specific antigen, chromogranin A, and lactate dehydrogenase. *J Nucl Med.* 2020;61:689–695.
41. Rahbar K, Boegemann M, Yordanova A, et al. PSMA targeted radioligandtherapy in metastatic castration resistant prostate cancer after chemotherapy, abiraterone and/or enzalutamide. A retrospective analysis of overall survival. *Eur J Nucl Med Mol Imaging.* 2018;45:12–19.
42. Grubmüller B, Senn D, Kramer G, et al. Response assessment using $^{68}$Ga-PSMA ligand PET in patients undergoing $^{177}$Lu-PSMA radioligand therapy for metastatic castration-resistant prostate cancer. *Eur J Nucl Med Mol Imaging.* 2019;46:1063–1072.
43. Kratochwil C, Fendler WP, Eiber M, et al. EANM procedure guidelines for radionuclide therapy with $^{177}$Lu-labelled PSMA-ligands ($^{177}$Lu-PSMA-RLT). *Eur J Nucl Med Mol Imaging.* 2019;46:2536–2544.
44. Gafita A, Calais J, Grogan TR, et al. Nomograms to predict outcomes after $^{177}$Lu-PSMA therapy in men with metastatic castration-resistant prostate cancer: an international, multicentre, retrospective study. *Lancet Oncol.* 2021;22:1115–1125.
45. Chen WJ, Kong DM, Li L. Prognostic value of ECOG performance status and Gleason score in the survival of castration-resistant prostate cancer: a systematic review. *Asian J Androl.* 2021;23:163–169.

# Molecular Imaging of Myocardial Fibroblast Activation in Patients with Advanced Aortic Stenosis Before Transcatheter Aortic Valve Replacement: A Pilot Study

Johanna Diekmann*[1], Jonas Neuser*[2], Manuel Röhrich[3], Thorsten Derlin[1], Carolin Zwadlo[2], Tobias Koenig[2], Desiree Weiberg[1], Felix Jäckle[2], Tibor Kempf[2], Tobias L. Ross[1], Jochen Tillmanns[2], James T. Thackeray[1], Julian Widder[2], Uwe Haberkorn[3], Johann Bauersachs*[2], and Frank M. Bengel*[1]

[1]*Department of Nuclear Medicine, Hannover Medical School, Hannover, Germany;* [2]*Department of Cardiology and Angiology, Hannover Medical School, Hannover, Germany; and* [3]*Department of Nuclear Medicine, University Hospital Heidelberg, Heidelberg, Germany*

Using multimodal imaging, we investigated the extent and functional correlates of myocardial fibroblast activation in patients with aortic stenosis (AS) scheduled for transcatheter aortic valve replacement (TAVR). AS may cause myocardial fibrosis, which is associated with disease progression and may limit response to TAVR. Novel radiopharmaceuticals identify upregulation of fibroblast activation protein (FAP) as a cellular substrate of cardiac profibrotic activity. **Methods:** Twenty-three AS patients underwent $^{68}$Ga-FAP inhibitor 46 ($^{68}$Ga-FAPI) PET, cardiac MRI, and echocardiography within 1–3 d before TAVR. Imaging parameters were correlated and then were integrated with clinical and blood biomarkers. Control cohorts of subjects without a history of cardiac disease and with ($n = 5$) and without ($n = 9$) arterial hypertension were compared with matched AS subgroups. **Results:** Myocardial FAP volume varied significantly among AS subjects (range, 1.54–138 cm$^3$, mean ± SD, 42.2 ± 35.6 cm$^3$) and was significantly higher than in controls with (7.42 ± 8.56 cm$^3$, $P = 0.007$) and without (2.90 ± 6.67 cm$^3$; $P < 0.001$) hypertension. FAP volume correlated with N-terminal prohormone of brain natriuretic peptide ($r = 0.58$, $P = 0.005$), left ventricular ejection fraction ($r = -0.58$, $P = 0.02$), mass ($r = 0.47$, $P = 0.03$), and global longitudinal strain ($r = 0.55$, $P = 0.01$) but not with cardiac MRI T1 (spin–lattice relaxation time) and extracellular volume ($P$ = not statistically significant). In-hospital improvement in left ventricular ejection fraction after TAVR correlated with pre-TAVR FAP volume ($r = 0.440$, $P = 0.035$), N-terminal prohormone of brain natriuretic peptide, and strain but not with other imaging parameters. **Conclusion:** FAP-targeted PET identifies varying degrees of left ventricular fibroblast activation in TAVR candidates with advanced AS. $^{68}$Ga-FAPI signal does not match other imaging parameters, generating the hypothesis that it may become useful as a tool for personalized selection of optimal TAVR candidates.

**Key Words:** aortic stenosis; myocardial fibrosis; molecular imaging; fibroblast activation protein; PET

**J Nucl Med 2023; 64:1279–1286**
DOI: 10.2967/jnumed.122.265147

Advanced aortic stenosis (AS) is associated with significant morbidity and mortality (*1–3*). Transcatheter aortic valve replacement (TAVR) is increasingly used, primarily in high-risk patients (*4*), although a broader use in lower-risk AS has been suggested (*5*). Myocardial fibrosis is thought to play a critical role in AS, in the response to therapy and in subsequent outcome (*6*). In TAVR recipients, the histologic severity of myocardial fibrosis varies significantly and independently predicts left ventricular (LV) remodeling and survival (*7,8*). Accordingly, myocardial fibrosis has emerged as an imaging target in AS. Strain analysis from transthoracic echocardiography (TTE) provides indirect measures of fibrosis in cardiomyopathies (*9,10*) and in AS (*11*). In cardiac MRI (CMR), late gadolinium enhancement (LGE) identifies scars and areas of replacement fibrosis (*12*). Parametric T1 (spin–lattice relaxation time) mapping describes altered tissue composition as an indicator of diffuse interstitial fibrosis (*13,14*). However, LGE and elevated T1 are, for example, also found in areas with extracellular expansion due to edema or infiltration (*12*), and T1 may have limited specificity for discriminating AS patients from healthy controls (*15*).

Recently, specific radioligands for fibroblast activation protein (FAP) have been developed for targeted PET and were initially used to characterize tumor stroma (*16*). FAP is a membrane-bound serine protease (*17,18*) that is highly expressed by activated myofibroblasts. In profibrotic conditions, it therefore identifies the biologic activity of tissue fibroblasts as a cell-based mechanism that is distinct from the extracellular matrix. The feasibility of noninvasive PET-based interrogation of cardiac $^{68}$Ga-FAPI expression has, for example, been shown after acute myocardial infarction (*19–23*). Moreover, among oncologic patients, a less intense but variable myocardial $^{68}$Ga-FAPI signal was proportional to cardiovascular risk factors such as hypertension and diabetes mellitus (*24*).

We hypothesized that FAP-targeted PET will identify the presence and inter- and intraindividual heterogeneity of myocardial fibroblast activation in AS. We also hypothesized that this signal of profibrotic activity will be distinct from, and thereby complementary to, other imaging parameters that reflect tissue composition. We tested our hypotheses by a comprehensive global and regional integration of multimodality noninvasive imaging parameters and their relation to established clinical risk markers and short-term response to TAVR. We speculate that confirmation of our hypotheses may support the use of FAP-targeted PET in future

Received Nov. 7, 2022; revision accepted Apr. 10, 2023.
For correspondence or reprints, contact Johanna Diekmann (diekmann.johanna@mh-hannover.de).
*Contributed equally to this work.
Published online Jun. 8, 2023.

studies seeking to optimize candidate selection for TAVR based on their individual fibrotic disease profile.

## MATERIALS AND METHODS

### Study Design and Participants

We included 23 patients (11 men, 12 women; mean age ± SD, 84.1 ± 3.3 y) who had undergone clinical evaluation including CMR, TTE, and FAP-targeted PET with $^{68}$Ga-FAP inhibitor 46 ($^{68}$Ga-FAPI) before TAVR at Hannover Medical School. AS had been evaluated, and eligibility for TAVR determined, according to clinical guidelines (*25*). All patients had classic high-gradient AS and sinus rhythm. Patients equipped with a permanent pacemaker or implantable cardioverter defibrillator and who had severe renal dysfunction (glomerular filtration rate < 30 mL/min), chronic inflammatory disease, or eminent frailty were excluded. All patients gave written informed consent before undergoing imaging. The study was in accordance with the ethical guidelines of the 1975 Declaration of Helsinki, and the local ethical committee approved the project (approval 9553_BO_K_2021).

### Radionuclide Imaging

FAP-targeted PET was conducted 1–3 d before TAVR, using the specific ligand $^{68}$Ga-FAPI-46, which was synthesized in house according to good manufacturing practices as previously described (*26*) and was used clinically according to §13.2b of the German Pharmaceuticals Act for determination of myocardial profibrotic activity. Static PET images were acquired for 20 min using a Biograph mCT 128 system (Siemens), beginning 60 min after intravenous injection of 118 ± 16 MBq of $^{68}$Ga-FAPI-46. Low-dose CT was used for attenuation correction. Images were iteratively reconstructed, using time-of-flight and point-spread function information (True X; Siemens). Peak and $SUV_{mean}$ were obtained for myocardium, blood pool (left atrium), and other organs (liver, spleen, bone marrow, lungs) using volumes of interest of 1 $cm^3$ and commercial software (syngo.via, V50B; Siemens Healthcare). Myocardial FAP volume was determined using an isocontour volume of interest including all voxels above an individually determined threshold (blood pool $SUV_{mean}$ + 2 SDs) with exclusion of valve regions. Additionally, the area of FAP upregulation was calculated by polar map analysis as previously described (*19*). Segmental $SUV_{mean}$ was calculated using the American Heart Association 17-segment model and polar maps. Apical segments were merged for comparability to CMR and echocardiography.

### CMR

CMR was performed using a 1.5-T scanner (Magnetom Avanto; Siemens) in 22 of 23 patients (97%) at 1–4 d before TAVR. In 2 of 22 patients, T1 mapping was not performed because of technical problems. Cine images were obtained using a balanced steady-state free-precession sequence (True FISP; Siemens). Parametric T1 maps were acquired in 3 short-axis slices (basal, midventricular, and apical LV) covering 16 segments (available for 16 patients), using the modified look-locker sequence before and after administration of contrast agent. LGE was imaged by phase-sensitive inversion recovery sequences, 10–15 min after bolus injection of a 0.15 mmol/kg dose of gadolinium-diethylenetriamine pentaacetate (Gadavist; Bayer Healthcare). Extracellular volume fraction was calculated from myocardial and blood T1 relaxation times before and after contrast administration, using the most recent hematocrit level. Global analysis included determination of LV ejection fraction (LVEF), volumes, mass, and extent of LGE, indexed by body surface area (*27*). Segmental analysis included native T1 and postcontrast T1 relaxation times, using the 16-segment model. Threshold analysis using the mean + 2 SDs of healthy controls' identified segments with prolonged native T1 relaxation times (*28*). Cvi42 software (Circle Cardiovascular Imaging) was used.

### TTE

TTE was performed 1–3 d before and after TAVR, using an EPIQ7 equipped with an X5-1 transducer (Philips). LV strain images were recorded using standard apical views. Speckle tracking for measurement of global longitudinal strain and LVEF were assessed offline using a TomTec Imaging Systems ultrasound software. Segmental longitudinal strain was assessed using 18 segments, and 4 apical segments were merged for comparability to CMR and PET. Threshold analysis using the mean + 2 SDs of healthy controls (*29*) identified segments with impaired longitudinal strain.

### Control Groups

From a historic sample of cancer patients having undergone $^{68}$Ga-FAPI-46 PET for staging at the University of Heidelberg, 2 control groups were identified and matched to AS subgroups by age and sex. Imaging modalities, tracers, and evaluations were identical to the Hannover protocol (image acquisition 60 min after injection). First, a group of 9 control subjects (4 with glioblastoma, 3 with adenoid cystic carcinoma, 1 with pancreas carcinoma, and 1 with a suspected cancerous polyp) was selected and matched 1:2 to 18 AS patients. This group had no history of cardiac disease, cardiotoxic chemotherapy, or radiation therapy of the chest; no coronary calcification; and no known cardiovascular risk factors, including smoking, diabetes mellitus, or

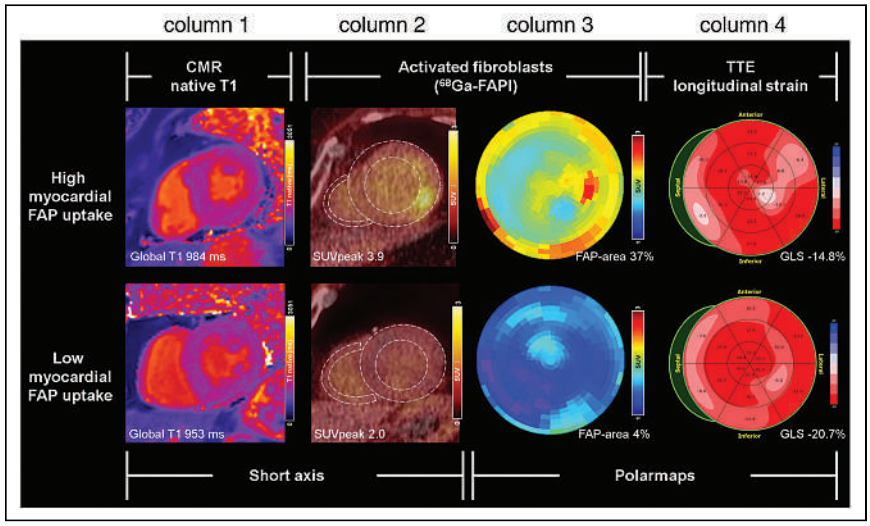


**FIGURE 1.** Multimodal characterization of myocardial fibrosis in AS patients before TAVR. Shown are 2 cases with high and low myocardial $^{68}$Ga-FAPI signal, as indicated by representative midventricular short-axis PET/CT image (column 2) and parametric polar maps of $^{68}$Ga-FAPI uptake (column 3; polar maps are 2-dimensional display of 3-dimensional LV activity with apex in center, base in periphery, anterior wall on top, inferior wall on bottom, septum on left, and lateral wall on right). High $^{68}$Ga-FAPI signal was associated with mild elevation of native T1 from CMR (column 1) and mild reduction of global longitudinal strain at TTE (column 4). Yet, neither CMR T1 nor TTE global longitudinal strain show similarly clear distinction between patients when compared with $^{68}$Ga-FAPI signal. GLS = global longitudinal strain.

**TABLE 1**
PET Parameters

| Variable | All AS patients ($n$ = 23) | | Sex-matched AS patients ($n$ = 18) | | Oncologic sex-matched controls ($n$ = 9) | | | Age-and sex-matched AS patients ($n$ = 5) | | Oncologic age-and sex-matched controls with AHT ($n$ = 5) | | |
|---|---|---|---|---|---|---|---|---|---|---|---|---|
| | Mean ± SD | Range | Mean ± SD | Range | Mean ± SD | Range | $P$ | Mean ± SD | Range | Mean ± SD | Range | $P$ |
| Area of FAP upregulation (% of LV) | 32.0 ± 29.1 | 0–91 | 29.6 ± 30.6 | 0–91 | 4.44 ± 7.83 | 0–24 | 0.004 | 43.4 ± 20.6 | 17–68 | 9.40 ± 11.2 | 0–27 | 0.012 |
| $SUV_{mean}$ (of total LV) | 2.50 ± 0.43 | 1.88–3.51 | 2.58 ± 0.42 | 1.93–3.51 | 1.89 ± 0.46 | 1.44–2.63 | <0.001 | 2.28 ± 0.45 | 1.81–2.93 | 1.47 ± 0.34 | 1.12–1.91 | 0.014 |
| FAP volume ($cm^3$) | 42.2 ± 35.6 | 1.54–137.8 | 37.9 ± 35.4 | 1.54–137.8 | 2.90 ± 6.67 | 0.01–20.62 | <0.001 | 43.1 ± 20.4 | 23.2–75.9 | 7.42 ± 8.56 | 0.71–18.3 | 0.007 |
| Myocardial SUV–to–blood pool ratio | 1.87 ± 0.5 | 1.20–3.15 | 1.81 ± 0.53 | 1.09–2.78 | 1.30 ± 0.56 | 0.74–2.57 | 0.030 | 1.86 ± 0.25 | 1.44–2.12 | 1.47 ± 0.34 | 1.18–1.99 | 0.003 |
| Organ $^{68}$Ga-FAPI signal ($SUV_{peak}$) | | | | | | | | | | | | |
| Myocardium | 3.35 ± 0.91 | 1.87–5.42 | 3.46 ± 0.96 | 1.87–5.42 | 3.46 ± 0.96 | 1.21–3.86 | <0.001 | 3.44 ± 0.67 | 2.48–4.21 | 1.62 ± 0.25 | 1.41–1.93 | <0.001 |
| Spleen | 1.39 ± 0.38 | 0.79–2.12 | 1.41 ± 0.38 | 0.79–2.12 | 1.13 ± 0.25 | 0.83–1.51 | 0.052 | 1.35 ± 0.34 | 1.05–1.91 | 1.01 ± 0.04 | 0.99–1.06 | 0.147 |
| Liver | 1.33 ± 0.35 | 0.81–2.64 | 1.36 ± 0.38 | 0.81–2.31 | 1.29 ± 0.67 | 0.80–3.49 | 0.731 | 1.35 ± 0.41 | 0.99–1.88 | 1.41 ± 0.49 | 0.92–2.12 | 0.817 |
| Bone marrow | 0.90 ± 0.25 | 1.05–4.05 | 0.92 ± 0.26 | 0.43–1.29 | 0.99 ± 0.27 | 0.60–1.35 | 0.540 | 1.05 ± 0.29 | 0.74–1.90 | 0.78 ± 0.18 | 0.50–1.00 | 0.122 |
| Lung | 0.58 ± 0.21 | 0.23–1.13 | 0.63 ± 0.20 | 0.35–1.13 | 0.52 ± 0.33 | 0.30–1.39 | 0.326 | 0.66 ± 0.22 | 0.54–0.99 | 0.56 ± 0.17 | 0.40–0.74 | 0.417 |
| Blood pool (left atrium) | 1.89 ± 0.30 | 1.48–2.84 | 1.94 ± 0.31 | 1.48–2.84 | 1.43 ± 0.24 | 1.20–1.90 | <0.001 | 1.71 ± 0.29 | 1.64–2.38 | 1.24 ± 0.52 | 1.41–1.80 | 0.082 |

AHT = arterial hypertension.

**TABLE 2**
CMR

| Variable | All patients | All patients indexed (mL/m$^2$) |
|---|---|---|
| Global function ($n$ = 22) | | |
| EDV (mL) | 118.6 ± 26.7 (83–191) | 66.5 ± 12.9 (45.0–102.0) |
| ESV (mL) | 43.5 ± 13.8 (29–84) | 24.3 ± 6.8 (15.0–43.0) |
| SV (mL) | 75.2 ± 14.8 (53–119) | 42.1 ± 7.0 (30.0–64.0) |
| LVM (g) | 116.2 ± 21.3 (77–157) | 66.3 ± 11.9 (40.0–86.0) |
| LVEF (%) | 63.8 ± 4.4 (53–72) | |
| Global mapping ($n$ = 20) | | |
| T1 global native (ms) | 977.2 ± 25.8 (939–1,049) | |
| T1 global contrast (ms) | 448.8 ± 48.8 (363–539) | |
| ECV global (%) | 28.0 ± 3.9 (22–38) | |

ECV = extracellular volume fraction; EDV = end-diastolic volume; ESV = end-systolic volume; SV = stroke volume; LVM = LV mass. Data are mean ± SD and range.

arterial hypertension. Second, 5 control subjects (all with pancreas carcinoma) with arterial hypertension were identified and matched to 5 AS patients.

### Statistical Analysis

Statistical analyses were performed using SPSS, version 27 (IBM), for Microsoft Windows and Prism, version 9 (GraphPad Software). Categoric variables are presented with absolute and relative frequencies. For quantitative continuous variables, testing for a gaussian distribution was performed using Shapiro–Wilk tests. For data with a gaussian distribution, paired Student $t$ tests or 1-way ANOVA with Tukey multiple-comparison tests were used depending on the number of compared groups. Paired continuous variables were compared using the Wilcoxon test; nonpaired continuous variables were compared using a 2-sided $t$ test. Categoric variables was compared using the $\chi^2$ test. Nonparametric unpaired data were analyzed with Mann–Whitney $U$ tests. Pearson correlation coefficients were calculated for bivariate correlation analyses. All statistical analyses were performed 2-sided, and a $P$ value of less than 0.05 was considered to indicate statistical significance.

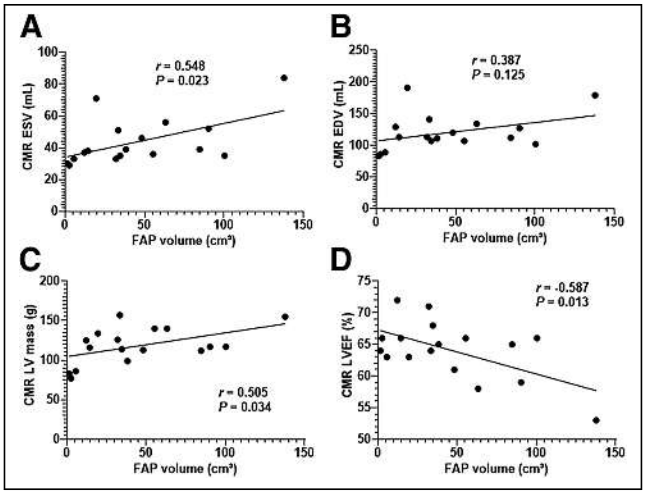


**FIGURE 2.** Regression plot for myocardial volume of elevated $^{68}$Ga-FAPI signal (FAP volume) and LV function parameters derived from CMR: end-systolic volume (A), end-diastolic volume (B), LV mass (C), and LVEF (D). EDV = end-diastolic volume.

## RESULTS

Patient characteristics are summarized in Supplemental Table 1 (supplemental materials are available at http://jnm.snmjournals.org). Mean age was 84 ± 3 y, and 52% were female. Most AS patients presented with a high burden of cardiovascular comorbidities (Supplemental Tables 1 and 2).

### Myocardial $^{68}$Ga-FAPI Signal Is Elevated in AS and Shows Inter- and Intraindividual Variability

A wide range of myocardial $^{68}$Ga-FAPI signal patterns was detected in the AS cohort (Fig. 1; Table 1). The area of significant FAP upregulation versus the blood pool ranged from 0% to 91% of the left ventricle (median, 20.0%; interquartile range, 4.0%–58.0%); Supplemental Fig. 1). Similarly, the global volume of elevated $^{68}$Ga-FAPI signal displayed high variance among patients, with a range of 1.5–138 cm$^3$ (median, 33.4 cm$^3$; interquartile range, 14.4–63.3 cm$^3$). Mean myocardial SUV as a measure of $^{68}$Ga-FAPI signal intensity ranged from 1.9 to 3.5 ($SUV_{mean}$, 2.5 ± 0.4). Interindividual regional LV distribution patterns were highly variable, whereas basal myocardial regions were more frequently involved.

Myocardial FAP volume was significantly higher in AS patients than in controls without hypertension (37.9 ± 35.4 cm$^3$ vs. 2.90 ± 6.67 cm$^3$, $P < 0.001$; Table 1; Supplemental Fig. 2). The area of FAP upregulation, $SUV_{mean}$, and $SUV_{peak}$ of the total left ventricle were equally higher in AS patients ($P < 0.001$ each). Additionally, matched comparison with hypertensive controls also showed that FAP volume was significantly higher in AS patients (43.1 ± 20.4 cm$^3$ vs. 7.42 ± 8.56 cm$^3$, $P < 0.001$; Supplemental Fig. 2).

### $^{68}$Ga-FAPI Signal Elevation Is Specific to Myocardium in AS

Signal intensity was very low in the blood pool, albeit slightly higher in AS than in controls (1.94 ± 0.31 vs. 1.43 ± 0.24, $P < 0.001$), confirming the feasibility of detecting mild $^{68}$Ga-FAPI signal elevation in the heart. Additionally, no elevated signal and no difference between AS and controls was identified in potential networking organs such as lung, liver, spleen, and bone marrow, suggesting that profibrotic activity in AS is specific to the myocardium (Table 1). No significant correlation between myocardial $^{68}$Ga-FAPI signal and the SUV of other organs was detected (Supplemental Fig. 3).

**TABLE 3**
TTE and TAVR Procedure

| Variable | Data |
|---|---|
| LVEF (%, 2-dimensional) | 60.1 ± 5.9 (44–70) |
| LVEF (%, 2-dimensional) after TAVR | 61.8 ± 3.7 (57–72) |
| Transaortic gradient (mm Hg, maximum) | 79.0 ± 13.6 (54–110) |
| Transaortic gradient (mm Hg, mean) | 50.4 ± 8.1 (38–70) |
| Aortic regurgitation | 7 (30.4) |
| AVA ($cm^2$) | 0.68 ± 0.18 (0.37–0.95) |
| THV SAPIEN (Edwards Lifesciences) | 14 (60.9) |
| THV CoreValve (Medtronic) | 9 (39.1) |
| Device success | 23 (100) |
| New permanent pacemaker | 1 (4.3) |

AVA = aortic valve area; THV = transcatheter heart valve.
Qualitative data are number and percentage ($n$ = 23); continuous data are mean ± SD and range.

### Global Myocardial $^{68}$Ga-FAPI Signal Correlates with Markers of Heart Failure Severity in AS

FAP volume significantly correlated with the levels of serum N-terminal prohormone of brain natriuretic peptide ($r$ = 0.58, $P$ = 0.004; Supplemental Fig. 4). No other correlations between $^{68}$Ga-FAPI imaging parameters and blood biomarkers were observed. CMR parameters are summarized in Table 2. Of note, FAP volume correlated significantly with volume, LV mass, and LVEF (all $P$ < 0.05; Fig. 2; Supplemental Fig. 5). No significant correlations between FAP volume and global mapping parameters could be detected (T1 global native: $r$ = −0.058, $P$ = 0.804; T1 global contrast: $r$ = −0.143, $P$ = 0.525, extracellular volume fraction global: $r$ = 0.011, $P$ = 0.990).

Also, TTE was available for all patients before and after TAVR (in-hospital follow-up, Table 3). Mean aortic valve area was severely reduced (0.68 ± 0.18 $cm^2$, severe AS < 1 $cm^2$) (*30*), and mean transaortic pressure gradient was severely increased (50.4 ± 8.1 mm Hg, severe AS > 40 mm Hg) (*30*) before TAVR. FAP volume significantly correlated with TTE-derived cardiac function (Fig. 3), including LVEF before TAVR ($r$ = −0.58, $P$ = 0.012) and LV global longitudinal strain ($r$ = 0.58, $P$ = 0.012) and tended to correlate with the mean transaortic gradient ($r$ = 0.44, $P$ = 0.07).

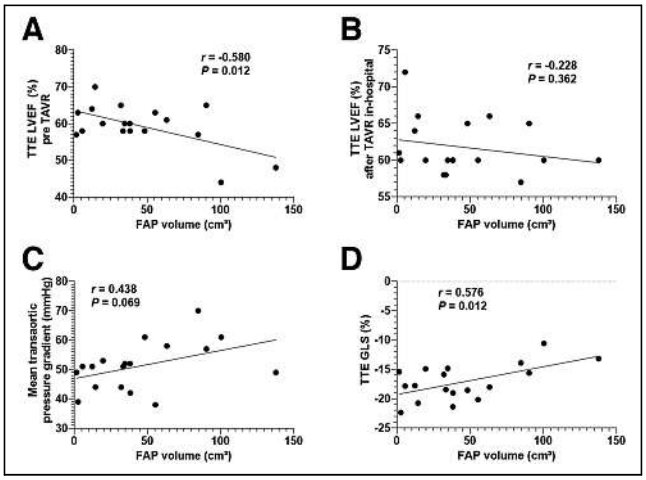


**FIGURE 3.** Regression plot for myocardial volume of elevated $^{68}$Ga-FAPI signal (FAP volume) and LV function parameters derived from TTE: LVEF before TAVR (A), LVEF after TAVR (B), mean transaortic gradient (C), and global longitudinal strain (D). GLS = global longitudinal strain.

### Segmental $^{68}$Ga-FAPI Signal Is Not Identical to Other Imaging Markers of Fibrosis in AS

In total, 299 segments with complete data from PET, CMR, and TTE were analyzed. Segmental $^{68}$Ga-FAPI $SUV_{mean}$ was significantly higher in basal than in midventricular ($P$ [ANOVA] = 0.022) and apical segments ($P$ [ANOVA] = 0.034, Fig. 4). Segmental $SUV_{mean}$ correlated weakly but significantly with segmental longitudinal strain from TTE ($r$ = 0.119, $P$ = 0.002; Supplemental Fig. 6), native T1 ($r$ = 0.271, $P$ < 0.001), and postcontrast T1 from CMR ($r$ = −0.330, $P$ < 0.001). To define $^{68}$Ga-FAPI signal elevation in a segment, an $SUV_{mean}$ more than 2 SDs above the blood pool level was chosen. This yielded 110 of 299 segments (37%) as $^{68}$Ga-FAPI–positive (Fig. 5). The native T1 relaxation time was mildly but significantly longer in the $^{68}$Ga-FAPI–positive segments (973 ± 35 vs. 961 ± 37 ms for $^{68}$Ga-FAPI–negative, $P$ = 0.015), and longitudinal strain was mildly but significantly reduced (−13.0 ± 7.1 vs. −16.0% ± 8.4%, $P$ = 0.003) in $^{68}$Ga-FAPI–positive segments. Also, 19 of 299 segments (6%) showed LGE, but only 11 of 19 (58%) segments with LGE were $^{68}$Ga-FAPI–positive. There was a relevant mismatch between $^{68}$Ga-FAPI positivity and elevated T1 at CMR (congruent signal in 51/110 segments), as well as impaired longitudinal strain at TTE (congruent signal in 78/110 segments), suggesting that the 3 modalities do not identify the same components of the fibrotic process.

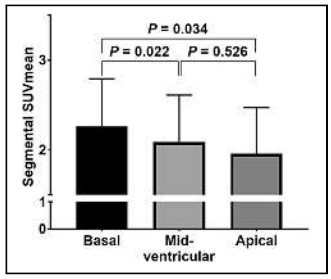


**FIGURE 4.** Segmental analysis: $SUV_{mean}$ of $^{68}$Ga-FAPI ligand at PET was significantly higher in basal than midventricular and distal myocardial segments.

### $^{68}$Ga-FAPI Signal Is Predictive of Short-Term Change in LVEF After TAVR

After TAVR, LVEF did not change significantly in

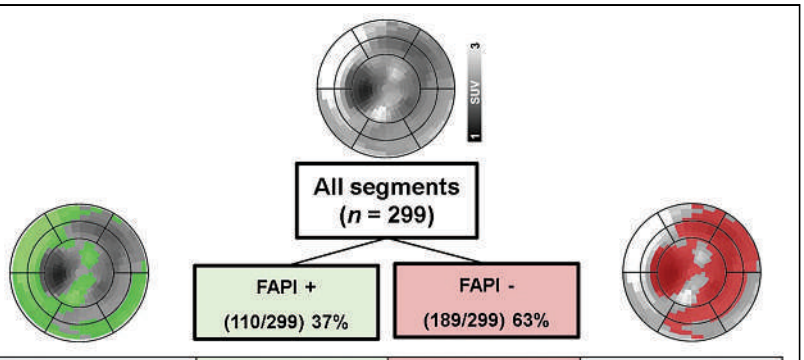


| | | | |
|---|---|---|---|
| T1 native (ms, mean ± SD) | 973 ± 35 | 961 ± 37 | **P = 0.015** |
| T1 native prolonged (n (%)) | 55/110 (50.0) | 59/189 (31.2) | **P = 0.021** |
| LGE present (n (%)) | 11/110 (10.0) | 8/189 (4.2) | P = 0.062 |
| LS (%, mean ± SD) | -13.0 ± 7.1 | -16.0 ± 8.4 | **P = 0.002** |
| LS impaired (n (%)) | 78/110 (70.9) | 101/189 (53.5) | **P = 0.003** |

**FIGURE 5.** Classification of segments into $^{68}$Ga-FAPI–upregulated (FAPI+) and $^{68}$Ga-FAPI–negative segments (FAPI−) when compared with blood pool background signal, illustrated by patient example (polar map). Native T1 relaxation time was significantly longer in $^{68}$Ga-FAPI–positive segments. More LGE was found in $^{68}$Ga-FAPI–positive segments, and global longitudinal strain was significantly impaired in $^{68}$Ga-FAPI–positive segments. Yet, agreement between $^{68}$Ga-FAPI, T1, and longitudinal strain elevation was only partial. FAPI+ = $^{68}$Ga-FAPI–upregulated; FAPI− = $^{68}$Ga-FAPI–negative; LS = longitudinal strain.

the entire group (60.1% ± 5.9% vs. 61.8% ± 3.7% before, $P$ = 0.19). Individually, however, in-hospital LVEF improvement significantly correlated with myocardial FAP volume ($r$ = 0.440, $P$ = 0.035), N-terminal prohormone of brain natriuretic peptide ($r$ = 0.480, $P$ = 0.024), and global longitudinal strain ($r$ = 0.440, $P$ = 0.013; Fig. 6). No correlation between in-hospital LVEF improvement and other parameters from CMR or TTE was observed.

## DISCUSSION

AS is the most common valvular disease in the Western world, and early treatment is recommended in symptomatic patients (*25*). However, symptoms often occur late, after adverse cardiac remodeling has led to overt heart failure. Progressive valve narrowing causing an increased afterload, along with adaptive LV hypertrophy, facilitates the transition to heart failure (*6,31*). It is thought that myocyte death and interstitial fibrosis are key mechanisms in this transformation (*32*). With new $^{68}$Ga-FAPI tracers, imaging of activated fibroblasts is now feasible. In oncologic patients, myocardial FAP upregulation was incidentally identified and associated with preexisting cardiovascular comorbidities (*33*). More recently, further studies have demonstrated the feasibility of myocardial $^{68}$Ga-FAPI imaging, particularly after acute myocardial infarction (*19,20,22–24*). A strong and specific $^{68}$Ga-FAPI signal was detected in the infarct region, where fibroblasts need to form a robust scar. Yet, in addition to this area of replacement fibrosis, there was also an elevated $^{68}$Ga-FAPI signal in viable periinfarct tissue, as a possible substrate for development of interstitial fibrosis.

Ex vivo analysis of human heart tissue identified significant $^{68}$Ga-FAPI expression in the LV tissue of failing hearts, whereas normal hearts had minimal $^{68}$Ga-FAPI expression (*34*). Thus, FAP is a suitable target marker of activated cardiac fibroblasts, and $^{68}$Ga-FAPI radioligands (*16,26*) are promising for noninvasive detection. Our study was the first, to our knowledge, to describe high inter- and intraindividual heterogeneity for myocardial $^{68}$Ga-FAPI uptake patterns in AS patients before TAVR. Expectedly $^{68}$Ga-FAPI uptake was not as intense and not as extensive as in patients with acute myocardial infarction but was significantly higher than in our matching controls, indicating that the myocardial $^{68}$Ga-FAPI signal is not caused primarily by the presence of cardiovascular comorbidities. Nevertheless, there were various regional distribution patterns and differences between individuals. These differences help to generate a hypothesis that the range of $^{68}$Ga-FAPI signal may be associated with the benefit from TAVR, which is known to be variable (*25*). Of note, a higher myocardial FAP volume led to a greater direct improvement of in-hospital LVEF after TAVR. This finding is somewhat unexpected, as more severe fibrosis is thought to inhibit LVEF improvement. It should be considered, however, that $^{68}$Ga-FAPI signal identifies not the extracellular matrix component of fibrosis but rather the activation state of fibroblasts as the cellular substrate of profibrotic activity. FAP elevation may potentially reflect a more dynamic remodeling process that involves reversible fibrotic cell activity, as opposed to a burnt-out chronic fibrotic state including irreversible scarring. However, because of the study design, our interpretations need to be verified by prospective studies and should be considered hypothesis-generating at this point.

Interestingly, in our patient cohort, higher preprocedural levels of N-terminal prohormone of brain natriuretic peptide significantly correlated with a greater global volume of fibroblast activation, which supports the possibility that FAP-targeted imaging has potential value as a prognostic biomarker. Globally, the PET results also correlated with functional measures and markers of extracellular matrix expansion and stiffness from CMR and TTE, but no exact regional matching—such as with LGE and T1 relaxation times and longitudinal strain—was detected. T1 relaxation times (*28*) and extracellular volume fraction (*35*) were in the expected range for this cohort. The underlying reason for these findings remains uncertain. Targeted imaging of activated fibroblasts

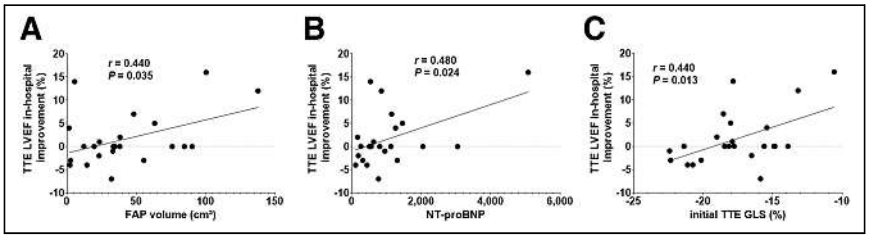


**FIGURE 6.** Regression plot for in-hospital LVEF improvement in percentage and myocardial volume of elevated $^{68}$Ga-FAPI signal (FAP volume) (A), preprocedural levels of N-terminal prohormone of brain natriuretic peptide (B), and preprocedural global longitudinal strain (%) (C). GLS = global longitudinal strain; NT-proBNP = N-terminal prohormone of brain natriuretic peptide.

may be a complementary asset with potential prognostic value in a multimodal fibrosis imaging toolbox and may be further explored for guidance of existing and novel therapies in AS.

Some limitations of this study should be considered. First, the patient population was small, consistent with the hypothesis-generating nature of this early observational project. Indeed, patients were carefully selected to derive a homogeneous cohort without low-flow, low-gradient AS. Another focus was the availability of all imaging modalities, thereby excluding subjects with implantable cardioverter defibrillators, reduced glomerular filtration rate, arrhythmia, or poor TTE windows. Second, because patients had significant cardiovascular comorbidities, myocardial $^{68}$Ga-FAPI signal may have been affected by other factors, including preexisting cardiovascular medication. Coronary angiography and CMR ruled out ischemic cardiomyopathy and cardiac amyloidosis in all patients; however, 48% of patients had preexisting coronary artery disease. Ultimately, effects on cardiac fibroblast activation cannot be ruled out. Yet, this reflects the expected clinical reality of AS before TAVR, and the heterogeneity of observed $^{68}$Ga-FAPI signals provides a foundation for testing prognostic value in larger samples in future projects. Third, PET, CMR, and TTE were performed at different time points using different systems. Coregistration was performed as thoroughly as possible, but slight local mismatches cannot be completely ruled out. Last, a longer-term follow-up after TAVR was not available and will have to be a focus of larger-sample subsequent projects to explore whether TAVR can be guided by $^{68}$Ga-FAPI imaging. Lastly, the matching control patients from our collaborating site in Heidelberg were oncologic patients undergoing $^{68}$Ga-FAPI PET for staging without in-depth information on severity or a detailed individual history of cardiovascular comorbidities. Cardiovascular diagnoses were retrospectively obtained from medical records.

## CONCLUSION

Molecular imaging identifies globally and regionally heterogeneous fibroblast activation in the LV myocardium of patients with severe AS. The $^{68}$Ga-FAPI signal correlates with LV dysfunction and altered extracellular matrix composition, but the FAPI-PET signal remains a distinct imaging biomarker that cannot be replaced by other clinical, blood, or imaging parameters. The present work provides a stimulus for subsequent studies focusing on strategies for image-guided therapy in AS, including fibroblast activation–targeted assays.

## DISCLOSURE

This work was supported by the Deutsche Forschungsgemeinschaft (DFG, Clinical Research Unit KFO 311 [Johann Bauersachs and Frank Bengel] and the Clinician Scientist Program PRACTIS [Johanna Diekmann]), the Leducq Foundation (Transatlantic Network "Immunofib" [Frank Bengel, James Thackeray, and Johanna Diekmann]), and "REBIRTH—Research Center for Translational Regenerative Medicine" (State of Lower Saxony [James Thackeray, Johann Bauersachs, and Frank Bengel]). Uwe Haberkorn has a patent application for quinolone-based FAP-targeting agents for imaging and therapy in nuclear medicine and has shares of a consultancy group for iTheranostics outside the submitted work. No other potential conflict of interest relevant to this article was reported.

## ACKNOWLEDGMENT

Precursor for $^{68}$Ga-FAPI-46 was kindly provided by Uwe Haberkorn.

## KEY POINTS

**QUESTION:** Is FAP-targeted PET a valuable marker of individual profibrotic activity in patients with AS, and is the PET signal linked to TAVR response?

**PERTINENT FINDINGS:** Using a multimodality, multiparametric correlative analysis, this cross-sectional, observational cohort study confirmed that noninvasive imaging of fibroblast activation in the myocardium of patients with advanced AS is feasible using the radiotracer $^{68}$Ga-FAPI-46 and targeted PET. The severity and regional pattern of fibroblast activation were heterogeneous among patients, and higher FAP volumes determined greater direct functional improvement immediately after TAVR.

**IMPLICATIONS FOR PATIENT CARE:** The observed heterogeneity of fibroblast activation provides a foundation for further studies testing its role as a predictor of outcome and response to valvular replacement or other therapies. The novel imaging assay may be integrated with other imaging and blood biomarkers for a future concept of fibrosis-targeted, image-guided therapeutic decision-making in AS.

## REFERENCES

1. Rosenhek R, Zilberszac R, Schemper M, et al. Natural history of very severe aortic stenosis. *Circulation.* 2010;121:151–156.
2. Coffey S, Cox B, Williams MJ. The prevalence, incidence, progression, and risks of aortic valve sclerosis: a systematic review and meta-analysis. *J Am Coll Cardiol.* 2014;63:2852–2861.
3. Généreux P, Stone GW, O'Gara PT, et al. Natural history, diagnostic approaches, and therapeutic strategies for patients with asymptomatic severe aortic stenosis. *J Am Coll Cardiol.* 2016;67:2263–2288.
4. Vahanian A, Beyersdorf F, Praz F, et al. 2021 ESC/EACTS guidelines for the management of valvular heart disease. *Eur Heart J.* 2022;43:561–632.
5. Ullah W, Gowda SN, Khan MS, et al. Early intervention or watchful waiting for asymptomatic severe aortic valve stenosis: a systematic review and meta-analysis. *J Cardiovasc Med (Hagerstown).* 2020;21:897–904.
6. Dweck MR, Boon NA, Newby DE. Calcific aortic stenosis: a disease of the valve and the myocardium. *J Am Coll Cardiol.* 2012;60:1854–1863.
7. Herrmann S, Fries B, Salinger T, et al. Myocardial fibrosis predicts 10-year survival in patients undergoing aortic valve replacement. *Circ Cardiovasc Imaging.* 2018;11:e007131.
8. Puls M, Beuthner BE, Topci R, et al. Impact of myocardial fibrosis on left ventricular remodelling, recovery, and outcome after transcatheter aortic valve implantation in different haemodynamic subtypes of severe aortic stenosis. *Eur Heart J.* 2020;41:1903–1914.
9. Pagourelias ED, Mirea O, Duchenne J, et al. Speckle tracking deformation imaging to detect regional fibrosis in hypertrophic cardiomyopathy: a comparison between 2D and 3D echo modalities. *Eur Heart J Cardiovasc Imaging.* 2020;21:1262–1272.
10. Krämer J, Niemann M, Liu D, et al. Two-dimensional speckle tracking as a non-invasive tool for identification of myocardial fibrosis in Fabry disease. *Eur Heart J.* 2013;34:1587–1596.
11. Hoffmann R, Altiok E, Friedman Z, Becker M, Frick M. Myocardial deformation imaging by two-dimensional speckle-tracking echocardiography in comparison to late gadolinium enhancement cardiac magnetic resonance for analysis of myocardial fibrosis in severe aortic stenosis. *Am J Cardiol.* 2014;114:1083–1088.
12. Bing R, Cavalcante JL, Everett RJ, Clavel MA, Newby DE, Dweck MR. Imaging and impact of myocardial fibrosis in aortic stenosis. *JACC Cardiovasc Imaging.* 2019;12:283–296.
13. Puntmann VO, Peker E, Chandrashekhar Y, Nagel E. T1 Mapping in characterizing myocardial disease: a comprehensive review. *Circ Res.* 2016;119:277–299.

14. Messroghli DR, Moon JC, Ferreira VM, et al. Clinical recommendations for cardiovascular magnetic resonance mapping of T1, T2, T2* and extracellular volume: a consensus statement by the Society for Cardiovascular Magnetic Resonance (SCMR) endorsed by the European Association for Cardiovascular Imaging (EACVI). *J Cardiovasc Magn Reson.* 2017;19:75.
15. Podlesnikar T, Delgado V, Bax JJ. Cardiovascular magnetic resonance imaging to assess myocardial fibrosis in valvular heart disease. *Int J Cardiovasc Imaging.* 2018;34:97–112.
16. Kratochwil C, Flechsig P, Lindner T, et al. $^{68}$Ga-FAPI PET/CT: tracer uptake in 28 different kinds of cancer. *J Nucl Med.* 2019;60:801–805.
17. Tillmanns J, Hoffmann D, Habbaba Y, et al. Fibroblast activation protein alpha expression identifies activated fibroblasts after myocardial infarction. *J Mol Cell Cardiol.* 2015;87:194–203.
18. Furtado MB, Nim HT, Boyd SE, Rosenthal NA. View from the heart: cardiac fibroblasts in development, scarring and regeneration. *Development.* 2016;143:387–397.
19. Diekmann J, Koenig T, Zwadlo C, et al. Molecular imaging identifies fibroblast activation beyond the infarct region after acute myocardial infarction. *J Am Coll Cardiol.* 2021;77:1835–1837.
20. Kessler L, Kupusovic J, Ferdinandus J, et al. Visualization of fibroblast activation after myocardial infarction using $^{68}$Ga-FAPI PET. *Clin Nucl Med.* 2021;46:807–813.
21. Notohamiprodjo S, Nekolla SG, Robu S, et al. Imaging of cardiac fibroblast activation in a patient after acute myocardial infarction using $^{68}$Ga-FAPI-04. *J Nucl Cardiol.* 2022;29:2254–2261.
22. Varasteh Z, Mohanta S, Robu S, et al. Molecular imaging of fibroblast activity after myocardial infarction using a $^{68}$Ga-labeled fibroblast activation protein inhibitor, FAPI-04. *J Nucl Med.* 2019;60:1743–1749.
23. Diekmann J, Koenig T, Thackeray JT, et al. Cardiac fibroblast activation in patients early after acute myocardial infarction: integration with magnetic resonance tissue characterization and subsequent functional outcome. *J Nucl Med.* 2022;63:1415–1423.
24. Siebermair J, Kohler MI, Kupusovic J, et al. Cardiac fibroblast activation detected by Ga-68 FAPI PET imaging as a potential novel biomarker of cardiac injury/remodeling. *J Nucl Cardiol.* 2021;28:812–821.
25. Vahanian A, Beyersdorf F, Praz F, et al. 2021 ESC/EACTS guidelines for the management of valvular heart disease. *EuroIntervention.* 2022;17:e1126–e1196.
26. Loktev A, Lindner T, Burger EM, et al. Development of fibroblast activation protein-targeted radiotracers with improved tumor retention. *J Nucl Med.* 2019;60:1421–1429.
27. Kawel-Boehm N, Maceira A, Valsangiacomo-Buechel ER, et al. Normal values for cardiovascular magnetic resonance in adults and children. *J Cardiovasc Magn Reson.* 2015;17:29.
28. Bull S, White SK, Piechnik SK, et al. Human non-contrast T1 values and correlation with histology in diffuse fibrosis. *Heart.* 2013;99:932–937.
29. Sugimoto T, Dulgheru R, Bernard A, et al. Echocardiographic reference ranges for normal left ventricular 2D strain: results from the EACVI NORRE study. *Eur Heart J Cardiovasc Imaging.* 2017;18:833–840.
30. Baumgartner H, Hung J, Bermejo J, et al. Recommendations on the echocardiographic assessment of aortic valve stenosis: a focused update from the European Association of Cardiovascular Imaging and the American Society of Echocardiography. *J Am Soc Echocardiogr.* 2017;30:372–392.
31. Chin CWL, Everett RJ, Kwiecinski J, et al. Myocardial fibrosis and cardiac decompensation in aortic stenosis. *JACC Cardiovasc Imaging.* 2017;10:1320–1333.
32. Hein S, Arnon E, Kostin S, et al. Progression from compensated hypertrophy to failure in the pressure-overloaded human heart: structural deterioration and compensatory mechanisms. *Circulation.* 2003;107:984–991.
33. Heckmann MB, Reinhardt F, Finke D, et al. Relationship between cardiac fibroblast activation protein activity by positron emission tomography and cardiovascular disease. *Circ Cardiovasc Imaging.* 2020;13:e010628.
34. Aghajanian H, Kimura T, Rurik JG, et al. Targeting cardiac fibrosis with engineered T cells. *Nature.* 2019;573:430–433.
35. Nagaraju CK, Dries E, Popovic N, et al. Global fibroblast activation throughout the left ventricle but localized fibrosis after myocardial infarction. *Sci Rep.* 2017;7:10801.

# Importance of Blood Glucose Management Before $^{18}$F-FDG PET/CT in 322 Patients with Bacteremia of Unknown Origin

Jordy P. Pijl[1], Andor W.J.M. Glaudemans[1], Olivier Gheysens[2], Riemer H.J.A. Slart[1,3], and Thomas C. Kwee[1]

[1]*Medical Imaging Center, Department of Radiology, Nuclear Medicine and Molecular Imaging, University Medical Center Groningen, University of Groningen, Groningen, The Netherlands;* [2]*Department of Nuclear Medicine, Cliniques Universitaires Saint-Luc and Institute of Clinical and Experimental Research, Université Catholique de Louvain, Brussels, Belgium; and* [3]*Department of Biomedical Photonic Imaging, University of Twente, Enschede, The Netherlands*

We investigated the effects of blood glucose levels on the performance of $^{18}$F-FDG PET/CT for detecting an infection focus in patients with bacteremia. **Methods:** A total of 322 consecutive patients with bacteremia who underwent $^{18}$F-FDG PET/CT between 2010 and 2021 were included. Logistic regression analysis was performed to evaluate the association between finding a true-positive infection focus on $^{18}$F-FDG PET/CT and blood glucose level, type of diabetes, and use of hypoglycemic medication. C-reactive protein, leukocyte count, duration of antibiotic treatment, and type of isolated bacteria were considered as well. **Results:** Blood glucose level (odds ratio, 0.76 per unit increase; $P = <0.001$) was significantly and independently associated with $^{18}$F-FDG PET/CT outcome. In patients with a blood glucose level between 3.0 and 7.9 mmol/L (54–142 mg/dL), the true-positive detection rate of $^{18}$F-FDG PET/CT varied between 61% and 65%, whereas in patients with a blood glucose level between 8.0 and 10.9 mmol/L (144–196 mg/dL), the true-positive detection rate decreased to 30%–38%. In patients with a blood glucose level greater than 11.0 mmol/L (200 mg/dL), the true-positive detection rate was 17%. In addition to C-reactive protein (odds ratio, 1.004 per point increase; $P = 0.009$), no other variables were independently associated with $^{18}$F-FDG PET/CT outcome. **Conclusion:** In patients with moderate to severe hyperglycemia, $^{18}$F-FDG PET/CT was much less likely to identify the focus of infection than in normoglycemic patients. Although current guidelines recommend postponing $^{18}$F-FDG PET/CT only in cases of severe hyperglycemia with glucose levels greater than 11 mmol/L (200 mg/dL), a lower blood glucose threshold seems to be more appropriate in patients with bacteremia of unknown origin and other infectious diseases.

**Key Words:** bacteremia; diabetes; $^{18}$F-FDG PET/CT; blood glucose; sepsis

**J Nucl Med 2023; 64:1287–1294**
DOI: 10.2967/jnumed.122.264839

Bacteremia is defined by the presence of viable bacteria in the bloodstream. With an incidence between 100 and 200 cases per 100,000 people per year, bacteremia is one of the most common causes of hospital admission (*1,2*). As source control is the most important treatment for bacteremia, the mortality rate of bacteremia strongly depends on the ability to locate the source of infection (*3*). When no source can be identified, patients are diagnosed with bacteremia of unknown origin (*4*).

$^{18}$F-FDG PET/CT has proven to be very useful in diagnosing numerous infectious diseases, including infection foci in patients with bacteremia of unknown origin (*5,6*). As leukocytes and other inflammatory cells such as cytokines are recruited to infection sites and usually consume more glucose than does the surrounding tissue, infection foci are often readily visible on $^{18}$F-FDG PET/CT (*7*). Most bacteria consume glucose as well (*8*).

Even though glucose metabolism plays a vital role in $^{18}$F-FDG PET/CT, the effect of hyperglycemia on the diagnostic performance of $^{18}$F-FDG PET/CT in patients with infectious disease remains poorly understood. Theoretically, hyperglycemia can cause reduced cellular $^{18}$F-FDG uptake due to direct competition with plasmatic glucose at glucose binding sites (*9*). Hyperglycemia can also lead to hyperinsulinemia, which causes upregulation of glucose type 4 transporters and subsequently higher skeletal and myocardial $^{18}$F-FDG uptake (*10*). Both mechanisms could potentially cause false-negative results in hyperglycemic patients with infectious disease, but literature on the clinical consequences of hyperglycemia on the diagnostic accuracy of $^{18}$F-FDG PET/CT is limited and conflicting (*11–17*). Infection foci may also show a large variation in location and in $^{18}$F-FDG avidity. For example, endocarditis may be obscured by physiologic high myocardial uptake due to hyperglycemia and osteomyelitis by just a marginally elevated $^{18}$F-FDG uptake compared with the background in low-grade infections. Additionally, the prevalence of diabetes mellitus in the community is rapidly increasing, especially in high-income countries (*18*).

In the current PET imaging guidelines, the recommended upper threshold of plasma glucose before clinical $^{18}$F-FDG PET/CT studies are performed is 11 mmol/L (200 mg/dL) (*15–18*). For research studies, an upper glucose threshold of 8.3 mmol/L (150 mg/dL) is recommended (*19*). Although these thresholds are widely applied, the effects of moderate (7.8–10.0 mmol/L or 140–180 mg/dL) to severe hyperglycemia (>10.0 mmol/L or >180 mg/dL) on the diagnostic performance of $^{18}$F-FDG PET/CT remain unclear, especially in patients with infectious disease (*20*).

Therefore, the aim of this study was to assess the effects of hyperglycemia on the diagnostic performance of $^{18}$F-FDG PET/CT in patients with bacteremia of unknown origin.

## MATERIALS AND METHODS

### Study Design and Patients

The electronic patient information system of University Medical Center Groningen was searched for all patients who underwent $^{18}$F-FDG

Received Oct. 1, 2022; revision accepted Apr. 14, 2023.
For correspondence or reprints, contact Jordy P. Pijl (j.p.pijl@umcg.nl).
Published online Jun. 29, 2023.

PET/CT between 2010 and 2021 to find the focus of infection using the keywords "sepsis," "bacteremia," "infection," "fever," and "blood culture." All patients for whom bacteremia was confirmed by blood cultures taken within 2 mo before $^{18}$F-FDG PET/CT were included. Patients with negative blood cultures or blood cultures that were considered contaminated by medical microbiologists were excluded. Follow-up $^{18}$F-FDG PET/CT scans and $^{18}$F-FDG PET/CT scans performed for other reasons than locating the source of infection, such as oncologic follow-up, were excluded as well. The local institutional review board approved this retrospective, single-center study and waived the requirement for written informed consent (Institutional Review Board number 201700145).

### Patient Data Review and Reference Standard

The medical files of all patients were reviewed for relevant clinical and biochemical data (age, sex, medical history [including the presence of diabetes], laboratory values [blood glucose before $^{18}$F-FDG PET/CT, C-reactive protein (CRP), leukocyte count, type of isolated bacteria]; duration of hospital stay; use of hypoglycemic medication, antibiotics, and immunosuppressive medication; final diagnosis at hospital discharge; and 6-mo follow-up data).

### $^{18}$F-FDG PET/CT Acquisition

All scans were performed using an integrated PET/CT system (Biograph mCT 40- or 64-slice PET/CT or Biograph Vision PET/CT; Siemens) with 3 min per bed position. Low-dose CT was performed for attenuation correction and anatomic mapping at 100 kV and 30 mAs. Data acquisition and reconstruction were in accordance with European Association of Nuclear Medicine/Research 4 Life guidelines (*19*). In 60 patients, concomitant full-dose CT of the neck, thorax, or abdomen was performed with a constant tube potential of 100 or 120 kV and automatic adjustment of milliampere seconds in the *z*-direction.

Patients fasted for a minimum of 6 h, and blood glucose concentration was ensured to be less than 11 mmol/L (200 mg/dL) before 3 MBq of $^{18}$F-FDG/kg of body weight were administered intravenously. In 7 patients, $^{18}$F-FDG PET/CT was performed even though the blood glucose level was greater than 11 mmol/L because of clinical urgency and poorly manageable diabetes. When there was a clinical suspicion of infective endocarditis, patients were also prepared with a high-fat, low-carbohydrate diet for at least 24 h. In some patients suspected of endocarditis, a heparin loading dose of 50 IU/kg was administered 15 min before imaging to reduce myocardial $^{18}$F-FDG uptake. PET/CT imaging was performed approximately 60 min after intravenous $^{18}$F-FDG administration.

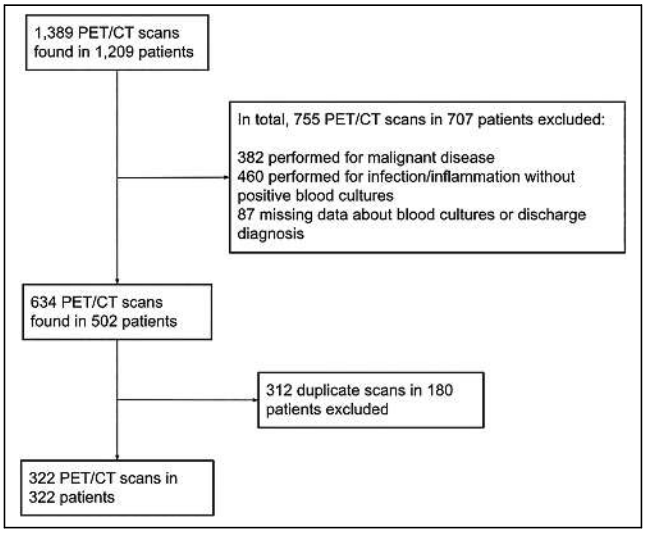


**FIGURE 1.** Patient inclusion tree.

### $^{18}$F-FDG PET Interpretation and Reference Standard

$^{18}$F-FDG PET/CT scans were interpreted by experienced nuclear medicine physicians as part of routine clinical care using Syngo.Via software

**TABLE 1**
Patient Characteristics

| Characteristic | Data |
|---|---|
| Age (y) | 63.5 (20) |
| Sex | |
| Men | 206 (64%) |
| Women | 116 (36%) |
| Diabetes | |
| Type 1 | 7 (2%) |
| Type 2 | 66 (20%) |
| NODAT | 4 (1%) |
| No diabetes | 245 (76%) |
| Use of hypoglycemic medication | |
| Sulfonylurea derivatives | 6 (2%) |
| Metformin | 27 (8%) |
| Insulin | 54 (17%) |
| None | 235 (73%) |
| Use of immunosuppressive medication | |
| Yes | 99 (31%) |
| No | 223 (69%) |
| Duration of hospital stay (d) | 23 (25) |
| CRP (mg/L) | 87 (116) |
| Leukocyte count ($\times 10^9$/L) | 8.9 (6.7) |
| Blood glucose level (mmol/L) | 5.4 (1.8) |
| Type of isolated bacteria | |
| Coagulase-negative *Staphylococci* | 35 (11%) |
| *Enterococci* | 38 (12%) |
| *Streptococci* | 44 (14%) |
| Gram-negative rods | 66 (20%) |
| *S. aureus* | 97 (30%) |
| Polymicrobial | 31 (10%) |
| Other | 11 (3%) |
| Duration between last positive blood cultures and $^{18}$F-FDG PET/CT (d) | 6 (7) |
| Duration of antibiotic treatment before $^{18}$F-FDG PET/CT (d) | 7 (7) |
| Quality of PET image | |
| Poor | 34 (11%) |
| Reasonable | 49 (15%) |
| Good | 239 (74%) |
| In-hospital mortality | 45 (14%) |

NODAT = New-onset diabetes after transplant.
Qualitative data are number and percentage; continuous data are median and IQR.

(Siemens Healthcare). All $^{18}$F-FDG PET/CT scans were reevaluated by one of the authors. In the case of any doubt or inconsistencies with previous reports and $^{18}$F-FDG PET/CT images, the images were reevaluated by another author, a nuclear medicine physician, who was unaware of the original $^{18}$F-FDG PET/CT interpretations and the results of all other imaging and clinical, laboratory, and microbiologic tests. $^{18}$F-FDG PET/CT scans showing at least 1 $^{18}$F-FDG–avid lesion localized to an area that did not correspond to physiologic biodistribution of $^{18}$F-FDG and did not suggest a pathology other than infection were considered to be positive for an infection focus. The final clinical diagnosis at hospital discharge was used as a reference standard for $^{18}$F-FDG PET/CT results. This clinical diagnosis was based on all clinically available data including histology or microbiology reports; other imaging results, such as ultrasonography or MRI, confirming the infection focus found on $^{18}$F-FDG PET/CT; and clinical follow-up and treatment outcome for at least 6 mo. The final diagnosis was never based on $^{18}$F-FDG PET/CT results alone.

### Statistical Analyses

Continuous variables were checked for normal distribution using Shapiro–Wilk tests. Data were presented as mean ± SD or median with interquartile range (IQR) for normally or nonnormally distributed data, respectively. The sensitivity, specificity, positive predictive value, and negative predictive value of $^{18}$F-FDG PET/CT for detecting an infection focus were calculated, along with 95% CI. Age, sex, medical history (including the presence of diabetes), laboratory values (blood glucose before $^{18}$F-FDG PET/CT, CRP, leukocyte count, type of isolated bacteria), and duration of hospital stay, as well as the use of hypoglycemic medication, antibiotics, and immunosuppressive medication, were analyzed with univariable logistic regression as independent variables and the $^{18}$F-FDG PET/CT result as the dependent variable. The $^{18}$F-FDG PET/CT result based on the final discharge diagnosis was either true-positive or not true-positive. As such, all true-positive results were analyzed against true-negative, false-positive, and false-negative results. Corresponding odds ratios (ORs) and 95% CIs were calculated, and $P$ values of less than 0.05 were considered to be statistically detectable. Variables with a $P$ value of 0.10 or less on univariable analysis were included in the backward multivariable logistic regression model. All statistical analyses were performed using IBM Statistical Package for the Social Sciences, version 28.

## RESULTS

### Patient Population

In total, 1,389 $^{18}$F-FDG PET/CT scans from 1,209 individual patients were potentially eligible for inclusion. After the inclusion and exclusion criteria were reviewed, 322 $^{18}$F-FDG PET/CT scans from 322 patients were finally included (Fig. 1). These included 206 men and 116 women, with a median age of 63.5 y (IQR, 20 y) (Table 1). Of these, 66 patients had type 2 diabetes (20%), 7 patients had type 1 diabetes (2%), and 4 patients had new-onset diabetes after transplantation (1%). Fifty-four patients (17%) were using

**TABLE 2**
Diagnostic Performance of $^{18}$F-FDG PET/CT for Detecting Infection Focus

| Statistic | Value (%) | 95% CI |
|---|---|---|
| Sensitivity | 83.6 | 78.1–88.2 |
| Specificity | 80.4 | 71.1–87.8 |
| Positive predictive value | 90.8 | 86.8–93.7 |
| Negative predictive value | 67.8 | 60.7–74.2 |

**TABLE 3**
True-Positive, False-Positive, True-Negative, and False-Negative Infections Based on $^{18}$F-FDG PET/CT Results and Final Discharge Diagnosis

| Infection type | *n* |
|---|---|
| True-positive | 188 |
| Central line infection | 6 (2%) |
| Cyst infection | 15 (5%) |
| Diffusely disseminated disease | 5 (2%) |
| Endocarditis | 15 (5%) |
| Gastrointestinal infection/abscess | 11 (3%) |
| Hepatobiliary infection | 18 (6%) |
| Musculoskeletal infection | 22 (7%) |
| Pulmonary infection | 21 (7%) |
| Renal abscess | 8 (2%) |
| Spondylodiskitis/sacroiliitis | 38 (12%) |
| Splenic abscess | 3 (1%) |
| Subcutaneous infection | 5 (2%) |
| Vascular graft infection | 13 (4%) |
| Vascular infection | 8 (2%) |
| False-positive | 18 |
| Endocarditis | 1 (<1%) |
| Gastrointestinal | 2 (<1%) |
| Infected hematoma after surgery | 3 (1%) |
| Mediastinitis after sternotomy | 1 (<1%) |
| Mucositis | 2 (<1%) |
| Musculoskeletal | 3 (1%) |
| Pulmonary infection | 3 (1%) |
| Vascular graft infection | 1 (<1%) |
| Vascular infection | 2 (<1%) |
| True-negative | 78 |
| Bloodstream infection of unknown origin | 63 (20%) |
| Central line infection* | 7 (2%) |
| Infected toe† | 2 (<1%) |
| Urinary tract infection‡ | 6 (2%) |
| False-negative infections | 37 |
| Cyst infection | 2 (<1%) |
| Endocarditis | 16 (5%) |
| Enterocolitis | 1 (<1%) |
| Cholangitis | 3 (1%) |
| Venous access port | 4 (1%) |
| Mucositis | 1 (<1%) |
| Parotitis | 1 (<1%) |
| Pulmonary infection | 2 (<1%) |
| Renal abscess | 4 (1%) |
| Vascular infection | 3 (1%) |

*Central line was already removed before $^{18}$F-FDG PET/CT was performed.

†Patients were only scanned from head to femur. Therefore, their legs are not depicted on $^{18}$F-FDG PET/CT.

‡These infections were considered true-negative as well, because $^{18}$F-FDG excretion through urinary tract masks urinary tract infections.

insulin, 27 patients (8%) metformin, and 6 patients (2%) sulfonylurea derivatives. Ninety-nine patients (31%) were using immunosuppressive medication such as prednisolone or tacrolimus. The median duration of antibiotic treatment before $^{18}$F-FDG PET/CT was 7 d (IQR, 7 d); the median duration between the last positive blood cultures and $^{18}$F-FDG PET/CT was 6 d (IQR, 7 d), and the median duration of the hospital stay was 23 d (IQR, 25 d). The median CRP level was 87 mg/L (IQR, 116 mg/L), with a median leukocyte count of $8.9 \times 10^9$/L (IQR, $6.7 \times 10^9$/L) and a median blood glucose level of 5.4 (IQR, 1.8 mmol/L). Most patients had bacteremia caused by *Staphylococcus aureus* (30%), followed by gram-negative rods (20%) and *Streptococci* (14%). The in-hospital mortality rate was 14%.

### Diagnostic Performance of $^{18}$F-FDG PET/CT

According to the reference standard, $^{18}$F-FDG PET/CT yielded 188 true-positive results, 19 false-positive results, 78 true-negative results, and 37 false-negative results for finding the infection focus. The resulting sensitivity was 83.6% and specificity was 80.4%, with a positive predictive value of 90.8% and a negative predictive value of 67.8% (Table 2). The most commonly diagnosed (true-positive) infections were spondylodiskitis or sacroiliitis (38 patients, 12%); other musculoskeletal infections, such as septic arthritis or osteomyelitis (22 patients, 7%); and pulmonary infections (21 patients, 7%) (Table 3). The most common false-positive diagnoses were infected hematomas shortly after surgery ($n$ = 3, 1%), for which elevated $^{18}$F-FDG uptake caused by inflammation was misinterpreted as an infection; musculoskeletal infection such as mediastinitis shortly after sternotomy ($n$ = 3, 1%), for which $^{18}$F-FDG avidity caused by postoperative changes was misinterpreted as an infection; and pulmonary infection ($n$ = 3), for which $^{18}$F-FDG PET/CT mostly showed mildly elevated $^{18}$F-FDG uptake in pleural effusion possibly caused by infection, but the final diagnosis was bacteremia of unknown origin. The most common false-negative diagnoses included endocarditis (16 patients, 5%) and infected venous access ports (4 patients, 1%) (*21*).

### Factors Associated with $^{18}$F-FDG PET/CT Outcome

On univariable logistic regression, not having diabetes (OR, 1.67; $P$ = 0.050), an increase in CRP level (OR, 1.003 per unit increase;

**TABLE 4**
Factors Associated with Detecting True-Positive Infection Focus on $^{18}$F-FDG PET/CT

| | Univariable OR | | Multivariable OR | |
|---|---|---|---|---|
| Factor | Value | *P* | Value | *P* |
| Clinical | | | | |
| Age | 1.0 (0.99–1.01) | 0.99 | | |
| Male sex | 0.72 (0.45–1.15) | 0.17 | | |
| Diabetes, type 1 | 0.93 (0.20–4.22) | 0.92 | | |
| Diabetes, type 2 | 0.61 (0.36–1.03) | 0.076 | | |
| No diabetes | 1.67 (0.99–2.81) | 0.050 | | |
| Duration of hospital stay | 1.0 (0.99–1.00) | 0.44 | | |
| Laboratory values | | | | |
| CRP | 1.004 (1.002–1.007) | 0.003 | 1.004 (1.001–1.007) | 0.009 |
| Leukocyte count | 1.01 (0.98–1.04) | 0.64 | | |
| Blood glucose level | 0.82 (0.72–0.93) | 0.003 | 0.76 (0.65–0.89) | <0.001 |
| Medication use | | | | |
| Immunosuppressives | 0.61 (0.38–0.99) | 0.044 | | |
| Sulfonylurea derivatives | 0.93 (0.20–4.22) | 0.92 | | |
| Metformin | 0.48 (0.21–1.08) | 0.077 | | |
| Insulin | 0.71 (0.39–1.29) | 0.26 | | |
| Days of antibiotic treatment | 0.99 (0.97–1.01) | 0.25 | | |
| Microbiology | | | | |
| Coagulase-negative *Staphylococci* ($n$ = 35) | 0.62 (0.31–1.26) | 0.19 | | |
| *Enterococci* ($n$ = 38) | 0.45 (0.23–0.92) | 0.028 | | |
| *Streptococci* ($n$ = 44) | 1.13 (0.59–2.16) | 0.72 | | |
| Gram-negative rods ($n$ = 66) | 1.51 (0.86–2.67) | 0.15 | | |
| *S. aureus* ($n$ = 97) | 1.24 (0.76–2.02) | 0.40 | | |
| Polymicrobial ($n$ = 31) | 0.96 (0.45–2.04) | 0.91 | | |
| Other ($n$ = 11) | 1.23 (0.35–4.28) | 0.75 | | |

Data in parentheses are 95% CI.

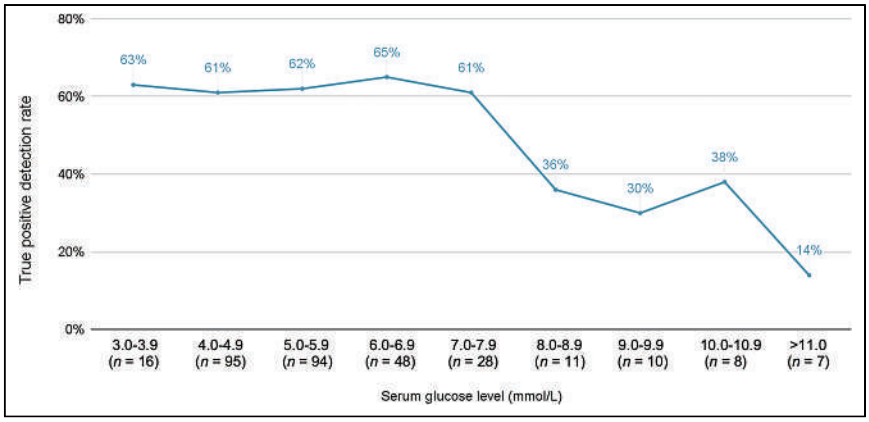


**FIGURE 2.** Blood glucose level and detection rate of true-positive infection focus on $^{18}$F-FDG PET/CT.

$P = 0.003$), an increase in blood glucose level (OR, 0.82 per unit increase; $P = 0.003$), use of immunosuppressants (OR, 0.61; $P = 0.044$), and bacteremia caused by *Enterococci* (OR, 0.028; $P = 0.028$) were significantly associated with detecting a true-positive infection focus on $^{18}$F-FDG PET/CT (Table 4). On multivariable logistic regression, only an increase in CRP level (OR, 1.004 per unit increase; $P = 0.009$) and blood glucose level (OR, 0.76 per unit increase; $P = <0.001$) before $^{18}$F-FDG PET/CT remained independently associated with detecting an infection focus on $^{18}$F-FDG PET/CT.

In 253 patients with a blood glucose level between 3.0 and 7.9 mmol/L (54–142 mg/dL), the true-positive detection rate of $^{18}$F-FDG PET/CT varied between 61% and 65% (Fig. 2). In 57 patients with a blood glucose level between 8.0 and 10.9 mmol/L (144–196 mg/dL), the true-positive detection rate decreased to 30%–38%. $^{18}$F-FDG PET/CT was performed on 7 patients with a blood glucose level greater than the recommended threshold of 11.0 mmol/L (200 mg/dL). In only 1 of these patients (17%) was a true-positive infection focus found. Two patient examples are shown in Figures 3 and 4.

### Effect of Hypoglycemic Medication Use on $^{18}$F-FDG PET/CT Outcome

On univariable logistic regression, only the use of metformin approached statistical significance (OR, 0.48; $P = 0.077$). Use of insulin (OR, 0.71; $P = 0.26$) or sulfonylurea derivatives (OR, 2.11; $P = 0.52$) was not significantly associated with $^{18}$F-FDG PET/CT outcome. The individual dosages were not specifically analyzed.

## DISCUSSION

The results of this study show that managing blood glucose before performing $^{18}$F-FDG PET/CT has a large impact on its ability to identify the infection focus in patients with bacteremia of unknown origin.

On univariable and multivariable logistic regression, a higher blood glucose level was associated with significantly lower odds of detecting an infection focus on $^{18}$F-FDG PET/CT (OR, 0.76; $P = 0.003$). The detection rate of $^{18}$F-FDG PET/CT was 60%–65% in patients with a blood glucose level less than 8.0 mmol/L (144 mg/dL) but decreased to 14%–38% in patients with a blood glucose level less than 8.0 mmol/L.

Most nuclear imaging guidelines recommend that $^{18}$F-FDG PET/CT not be postponed unless the glucose level exceeds an upper threshold of 11 mmol/L (200 mg/dL) (*22*). However, this threshold also depends on the indication for $^{18}$F-FDG PET/CT and the setting in which $^{18}$F-FDG PET/CT is performed. For example, the recommended upper threshold for brain imaging is 8.8 mmol/L (160 mg/dL), and the European Association of Nuclear Medicine recommends an upper threshold of 7.0–8.3 mmol/L (126–150 mg/dL) for clinical trials (*16*). The procedure guideline for tumor imaging from the Society of Nuclear Medicine and Molecular Imaging recommends an upper threshold between 8.3 and 11 mmol/L (150–200 mg/dL) (*23*). The rationale behind these differences in upper threshold is unclear. Also, there is no distinction between the glucose threshold in patients who undergo $^{18}$F-FDG PET/CT for oncologic disease and that in patients who undergo $^{18}$F-FDG PET/CT for infectious disease, even though the physiology behind

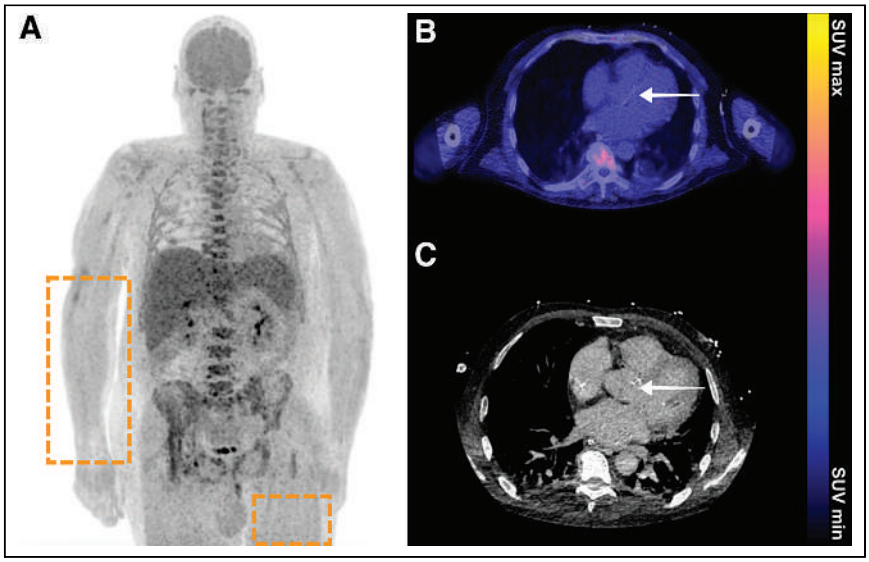


**FIGURE 3.** A 64-y-old man presented to hospital with septic shock. His medical history showed type 2 diabetes mellitus, hypertension, and myocardial infarction. At presentation, his CRP level was 78 mg/L, and his leukocyte count was 13.3 × $10^9$/L. Blood cultures were positive for *S. aureus*. To identify focus of infection, $^{18}$F-FDG PET/CT was performed. Before $^{18}$F-FDG PET/CT, his blood glucose level measured 11.1 mmol/L (200 mg/dL). (A) Coronal maximum-intensity-projection $^{18}$F-FDG PET showed diffusely increased $^{18}$F-FDG uptake in skeletal muscle (rectangles), which made images difficult to interpret. High glucose level was deemed to be most probable cause for this elevated skeletal muscle uptake. (B and C) Axial $^{18}$F-FDG PET/CT (B) and low-dose CT (C) did not show elevated $^{18}$F-FDG uptake at aortic valve (arrows), even though valvular vegetation of aortic valve was seen on transesophageal ultrasound, suggestive of endocarditis. Thus, $^{18}$F-FDG PET/CT result was deemed to be false-negative. Despite antibiotic treatment, patient died several days after $^{18}$F-FDG PET/CT was performed. Autopsy was not performed.

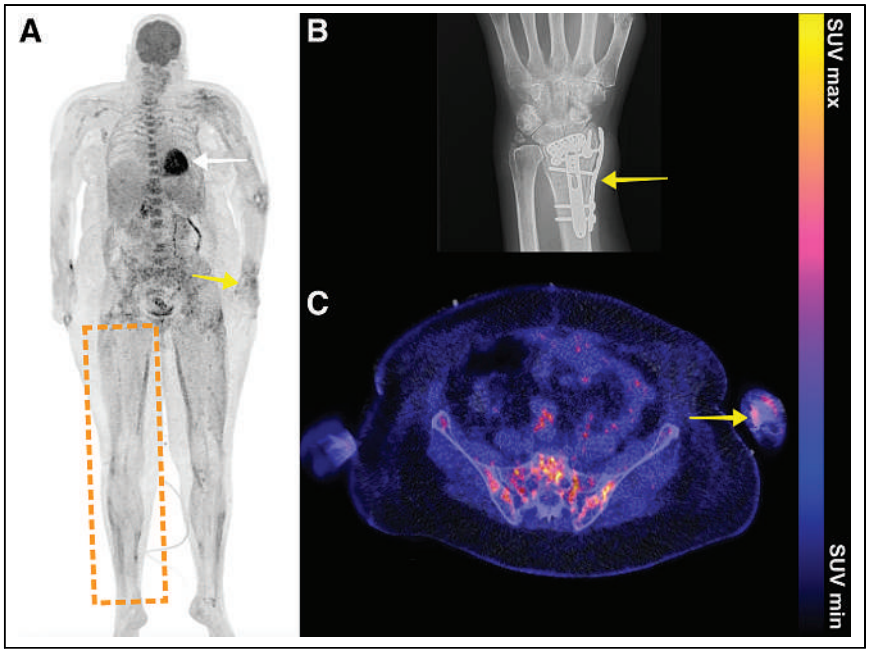


**FIGURE 4.** A 64-y-old woman presented to hospital with painful left wrist and fever. Her medical history showed bilateral hip replacement and internal fixation of left wrist fracture with plates and screws earlier that year. On admittance, she had CRP of 274 mg/L and leukocyte count of $18.4 \times 10^9$/L. Blood cultures were positive for *S. aureus*. $^{18}$F-FDG PET/CT was performed to identify primary infection focus and potential metastatic foci. By accident, insulin was administered to patient shortly before $^{18}$F-FDG PET/CT was performed. (A) Coronal maximum-intensity projection showed diffusely increased $^{18}$F-FDG uptake in skeletal muscle (rectangle), rendering $^{18}$F-FDG PET images difficult to interpret. Myocardium also showed elevated $^{18}$F-FDG uptake (white arrow). Pathologic $^{18}$F-FDG uptake was seen at left wrist (yellow arrow). (B and C) On radiography (B), wrist uptake on PET was interpreted as infected osteosynthetic material (arrow), also visible on axial $^{18}$F-FDG PET/CT (C, arrow). Plates and screws of left wrist were surgically removed and cultured. These cultures were also positive for *S. aureus*. Despite antibiotic treatment, patient died of septic shock 1 wk after $^{18}$F-FDG PET/CT was performed.

elevated $^{18}$F-FDG uptake in oncologic and infectious lesions is different. Cancer cells consume much glucose because of increased proliferation and inefficient metabolism with glycolysis instead of oxidative phosphorylation as their main metabolic pathway (*24*). An infection focus is thought to be $^{18}$F-FDG–avid mainly because of the recruitment of other metabolically active cells such as granulocytes. Additionally, most bacteria consume glucose and therefore $^{18}$F-FDG. As the $^{18}$F-FDG avidity of different types of bacteria also differs, it could be hypothesized that $^{18}$F-FDG uptake in infection foci with more fulminant bacteria, such as *S. aureus,* is less easily affected by high blood glucose levels than are the less fulminant pathogens (*8*). On univariable regression, an *Enterococcus* bacteremia was also significantly associated with lower odds of identifying an infection focus on $^{18}$F-FDG PET/CT (OR, 0.45; $P = 0.028$). However, the statistical significance of this variable was not maintained in the multivariate model.

In both cancer and infectious disease, high blood glucose can cause reduced cellular $^{18}$F-FDG uptake due to direct competition with plasmatic glucose at glucose binding sites and upregulation of the glucose transporters of other tissues, resulting in a lower lesion-to-background ratio (*9*). Some studies also suggest that cancer cells are less easily saturated by glucose than are other tissues (*14,25*).

Not having diabetes was significantly associated with identifying an infection focus on $^{18}$F-FDG PET/CT with univariable logistic regression (OR, 1.67; $P = 0.050$) but not with multivariable logistic regression. This finding suggests that diabetic patients may not be at a disadvantage for detection of their infection focus on $^{18}$F-FDG PET/CT when their blood glucose is properly managed. This includes fasting for 4–6 h and also making sure that no external glucose is intravenously administered. Rapid-acting insulin should be administered only up to 4 h before $^{18}$F-FDG PET/CT, short-acting insulin should be administered within 6 h, and intermediate- or long-acting insulin should not be used on the day $^{18}$F-FDG PET/CT is scheduled (*26*). Interestingly, the use of hypoglycemic medication such as metformin or insulin was not statistically associated with $^{18}$F-FDG PET/CT outcome, implying that a satisfactory effect of these medications on glucose level and not the use of these medications alone is important for $^{18}$F-FDG PET/CT outcome.

In addition to blood glucose, CRP was the only other factor independently associated with $^{18}$F-FDG PET/CT outcome. This finding is in line with previous studies, which also found that a higher CRP increases the chance of identifying an infection focus on $^{18}$F-FDG PET/CT in patients with bacteremia (*27–29*). Although a previous study of our own (*30*) showed a statistically detectable relation between duration of antibiotic use and $^{18}$F-FDG PET/CT outcome, this relation was not shown in our current study (OR, 0.99 per day; $P = 0.25$), perhaps because much more recent patients were included in the current study. Our hospital became more selective in only providing specialized tertiary care over the past few years, resulting in the inclusion of more patients with comorbidities such as infected vascular grafts or prostheses requiring chronic antibiotic suppressive therapy or immunocompromised patients requiring prophylactic antibiotic treatment.

Previous literature on the effects of hyperglycemia on $^{18}$F-FDG PET/CT outcome in patients with infectious disease is limited. In a study by Rabkin et al., 123 patients with infection or inflammation were included (*12*). Nineteen patients had a glucose level greater than 10 mmol/L (180 mg/dL), and in 11 patients (58%), a true-positive infection or inflammation focus was found. No statistically detectable difference was found in the number of false-negative results between normoglycemic and hyperglycemic patients. Because patients with both inflammatory and infectious diseases were included, it is unclear how many of these 11 patients had infectious disease. Additionally, not all patients had an infection of unknown origin. Twenty-six of 123 patients (21%) underwent $^{18}$F-FDG PET/CT to evaluate their diabetic foot. A higher number of true-positive results in hyperglycemic patients than in our patient population could have resulted from the fact that hyperglycemia is more likely in patients with a diabetic foot than in general patients with bacteremia of unknown origin, and the a priori chance of detecting an infection in patients with a

chronic wound such as diabetic foot is likely higher than in all patients with bacteremia of unknown origin (*12*).

In a large metaanalysis by Eskian et al., which was conducted to evaluate the effect of prescan blood glucose levels on the SUVs of healthy tissue, 8,380 patients were included with SUV measurements of the liver, brain, muscle, blood pool, or tumors (*14*). Patients were categorized in 5 groups based on blood glucose: less than 109 mg/dL (euglycemic), 110–125 mg/dL (mild hyperglycemia), 126–150 mg/dL (moderate hyperglycemia), 151–200 mg/dL (high moderate hyperglycemia), and greater than 200 mg/dL (severe hyperglycemia). Eskian et al. concluded that blood glucose affected $^{18}$F-FDG uptake in tumors only when the glucose level was greater than 11 mmol/L (200 mg/dL). Blood glucose showed a statistically detectable negative correlation with $^{18}$F-FDG uptake in the muscles and brains in all hyperglycemic groups and a statistically detectable positive correlation in all hyperglycemic patients with $^{18}$F-FDG uptake in the blood pool and livers. Unfortunately, patients with infectious disease were not included, and the underlying mechanism of $^{18}$F-FDG avidity for infectious and oncologic lesions is different.

Our study was compromised by some limitations. First, because of the retrospective nature of this study, selection bias may have occurred. Although all patients were selected using objective criteria, not all patients from our hospital with bacteremia underwent $^{18}$F-FDG PET/CT because this indication was set by the treating physician. Second, the reference standard for $^{18}$F-FDG PET/CT, namely the clinical diagnosis at hospital discharge, was suboptimal because this diagnosis also included $^{18}$F-FDG PET/CT results. However, this diagnosis was never based on $^{18}$F-FDG PET/CT results alone. For future research, it would be interesting to conduct quantitative measurements of infection foci in patients with bacteremia to examine whether there may be not only a lower detection rate on $^{18}$F-FDG PET/CT but also a lower $^{18}$F-FDG uptake in infection foci in patients with moderate to hyperglycemia than in normoglycemic patients. The difference in the $^{18}$F-FDG avidity of infections caused by different types of bacteria (e.g., *Enterococci* vs. *S. aureus*) could be investigated as well.

**KEY POINTS**

**QUESTION:** Does moderate hyperglycemia affect the ability of $^{18}$F-FDG PET/CT to find the infection focus in patients with bacteremia of unknown origin?

**PERTINENT FINDINGS:** In our study including 322 patients, the true-positive detection rate of $^{18}$F-FDG PET/CT was 61%–65% in patients with a blood glucose level of 3.0–7.9 mmol/L (54–142 mg/dL), 30%–38% for a level of 8.0–10.9 mmol/L (144–196 mg/dL), and 17% for a level greater than 11.0 mmol/L (200 mg/dL).

**IMPLICATIONS FOR PATIENT CARE:** Nuclear medicine physicians should be aware that even only moderate hyperglycemia negatively affects the ability of $^{18}$F-FDG PET/CT to locate the source of infection in patients with bacteremia of unknown origin. This may warrant adjustment of current scanning protocols, in which an upper prescan blood glucose threshold of 11.0 mmol/L (200 mg/dL) is generally maintained.

## CONCLUSION

In patients with bacteremia with a glucose level greater than 8 mmol/L (144 mg/dL), $^{18}$F-FDG PET/CT was much less likely to identify the infection focus. Although current guidelines recommend postponing $^{18}$F-FDG PET/CT only in cases of severe hyperglycemia with a glucose level greater than 11 mmol/L (200 mg/dL), the diagnostic power of $^{18}$F-FDG PET/CT already seems to be affected in patients with only moderate hyperglycemia (>8.0 mmol/L or 144 mg/dL). Stricter blood glucose management seems appropriate in patients who undergo $^{18}$F-FDG PET/CT for bacteremia of unknown origin or other infectious diseases. Diabetic patients with adequately controlled blood glucose levels had detection rates on $^{18}$F-FDG PET/CT similar to those of nondiabetic patients.

## DISCLOSURE

No potential conflict of interest relevant to this article was reported.

## REFERENCES


1. Laupland KB. Incidence of bloodstream infection: a review of population-based studies. *Clin Microbiol Infect.* 2013;19:492–500.
2. Anderson DJ, Moehring RW, Sloane R, et al. Bloodstream infections in community hospitals in the 21st century: a multicenter cohort study. *PLoS One.* 2014;9:e91713.
3. Tabah A, Koulenti D, Laupland K, et al. Characteristics and determinants of outcome of hospital-acquired bloodstream infections in intensive care units: the EUROBACT International Cohort Study. *Intensive Care Med.* 2012;38:1930–1945.
4. Courjon J, Demonchy E, Degand N, et al. Patients with community-acquired bacteremia of unknown origin: clinical characteristics and usefulness of microbiological results for therapeutic issues: a single-center cohort study. *Ann Clin Microbiol Antimicrob.* 2017;16:40.
5. Kung BT, Seraj SM, Zadeh MZ, et al. An update on the role of $^{18}$F-FDG PET/CT in major infectious and inflammatory diseases. *Am J Nucl Med Mol Imaging.* 2019;9:255–273.
6. Hess S, Hansson SH, Pedersen KT, Basu S, Høilund-Carlsen PF. $^{18}$F-FDG PET/CT in infectious and inflammatory diseases. *PET Clin.* 2014;9:497–519.
7. Vos FJ, Bleeker-Rovers CP, Sturm PD, et al. $^{18}$F-FDG PET/CT for detection of metastatic infection in gram-positive bacteremia. *J Nucl Med.* 2010;51:1234–1240.
8. Heuker M, Sijbesma JWA, Aguilar Suárez R, et al. In vitro imaging of bacteria using $^{18}$F-fluorodeoxyglucose micro positron emission tomography. *Sci Rep.* 2017;7:4973.
9. Finessi M, Bisi G, Deandreis D. Hyperglycemia and $^{18}$F-FDG PET/CT, issues and problem solving: a literature review. *Acta Diabetol.* 2020;57:253–262.
10. Shao D, Tian R. Glucose transporters in cardiac metabolism and hypertrophy. *Compr Physiol.* 2015;6:331–351.
11. Hess S, Scholtens AM, Gormsen LC. Patient preparation and patient-related challenges with $^{18}$F-FDG PET/CT in infectious and inflammatory disease. *PET Clin.* 2020;15:125–134.
12. Rabkin Z, Israel O, Keidar Z. Do hyperglycemia and diabetes affect the incidence of false-negative $^{18}$F-FDG PET/CT studies in patients evaluated for infection or inflammation and cancer? A comparative analysis. *J Nucl Med.* 2010;51:1015–1020.
13. Zhao S, Kuge Y, Tsukamoto E, et al. Effects of insulin and glucose loading on $^{18}$F-FDG uptake in experimental malignant tumours and inflammatory lesions. *Eur J Nucl Med.* 2001;28:730–735.
14. Eskian M, Alavi A, Khorasanizadeh M, et al. Effect of blood glucose level on standardized uptake value (SUV) in $^{18}$F-FDG PET-scan: a systematic review and meta-analysis of 20,807 individual SUV measurements. *Eur J Nucl Med Mol Imaging.* 2019;46:224–237.
15. Yang H, Zhuang H, Rubello D, Alavi A. Mild-to-moderate hyperglycemia will not decrease the sensitivity of $^{18}$F-FDG PET imaging in the detection of pedal osteomyelitis in diabetic patients. *Nucl Med Commun.* 2016;37:259–262.
16. Sprinz C, Altmayer S, Zanon M, et al. Effects of blood glucose level on $^{18}$F-FDG uptake for PET/CT in normal organs: a systematic review. *PLoS One.* 2018;13:e0193140.
17. Slart RHJA, Glaudemans AWJM, Gheysens O, et al. Procedural recommendations of cardiac PET/CT imaging: standardization in inflammatory-, infective-, infiltrative-,

and innervation (4Is)-related cardiovascular diseases: a joint collaboration of the EACVI and the EANM. *Eur J Nucl Med Mol Imaging.* 2021;48:1016–1039.
18. Saeedi P, Petersohn I, Salpea P, et al. Global and regional diabetes prevalence estimates for 2019 and projections for 2030 and 2045: results from the International Diabetes Federation Diabetes Atlas, 9th ed. *Diabetes Res Clin Pract.* 2019;157:107843.
19. Boellaard R, Delgado-Bolton R, Oyen WJG, et al. $^{18}$F-FDG PET/CT: EANM procedure guidelines for tumour imaging: version 2.0. *Eur J Nucl Med Mol Imaging.* 2015;42:328–354.
20. Qureshi AI, Huang W, Lobanova I, et al. Effect of moderate and severe persistent hyperglycemia on outcomes in patients with intracerebral hemorrhage. *Stroke.* 2022;53:1226–1234.
21. Li JS, Sexton DJ, Mick N, et al. Proposed modifications to the Duke criteria for the diagnosis of infective endocarditis. *Clin Infect Dis.* 2000;30:633–638.
22. Dudoignon D, Pattison DA, Legallois D, Hicks RJ, Aide N. The utility of pharmacological and radiological interventions to optimize diagnostic information from PET/CT. *Cancer Imaging.* 2020;20:68.
23. Delbeke D, Coleman RE, Guiberteau MJ, et al. Procedure guideline for tumor imaging with $^{18}$F-$^{18}$F-FDG PET/CT 1.0. *J Nucl Med.* 2006;47:885–895.
24. Yu L, Chen X, Sun X, Wang L, Chen S. The glycolytic switch in tumors: how many players are involved? *J Cancer.* 2017;8:3430–3440.
25. Gorenberg M, Hallett WA, O'Doherty MJ. Does diabetes affect [$^{18}$F]FDG standardised uptake values in lung cancer? *Eur J Nucl Med Mol Imaging.* 2002;29:1324–1327.
26. Evangelista L, Gori S, Rubini G, Gallo M. Management of hyperglycemia in oncological patients scheduled for an FDG-PET/CT examination. *Clin Transl Imaging.* 2019;7:447–450.
27. Pijl JP, Kwee TC, Slart RHJA, Yakar D, Wouthuyzen-Bakker M, Glaudemans AWJM. Clinical implications of increased uptake in bone marrow and spleen on $^{18}$F-FDG PET in patients with bacteremia. *Eur J Nucl Med Mol Imaging.* 2021;48:1467–1477.
28. Tsai H-Y, Lee M-H, Wan C-H, et al. C-reactive protein levels can predict positive $^{18}$F-FDG PET/CT findings that lead to management changes in patients with bacteremia. *J Microbiol Immunol Infect.* 2018;51:839–846.
29. Okuyucu K, Alagoz E, Demirbas S, et al. Evaluation of predictor variables of diagnostic [$^{18}$F]FDG-PET/CT in fever of unknown origin. *Q J Nucl Med Mol Imaging.* 2018;62:313–320.
30. Pijl JP, Glaudemans AWJM, Slart RHJA, Yakar D, Wouthuyzen-Bakker M, Kwee TC. FDG-PET/CT for detecting an infection focus in patients with bloodstream infection: factors affecting diagnostic yield. *Clin Nucl Med.* 2019;44:99–106.

# MIRD Pamphlet No. 28, Part 2: Comparative Evaluation of MIRDcalc Dosimetry Software Across a Compendium of Diagnostic Radiopharmaceuticals

Lukas M. Carter[1], Juan C. Ocampo Ramos[1], Edmond A. Olguin[2], Justin L. Brown[3], Daniel Lafontaine[1], Derek W. Jokisch[4,5], Wesley E. Bolch[3], and Adam L. Kesner[1]

*[1]Department of Medical Physics, Memorial Sloan Kettering Cancer Center, New York, New York; [2]Beth Israel Deaconess Medical Center, Department of Radiology, Harvard Medical School, Boston, Massachusetts; [3]J. Crayton Pruitt Department of Biomedical Engineering, University of Florida, Gainesville, Florida; [4]Department of Physics and Engineering, Francis Marion University, Florence, South Carolina; and [5]Center for Radiation Protection Knowledge, Oak Ridge National Laboratory, Oak Ridge, Tennessee*

Radiopharmaceutical dosimetry is usually estimated via organ-level MIRD schema-style formalisms, which form the computational basis for commonly used clinical and research dosimetry software. Recently, MIRDcalc internal dosimetry software was developed to provide a freely available organ-level dosimetry solution that incorporates up-to-date models of human anatomy, addresses uncertainty in radiopharmaceutical biokinetics and patient organ masses, and offers a 1-screen user interface as well as quality assurance tools. The present work describes the validation of MIRDcalc and, secondarily, provides a compendium of radiopharmaceutical dose coefficients obtained with MIRDcalc. Biokinetic data for about 70 currently and historically used radiopharmaceuticals were obtained from the International Commission on Radiological Protection (ICRP) publication 128 radiopharmaceutical data compendium. Absorbed dose and effective dose coefficients were derived from the biokinetic datasets using MIRDcalc, IDAC-Dose, and OLINDA software. The dose coefficients obtained with MIRDcalc were systematically compared against the other software-derived dose coefficients and those originally presented in ICRP publication 128. Dose coefficients computed with MIRDcalc and IDAC-Dose showed excellent overall agreement. The dose coefficients derived from other software and the dose coefficients promulgated in ICRP publication 128 both were in reasonable agreement with the dose coefficients computed with MIRDcalc. Future work should expand the scope of the validation to include personalized dosimetry calculations.

**Key Words:** MIRDcalc; MIRD; dosimetry; radiopharmaceuticals

**J Nucl Med 2023; 64:1295–1303**
DOI: 10.2967/jnumed.122.264230

Accurate estimations of absorbed radiation dose are required to ensure patient safety in nuclear medicine. The MIRD schema (*1*) provides a computational basis for assessing absorbed dose at the organ level, tissue level, cellular level, or various spatial subdivisions; however, organ-level dosimetry remains the prevailing methodologic paradigm for routine clinical dose assessment.

Received Apr. 4, 2022; revision accepted Mar. 21, 2023.
For correspondence or reprints, contact Lukas M. Carter (carterl1@mskcc.org).
Published online Jun. 2, 2023.


Implementation of the MIRD schema or equivalent formalisms in dosimetry software generally requires 2 underlying elements: a mathematic representation of anatomy known as a computational phantom, and a database of radionuclide S values (*1*) specific to the phantom (usually derived via Monte Carlo simulation). Reference phantoms, which model representative individuals of particular sex and age groups, have undergone several important revisions over the past 50 y. First, the consensus anatomic reference data have been revised, with the data of the International Commission on Radiological Protection (ICRP) publication 23 (*2*) being superseded by ICRP publication 89 (*3*). Second, the computerized formats for depicting anatomy have been refined.

Recently, the MIRDsoft project was initiated to provide the community with a suite of free dosimetry software programs endorsed by the MIRD committee of the Society of Nuclear Medicine and Molecular Imaging. MIRDcalc, the flagship program in the MIRDsoft suite, is a Microsoft Excel–based executable program implementing the MIRD schema at the organ level. It incorporates up-to-date anatomic models, including the ICRP publication 110 series adult computational reference phantoms (*4*) and the ICRP publication 143 series pediatric reference phantoms (*5,6*). These phantoms offer numerous advantages over the first-generation stylized phantoms, including anatomically realistic organ shapes and interorgan spacing. MIRDcalc also factors uncertainty into the dose coefficients by propagating uncertainties in the input biokinetics and organ masses. Additional features include a single-screen interface, quality assurance tools, and batch processing capabilities.

An overview of the development and features of MIRDcalc is provided in part 1 of this 2-part article (*7*). In this second part, the primary aim was to comprehensively benchmark the dose coefficients obtained from MIRDcalc against a compendium of published reference dose coefficients (*8*) and the output of other reference dosimetry software.

## COMPUTATION OF DOSIMETRIC QUANTITIES

### Absorbed Dose

The present investigation considers organ-level mean absorbed doses and assumes that the masses of phantom regions remain constant over the period of irradiation. The organ-level time-independent formulation of the MIRD schema therefore applies (*1*). Given a target

region $r_T$ irradiated over a time period $T_D$, the absorbed dose coefficient $d(r_T, T_D)$ (mGy/MBq) is defined as the absorbed dose (mGy) normalized to the administered activity (MBq):

$$d(r_T, T_D) = \sum_{r_S} \tilde{a}(r_S, T_D) S(r_T \leftarrow r_S). \quad \text{Eq. 1}$$

Here, $\tilde{a}(r_S, T_D)$ is the time-integrated activity coefficient (TIAC), and $S(r_T \leftarrow r_S)$ is known as the S value (or S coefficient), the absorbed dose rate to $r_T$ per unit activity in source region $r_S$. S values are specific to a radionuclide and computational phantom. For monoenergetic emissions:

$$S(r_T \leftarrow r_S) = \sum_i E_i Y_i \Phi(r_T \leftarrow r_S, E_i), \quad \text{Eq. 2}$$

where $E_i$ is the energy of the $i^{\text{th}}$ nuclear transition, $Y_i$ is the number of $i^{\text{th}}$ transitions per nuclear transformation, and $\Phi(r_T \leftarrow r_S, E_i)$ is the specific absorbed fraction (SAF) ($\text{kg}^{-1}$). The SAF represents the fraction of $E_i$ absorbed in $r_T$ for transition $i$ occurring in source $r_S$, normalized to the mass of the target region. For β-emissions, the spectrum of energies is considered:

$$S(r_T \leftarrow r_S) = \int_0^{E_0} P(E) E \Phi(r_T \leftarrow r_S, E) dE, \quad \text{Eq. 3}$$

where $E_0$ is the β-endpoint energy, and $P(E)$ is the distribution for the number of β-particles emitted per megaelectron volt per nuclear transformation, as a function of energy.

The TIAC represents the number of nuclear transformations occurring in a source region over a specified time period $T_D$:

$$\tilde{a}(r_S, T_D) = \frac{1}{A_0} \int_0^{T_D} A(r_S, t) dt, \quad \text{Eq. 4}$$

where $A(r_S, t)$ is the time-dependent activity in $r_S$, and $A_0$ is the administered activity.

All programs used in this work use the MIRD or mathematically equivalent formalism for absorbed dose computation.

### Effective Dose

The effective dose (mSv) is considered a measure of risk related to radiation-induced stochastic effects. It is a sex-averaged, tissue-weighted sum of mean organ equivalent doses (*9*). The effective dose coefficient (mSv/MBq) (i.e., effective dose per unit administered activity) can be calculated as …

$$e = \sum_T \frac{w_T h(r_T, T_D)^{\text{male}} + w_T h(r_T, T_D)^{\text{female}}}{2}, \quad \text{Eq. 5}$$

where $w_T$ is the tissue-weighting factor for tissue $T$, and $h(r_T, T_D)$ is the equivalent dose, wherein the radiation-weighting factor $w_R$ accounts for the differential biologic effectiveness of each radiation type $R$:

$$h(r_T, T_D) = \sum_R w_R d_R(r_T, T_D). \quad \text{Eq. 6}$$

## DOSIMETRY SOFTWARE AND PHANTOMS

### MIRDcalc

MIRDcalc is Excel-based software freely obtainable at www.mirdsoft.org. For dose computation, MIRDcalc uses a database of S values for the ICRP publication 110 (*4*) reference adult phantoms and ICRP publication 143 (*6*) reference pediatric phantoms (Fig. 1). The reference phantom S-value database was generated using SAFs promulgated by the ICRP (*10,11*). The SAFs were used in combination with the radionuclide decay data of ICRP publication 107 (*12*) to compute the S values (Eq. 2); in the case of β-particles, the full spectrum was used (Eq. 3). Effective dose coefficients are computed using the tissue-weighting factors of ICRP publication 103 (*13*).

In addition to the S values for each phantom, the organ masses and organ fractional blood content are stored within MIRDcalc for use in various computations. The organ masses and fractional blood content of the adult phantoms are defined in ICRP publication 89. For the pediatric phantoms, the suggested reference values of Wayson et al. (*14*) were used, which, notably, account for volumetric changes and changes in blood vascularization across the different reference ages. A summary of all phantom organ, parenchyma, and blood masses used in MIRDcalc is presented as supplemental material in part 1 of this article (supplemental materials are available at http://jnm.snmjournals.org) (*7*).

### IDAC-Dose

IDAC-Dose 2.1 (*15*) organ-level dosimetry software is MATLAB-based and uses S values for the ICRP publication 110 adult reference phantoms (Fig. 1) for dose computation; similar to MIRDcalc, IDAC S values were derived from ICRP publication 133 SAFs.

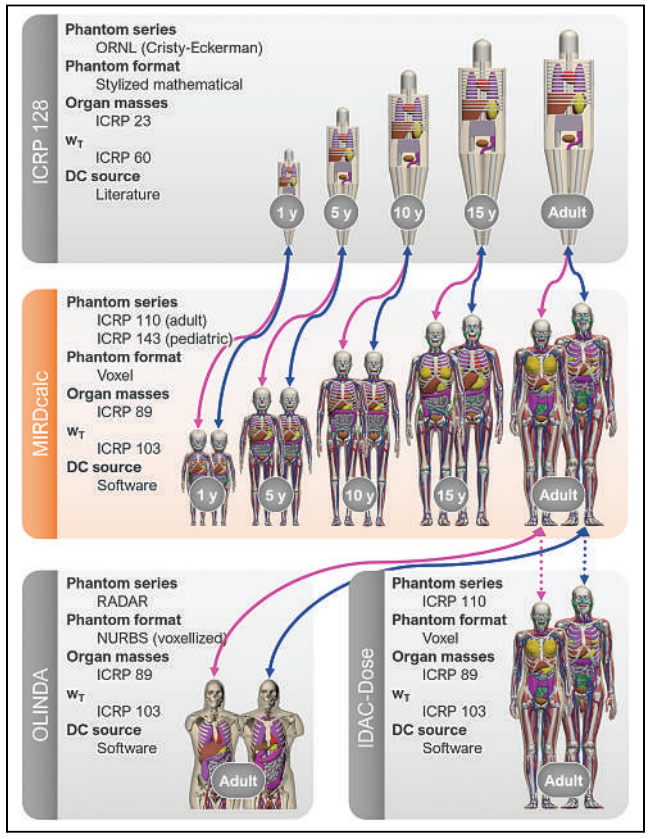


**FIGURE 1.** Phantoms used to derive dose coefficients compared in this work. Solid arrows denote comparisons using different phantoms and different software. Dashed arrows represent comparisons using same phantoms but different software. DC = dose coefficient; ORNL = Oak Ridge National Laboratory; $w_T$ = tissue-weighting factor.

Effective dose coefficients are computed using ICRP publication 103 tissue-weighting factors. IDAC-Dose is freely obtainable from www.idac-dose.org.

Notably, IDAC-Dose and MIRDcalc are based on identical phantoms.

### OLINDA

OLINDA 2.1, preceded by OLINDA 1.0 and MIRDOSE software, is Java-based. It uses an S-value database derived from the Radiation Dose Assessment Resource (RADAR) phantom series (Fig. 1) (*16,17*). Effective dose coefficients are computed using ICRP publication 103 tissue-weighting factors. OLINDA is obtainable under license from Hermes Medical Solutions (www.hermesmedical.com). Only the RADAR reference adult male and female phantoms were used for comparisons in this work.

The RADAR phantoms of OLINDA and the ICRP publication 110 phantoms of MIRDcalc are based on the same reference organ parenchyma masses but possess different organ shapes and positioning. The RADAR phantoms do not contain a blood source region or account for organ fractional blood content. For walled organs, a different dose estimation methodology is used (*18,19*).

## REFERENCE DOSE COEFFICIENTS AND BIOKINETIC DATA

ICRP publication 128 is a compendium of reference dosimetric information for about 70 currently or historically used radiopharmaceuticals. For certain radiopharmaceuticals, several use scenarios or administration routes are considered. Organ-level TIACs and mean organ-absorbed dose coefficients are provided for the Cristy–Eckerman stylized mathematic reference adult and pediatric phantoms (15-, 10-, 5-, and 1-y-old) (*20*). The effective dose coefficients reported in ICRP publication 128 were computed using ICRP publication 60 tissue-weighting factors.

The Cristy–Eckerman phantoms used to compute the dose coefficients reported in ICRP publication 128 possess similar organ masses to the phantoms of MIRDcalc but have drastically different shapes and different interorgan spacing. For walled organs, a different dose estimation methodology is used (*18,19*).

## MODIFICATIONS OF ICRP PUBLICATION 128 REFERENCE BIOKINETIC DATA FOR USE IN OTHER PHANTOMS

The ICRP publication 128 TIACs are the biokinetic source data used in all our calculations. However, these TIACs are specific to the source regions of the Cristy-Eckerman stylized reference phantoms; some of these source regions have been redefined or modified in more modern reference phantoms, such as those used in MIRDcalc, IDAC, or OLINDA. Therefore, TIACs for the Cristy–Eckerman phantom source regions were transposed into the other phantom source regions using the approach of Andersson et al. (*21*). Specific assumptions and adjustments are detailed here.

### Colon Wall

The colon wall of the Cristy-Eckerman phantoms is partitioned into 2 regions: the upper large intestine, comprising the ascending and transverse colon, and the lower large intestine, comprising the descending and sigmoid colon. In modern reference phantoms, the colon wall is instead partitioned into 3 regions consonant with the updated ICRP human alimentary tract model: the right colon, comprising the ascending colon and the proximal half of the transverse colon; the left colon, comprising the descending colon and the distal half of the transverse colon; and the rectosigmoid colon. TIACs provided in ICRP publication 128 for the walls of the upper or lower large intestine were transposed into the modern phantoms using the following formulas (*20*):

$$\tilde{a}(\text{right colon wall}, T_D) = 0.71\ \tilde{a}(\text{upper large intestine wall}, T_D), \quad \text{Eq. 7}$$

$$\tilde{a}(\text{left colon wall}, T_D) = 0.29\ \tilde{a}(\text{upper large intestine wall}, T_D) + 0.56\ \tilde{a}(\text{lower large intestine wall}, T_D), \quad \text{Eq. 8}$$

$$\tilde{a}(\text{rectosigmoid colon wall}, T_D) = 0.44\ \tilde{a}(\text{lower large intestine wall}, T_D). \quad \text{Eq. 9}$$

### Colon Contents

The colon content source regions follow the same partitioning scheme as above, but with different coefficients required to account for the region masses:

$$\tilde{a}(\text{right colon contents}, T_D) = 0.71\ \tilde{a}(\text{upper large intestine contents}, T_D), \quad \text{Eq. 10}$$

$$\tilde{a}(\text{left colon contents}, T_D) = 0.29\ \tilde{a}(\text{upper large intestine contents}, T_D) + 0.74\ \tilde{a}(\text{lower large intestine contents}, T_D), \quad \text{Eq. 11}$$

$$\tilde{a}(\text{rectosigmoid colon contents}, T_D) = 0.26\ \tilde{a}(\text{lower large intestine contents}, T_D). \quad \text{Eq. 12}$$

### Walled Organs (General Case)

In MIRDcalc and IDAC-Dose, which have the option to assign TIACs to the entire wall or constituent subregions, the entire wall was considered as the source.

OLINDA does not support the use of walled organs as source regions; only the contents of walled organs may be used as sources. When ICRP publication 128 provided a TIAC for a wall source, this was appended to the TIAC for the other-organs-and-tissues region. We note that this approach may critically underestimate the absorbed dose coefficients for radiopharmaceuticals with elevated uptake or prolonged retention in walled organs.

### Skeleton

For radiopharmaceuticals for which ICRP publication 128 explicitly specified TIACs for the cortical or trabecular bone source regions, those values were used without modification. When a TIAC was specified for a generic bone-surface source region (i.e., bone surface–seeking radionuclides), the TIAC was reapportioned to the cortical and trabecular bone surfaces in a 40:60 ratio for the adult, 15-y-old, or 10-y-old phantoms or in a 30:70 ratio for the 5-y-old or 1-y-old phantoms (*8*). For bone volume–seeking radionuclides, 80:20 and 60:40 cortical-to-trabecular ratios, respectively, were used to define bone volume sources for the age groups above (*8*).

### Blood

A salient difference among the dosimetry programs used here relates to the treatment of blood. The stylized phantoms used in

**TABLE 1**
Adult Effective Dose Coefficients and Relative Differences Compared Among MIRDcalc, IDAC-Dose, and ICRP Publication 128

| Radiopharmaceutical | Effective dose coefficient (mSv/MBq) | | | | $\Delta^{\text{IDAC-Dose}}_{\text{MIRDcalc}}$ | $PE^{\text{IDAC-Dose 2.1 2.1}}_{\text{MIRDcalc}}$ | $\Delta^{\text{OLINDA}}_{\text{MIRDcalc}}$ | $PE^{\text{OLINDA}}_{\text{MIRDcalc}}$ | $\Delta^{\text{ICRP 128}}_{\text{MIRDcalc}}$ | $PE^{\text{ICRP 128}}_{\text{MIRDcalc}}$ |
|---|---|---|---|---|---|---|---|---|---|---|
| | MIRDcalc | IDAC-Dose | OLINDA | ICRP 128 | | | | | | |
| $^{111}$In-octreotide | 5.49E−02 | 5.38E−02 | 5.89E−02 | 5.40E−02 | −2.0 | −2.0% | 7.0 | 7.3% | −1.7 | −1.6% |
| $^{123}$I-ioflupane | 2.50E−02 | 2.36E−02 | 2.16E−02 | 2.50E−02 | −5.8 | −5.6% | −15 | −14% | 0.00 | 0.00% |
| $^{123}$I-NaI capsules (high thyroid uptake) | 2.45E−01 | 2.45E−01 | 2.77E−01 | 3.00E−01 | 0.00 | 0.00% | 12 | 13% | 20 | 22% |
| $^{123}$I-NaI capsules (thyroid blocked) | 3.04E−02 | 3.02E−02 | 2.04E−02 | 3.70E−02 | −0.66 | −0.7% | −40 | −33% | 20 | 22% |
| $^{131}$I-NaI capsules (high thyroid uptake) | 2.17E+01 | 2.16E+01 | 2.64E+01 | 2.90E+01 | −0.46 | −0.50% | 20 | 22% | 29 | 34% |
| $^{131}$I-NaI (thyroid blocked) | 2.10E−01 | 2.08E−01 | 1.55E−01 | 2.80E−01 | −0.96 | −1.0% | −30 | −26% | 29 | 33% |
| $^{133}$Xe gas | 1.99E−04 | 1.64E−04 | 1.86E−04 | 1.80E−04 | −19 | −18% | −6.8 | −6.5% | −10 | −9.5% |
| $^{133}$Xe gas (rebreathing for 10 min) | 1.27E−03 | 1.21E−03 | 1.11E−03 | 1.10E−03 | −4.8 | −4.7% | −13 | −13% | −14 | −13% |
| $^{14}$C-urea, *Heliobacter* positive | 8.68E−02 | 7.75E−02 | 8.93E−02 | 8.10E−02 | −11 | −11% | 2.8 | 2.9% | −6.9 | −6.7% |
| $^{14}$C-urea, normal case | 2.42E−02 | 2.16E−02 | 2.93E−02 | 3.10E−02 | −11 | −11% | 19 | 21% | 25 | 28% |
| $^{18}$F-FDG | 1.67E−02 | 1.61E−02 | 1.92E−02 | 1.90E−02 | −3.7 | −3.6% | 14 | 15% | 13 | 14% |
| $^{18}$F-NaF | 1.30E−02 | 1.28E−02 | 1.65E−02 | 1.70E−02 | −1.6 | −1.5% | 24 | 27% | 27 | 31% |
| $^{201}$Tl-TlCl | 1.13E−01 | 1.09E−01 | 8.47E−02 | 1.40E−01 | −3.6 | −3.5% | −29 | −25% | 21 | 24% |
| $^{67}$Ga-citrate | 9.43E−02 | 8.97E−02 | 8.72E−02 | 1.00E−01 | −5.0 | −4.9% | −7.8 | −7.5% | 5.9 | 6.0% |
| $^{82}$Rb-chloride | 1.05E−03 | 1.00E−03 | 7.77E−04 | 1.10E−03 | −4.9 | −4.8% | −30 | −26% | 4.7 | 4.8% |
| $^{99m}$Tc-DMSA | 7.02E−03 | 6.92E−03 | 7.24E−03 | 8.80E−03 | −1.4 | −1.4% | 3.1 | 3.1% | 23 | 25% |
| $^{99m}$Tc-DTPA | 3.37E−03 | 3.26E−03 | 4.57E−03 | 4.90E−03 | −3.3 | −3.3% | 30 | 36% | 37 | 45% |
| $^{99m}$Tc-ECD | 5.56E−03 | 5.52E−03 | 5.08E−03 | 7.70E−03 | −0.72 | −0.70% | −9.0 | −8.6% | 33 | 39% |
| $^{99m}$Tc-iminodiacetic acid derivatives | 9.44E−03 | 9.55E−03 | 3.84E−03 | 1.60E−02 | 1.2 | 1.2% | −90 | −59% | 53 | 70% |
| $^{99m}$Tc-macroaggregated albumin | 1.40E−02 | 1.15E−02 | 1.37E−02 | 1.10E−02 | −20 | −18% | −2.2 | −2.1% | −24 | −21% |
| $^{99m}$Tc-MAG3 | 4.12E−03 | 4.09E−03 | 6.38E−03 | 7.00E−03 | −0.73 | −0.70% | 44 | 55% | 53 | 70% |
| $^{99m}$Tc-sestamibi, exercise | 6.19E−03 | 6.03E−03 | 3.74E−03 | 7.90E−03 | −2.6 | −2.6% | −50 | −40% | 24 | 28% |
| $^{99m}$Tc-sestamibi, rest | 7.09E−03 | 6.89E−03 | 4.64E−03 | 9.00E−03 | −2.9 | −2.8% | −42 | −35% | 24 | 27% |
| $^{99m}$Tc-HMPAO | 8.35E−03 | 7.99E−03 | 7.10E−03 | 9.30E−03 | −4.4 | −4.3% | −16 | −15% | 11 | 11% |
| $^{99m}$Tc sulfur colloid | 1.10E−02 | 1.09E−02 | 1.11E−02 | 9.10E−03 | −0.91 | −0.90% | 0.90 | 0.90% | −19 | −17% |
| $^{99m}$Tc-pertechnetate, with blocking agent | 4.07E−03 | 3.78E−03 | 4.47E−03 | 4.60E−03 | −7.4 | −7.1% | 9.4 | 9.8% | 12 | 13% |
| $^{99m}$Tc-pertechnetate, no blocking agent | 9.99E−03 | 9.87E−03 | 4.24E−03 | 1.30E−02 | −1.2 | −1.2% | −86 | −58% | 26 | 30% |
| $^{99m}$Tc-MDP | 4.32E−03 | 4.25E−03 | 5.10E−03 | 4.90E−03 | −1.6 | −1.6% | 17 | 18% | 13 | 13% |
| $^{99m}$Tc-tetrofosmin, exercise | 5.63E−03 | 5.37E−03 | 4.51E−03 | 6.90E−03 | −4.7 | −4.6% | −22 | −20% | 20 | 23% |
| $^{99m}$Tc-tetrofosmin, rest | 6.09E−03 | 5.89E−03 | 4.56E−03 | 8.00E−03 | −3.3 | −3.3% | −29 | −25% | 27 | 31% |

Fluorodeoxyglucose (FDG), dimercaptosuccinic acid (DMSA), diethylenetriaminepentaacetic acid (DTPA), ethylenedicysteine diester (ECD), mercaptoacetyltriglycine (MAG3), hexamethylpropyleneamine oxime (HMPAO), methyl diphosphonate (MDP).

the ICRP publication 128 dose calculations did not directly define a blood source; instead, ignoring differences in fractional blood content among organs, a blood source was approximated using a uniform whole-body source region for those calculations. Similarly, the hybrid phantoms of OLINDA do not directly implement a blood source. In IDAC-Dose, a blood source is defined and is based on ICRP publication 133 SAFs for total-body blood content; this blood source was designed to be used in combination with organ TIACs supplied for the organ parenchyma only (i.e., exclusive of blood contained within the organs). The ICRP publication 133 blood source region is available in MIRDcalc. MIRDcalc also contains novel dynamic blood and parenchyma regions to support either blood-inclusive or blood-exclusive TIAC inputs. Namely, this feature supports 2 areas of dosimetry research: the first is routine nuclear medicine dosimetry, with blood-inclusive organ uptake being quantified via imaging (e.g., volume-of-interest delineation, with the volume including organ parenchyma and organ blood content), and the second is radiation protection, with TIACs for organ parenchyma often being obtained through pharmacokinetic modeling. The MIRDcalc dynamic blood model actively removes blood and parenchyma subregions from the dynamic rest-of-blood and rest-of-parenchyma source regions, respectively, as well as from the rest-of-body source region, as individual organ TIACs are entered. To implement the dynamic blood model in MIRDcalc, SAFs for blood regions including heart contents, major vessels, and miscellaneous connective tissues were required. These SAFs were computed via methods described previously (*10*).

ICRP publication 128 considers 2 separate approaches for specifying TIACs associated with the blood—either explicit or implicit assignment. For radiopharmaceuticals for which a blood source is not explicitly given in ICRP publication 128, the ICRP publication 128 organ TIACs are assumed to apply to the whole organ (i.e., both parenchyma and blood contained within the organ). In contrast, for radiopharmaceuticals for which a blood source is explicitly given by the pharmacokinetic model, the organ TIACs are assumed to apply to the parenchyma only. Specific methods used for blood source input in each type of software are described in this article.

In IDAC-Dose, the blood, organ, and other-organs-and-tissues TIACs for each ICRP publication 128 radiopharmaceutical were input directly.

In OLINDA, when a blood source TIAC was available for a radiopharmaceutical, the total body was used as a surrogate for the blood. This was accomplished by running 2 separate calculations: the first was a calculation in which only the blood TIAC was input into the whole-body region (i.e., approximating the blood distribution as uniform throughout the body), and the second was a calculation in which the organ and ICRP publication 128 other-organs-and-tissues TIACs were input. The 2 respective dose calculations were then summed. For radiopharmaceuticals for which no explicit blood TIAC was given, a single calculation was run normally.

In MIRDcalc, when ICRP publication 128 provided a blood source TIAC, this was assigned to the classic ICRP blood source, and the ICRP publication 128 other-organs-and-tissues TIAC was assigned to the rest-of-parenchyma source region to avoid double-counting (i.e., to avoid source region overlap). For radiopharmaceuticals in the absence of a blood source, the ICRP publication 128 other-organs-and-tissues TIAC was assigned to the rest-of-body source region. In the latter case, the rest-of-body TIAC is distributed to its constituent regions in proportion to the blood-inclusive region masses.

## COMPARISON OF DOSE COEFFICIENTS

Relative differences in dose coefficients are presented on the basis of 2 metrics. First, we define the logarithmic relative difference metric:

$$\Delta^{\text{other}}_{\text{MIRDcalc}}(r_T, T_D, RP) = 100\times\ln\frac{d_{\text{other}}(r_T, T_D, RP)}{d_{\text{MIRDcalc}}(r_T, T_D, RP)}, \qquad \text{Eq. 13}$$

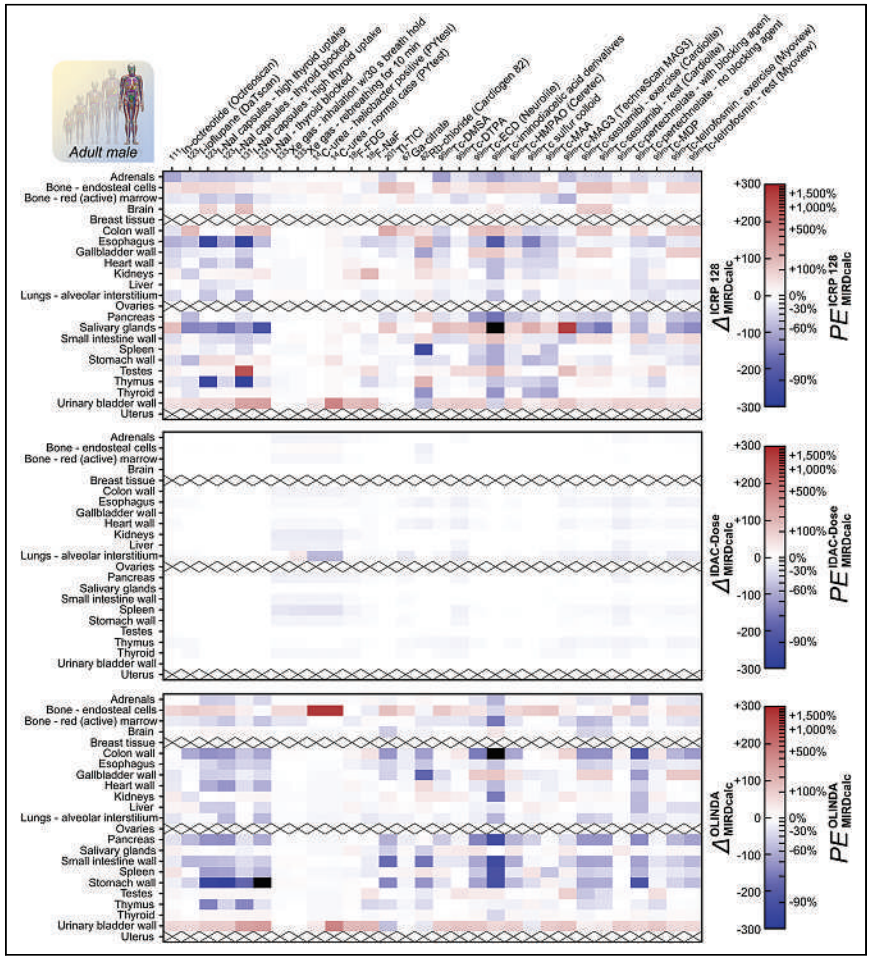


**FIGURE 2.** Organ-level absorbed dose coefficients for adult male compared via log relative differences (Eq. 13). (Top) ICRP publication 128 compared against MIRDcalc. (Middle) IDAC-Dose compared against MIRDcalc. (Bottom) OLINDA 2.1 compared against MIRDcalc. Red indicates a dose coefficient estimate higher than that of MIRDcalc; blue indicates lower. Black indicates off-scale values ($|\Delta| > 300$).

where, for radiopharmaceutical $RP$, $\Delta^{\text{other}}_{\text{MIRDcalc}}(r_T, T_D, RP)$ is the log relative difference (we refer to these here as Δ-values), $d_{\text{MIRDcalc}}(r_T, T_D, RP)$ is the dose coefficient for target organ $r_T$ computed by MIRDcalc, and $d_{\text{other}}(r_T, T_D, RP)$ is the corresponding dose coefficient computed by another software/data source. The approach of quantifying differences via the log relative difference was selected to alleviate dependence on reference choice; the magnitude of the reported log relative differences is equivalent regardless of which method is chosen as the reference. Second, we consider the traditional percentage error, with MIRDcalc taken as the gold standard reference:

$$PE^{\text{other}}_{\text{MIRDcalc}}(r_T, T_D, RP) = \frac{d_{\text{other}}(r_T, T_D, RP) - d_{\text{MIRDcalc}}(r_T, T_D, RP)}{d_{\text{MIRDcalc}}(r_T, T_D, RP)} \times 100\ (\%). \quad \text{Eq. 14}$$

We note that in the second case, the relative error approaches the log relative difference for very small differences, namely,

$$\Delta^{\text{other}}_{\text{MIRDcalc}}(r_T, T_D, RP) \approx PE^{\text{other}}_{\text{MIRDcalc}}(r_T, T_D, RP), \text{ when } |\, PE^{\text{other}}_{\text{MIRDcalc}}(r_T, T_D, RP)\,| \ll 100\%. \quad \text{Eq. 15}$$

Dose coefficients for 116 radiopharmaceutical-use scenarios were obtained with MIRDcalc dosimetry software and compared against the established reference data of ICRP publication 128 and against the output of other validated software (IDAC-Dose and OLINDA). Of the radiopharmaceuticals considered in ICRP publication 128, we have selected the subset with U.S. Food and Drug Administration approval as of the year 2020 for presentation in most of the figures and tables in the print version of this article (30 radiopharmaceuticals). Effective dose coefficients and associated relative differences are provided in Table 1 for adult reference phantoms; for pediatric phantoms, the corresponding data are given in Supplemental Tables 1–4. Graphical presentation (heat maps) of log relative differences in organ-absorbed dose coefficients are provided for reference adults in Figures 2 and 3. Corresponding heat maps for pediatric reference phantoms are given in Supplemental Figures 1–4. The underlying organ-absorbed dose coefficients for all phantoms and all ICRP publication 128 radiopharmaceuticals are available in the Supplemental Dose Coefficient Compendium.

All summary statistics (e.g., mean and SD) mentioned in the text consider the entire ICRP publication 128 radiopharmaceutical ensemble.

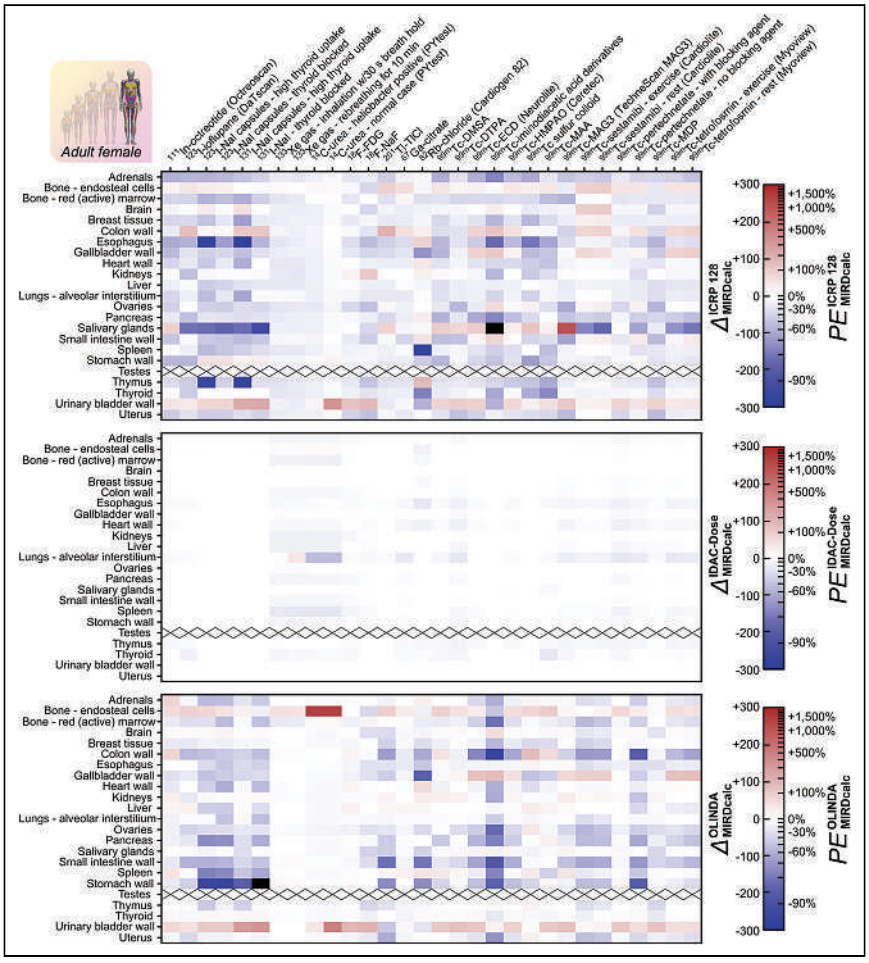


**FIGURE 3.** Organ-level absorbed dose coefficients for adult female compared via log relative differences (Eq. 13). (Top) ICRP publication 128 compared against MIRDcalc. (Middle) IDAC-Dose compared against MIRDcalc. (Bottom) OLINDA compared against MIRDcalc. Red indicates a dose coefficient estimate higher than that of MIRDcalc; blue indicates lower. Black indicates off-scale values ($|\,\Delta\,| > 300$).

## COMPARISON OF MIRDCALC AND IDAC-DOSE

Overall, the effective dose coefficients calculated from MIRDcalc and IDAC-Dose were in close agreement. On average, the IDAC-Dose effective dose estimates were marginally lower than MIRDcalc (mean $\Delta^{\text{IDAC-Dose}}_{\text{MIRDcalc}} = -2.8$, SD = 4.2; Eq. 13). The largest differences were observed for pulmonary perfusion imaging agents (e.g., $^{99m}$Tc-macroaggregated albumin and $^{133}$Xe gas), for which the lung tissues were the critical organs; in these cases, the effective dose coefficients computed with IDAC-Dose were lower by approximately 5%–21%. These differences in effective dose reflected larger underlying differences in the aborbed doses computed for the bronchial and bronchiolar epithelial regions of the lung. Acute underestimates in the SAFs of ICRP publication 133 were originally published for the lung regions of the reference adult phantoms for low-energy electrons and photons (<100 keV), which would lead to underestimates of lung tissue–absorbed doses if uncorrected. These issues were corrected before generation of the MIRDcalc S-value database (*22*).

Since MIRDcalc and IDAC-Dose use the same phantoms and the same radionuclide decay data, very close agreement was expected. Exact agreement was not observed. Implementation details related to the blood source in each program are expected to be the major source of disagreement.

### COMPARISON OF MIRDCALC AND ICRP PUBLICATION 128

Effective dose coefficients calculated from MIRDcalc differed considerably from those provided in ICRP publication 128 (adult subjects: mean $\Delta_{\text{MIRDcalc}}^{\text{ICRP 128}} = +6.1$, SD = 67), indicating a bias toward lower values than the ICRP publication 128 dose estimates. Absorbed dose coefficients for the urinary bladder wall were 2- to 3-fold higher for the ICRP publication 128 estimates than for MIRDcalc, for renally excreted radiopharmaceuticals (Figs. 2 and 3). This feature has been observed in many investigations and relates to conservative simplified methods for estimating the bladder wall irradiation from the bladder contents (*18,19,23*). ICRP publication 128 absorbed dose coefficients for the endosteal cells and adrenals showed consistent positive and negative biases, respectively, though to a lesser degree than seen with the urinary bladder. The definition of the radiosensitive endosteal cell target region has been refined in modern skeletal models and comprises a 50-μm layer at the surfaces of the trabecular spongiosa and cortical surfaces of the medullary cavities of the long bones of the limbs. This is a potential source of disagreement with dose coefficients derived in ICRP publication 128, which assume a 10-μm endosteal layer. The negatively biased adrenal-absorbed doses are likely due to the exaggeration of interorgan spacing in stylized phantoms. Cross-irradiation from the kidneys is an important contributor to the adrenal-absorbed dose for renally cleared agents and exacerbates the error due to adrenal–kidney spacing mismatch. Few other trends were evident between the absorbed dose coefficients of ICRP publication 128 and MIRDcalc. A similar variation was seen between the age-matched pediatric phantoms.

### COMPARISON OF MIRDCALC AND OLINDA

Effective dose coefficients calculated with MIRDcalc also differed from those calculated with OLINDA (adult subjects: mean $\Delta_{\text{MIRDcalc}}^{\text{OLINDA}} = -11$, SD = 50). The largest relative differences were generally observed for radiopharmaceuticals with gastrointestinal tract wall TIACs given by ICRP publication 128 (e.g., radioiodides)—which OLINDA was not designed to accommodate. OLINDA estimates for the urinary bladder–absorbed and bone endosteum–absorbed dose coefficients were positively biased relative to MIRDcalc. Compared with the stylized phantoms of ICRP publication 128, the phantoms used in OLINDA more closely match those used in MIRDcalc in terms of organ mass, contour, and spacing; however, $\Delta_{\text{MIRDcalc}}^{\text{OLINDA}}$ was not significantly improved relative to $\Delta_{\text{MIRDcalc}}^{\text{ICRP 128}}$.

### COMPARISON OF RESULTS: WHAT CONSTITUTES REASONABLE AGREEMENT?

This investigation compares radiopharmaceutical dose coefficients derived from different reference phantoms with different software. Reference phantoms are designed to characterize the average individual of a specified age and sex—that is, the only criterion a phantom must meet to qualify as a reference phantom is that the organ masses defined within the phantom should match accepted reference values for the corresponding age and sex. Dose coefficients depend strongly on organ mass but are also influenced by other phantom-specific factors including organ shape, interorgan spacing, target volumes, degree of detail, and other factors, none of which are standardized. To generate phantom SAFs/S values needed for software using MIRD-style formalisms, Monte Carlo radiation transport simulations are performed within the phantoms. The details of the Monte Carlo simulations also lack standardization. Because such factors are not controlled, it is difficult to stipulate how well dose coefficients derived from different reference phantoms should agree.

It is generally accepted that variation in the body morphometry of specific patients—which may deviate substantially from the reference individual—imparts variation in organ-absorbed dose coefficients on the order of 20%–60% (*8,24*); this percentage range expressed in terms of Δ-values (Eq. 13) is approximately 18–47. We are unaware of any studies providing a ballpark guideline on agreement for reference phantoms, but the variation should be considerably lower because the organ masses are consistent (*8*). Therefore, we consider this range to be an upper limit regarding reasonable agreement. It is evident in Figures 2 and 3 that there are many instances in which $\Delta_{\text{MIRDcalc}}^{\text{OLINDA}}$ and $\Delta_{\text{MIRDcalc}}^{\text{ICRP 128}}$ lie well outside this range, and many instances were also present for the radiopharmaceuticals not shown. To gain a more comprehensive but condensed view, we expanded the scope over all 116 cases examined and aggregated the Δ-values for each software comparison into histograms (Figs. 4 and 5, left panel). In each histogram, the red–green shading encompasses the Δ-values within the upper limit of the range of expected variation (Δ = 47). The left panel includes Δ-values for all available target regions that correspond directly between the software being compared.

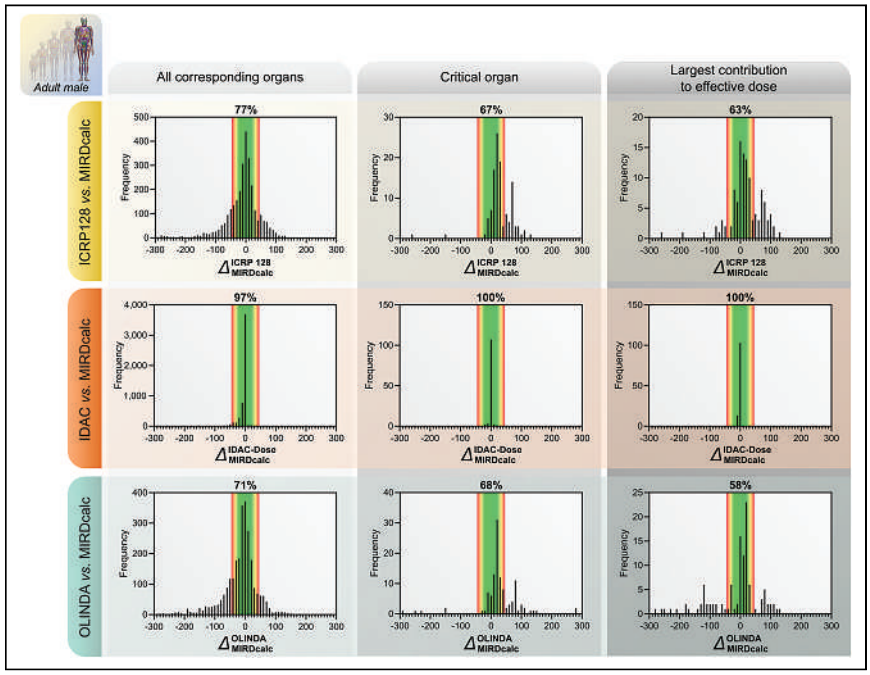


**FIGURE 4.** Distribution of log relative differences in organ-level absorbed dose coefficients for adult male phantoms. (Top) ICRP publication 128 compared against MIRDcalc. (Middle) IDAC-Dose compared against MIRDcalc. (Bottom) OLINDA compared against MIRDcalc. Red–green shaded region represents range of reasonable agreement discussed in text; percentage value overlying this region indicates fraction of Δ-values that fall within this range. Histogram bin width is 10.

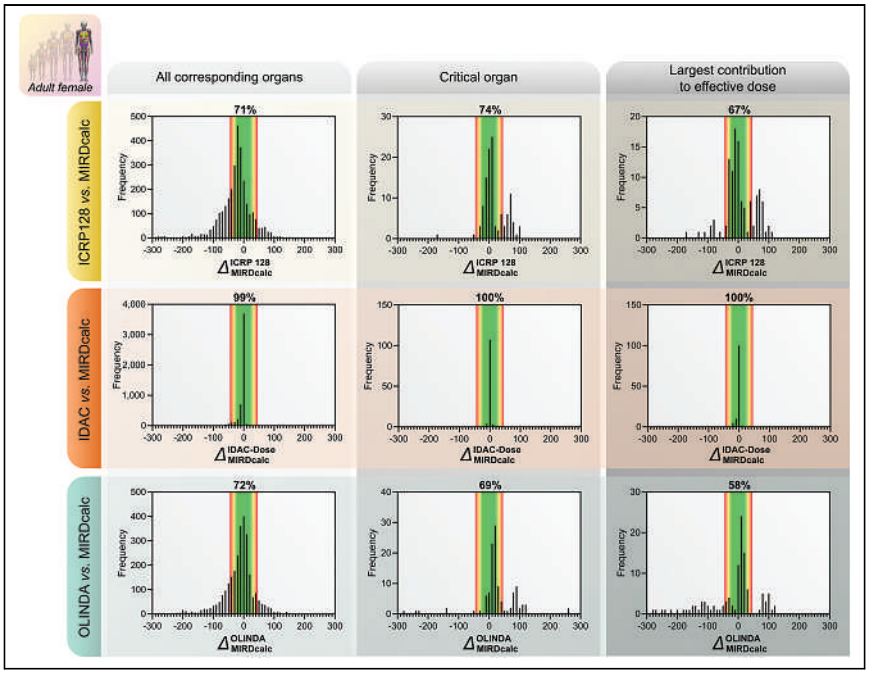


**FIGURE 5.** Distribution of log relative differences in organ-level absorbed dose coefficients for adult female phantoms. (Top) ICRP publication 128 compared against MIRDcalc. Upper left histogram is negatively skewed because ICRP publication 128 dose estimates are derived from single 70-kg hermaphroditic adult phantom, whereas MIRDcalc, IDAC-Dose, and OLINDA use a 60-kg female phantom. (Middle) IDAC-Dose compared against MIRDcalc. (Bottom) OLINDA compared against MIRDcalc. Red-green shaded region represents range of reasonable agreement discussed in text; percentage value overlying this region indicates fraction of Δ-values that fall within this range. Histogram bin width is 10.

We questioned whether the outlying Δ-values (Figs. 4 and 5, left panel) were likely to be dosimetrically significant. For example, the critical organ (the organ receiving the highest absorbed dose) is important in planning administered activities for clinical trials for new imaging agents and is of greater importance if the agent is being used in a theranostic role (e.g., to plan therapeutic administrations based on pretherapy imaging). Is there consensus among the software and phantoms regarding absorbed dose to critical organs? To gain insight into this question, we restricted the histograms to include only the critical organ for each radiopharmaceutical (Figs. 4 and 5, middle panel). Notably, the histograms of $\Delta^{\text{OLINDA}}_{\text{MIRDcalc}}$ and $\Delta^{\text{ICRP 128}}_{\text{MIRDcalc}}$ for the critical organs showed a reduced frequency of negative Δ-values. This finding indicates that OLINDA and ICRP publication 128, when compared with MIRDcalc, tend to provide higher estimates of the dose coefficients for critical organs. This tendency seems logical, because a large proportion of the radiopharmaceuticals included in ICRP publication 128 are rapidly excreted small molecules, which often irradiate the walled clearance organs to the largest extent, and because OLINDA and ICRP publication 128 are known to provide conservative overestimates for the walled organs (*18,19,21,23*). Analogous to the critical organ, we have also provided histograms that include only the organ contributing maximally to the effective dose (i.e., the maximal $w_T \cdot h(r_T, T_D)$; Figs. 4 and 5, right panel). When considering only critical organs or maximal contributors to the effective dose, agreement between MIRDcalc and IDAC-Dose improved such that no $\Delta^{\text{IDAC-Dose}}_{\text{MIRDcalc}}$ lay outside the range of expected variation.

## LIMITATIONS AND FUTURE WORK

We provide revised reference dose estimates for the ICRP publication 110 phantoms (or other modernized phantoms) based on biokinetic data of ICRP publication 128. There are recognized uncertainties inherent in the ICRP 128 TIACs—uncertainties that exist largely because of the limited availability of quantitative biodistribution measurements for many radiopharmaceuticals. Aside from these uncertainties, the main limitation in our dosimetric evaluation strategy is that the TIACs were derived using older compartmental pharmacokinetic models or exponential retention functions intended for use with the Cristy–Eckerman stylized phantoms. Therefore, the dose coefficients provided here should not supersede those originally published in ICRP publication 128. Rather, the dose coefficients we present should be used for comparative purposes; for example, in software validation, as we show. A current effort within the ICRP focuses on updating the ICRP publication 128 biokinetic datasets to full compartmental models consistent with the updated phantoms. After favorable reception of these datasets by the field, the dose coefficients should be recalculated with MIRDcalc and other current dosimetry software.

The scope of this validation was limited to diagnostic cases only; future validation should investigate agreement of MIRDcalc with other software supporting personalized dosimetry for therapy and theranostic-use cases.

## CONCLUSION

We report comprehensive testing and validation of MIRDcalc software based on comparison of dose coefficients for multiple radiopharmaceuticals across adult and pediatric phantoms, using validated data sources. Dose coefficients computed with MIRDcalc showed overall excellent agreement with other types of dosimetry software implementing the ICRP publication 110 series reference adult voxel phantoms and showed reasonable agreement with most dose coefficients derived using other reference phantoms.

## DISCLOSURE

This research was funded in part through the NIH/NCI Cancer Center support grant P30 CA008748 and NIH U01 EB028234. Lukas Carter acknowledges support from the Ruth L. Kirschstein NRSA postdoctoral fellowship (NIH F32 EB025050). No other potential conflict of interest relevant to this article was reported.

## ACKNOWLEGMENTS

This work was done in collaboration with the Society of Nuclear Medicine and Molecular Imaging MIRD Committee: Vikram Adhikarla, Rachel M. Barbee, Wesley E. Bolch, Yuni K. Dewaraja,

William D. Erwin, Darrell R. Fisher, Roger W. Howell, Adam L. Kesner, Richard Laforest, Joseph G. Rajendran, George Sgouros, and Pat B. Zanzonico (chair). We thank Dr. Pat Zanzonico from Memorial Sloan Kettering Cancer Center for providing guidance and support to the MIRDcalc development effort.

## REFERENCES

1. Bolch WE, Eckerman KF, Sgouros G, Thomas SR. MIRD pamphlet no. 21: a generalized schema for radiopharmaceutical dosimetry—standardization of nomenclature. *J Nucl Med.* 2009;50:477–484.
2. Snyder WS, Cook MJ, Nasset ES, Karhausen LR, Howells GP, Tipton IH. *ICRP Publication 23: Report of the Task Group on Reference Man.* Pergamon Press; 1975:1–480.
3. ICRP publication 89: basic anatomical and physiological data for use in radiological protection: reference values. *Ann ICRP.* 2002;32:5–265.
4. Menzel HG, Clement C, DeLuca P. ICRP Publication 110: adult reference computational phantoms. *Ann ICRP.* 2009;39:1–164.
5. Lee C, Lodwick D, Hurtado J, Pafundi D, Williams JL, Bolch WE. The UF family of reference hybrid phantoms for computational radiation dosimetry. *Phys Med Biol.* 2010;55:339–363.
6. Bolch WE, Eckerman K, Endo A, et al. ICRP publication 143: paediatric reference computational phantoms. *Ann ICRP.* 2020;49:5–297.
7. Kesner AL, Carter LM, Ocampo Ramos JC, et al. MIRD pamphlet no. 28, part 1: MIRDcalc—a software tool for medical internal radiation dosimetry. *J Nucl Med.* 2023. In press.
8. Mattsson S, Johansson L, Svegborn LS, et al. ICRP publication 128: radiation dose to patients from radiopharmaceuticals: a compendium of current information related to frequently used substances. *Ann ICRP.* 2015;44:1–321.
9. ICRP publication 103: the 2007 recommendations of the International Commission on Radiological Protection. *Ann ICRP.* 2007;37:1–332.
10. Bolch WE, Jokisch D, Zankl M, et al. ICRP publication 133: the ICRP computational framework for internal dose assessment for reference adults: specific absorbed fractions. *Ann ICRP.* 2016;45:5–73.
11. Jokisch DW, Bolch WE, Schwarz BC, et al. Specific absorbed fractions for reference paediatric individuals. *Ann ICRP.* In press.
12. Eckerman K, Endo A. ICRP publication 107: nuclear decay data for dosimetric calculations. *Ann ICRP.* 2008;38:7–96.
13. Vetter RJ. The 2007 recommendations of the International Commission on Radiological Protection: ICRP Publication 103. *Health Phys.* 2008;95:445.
14. Wayson MB, Leggett RW, Jokisch DW, et al. Suggested reference values for regional blood volumes in children and adolescents. *Phys Med Biol.* 2018;63:155022.
15. Andersson M, Johansson L, Eckerman K, Mattsson S. IDAC-Dose 2.1, an internal dosimetry program for diagnostic nuclear medicine based on the ICRP adult reference voxel phantoms. *EJNMMI Res.* 2017;7:88.
16. Segars WP, Lalush DS, Frey EC, Manocha D, King MA, Tsui BM. Improved dynamic cardiac phantom based on 4D NURBS and tagged MRI. *IEEE Trans Nucl Sci.* 2009;56:2728–2738.
17. Segars PW, Tsui BM. MCAT to XCAT: the evolution of 4-D computerized phantoms for imaging research—computer models that take account of body movements promise to provide evaluation and improvement of medical imaging devices and technology. *Proc IEEE Inst Electr Electron Eng.* 2009;97:1954–1968.
18. Stabin MG. MIRDOSE: personal computer software for internal dose assessment in nuclear medicine. *J Nucl Med.* 1996;37:538–546.
19. Stabin MG, Siegel JA. Physical models and dose factors for use in internal dose assessment. *Health Phys.* 2003;85:294–310.
20. Cristy M, Eckerman KF. *Specific Absorbed Fractions of Energy at Various Ages from Internal Photon Sources. VII. Adult Male.* Oak Ridge National Laboratory; 1987.
21. Andersson M, Johansson L, Minarik D, Leide-Svegborn S, Mattsson S. Effective dose to adult patients from 338 radiopharmaceuticals estimated using ICRP biokinetic data, ICRP/ICRU computational reference phantoms and ICRP 2007 tissue weighting factors. *EJNMMI Phys.* 2014;1:9.
22. Corrigendum to ICRP publication 133: the ICRP computational framework for internal dose assessment for reference adults: specific absorbed fractions. *Ann ICRP.* 2017;46:487.
23. Carter LM, Crawford TM, Sato T, et al. PARaDIM: a PHITS-based Monte Carlo tool for internal dosimetry with tetrahedral mesh computational phantoms. *J Nucl Med.* 2019;60:1802–1811.
24. Roedler HD. Accuracy of internal dose calculations with special consideration of radiopharmaceutical biokinetics. Abstract presented at: Third International Radiopharmaceutical Dosimetry Symposium; October 6, 1980; Oak Ridge, TN.

# Facial Anonymization and Privacy Concerns in Total-Body PET/CT

Aaron R. Selfridge[1], Benjamin A. Spencer[1,2], Yasser G. Abdelhafez[2,3], Keisuke Nakagawa[4], John D. Tupin[5], and Ramsey D. Badawi[1,2]

*[1]Department of Biomedical Engineering, University of California–Davis, Davis, California; [2]Department of Radiology, University of California–Davis, Davis, California; [3]Radiotherapy and Nuclear Medicine Department, South Egypt Cancer Institute, Assiut University, Assiut, Egypt; [4]Cloud Innovation Center, University of California–Davis, Davis, California; and [5]IRB Administration, University of California–Davis, Davis, California*

Total-body PET/CT images can be rendered to produce images of a subject's face and body. In response to privacy and identifiability concerns when sharing data, we have developed and validated a workflow that obscures (defaces) a subject's face in 3-dimensional volumetric data. **Methods:** To validate our method, we measured facial identifiability before and after defacing images from 30 healthy subjects who were imaged with both [$^{18}$F]FDG PET and CT at either 3 or 6 time points. Briefly, facial embeddings were calculated using Google's FaceNet, and an analysis of clustering was used to estimate identifiability. **Results:** Faces rendered from CT images were correctly matched to CT scans at other time points at a rate of 93%, which decreased to 6% after defacing. Faces rendered from PET images were correctly matched to PET images at other time points at a maximum rate of 64% and to CT images at a maximum rate of 50%, both of which decreased to 7% after defacing. We further demonstrated that defaced CT images can be used for attenuation correction during PET reconstruction, introducing a maximum bias of −3.3% in regions of the cerebral cortex nearest the face. **Conclusion:** We believe that the proposed method provides a baseline of anonymity and discretion when sharing image data online or between institutions and will help to facilitate collaboration and future regulatory compliance.

**Key Words:** total-body PET/CT; facial anonymization; uEXPLORER; facial recognition

**J Nucl Med 2023; 64:1304–1309**
DOI: 10.2967/jnumed.122.265280

Improving the resolution of medical imaging systems and facial recognition algorithms has given rise to concerns about the identifiability of CT, MRI, and PET image data. In any imaging study including the head, the surface of the 3-dimensional (3D) volume can be rendered to visualize the subject's face. When shared outside a healthcare setting, such an image could be recognizable to an individual or computer vision system, potentially compromising the confidentiality of any findings or linked information. With the introduction of total-body PET/CT, images of the entire human body can be acquired during normal clinical or research examinations (*1,2*). Renderings of total-body images contain all the same facial information as dedicated brain studies, as well as any sensitive or identifiable structure in the remainder of the body. Total-body PET/CT is a growing field with diverse and valuable prospects, making such concerns all the more pressing (*3–6*). Continued use of total-body PET/CT must consider how differences from conventional PET/CT may compromise patient privacy and anonymity. This is especially true when data are shared between institutions or uploaded to online research archives, a practice that will likely become more common given recent changes to the National Institutes of Health policies on data sharing (*7–9*).

Prior studies have focused on the degree to which surface-rendered MRI and CT images are identifiable to a subject's photograph (*10–15*). The identifiability of PET images using various tracers and changes to quantification after defacing were first studied in 2022 (*16*). These studies typically assume a motivated attacker with access to several photographs of a subject, and knowledge that the subject's CT or MRI study exists within a certain cohort. Under these conditions, the chances of correct identification can approach 100% for MRI data (*15*). Defacing and refacing can reduce this probability to 8%, using a method in which face regions are registered to and replaced with a population average (*16*). These methods are all tailored for dedicated head scans and assume some approximate position of the face within the imaging field of view. Working with total-body data presents the challenge that the face is not restricted within the field of view and that the head is typically not fixed. Patient height, rotation of the head, and positioning of the arms can all complicate the process of locating the patient's face as part of the defacing process.

The uEXPLORER PET/CT scanner is the first total-body PET/CT scanner and was installed at the University of California–Davis Health in 2019 for clinical and research use (*1,17*). The uEXPLORER has an axial field of view of 194 cm, permitting simultaneous PET acquisition of the whole body. The uEXPLORER also contains an 80-row 160-slice CT scanner capable of image acquisition with a minimal slice thickness of 0.5 mm. A head-to-foot CT scan is acquired with each PET scan and used for attenuation correction and anatomic localization. Because of the potential for high-resolution, low-noise imaging of the whole body, we believe that facial anonymization is an important consideration for data acquired on the uEXPLORER or any other high-resolution PET scanner with a long axial field of view.

In this work, we first present a method for surface rendering of total-body PET/CT data obtained from the uEXPLORER scanner. Subsequently, we present a method to locate and obscure faces in a way that provides a baseline of anonymity when sharing data. After applying our defacing workflow, we then tested the identifiability of the initial and defaced PET and CT images using a facial recognition system built on Google's FaceNet (*18,19*). Finally, we have

Received Dec. 1, 2022; revision accepted Mar. 30, 2023.
For correspondence or reprints, contact Aaron Selfridge (arselfridge@ucdavis.edu).
Published online Jun. 2, 2023.

**TABLE 1**
Scan Details for 30 Subjects Imaged at 3 or 6 Time Points

| Cohort | Participants (*n*) | Modality | Initial* | 90 min | 3 h | 6 h | 9 h | 12 h |
|---|---|---|---|---|---|---|---|---|
| Low-dose cohort | 15 | CT parameter | 140 kVp/ 5 mAs | 140 kVp/ 50 mAs | 140 kVp/ 5 mAs | NA | NA | NA |
| | | PET activity† | 15 MBq | 11 MBq | 6.3 MBq | NA | NA | NA |
| Full-dose cohort | 15 | CT parameter | 140 kVp/ 5 mAs | 140 kVp/ 50 mAs | 140 kVp/ 5 mAs | 140 kVp/ 5 mAs | 140 kVp/ 5 mAs | 140 kVp/ 5 mAs |
| | | PET activity† | 288 MBq | 209 MBq | 117 MBq | 36.8 MBq | 11.6 MBq | 3.65 MBq |

*Initial CT and PET images were at 0 and 40 min, respectively.
†Reported PET activity is actual injected dose averaged over all subjects. Later time points indicate remaining activity after decay of [$^{18}$F] (not accounting for excreted activity).
NA = not applicable.

considered the use of a defaced CT scan for attenuation correction during PET reconstruction to evaluate the impact of CT defacing on PET quantitation.

## MATERIALS AND METHODS

### uEXPLORER PET/CT Data Acquisition

In this work, we used a group of healthy volunteers who underwent uEXPLORER [$^{18}$F]FDG PET/CT scanning at multiple time points during a single visit. The study was approved by the Institutional Review Board at the University of California–Davis, and all subjects provided written informed consent. One cohort of 15 participants was injected with 20 ± 2 MBq of [$^{18}$F]FDG and underwent total-body PET/CT imaging at 0, 1.5, and 3 h after injection. A second cohort of 15 participants was injected with 372 ± 17 MBq and underwent 6 PET/CT scans at 0, 1.5, 3, 6, 9, and 12 h after injection. In full, the study contained 30 participants, 16 of whom were female (mean age, 47 ± 13 y; mean body mass index, 28 ± 5 kg/m$^2$; mean height, 175 ± 10 cm), with 135 PET scans and 135 CT scans. CT images were reconstructed with a voxel size of 0.97 × 0.97 × 2.3 mm, whereas PET images were reconstructed with a 2.3-mm isotropic voxel size. The details of each acquisition for the 2 cohorts are shown in Table 1.

For all 30 participants, the CT scan obtained at the 90-min time point was acquired following the PET/CT clinical low-dose protocol with 140 kVp, an average of 50 mAs, and automatic dose modulation. For all other time points, the CT scan followed a research ultra-low-dose protocol with 140 kVp, an average of 5 mAs, and automatic dose modulation.

PET imaging was performed for 60 min at the first time point (0–60 min) and 20 min for all other scans (e.g., 90–110 min). The PET image at the initial time point was reconstructed from 40 to 60 min to produce a static image matching the acquisition duration of other time points. Reconstructed PET images from all other time points were generated from data acquired over 20 min. As the injected activity decays over time, it is expected that the quality of surface-rendered images will also decrease.

### Surface Rendering

Rendering of surfaces from PET or CT follows several steps. The first is identification of an optimal threshold to create a binary image, capturing the surface structure from either modality. In CT, Otsu's method (*20*) for binarization is applied to the central transverse slice. In PET, half the mean value of the central coronal slice is used as the threshold. Voxels exceeding the threshold and not attached to the largest region (the body) are removed to provide a clearer surface rendering. In the second step, a 2-dimensional distance image is computed in which pixel value represents the distance from the back of the imaging volume to the first nonzero voxel in the binary image mask. The third step is computing of the 2-dimensional Sobel filter on the distance image, with gradient values being clipped at 10 times the pixel size for PET or 20 times the pixel size for CT. Finally, for a more realistic rendering, the gradient image is inverted. This step ensures that pixels in flatter regions are brighter and that those on edges are darker, creating a more natural-looking, front-lit image (Supplemental Fig. 1; supplemental materials are available at http://jnm.snmjournals.org).

Other software packages exist for rendering surfaces from 3D image volumes and have been used successfully in dedicated head and brain studies (*15,21*). Our purpose in developing a custom rendering process was to establish a fast, automated method optimized for total-body data. Furthermore, we wished to minimize external dependencies, for easier integration into an in-house defacing workflow.

### Face Detection and Blurring

For face detection in the rendered images, 2 methods were used. In the first method, a multitask cascaded convolutional neural network (MTCNN) was trained for face detection (*22,23*). This approach requires

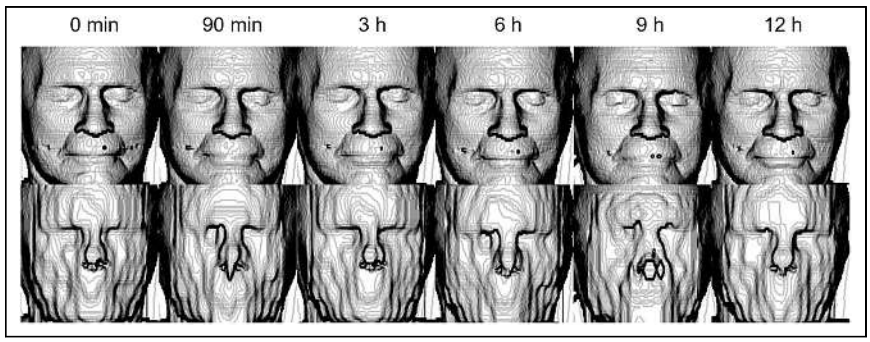


**FIGURE 1.** (Top) Faces rendered from CT images at 6 time points. Ninety-minute time point used clinical low-dose CT protocol. All others used research ultra-low-dose protocol. (Bottom) Rendering of defaced images at each time point.

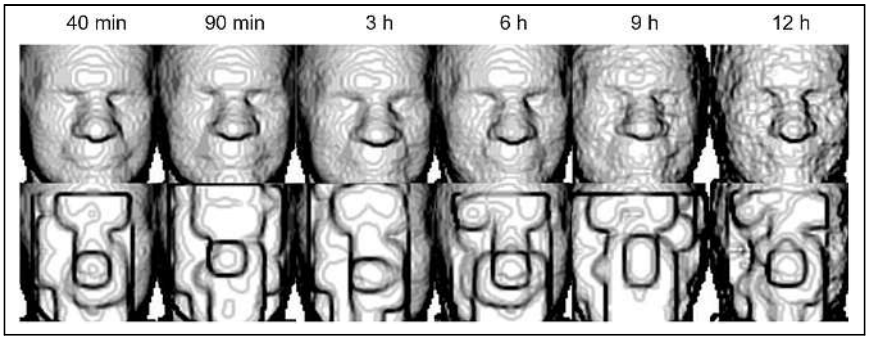


**FIGURE 2.** (Top) Faces rendered from PET images at 6 time points. (Bottom) Rendering of defaced images at each time point.

minimal preprocessing and is robust for varying face angle and lighting. However, we found that the MTCNN struggles to identify faces in low-resolution images or when facial features are not prominent, as may occur in rendered PET images. In the second method, a Haar cascade classifier was implemented in OpenCV (*24*). This approach is computationally inexpensive but more susceptible to noise and false-positives. Compared with the MTCNN detector, we found that this approach may not accurately detect faces at an angle or in different lighting conditions.

The MTCNN face detector was applied first, as we found it to provide an accurate face-bounding box with few false-positive detections. If no face was identified by the MTCNN detector, the Haar cascade classifier was applied as a fallback option since it could be tuned for greater sensitivity. The resultant bounding boxes tended to be smaller, with a greater tendency for false-positives on nonface regions.

The process of obscuring the face in a 3D volume followed several steps. The first was to create a 3D mask of face and nonface voxels using the 2-dimensional distance image and the coordinates of the face rectangle identified by the face detection algorithm. The 3D mask indicates the surface of the face and can be extended to cover an appropriate volume. In our case, we extended the mask 1 cm inward and 3 cm outward from the face surface. The second step was to down-sample the original image by a factor of 8 and then up-sample to create a pixelated or blurred version of the input with equal dimensions. Linear interpolation was used while resampling to preserve an approximation of a face structure without any clearly identifying features. The third step was to replace voxels in the original image with those in the pixelated image according to the 3D face mask.

### Defacing Workflow

The defacing workflow (illustrated in Supplemental Fig. 1) consists of creating a surface rendering, identifying the face position in the image, and blurring the corresponding surface in the input 3D image. This workflow was applied to PET and CT images acquired for all subjects at all time points. We subsequently visually evaluated whether the face detection algorithm had correctly identified a face in each image. Visual evaluation allowed us to gauge the quality of rendered images, to tune the binarization threshold selection and image contrast to provide more realistic renderings, and to ensure that the pixelation process sufficiently obscured the face. All algorithms were implemented in Python, version 3.10, and run on a dedicated server without multithreading or acceleration. Defacing a single PET or CT image took approximately 16 s and 8 GB of memory. Code for running the defacing workflow is available at a public GitHub repository (https://github.com/aaron-rohn/total-body-anonymization).

### Facial Recognition and Validation

We further validated our method by quantifying the identifiability of PET and CT images before and after defacing. An implementation of FaceNet was used to map each face image to a 128-dimension embedding vector, where Euclidian distance is used as a measure of similarity (*18,19*). After embeddings for a cohort are measured, clustering methods can be applied to identify distinct members.

We first considered the 15 participants of the full-dose cohort since images could be rendered at 6 separate time points (90 images for each modality). After rendering and creating facial embeddings for each PET and CT image, a nearest-neighbor classifier was used to identify the most likely matching subject. Cross validation was repeated 6 times (folds), at each stage leaving out 1 time point for each subject during training. The remaining time point was then used for testing. Accuracy at each stage was then measured as the fraction of faces matched to the correct subject and averaged over the 6-folds. To create a visual representation of clusters within the 128-dimension FaceNet-generated embeddings, we applied t-distributed stochastic neighbor embedding (t-SNE) to reduce dimensionality from 128 to 2 and plotted the resulting values (*25*). To estimate the degree of clustering in t-SNE plots, the mean within-cluster and between-cluster deviations were measured. Deviation was measured as …

$$\text{Mean deviation} = \frac{\sum_i^n ||x_i - \hat{x}||}{n},$$

where $n$ is the number of imaging time points and $\hat{x}$ is the centroid of the cluster on the t-SNE plot. For within-cluster deviation, the mean deviation was averaged over all subjects. For between-cluster deviation, the mean deviation of the per-subject centroids was calculated. The Levene test for unequal variance was used to calculate the likelihood that the within-cluster deviation was significantly different from that of the between-cluster deviation (*26*). $P$ values are reported on the t-SNE plots. Significantly lower within-cluster deviation indicates identifiability. Within-cluster deviation equal to or greater than between-cluster deviation indicates a loss of identifiability.

In addition to these evaluations of the high-dose cohort, we measured the identifiability of CT images acquired from all 30 subjects at the

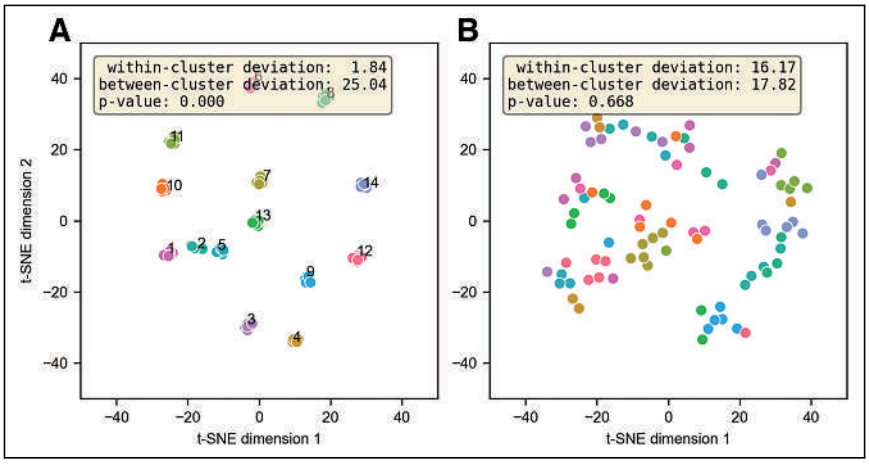


**FIGURE 3.** (A) Facial embeddings for 15 full-dose cohort subjects at 6 time points, plotted in 2 dimensions using t-SNE. Before defacing, facial embeddings are highly clustered. (B) After defacing, data are no longer clustered.

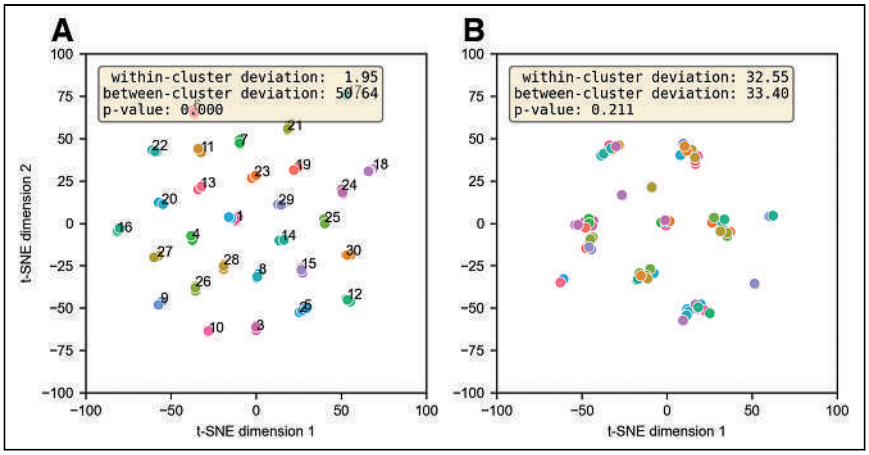


**FIGURE 4.** (A) Facial embeddings for all 30 full- and low-dose cohort subjects at first 3 time points. Before defacing, clusters are present for each participant. (B) After defacing, participants are not uniquely associated with clusters.

**TABLE 2**
Identifiability of PET Images Using Classifier Trained with PET (PET-to-PET) or CT (PET-to-CT) Images

| Identifiability (%) | Initial | 90 min | 3 h | 6 h | 9 h | 12 h |
|---|---|---|---|---|---|---|
| PET-to-PET | 64.3 | 50.0 | 57.1 | 57.1 | 28.6 | 7.1 |
| PET-to-CT | 50.0 | 42.9 | 28.6 | 21.4 | 28.6 | 14.3 |

first 3 time points only (90 images). We performed a similar series of cross-validations as well as clustering through t-SNE with this larger cohort.

When measuring the identifiability of PET images, we considered both PET-to-PET identification and PET-to-CT identification. The latter is more alike to some prior studies, which matched renderings to facial photographs (*15,16*). Identifiability was measured at each time point, as activity decayed and image quality decreased.

To verify the quantitative impact of our defacing method, we reconstructed PET raw data twice: first using the original CT image for attenuation correction and then using the defaced CT image for attenuation correction. Various brain regions of interest (ROIs) were compared with measured quantitative differences between the 2 reconstructed PET images. Five 1-cm-diameter spheric ROIs were placed at 5 positions along the outer aspect of the cerebral cortex, from the front of the brain moving posteriorly. The selected transverse plane was near the top of the defaced region, just above the brow. The relative difference at each point was measured and plotted.

## RESULTS

### Performance of Automated Workflow

Among 135 CT images, faces were correctly identified for all subjects using the MTCNN detector, and the Haar cascade classifier was not needed as a fallback option. The CT protocol (low-dose vs. ultra-low-dose) had no major visual impact on the quality of the rendered image or the performance of the face detector (Fig. 1). Among the 135 PET images (Fig. 2), the success of the face detector was influenced by the image activity; high-activity images produced renderings of the face with lower noise and a smoother surface, from which faces were more easily identified. The MTCNN detector performed better at earlier time points, and the Haar cascade classifier was necessary for robust face detection at later time points (Supplemental Fig. 2). In either case, faces were completely obscured after correct detection in all cases (Fig. 2, bottom).

### CT Identification Accuracy—Full-Dose Cohort

Before defacing, faces rendered from CT scans were matched to the correct subject at a rate of 96% ± 4%. After defacing, faces were matched in 10% of cases, marginally exceeding the probability of random chance (7%, 1/15). In the t-SNE plot before defacing (Fig. 3A), 15 well-defined clusters corresponded to faces rendered from the CT images of each subject. Variance of the within- and between-cluster deviance was statistically different in the original CT images, with a $P$ value of $8.53 \times 10^{-20}$. After defacing, no statistical difference was observed between with within- and between-cluster deviance, with a $P$ value of 0.668. The absence of subject-specific clusters after facial blurring (Fig. 3B) implies a relative loss of distinction between faces.

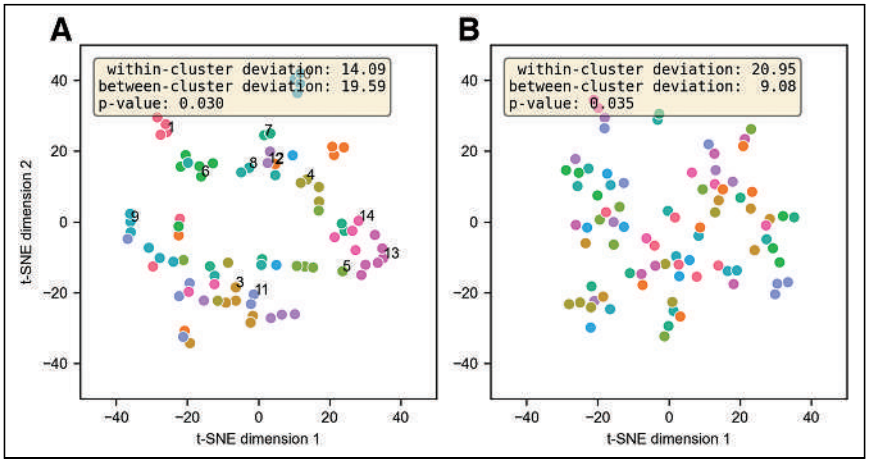


**FIGURE 5.** (A) Facial embeddings for 15 full-dose cohort subjects at 6 time points. Clustered facial embeddings for PET images indicate modest but significant ($P < 0.05$) degree of identifiability. (B) No clusters are present after defacing. Within-cluster deviation is significantly greater than between-cluster deviation.

### CT Identification Accuracy—Full- and Low-Dose Cohorts

When the first 3 time points were used for all 30 subjects, the identification accuracy of rendered images from CT scans was 93% ± 3%. After anonymization, faces were matched in 6% of cases, marginally exceeding the probability of random chance (3.3%, 1/30). The t-SNE plots showed 30 distinct clusters corresponding to each subject—the $P$ value for clustering was $3.32 \times 10^{-26}$ (Fig. 4A). After defacing, the $P$ value for clustering was 0.211, indicating a loss of identifiability (Fig. 4B). Some clusters were still present after defacing; these were random

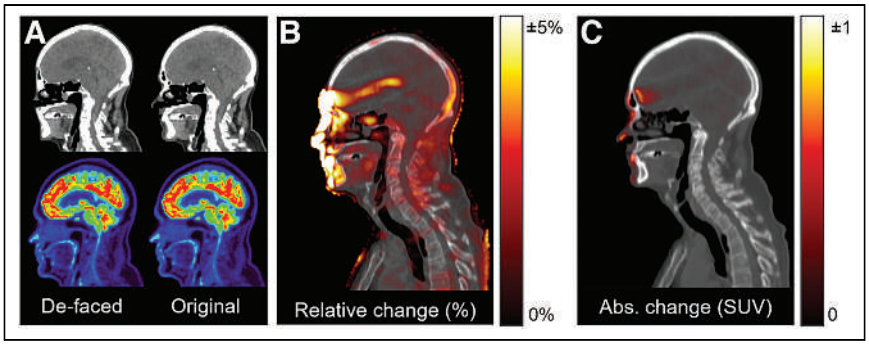


**FIGURE 6.** (A) Grid showing CT slices before and after defacing. PET images are reconstructed from same raw data, with different CT scans for attenuation correction. (B) Normalized difference image showing percentage change in PET activity. High-intensity region in brain largely overlaps ventricles, which have low [$^{18}$F]FDG uptake. (C) Absolute difference in PET SUV.

and related to t-SNE parameter selection. The number of clusters was less than the number of subjects, and subjects were no longer uniquely associated with individual clusters.

### PET Identification Accuracy—Full-Dose Cohort

In cross-validation of faces rendered from PET images, identifiability depended on the imaging time point (Table 2). PET-to-PET identifiability reflects the accuracy of a classifier trained using PET images only, when querying the identity of a PET image. PET-to-CT identifiability reflects the accuracy of a classifier trained using CT images, when querying the identity of a PET image. Before defacing, the maximum PET-to-PET identifiability was 64% and PET-to-CT identifiability was 50%, both at the initial 40-min time point. After defacing, the average PET-to-CT and PET-to-PET identifiability were both 7%, equivalent to the probability of random chance (7%, 1/15).

The *P* value for clustering in the original PET images was 0.03, although the magnitude of the difference between the within- and between-cluster deviations was less than for CT-derived faces (Fig. 5A). The *P* value for clustering after defacing was 0.035, in this case indicating that the within-cluster deviation was significantly greater than the between-cluster deviation, as is consistent with a lack of identifiability (Fig. 5B).

### PET Quantitation with Anonymized CT for Attenuation Correction

After reconstruction of the PET raw data with the original and defaced CT scans, the images were qualitatively similar (Fig. 6A). The normalized difference approached 30% in the face and around the chin and eyebrow, in the regions where the CT image was modified (Supplemental Fig. 3). Immediately behind the face and modified regions, the percentage change decreased rapidly. As shown in Figure 7, the difference in PET activity in ROI 0, nearest the modified face region, was −3.3%. In ROI 4, the difference was −0.24%.

## DISCUSSION

The proposed workflow reliably detected and obscured faces in both CT (Fig. 1) and [$^{18}$F]FDG PET (Fig. 2) images. It should also scale equally well to other tracers, provided that there is sufficient superficial uptake and that an appropriate threshold for binarization is selected. Validation will be required, however. Images in this study included scans with both arms up and arms down and of patients with a range of heights and sizes—factors that pose a unique challenge to defacing in total-body PET images. Although the quality of the facial rendering is consistently high in CT (Fig. 1), PET images vary greatly depending on the degree to which the radiotracer has decayed, resulting in degraded image quality (Fig. 2). At delayed time points (or when scan duration or injected activity is reduced), automated face detection is prone to false-negative and -positive detections due to increased image noise (Supplemental Fig. 2). In these cases, however, the images retain fewer potentially identifying facial features. For reference, the 3-h time point in the high-dose cohort is closest to the standard clinical protocol used at our institution (296 MBq, 120 min after injection) (*17*). At this time point, PET-to-CT identifiability was 28.6% (Table 2).

In our validation, we found that identifiability between modalities (PET-to-CT) was generally lower than that within a single modality (Table 2). This difference likely reflects the changing appearance of faces rendered from PET and CT. PET images have a lower resolution, and patterns of [$^{18}$F]FDG uptake may not directly correspond to the structures imaged in CT. This difference in identifiability is notable since prior studies on image defacing have focused primarily on the identifiability of medical images to photographs, such as those mined from social media (*16*). Using the Microsoft Azure Face application programming interface, 1 prior study measured an identification rate of 78% between faces rendered from CT and photographs (*14*). This rate is consistent with the high rate of CT-to-CT identification measured here, although different numbers of participants and methods for facial recognition will lead to different identification rates.

For most purposes, the defacing process should have no major impact on image quantitation. Image voxels outside the immediate region of the face are not altered. We have not tested the impact of our defacing process on automated brain segmentation methods, which may be impacted by defaced images (*15*). When defaced PET or CT images are used for reconstruction or reprojection, as in motion correction or other advanced applications, we expect that PET values outside the immediate region of the face should not

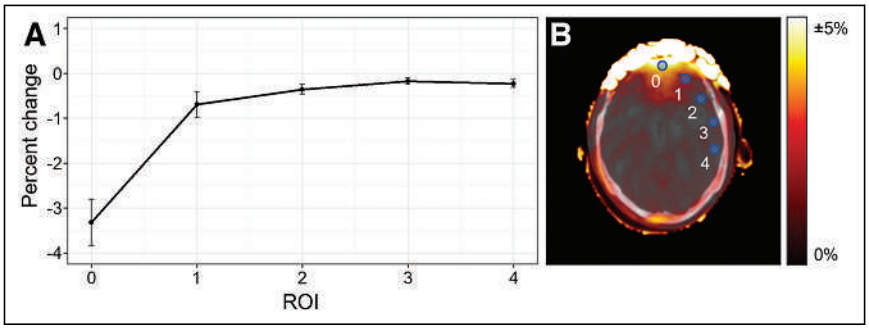


**FIGURE 7.** (A) Percentage change when using defaced CT for PET attenuation correction. Values were measured at 5 spheric ROIs along cerebral cortex. Error bars correspond to SD within ROI. (B) Difference image and corresponding CT slice, overlaid with 5 ROIs.

show substantial changes beyond a few percentage points (Fig. 7). When defacing is called for, it is a necessary trade-off that the measured uptake or attenuation in regions around the nose, eyes, and cheeks will be altered substantially, potentially obscuring skin or other superficial lesions.

We note that for many institutions and applications, defacing of volumetric image data is not standard practice and is not currently required for regulatory compliance. Furthermore, whereas we have demonstrated identifiability of faces under very specific circumstances, these do not necessarily represent those of our presumed motivated attacker. As in any task of identifying anonymized data, there still exists the problem of the perfect register—a reference database with one and only one match for the desired target (*27*). Image data may indeed make creation of such a database more possible, since an individual's face has the potential to be a highly identifying feature (as opposed to name, address, birthday, or other identifiers). However facial recognition is probabilistic, and images must still be mined from social media or elsewhere, which may not be trivial. Institutional bodies considering the adoption of defacing should weigh these factors against the associated complexity and loss of image information.

## CONCLUSION

We have described a method for defacing total-body [$^{18}$F]FDG PET and CT data that makes facial identification of volumetric images more challenging and has a minimal impact on PET quantification. We believe that the presented workflow provides a baseline of patient privacy and discretion and will be a valuable component of data-sharing workflows, which are expected to become more widespread in the future.

## DISCLOSURE

This work was funded in part through National Institutes of Health grants R01CA249422 and R01CA206187. The University of California–Davis has a research agreement and a sales-based revenue-sharing agreement with United Imaging Healthcare. No other potential conflict of interest relevant to this article was reported.

**KEY POINTS**

**QUESTION:** What are the unique privacy concerns from surface renderings in total-body PET/CT, and how can we mitigate them?

**PERTINENT FINDINGS:** Total-body PET/CT images are identifiable and uniquely sensitive because of their capacity for rendering of the whole surface of the body. The presented defacing workflow minimizes the possibility of facial identification without impacting image quantitation.

**IMPLICATIONS FOR PATIENT CARE:** Image processing developments that benefit patient care often depend on the availability of large volumes of image data. Robust anonymization processes, such as facial anonymization, help to support the requisite data sharing and archiving.

## REFERENCES

1. Badawi RD, Shi H, Hu P, et al. First human imaging studies with the EXPLORER total-body PET scanner. *J Nucl Med.* 2019;60:299–303.
2. Spencer BA, Berg E, Schmall JP, et al. Performance evaluation of the uEXPLORER total-body PET/CT scanner based on NEMA NU 2-2018 with additional tests to characterize PET scanners with a long axial field of view. *J Nucl Med.* 2021;62:861–870.
3. Wang G, Nardo L, Parikh M, et al. Total-body PET multiparametric imaging of cancer using a voxelwise strategy of compartmental modeling. *J Nucl Med.* 2022; 63:1274–1281.
4. Derlin T, Spencer BA, Mamach M, et al. Exploring vessel wall biology in vivo by ultrasensitive total-body PET. *J Nucl Med.* 2023;64:416–422.
5. Abdelhafez Y, Raychaudhuri SP, Mazza D, et al. Total-body $^{18}$F-FDG PET/CT in autoimmune inflammatory arthritis at ultra-low dose: initial observations. *J Nucl Med.* 2022;63:1579–1585.
6. Sundar LKS, Yu J, Muzik O, et al. Fully-automated, semantic segmentation of whole-body $^{18}$F-FDG PET/CT images based on data-centric artificial intelligence. *J Nucl Med.* 2022;63:1941–1948.
7. Clark K, Vendt B, Smith K, et al. The cancer imaging archive (TCIA): maintaining and operating a public information repository. *J Digit Imaging.* 2013;26:1045–1057.
8. Data management and sharing policy. National Institutes of Health website. https://sharing.nih.gov/data-management-and-sharing-policy. Accessed May 16, 2023.
9. Larson DB, Magnus DC, Lungren MP, Shah NH, Langlotz CP. Ethics of using and sharing clinical imaging data for artificial intelligence: a proposed framework. *Radiology.* 2020;295:675–682.
10. Chen JJ, Siddiqui KM, Fort L, et al. Observer success rates for identification of 3D surface reconstructed facial images and implications for patient privacy and security. In: *Medical Imaging 2007: PACS and Imaging Informatics.* Vol 6516. SPIE; 2007:407–414.
11. Prior FW, Brunsden B, Hildebolt C, et al. Facial recognition from volume-rendered magnetic resonance imaging data. *IEEE Trans Inf Technol Biomed.* 2009; 13:5–9.
12. Mazura JC, Juluru K, Chen JJ, Morgan TA, John M, Siegel EL. Facial recognition software success rates for the identification of 3D surface reconstructed facial images: implications for patient privacy and security. *J Digit Imaging.* 2012;25: 347–351.
13. Chen JJ-S, Juluru K, Morgan T, Moffitt R, Siddiqui KM, Siegel EL. Implications of surface-rendered facial CT images in patient privacy. *AJR.* 2014;202: 1267–1271.
14. Schwarz CG, Kremers WK, Therneau TM, et al. Identification of anonymous MRI research participants with face-recognition software. *N Engl J Med.* 2019;381: 1684–1686.
15. Schwarz CG, Kremers WK, Wiste HJ, et al. Changing the face of neuroimaging research: comparing a new MRI de-facing technique with popular alternatives. *Neuroimage.* 2021;231:117845.
16. Schwarz CG, Kremers WK, Lowe VJ, et al. Face recognition from research brain PET: an unexpected PET problem. *Neuroimage.* 2022;258:119357.
17. Nardo L, Abbelhafez YG, Spencer BA, Badawi RD. Clinical implementation of total-body PET/CT at University of California, Davis. *PET Clin.* 2021;16:1–7.
18. keras-facenet. GitHub website. https://github.com/nyoki-mtl/keras-facenet. Published February 23, 2018. Accessed May 16, 2023.
19. Schroff F, Kalenichenko D, Philbin J. FaceNet: a unified embedding for face recognition and clustering. In: *2015 IEEE Conference on Computer Vision and Pattern Recognition (CVPR)*. IEEE; 2015:815–823.
20. Otsu N. A threshold selection method from fray-level histograms. *IEEE Trans Syst Man Cybern.* 1979;9:62–66.
21. Surf Ice. NITRC website. https://www.nitrc.org/projects/surfice/. Published October 19, 2015. Accessed May 16, 2023.
22. Face recognition using Tensorflow. GitHub website. https://github.com/davidsandberg/facenet. Published April 16, 2018. Accessed May 16, 2023.
23. Zhang K, Zhang Z, Li Z, Qiao Y. Joint face detection and alignment using multitask cascaded convolutional networks. *IEEE Signal Process Lett.* 2016;23: 1499–1503.
24. Bradski G. The OpenCV library. *Dr Dobb's J Softw Tools.* 2000;120:122–125.
25. van der Maaten L, Hinton G. Visualizing data using t-SNE. *J Mach Learn Res.* 2008;9:2579–2605.
26. Levene H. Robust tests for equality of variances. In: Olkin I, ed. *Contributions to Probability and Statistics: Essays in Honor of Harold Hotelling.* Stanford University Press; 1960:278–292.
27. Barth-Jones D. The 're-identification' of governor William Weld's medical information: a critical re-examination of health data identification risks and privacy protections, then and now. SSRN website. http://dx.doi.org/10.2139/ssrn.2076397. Published July 2012. Accessed May 16, 2023.

# Endogenous Opioid Release After Orgasm in Man: A Combined PET/Functional MRI Study

Patrick Jern[1], Jinglu Chen[2,3], Jouni Tuisku[2,3], Tiina Saanijoki[2,7], Jussi Hirvonen[2–4], Lasse Lukkarinen[2,3], Sandra Manninen[2,3], Semi Helin[2], Vesa Putkinen[2,3,5], and Lauri Nummenmaa[2,3,6]

*[1]Department of Psychology, Åbo Akademi University, Turku, Finland; [2]Turku PET Centre, University of Turku, Turku, Finland; [3]Turku University Hospital, University of Turku, Turku, Finland; [4]Department of Radiology, University of Turku, Turku, Finland; [5]Turku Institute for Advanced Study, University of Turku, Turku, Finland; [6]Department of Psychology, University of Turku, Turku, Finland; and [7]Turku BioImaging, University of Turku and Åbo Akademi University, Turku, Finland*

The endogenous μ-opioid receptor (MOR) system plays a key role in the mammalian reward circuit. Human and animal experiments suggest the involvement of MORs in human sexual pleasure, yet this hypothesis currently lacks in vivo support. **Methods:** We used PET with the radioligand [$^{11}$C]carfentanil, which has high affinity for MORs, to quantify endogenous opioid release after orgasm in man. Participants were scanned once immediately after orgasm and once in a baseline state. Hemodynamic activity was measured with functional MRI during penile stimulation. **Results:** The PET data revealed significant opioid release in the hippocampus. Hemodynamic activity in the somatosensory and motor cortices and in the hippocampus and thalamus increased during penile stimulation, and thalamic activation was linearly dependent on self-reported sexual arousal. **Conclusion:** Our data show that endogenous opioidergic activation in the medial temporal lobe is centrally involved in sexual arousal, and this circuit may be implicated in orgasmic disorders.

**Key Words:** orgasm; manual penile stimulation; arousal; opioids; fMRI; PET

**J Nucl Med 2023; 64:1310–1313**
DOI: 10.2967/jnumed.123.265512

The endogenous opioid system plays a key role in the mammalian reward circuit (*1*), and the opioid receptor also regulates sexual desire and arousal (*2*). Opiates suppress sexual behaviors in both humans and animals (*3*), and μ-opioid receptor (MOR) agonists, in particular, decrease human sexual desire and pleasure acutely and chronically (*4*). The roles of opioid receptor agonists and antagonists in exciting and suppressing sexual behaviors is complex and varies between species and conditions. Opioid antagonists and agonists may also promote sexual behavior: naltrexone stimulates ejaculations and increases copulation rates in male rats (*5*). Opioid agonists may also induce copulation when injected to the medial preoptic area (*6*), whereas striatal administration does not, at least not consistently (*7*). A recent study also showed that MOR availability in cortical and subcortical areas correlated positively with sex drive in men (*2*). Animal studies also demonstrate postcoital endogenous opioid release: copulation releases endogenous opioid peptides in rats in the medial preoptic area of the hypothalamus (*8*). In humans, opioid agonists increase pleasure, and opioid abusers describe the sensations after opioid administration as euphoric and orgasmic (*9*). Accordingly, evidence suggests that the opioid receptor contributes to human sexual drive and pleasure, but in vivo evidence for endogenous opioid release after sexual behaviors is lacking. Here, because of the potential implications in orgasmic disorders, we tested the hypothesis that sexual arousal peaking in orgasm leads to endogenous opioid release in men.

## MATERIALS AND METHODS

The participants were 6 heterosexual males (mean age, 35.4 y, range, 21.6–43.2 y). Participants gave informed, written consent and were compensated for their participation. The Hospital District of Southwest Finland's ethics board approved the protocol. The study was conducted in accordance with the Declaration of Helsinki. The participants' female partners served as confederates, providing tactile penile stimulation (scanning details are provided in the supplemental materials (available at http://jnm.snmjournals.org). The participants were scanned with PET at baseline and after receiving orgasm-leading penile stimulation. The scans were done on separate days, and their order was counterbalanced (Fig. 1, top row). The mean time between PET and MRI scans was 14.67 d (SD, 12.59 d). The couple was led to a private room 30 min before the orgasm scan; the partner was instructed to time the participant's orgasm as close to the PET scan as possible. MOR availability was measured with the radioligand [$^{11}$C]carfentanil (*10*), synthesized as described previously (*11*). Regional time–activity curves were obtained from 21 regions of interest, and regional nondisplaceable binding potential values were obtained for each scan using the simplified reference tissue model with the occipital cortex as a reference (Supplemental Table 1) (*10–22*). PET imaging was performed with a Discovery 690 PET/CT scanner. The tracer was administered as a single bolus via a catheter placed in each participant's antecubital vein. PET emission data were acquired for 51 min after injection. Regional nondisplaceable binding potentials across the orgasm and baseline conditions were compared using paired-sample *t* tests without multiple-comparison correction across regions of interest.

The MRI data were acquired using a Phillips Ingenuity TF PET/MRI 3-T scanner. The participant was covered with a blanket, and the partner was sitting next to the MRI bed. The partner received auditory instructions to stimulate her partner in approximately 10-s blocks (Fig. 1).

Received Jan. 24, 2023; revision accepted May 10, 2023.
For correspondence or reprints, contact Patrick Jern (patrick.jern@abo.fi).
Published online Jul. 13, 2023.

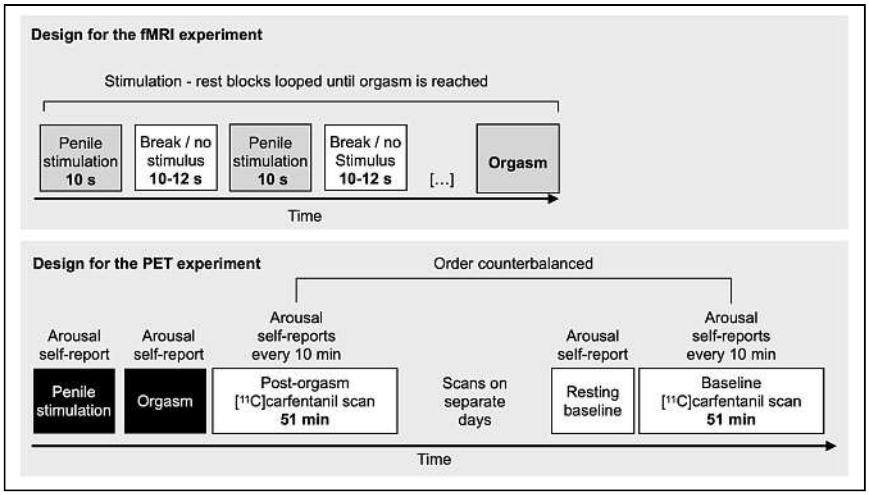


**FIGURE 1.** Depiction of study design. fMRI = functional MRI.

The participant used buttons to indicate his moment-to-moment sexual arousal (on a scale of 0–100). Stimulation blocks were interspersed with approximately 11-s rest blocks (±1-s jitter). Functional data were preprocessed with FMRIPREP (version 1.3.0) (*15*) and analyzed using a general linear model with t-contrast for manual penile stimulation versus rest as well as moment-to-moment parametric modulation of sexual arousal. All results were corrected using a false-discovery-rate $P$ value of less than 0.05.

## RESULTS

The mean pleasure rating for the orgasm was 8.1 units, and the mean arousal rating was 6.33 units (scale, 1–10 units; Supplemental Fig. 1). Arousal after the orgasm was significantly higher than during any other time point ($t$s $>$ 3.27, $P$s $<$ 0.02 in paired-sample $t$ test). Figure 2 shows mean MOR availability during baseline and orgasm scans. The region-of-interest analysis (Fig. 3) yielded a significant effect in the hippocampus ($t(5) = 2.90$, $P = 0.03$), indicating endogenous opioid release after orgasm ($\Delta M = 13\%$). No other significant effects were observed. Sexual arousal increased linearly during functional MRI (fMRI) scans (Supplemental Fig. 2). Hemodynamic responses to receiving penile stimulation minus rest were stronger in the hippocampus and thalamus and in the posterior parietal, primary motor, and somatosensory cortices. Deactivations were observed in the anterior cingulate cortex in the nucleus accumbens and insula (Fig. 4A). The parametric model for pleasure yielded positive effects in the thalamus and inferior parietal cortices. Negative associations were observed in the insula, putamen, and frontal pole (Fig. 4B).

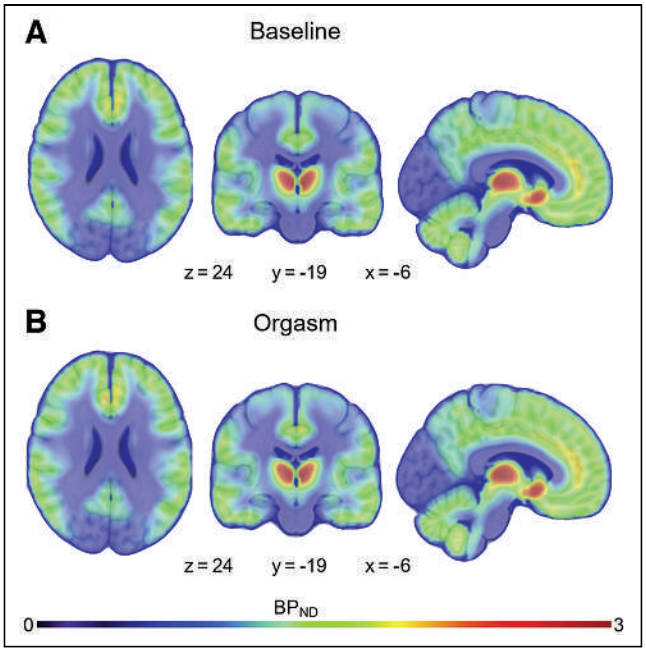


**FIGURE 2.** Mean MOR availability during baseline and orgasm scans.

## DISCUSSION

We provide an indication that in vivo endogenous opioid release may be raised in the male hippocampus after orgasm. Orgasm led to increased opioid release in the medial temporal lobe. Hemodynamic activity during penile stimulation increased in limbic regions and the somatosensory cortex, whereas responses in the thalamus reflected the moment-to-moment intensity of sexual arousal.

PET data revealed higher nondisplaceable binding potential in the hippocampus in the baseline versus orgasm scan, consistent with increased neurotransmitter release after an orgasm. These changes were paralleled by hemodynamic responses in the hippocampus during penile stimulation. The fMRI results also implied a central role of the thalamus in modulating sexual arousal. To our knowledge, these data yield the most detailed picture, to date, of the functional and molecular brain basis of sexual arousal and climax in man and support the general role of the MOR system in modulating the calmness–arousal axis (*2,23*).

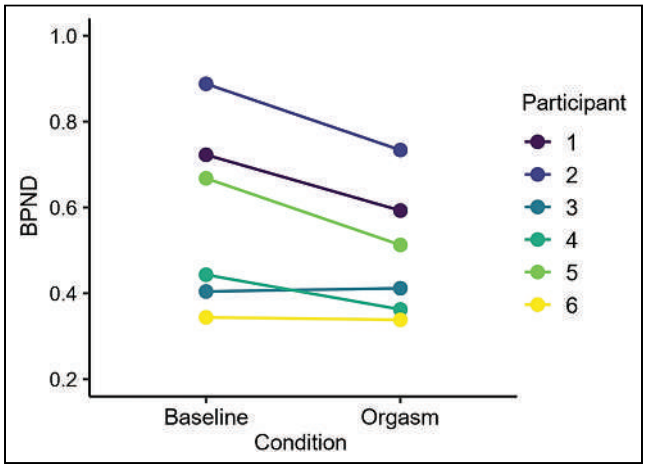


**FIGURE 3.** Mean participantwise nondisplaceable binding potential in hippocampus for baseline and orgasm scans. Difference is statistically significant at $P < 0.05$ (paired $t$ test). BPND = nondisplaceable binding potential.

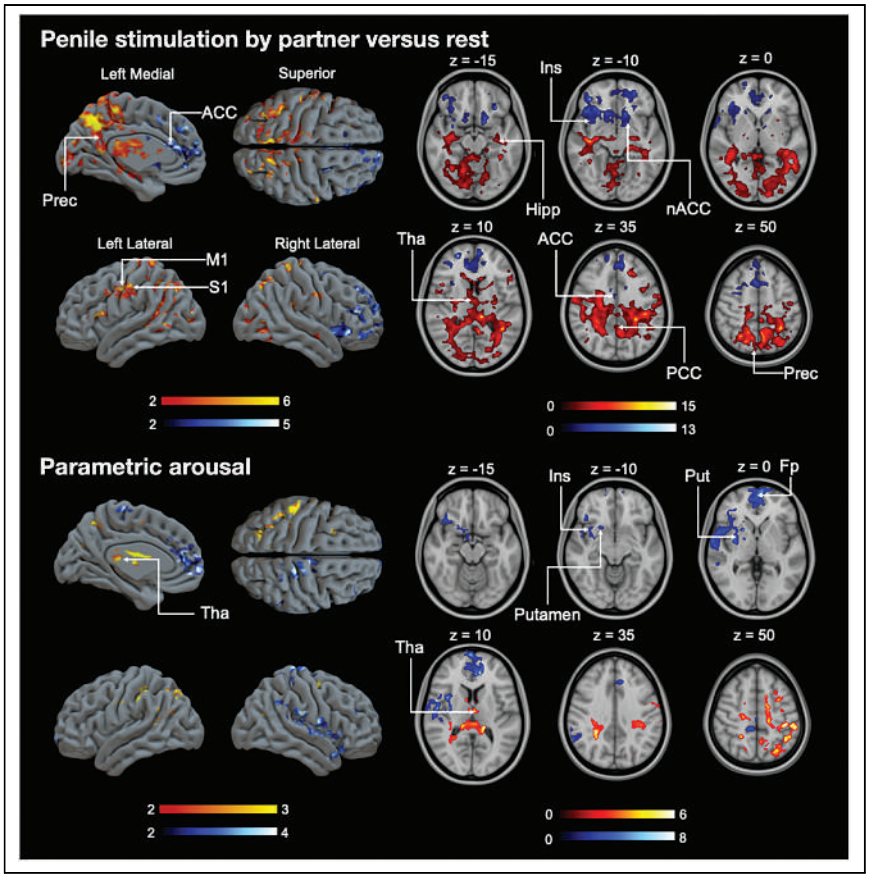


**FIGURE 4.** (Top) Brain regions showing amplified responses during manual penile stimulation minus rest. (Bottom) Brain regions whose activity increased linearly as function of sexual arousal during scans. Data are thresholded at $P < 0.05$, false-discovery-rate–corrected at cluster level. Color bar indicates *t* statistic range. ACC = anterior cingulate cortex; Hipp = hippocampus; Ins = insula; Fp = frontal pole; Put = putamen; M1 = primary motor cortex; nACC = nucleus accumbens; PCC = posterior cingulate cortex; Prec = precuneus; S1 = primary somatosensory cortex; Tha = thalamus.

Opioid release after sexual activity corroborates findings of increased opioid receptor activity after sexual behaviors in other mammals (*8*). This finding parallels human PET studies demonstrating endogenous opioid release after consumption of rewards ranging from feeding to sociability (*24*) and extends the role of the human MOR system to sexual pleasure. Data were also in line with recent PET data indicating MOR-dependent individual differences in male sex drive, corroborating the role of MORs in sexual motivation and pleasure (*2*). Because of the temporal resolution of PET, we cannot, however, state whether opioid release reflects pleasure evoked by sexual stimulation, orgasm, or refractory activity in the postorgasmic phase.

Perhaps surprisingly, orgasm-dependent MOR activation was observed only in the hippocampus. However, animal electrophysiologic studies have demonstrated hippocampal activity during orgasm (*25*). Furthermore, θ-hippocampal activity can be induced by injecting opiates into the brain stem (*26*). Indeed, the rat brain may enter a learning mode during the postorgasmic phase, analogous to the memory consolidation that is known to occur during sleep after learning (*27*). We did not observe MOR activity in the hypothalamus despite its role in sexual functioning in rodents (*6*). This may reflect insufficient statistical power, yet we observed no hypothalamic effects even at lower statistical thresholds. The hypothalamus is, however, a small structure whose accurate quantification using PET with limited spatial resolution is complicated.

Brain activity increases during sexual reward in humans and animals. fMRI revealed increased activation in the hippocampus and thalamus during penile stimulation versus rest, the former according with increased MOR activation observed in the PET study. The thalamus modulates arousal and awareness (*28*), and the male thalamus becomes activated during penile erection, acting as a relay station transmitting peripheral sexual sensations to the brain (*29*). We also observed deactivation in the anterior cingulate and activation in the posterior parietal, primary motor, and somatosensory cortices. These areas have been shown to activate during sexual arousal and orgasm in men (*30*).

Our study had some limitations. Evidence for opioid release was found only in 1 region (hippocampus) of 21 a priori regions of interest, and although the hippocampus contains MORs, the regional nondisplaceable binding potentials were moderately low. Because full-volume false-discovery-rate–corrected results were not observed, the finding should be considered preliminary until replicated. Only men were studied, and the sample size was limited by the complex multimodal imaging setup; however, significant effects were nonetheless observed. Brain responses during the orgasm phase in fMRI could not be analyzed because of head motion.

## CONCLUSION

We observed endogenous opioid release in the male brain after orgasm in 6 healthy volunteers. In a parallel fMRI experiment, we observed activation of—above all—the hippocampus. Altogether, these data show that endogenous opioidergic activation in the medial temporal lobe is centrally involved in sexual arousal, whereas modulation of sexual arousal in the thalamus and striatum may be supported by other neuromodulators.

## DISCLOSURE

The study was supported by the Sigrid Juselius Stiftelse and Academy of Finland (294897, 332225). No other potential conflict of interest relevant to this article was reported.

## ACKNOWLEDGMENTS

We thank Henry Karlsson for generating the audio cues for the experiment, and we thank Profs. Juha Rinne and Matti Laine for discussing the research protocol.

**KEY POINTS**

**QUESTION:** Does sexual arousal peaking in orgasm lead to endogenous opioid release in men?

**PERTINENT FINDINGS:** In a combined PET/fMRI study involving 6 healthy participants, we found evidence of opioid release in the hippocampus ($P < 0.05$).

**IMPLICATIONS FOR PATIENT CARE:** Endogenous opioidergic activation in the medial temporal lobe is centrally involved in sexual arousal, and this circuit may be implicated in orgasmic disorders.

## REFERENCES


1. Nummenmaa L, Tuominen LJ. Opioid system and human emotions. *Br J Pharmacol.* 2018;175:2737–2749.
2. Nummenmaa L, Jern P, Malén T, et al. M-opioid receptor availability is associated with sex drive in human males. *Cogn Affect Behav Neurosci.* 2022;22:281–290.
3. Pfaus JG, Gorzalka BB. Opioids and sexual behavior. *Neurosci Biobehav Rev.* 1987;11:1–34.
4. Birke H, Ekholm O, Hojsted J, Sjogren P, Kurita GP. Chronic pain, opioid therapy, sexual desire, and satisfaction in sexual life: a population-based survey. *Pain Med.* 2019;20:1132–1140.
5. Rodríguez-Manzo G, Fernández-Guasti A. Opioid antagonists and the sexual satiation phenomenon. *Psychopharmacology (Berl).* 1995;122:131–136.
6. Hughes AM, Everitt BJ, Herbert J. Comparative effects of preoptic area infusions of opioid peptides, lesions and castration on sexual behaviour in male rats: studies of instrumental behaviour, conditioned place preference and partner preference. *Psychopharmacology (Berl).* 1990;102:243–256.
7. Le Merrer J, Becker JAJ, Befort K, Kieffer BL. Reward processing by the opioid system in the brain. *Physiol Rev.* 2009;89:1379–1412.
8. Coolen LM, Fitzgerald ME, Yu L, Lehman MN. Activation of μ opioid receptors in the medial preoptic area following copulation in male rats. *Neuroscience.* 2004; 124:11–21.
9. Chessick RD. The pharmacogenic orgasm in the drug-addict. *Arch Gen Psychiatry.* 1960;3:545–556.
10. Eriksson O, Antoni G. [$^{11}$C]carfentanil binds preferentially to μ-opioid receptor subtype 1 compared to subtype 2. *Mol Imaging.* 2015;14:476–483.
11. Kantonen T, Pekkarinen L, Karjalainen T, et al. Obesity risk is associated with altered cerebral glucose metabolism and decreased μ-opioid and $Cb_1$-receptor availability. *Int J Obes.* 2022;46:400–407.
12. Karjalainen T, Tuisku J, Santavirta S, et al. Magia: robust automated image processing and kinetic modeling toolbox for PET neuroinformatics. *Front Neuroinform.* 2020;14:3.
13. Lammertsma AA, Hume SP. Simplified reference tissue model for PET receptor studies. *Neuroimage.* 1996;4:153–158.
14. Gunn RN, Lammertsma AA, Hume SP, Cunningham VJ. Parametric imaging of ligand-receptor binding in PET using a simplified reference region model. *Neuroimage.* 1997;6:279–287.
15. Esteban O, Markiewicz CJ, Blair RW, et al. Fmriprep: a robust preprocessing pipeline for functional MRI. *Nat Methods.* 2019;16:111–116.
16. Abraham A, Pedregosa F, Eickenberg M, et al. Machine learning for neuroimaging with Scikit-learn. *Front Neuroinform.* 2014;8:14.
17. Tustison NJ, Avants BB, Cook PA, et al. N4itk: improved N3 bias correction. *IEEE Trans Med Imaging.* 2010;29:1310–1320.
18. Dale AM, Fischl B, Sereno MI. Cortical surface-based analysis: I. Segmentation and surface reconstruction. *Neuroimage.* 1999;9:179–194.
19. Klein A, Ghosh SS, Bao FS, et al. Mindboggling morphometry of human brains. *PLOS Comput Biol.* 2017;13:e1005350.
20. Fonov VS, Evans AC, McKinstry RC, Almli CR, Collins DL. Unbiased nonlinear average age-appropriate brain templates from birth to adulthood. *Neuroimage.* 2009;47(suppl 1):S102.
21. Avants BB, Epstein CL, Grossman M, Gee JC. Symmetric diffeomorphic image registration with cross-correlation: evaluating automated labeling of elderly and neurodegenerative brain. *Med Image Anal.* 2008;12:26–41.
22. Zhang Y, Brady M, Smith S. Segmentation of brain MR images through a hidden Markov random field model and the expectation-maximization algorithm. *IEEE Trans Med Imaging.* 2001;20:45–57.
23. Karjalainen T, Seppälä K, Glerean E, et al. Opioidergic regulation of emotional arousal: a combined PET-fMRI study. *Cereb Cortex.* 2019;29:4006–4016.
24. Nummenmaa L, Saanijoki T, Tuominen L, et al. μ-opioid receptor system mediates reward processing in humans. *Nat Commun.* 2018;9:1500.
25. McIntosh TK, Barfield RJ, Thomas D. Electrophysiological and ultrasonic correlates of reproductive behavior in the male rat. *Behav Neurosci.* 1984;98:1100–1103.
26. Leszkowicz E, Kusmierczak M, Matulewicz P, Trojniar W. Modulation of hippocampal theta rhythm by the opioid system of the pedunculopontine tegmental nucleus. *Acta Neurobiol Exp (Warsz).* 2007;67:447–460.
27. Coria-Avila GA, Herrera-Covarubias D, Ismail N, Pfaus JG. The role of orgasm in the development and shaping of partner preferences. *Socioaffect Neurosci Psychol.* 2016;6:31815.
28. Schiff ND. Central thalamic contributions to arousal regulation and neurological disorders of consciousness. *Ann N Y Acad Sci.* 2008;1129:105–118.
29. Temel Y, Visser-Vandewalle V, Ackermans L, Beuls EAM. Thalamus and penile erection. *Int J Impot Res.* 2004;16:505–511.
30. Stoléru S, Fonteille V, Cornélis C, Joyal C, Moulier V. Functional neuroimaging studies of sexual arousal and orgasm in healthy men and women: a review and meta-analysis. *Neurosci Biobehav Rev.* 2012;36:1481–1509.

# Comparative Evaluation of [$^{18}$F]5-Fluoroaminosuberic Acid and (4*S*)-4-3-[$^{18}$F]fluoropropyl)-L-Glutamate as System $x_C^-$–Targeting Radiopharmaceuticals

Milena Colovic[1,2], Hua Yang[1], Lily Southcott[1], Helen Merkens[2], Nadine Colpo[2], Francois Bénard[2,3], and Paul Schaffer[1,3,4]

[1]*Life Sciences Division, TRIUMF, Vancouver, British Columbia, Canada;* [2]*Department of Molecular Oncology, BC Cancer Research Institute, Vancouver, British Columbia, Canada;* [3]*Department of Radiology, University of British Columbia, Vancouver, British Columbia, Canada; and* [4]*Department of Chemistry, Simon Fraser University, Burnaby, British Columbia, Canada*

System $x_C^-$ is an appealing biomarker for targeting oxidative stress with oncologic PET imaging and can serve as an alternative PET biomarker to other metabolic indicators. In this paper, we report a direct comparison of 2 $^{18}$F-labeled amino acid radiopharmaceuticals targeting system $x_C^-$, [$^{18}$F]5-fluoroaminosuberic acid ([$^{18}$F]FASu) and (4*S*)-4-(3-[$^{18}$F]fluoropropyl)-L-glutamate ([$^{18}$F]FSPG), in terms of their uptake specificity and ability to image glioma and lung cancer xenografts in vivo. **Methods:** Both tracers were synthesized according to previously published procedures. In vitro uptake specificity assays were conducted using prostate (PC-3), glioblastoma (U-87), colorectal (HT-29), ovarian (SKOV3), breast (MDA-MB-231), and lung cancer (A549) cell lines. PET/CT imaging and biodistribution studies were conducted in immunocompromised mice bearing U-87 or A549 xenografts. **Results:** In vitro cell uptake assays showed that the tracers accumulated in cancer cells in a time-dependent manner and that the uptake of [$^{18}$F]FASu was blocked by the system $x_C^-$ inhibitor sulfasalazine and rose bengal, but not by system L inhibitor 2-aminobicyclo-(2,2,1)-heptane-2-carboxylic acid, system $x_{AG}^-$ inhibitor L-*trans*-pyrrolidine-2,4-dicarboxylic acid, or L-serine, which is a substrate for transporter systems A, ACS, $B^0$, and $B^{0,+}$. Conversely, [$^{18}$F]FSPG uptake decreased significantly in the presence of an excess of L-*trans*-pyrrolidine-2,4-dicarboxylic acid in 2 of 3 tested cell lines, indicating some reliance on system $x_{AG}^-$ in these cells. In an in vivo setting, [$^{18}$F]FASu and [$^{18}$F]FSPG generated good-contrast PET images in U-87 and A549 tumor–bearing mice. Tracer accumulation in A549 tumors was 5.0 ± 0.8 percentage injected dose (%ID)/g ([$^{18}$F]FASu, $n \geq 5$) and 6.3 ± 1.3 %ID/g ([$^{18}$F]FSPG, $n \geq 6$, $P = 0.7786$), whereas U-87 xenografts demonstrated uptake of 6.1 ± 2.4 %ID/g ([$^{18}$F]FASu, $n \geq 4$) and 11.2 ± 4.1 %ID/g ([$^{18}$F]FSPG, $n \geq 4$, $P = 0.0321$) at 1 h after injection. **Conclusion:** [$^{18}$F]FSPG had greater in vitro uptake than [$^{18}$F]FASu in all cell lines tested; however, our results indicate that residual uptake differences exist between [$^{18}$F]FSPG and [$^{18}$F]FASu, suggesting alternative transporter activity in the cell lines tested. In vivo studies demonstrated the ability of both [$^{18}$F]FASu and [$^{18}$F]FSPG to image glioblastoma (U-87) and non–small cell lung cancer (A549) xenografts.

**Key Words:** system $x_C^-$ transporter; tumor imaging; amino acid tracer; $^{18}$F; rose bengal

**J Nucl Med 2023; 64:1314–1321**
DOI: 10.2967/jnumed.122.265254

Oxidative stress (OS), resulting from the imbalance between the production of reactive oxygen species and their elimination by antioxidants (*1*), has been implicated in the metabolic reprogramming of cancer cells, causing them to become less sensitive to high levels of reactive oxygen species than normal cells (*1,2*). System $x_C^-$ is a transmembrane transporter protein playing a partial role in this process through its action as the primary importer of intracellular cystine (*3*), which on entry into the cell is reduced to cysteine, the rate-limiting precursor in the biosynthesis of glutathione (*2*). Glutathione is vital for the maintenance of cellular redox balance and protection from OS (*4,5*). Consequently, system $x_C^-$ is upregulated under OS and is found to be overexpressed in several different malignancies, including breast, pancreatic, and brain cancers (*6–8*). As a result, system $x_C^-$ has emerged as a promising target in PET imaging, with several $^{18}$F or $^{11}$C radiopharmaceuticals reported to target system $x_C^-$ to date (*9–14*). Among them, [$^{18}$F]5-fluoro-ASu ([$^{18}$F]FASu) and (4*S*)-4-(3-[$^{18}$F]fluoropropyl)-L-glutamate ([$^{18}$F]FSPG) are the most studied (Figs. 1A and 1B). [$^{18}$F]FSPG, a glutamate analog that demonstrated specific tumor uptake, is currently under evaluation in multiple multicenter clinical trials to determine its efficacy in detection and staging of various types of cancer, including, but not limited to, colorectal, breast, pulmonary, abdominal, and head and neck neoplasms (*15*). [$^{18}$F]FASu has been used in preclinical evaluations of breast cancer, lung cancer, and glioblastoma (*16,17*). Both tracers demonstrated the ability to target tumors with good specificity and contrast.

Herein, we report a comparative preclinical evaluation of 2 system $x_C^-$–imaging agents, [$^{18}$F]FASu and [$^{18}$F]FSPG, in tumor accumulation and specificity toward $x_C^-$. The comparison study was performed in non–small cell lung cancer (A549) and glioblastoma (U-87) cell lines and xenograft-bearing mice.

## MATERIALS AND METHODS

### Chemicals and Instrumentation

All chemicals and solvents were obtained from commercial sources and used without further purification. The quantity of injected radiofluorinated tracers was measured using a Capintec CRC-25R/W dose calibrator, and the radioactivity of mouse tissues collected from biodistribution studies was counted using a Perkin Elmer Wizard 2480 γ-counter. PET imaging experiments were conducted using an Inveon multimodality small-animal PET/CT system (Siemens Healthineers).

Received Dec. 5, 2022; revision accepted Mar. 21, 2023.
For correspondence or reprints, contact Paul Schaffer (pschaffer@triumf.ca).
Published online Apr. 28, 2023.

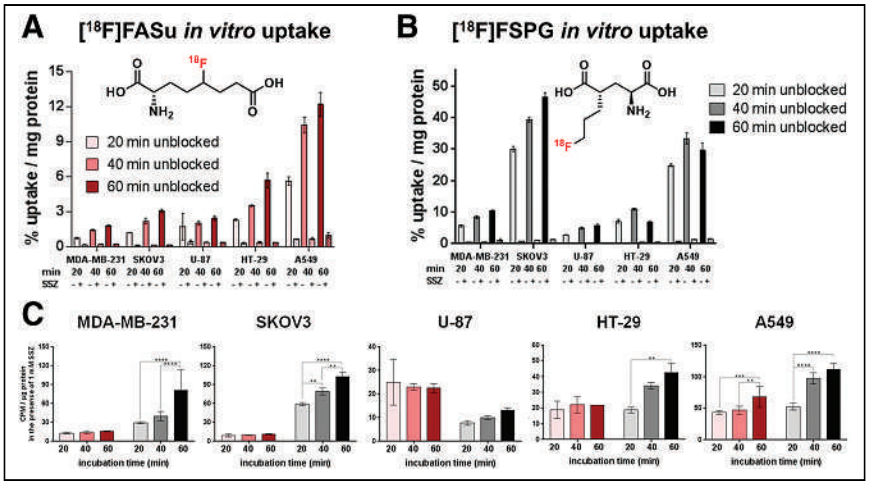


**FIGURE 1.** (A) [$^{18}$F]FASu in vitro uptake at 20, 40, and 60 min in absence and presence of xCT inhibitor sulfasalazine (1 mM). (B) [$^{18}$F]FSPG in vitro uptake at 20, 40, and 60 min in absence and presence of 1 mM sulfasalazine. Radiotracer structures are embedded into graphs. (C) [$^{18}$F]FASu and [$^{18}$F]FSPG in vitro uptake in presence of sulfasalazine (1 mM). Cells were incubated with tracer (red bars for [$^{18}$F]FASu, black bars for [$^{18}$F]FSPG) for 20, 40, or 60 min. Sulfasalazine was coadded with tracer. All uptake values are normalized to protein concentration and presented as percentage uptake per minute per milligram of protein (A and B) or as counts per minute per microgram of protein (C). SSZ = sulfasalazine. *$P < 0.05$. **$P < 0.01$. ***$P < 0.001$. ****$P < 0.0001$.

### [$^{18}$F]FASu Synthesis

[$^{18}$F]FASu was synthesized as previously reported (*18*), with a minor change in formulation. The supplemental materials provide further details (available at http://jnm.snmjournals.org). The original [$^{18}$F]FASu formulation used a trifluoroacetic acetate counterion, but for this study, we used a tracer formulated with a chloride counterion. This change was implemented to match formulations between [$^{18}$F]FASu and [$^{18}$F]FSPG. Our validation biodistribution studies indicated no statistically significant differences in biodistribution of [$^{18}$F]FASu based on the formulation used (Supplemental Fig. 1). Decay-corrected radiochemical yield (d.c. RCY) was 18 ± 6% ($n = 6$), radiochemical purity was greater than 98%, and molar activity was 17.5 ± 7 GBq/mmol ($n = 6$).

### [$^{18}$F]FSPG Synthesis

[$^{18}$F]FSPG was synthesized as previously reported (*12*). The final product was purified by an SCX cation exchange column and taken up in phosphate-buffered saline buffer. The decay-corrected radiochemical yield was 28 ± 7% ($n = 4$), radiochemical purity was greater than 98%, and molar activity was 15 ± 5 GBq/mmol ($n = 4$).

### In Vitro Uptake Specificity Studies

All cell lines used in this study were authenticated by DDC Medical.

For tracer uptake and competition studies, the tumor cells were seeded in 24-well plates at appropriate concentrations. The cell number used for seeding was adjusted for every tumor cell line to yield approximately 200,000 cells per well on the day of the uptake study. Cells were usually grown for 2–3 d under standard conditions (37°C, 5% $CO_2$) until subconfluency. The cell number on the day of the uptake assay was determined by detaching cells in 3 representative wells and counting the cells using the MOXI Z mini automated cell counter kit (Orflo). Uptake data were normalized to 100,000 cells or per the protein content in representative wells.

Before the radioactive uptake assay, the cell culture medium was removed, and the cells were washed twice with *N*-(2-hydroxyethyl)piperazine-*N*′-(2-ethanesulfonic acid) basal salt solution buffer. Radiotracers were added to the assay buffer using 148 kBq per well. For competition experiments, the cells were coincubated with competitors either in excess at 1 mM or in a dose-dependent manner (0.001–1 mM). Tracer uptake was stopped by removal of the assay buffer at the indicated time points. Cells were quickly washed twice with 400 μL of ice-cold *N*-(2-hydroxyethyl)-piperazine-*N*′-(2-ethanesulfonic acid) basal salt solution buffer and lysed with the addition of 1 M NaOH. The cell lysate was removed from the plates. Radioactivity of $^{18}$F samples was determined using a γ-counter.

### Animal Studies

All animal experiments were conducted in accordance with the guidelines established by the Canadian Council on Animal Care and approved by the Animal Ethics Committee of the University of British Columbia. Immunodeficient 129S6/SvEvTac-*Rag2*$^{tm1Fwa}$ (Rag2M) mice were bred in-house at the Animal Research Centre, British Columbia Cancer Research Institute, and used in this study. Food and water were provided ad libitum for the entire duration of the study.

### Tumor Inoculation

Mice were anesthetized briefly with 2.5% isoflurane in oxygen, 2.0 L/min, during cell implantation. After the upper back area below the left shoulder was shaved, the injection site was wiped with an alcohol prep pad, and a 28.5-gauge needle was used to subcutaneously inject approximately $5 \times 10^6$ U-87 cells or approximately $2 \times 10^6$ A549 cells (in 100 μL 1× phosphate-buffered saline and BD Matrigel Matrix at a 1:1 ratio). Biodistribution studies and PET/CT imaging were performed when tumors reached 5–7 mm in diameter.

### Biodistribution Studies

Tumor-bearing mice were briefly anesthetized with isoflurane inhalation and injected with 0.9–2.5 MBq of [$^{18}$F]FASu or [$^{18}$F]FSPG (100–200 μL in saline, intravenously). The mice were allowed to roam freely in their cages for 1 h and were then killed by $CO_2$ asphyxiation. Their blood was promptly harvested by cardiac puncture. Organs or tissues of interest were collected in a subsequent necropsy, washed with phosphate-buffered saline, blotted dry, and weighed, and their activity was counted, normalized to the injected dose, and expressed as the percentage injected dose per gram of tissue (%ID/g).

### PET Imaging and Data Analysis

Anesthetized mice were injected with 3.94–5.22 MBq through the caudal vein. A 10-min CT scan was performed, followed by a 15-min static or 60-min dynamic PET acquisition on the small-animal PET/CT scanner. PET data were acquired in list mode. After the static acquisition at 1 h after injection, the mice were killed by $CO_2$ asphyxiation, followed by cardiac puncture. The tissues of interest were harvested, weighed, and counted on the γ-counter. The PET data were reconstructed using the 3-dimensional ordered-subset expectation maximization (2 iterations) maximum a priori (18 iterations) algorithm with CT-based attenuation correction. Inveon Research Workplace software (Siemens Healthineers) was used for image analysis and drawing 3-dimensional regions of interest to determine the %ID/g of tissue for selected organs. In addition, Inveon Research Workplace software was used to generate maximum-intensity projection images for visualization.

### Statistical Analysis

All data are expressed as mean ± SD. Statistical analysis was performed using GraphPad (7.0-h) software. Two-way ANOVA analysis was performed for all tracer comparisons for in vitro and biodistribution studies. Multiple comparisons were corrected using the Šidak method. Student *t* tests were performed for all organs and tumor-to-organ ratios in the biodistribution blocking studies. The difference was considered statistically significant at a *P* value of less than 0.05.

## RESULTS

### In Vitro Cell Uptake Studies

Uptake of both [$^{18}$F]FASu and [$^{18}$F]FSPG was measured in 5 different human cancer cell lines: MDA-MB-231 (breast), U-87 (glioblastoma), HT-29 (colorectal), A549 (lung), and SKOV3 (ovarian). The uptake generally increased over time and was blocked by the system $x_C^-$ inhibitor sulfasalazine (1 mM) in all cases (Figs. 1A and 1B). [$^{18}$F]FSPG had greater uptake overall, with U-87 cells retaining 5.8% ± 0.5% activity/mg of protein at 60 min and A549 and SKOV3 exceeding 29.6% ± 2.4% uptake/mg of protein (Fig. 1B). [$^{18}$F]FASu uptake was also inhibited by the addition of sulfasalazine in all cell lines studied (Fig. 1A); however, the activity taken up by the cells in the absence of sulfasalazine ranged from 1.8% ± 0.1% uptake/mg of protein to 12.2% ± 1.0% uptake/mg of protein at 60 min in A549 cells. Figure 1C illustrates uptake values in the presence of excess sulfasalazine, where it is evident that the uptake of the 2 tracers no longer differed by severalfold, in all cell lines except SKOV3. Furthermore, we observed that the uptake of [$^{18}$F]FASu in the presence of 1 mM sulfasalazine did not change with increasing incubation time, except in A549 cells, where it increased from 0.650% ± 0.042% uptake/mg of protein at 20 min to 0.988% ± 0.242% uptake/mg of protein at 60 min ($P < 0.0001$). Under the same conditions, [$^{18}$F]FSPG uptake continued increasing with prolonged incubation in all cell lines despite the presence of 1 mM sulfasalazine, with the exception of U-87 cells, which demonstrated no significant change over time ($P = 0.7069$ for 20- vs. 60-min comparison and $P > 0.89$ for 20- vs. 40-min and 40- vs. 60-min comparisons; Fig. 1C).

In vitro specificity assays were performed in A549, U-87, and MDA-MB-231 cell lines using the system $x_C^-$ inhibitor sulfasalazine and inhibitors of the excitatory amino acid transporter protein (EAAT) family of transporters (L-*trans*-pyrrolidine-2,4-dicarboxylic acid [PDC]) (*19*) of vesicular glutamate transporters (rose bengal) (*20*) and of system L transporter (2-aminobicyclo-[2,2,1]-heptane-2-carboxylic acid) (*21–23*), in addition to L-serine, which is a known substrate of transporter systems A, ASC, $B^0$, and asc (*24*). Once again, sulfasalazine significantly inhibited uptake of both [$^{18}$F]FASu and [$^{18}$F]FSPG ($P < 0.05$ for each comparison, $n = 3$; Fig. 2; Supplemental Fig. 2). [$^{18}$F]FASu uptake was not significantly inhibited in the presence of excess PDC, L-serine, or 2-aminobicyclo-[2,2,1]-heptane-2-carboxylic acid (*P* value varied but exceeded 0.463 for each comparison). Conversely, [$^{18}$F]FSPG uptake decreased significantly in the presence of excess PDC in A549 and MDA-MB-231 cells ($P = 0.0006$ and $P = 0.0002$, respectively, equivalent to 26.7% and 28.7% uptake inhibition), but not in the U-87 cell line ($P = 0.4570$, corresponding to 8.9% uptake inhibition), which indicated possible involvement of EAATs in these cell lines. This finding is consistent with those of Koglin et al. and Greenwood et al., who also reported competition of [$^{18}$F]FSPG uptake with both aspartate and glutamate, which are the natural substrates of the EAATs (*12,24*). Moreover, we observed significant uptake blocking in the presence of L-serine in all 3 cell lines ($P = 0.0047$ for A549, $P = 0.0340$ for U-87, and $P = 0.0001$ for MDA-MB-231 cells, equivalent to 21.7%, 17.0%, and 40.2% [$^{18}$F]FSPG uptake inhibition, respectively). We also found that the most potent vesicular glutamate transporter inhibitor, rose bengal (*25*), inhibited the uptake of both [$^{18}$F]FASu and [$^{18}$F]FSPG (*P* value varied but was ≤0.0015 for each comparison) and that it had better blocking efficacy than sulfasalazine in the case of both tracers and across all cell lines studied (Fig. 2; Supplemental Fig. 3). Western blotting indicated expression of EAAT3 and EAAT4 transporters in U-87 and MDA-MB-231 whole-cell lysates (Supplemental Fig. 4). Furthermore, blotting of EAAT1 and EAAT2 indicated bands corresponding to the expression of glycosylated proteins, causing a band shift of 5–15 kDa (*26*), as well as detection of EAAT1 homodimers and homotrimers in all 3 cell lines tested.

The affinity of [$^{18}$F]FASu and [$^{18}$F]FSPG to system $x_C^-$ transporter was further studied in a dose-dependent manner in competition assays

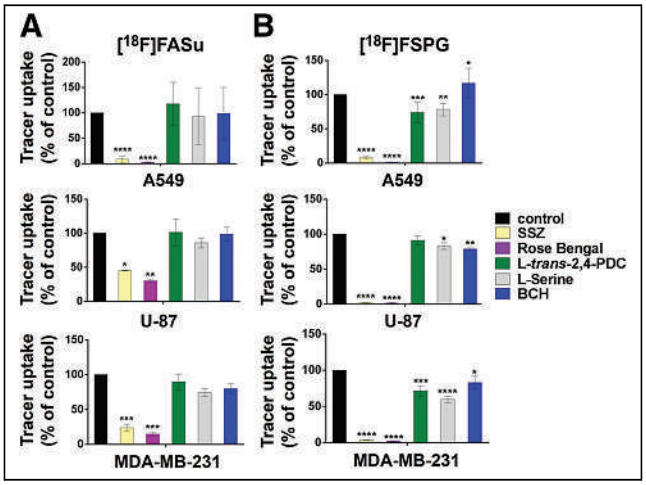


**FIGURE 2.** Two-way ANOVA analysis of 1-h uptake of [$^{18}$F]FASu (A) and [$^{18}$F]FSPG (B) in A549, U-87, and MDA-MB-231 cells, expressed as percentage of control sample uptake. BCH = 2-aminobicyclo-(2,2,1)-heptane-2-carboxylic acid. *$P < 0.05$. **$P < 0.01$. ***$P < 0.001$. ****$P < 0.0001$.

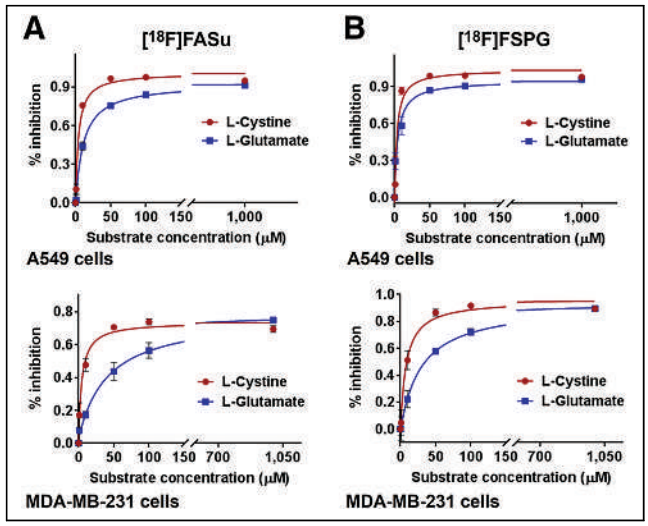


**FIGURE 3.** Dose-dependent competition cell uptake assays were performed in A549 (top) and MDA-MB-231 (bottom) cells using 148 kBq per well of either [$^{18}$F]FASu (A) or [$^{18}$F]FSPG (B) and increasing concentration of L-cystine or L-glutamate.

**TABLE 1**
Half-Maximal Inhibitory Concentrations (μM) from Tracer Competition Uptake Assays Against L-Cystine and L-Glutamate

| Substrate | Cell line | [$^{18}$F]FASu (±SE) | [$^{18}$F]FSPG (±SE) |
|---|---|---|---|
| L-Cystine | A549 | 3.92 ± 0.60 | 3.23 ± 1.01 |
| L-Glutamate | A549 | 10.93 ± 1.00 | 5.20 ± 1.18 |
| L-Cystine | MDA-MB-231 | 4.56 ± 0.89 | 7.88 ± 1.36 |
| L-Glutamate | MDA-MB-231 | 41.01 ± 6.32 | 29.29 ± 3.60 |

Assays were performed in A549 and MDA-MB-231 cells ($n$ = 3).

against the natural substrates of system $x_C^-$: L-cystine and L-glutamate. Half-maximal inhibitory concentrations of 3.92 ± 0.60 and 3.23 ± 1.01 μM were determined for L-cystine in competition with [$^{18}$F]FASu and [$^{18}$F]FSPG, respectively, in A549 cells (Fig. 3; Table 1). These values are less than the values determined in competition with L-glutamate: 10.93 ± 1.00 μM for [$^{18}$F]FASu and 5.20 ± 1.18 μM for [$^{18}$F]FSPG. Although the difference in half-maximal inhibitory concentrations for L-cystine was not significant ($P$ = 0.6503), the L-glutamate half-maximal inhibitory concentrations significantly differed ($P$ = 0.0002).

### In Vivo PET Imaging

[$^{18}$F]FASu and [$^{18}$F]FSPG were evaluated in subcutaneous models of glioblastoma (U-87) and non–small cell lung cancer (A549). The expression of xCT, the light chain subunit of system $x_C^-$, in these tumors was confirmed ex vivo with Western blotting (Supplemental Fig. 5), which revealed a greater abundance of xCT in the A549 tumor lysate. Representative decay-corrected fused PET/CT images and biodistribution data of A549 tumor–bearing Rag2M mice are shown in Figure 4A and Table 2. Both [$^{18}$F]FASu and [$^{18}$F]FSPG gave PET images with low background uptake, high image contrast, and clear tumor visualization. Renal clearance was evident from both biodistribution data and images. [$^{18}$F]FASu and [$^{18}$F]FSPG both had high pancreatic uptake: 24.93 ± 2.92 and 17.71 ± 3.63 %ID/g, respectively. Both A549 tumor and pancreatic uptake were blocked with coinjection of the nonradioactive standard aminosuberic acid (ASu, 100 mg/kg, intravenously), indicating uptake specificity of the tracers to system $x_C^-$ (Table 2) (*17*). Moreover, ASu coinjection resulted in measurable decreases in tumor-to-muscle, -brain, and -lung uptake ratios for [$^{18}$F]FASu and a decrease in tumor-to-blood ratio for [$^{18}$F]FSPG, as indicated in Table 2. Although [$^{18}$F]FSPG tumor uptake reduction with ASu coinjection was not statistically significant ($P$ = 0.0688), it is worth noting that tumor uptake decreased more than 40% with ASu coinjection. It may also be worth noting that differences in [$^{18}$F]FSPG tumor-to-brain and -muscle uptake were not significant in the presence of ASu, which is in contrast to the results obtained for [$^{18}$F]FASu. Tumor uptake of [$^{18}$F]FASu and [$^{18}$F]FSPG was 5.00 ± 0.83 and 6.27 ± 1.32 %ID/g, respectively, although it was not significantly different between [$^{18}$F]FASu and [$^{18}$F]FSPG (Figs. 4B and 4C). [$^{18}$F]FSPG had a significantly greater tumor-to-brain ratio than [$^{18}$F]FASu ($P < 0.05$); otherwise, there were no significant differences in the biodistribution of these 2 tracers.

In the case of U-87 tumor–bearing Rag2M mice, the images (Fig. 5A) and biodistribution data (Table 3) resemble those of A549 tumor–bearing animals. Radiofluorinated amino acids [$^{18}$F]FASu and [$^{18}$F]FSPG generated good-contrast PET images in xCT-expressing glioblastoma xenografts. The 2 tracers indicated a similar biodistribution pattern in the organs and tissues that were studied (Table 3). In addition to tumor, excretory organs such as the kidneys and bladder showed uptake, indicating a renal excretion pathway (Fig. 5). Blood clearance was rapid, with 0.84 ± 0.50 and 0.59 ± 0.08 %ID/g of [$^{18}$F]FASu and [$^{18}$F]FSPG present at 1 h after injection, respectively. [$^{18}$F]FASu and [$^{18}$F]FSPG both had high pancreatic uptake, 26.42 ± 11.59 and 16.81 ± 1.38 %ID/g, respectively, because of high xCT expression in this organ (*27*). U-87 tumor uptake of [$^{18}$F]FASu and [$^{18}$F]FSPG at 1 h after injection was 6.05 ± 2.40

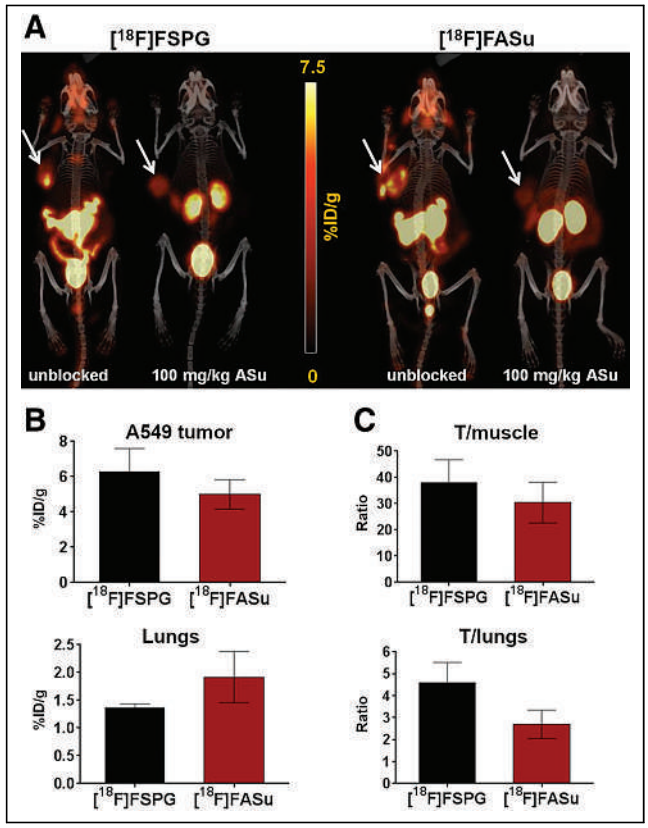


**FIGURE 4.** (A) Uptake of [$^{18}$F]FSPG and [$^{18}$F]FASu in A549 tumor–bearing mice at 1 h after injection with and without blocking reagent (100 mg/kg ASu). Arrows indicate location of A549 tumors on fused PET/CT maximum-intensity projection images. (B and C) Two-way ANOVA of tumor-to-muscle and tumor-to-lung ratios (C) and tumor and lung uptake (B) for [$^{18}$F]FSPG and [$^{18}$F]FASu in A549 tumor–bearing mice at 1 h after injection. $P$ value varied for each comparison but was always >0.05. T = tumor.

**TABLE 2**
Biodistribution and Tumor-to-Nontarget Ratios of [$^{18}$F]FASu and [$^{18}$F]FSPG in A549 Xenograft–Bearing Rag2M Mice

| | [$^{18}$F]FASu | | [$^{18}$F]FSPG | |
|---|---|---|---|---|
| Organ | Unblocked ($n$ = 6) | 100 mg/kg ASu* ($n$ = 4) | Unblocked ($n$ = 6) | 100 mg/kg ASu* ($n$ = 4) |
| Blood | 0.78 ± 0.44 | 0.64 ± 0.11 | 0.51 ± 0.08 | 0.55 ± 0.16 |
| Fat | 0.04 ± 0.01 | 0.04 ± 0.01 | 0.03 ± 0.01 | 0.02 ± 0.00 |
| Ovaries | 2.91 ± 0.50 | 0.91 ± 0.21† | 9.13 ± 2.77 | 1.14 ± 0.20† |
| Uterus | 7.96 ± 2.88 | 0.59 ± 0.11† | 6.29 ± 2.99 | 0.91 ± 0.34 |
| Small intestine | 2.53 ± 0.21 | 0.87 ± 0.61† | 2.51 ± 0.37 | 0.46 ± 0.13† |
| Stomach | 0.66 ± 0.12 | 0.61 ± 0.42 | 0.85 ± 0.29 | 0.33 ± 0.18 |
| Pancreas | 24.93 ± 2.92 | 3.96 ± 1.18† | 17.71 ± 3.63 | 3.99 ± 0.70† |
| Spleen | 3.89 ± 2.01 | 1.04 ± 0.26 | 6.14 ± 0.84 | 1.02 ± 0.20† |
| Adrenal glands | 0.65 ± 0.15 | 0.51 ± 0.24 | 0.53 ± 0.05 | 0.59 ± 0.16 |
| Kidneys | 13.29 ± 1.60 | 22.19 ± 5.85 | 17.49 ± 2.11 | 21.07 ± 10.60 |
| Liver | 0.74 ± 0.08 | 0.75 ± 0.17 | 0.63 ± 0.13 | 0.60 ± 0.32 |
| Heart | 0.24 ± 0.06 | 0.26 ± 0.05 | 0.16 ± 0.03 | 0.17 ± 0.08 |
| Lungs | 1.92 ± 0.46 | 2.66 ± 0.28 | 1.36 ± 0.07 | 1.00 ± 0.37 |
| Muscle | 0.15 ± 0.02 | 0.16 ± 0.03 | 0.17 ± 0.05 | 0.10 ± 0.03 |
| Bone | 0.56 ± 0.08 | 0.33 ± 0.07† | 0.14 ± 0.04 | 0.20 ± 0.07 |
| Brain | 0.13 ± 0.02 | 0.09 ± 0.01 | 0.64 ± 0.21 | 0.09 ± 0.04 |
| Tail | 1.25 ± 0.20 | 0.75 ± 0.29 | 0.21 ± 0.01 | 0.44 ± 0.20† |
| A549 tumor | 5.00 ± 0.83 | 2.04 ± 0.36† | 6.27 ± 1.32 | 3.53 ± 0.69 |
| Tumor/blood | 7.61 ± 3.58 | 3.22 ± 0.58 | 12.36 ± 2.52 | 6.67 ± 1.81† |
| Tumor/muscle | 33.18 ± 4.39 | 13.72 ± 4.40† | 37.92 ± 9.55 | 39.15 ± 11.34 |
| Tumor/lungs | 2.70 ± 0.65 | 0.78 ± 0.20† | 4.59 ± 0.92 | 3.77 ± 1.17 |
| Tumor/brain | 39.79 ± 6.67 | 23.40 ± 6.53† | 52.95 ± 10.29 | 45.58 ± 17.86 |

*Blocked with coinjection of cold standard, ASu.
†Coinjection significantly reduced uptake of same organ for tracer or tumor-to-organ ratio ($P < 0.05$).
Biodistributions and ratios are at 1 h after injection. Values (%ID/g) are presented as mean ± SD.

and 11.18 ± 4.12 %ID/g, respectively. Glioblastoma xenograft uptake of [$^{18}$F]FSPG was significantly greater than that of [$^{18}$F]FASu ($P < 0.05$), as were tumor-to-muscle and tumor-to-brain uptake ratios ($P < 0.0001$; Figs. 5B and 5C). Region-of-interest analysis of the dynamic scans with [$^{18}$F]FASu and [$^{18}$F]FSPG in U-87 tumor–bearing mice showed a steady increase of tracer uptake by the tumor and a clear delineation from the background activity, as evident on the time–activity curves (Supplemental Fig. 6).

## DISCUSSION

Cellular antioxidant machinery functions as a tightly controlled system, in which the purpose is to maintain an intracellular redox balance (*28,29*). Glutathione is a major endogenous nonenzymatic antioxidant involved in reactive oxygen species neutralization and containment of intracellular OS levels (*30*). Given the dependency of glutathione biosynthesis on the import of cystine into the cell, system $x_C^-$ is considered a marker of cellular OS (*10*) and, as such, has become an appealing target for therapeutic and imaging purposes. The aim of this study was to directly compare the uptake specificity, biodistribution profile, and imaging utility of 2 tracers targeting system $x_C^-$, both of which have previously been reported as promising noninvasive tools for imaging of intracellular redox status.

In vitro uptake studies indicate system $x_C^-$–mediated uptake of both [$^{18}$F]FASu and [$^{18}$F]FSPG. We found that [$^{18}$F]FSPG was taken up more readily in vitro and that it had severalfold greater uptake than [$^{18}$F]FASu in all tested cell lines. We hypothesize that this could be because of reliance of [$^{18}$F]FSPG on other modes of transport across the plasma membrane, and we tested this hypothesis in a series of specificity assays in which we measured uptake of each tracer in the presence of several different amino acid transporter inhibitors (Fig. 2). In at least 2 of 3 tested cell lines, [$^{18}$F]FSPG uptake was significantly inhibited by PDC and L-serine ($P < 0.05$), indicating some involvement of EAATs and numerous serine transporters in the import of this tracer into these cells. Furthermore, we were able to detect the expression of EAAT3 and EAAT4 and predicted glycoproteins of EAAT1 and EAAT2 (*26*) in these cell lines (Supplemental Fig. 4), further supporting our hypothesis that there might be some reliance on EAATs in the import of [$^{18}$F]FSPG into these cells. An additional finding in this study was the ability of rose bengal, a known vesicular glutamate transporter inhibitor, to block transport of both [$^{18}$F]FASu and [$^{18}$F]FSPG across the plasma membrane in all cell lines studied

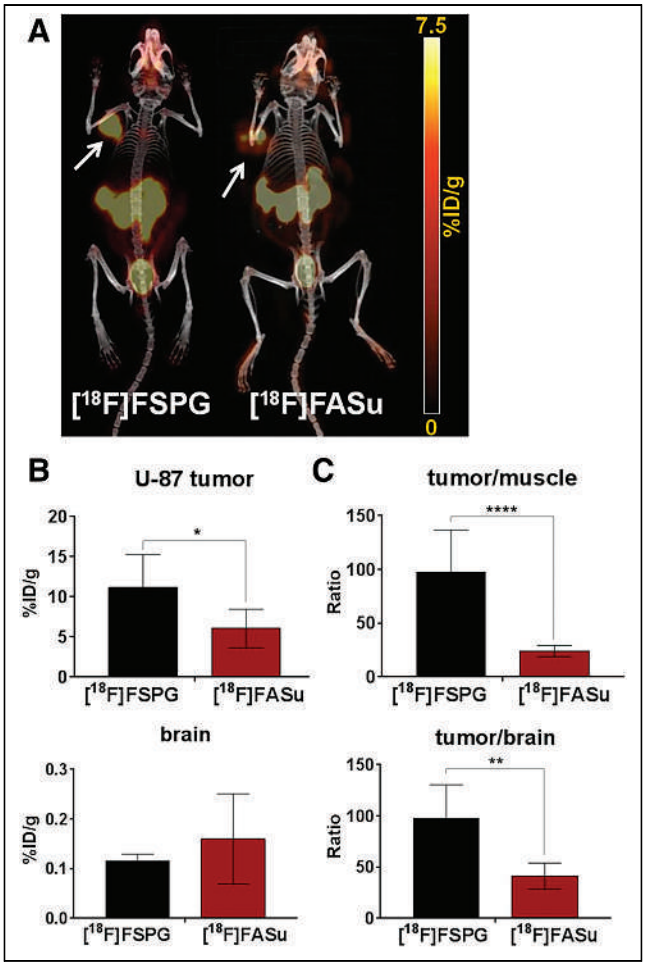


**FIGURE 5.** Comparative study. (A) Uptake of [$^{18}$F]FSPG and [$^{18}$F]FASu in U-87 tumor–bearing mice at 1 h after injection. Arrows indicate location of U-87 tumors on fused PET/CT maximum-intensity projection images. (B and C) Two-way ANOVA of tumor-to-muscle and tumor-to brain ratios (C) and tumor and brain uptake (B) for [$^{18}$F]FSPG and [$^{18}$F]FASu in U-87 tumor–bearing mice at 1 h after injection. *$P < 0.05$. **$P < 0.01$. ****$P < 0.0001$.

($P < 0.01$; Fig. 2). When coincubated with either one of these 2 radiotracers, rose bengal caused a dose-dependent reduction in intracellular tracer content (Supplemental Fig. 3). Only 10 μM rose bengal was sufficient to prevent greater than 90% of activity from entering A549 cells, which is equivalent to the percentage inhibition achieved by 1 mM sulfasalazine in this study. With these results, the finding that rose bengal inhibits system $x_C^-$ raises the prospect that this compound may induce a therapeutic response (*31,32*) via glutathione depletion, thus sensitizing the target tissue to other chemotherapeutics (*6,33–35*).

[$^{18}$F]FASu and [$^{18}$F]FSPG biodistribution and imaging potential was tested in mice bearing U-87 and A549 xenografts. These 2 tumor models were selected for the in vivo experiments because of their disparate uptake pattern in vitro. U-87 cells were on the lower end of the uptake spectra of both tracers, and no increase in blocked uptake of either tracer was evident in vitro. The lung cancer cells, A549, conversely, demonstrated high in vitro uptake of both radiotracers and increasing uptake over time despite oversaturation with sulfasalazine, which is a system $x_C^-$ inhibitor.

**TABLE 3**
Biodistribution and Tumor-to-Nontarget Ratios of [$^{18}$F]FASu and [$^{18}$F]FSPG in U-87 Xenograft–Bearing Rag2M Mice

| Organ | [$^{18}$F]FASu | [$^{18}$F]FSPG |
|---|---|---|
| Organ | Unblocked ($n \geq 4$) | Unblocked ($n \geq 4$) |
| Blood | 0.84 ± 0.50 | 0.59 ± 0.08 |
| Fat | 0.04 ± 0.02 | 0.02 ± 0.00 |
| Ovaries | 3.07 ± 1.48 | 5.62 ± 4.09 |
| Uterus | 5.97 ± 3.08 | 5.07 ± 0.73 |
| Small intestine | 1.83 ± 0.64 | 2.18 ± 0.40 |
| Stomach | 1.66 ± 1.13 | 1.08 ± 0.73 |
| Pancreas | 26.42 ± 11.59 | 16.81 ± 1.38 |
| Spleen | 4.47 ± 1.65 | 6.58 ± 1.58 |
| Adrenal glands | 0.46 ± 0.15 | 0.55 ± 0.05 |
| Kidneys | 17.79 ± 7.20 | 17.92 ± 2.49 |
| Liver | 0.95 ± 0.44 | 0.59 ± 0.14 |
| Heart | 0.36 ± 0.21 | 0.17 ± 0.01 |
| Lungs | 3.41 ± 2.20 | 1.39 ± 0.16 |
| Muscle | 0.26 ± 0.11 | 0.12 ± 0.02 |
| Bone | 0.76 ± 0.46 | 0.76 ± 0.17 |
| Brain | 0.16 ± 0.09 | 0.12 ± 0.01 |
| Tail | 1.82 ± 0.90 | 1.26 ± 0.24 |
| U-87 tumor | 6.05 ± 2.40 | 11.18 ± 4.12 |
| Tumor/blood | 7.96 ± 2.81 | 18.67 ± 6.30 |
| Tumor/muscle | 24.08 ± 5.20 | 97.86 ± 38.99 |
| Tumor/lungs | 1.96 ± 0.51 | 8.04 ± 2.60 |
| Tumor/brain | 41.30 ± 12.73 | 97.22 ± 33.15 |

Biodistributions and ratios are at 1 h after injection. Values (%ID/g) are presented as mean ± SD.

In contrast to the in vitro uptake, [$^{18}$F]FASu and [$^{18}$F]FSPG have similar biodistribution profiles and excretion pathways, irrespective of the tumor inoculated (A549 or U-87; Tables 2 and 3). Both tracers exhibited low background uptake and moderate to high tumor-to-blood, tumor-to-brain, and tumor-to-muscle ratios. The principal difference between [$^{18}$F]FASu and [$^{18}$F]FSPG was found in the greater in vivo tumor uptake of the latter, with significantly greater uptake in the U-87 tumor (Fig. 5B; $P < 0.05$) yet nonsignificantly greater uptake in A549 tumors (Fig. 4B; $P = 0.79$), despite greater xCT expression in these tumors (Supplemental Fig. 5). This may be an indication that [$^{18}$F]FSPG is transported into the cells by the action of alternative transporters, including the EAATs, or system $x_{AG}^-$, in addition to system $x_C^-$ (*36*). Moreover, an early report on the specificity of [$^{18}$F]FSPG by Koglin et al. (*12*) demonstrated that, although [$^{18}$F]FSPG does predominantly use system $x_C^-$ to enter cells, both L-cystine and L-glutamate achieved higher levels of tracer uptake inhibition than a potent system $x_C^-$ inhibitor, *p*-carboxy-phenylglycine, indicating that [$^{18}$F]FSPG may be a suitable substrate for other AATs that include L-glutamate or L-cystine as substrates, such as EAATs (EAAT1, EAAT2, EAAT4, and EAAT5 for L-glutamate and EAAT3 for both) (*24*). The authors also reported observing a minor competition with either L- or

D-aspartate, both of which are substrates along with L-glutamate for the EAAT family members 1–5 (*24*). Webster et al. (*10*) performed a similar in vitro uptake inhibition uptake assay with [$^{18}$F]FASu, and in their study, sulfasalazine was more effective in blocking tracer uptake than L-glutamate, signifying a preference of [$^{18}$F]FASu for system $x_C^-$. The authors reported observing little effect of D-aspartate on [$^3$H]ASu, [$^3$H]Glu, and [$^3$H]Leu uptake, which is in agreement with our finding reported here that [$^{18}$F]FASu uptake was not affected by the system $x_{AG}^-$ inhibitor PDC.

Notwithstanding the data presented here, we are aware of other potential explanations for the in vitro uptake fluctuations of [$^{18}$F]FSPG involving the complex interplay between amino acid transporters and their respective substrates. Inhibition of EAATs has been previously shown to alter intracellular glutamate levels, which are known to affect system $x_C^-$ activity (*37*). Given that fluctuations in intracellular glutamate levels also affect [$^{18}$F]FSPG retention (*38*) because of system $x_C^-$–mediated exchange, this phenomenon may account for changes in cell retention together with alternative transport mechanisms. Moreover, serine is a precursor for the biosynthesis of cysteine, the levels of which have been shown to affect [$^{18}$F]FSPG retention in cells through $x_C^-$ exchange (*38*).

Several recent studies have examined the potential use of [$^{18}$F]FSPG and [$^{18}$F]FASu for measuring intracellular redox status. McCormick et al. found that in vitro [$^{18}$F]FSPG uptake in ovarian cancer cells was sensitive to an elevation in glutathione biosynthesis after drug-induced OS (*38*). Our group recently reported a positive correlation between in vitro [$^{18}$F]FASu uptake and intracellular glutathione fluctuations in breast cancer models caused by radiation- and diethylmaleate-induced OS (*17*). Despite the methodic and detailed approach taken in previous studies, a side-by-side study comparing [$^{18}$F]FASu and [$^{18}$F]FSPG in the same cancer model became warranted to better understand the subtleties in tracer behavior. The data presented here suggest that the degree of non–system $x_C^-$ uptake may vary depending on the cancer model studied and the mode of action of the OS-inducing drug used. Other reports testify to the emerging (poor) prognostic significance of xCT/*SLC7A11* overexpression in several different malignancies, including non–small cell lung cancer (*39*), laryngeal squamous cell carcinoma (*40*), glioblastoma (*41,42*), hepatocellular carcinoma (*43*), colorectal cancer (*44,45*), and acute myeloid leukemia (*46,47*). Additional studies speak to the increasing potential of using xCT-targeting therapeutics to sensitize cancers to chemotherapy or radiation therapy (*6,33–35,48–50*). Therefore, early identification of xCT-expressing tumors would help with patient stratification, treatment plan development, and therapeutic monitoring and intervention because xCT has been recognized as an emerging therapeutic or adjuvant target.

The main objective of this work was to compare the 2 tracers with respect to their specificity for the target transporter and tumor visualization potential. [$^{18}$F]FSPG is currently in use in pilot clinical studies (*51–53*) and is showing promise as a marker of therapeutic response in the preclinical setting in high-grade serous ovarian cancer models (*54*). [$^{18}$F]FASu performed as well as [$^{18}$F]FSPG as an in vivo oncologic imaging agent in a preclinical setting and may warrant further consideration for clinical use.

## CONCLUSION

We found that [$^{18}$F]FSPG is taken up more readily in vitro by all cell lines tested, whereas ex vivo biodistribution was generally equivalent between [$^{18}$F]FSPG and [$^{18}$F]FASu, with the exception of greater [$^{18}$F]FSPG uptake in glioblastoma xenografts. This study examined the participation of alternative AATs, such as system $x_{AG}^-$, in the transport of both tracers. Nevertheless, we found that [$^{18}$F]FSPG and [$^{18}$F]FASu have comparable biodistribution and tumor-imaging ability in vivo, supporting the further pursuit of either tracer for non-[$^{18}$F]FDG oncologic imaging.

## DISCLOSURE

This work was supported by the CIHR (grants 201403COP and 329895). TRIUMF receives federal funding via a contribution agreement with the National Research Council of Canada. This work was supported in part by the BC Leading Edge Endowment Fund. Milena Colovic received support from an NSERC CREATE IsoSiM fellowship, grant 448110, competition year 2014. No other potential conflict of interest relevant to this article was reported.

## ACKNOWLEDGMENTS

We thank the TRIUMF TR13 cyclotron team, in particular David Prevost, Linda Graham, and Samuel Varah, for technical assistance.

**KEY POINTS**

**QUESTION:** How do the 2 system $x_C^-$ imaging agents, [$^{18}$F]FASu and [$^{18}$F]FSPG, compare with respect to their uptake specificity and tumor imaging potential?

**PERTINENT FINDINGS:** Our in vitro specificity assays indicated greater overall uptake of [$^{18}$F]FSPG than of [$^{18}$F]FASu but also potential participation of other AA transporters. Moreover, we found that rose bengal inhibited uptake of both tracers in vitro. In preclinical subjects, however, both tracers were successful at visualizing glioma (U-87) and lung cancer (A549) xenografts and had comparable tumor uptake and pharmacokinetics.

**IMPLICATIONS FOR PATIENT CARE:** [$^{18}$F]FASu and [$^{18}$F]FSPG are redox PET tracers that, when translated into the clinic, have the potential to serve as indicators of the redox state of the lesion, companion diagnostics, and, potentially, patient prognosis.

## REFERENCES

1. Reuter S, Gupta SC, Chaturvedi MM, Aggarwal BB. Oxidative stress, inflammation, and cancer: how are they linked? *Free Radic Biol Med.* 2010;49:1603–1616.
2. Gorrini C, Harris IS, Mak TW. Modulation of oxidative stress as an anticancer strategy. *Nat Rev Drug Discov.* 2013;12:931–947.
3. Bridges RJ, Natale NR, Patel SA. System $x_c^-$ cystine/glutamate antiporter: an update on molecular pharmacology and roles within the CNS. *Br J Pharmacol.* 2012;165:20–34.
4. Conrad M, Sato H. The oxidative stress-inducible cystine/glutamate antiporter, system $x_c^-$: cystine supplier and beyond. *Amino Acids.* 2012;42:231–246.
5. Sato H, Ishii T, Kuriyama-Matsumura K, et al. Effect of oxygen on induction of the cystine transporter by bacterial lipopolysaccharide in mouse peritoneal macrophages. *J Biol Chem.* 2002;276:10407–10412.
6. Timmerman LA, Holton T, Yuneva M, et al. Glutamine sensitivity analysis identifies the xCT antiporter as a common triple negative breast tumor therapeutic target. *Cancer Cell.* 2013;24:450–465.
7. Nakanishi T, Tamai I. Solute carrier transporters as targets for drug delivery and pharmacological intervention for chemotherapy. *J Pharm Sci.* 2011;100:3731–3750.
8. Ganapathy V, Thangaraju M, Prasad PD. Nutrient transporters in cancer: relevance to Warburg hypothesis and beyond. *Pharmacol Ther.* 2009;121:29–40.
9. Yang H, Miao Q, Johnson BF, et al. A simple route to [$^{11}$C]N-Me labeling of aminosuberic acid for proof of feasibility imaging of the $x_C^-$ transporter. *Bioorg Med Chem Lett.* 2014;24:5512–5515.

10. Webster JM, Morton CA, Johnson BF, et al. Functional imaging of oxidative stress with a novel PET imaging agent, $^{18}$F-5-fluoro-L-aminosuberic acid. *J Nucl Med.* 2014;55:657–664.
11. Krasikova RN, Kuznetsova OF, Fedorova OS, et al. 4-[$^{18}$F]fluoroglutamic acid (BAY 85-8050), a new amino acid radiotracer for PET imaging of tumors: synthesis and in vitro characterization. *J Med Chem.* 2011;54:406–410.
12. Koglin N, Mueller A, Berndt M, et al. Specific PET imaging of $x_C^-$ transporter activity using a $^{18}$F-labeled glutamate derivative reveals a dominant pathway in tumor metabolism. *Clin Cancer Res.* 2011;17:6000–6011.
13. Beinat C, Gowrishankar G, Shen B, et al. The characterization of $^{18}$F-hGTS13 for molecular imaging of $x_C^-$ transporter activity with positron emission tomography. *J Nucl Med.* 2019;60:1812–1817.
14. Greenwood HE, Edwards R, Koglin N, et al. Radiotracer stereochemistry affects substrate affinity and kinetics for improved imaging of system $x_C^-$ in tumors. *Theranostics.* 2022;12:1921–1936.
15. ClinicalTrial.gov website. https://clinicaltrials.gov/ct2/results?cond=cancer&term=fspg&cntry=&state=&city=&dist=. Published November 2015. Accessed April 12, 2023.
16. Yang H, Jenni S, Colovic M, et al. $^{18}$F-5-fluoroaminosuberic acid as a potential tracer to gauge oxidative stress in breast cancer models. *J Nucl Med.* 2017; 58:367–373.
17. Čolović M, Yang H, Merkens H, Colpo N, Bénard F, Schaffer P. Non-invasive use of positron emission tomography to monitor diethyl maleate and radiation-induced changes in system $x_C^-$ activity in breast cancer. *Mol Imaging Biol.* 2019; 21:1107–1116.
18. Yang H, Tam B, Čolović M, et al. Addressing chirality in the structure and synthesis of [$^{18}$F]5-fluoroaminosuberic acid ([$^{18}$F]FASu). *Chemistry.* 2017;23: 11100–11107.
19. Lewerenz J, Klein M, Methner A. Cooperative action of glutamate transporters and cystine/glutamate antiporter system $x_c^-$ protects from oxidative glutamate toxicity. *J Neurochem.* 2006;98:916–925.
20. Neale SA, Copeland CS, Salt TE. Effect of VGLUT inhibitors on glutamatergic synaptic transmission in the rodent hippocampus and prefrontal cortex. *Neurochem Int.* 2014;73:159–165.
21. Haase C, Bergmann R, Fuechtner F, Hoepping A, Pietzsch J. L-type amino acid transporters LAT1 and LAT4 in cancer: uptake of 3-O-methyl-6-$^{18}$F-fluoro-L-dopa in human adenocarcinoma and squamous cell carcinoma in vitro and in vivo. *J Nucl Med.* 2007;48:2063–2071.
22. Kim CS, Cho SH, Chun HS, Lee SY, Ndou HE. BCH, an inhibitor of system L amino acid transporters, induces apoptosis in cancer cells. *Biol Pharm Bull.* 2008; 31:1096–1100.
23. Wagner CA, Lang F, Broer S. Function and structure of heterodimeric amino acid transporters. *Am J Physiol Cell Physiol.* 2001;281:C1077–C1093.
24. Bröer S, Bröer A. Amino acid homeostasis and signalling in mammalian cells and organisms. *Biochem J.* 2017;474:1935–1963.
25. Pietrancosta N, Kessler A, Favre-Besse FC, et al. Rose Bengal analogs and vesicular glutamate transporters (VGLUTs). *Bioorg Med Chem.* 2010;18:6922–6933.
26. Parkin GM, Udawela M, Gibbons A, Dean B. Glutamate transporters, EAAT1 and EAAT2, are potentially important in the pathophysiology and treatment of schizophrenia and affective disorders. *World J Psychiatry.* 2018;8:51–63.
27. Lewerenz J, Hewett SJ, Huang Y, et al. The cystine/glutamate antiporter system $x_c^-$ in health and disease: from molecular mechanisms to novel therapeutic opportunities. *Antioxid Redox Signal.* 2013;18:522–555.
28. Phaniendra A, Jestadi DB, Periyasamy L. Free radicals: properties, sources, targets, and their implication in various diseases. *Indian J Clin Biochem.* 2015;30:11–26.
29. Cairns RA, Harris IS, Mak TW. Regulation of cancer cell metabolism. *Nat Rev Cancer.* 2011;11:85–95.
30. Trachootham D, Alexandre J, Huang P. Targeting cancer cells by ROS-mediated mechanisms: a radical therapeutic approach? *Nat Rev Drug Discov.* 2009;8:579–591.
31. Ross MI. Intralesional therapy with PV-10 (Rose Bengal) for in-transit melanoma. *J Surg Oncol.* 2014;109:314–319.
32. Read TA, Smith A, Thomas J, et al. Intralesional PV-10 for the treatment of in-transit melanoma metastases: results of a prospective, non-randomized, single center study. *J Surg Oncol.* 2018;117:579–587.
33. Daher B, Parks SK, Durivault J, et al. Genetic ablation of the cystine transporter xCT in PDAC cells inhibits mTORC1, growth, survival, and tumor formation via nutrient and oxidative stresses. *Cancer Res.* 2019;79:3877–3890.
34. Sato M, Kusumi R, Hamashima S, et al. The ferroptosis inducer erastin irreversibly inhibits system $x_c^-$ and synergizes with cisplatin to increase cisplatin's cytotoxicity in cancer cells. *Sci Rep.* 2018;8:968.
35. Yoshikawa M, Tsuchihashi K, Ishimoto T, et al. XCT inhibition depletes CD44v-expressing tumor cells that are resistant to EGFR-targeted therapy in head and neck squamous cell carcinoma. *Cancer Res.* 2013;73:1855–1866.
36. Hyde R, Taylor PM, Hundal HS. Amino acid transporters: roles in amino acid sensing and signalling in animal cells. *Biochem J.* 2003;373:1–18.
37. Bannai S, Ishii T. A novel function of glutamine in cell culture: utilization of glutamine for the uptake of cystine in human fibroblasts. *J Cell Physiol.* 1988;137: 360–366.
38. McCormick PN, Greenwood HE, Glaser M, et al. Assessment of tumor redox status through (S)-4-(3-[$^{18}$F]fluoropropyl)-L-glutamic acid PET imaging of system $x_C^-$ activity. *Cancer Res.* 2019;79:853–863.
39. Ji X, Qian J, Rahman SMJ, et al. xCT (SLC7A11)-mediated metabolic reprogramming promotes non-small cell lung cancer progression. *Oncogene.* 2018;37:5007–5019.
40. Ma Z, Zhang H, Lian M, et al. SLC7A11, a component of cysteine/glutamate transporter, is a novel biomarker for the diagnosis and prognosis in laryngeal squamous cell carcinoma. *Oncol Rep.* 2017;38:3019–3029.
41. Takeuchi S, Wada K, Toyooka T, et al. Increased xCT expression correlates with tumor invasion and outcome in patients with glioblastomas. *Neurosurgery.* 2013; 72:33–41.
42. Robert SM, Buckingham SC, Campbell SL, et al. SLC7A11 expression is associated with seizures, predicts poor survival in patients with malignant glioma. *Sci Transl Med.* 2015;7:289ra86.
43. Zhang L, Huang Y, Ling J, et al. Overexpression of SLC7A11: a novel oncogene and an indicator of unfavorable prognosis for liver carcinoma. *Future Oncol.* 2018; 14:927–936.
44. Lim JKM, Delaidelli A, Minaker SW, et al. Cystine/glutamate antiporter xCT (SLC7A11) facilitates oncogenic RAS transformation by preserving intracellular redox balance. *Proc Natl Acad Sci USA.* 2019;116:9433–9442.
45. Sugano K, Maeda K, Ohtani H, Nagahara H, Shibutani M, Hirakawa K. Expression of xCT as a predictor of disease recurrence in patients with colorectal cancer. *Anticancer Res.* 2015;35:677–682.
46. Zhao X, Li Y, Wu H. A novel scoring system for acute myeloid leukemia risk assessment based on the expression levels of six genes. *Int J Mol Med.* 2018;42: 1495–1507.
47. Lin W, Wang C, Liu G, et al. SLC7A11/xCT in cancer: biological functions and therapeutic implications. *Am J Cancer Res.* 2020;10:3106–3126.
48. Wada F, Koga H, Akiba J, et al. High expression of CD44v9 and xCT in chemoresistant hepatocellular carcinoma: potential targets by sulfasalazine. *Cancer Sci.* 2018;109:2801–2810.
49. Polewski MD, Reveron-Thornton RF, Cherryholmes GA, Marinov GK, Aboody KS. SLC7A11 overexpression in glioblastoma is associated with increased cancer stem cell-like properties. *Stem Cells Dev.* 2017;26:1236–1246.
50. Cobler L, Zhang H, Suri P, Park C, Timmerman LA. xCT inhibition sensitizes tumors to γ-radiation via glutathione reduction. *Oncotarget.* 2018;9:32280–32297.
51. Baek S, Choi CM, Ahn S, et al. Exploratory clinical trial of (4S)-4-(3-[$^{18}$F]fluoropropyl)-L-glutamate for imaging $x_C^-$ transporter using positron emission tomography in patients with non-small cell lung or breast cancer. *Clin Cancer Res.* 2012; 18:5427–5437.
52. Baek S, Mueller A, Lim Y, et al. (4S)-4-(3-$^{18}$F-fluoropropyl)-L-glutamate for imaging of $x_C^-$ transporter activity in hepatocellular carcinoma using PET: preclinical and exploratory clinical studies. *J Nucl Med.* 2013;54:117–123.
53. Kavanaugh G, Williams J, Morris AS, et al. Utility of [$^{18}$F]FSPG PET to image hepatocellular carcinoma: first clinical evaluation in a US population. *Mol Imaging Biol.* 2016;18:924–934.
54. Greenwood HE, McCormick PN, Gendron T, et al. Measurement of tumor antioxidant capacity and prediction of chemotherapy resistance in preclinical models of ovarian cancer by positron emission tomography. *Clin Cancer Res.* 2019;25: 2471–2482.

# $^{161}$Tb-PSMA Radioligand Therapy: First-in-Humans SPECT/CT Imaging

Akram Al-Ibraheem[1], Rahma M. Doudeen[1], Diyaa Juaidi[1], Alaa Abufara[2], and Stephan Maus[3]

*[1]Department of Nuclear Medicine, King Hussein Cancer Center, Amman, Jordan; [2]Department of Internal Medicine, King Hussein Cancer Center, Amman, Jordan; and [3]Department of Nuclear Medicine, Universitätsklinikum des Saarlandes, Homburg, Germany*

Terbium-161 is a β-emitting radionuclide that resembles $^{177}$Lu in terms of its in vivo and in vitro chemical and pharmacokinetic properties, exhibiting similar behavior with regard to radioligand-specific cell uptake and internalization, as well as emitting a modest fraction of photons useful for post-therapy imaging. Unlike $^{177}$Lu, a significant amount of conversion and Auger electrons are emitted per decay, making it particularly appealing for targeted radionuclide therapy (*1*).

Here, we present whole-body scintigraphic and SPECT/CT images acquired with $^{161}$Tb-PSMA-617 in a 69-y-old man diagnosed with metastatic prostate cancer refractory to hormonal therapy and chemotherapy who was referred for PSMA radioligand therapy (Fig. 1).

The patient received an empiric well-tolerated dose of $^{161}$Tb-PSMA-617 (5,550 MBq) without having acute or early adverse events (compassionate use on a named-patient basis under the local regulatory framework and international ethical and radiation safety standards).

Two γ-energies with high frequencies were identified from the decay scheme of $^{161}$Tb: 48.9 keV with a 17% frequency and 74.5 keV with a 10.2% frequency (*1*). As a result, whole-body planar and SPECT/CT scanning protocols have been created. Spatiotemporal distribution of the radionuclide in the target and nontarget potentially dose-limiting organs was obtained by acquiring time-sequential planar and SPECT/CT datasets: 18 h after injection, 69 h after injection, and 90 h after injection. SPECT/CT images were acquired from the lower cervical level to the pelvis at 69 h after injection, aiding in more refined image-derived activity quantification and characterization of tissue kinetics. The obtained images were of

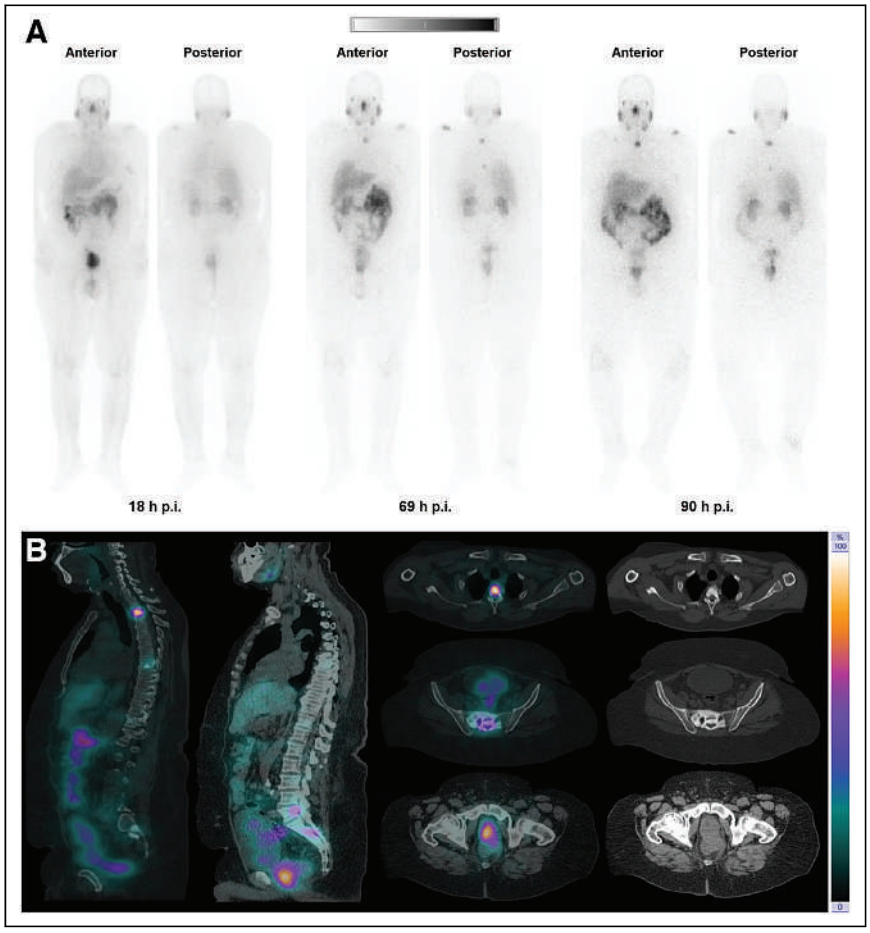


**FIGURE 1.** (A) Whole-body images at different time points after injection. (B) Representative SPECT/CT sagittal and axial slices and CT axial slices demonstrating physiologic biodistribution of $^{161}$Tb-PSMA in lacrimal, parotid, and submandibular glands; nasopharyngeal mucosa; liver; intestinal tract; kidneys; and urinary bladder, as well as pathologic uptake in primary prostate tumor and metastatic bone lesions. p.i. = after injection.

Received Dec. 5, 2022; revision accepted Jan. 31, 2023.
For correspondence or reprints, contact Akram Al-Ibraheem (aibraheem@khcc.jo).
Published online Feb. 9, 2023.

DOI: 10.2967/jnumed.122.265291

good quality, enabling visualization of all previously identified PSMA-avid primary and metastatic bone lesions using a $^{68}$Ga-PSMA PET/CT scan.

In-human posttherapy imaging with $^{161}$Tb SPECT/CT has been proposed as a predefined clinical protocol using a radiolabeled somatostatin analog of up to 113 h after injection (*2*). We present here, to the best of our knowledge, the first-in-humans posttherapy $^{161}$Tb-PSMA SPECT/CT imaging.

## DISCLOSURE

No potential conflict of interest relevant to this article was reported.

## REFERENCES


1. Müller C, Umbricht CA, Gracheva N, et al. Terbium-161 for PSMA-targeted radionuclide therapy of prostate cancer. *Eur J Nucl Med Mol Imaging.* 2019;46:1919–1930.
2. Baum RP, Singh A, Kulkarni HR, et al. First-in-humans application of $^{161}$Tb: a feasibility study using $^{161}$Tb-DOTATOC. *J Nucl Med.* 2021;62:1391–1397.

## Radiopharmaceutical Extravasations Can Have Consequences

**TO THE EDITOR:** Regarding "Adverse Clinical Events at the Injection Site Are Exceedingly Rare After Reported Radiopharmaceutical Extravasation in Patients Undergoing $^{99m}$Tc-MDP Whole-Body Bone Scintigraphy: A 12-Year Experience" (*1*), I read this article with some interest from a purely scientific perspective. I am concerned that the results reported might be used to justify certain courses of action, or inaction, without the evidence to support these approaches. I have several misgivings about this article.

First, the numbers that have been reported for inclusion in this study are likely to be significantly underestimated. Of the approximately 32,000 scans that the authors examined, they found 118 cases of documented extravasation in the clinical reports, of which only 96 could be followed up. The authors cite other audits of bone scan administrations that quote extravasation rates of around 15%–20% in routine clinical practice. On the basis of the 15%–20% rate, the number of extravasations should have been more like 4,750–6,300 cases in the 12-y cohort. A rate of 15%–20% seems, from my experience, to be not unexpected for some degree of extravasation at the injection site. As the authors have included only patients for whom an extravasation had been noted in the clinical report—a notation that is rarely made—they acknowledge that this could lead to an underestimation of the incidence of extravasation. Indeed, the authors state that "this approach has the *possibility* [my emphasis] of missing studies in which [a radiopharmaceutical extravasation] occurred but was not documented in the report." The lack of documentation by the reporting physicians may be because the technologist or nurse injecting the patient did not recognize the extravasation at the time of injection (often due to the low injected volumes used) and, hence, the extravasation was detected only when the scan was acquired some hours later. This is a serious underestimate and tends to undermine the authors' conclusions.

Second, the authors have little clinical or other follow-up information on extravasations that were not documented (assuming the true incidence of around 5,000–6,000 is correct) and seem to assume that if they did not hear anything from the patient then there was no problem. I propose that it is likely most extravasations will not lead to any significant unintended acute or chronic tissue damage but that just because one does not follow up about extravasation does not mean one has evidence of no extravasation issues. The authors may suggest that, on the basis of my estimates, in a cohort of 5,000–6,000 individuals the authors would likely learn of an adverse event even if there is only the slightest possibility of it. However, in complex, fragmented health-care systems, the feedback between primary-care and secondary or tertiary service providers is often tenuous at best, and many primary-care practitioners may not make a connection between the bone scan performed 1 mo previously and the ongoing issue at the patient's injection site.

Third, whereas the impact of quantification on clinical interpretation is mentioned in the introduction, little emphasis is given to the fact that any quantitative procedure, such as measuring an $SUV_{max}$ in a PET scan or a bone scan, or even a glomerular filtration rate estimation based on blood sampling, is invalidated when the entire dose is not delivered into the bloodstream for full mixing and redistribution throughout the body. This is a concern for any nuclear medicine procedure but takes on greater importance in serial studies when monitoring changes in organ function or tumor response.

Finally, as the interest in the use of $\alpha$-particles for therapy increases, the spectre of issues that arise from an extravasated $\alpha$-emitting therapeutic radiopharmaceutical injection becomes a consideration. There has already been at least one case report of a skin lesion (squamous cell carcinoma) attributed to an extravasated injection of $^{223}$Ra (*2*). Although molecules and small vectors such as peptides may be able to readily drain from a site of extravasation via the lymphatics, larger biologic agents such as antibodies would be particularly concerning.

Although the authors have presented their data with full disclosure about the methodology used, they would appear to have underestimated the limitations of their approach. Readers could be misled were this article to be quoted as a "definitive reference based on large numbers," suggesting that extravasations in nuclear medicine procedures are without consequence. It is clear that they are not.

### REFERENCES

1. Parihar AS, Schmidt LR, Crandall J, Dehdashti F, Wahl RL. Adverse clinical events at the injection site are exceedingly rare after reported radiopharmaceutical extravasation in patients undergoing $^{99m}$Tc-MDP whole-body bone scintigraphy: a 12-year experience. *J Nucl Med.* 2023;64:485–490.
2. Benjegerdes KE, Brown SC, Housewright CD. Focal cutaneous squamous cell carcinoma following radium-223 extravasation. *Proc Bayl Univ Med Cent.* 2017;30:78–79.

**Dale L. Bailey**
*Royal North Shore Hospital*
*Sydney, Australia*
*E-mail: dale.bailey@sydney.edu.au*

Published online Jun. 29, 2023.
DOI: 10.2967/jnumed.123.265717

**REPLY:** We would like to thank the author for his interest in our work and for this opportunity to address his queries. The author raises several concerns about our large retrospective study.

We had described a limitation of our methodology that involved reviewing the clinical reports for reported radiopharmaceutical extravasation (RPE) instead of reviewing the scintigraphy images (*1*). Reviewing the scintigraphy images of around 32,000 studies would surely have been a more accurate but certainly a much less feasible exercise in a finite period. Further, the primary objective of this study was not to detect the rate of RPE of any magnitude but to evaluate the clinical adverse events, if any, associated with the RPE events. We agree that although the actual RPE rate (of any extent) might likely be higher than the clinically reported RPE rates, it is also expected that major RPEs are the most likely to be documented in the report, compared with minimal RPEs. Our results showing no long-term adverse events in patients with reported RPE (likely to represent major RPEs) therefore validate our conclusion. In the absence of clinical adverse events with the documented RPEs, it is highly

implausible that the undocumented RPEs (likely of minor extent) would lead to a significant number of clinical adverse events that could change our estimates. Despite the perceived and existent limitations with the health-care systems, clinical follow-up was available for over 80% patients, with the studies performed over approximately 12 y. In addition, comprehensive review of the clinical charts of these patients (including clinical encounters from our medical center and other centers) ensured that we would very likely detect symptoms or signs at the local RPE site, irrespective of whether they were attributed to the RPE event. Our conclusion that clinical adverse events are rare with reported RPEs is therefore firmly supported by our research methodology and the results. We agree that it might be of interest to review all of the approximately 32,000 scintigraphy images directly, and we suggest that an international experience would provide a greater breadth of understanding.

We have endorsed and advocate for improving quantification in nuclear medicine studies. Accurate delivery of radiopharmaceutical activity is important for obtaining reproducible and precise estimates of quantitative parameters such as SUV (*2,3*). We also acknowledged the potential impact of extravasations on quantification and clinical interpretation of studies in our article. However, quantitative evaluation is not routinely performed and is not required for clinical interpretation of planar bone scintigraphy studies, the study population we assessed. Planar bone scintigraphy studies are generally interpreted with qualitative assessment, hence the rationale for incorporating the requirement of a repeat scan as a surrogate metric for scan quality. The focus of the current study, as mentioned earlier, was on adverse clinical events at the injection site rather than the impact on quantification, which can be addressed in future investigations. Additionally, whereas delivery of the entire radiopharmaceutical activity into the appropriate compartment is surely desired, labeling quantitative results as invalid with less than 100% activity delivery is certainly an overstatement (e.g., a 0.1% extravasation would not meaningfully change quantitation).

Lastly, the consideration of extravasations of therapeutic radiopharmaceuticals is a valid concern for future research. Although this was not an objective of the current study, the need to exercise caution while administering therapeutic radiopharmaceuticals is well recognized in view of their high-energy emissions. However, the author cites a case report attributing extravasation of $^{223}$Ra to the development of cutaneous squamous cell carcinoma a few months later (*4*). All the methodologic limitations of a descriptive single-case report set aside, this report has several additional complexities that make the conclusion of local-radiation–induced carcinogenesis debatable. We would like to highlight some of the major concerns here. The development of a radiation-induced solid tumor at 4 mo after radiation exposure is highly unusual. Several prior studies have reported that solid tumors typically occur 10–15 y after exposure to high-dose ionizing radiation (*5–7*). It is thus improbable that the extravasation of $^{223}$Ra led to exceptionally rapid mutagenesis in the absence of any local tissue damage, with the latter widely recognized as an acute effect of ionizing radiation (*8*). The likely explanation for these discrepancies in the case report, as well as the absence of other literature documenting similar results, is the possibility of confusing correlation with causation. A brief review of the Bradford Hill criteria for causation clearly shows that the report describes an unfortunate possible correlation and not necessarily causation (*9*). A very interesting read that emphatically represents this issue is the correlation of annual chocolate consumption with the number of Nobel laureates produced (*10*). We, however, share the concern that RPE with radiopharmaceutical therapies must be avoided. The author also raises the issue of RPE with antibodies. Although any RPE should certainly be avoided, the clearance of radiolabeled antibodies (whole antibodies and fragments) from the interstitial compartment is relatively rapid (*11*).

In conclusion, whereas we appreciate the queries raised by the author and his interest in our study, we firmly stand by the findings of our study and believe that our concluding remarks are data-driven and well supported by an appropriate research methodology. We also recognize the potential of future studies with larger patient populations to assess for potential clinical risks of RPE. The sample size of these studies would likely need to be large because the risk of clinical adverse events after radiopharmaceutical injections for diagnostic bone scans appears to be vanishingly low.

## REFERENCES


1. Parihar AS, Schmidt LR, Crandall J, Dehdashti F, Wahl RL. Adverse clinical events at the injection site are exceedingly rare after reported radiopharmaceutical extravasation in patients undergoing $^{99m}$Tc-MDP whole-body bone scintigraphy: a 12-year experience. *J Nucl Med.* 2023;64:485–490.
2. Parihar AS, Dehdashti F, Wahl RL. FDG PET/CT-based response assessment in malignancies. *Radiographics.* 2023;43:e220122.
3. Wahl RL, Jacene H, Kasamon Y, Lodge MA. From RECIST to PERCIST: evolving considerations for PET response criteria in solid tumors. *J Nucl Med.* 2009;50(suppl 1):122S–150S.
4. Benjegerdes KE, Brown SC, Housewright CD. Focal cutaneous squamous cell carcinoma following radium-223 extravasation. *Proc Bayl Univ Med Cent.* 2017;30:78–79.
5. Berrington de Gonzalez A, Gilbert E, Curtis R, et al. Second solid cancers after radiation therapy: a systematic review of the epidemiologic studies of the radiation dose-response relationship. *Int J Radiat Oncol Biol Phys.* 2013;86:224–233.
6. Little MP. Comparison of the risks of cancer incidence and mortality following radiation therapy for benign and malignant disease with the cancer risks observed in the Japanese A-bomb survivors. *Int J Radiat Biol.* 2001;77:431–464.
7. Hodgson DC, Gilbert ES, Dores GM, et al. Long-term solid cancer risk among 5-year survivors of Hodgkin's lymphoma. *J Clin Oncol.* 2007;25:1489–1497.
8. Stone HB, Coleman CN, Anscher MS, McBride WH. Effects of radiation on normal tissue: consequences and mechanisms. *Lancet Oncol.* 2003;4:529–536.
9. Hill AB. The environment and disease: association or causation? *Proc R Soc Med.* 1965;58:295–300.
10. Messerli FH. Chocolate consumption, cognitive function, and Nobel laureates. *N Engl J Med.* 2012;367:1562–1564.
11. Wahl RL, Geatti O, Liebert M, Wilson B, Shreve P, Beers BA. Kinetics of interstitially administered monoclonal antibodies for purposes of lymphoscintigraphy. *J Nucl Med.* 1987;28:1736–1744.



**Ashwin Singh Parihar**
**Lisa Raymond-Schmidt**
**John P. Crandall**
**Farrokh Dehdashti**
**Richard L. Wahl***
**Washington University School of Medicine*
*St. Louis, Missouri*
*E-mail: rwahl@wustl.edu*



Published online Jun. 29, 2023.
DOI: 10.2967/jnumed.123.265920

## PSMA Is Not Specific to Prostate Cancer

**TO THE EDITOR:** Since the large-scale deployment of coronavirus disease 2019 vaccination, several publications have mentioned many false-positive findings on PET examinations, mainly with $^{18}$F-FDG but also with other radiopharmaceuticals (*1*). For instance, Notohamiprodjo et al. recently reported that the prevalence of vaccine-associated lymphadenopathy (VAL) on $^{18}$F-rhPSMA-7.3 PET/CT was high, at 45% (*2*), but some points of the study deserve comment.

First, the authors stated that "increased ipsilateral axillary uptake of [prostate-specific membrane antigen (PSMA)] ligand is common" but omitted to mention some contradictory results in the literature. In fact, we prospectively constituted a cohort in which 120 and 79 patients underwent $^{18}$F-fluorocholine or $^{68}$Ga-PSMA-11 PET/CT, respectively, and we reported a 42.5% incidence of VAL for $^{18}$F-fluorocholine PET/CT (which was comparable to the findings with $^{18}$F-FDG) but only a 12% incidence for $^{68}$Ga-PSMA-11 PET/CT (*3*). This difference cannot be due entirely to variable definitions of VAL between studies but may be explained by differences in the studied populations or in the radiopharmaceutical itself (*4*).

Second, the authors did not provide a documented hypothesis explaining the false-positive cases. A possible explanation comes from PSMA uptake in the context of neoangiogenesis (*5*). We hypothesized that coronavirus disease 2019 vaccination could induce production of vascular cell adhesion molecules and vascular endothelial growth factor, as observed during severe acute respiratory syndrome coronavirus 2 infection (*6*), leading to neovasculature and therefore PSMA uptake.

Third, as mentioned by the authors, "separate analysis among those vaccines was not performed." Nevertheless, differences between vaccines could be expected since a metaanalysis found VAL more frequently after the Moderna vaccine than after the Pfizer-BioNTech vaccine (*7*), whereas a comparative study reported higher metabolic activity in the lymph nodes after Pfizer-BioNTech than after AstraZeneca (*8*).

Last, the authors do not suggest a clear management plan for these lymph nodes in clinical practice. Should they be closely monitored for development or regression by physical examination or by imaging? Should they be systematically analyzed by a pathologist? Some researchers are exploring ways to address this issue. For instance, radiomics could help differentiate VAL from malignant lymphadenopathies (*9*). Besides, innovative radiopharmaceuticals are under development and capable of overcoming postvaccination pitfalls, such as use of the $^{68}$Ga-fibroblast-activation protein inhibitor, which showed no fixation in postvaccination axillary nodes, to replace $^{18}$F-FDG (*10*).

In conclusion, the study provides valuable information about false-positive cases on PET imaging due to vaccination—a recurrent issue that needs to be addressed, even if some results can be challenged by other existing findings, notably in our work published previously. However, this study has the merit of reminding the imaging interpreter and the prescriber that PSMA ligand is not specific to prostate cancer and not even to the prostatic gland.


### ACKNOWLEDGMENTS

We would like to thank the French National Agency for Research (Investissements d'Avenir), LabexIRON no. ANR-11-LABX-0018-01 and EquipexArronaxPlus no. ANR-11-EQPX-0004, for their support.


### REFERENCES


1. Minamimoto R. Oncology and cardiology positron emission tomography/computed tomography faced with COVID-19: a review of available literature data. *Front Med (Lausanne).* 2022;9:1052921.
2. Notohamiprodjo S, Eiber M, Lohrmann C, Weber WA. Temporary reactive response of axillary lymph nodes to COVID-19 vaccination on $^{18}$F-rhPSMA-7.3 PET/CT in patients with prostate cancer. *J Nucl Med.* 2022;63:1673–1676.
3. Ah-Thiane L, Ferrer L, Maucherat B, et al. Vaccine-related lymph nodes: the emerging pitfalls of $^{18}$F-fluorocholine and $^{68}$Ga-PSMA-11 PET/CT in the era of COVID-19 vaccination. *Clin Nucl Med.* 2022;47:575–582.
4. Piron S, Verhoeven J, Vanhove C, De Vos F. Recent advancements in $^{18}$F-labeled PSMA targeting PET radiopharmaceuticals. *Nucl Med Biol.* 2022;106-107:29–51.
5. Chang SS, O'Keefe DS, Bacich DJ, Reuter VE, Heston WD, Gaudin PB. Prostate-specific membrane antigen is produced in tumor-associated neovasculature. *Clin Cancer Res.* 1999;5:2674–2681.
6. Amraei R, Rahimi N. COVID-19, renin-angiotensin system and endothelial dysfunction. *Cells.* 2020;9:1652.
7. Treglia G, Cuzzocrea M, Giovanella L, Elzi L, Muoio B. Prevalence and significance of hypermetabolic lymph nodes detected by 2-[$^{18}$F]FDG PET/CT after COVID-19 vaccination: a systematic review and a meta-analysis. *Pharmaceuticals (Basel).* 2021;14:762.
8. Ayati N, Evans S, Zakavi SR, Gruenewald SM. Comparison between viral vector and mRNA based COVID-19 vaccination in prevalence and severity of regional immune reactions, and $^{18}$F-FDG PET/CT features. *Asia Ocean J Nucl Med Biol.* 2023;11:4–12.
9. Eifer M, Pinian H, Klang E, et al. FDG PET/CT radiomics as a tool to differentiate between reactive axillary lymphadenopathy following COVID-19 vaccination and metastatic breast cancer axillary lymphadenopathy: a pilot study. *Eur Radiol.* 2022; 32:5921–5929.
10. Demmert TT, Maric I, Pomykala KL, et al. Novel $^{68}$Ga-FAPI PET/CT offers oncologic staging without COVID-19 vaccine-related pitfalls. *J Nucl Med.* 2023;64: 368–371.



**Loic Ah-Thiane***
**Ludovic Ferrer**
**Caroline Rousseau**
**ICO René Gauducheau*
*St-Herblain, France*
*E-mail: loic.ah-thiane@ico.unicancer.fr*



Published online Jun. 22, 2023.
DOI: 10.2967/jnumed.123.265720


**REPLY:** We are grateful for the commentary on our paper (*1*) by Ah-Thiane et al. and appreciate the reference to their publication on prostate-specific membrane antigen (PSMA) radioligand uptake by axillary lymph nodes after vaccination. We submitted the final version of our manuscript to *The Journal of Nuclear Medicine* on February 17, 2022, and their study was published in July 2022 (*2*). Therefore, we were unfortunately unable to discuss the study by Ah-Thiane et al.

It is interesting that Ah-Thiane et al. reported a substantially lower incidence of PSMA-positive axillary lymph nodes with $^{68}$Ga-PSMA-11 (12%) than we found for $^{18}$F-rhPSMA 7.3 (45%). This large difference may indeed point to differences in the studied population or of the radiopharmaceutical itself, but confirmation will require future studies.

We also thank Ah-Thiane et al. for pointing out that PSMA expression during angiogenesis may contribute to PSMA expression after vaccination. We had discussed that PSMA expression is not specific to the prostate and that PSMA RNA is found in many tissues, including lymph nodes (*3,4*). At the moment, there are, to our knowledge, no data to allow for definitive statements on what precisely causes PSMA radioligand uptake after vaccination.

It is well conceivable that different vaccines or vaccine dosages cause different degrees of PSMA radioligand uptake. Unfortunately, information on the vaccine type was not available for all patients in this retrospective study. However, we assume that most patients received the Pfizer-BioNTech vaccine, which was the most commonly used coronavirus disease 2019 vaccine in Germany.

With respect to the clinical consequences of PSMA radioligand uptake in axillary lymph nodes, it is important to remember that the axilla is an uncommon site of metastatic disease in prostate cancer patients. Axillary lymph nodes may be involved in advanced stages of prostate cancer, but in this setting, the presence or absence of metastases in the axilla will only rarely affect therapeutic decisions. In such cases, we believe that histologic confirmation will be required to differentiate between inflammatory and metastatic nodes because we are not aware of alternative radiotracers that are similar to PSMA ligands in sensitivity for prostate cancer metastases but have a substantially higher specificity. As pointed out by Ah-Thiane et al., the main message of our paper is that PSMA is not specific for prostate cancer and that substantial PSMA radioligand uptake may be observed in activated lymph nodes. We hope that our study stimulates future research in this area, which will be important to understand the strengths and limitations of PSMA PET imaging in the clinic. A particularly intriguing question is perhaps why the specificity of PSMA PET/CT for pelvic lymph node metastases has been extremely high in almost all studies, despite the fact that inflammatory nodes in the axilla can show such high uptake of PSMA radioligands.

## REFERENCES


1. Notohamiprodjo S, Eiber M, Lohrmann C, Weber WA. Temporary reactive response of axillary lymph nodes to COVID-19 vaccination on $^{18}$F-rhPSMA-7.3 PET/CT in patients with prostate cancer. *J Nucl Med.* 2022;63:1673–1676.
2. Ah-Thiane L, Ferrer L, Maucherat B, et al. Vaccine-related lymph nodes: the emerging pitfalls of $^{18}$F-fluorocholine and $^{68}$Ga-PSMA-11 PET/CT in the era of COVID-19 vaccination. *Clin Nucl Med.* 2022;47:575–582.
3. de Galiza Barbosa F, Queiroz MA, Nunes RF, et al. Nonprostatic diseases on PSMA PET imaging: a spectrum of benign and malignant findings. *Cancer Imaging.* 2020;20:23.
4. Kinoshita Y, Kuratsukuri K, Landas S, et al. Expression of prostate-specific membrane antigen in normal and malignant human tissues. *World J Surg.* 2006;30:628–636.



**Susan Notohamiprodjo***
**Matthias Eiber**
**Christian Lohrmann**
**Wolfgang A. Weber**
**Technical University of Munich*
*Munich, Germany*
*E-mail: s.notohamiprodjo@tum.de*



Published online Jun. 22, 2023.
DOI: 10.2967/jnumed.123.265921

# BE PREPARED. GET CERTIFIED.

## 2023 SNMMI Nuclear Medicine Review Course – Live Virtual Meeting

This comprehensive review course is designed to help individuals prepare for their ABNM board certification, as well as providing a refresher for more experience clinicians. The program will be offered in a live virtual environment over two days, covering the following topics:

### Day 1 Program – September 9, 2023

- Neurology
- Thyroid/Parathyroid/Head & Neck
- Pediatrics
- PET/CT
- Pulmonary/Thoracic
- Cardiovascular
- Infection/Inflammation
- Musculoskeletal

### Day 2 Program – September 10, 2023

- Renal
- Gastrointestinal
- Male/Female-Benign/Malignant
- Therapies
- Treatment Response-Criteria/Imaging
- NRC Regulations/Radiation Safety
- Artifacts/Corrections
- Physics/Instrumentation

**Register Today:**
**www.snmmi.org/nmrc**

SNMMI | SOCIETY OF NUCLEAR MEDICINE & MOLECULAR IMAGING

# SEPT 21-23 2023 SNMMI THERAPEUTICS CONFERENCE

MARYLAND
MARRIOTT WATERFRONT BALTIMORE

The **SNMMI Therapeutics Conference** is coming to **Baltimore, Maryland** on **September 21-23**, 2023! This exciting event will bring together leaders in radiopharmaceutical therapy to explore the latest innovations and advancements in the field.

This conference is a must-attend if you want to expand your knowledge and stay up-to-date on the latest developments. With two-and-a-half days of informative sessions and networking opportunities, you'll have the chance to connect with colleagues, enhance your knowledge, learn from experts, and gain invaluable insights.

This year's program will focus on the latest innovations and clinical applications in radiopharmaceutical therapy, including the following topic areas:

- Setting up a Theranostics Clinic
- Radiopharmaceutical Supply Chain
- Thyroid Therapies Lectures & Mock Tumor Board
- Prostate Therapies Lectures & Mock Tumor Board
- GI/Neuroendocrine Therapies Lectures & Mock Tumor Board
- Pediatric Therapies Lectures & Mock Tumor Board
- Radiopharmaceutical Dosimetry
- Updates on Clinical Trials

Remember to register by the **Early-Bird Deadline: August 17, 2023** to lock in the best registration rates!

## VISIT WWW.SNMMI.ORG/TC2023 TO REGISTER

## SPONSORS

▶ **TITLE SPONSOR:**

itm PASSION FOR PRECISION

▶ **GOLD SPONSORS:**

GE HealthCare · NOVARTIS · Telix

▶ **SILVER SPONSOR:**

HERMES MEDICAL SOLUTIONS · POINT BIOPHARMA

▶ **SATELLITE SYMPOSIA SPONSORS:**

GE HealthCare · mim SOFTWARE · Telix

Don't miss out on this incredible opportunity – become a **Therapeutics Conference Sponsor**.
Contact us today and join us in Baltimore for what promises to be an unforgettable event:

▶ Sharon G. Jenkins, EdD: sjenkins@snmmi.org ▶ Catherine Lamb: clamb@snmmi.org

SNMMI


BEDPRC23-0033 05/23